



UNIVERSITAT DE
BARCELONA

New organic semiconductors based on the carbazole core: synthesis and application in optoelectronic devices

Roger Bujaldón Carbó



Aquesta tesi doctoral està subjecta a la llicència **Reconeixement- NoComercial – SenseObraDerivada 4.0. Espanya de Creative Commons.**

Esta tesis doctoral está sujeta a la licencia **Reconocimiento - NoComercial – SinObraDerivada 4.0. España de Creative Commons.**

This doctoral thesis is licensed under the **Creative Commons Attribution-NonCommercial-NoDerivs 4.0. Spain License.**



UNIVERSITAT DE
BARCELONA

Programa de Doctorat de Química Orgànica

**New organic semiconductors based on the carbazole core:
synthesis and application in optoelectronic devices**

Roger Bujaldón Carbó

Supervised by:

Prof. Dolores Velasco Castrillo

Dept. Química Inorgànica i Orgànica

Secció de Química Orgànica

Facultat de Química

Universitat de Barcelona

Als meus pares i a la Gisela

17

AGRAÏMENTS

Abans d'aprofundir en el treball realitzat al llarg de la Tesi doctoral, m'agradaria fer un incís i agrair a tothom que ha participat, d'una manera o altra, a fer-la possible. Sóc conscient que aquestes paraules són molt generals i em semblen insuficients. Tot i així, si hagués expressat tots els agraïments amb paraules i hagués inclòs totes les persones que han estat importants, el contingut de la tesi que ve a continuació hauria quedat reduït a un mer fragment del conjunt de la memòria. Per tant, espero poder-los sintetitzar en aquest apartat.

En primer lloc, voldria donar les gràcies a la Prof. Dolors Velasco per haver-me donat la oportunitat de realitzar la tesi doctoral sota la seva direcció. Sense el seu suport, no hauria estat possible aquesta etapa. Per tant, bona part de les experiències i aprenentatge que he adquirit al llarg d'aquests anys, es deuen al fet que en un inici va confiar en mi. Gràcies per haver-me guiat en els moments adequats i deixar-me autonomia en d'altres per poder desenvolupar les competències que crec que són importants en la recerca.

També vull destacar el suport i l'ajuda inestimable que m'ha brindat el Dr. Jaume Garcia en tot moment. Com que no hi ha prou paraules per agrair-li, espero que pugui apreciar tot el reconeixement que hi ha condensat en aquest minúscul "gràcies".

També voldria agrair especialment al Prof. Joaquim Puigdollers l'oportunitat de realitzar part de la recerca a les instal·lacions del departament d'Enginyeria Electrònica de la Universitat Politècnica de Catalunya, on sempre m'hi ha fet sentir com a casa. M'agradaria posar èmfasi en la disposició que ha tingut i té en tot moment d'ajudar-me, aconsellar-me i resoldre qualsevol dubte o problema.

Així mateix, voldria donar les gràcies a la Dra. Eugenia Martínez per la confiança i la possibilitat d'incorporar-me a la Unitat de *Printed Electronics & Embedded Devices* del Centre Tecnològic de Catalunya Eurecat per poder aprofundir en el camp de la tecnologia OLED. També voldria agrair l'ajut, la disposició i el suport en primer lloc del Dr. Nikola Peřinka i posteriorment de la Dra. Laura López.

Voldria agrair també als membres de la Unitat de Raigs-X dels CCiTUB l'assessorament i la disposició que m'han ofert sempre. M'agradaria recalcar la paciència, la voluntat i l'atenció que sempre m'han mostrat en totes les explicacions, mesures i consells. Especialment a la Dra. Mercè Font, a la Dra. Cristina Puigjaner, al Dr. Xavier Alcobé i al Dr. Josep Maria Bassas.

A la Dra. Elvira Gómez i la Dra. Elisa Vallés per obrir-nos les portes del seu laboratori i pel seu assessorament en les mesures electroquímiques.

Evidentment, també m'agradaria agrair de forma especial a la resta de companys amb qui he compartit el dia a dia al grup de Materials Orgànics per fer que aquesta etapa sigui inoblidable: a l'Alba i la Marta, que sempre han tingut la paciència d'orientar-me i d'aconsellar-me amb l'experiència d'haver viscut aquest procés abans que jo; a la Clara, que sempre està disposada a ajudar i a escoltar, i a qui desitjo tota la sort del món en la seva pròpia tesi; al Raoul, que sempre m'ha donat els consells adequats; al Raül (espero que gràcies a ell aquesta memòria no sigui tan grisa, tot i que segur que encara l'hi troba), a la Mireia i a l'Ernesto per les *Raids* i estones compartides; i al Guillem, pels records i les converses de quan vam començar. Hi ha molts noms més que m'agradaria afegir de la gent que he anat coneixent al llarg d'aquests anys i que espero que quedin implícits, ja que tots i cada un han contribuït d'alguna manera a enriquir aquesta experiència.

També vull fer menció a les amistats amb qui he compartit tants moments des de l'inici de la carrera fins ara, en especial la Mariona, la Bea i la Marta. I també a la Rosanna, ja que tot i que no pertanyi a l'àmbit químic, sé que sempre hi he pogut comptar i compartir els problemes i els èxits de la tesi.

I deixo el que segurament és l'agraïment més important pel final: a la meva família. Especialment als meus pares, que sempre m'han fet costat i m'han ajudat en tot el que han pogut. M'han aportat la confiança necessària per seguir endavant i han viscut la tesi com a pròpia, en tots els aspectes. I a la meva germana Gisela, amb qui sempre he pogut compartir experiències, anècdotes i idees relacionades amb la tesi. Tant, que a vegades sembla que hagi estat una més del grup de recerca. I evidentment, moltes gràcies per fer brillar la tesi amb els teus acabats artístics que han millorat molt els meus dissenys originals. I no em vull deixar la Lluna, per ser-hi en tot moment. La veritat és que, inevitablement, la tesi també porta els vostres noms.

ABBREVIATIONS AND SYMBOLS

ACN	Acetonitrile
ACQ	Aggregation-Caused Quenching
AIE	Aggregation-Induced Emission
BTBT	[1]Benzothieno[3,2- <i>b</i>][1]benzothiophene
CB	Chlorobenzene
CE	Current Efficiency
CH	Cyclohexane
CHO	Cyclohexanone
CIE	<i>Commission Internationale de l'Eclairage</i>
CV	Cyclic Voltammetry
D	Drain electrode
<i>d</i>	Thickness
DCM	Dichloromethane
<i>d</i> _{hkl}	Interplanar spacing
DMF	<i>N,N</i> -dimethylformamide
DMSO	Dimethylsulfoxide
DNTT	Dinaphtho[2,3- <i>b</i> :2',3'- <i>f</i>]thieno[3,2- <i>b</i>]thiophene
DSC	Differential Scanning Calorimetry
E_{ox}^0	Oxidation standard potential
E_{red}^0	Reduction standard potential
EA	Electron Affinity
E_{gap}	HOMO/LUMO energy gap
EL	Electroluminescence
E_{onset}	Onset potential
EQE	External Quantum Efficiency
ESI	Electrospray ionization
ETL	Electron-Transporting Layer
Fc	Ferrocene
G	Gate electrode
GIXRD	Grazing Incidence X-Ray Diffraction

HOMO	Highest Occupied Molecular Orbital
HPLC	High-Performance Liquid Chromatography
HRMS	High Resolution Mass Spectrometry
HTL	Hole-Transporting Layer
I_D	Drain-source current
IP	Ionization Potential
$\text{Ir}(\text{MDQ})_2\text{acac}$	Bis(2-methyldibenzo[<i>f,h</i>]quinoxaline)(acetylacetonate) iridium (III)
$\text{Ir}(\text{ppy})_3$	Tris(2-phenylpyridine)iridium (III)
ITO	Indium Tin Oxide
J	Coupling constant
JohnPhos	(2-Biphenyl)di- <i>tert</i> -butylphosphine
L	Length
L	Luminance
LE	Locally Excited
LUMO	Lowest Unoccupied Molecular Orbital
MS	Mass Spectrometry
NBS	<i>N</i> -bromosuccinimide
NMR	Nuclear Magnetic Resonance
NRD	Non-Radiative Decay
OLED	Organic Light-Emitting Diode
ORTEP	Oak Ridge Thermal Ellipsoid Plot
OTFT	Organic Thin-Film Transistor
OTS	Octadecyltrichlorosilane
PEDOT:PSS	Poly(3,4-ethylenedioxythiophene)-poly(styrenesulfonate)
POPOP	1,4-Bis(5-phenyl-2-oxazolyl)benzene
ppm	Parts per million
PS	Polystyrene
PXRD	Powder X-Ray Diffraction
rpm	Revolutions per minute
RT	Room temperature
S	Source electrode
S_0	Singlet ground state
S_1	Singlet first excited state
SAM	Self-Assembled Monolayer

T_1	Triplet first excited state
TADF	Thermally Activated Delayed Fluorescence
TBAP	Tetrabutylammonium hexafluorophosphate
T_c	Crystallization temperature
T_d	Decomposition temperature
T_g	Glass transition temperature
TGA	Thermogravimetric analysis
THF	Tetrahydrofuran
TICT	Twisted Intramolecular Charge Transfer
TIPS	Triisopropylsilyl
T_m	Melting point
TOF	Time of Flight
TPBi	2,2',2''-(1,3,5-Benzinetriyl)-tris(1-phenyl-1- <i>H</i> -benzimidazole)
t_r	Retention time
THT	<i>N</i> -trihexyl triindole
UV	Ultraviolet
V_{DS}	Drain-source voltage
V_G	Gate voltage
V_{on}	Turn-on voltage
V_{th}	Threshold voltage
W	Width
XRD	X-Ray Diffraction
δ	Chemical shift
θ	Incident angle
λ	Wavelength
$\lambda_{abs,max}$	Wavelength of maximum absorption
$\lambda_{em,max}$	Wavelength of maximum emission
λ_{exc}	Excitation wavelength
μ	Charge carrier mobility
μ_e	Electron mobility
μ_h	Hole mobility
Φ_f	Fluorescence quantum yield

CONTENTS

INTRODUCTION.....	1
OBJECTIVES	11
GENERAL PART.....	15
PART 1. Characterization of organic materials.....	17
1.1. Optical properties.....	17
1.2. Electrochemical properties.....	21
1.3. Thermal properties.....	23
PART 2. Organic thin-film transistors (OTFTs).....	24
2.1. Geometry.....	25
2.2. Operation and characterization of the devices.....	26
PART 3. Organic light-emitting diodes (OLEDs).....	30
3.1. Structure, fabrication and operation.....	30
3.2. Characterization of the devices.....	33
PART 4. Solid-state characterization techniques.....	37
4.1. Crystal structure.....	38
4.2. Characterization of a thin film.....	42
RESULTS AND DISCUSSION	45
CHAPTER 1. Extending the carbazole heterocycle (I): the diindolocarbazole core.....	47
1.1. Introduction.....	49
1.2. Synthesis of the diindolocarbazole core.....	50
1.2.1. Synthesis through the Cadogan reaction: C-N coupling.....	51
1.2.2. Synthesis through the oxidative cyclisation: C-C coupling.....	55
1.3. Characterization of the organic materials.....	59
1.3.1. Aniline-containing intermediates.....	59
1.3.2. Diindolocarbazole derivatives.....	61
1.4. Organic thin-film transistors.....	64
1.5. Molecular order and disposition in the thin-films.....	67

1.5.1. Crystallographic study	67
1.5.2. GIXRD measurements.....	70
1.6. Conclusions	72
CHAPTER 2. Extending the carbazole heterocycle (II): the bisbenzothienocarbazole core	75
2.1. Introduction	77
2.2. Sulfurated carbazole precursors.....	78
2.2.1. Synthesis	79
2.2.2. Synthetic study towards the sulfonylated analogs	81
2.2.3. Crystal structure	83
2.2.4. Optical properties.....	84
2.3. Bisbenzothienocarbazole derivatives.....	87
2.3.1. Synthesis	87
2.3.2. Characterization of the organic semiconductors	88
2.3.3. Organic Thin-Film Transistors	90
2.3.4. Crystal structures.....	93
2.3.5. Molecular order in the thin films.....	95
2.4. Conclusions	96
CHAPTER 3. Extending the carbazole heterocycle (III): the diphenanthrocarbazole core	99
3.1. Introduction	101
3.2. Synthesis and design.....	102
3.2.1. Synthesis of the unbounded precursors	103
3.2.2. Synthesis of the diphenanthrocarbazole derivatives through the Scholl reaction	105
3.3. Optoelectronic characterization.....	106
3.3.1. Photophysical and thermal properties.....	106
3.3.2. Electrochemical properties.....	108
3.4. Application in final devices and characterization.....	110
3.4.1. Organic Thin-Film Transistors.....	110

3.4.2. Molecular order and morphology	114
3.5. Overview: influence of the studied extensions on 9 <i>H</i> -carbazole.....	116
3.6. Conclusions	119
CHAPTER 4. Beyond 9 <i>H</i> -carbazole: the potential of the dibenzothiophene nucleus	121
4.1. Introduction	123
4.2. Precedents of AIE studies on propeller-shaped materials	124
4.3. Homogeneously substituted compounds.....	125
4.3.1. Synthesis	126
4.3.2. Crystal structures.....	130
4.3.3. Photophysical properties.....	131
4.3.4. Electrochemical properties.....	134
4.4. Heterogeneously substituted compounds	135
4.4.1. Design and synthesis	135
4.4.2. Optoelectronic characterization.....	139
4.4.3. Organic Thin-Film Transistors.....	142
4.5. Conclusions	143
CHAPTER 5. Back to the start: remodeling the triindole core	145
5.1. Introduction	147
5.2. Design and synthesis.....	148
5.2.1. Triindole derivatives	148
5.2.2. Trioxatruxene core	149
5.2.3. Trithiatruxene core	151
5.3. Physical characterization	154
5.3.1. Thermal and photophysical properties	154
5.3.2. Electrochemical properties.....	156
5.4. Conclusions	157
CHAPTER 6. Shedding light on the performance of the 3-(phenylethynyl)- 9 <i>H</i> -carbazole unit in OLED devices	159
6.1. Introduction	161

6.2. Design and synthesis.....	162
6.2.1. 6,6'-bis(phenylethynyl)-9 <i>H</i> ,9' <i>H</i> -3,3'-bicarbazole derivatives.....	163
6.2.2. 1,3,5-tris((9 <i>H</i> -carbazol-3-yl)ethynyl)benzene derivatives.....	164
6.3. Characterization of the fluorophores.....	165
6.3.1. Thermal and photophysical properties.....	165
6.3.2. Single crystals.....	167
6.3.3. Electrochemical properties.....	168
6.4. Organic Light-Emitting Diodes.....	169
6.4.1. Non-doped devices.....	170
6.4.2. Iridium-containing devices.....	172
6.5. Conclusions.....	176
CONCLUSIONS.....	179
REFERENCES.....	183
EXPERIMENTAL PART.....	203
1. Materials, solvents and reagents.....	205
2. Instrumentation and methods.....	205
2.1. Characterization of organic compounds.....	205
2.2. Fabrication and characterization of OTFTs.....	207
2.3. Fabrication and characterization of OLEDs.....	208
2.4. X-ray diffraction measurements.....	209
3. Synthetic procedures and characterization data.....	210
APPENDIX.....	259
LIST OF PUBLICATIONS.....	261
SUMMARY.....	263
SUPPLEMENTARY INFORMATION.....	265

INTRODUCTION



INTRODUCTION

Electronic devices have settled so inherently in all aspects of our daily lives that it is challenging to conceive the current world without them. Semiconductors, being essential components of modern electronics, have therefore become indispensable materials. The definition of semiconductor relies on its electrical conductivity, which is situated between that of an insulator and a conductor and can be typically triggered and altered by external factors. Elemental semiconductors such as silicon and germanium or compound ones that combine two or more elements (e.g. GaAs or AlGaInP) are well-established within this industry.^[1-2]

On the contrary, organic materials had been only regarded as insulators in the early development of the electronic field. In fact, the advent of organic semiconductors goes back to the late 1940s with the study of phthalocyanine derivatives.^[3] In the 1950s, the discovery that polycyclic aromatic compounds in combination with molecular halogens could form semiconducting charge-transfer complex salts paved the way to subsequent advances.^[4] However, the upsurge of organic electronics started in 1977, when Heeger, MacDiarmid and Shirakawa pioneered in the discovery and development of conductive polymers.^[5] For this work, they were awarded with the Nobel Prize in Chemistry in 2000.^[6-7] Thereafter, the interest in organic semiconductors has increased considerably, inciting the research of novel materials by both academia and industry. Despite the extended predominance of traditional inorganic semiconductors, organic compounds have finally achieved to keep pace and establish in the market as a realistic alternative.

Indeed, organic compounds offer interesting and unique characteristics required in next-generation electronic products, which set them apart from their inorganic competitors. Their potential in the manufacturing of large-area and flexible devices or the lower cost attached to the production process are just a few of the advantages.^[8-11] Not only that, but their optical and electronic properties can be easily adapted from a structural point of view. The accessible variety of both small molecules and polymeric materials also offer additional characteristics to exploit. Thus, it is not surprising that the development of organic semiconductors featuring effective charge transport capabilities has spread to many applications like Organic Thin-Film Transistors (OTFTs)^[12-13], Organic Light-Emitting Diodes (OLEDs)^[14-15] and Organic Photovoltaic Cells (OPCs).^[16-17]

The semiconductor behavior in organic compounds is closely related to the molecular design, which is typically constructed from π -conjugated systems. Such architecture

facilitates the required overlap between π orbitals, promoting the delocalization of the corresponding electrons throughout the molecule.^[18-21] This feature is essential to fulfill the different processes involved within the active layers of organic-based devices, namely the introduction of charge carriers into the system, their transport and their eventual collection. In the case of inorganic materials, charge transport can be analyzed by means of the band model, which involves the valence and the conduction bands. Nevertheless, this approach is not applicable in organic compounds because of the weaker intermolecular interactions. Alternatively, the hopping model was proposed to describe the charge transport in more disordered or disjointed systems like those found in organics.^[22-23] This model considers that all relevant states are localized so the charge carriers “jump” between individual molecules to form the corresponding radical specie. It should be pointed out that, depending on the nature of the charge carriers, both inorganic and organic semiconductors can be classified as hole-transporting (p-type) or electron-transporting (n-type) materials. The feasibility to carry holes or electrons is conditioned by the electronic profile of the material.^[18] According to the hopping model, electrons are successively relocated from a neutral system to a cation radical through the highest occupied molecular orbital (HOMO) in the case of p-type semiconductors, whereas this process takes place from an anion radical to a neutral system through the lowest unoccupied molecular orbital (LUMO) in n-type ones. A schematic representation of such process is illustrated in Figure 1. In order to accomplish so, the disposition of the molecular units in the solid state should grant an effective overlap between neighboring π -systems. Consequently, the design of an organic semiconductor has to address not only the molecular but also the supramolecular level.

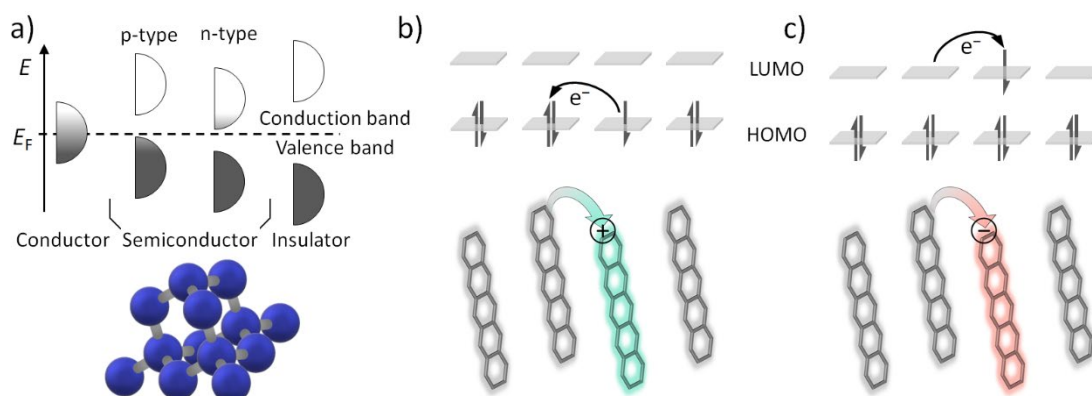


Figure 1. Schematic diagram showing the charge transport characteristics in: a) inorganic materials, showing the profiles of the conduction and valence bands (E_F indicates the Fermi level) and the structure of crystalline silicon; b) p-type organic semiconductors and c) n-type organic semiconductors through the hopping model.

The structural features of the π -conjugated backbone govern the intrinsic electronic and optoelectronic characteristics in organic semiconductors. The nature of the core also contributes to determining the intermolecular arrangement in the solid state, and thus it should be carefully chosen. Nevertheless, all these features can be synthetically tailored with the addition of electron-donating or electron-withdrawing moieties. It is especially notorious the case of the alkyl chains, which enhance the solubility of the material as well as modulating the intermolecular interactions and disposition in the solid state.^[24–28] Consequently, the molecular design of the semiconductor along with the device architecture and its processing are key aspects to analyze. The specific requirements of an organic semiconductor also depend on the final application. As abovementioned, the scope of applications encompasses several fields. Nevertheless, this thesis is mainly focused on the study of materials with potential use as active layers in OTFT and OLED devices, which are introduced herein and further described in the general part.

- **Organic Thin-Film Transistors**

Transistors, being one of the basic building blocks of modern electronics, are devices designed to amplify or switch electric signals. Specifically, they are able to control the current through the semiconductor by means of a voltage input that acts as an external trigger. The importance of this research becomes self-explanatory by the fact that it has yielded the Nobel Prize in Physics on two occasions: for “the research on semiconductors and the discovery of the transistor effect” in 1956^[29] and for “the invention of the integrated circuit” and “the development of semiconductor heterostructures used in high-speed- and opto-electronics” in 2000^[30].

In organics, the first OTFT device was reported in 1986 by Tsumura, Kozuka and Ando employing an electrochemically-prepared polythiophene thin-film as the semiconducting layer.^[31–32] After that, the extensive investigation on OTFTs has derived into a tremendous evolution of their performance, which implies a high charge-carrier mobility (μ), a low-operating voltage with a large on/off current ratio and air stability. Even though these parameters are still globally outpaced by inorganics, it is important to note that the aim of organics is not substituting them in high-performing applications, but open the door to new conceptual products. OTFTs are key components in organic electronics and therefore find their niche in, for instance, flexible and light-weight displays.^[9,33–35] From a research point of view, they are also typically utilized as a method to characterize the semiconductor properties of an organic material.^[36]

As abovementioned, organic semiconductors aimed to OTFT applications require several must-have characteristics that are mainly conferred through the structural design. In

general, π -conjugated systems with adequate energy levels that can grant a steady π - π stacking throughout the semiconductor layer are prone to providing a fast and efficient transport of charge carriers, i.e. high μ . Currently, there are some examples of OTFTs with charge carrier mobilities that have surpassed the milestone of $10 \text{ cm}^2 \text{ V}^{-1} \text{ s}^{-1}$, overcoming the results provided by amorphous silicon.^[33,37] Figure 2 collects some of the top organic molecules in terms of hole- and electron-transporting characteristics in OTFTs.

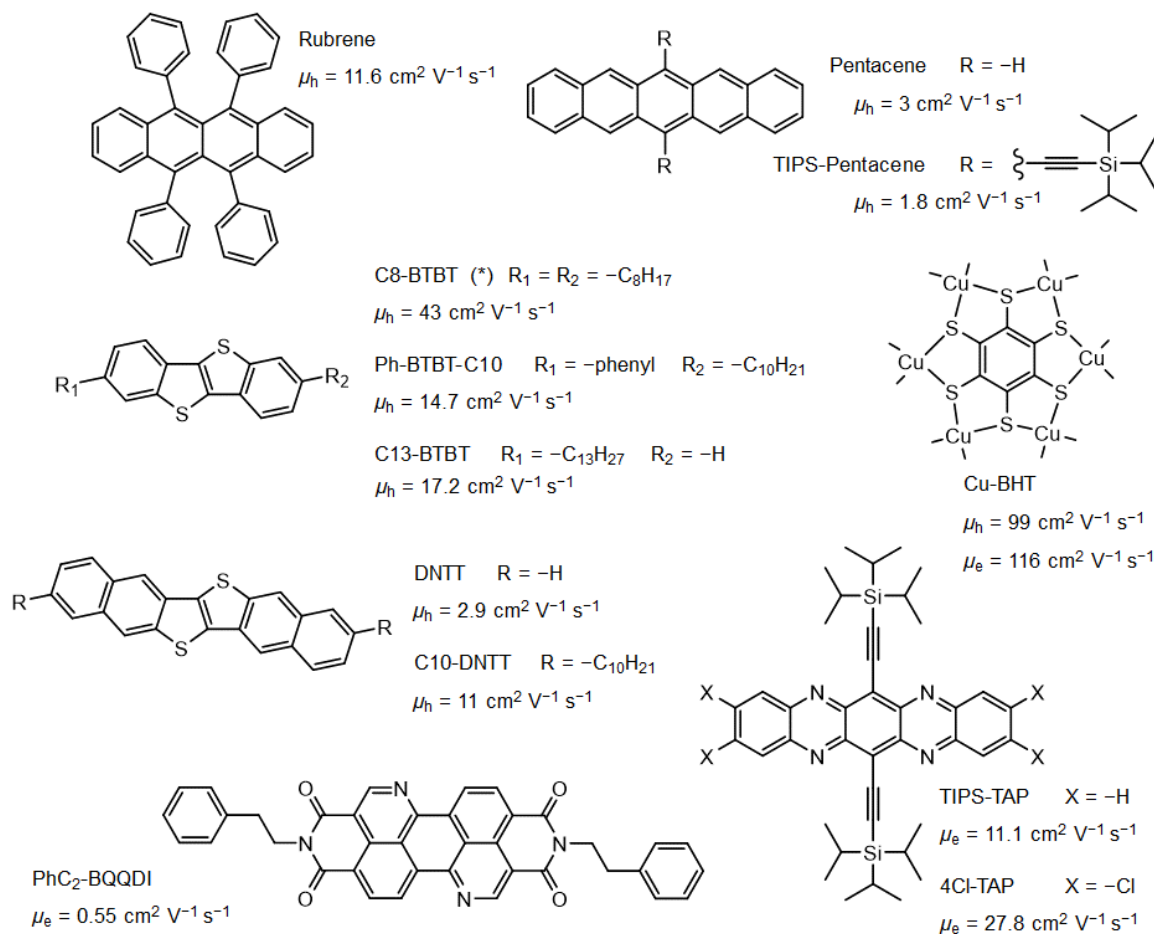


Figure 2. Overview on currently top hole- and electron-transporting materials for high-performing OTFTs and their reported charge mobility values (μ_h or/and μ_e). Hole-transporting materials (μ_h): rubrene^[38]; pentacene^[39-40] and its derivative 6,13-bis(triisopropylsilylethynyl)pentacene (TIPS-pentacene)^[41]; [1]benzothieno[3,2-*b*][1]benzothiophene (BTBT) derivatives C8-BTBT(*)^[42], Ph-BTBT-C10^[43] and C13-BTBT^[44]; dinaphtho[2,3-*b*:2',3'-*f*]thieno[3,2-*b*]thiophene (DNTT)^[45] and its alkylated derivative C10-DNTT^[46]. Electron-transporting materials (μ_e): (PhC₂-BQQDI)^[47]; 6,13-bis((triisopropylsilyl)ethynyl)-5,7,12,14-tetraazapentacene (TIPS-TAP)^[48] and its chlorinated derivative 4Cl-TAP^[49]. Ambipolar materials (μ_h and μ_e): the polymeric copper (II) benzenehexathiol (Cu-BHT)^[50]. (*) The semiconductor layer consists of a C8-BTBT:PS blend prepared *via* spin-coating.

The manufacturing of the device offers additional variables to extract the full potential of an organic semiconductor. The deposition of the organic semiconductor by means of the vacuum-evaporation technique generally affords more uniform and ordered films, which is

typically translated into a better charge mobility. Alternatively, the solution-processing implies a more versatile and economical method, but often at the cost of lower results and a huge investment to optimize the process. However, compounds like TIPS-pentacene can form highly crystalline films *via* solution deposition, outpacing the values of their vacuum-evaporated counterparts.^[51] Also, the use of single crystals instead of deposited thin-films grants a system with a long-range periodic order with minimal traps and defects.^[8] This is particularly useful for revealing the intrinsic properties of organic semiconductors and the structure-property relationship. For instance, a device based on a single crystal of pentacene can achieve a μ_h up to $40 \text{ cm}^2 \text{ V}^{-1} \text{ s}^{-1}$,^[52] which represents more than a 10-fold improvement with respect to that of an OTFT. However, the applicability of such devices is considerably more restricted.

The impact of the chemical structure over the electronic profile goes beyond the modulation of the μ , also influencing the stability and lifetime of the displays under ambient conditions.^[18,53–54] It is not uncommon that organic semiconductors underperform or even succumb to degradation after being exposed to air. The example of top performers like pentacene particularly illustrate this phenomenon.^[12] Consequently, the use of preserving strategies like operation under inert atmosphere or encapsulation are often imperative in such cases, hampering the viability of the material or implying undesired extra steps in the processing, respectively. To avoid these issues, materials featuring high air-stability and robustness are particularly sought-after. As predicted, a neutral p-type semiconductor should possess an ionization potential greater than 4.9 eV, i.e. a rather low-lying HOMO.^[18] Otherwise, a shallow HOMO energy level would make it susceptible to reducing ambient oxygen in the presence of humidity. The electron transport in n-type semiconductors is perturbed by reactions with air to an even further extent, so the electron affinity should surpass, or the LUMO energy level be below, the 4 eV to prevent excited electrons from reducing oxygen or water.^[55–56] Characteristics of the film such as a proper arrangement, morphology and even balanced inner strains can also enhance the device stability and prolong its shelf and operative lifetime.^[57] For instance, DNTT (Figure 2) has exhibited an outstanding five-year lifetime by engineering the intrinsic strains of the film.^[58] Despite the importance of this factor, the long-term stability of devices is seldom reported or analyzed, inciting further research in this direction.

- **Organic Light-Emitting Diodes**

The case of OLEDs is more self-explanatory because, unlike OTFTs, they represent the visible part of a display. Just as the name indicates, it is a device that aims the conversion of an electric input into light emission by means of the electroluminescent properties that exhibit certain materials, whether small molecules or polymers. The first proof to the

feasibility of this phenomenon in organics was brought by Benarose *et al.* in 1953, inducing a high-voltage alternating current to thin films of gonacrine and acridine orange E adsorbed upon a sheet of Cellophane.^[59] In the early 1960s, this was also demonstrated with anthracene crystals,^[60] whereas eosin was reported to emit delayed fluorescence.^[61] In 1987, Tang and VanSlyke from Eastman Kodak set the stage for the development of this field with the first efficient double-layered OLED device operated at relatively low voltages.^[62] In recent years, the industry has experienced a revolution with the long-awaited introduction of OLED-based products that comprise from displays of smartphones and TV screens to lighting applications. Figure 3 compiles representative products based on the OLED technology. Indeed, the assets of OLED displays with regard to the hitherto existing technologies are continuously claimed nowadays by commercial advertisement. In comparison to conventional liquid-crystal displays (LCD), OLED screens exhibit a better energy-efficiency because they do not rely upon a backlight system. This also translates into exceptionally pure black hues and high-contrast colors as well as thinner, lighter and even transparent displays.^[15,63] With the addition of the advantages attached to organic materials, the OLED technology permits the expansion of possibilities regarding the design, concept and application of next-generation displays and lighting sources.

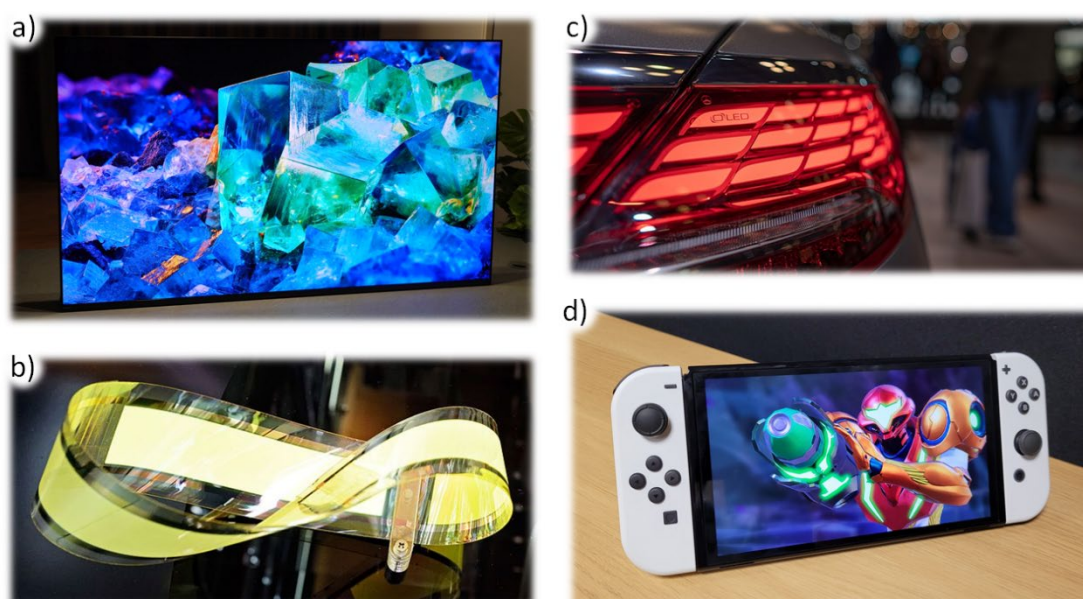


Figure 3. Representative displays and commercial products featuring the OLED technology: a) SONY BRAVIA XR A95K TV^[64]; b) example of flexible OLED lighting “Möbius”^[65]; c) OLED car taillights on Mercedes-Benz S560^[66]; d) videogame console Nintendo Switch - OLED model^[67].

Nevertheless, OLED technology still deals with key challenges with respect to both the organic materials and the device architecture, especially the improvement of their light output, efficiency, color purity, operational lifetime and low-cost manufacturing

techniques.^[68–69] Again, the molecular design and the supramolecular properties of the material in the solid state are crucial factors to address. This encompasses the π -conjugated core as well as the attachment of adequate groups and scaffolds. Whereas OTFT semiconductors prioritize large π -extended nuclei with a proper intermolecular overlap for an optimal charge mobility, these type of materials are typically not optimal for OLED applications due to their generally low emission output in the solid state.^[70–71] The evolution towards more efficient displays has led to diverse emitting materials that rely on fluorescence (first generation), phosphorescence (second generation) and the thermally activated delayed fluorescence (TADF) phenomenon (third generation). Each type of emitter requires particular structural characteristics.^[15,72–73]

The color of the emitted light in OLEDs is also closely related to the molecular system, which only reinforces the importance of an accurate design. The current research is particularly focalized on the study of improved blue OLEDs, which have historically fallen behind their red and green analogs in terms of both efficiency and stability.^[74–75] Indeed, the intrinsically large optical band gaps of blue emitters make them more susceptible to deterioration upon excitation, deriving into shorter lifetimes. The essentiality of blue OLEDs is not only limited to full-color displays, but are also compulsory to generate white light, highlighting the importance of enhanced blue-emitting materials.^[76–77] Deep-blue emitters, which are characterized by the *Comission Internationale de l'Éclairage* (CIE) chromaticity coordinates with a CIE_y value equal or below 0.10 (Figure 4), are especially sought-after.

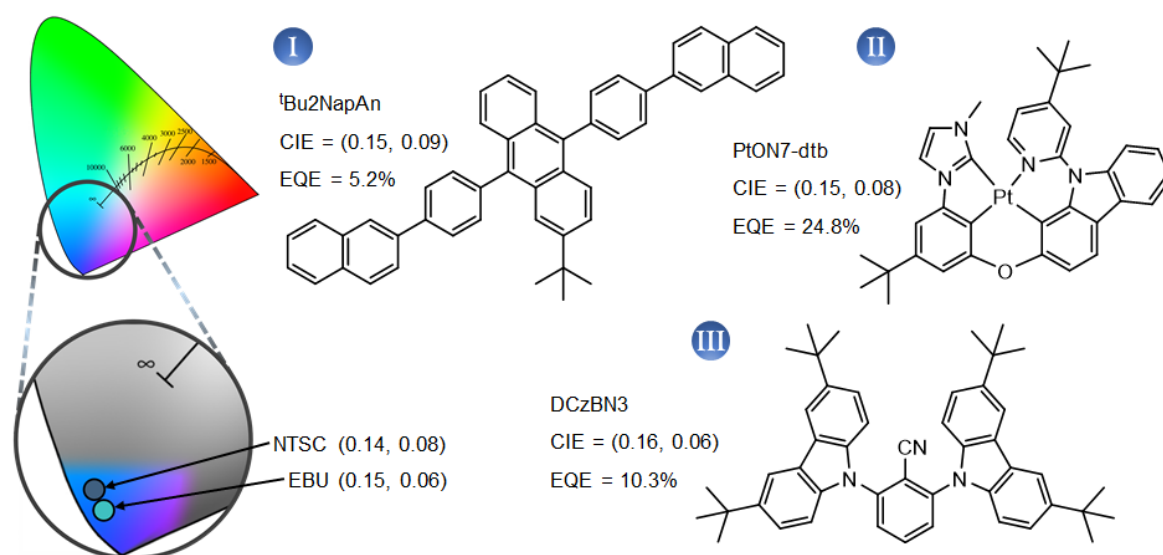


Figure 4. CIE 1931 color space with the deep-blue region and the NTSC and EBU blue coordinates highlighted in the amplified region. A representative example of each first^[78], second^[79] and third^[80] generation deep-blue emitter with their CIE coordinates and external quantum yields (EQE) are also collected.

Indeed, the standard CIE coordinates for blue are established as (0.14, 0.08) or (0.15, 0.06) by the National Television System Committee (NTSC) and the European Broadcast Union (EBU), respectively.^[75] Figure 4 compiles a representative deep-blue emitter from each generation and their respective characteristics.

- **9H-Carbazole as building block**

As stated, the π -conjugated backbone of an organic material rules fundamental properties such as the electronic profile, the arrangement in the solid state, the stability and the optical characteristics, which overall represent the cornerstone of a semiconductor. Hence, the investigation of this topic has led to countless molecular structures developed from a wide array of building blocks. In this way, 9H-carbazole emerges as a highly promising core that can fulfill all the requirements of novel materials. In fact, the carbazole heterocycle (depicted in Figure 5) is a frequently-resorted synthetic building block because of its easy availability and low cost, while also endows with hole-transporting properties^[81-82] and stability against oxidative doping by atmospheric oxygen^[83]. Nevertheless, the range of possibilities does not restrict to semiconductor applications, but it is also well-known for its excellent photophysical properties.^[81-82,84] Indeed, the occurrence of carbazole moieties in deep-blue emitters (such in examples 2 and 3 of Figure 4) exalts the relevance within all areas of optoelectronics. Another enticing feature resides in the feasibility to easily modify the properties of the main core through the attachment of diverse moieties to different positions, which also paves the way to the synthetic expansion of its π -system. Thus, the design of new semiconductor materials in this thesis will be based on the carbazole core.

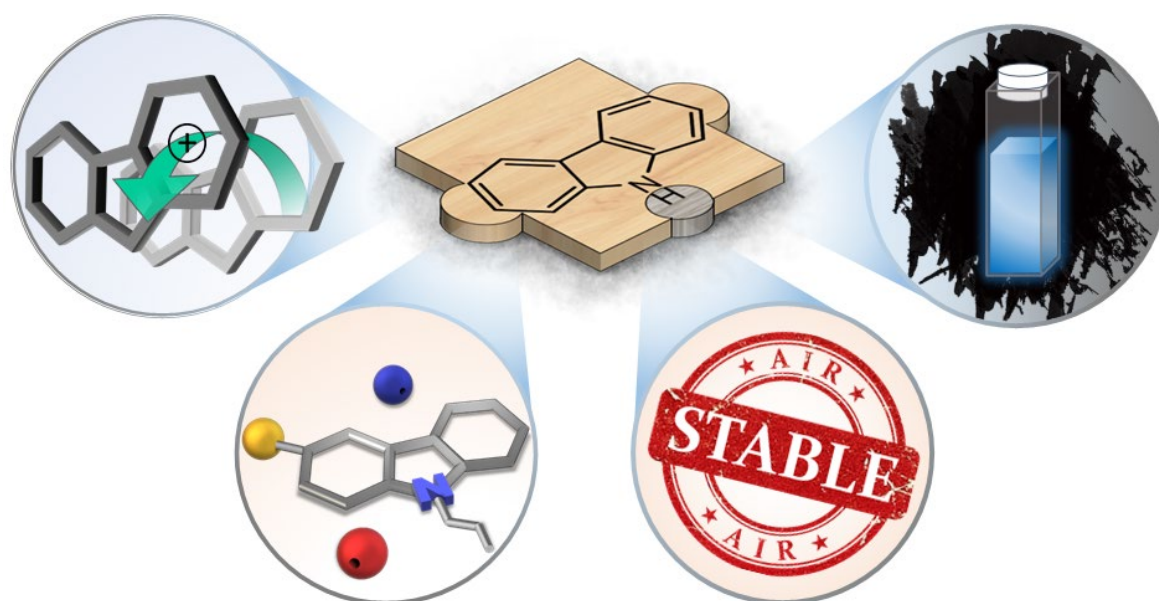


Figure 5. The structure and highlights of 9H-carbazole as a building block for optoelectronics.

OBJECTIVES



OBJECTIVES

This thesis is focused on the search of different carbazole-based materials as potential semiconductors for optoelectronic applications. Specifically, the derived core triindole was set as the model for conceiving and choosing the molecular constructions surveyed herein, since it has excelled as a p-type semiconductor in previous investigations of our research group. The study encompasses all stages of investigation, namely the design of new molecular structures, the synthetic processes, the characterization of the physical properties, the integration in optoelectronic devices and finally, the correlation of the device performance with the properties and intermolecular arrangement of the material. The materials surveyed in this work and their subsequent analyses have been classified in six chapters, depending on their structural features and their final application.

As a first approach to new hole-transporting materials, diverse ladder-type structures were projected from the expansion of the aromatic system of *9H*-carbazole. This strategy is particularly exploited in the trilogy of chapters 1, 2 and 3, which deal with the study of three different cores constructed from the fusion of carbazole with indole (diindolocarbazole core, Chapter 1), benzothiophene (bisbenzothiophenecarbazole core, Chapter 2) and phenanthrene (diphenanthrocarbazole core, Chapter 3). The effect of attaching alkyl chains of various lengths to different positions of the three studied systems also represents an important point of analysis. The integration of the resulting derivatives in OTFTs will ultimately determine the viability and adequacy of the three cores as organic semiconductors. A special emphasis is aimed to the evaluation of the stability and shelf lifetime of the devices, a crucial analysis that is often overlooked in the literature.

The study described in Chapter 4 is built upon the idea of substituting the nitrogen of *9H*-carbazole by sulfur as an alternative building block, namely dibenzothiophene core. In a more synthetically-conducted study, this chapter envisages the formation of assorted thiophene-centered constructions with potential in the optoelectronic field. Besides, it implies the evaluation of the synthetic route in terms of robustness and scope. The analysis of the photophysical properties of the tetraarylated precursors as well as the semiconductor potential of the final π -extended dibenzothiophene constructions constitutes a prime objective.

Chapter 5 resumes the analysis of the triindole core, which has been regarded as a highly-promising carbazole-based semiconductor in previous investigations of our research group. The different synthetic strategies explored throughout this thesis have been applied in the

redesign of triindole towards new derived constructions. The aimed synthetic variations comprise structural changes such as the attachment of peripheral carbazole moieties and the inclusion of oxygen and sulfur as alternative heteroatoms.

Finally, Chapter 6 pretends to highlight another important aspect of *9H*-carbazole, i.e. its photophysical properties. Thus, the search of new deep-blue emitting materials based on the 3-phenylethynylcarbazole moiety has been directed to their application in OLED devices. Specifically, the different fluorophores surveyed in this chapter target two distinct features apart from the emission in the deep-blue region in the solid state: the feasibility to be solution-processed and the flexibility to perform as both blue emitter and host in second-generation iridium-doped white OLEDs.

GENERAL PART



GENERAL PART

This section provides information about the fundamental concepts that are essential to comprehend the techniques employed throughout this thesis. Specifically, it encompasses from the characterization of the organic materials (Part 1) to the fabrication and evaluation of optoelectronic devices, namely OTFTs (Part 2) and OLEDs (Part 3). Finally, the techniques utilized to characterize the crystal structures of the organic semiconductors and their molecular order within the thin-films are also compiled (Part 4).

PART 1. Characterization of organic materials

1.1. Optical properties

The transitions that can take place between the electronic states of a molecule from the absorption to the emission of light are illustrated in the Jablonski diagram, represented in Figure 1. The ground state S_0 and the excited states S_1 and S_2 correspond to singlet states, while the counterpart triplet state is labeled as T_1 . The singlet state of a molecule with a closed-shell structure is characterized by the opposite spins of the involved pair of electrons. Additionally, each of the electronic energy levels presents several vibrational levels. The processes involved are herein described.^[85]

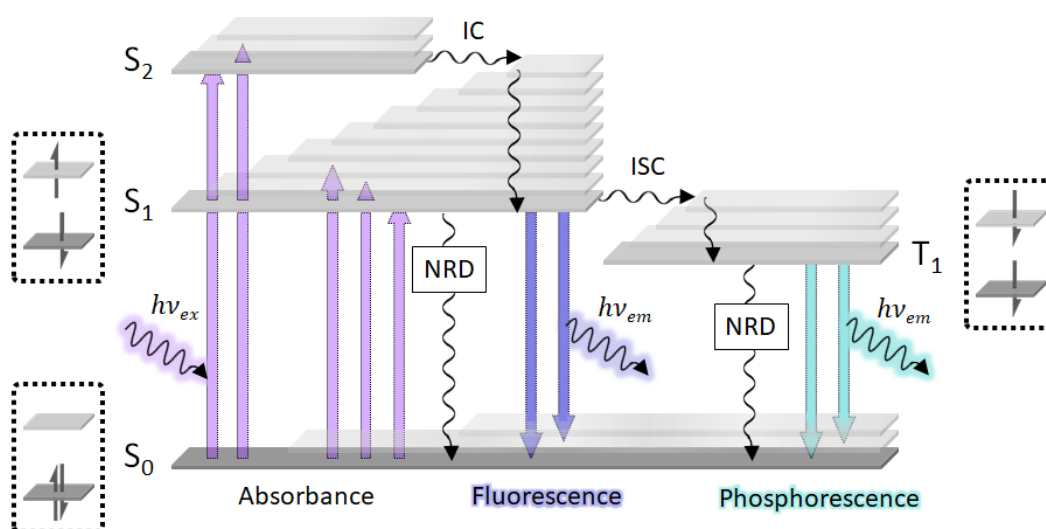


Figure 1. Schematic representation of the Jablonski diagram.

1.1.1. Absorbance

When the molecule absorbs a photon with the appropriate energy ($h\nu_{\text{ex}}$), one of the electrons from the orbital in the electronic ground state of the molecule is promoted to an unoccupied molecular orbital possessing higher energy. This transition takes place in a timescale of ca. 10^{-15} s, meaning that it is considerably faster than any other process like molecular vibrations. As stated by the Franck-Condon principle, such transition is most likely to proceed without changes in the positions of the nuclei in the molecular entity and its environment. Since the initial spin of the electrons is preserved in this process, the resulting promotion involves only singlet excited states. The least energetic transition, which occurs from $S_0 \rightarrow S_1$, is typically associated with the promotion from the HOMO to the LUMO energy levels. The optical energy gap ($E_{\text{gap}}^{\text{opt}}$), which quantifies the energy difference between both energy levels (usually given in electronvolts (eV)), can be estimated from the onset wavelength (λ_{onset}) of the corresponding absorption band (Figure 2) employing eqn. 1:

$$E_{\text{gap}}^{\text{opt}} = \frac{c \cdot h}{\lambda_{\text{onset}}} \quad (1)$$

where c is the speed of light (3×10^8 m s $^{-1}$) and h , the Planck constant (6.63×10^{-34} J s).

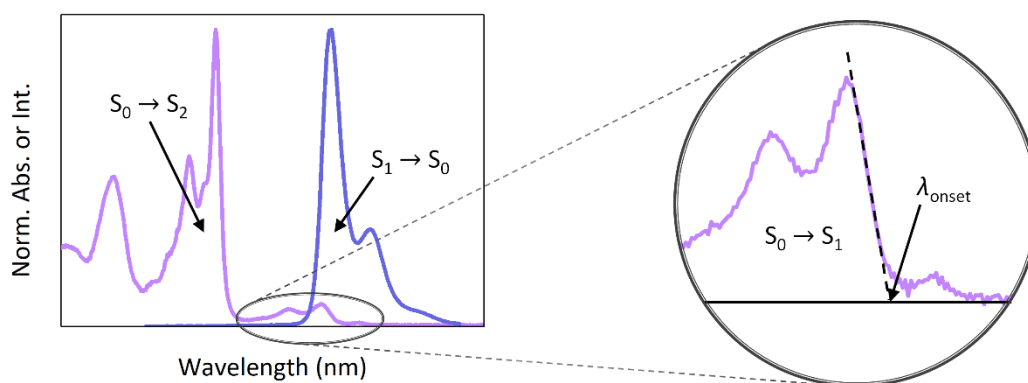


Figure 2. Representative absorption and emission spectra, indicating the corresponding transitions and the onset wavelength.

Experimentally, the efficiency of light absorption at a specific wavelength λ is characterized by the absorbance (A), which is defined by the Lambert-Beer Law (eqn. 2):

$$A(\lambda) = \log \frac{I_0}{I} = \varepsilon(\lambda)lc \quad (2)$$

where I_0 and I are the intensities of the beams entering and leaving the absorbing medium, respectively. The absorbance of a sufficiently diluted sample follows equation 2, where ε

represents the molar absorption coefficient (in $M^{-1} \text{ cm}^{-1}$) at a given λ , c is the concentration in molarity (M) and l is the path length or thickness of the absorbing medium (in cm). Otherwise, relatively concentrated samples can lead to light scattering due to aggregation, resulting into a loss of the linear dependence of the absorbance with respect to the concentration.

1.1.2. Fluorescence

The absorption of light generally promotes the excited electron to an energy level beyond the lowest vibrational level of the S_1 state. Consequently, the electron relaxes to that level through vibrational relaxation and internal conversion (IC) processes. The relaxation from the S_1 level to the ground state ($S_1 \rightarrow S_0$ transition) can be as whether a non-radiative decay (NRD) or associated to the emission of a photon. The latter case is known as fluorescence. Since the relaxation generally takes place from the lowest vibrational level, the fluorescence is not conditioned by the $h\nu_{\text{ex}}$. Besides, the energy of the emitted photons ($h\nu_{\text{em}}$) is lower than that of the absorbed photon ($h\nu_{\text{ex}}$), so the fluorescence is routinely red-shifted with respect to the absorbance.

The fluorescence quantum yield (Φ_f), which indicates the number of emitted photons relative to the number of absorbed photons, represents an important parameter to characterize a fluorophore. A Φ_f close to the unity implies that most of the excited electrons return to the ground state emitting a photon and NRD mechanisms are residual, so the resulting fluorescence is more intense and efficient. It can be experimentally determined with an integrating sphere or calculated using a reference compound according to eqn. (3):^[86]

$$\Phi_{f(x)} = \Phi_{f(r)} \frac{A_r}{A_x} \cdot \frac{n_x^2}{n_r^2} \cdot \frac{D_x}{D_r} \quad (3)$$

in which A represents the absorbance at λ_{ex} , n is the refractive index of the medium and D is the integrated area of the emission spectrum corresponding to the sample (x) and the reference (r). The chosen reference should display similar absorbance and emission profiles to those of the analyzed fluorophore and possess a tabulated $\Phi_{f(r)}$ value related to the λ_{ex} .

The Φ_f of a material as well as the wavelength of emission are conditioned by numerous structural and environmental factors. A commonly-observed phenomenon in organic fluorophores is the aggregation-caused quenching (ACQ), i.e. the drastic decrease of the Φ_f due to aggregation of the material when it is found in highly concentrated solutions or in the solid state.^[70-71] This phenomenon is usually accompanied by a bathochromic shift. Highly extended, aromatic systems tend to especially suffer from this effect, hampering

their use in optical applications. Contrarily, materials featuring aggregated-induced emission (AIE) exhibit the opposite effect, namely the lack of emission in solution and a prominent enhancement of the Φ_f in the solid state together with a hypsochromic shift.^[71,87–88]

1.1.3. Phosphorescence

The emission coming from the decay from the first triplet state to the singlet ground state ($T_1 \rightarrow S_0$ transition) is known as phosphorescence. As abovementioned, the spin of an electron does not change upon excitation, only resulting into the promotion to excited singlet states. However, an excited electron in the S_1 state can move to an isoenergetic vibrational level of the T_1 state through intersystem crossing (ISC). Since the ISC process can take place in the order of 10^{-7} – 10^{-9} s, it is able to compete with other pathways of de-excitation from S_1 . Even though crossing between states of different multiplicity is in principle forbidden, it can become more probable depending singlet and triplet states involved *via* spin–orbit coupling (i.e. coupling between the orbital magnetic moment and the spin magnetic moment).

Another obstacle to the phosphorescence is that non-radiative de-excitation greatly outweighs the radiative process in the $T_1 \rightarrow S_0$ transition, which is especially notorious in solution at room temperature. On the contrary, the emission of phosphorescence can be observed in a rigid medium and/or at low temperature. The lifetime of the T_1 state may be long enough under these conditions to observe phosphorescence on a time-scale up to seconds and even minutes. Considering that the lowest vibrational level of the T_1 state features a lower energy than that of the S_1 state, the phosphorescence spectrum is bathochromically shifted with respect to the fluorescence spectrum.

1.1.4. Delayed fluorescence

Another feasible radiative de-excitation process from T_1 is the delayed fluorescence. Similarly to the intersystem crossing ($S_1 \rightarrow T_1$), the opposite transition ($T_1 \rightarrow S_1$) can also occur if the lifetime of T_1 is long enough and the energy difference is sufficiently small. This process is known as reverse intersystem crossing (RISC). The resulting emission is analog to that of the fluorescence but with a longer decay time constant, since the molecules stay in the triplet state before emitting from the S_1 state. Because of the greater energy of the S_1 state in front of T_1 , this process can be thermally activated, so it is referred as thermally activated delayed fluorescence (TADF). This phenomenon has recently attracted a lot of attention due to its applicability in the highly efficient OLEDs of third generation (section 3.1).^[89–91]

1.2. Electrochemical properties

The electronic profile of a semiconductor material, i.e. the values of the HOMO and LUMO energy levels, is the base for any potential application.^[18] They do not only indicate the feasibility as p- or n-type semiconductor of the molecule, but are also fundamental to design the architecture of a device. The HOMO and LUMO energy levels of a molecule are typically associated with the ionization potential (IP) and electron affinity (EA) of the system, respectively. Cyclic voltammetry stands as a widely employed electrochemical technique to estimate their values.^[92–94] A cyclic voltammetry is carried out in a three-electrode cell consisting of a working electrode, a reference electrode and a counter electrode,^[95] as represented in Figure 3a. The application of a suitable, forward potential scan between the working and the reference electrodes under quiescent and inert conditions triggers the oxidation (or reduction) of the material onto the surface of the working electrode. The current generated in such process is simultaneously recorded between the working and the counter electrodes. The application of a forward potential scan is followed by an analog reverse potential scan, in which the oxidized (or reduced) species return into the initial state in the case of a reversible process. An example of a voltammogram corresponding to an oxidation process ($Sp \rightarrow e^- + Sp^+$) is shown in Figure 3b.

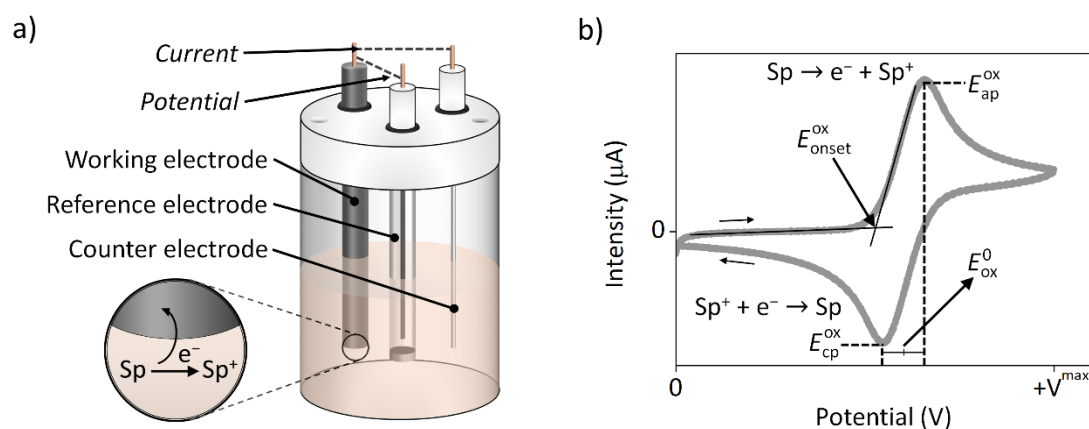


Figure 3. a) Schematic depiction of an electrochemical cell, displaying the three electrodes and indicating an oxidation process taking place on the working electrode, the generated current (between the working and the counter electrodes) and the applied potential (between the working and the reference electrodes); b) representative cyclic voltammogram showing an oxidation process, indicating all the parameters. The arrows specify the direction of the forward and reverse scans.

Specifically, it displays the anodic wave in the positive forward scan (\rightarrow) that derives from the oxidation of the electroactive species, whereas the reduction of the oxidized to the initial species are associated to the cathodic wave of the reverse scan (\leftarrow). The anodic and

cathodic waves culminate into the anodic (E_{ap}^{ox}) and cathodic (E_{cp}^{ox}) peaks, respectively. Such peaks originate from the steadily consumption of the initial species (Sp) in the anodic wave and the oxidized species (Sp^+) in the cathodic wave that are near the electrode, respectively. Since the cyclic voltammetry operates under quiescent conditions, the current thereafter depends upon the delivery of additional (Sp) in the former case or (Sp^+) in the latter *via* diffusion from the bulk solution, explaining the decrease of the current intensity after the peak.

In a reversible process, the current intensities of the cathodic and anodic peaks are typically analogous and the potential difference between them does not exceed the 57 mV/n (where n is the number of electrons transferred in the process).^[96] As represented in Figure 3b and described by eqn. (4), the average of the peak potentials of the anodic and cathodic waves of the reversible process is used as an approximation of the standard potential (E^0):

$$E^0 = \frac{E_{ap} + E_{cp}}{2} \quad (4)$$

The extraction of the standard potential is nevertheless limited to reversible or quasi-reversible redox couples. The calculi of the ionization potential and the electron affinity can be related to the onset potential of the first oxidation (E_{onset}^{ox} , represented in Figure 3b) or the first reduction (E_{onset}^{red}) peaks, respectively. To accomplish this, these potentials should be expressed with respect to the vacuum level, i.e. in the absolute potential scale. Therefore, the IP and EA values can be assessed considering the reference energy level of ferrocene as it is shown in eqn. (5) and (6):

$$IP = E_{onset}^{ox} - E^0(Fc^+/Fc) + 5.39 \quad (5)$$

$$EA = E_{onset}^{red} - E^0(Fc^+/Fc) + 5.39 \quad (6)$$

where $E^0(Fc^+/Fc)$ corresponds to the standard potential of the ferrocenium/ferrocene redox couple *vs.* the used reference electrode and the value of 5.39 eV stands as the formal potential of the Fc^+/Fc redox couple in the Fermi scale.^[92] Alternatively, the IP can be estimated from the EA and the E_{gap}^{opt} if the material does not display any oxidation process or, contrarily, the EA can be obtained from the IP and the E_{gap}^{opt} if it does not show any reduction process (eqn. 7 and 8):

$$IP = EA + E_{gap}^{opt} \quad (7)$$

$$EA = IP - E_{gap}^{opt} \quad (8)$$

1.3. Thermal properties

The thermal characterization of a material, namely the variation of its physical properties as a function of the temperature, represents a highly valuable information. In fact, it sheds light on several factors that influence into the applicability of the material as semiconductor. The thermogravimetric analysis (TGA) and the differential scanning calorimetry (DSC) are considered as two of the most widely used techniques to evaluate the thermal properties of materials.^[97] It should be mentioned that several experimental factors can influence both TGA and DSC curves, such as the atmosphere (reactive or nonreactive) and the applied heating rate.

1.3.1. Thermogravimetric analysis (TGA)

TGA is usually employed to evaluate the thermal decomposition of a compound by measuring the change of weight of a sample with the temperature in a controlled environment. It can be also applied to determine the thermal and oxidative stability of a material, the composition of a sample in the case of multi-component systems or the characteristics of chemical reactions. In this technique, the weight variations of the sample are monitored by a thermobalance. The sample is heated in a regulated environment at a given heating rate, while the weight is continuously and simultaneously recorded. Figure 4 exhibits a representative TGA curve, which expresses the percentage of weight with respect to the initial value versus the temperature.

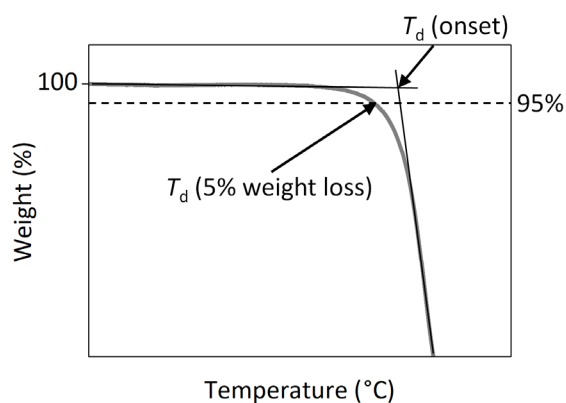


Figure 4. Representative thermogravimetric curve, showing the variation of weight of the compound with respect to the initial value (in %) vs. the temperature. As indicated, the decomposition temperature (T_d) can be associated to the 5% weight loss or the onset value.

The decomposition temperature (T_d) refers to the point where the weight of the sample starts to decrease. As shown in Figure 4, it can be estimated from the intersection point, i.e. the onset decomposition temperature, or the temperature corresponding to the 5% weight loss.

1.3.2. Differential scanning calorimetry (DSC)

DSC is a widely used technique for studying the phase transitions of materials. Whereas the instrumentation for DSC is similar to that of the TGA technique, it measures the difference of the heat flow between the sample and a reference. The sample can be heated or cooled in a controlled environment while the changes on the materials are monitored. Such changes include solid-phase transformations, glass transitions or melting points. Figure 5 records characteristic DSC curves for both amorphous and crystalline molecular materials, in which the heat flow (in W g^{-1}) is plotted versus the temperature.

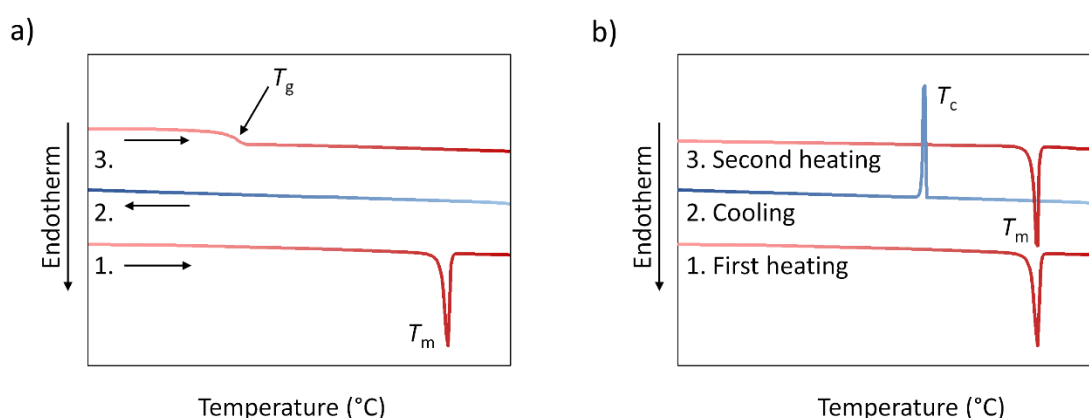


Figure 5. Representative DSC curves displaying a first heating, a cooling to the initial temperature and a second heating of two different materials: a) an amorphous molecular material; b) a crystalline molecular material. (T_m : melting point, T_c : crystallization temperature and T_g : glass transition temperature). The endothermic events are indicated as a downward feature, while the exothermic ones go upwards.

As represented, glass transitions can be observed in the case of polymeric and amorphous molecular materials (Figure 5a). A glass transition describes the change from a rigid non-crystalline solid to a glass phase or a rubber-like solid. Typically, it is observed in the second heating step and it is not preceded by a crystallization in the cooling step. Contrarily, crystalline materials display a characteristic melting point in the heating processes and the corresponding crystallization in the cooling step (Figure 5b).

PART 2. Organic thin-film transistors (OTFTs)

OTFTs are electronic devices capable of amplifying or switching electrical signals. Apart from their essentiality in diverse applications, OTFTs also represent a well-known system to determine the charge mobility of organic materials.^[36] The mobility (μ) indicates how easily charge carriers can move throughout a material when an electric field is applied, in $\text{cm}^2 \text{V}^{-1} \text{s}^{-1}$. It can be described with the following equation (9):

$$\mu = \frac{v}{E} \quad (9)$$

where v is the drift velocity of the charge carriers and E is the applied electric field. Even though there are several alternative methods to estimate the charge mobility of a material, such as the time-of-flight (TOF) or space-charge-limited current (SCLC) techniques,^[98] the results extracted from OTFT devices characterize more accurately the performance in final applications. Therefore, this section is centered on the architecture, manufacturing and characterization of OTFT devices to eventually define the charge mobility of the integrated organic material.

2.1. Geometry

OTFTs are three-terminal devices that control the current flow between the source and drain electrodes using the voltage applied to the gate electrode as an external trigger. Figure 6 depicts a typical bottom-gate top-contact OTFT architecture, highlighting the different parts.

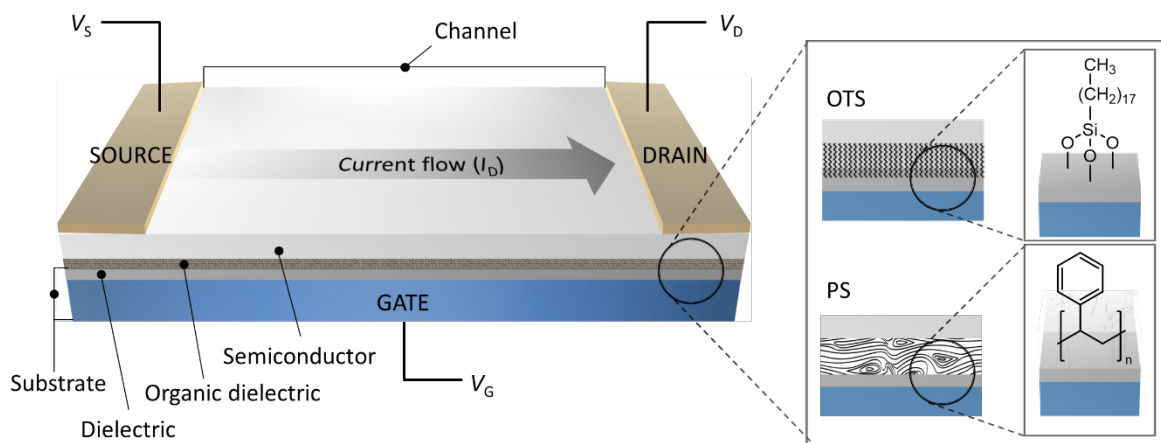


Figure 6. Schematic representation of an OTFT device. The amplified region details the structure of two types of commonly used organic dielectrics, namely octadecyltrichlorosilane (OTS) and polystyrene (PS).

As observed, the gate electrode is defined on a substrate that can be either rigid, such as the silicon wafer of the example, or flexible, such as plastic or even paper. The presented work is developed employing the former type of substrate. In it, the silicon typically acts as the gate and the silicon oxide coating as the dielectric layer. The properties of the interface between the semiconductor and the dielectric layer can be modulated by means of an additional organic dielectric. In fact, the presence and nature of this interfacial layer can be decisive in the performance of the device. Several organic dielectrics can fulfill this role, such as the functionalization of the SiO₂ dielectric with a self-assembled monolayer

(SAM).^[99-101] SAMs based on aliphatic chains like octadecyltrichlorosilane are the most resorted. The deposition of a polymer-based layer such as polystyrene through solution-processing also confers an interesting alternative.^[102] The deposition of the semiconductor layer is accomplished *via* vacuum thermal evaporation in this work. To achieve so, the organic material is heated inside a vacuum chamber under a pressure below 10^{-6} mbar. Parameters such as the evaporation rate or the thickness of the deposited film can be monitored throughout the process. The deposition of the metal that constitutes the drain and source electrodes, being gold the one chosen in our case, is likewise carried out at high vacuum. The geometry of both the semiconductor layer and the gold electrodes is imprinted by means of a shadow mask, which defines the dimensions of the channel.

It should be mentioned that an alternative geometry, namely bottom-contact, is also feasible. In it, the source and drain electrodes are deposited between the substrate and the semiconductor layer instead of the upper part.

2.2. Operation and characterization of the devices

The application of an appropriate gate voltage (V_G) triggers the generation of charges within the semiconductor layer, which accumulate in the interface with the dielectric.^[35,103] This is represented in Figure 7a for a hole-transporting OTFT as example, in which the operation under a $V_G < 0$ V prompts the formation of holes in the semiconductor/dielectric interface. As a result of the voltage applied between the source and the drain electrodes (V_{DS}), most of these generated charges can move across the semiconductor layer. The charge carriers are injected and collected from the source and drain electrodes, respectively. Ideally, the device rests in the off state in the absence of an adequate V_G , regardless of the V_{DS} that could be applied. The minimum V_G needed to activate the current flow is known as the threshold voltage (V_{th}). The threshold voltage depends on several factors such as the nature of the material or the presence of traps in the film. Consequently, the switching of the device between the off and the on states is controlled through the gate. This is exemplified in the output plot (Figure 7b), in which the current intensity from source to drain (I_D) is measured *vs.* the V_{DS} at different constant values of V_G . Each individual curve corresponds to a fixed value of V_G . As observed, the intensity remains almost negligible when $V_G = 0$ V (purple curve). When $|V_G| > |V_{th}|$, the intensity depends on the V_{DS} and is defined by the regime of operation. The linear regime is designated at $|V_{DS}| < |(V_G - V_{th})|$, in which the I_D current is proportional to the V_{DS} at a given V_G following the Ohm's Law, as described in eqn. (10):^[36]

$$I_D = \mu_{lin} C_{ox} \frac{W}{L} \left[(V_G - V_{th}) - \frac{V_{DS}}{2} \right] V_{DS} \quad (10)$$

where μ_{lin} refers to the charge carrier mobility in the linear regime, C_{ox} is the gate-dielectric capacitance per unit area and W and L indicate the width and length of the channel, respectively. On the other hand, the device is said to operate in the saturation regime when $|V_{DS}| > |(V_G - V_{th})|$, in which the I_D current is no longer dependent on V_{DS} and remains constant even if V_{DS} is further increased. This happens because of the excessive accumulation of charges near the drain electrode. In this case, I_D is governed by the mobility in the saturation regime (μ_{sat}) as described in eqn. (11):^[36]

$$I_D = \mu_{sat} C_{ox} \frac{W}{2L} (V_G - V_{th})^2 \quad (11)$$

The characterization of an OTFT also relies on the transfer plot, which, contrarily to the output curves, represents the I_D with respect to the V_G at a fixed V_{DS} value as shown in Figure 7c,d. Specifically, Figure 7c represents a transfer plot in the linear regime, so the applied V_{DS} must be considerably lower than the maximum V_G reached in the measurement. Accordingly to eqn. 10, I_D increases linearly with respect to V_G .

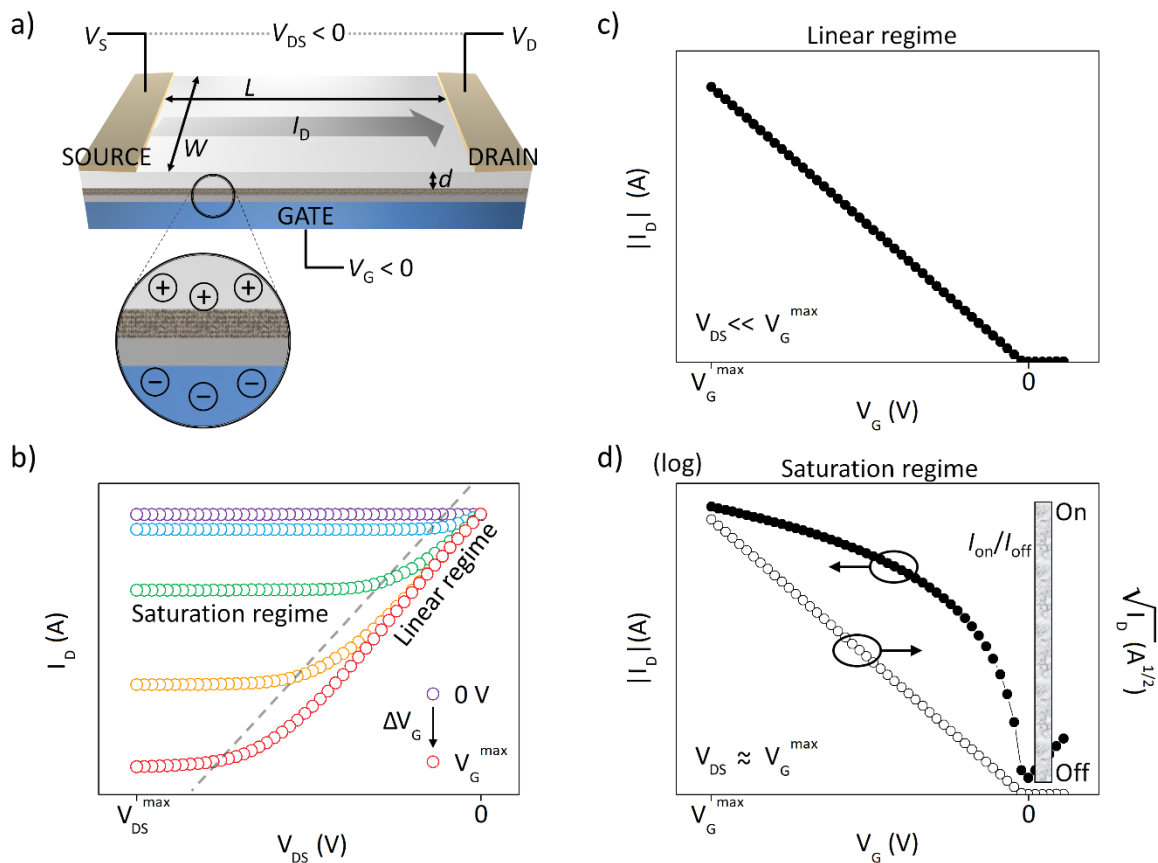


Figure 7. Characterization of a p-type OTFT: a) scheme of the different parameters of an operating device; b) output plot registered at different constant V_G values, delineating the linear and the saturation regimes; c) transfer plot in the linear regime at a given V_{DS} ; d) transfer plot in the saturation regime (in the log scale) at a given V_{DS} , illustrating the I_{on}/I_{off} ratio, and the resulting linear-scale plot ($I_D^{1/2}$ vs. V_G).

Alternatively, Figure 7d illustrates the transfer curve in the saturation regime represented in the logarithmic scale. Since the applied V_G is much higher in this case, so does the I_D . Thus, it enables the estimation of the I_{on}/I_{off} ratio, namely the difference of intensity between the on and off states. The I_D displays a quadratic growth in front of V_G in the saturation regime (eqn. 11), so the saturation plot ($I_D^{1/2}$ vs. V_G) is commonly expressed as well. Most importantly, the linear-scale plots (I_D vs. V_G in the linear regime and $I_D^{1/2}$ vs. V_G in the saturation regime) also permit the extraction of the charge carrier mobility (μ_{lin} and μ_{sat} , respectively) of a material, on the basis of the aforementioned equations 10 and 11. Even though some authors currently recommend the analysis of both μ_{lin} and μ_{sat} to provide more reliable results in top-performing OTFTs,^[104] this work is more focused on the characterization of the latter. Equation 11 can be rearranged to obtain the μ_{sat} (which is simply referred as μ in the subsequent sections) from the saturation linear-scale plot as follows (eqn. 12):

$$\sqrt{I_D} = \sqrt{\mu_{sat} C_{ox} \frac{W}{2L}} \cdot V_G - \sqrt{\mu_{sat} C_{ox} \frac{W}{2L}} \cdot V_{th} = A \cdot V_G - B \quad (12)$$

in which the μ_{sat} can be extracted from the slope A and the V_{th} can be estimated from parameter B (eqn. 13):

$$\mu_{sat} = \frac{2L}{C_{ox}W} \cdot A^2 \quad ; \quad V_{th} = -\frac{B}{A} \quad (13)$$

It must be noted that the description of an OTFT and the aforementioned equations are assimilated to those employed in metal-oxide silicon field-effect transistors (MOSFETs). Thus, it is assumed that the linearity of the dependence of $I_D^{1/2}$ (V_G) covers an extended range of V_G values, i.e. the OTFT displays ideal or close-to-ideal behavior. Nevertheless, most of the devices still exhibit different nonlinearities as a result of diverse structural and electronic factors. In these cases, the extraction of the charge mobility is still possible but the slope should be carefully selected.^[36,104–105] Figure 8 exemplifies the OTFT characteristics of a close-to-ideal device (a) and commonly found nonlinearities, namely linear with a considerable V_{th} (b), hump-like (c) and kink or double slope (d). As suggested in the literature, the estimation of the charge mobility in these cases should be carried out with the green slopes highlighted in each case.^[104]

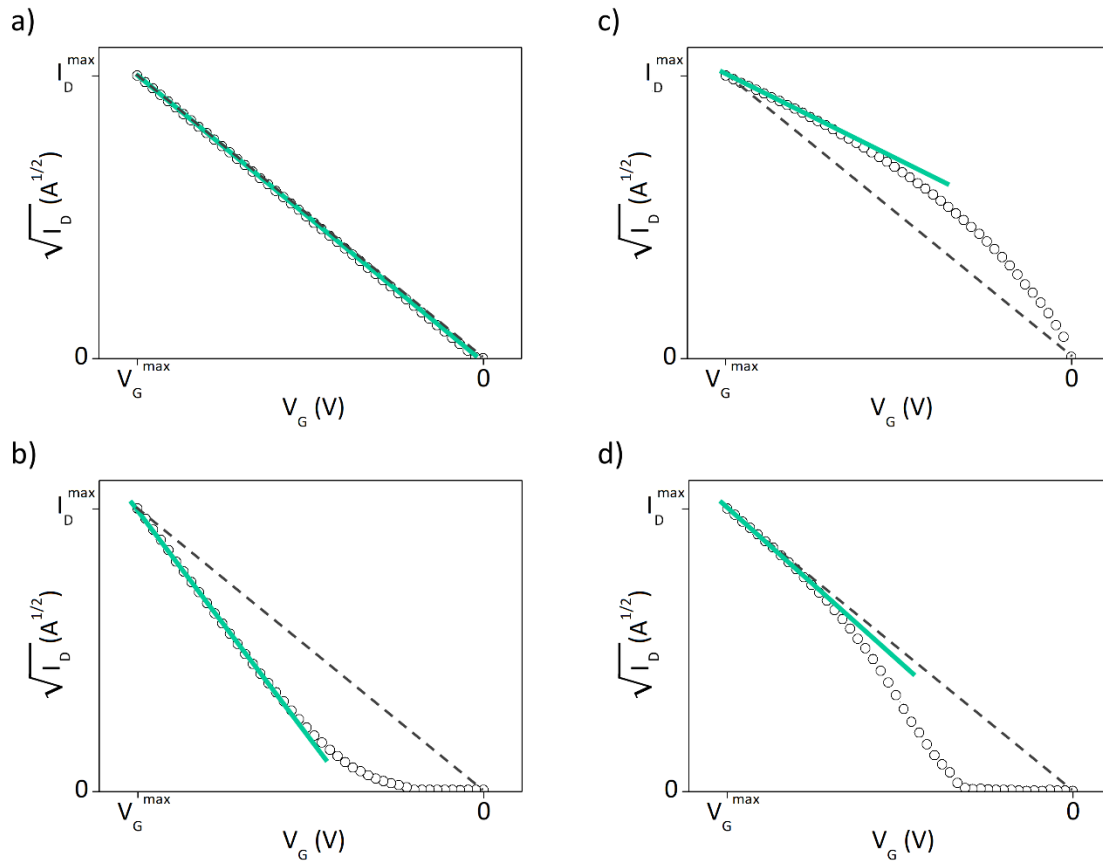


Figure 8. Extraction of the mobility from the saturation plot of an OTFT device featuring: a) a close-to-ideal behavior; b) a linear profile with a considerable V_{th} ; c) a hump-like nonlinearity; d) a kink or double slope. The characteristics of the equivalent ideal devices are indicated with the discontinuous grey lines and the recommended slopes to extract the mobility in green.

As observed, example (b) displays a superlinear behavior with respect to that of an electrically-equivalent ideal device (indicated by the dashed grey line). Consequently, the charge mobility extracted is lower than that of an analogous ideal device. Contrarily, example (c) features a sublinear behavior, so the charge mobility extracted is higher than that of an analogous ideal device. In the case of (d), the literature findings agree that the mobility extracted from the high V_G region, i.e. the lower slope, is the most appropriate. The empirical estimation of the V_{th} from eqn. (13), which is based on the extrapolated intercept point of the V_G axis, can lead to unrealistic values particularly in cases (b) and (d). The turn-on voltage (V_{on}), i.e. the voltage at which the current starts to depend on the gate voltage, is an alternative parameter. In an ideal device, both V_{th} and V_{on} should exhibit analogous values close to 0 V.

PART 3. Organic light-emitting diodes (OLEDs)

3.1. Structure, fabrication and operation

Organic Light-Emitting Diodes are multilayer devices that aim the conversion of electric current into light. To achieve so, OLEDs exploit the capability of an organic fluorophore to release energy as light when an electron returns from an excited to their ground state. The structure of the device typically consists of two electrodes sandwiching the emissive layer, enabling the electroluminescence (EL) of the organic material when a certain voltage is applied. The color of the emitted light is governed by the optical energy gap of the fluorophore. Figure 9 presents the architecture of a conventional multilayer OLED device.

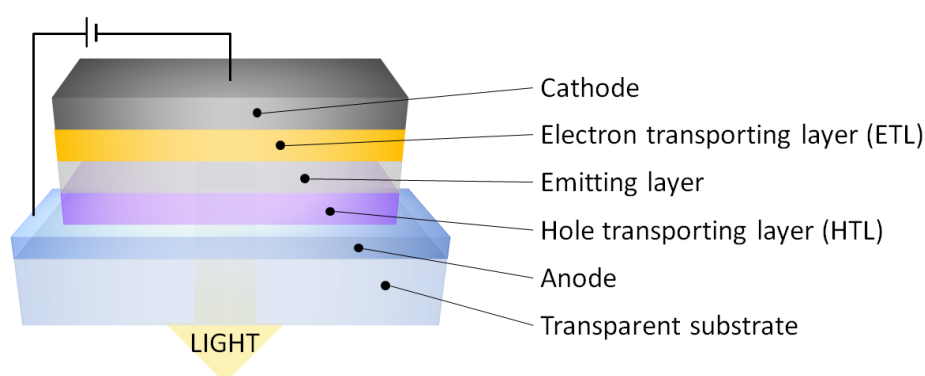


Figure 9. Schematic representation of a multilayer OLED device.

The fabrication of an OLED requires the successive deposition of each layer over the substrate. The deposition *via* vacuum thermal evaporation grants a lengthy but systematic procedure that normally provides layers with an improved morphology, translating into a better performance. On the other hand, the introduction of solution-processing techniques like spin-coating or ink-jet can drastically reduce both the cost and time of the manufacturing. However, the choice of the solvents and conditions involved should be carefully addressed in this case to avoid interlayer mixing.

The generation of the electroluminescence comprises several steps, namely the injection, migration and recombination of charge carriers, which culminate with the emission of light. The whole process is illustrated and detailed in Figure 10. In the absence of an external voltage, the system remains in the single ground state S_0 (step 1 in Figure 10). The induction of a voltage triggers the introduction of electrons from the cathode and withdrawing of electrons (or introduction of holes) from the anode (step 2 in Figure 10). In order to optimize the charge injection, the work function of the anode and the cathode should fit the LUMO and HOMO energy levels of the fluorophore, respectively.

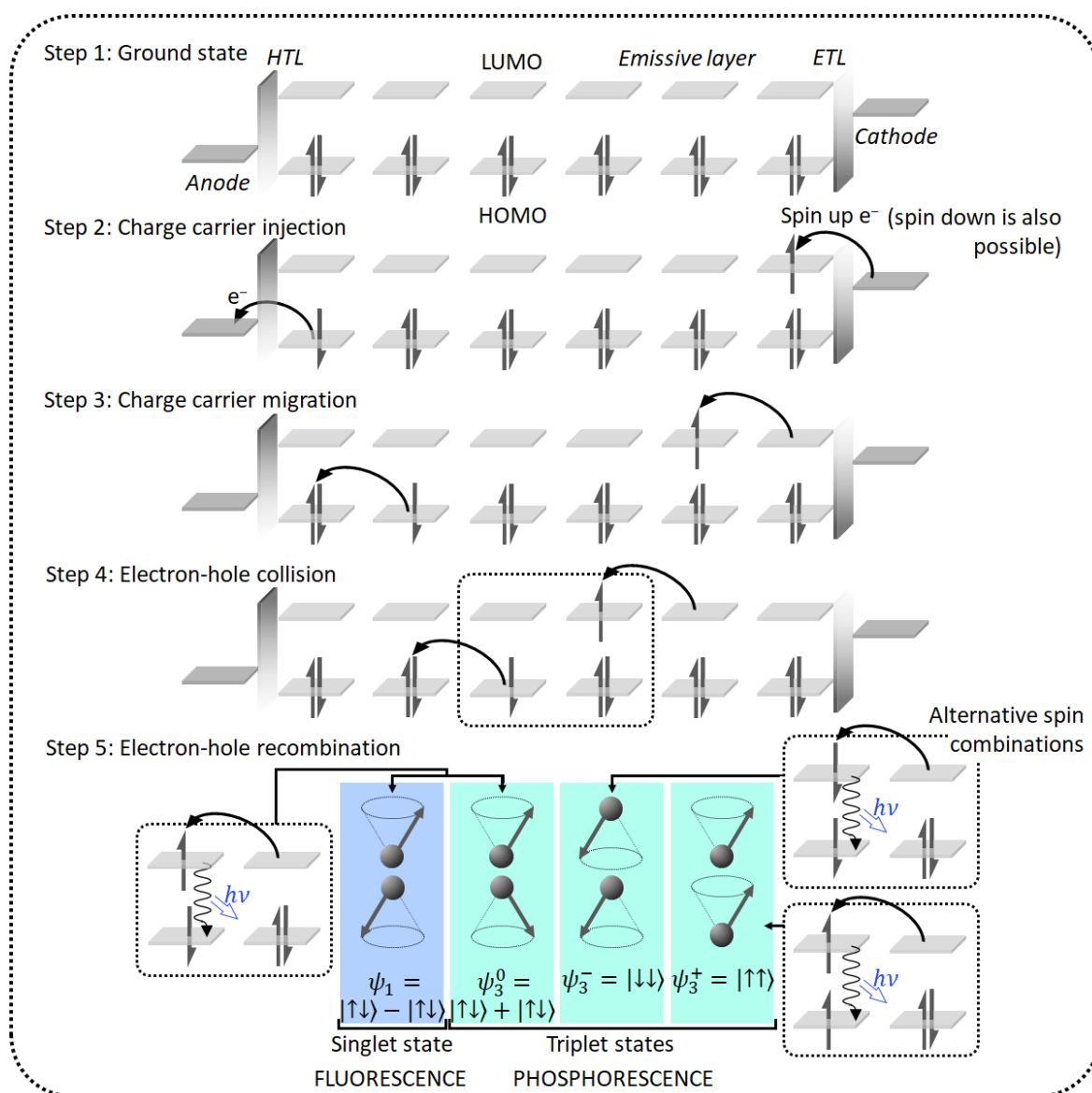


Figure 10. Schematic representation of the process that generates the electroluminescence in an OLED. The four eigenstates are also detailed. Adapted from the literature.^[106-107]

Another key point to consider is that at least one of the electrodes must permit the extraction of the generated light. Thus, ITO (Indium Tin Oxide) is usually the preferred anode option since, apart from being optically transparent, it features a conveniently low-lying work function of 4.8 eV.^[108] On the other hand, metals possessing relatively high-lying work functions are the most common choices for the cathode. As observed in both figures, several interfacial layers are included as well to smooth the transport of charges towards the emissive layer. Specifically, the hole-transporting layer (HTL) facilitates the transfer of holes from the anode to the HOMO of the fluorophore and blocks the transport of electrons, whereas the electron-transporting layer (ETL) performs in the opposite way between the cathode and the LUMO of the fluorophore. Considering that the charge

carriers migrate *via* the hopping mechanism across the emitting layer (step 3 in Figure 10), the fluorophore should exhibit certain semiconductor properties.

Once electrons and holes are sufficiently close within the emissive layer, they are attracted to each other to form excitons (steps 4 and 5 in Figure 10). It should be noted that, since the exciton state in OLEDs is promoted by an external current, both hole and electron are not spin-correlated. In fact, the spin is defined at the injection process and the electron-hole collision is arbitrary. For instance, Figure 10 depicts an injected spin-down hole and a spin-up electron. As represented in the step 5, the resulting exciton can conclude as both singlet (S) and triplet (T) states. Alternatively, the collision of an electron-hole pair with parallel spins also result in a triplet state. On the basis of the four possible eigenstates described in Figure 10, it is known that, statistically, the actual ratio of singlet and triplet states corresponds to 1:3. Knowing that the consequent decay from the latter is non-emissive in most organic fluorophores because it is a spin-forbidden transition, the internal efficiency cannot exceed 25% in first-generation fluorescent OLEDs (Figure 11a).^[14-15]

On the other hand, second-generation phosphorescent OLEDs (PhOLEDs) are able to emit from both the singlet and the triplet states (Figure 11b).^[14-15] Typical phosphorescent emitters are based on organometallic complexes of metals such as Ir, Pt and Os, in which the transition between the triplet and the ground state is permitted due to spin-orbit coupling.^[85] The emissive layer of PhOLEDs usually consists of a suitable organic fluorophore (host) that is doped with a phosphorescent complex (guest). The excitons are therefore formed in the host material, which can emit through the $S_1 \rightarrow S_0$ transition. In this case, however, the triplet states can still be harvested by the guest, which also permits the $T_1 \rightarrow S_0$ transition. As a result, the internal efficiency of the device could be theoretically enhanced to 100%. It should be mentioned that the triplet state of the host should be more energetic than that of the guest to enable this process. Since blue emitting hosts possess higher energies associated, they can be used universally in a wider spread of complexes. Even though the $S_1 \rightarrow S_0$ transition of the host also contributes to the emitted color, it is generally determined by the energy of the $T_1 \rightarrow S_0$ transition corresponding to the guest.

Third-generation OLEDs^[89-91] can also achieve theoretical internal efficiencies up to 100% due to the thermally activated delayed fluorescence (TADF), which enables the upconversion from nonradiative triplet excitons to radiative singlet ones *via* the reverse intersystem crossing (RISC) mechanism (Figure 11c). This case is especially enticing because it implies the fabrication of highly efficient non-doped devices, reducing the complexity and cost of fabrication. The structural design of TADF emitters targets a small energy difference between the excited triplet and singlet states and a high rate of radiative vs. non-radiative decay in the $S_1 \rightarrow S_0$ transition (i.e. high fluorescence). This can be achieved with structures

based on the combination of electron-donating and electron-withdrawing moieties, namely donor-acceptor (D-A) systems, with a twist angle between both driven by high steric hindrance.

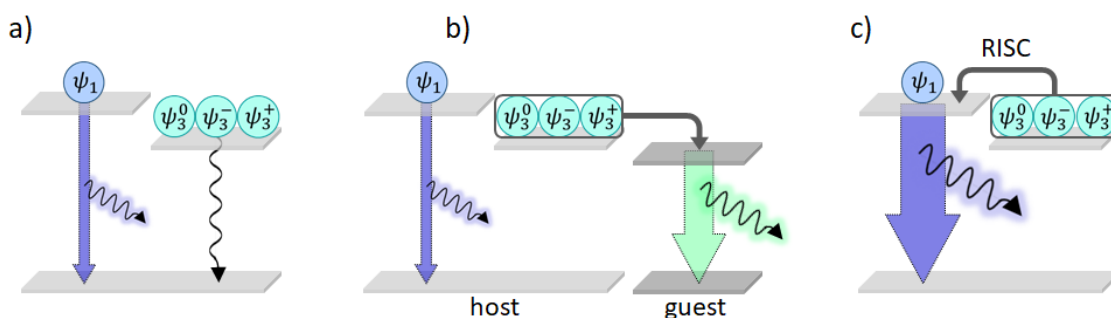


Figure 11. Schematic representation of the basis of electroluminescence in an OLED device of: a) first generation; b) second generation; c) third generation.

3.2. Characterization of the devices

3.2.1. Optoelectronic characterization

The optoelectronic characterization of an OLED device comprises different parameters, which are herein defined. Typically, the light that emits an OLED is registered as photocurrent through a photodiode detector, enabling the expression of the luminance (L). The luminance describes the luminous intensity per unit of area irradiated by a device in candela per square meter (cd m^{-2}). The electric current density (J) that goes throughout the device, triggering the generation of light, is referred to the area of the device. It is expressed as ampere per square meter (A m^{-2}). OLED devices should exhibit a high rectification ratio with minimal leakage current, since it does not contribute to the electroluminescence.^[109] Figure 12 shows representative curves of the luminance and current density with respect to the applied voltage ($V_{\text{appl.}}$).

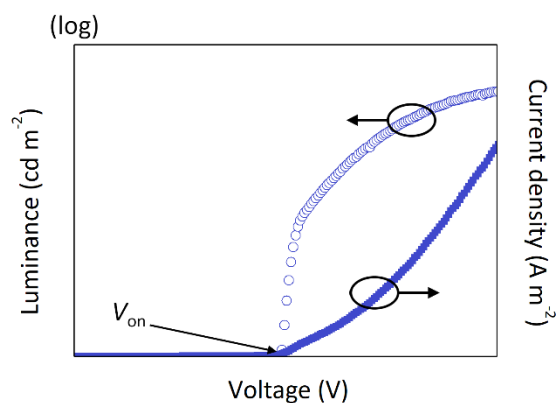


Figure 12. Representative optoelectronic characteristics of an OLED: a) luminance in the log scale and b) current density vs. the applied voltage.

The turn-on voltage (V_{on}) describes the potential at which the device is considered switched on, on the basis of a certain luminance value. The V_{on} depends on several factors, such as the energy barriers between the different interfaces, the charge transport properties and thicknesses of the active layers. Another key aspect is the efficiency of a device, which is evaluated with different parameters. The current efficiency (CE) is the ratio between the luminous intensity of the emitted light in the forward direction and the current density that goes through the device, and is expressed in candela per ampere (cd A^{-1}) as described by eqn. (14):

$$\text{CE} = \frac{L}{J} \quad (14)$$

The power efficiency (PE), sometimes known as luminous efficacy (LE), and the external quantum efficiency (EQE) also represent efficiency parameters. The formers are defined as the output luminous flux per electrical power input and are measured in lumen per watt (lm W^{-1}). The power efficiency can be estimated from the current efficiency according to eqn. (15):

$$\text{PE} = \text{CE} \times \frac{\pi}{V_{\text{appl.}}} \quad (15)$$

considering that the lumen depends on the visual angle, this approximation is valid at a perpendicular angle under the assumption of Lambertian emission. Regarding the external quantum efficiency, it indicates the ratio of photons emitted from the device with regard to the electrons injected from the cathode. Consequently, the EQE stands as a general measure of a device efficiency, whereas CE and PE of devices with different emission colors should be compared with caution. This is because the CE and PE parameters consider the sensitivity of the human eye to the diverse wavelengths of the visible spectrum. Since the EQE refers to the total number of photons emitted, its experimental determination requires the use of an integrating sphere. It can be theoretically expressed with eqn. (16):

$$\text{EQE} = \chi \times \eta_x \times \eta_c \times \Phi_f \quad (16)$$

where χ is the fraction of emissive excitons (which is 0.25 in fluorophores and 1 in phosphorophores or TADF emitters), η_x is the output coupling fraction, η_c is the charge balance between injected holes and electrons and Φ_f is the quantum yield of the emissive molecule.

3.2.2. Characterization of the emitted color

The chromaticity of the electroluminescence also represents a relevant factor to define. In 1931, the *Commission Internationale de l'Éclairage* (CIE) established a system to relate quantitatively the different wavelengths of the visible spectrum with the colors perceived by the human eye. As a result, the CIE chromaticity diagram (Figure 13a) stands as the most currently employed method to represent the color space two-dimensionally.

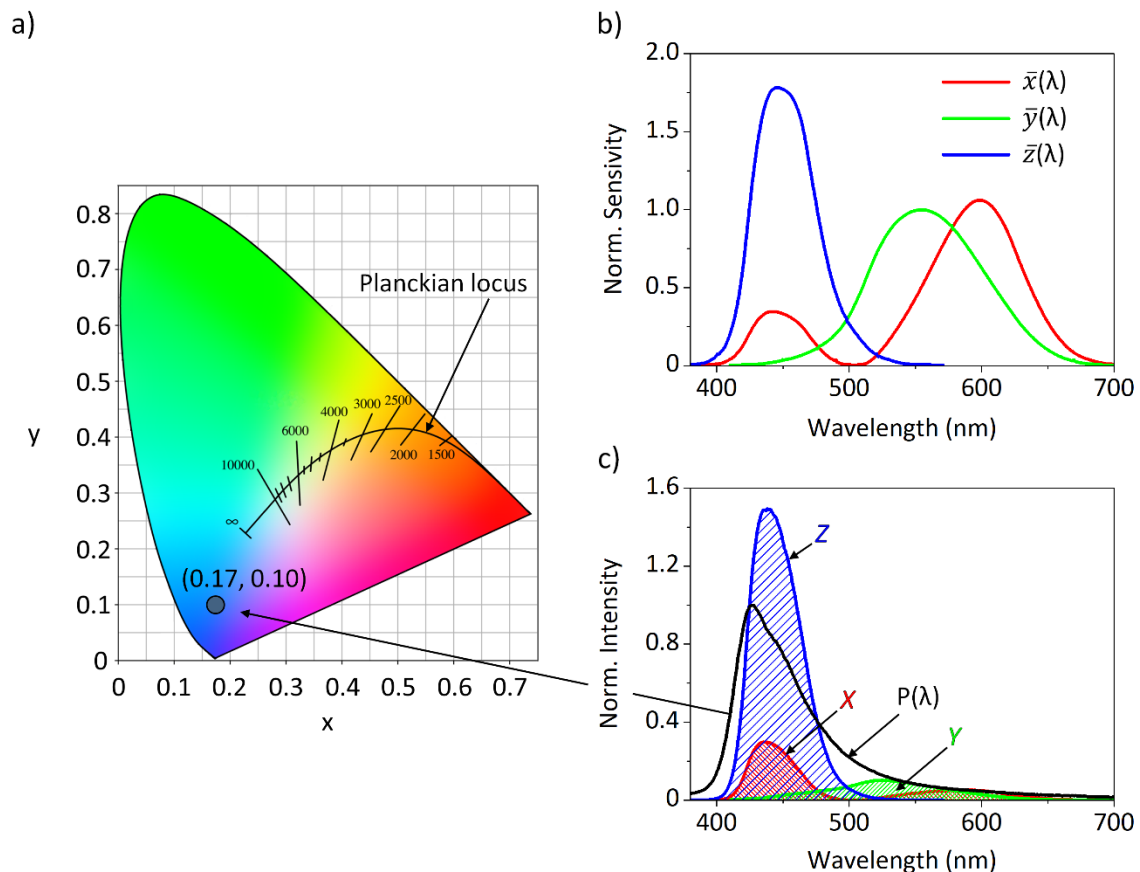


Figure 13. Evaluation of the chromaticity of light: a) CIE chromaticity diagram detailing the Planckian locus, with the coordinates of a deep-blue emitter shown as example; b) spectral responses of the three type of color receptive cells present in the human eye, described by functions $\bar{x}(\lambda)$, $\bar{y}(\lambda)$ and $\bar{z}(\lambda)$, normalized with respect to $\bar{y}(\lambda)$; c) example of a normalized emission spectrum $P(\lambda)$ corresponding to a deep-blue emitter and the functions resulting from eqn. (17). The tristimulus values X , Y and Z correspond to the areas below.

This diagram is constructed from the spectral responses of the three type of color receptive cells present in the human eye, which are described by the functions $\bar{x}(\lambda)$, $\bar{y}(\lambda)$ and $\bar{z}(\lambda)$ shown in Figure 13.^[110] As observed, functions $\bar{x}(\lambda)$, $\bar{y}(\lambda)$ and $\bar{z}(\lambda)$ can be roughly associated to the responsivities to the red, green and blue, respectively. The contribution of a given electroluminescence spectrum $P(\lambda)$ to the responsivity of each color receptive cell, namely the tristimulus values X , Y and Z , is calculated as follows (eqns. 17):

$$\begin{aligned}
X &= \int P(\lambda) \cdot \bar{x}(\lambda) d\lambda \\
Y &= \int P(\lambda) \cdot \bar{y}(\lambda) d\lambda \\
Z &= \int P(\lambda) \cdot \bar{z}(\lambda) d\lambda
\end{aligned}
\tag{17}$$

Finally, the corresponding CIE coordinates (x, y) can be obtained from values X, Y and Z as indicated in eqn (18):

$$(x, y) = \left(\frac{X}{X + Y + Z}, \frac{Y}{X + Y + Z} \right)
\tag{18}$$

Another parameter that should be described with regard to the characterization of white light is the color temperature, which is particularly important in illumination applications.^[111] The color temperature of a source of light is measured in reference to the radiation of a blackbody at a given temperature, expressed in Kelvin. The range of color temperatures are described by the Planckian locus in the CIE chromaticity diagram (Figure 13a). The correlated color temperature (CCT) is the closest point to the Planckian locus of hues possessing CIE coordinates outside of it. The McCamy's approximation^[112] stands as a widespread method to estimate the CCT of a given hue from the CIE coordinates. The associated empirical formula is shown in eqns. (19) and (20):

$$n = \frac{(x - x_e)}{(y - y_e)}
\tag{19}$$

$$CCT = an^3 + bn^2 + cn + d
\tag{20}$$

where x and y represent the given CIE coordinates, x_e and y_e correspond to the coordinates of the epicenter with values of 0.3320 and 0.1858, respectively, and constants a, b, c and d are estimated as 437, 3601, 6861 and 5517, respectively. Albeit this formula permits the calculation of the CCT of any CIE coordinates, it should be pointed out that it is meaningless to describe hues that are not close enough to the Planckian locus to be considered as "white". The scope of CIE coordinates that are considered as white in terms of illumination and possess analog CCT values are defined by the lines that are transversal to the Planckian locus in Figure 13a.

PART 4. Solid-state characterization techniques

When a solid is irradiated, it is able to scatter the incident beam if it possesses a wavelength close to the interatomic distances. Since the interatomic distances typically range from 1 to 3 Å,^[113] the use of X-ray irradiation is mandatory to achieve such phenomenon. The process by which the radiation, without changing its wavelength, is transformed into numerous reflections with characteristic directions in space through the interference with the solid is called X-ray diffraction (XRD).^[113] The intensity of the diffracted beams, which can derive into constructive or destructive interferences, can be measured to produce a diffraction pattern. The former interferences increase the intensity whereas the latter reduce it. In the case of a solid displaying a periodic and regular arrangement, the presence of constructive interferences will be concentrated in certain directions, providing information of the disposition of the atoms that form it. A constructive interference requires an angle of reflection equal to that of incidence and a value that permits the scattering in phase in the entire set of planes (Figure 14).^[113,114] As described by the Bragg's equation (21), the corresponding angles are defined as follows:

$$n\lambda = 2d_{hkl} \sin \theta \quad (21)$$

where n is the order of diffraction, λ is the wavelength of the X-ray source, d_{hkl} is the distance between parallel planes and θ is the incident angle, as indicated in Figure 14.

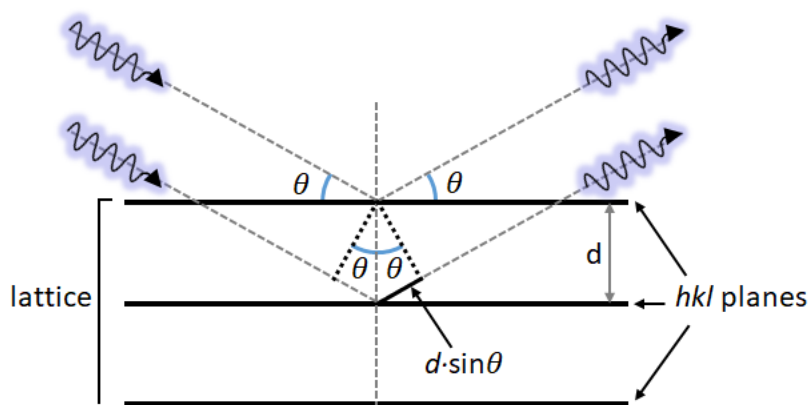


Figure 14. Bragg diffraction projected by crystal planes.

Knowing the incident angle and the wavelength of the X-ray source from the experimental conditions, the distance between planes can be extracted to shed light on the arrangement and composition of the atoms within. In fact, XRD represents the cornerstone of solid-state characterization, permitting the study of not only the crystallographic structure, but also the chemical composition and physical features of compounds and thin films as well.^[115] Since the semiconductor properties of organic materials are closely related to the

intermolecular packing, the structural characterization in the solid state represents a crucial part.^[20] This part pretends to delve into the main XRD techniques utilized in this work, which are crucial to unveil the molecular arrangement, orientation and degree of order within the thin films.

4.1. Crystal structure

The analysis of the crystal structure of a material provides a valuable insight into its intermolecular disposition and interactions that govern the packing. Thus, it permits the correlation of the molecular structure with its supramolecular features. The elucidation of the crystal structure involves the definition of the precise spatial arrangement in the crystalline state of all the present atoms, namely the connectivity, conformation, stoichiometry, symmetry, etc.^[113]

Crystals are solid constructions constituted of a basic pattern of atoms or molecules that is repeated over and over along all three dimensions.^[1,113] Hence, it is only necessary to define the simplest repeating motif, known as the unit cell, and the lengths and directions of the basis vectors to describe the structure of a crystal. By the operation of one unit cell upon another, a lattice is generated. Figure 15 illustrates the fragment of a lattice formed from equivalent unit cells and the parameters that define them, as well as two representative examples.

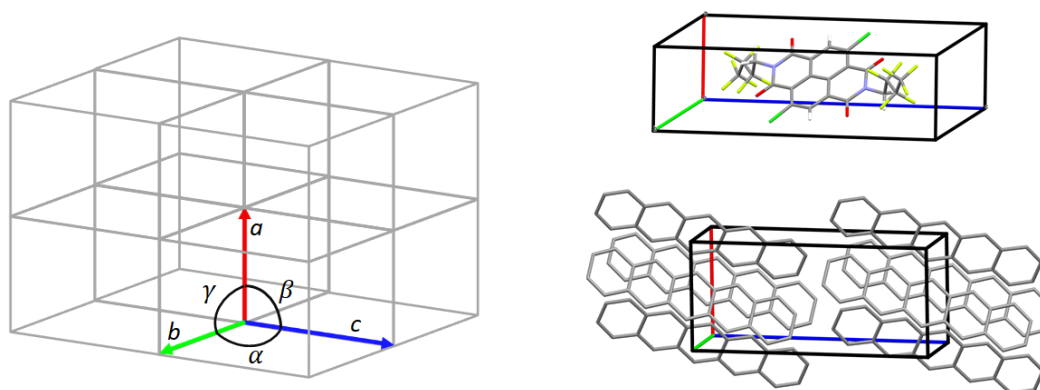


Figure 15. Part of a lattice formed by consecutive unit cells, indicating the basis vectors (a , b and c) and the angles that separate them (α , β and γ). Two examples of unit cells are also included, featuring a single molecule (4,9-dichloro-2,7-bis(2,2,3,3,4,4,4-heptafluorobutyl)benzo[lmn][3,8]-phenanthroline-1,3,6,8(2H,7H)-tetrone, crystallized in space group P_{-1} of the triclinic system, CCDC number 1018034) or several molecules (pentacene, crystallized in space group P_{-1} of the triclinic system, CCDC number 114447) inside.

The unit cell is characterized by the lengths of the basis vectors (a , b and c) and the angles that separate them (α , β and γ). Apart from their values with respect to the rest of the parameters, the symmetry present in the lattice is also important. Considering all the

possible symmetries for the lattice, seven different crystal systems are defined: triclinic, monoclinic, orthorhombic, tetragonal, trigonal, hexagonal and cubic. All of them possess unique shapes and characteristics that distinguish from each another. The symmetry operations in each one can be further specified with the space groups, with an overall range of 230 possibilities. The crystallographic data of a compound can be approached *via* two different techniques, which are briefly surveyed herein.

4.1.1. Determination *via* single crystal X-ray diffraction

Single crystal X-ray diffraction (SXRD) represents the most extensively employed technique to elucidate a crystal structure. A single crystal is usually obtained from the slow evaporation of the solvent (or mixture of solvents) of a dissolved compound. The success in furnishing a suitable single crystal depends on several factors, such as the solvent nature and polarity, the evaporation rate of the solvent or the proneness of the compound to assemble in a regular and continuous disposition.^[116] Since single crystals are composed of homogeneously repeated unit cells, the distances between the lattice planes (d_{hkl}) can be directly deduced through XRD measurements according to Bragg's Law. The lattice planes display an orientation relative to the lattice that can be defined by the Miller indices (hkl), as exemplified in Figure 16.^[113]

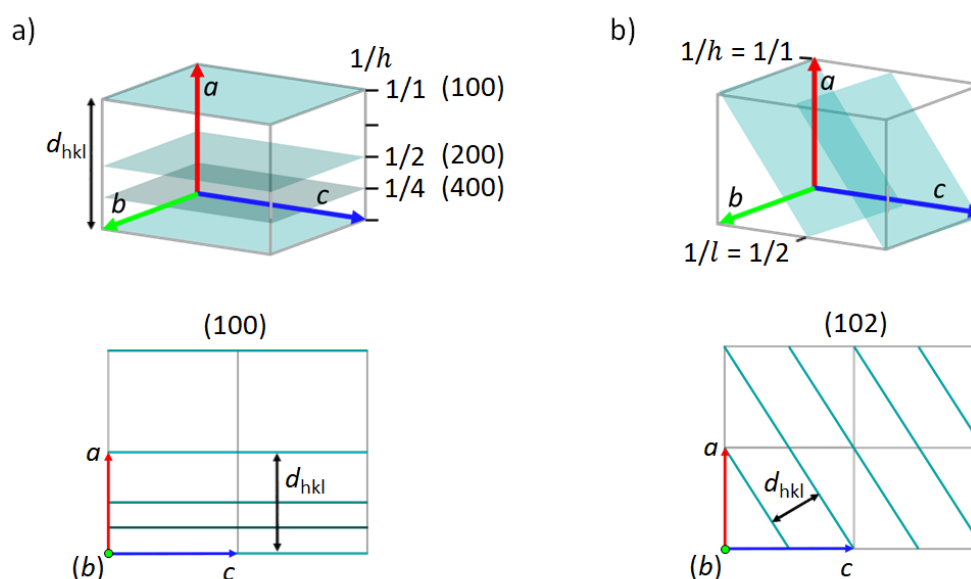


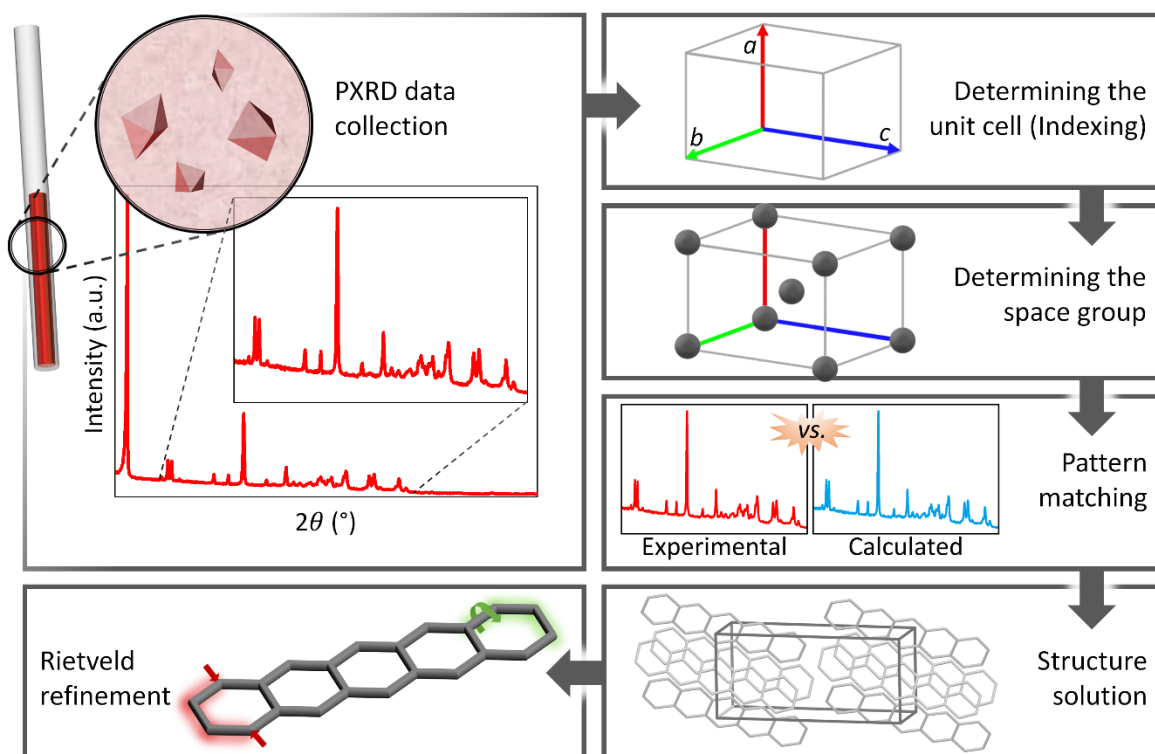
Figure 16. Examples of lattice planes and the corresponding d_{hkl} , represented in the unit cell (above) and in the 2D lattice where the b vector is perpendicular to the sheet (below): a) plane (100), with the complementary planes (200) and (400); b) plane (102).

As represented, the Miller indices refer to the points where the closest plane to the origin that do not pass through it intercepts the basis vectors a , b and c , being their values $1/h$, $1/k$ and $1/l$, respectively. Each set of lattice planes also has parallel, complementary planes

that feature Miller indices that are multiples of the original one (lattice planes (200) and (400) of Figure 16a), which are often translated into secondary reflections in XRD. The interpretation of the whole set of resulting diffractions leads to the unit cell and, subsequently, the crystal structure.

4.1.2. Determination *via* powder X-ray diffraction

Alternatively to the well-established resolution *via* SXR, the crystal structure can be also approached from a polycrystalline material. This method is especially enticing when the crystallization of the material is challenging or the production of single crystals results inaccessible. Structure determination from powder diffraction (SDPD), while by no means routine, has also emerged as a realistic option for determining crystal structures.^[117] Whereas the use of a microcrystalline powder compound is substantially more straightforward with respect to SXR in terms of sample preparation, the analysis of the XRD data is considerably more intricate. The diffraction patterns of single crystal and powder samples contain essentially the same information, but the diffraction data is distributed in the 3D space in the former and compressed into 1D in the latter. Consequently, this involves a considerable overlap of diffraction peaks in the powder diffraction pattern, resulting in a loss of information. The development of high resolution PXRD instrumentation, computational resources and well-developed algorithms, however, has prompted SDPD as a powerful tool of structural characterization.^[118] The SDPD procedure implies several steps, which are summarized in Scheme 1. The experimental conditions should be carefully addressed in order to collect high quality data. Specifically, they should provide angular accuracy and a proper choice of slits, control over the morphology and size of the sample and avoid preferential orientation problems.^[119] The determination of the unit cell, i.e. the indexing step, is the most challenging and crucial of the resolution process. The indexing involves the analysis of the Bragg reflections in the powder XRD data in terms of the diffraction angle 2θ or the corresponding d_{hkl} spacing. The aim is to find a set of unit-cell parameters and the corresponding set of Miller indices for each Bragg reflection that successfully account for the positions of all peaks in the PXRD data. Thereafter, it implies the assignment of the fitting space group. After establishing a proper initial approximation to the unit cell, it is improved in subsequent profile-fitting calculations where the PXRD pattern generated from the approximated structure is compared with the experimental one. This leads to a closer approach of the crystal structure that is further improved *via* the Rietveld refinement.



Scheme 1. General procedure of structure determination from powder X-ray diffraction (PXRD).

4.1.3. Classification of crystal structures in organic electronics

As stated, the analysis of the crystal structure provides vital information about the feasible charge-transport mechanisms and potential of the material as semiconductor. On the basis of the more frequent crystal arrangements observed in polycyclic aromatic hydrocarbons, four general categories have been defined.^[120–121] Each type of packing is characterized by the presence of different interactions between the aromatic systems, namely face-to-face (cofacial and parallel-displaced) and edge-to-face (Figure 17a). The herringbone packing (Figure 17b) is featured by several top-performing semiconductors like pentacene and BTBT, and is mainly governed by edge-to-face interactions whereas there is no effective face-to-face overlapping. Similarly, the sandwich herringbone packing displays an analogous disposition but composed of cofacial or parallel-displaced dimers instead of single molecules (Figure 17c). The γ packing consists of parallel-related molecules forming π -stacked columns through face-to-face interactions and edge-to-face interactions between columns (Figure 17d). It is often described as a flattened herringbone motif featuring direct π - π overlap. Finally, the β packing, sometimes referred as sheet-like, is basically composed by face-to-face interactions. Depending on the arrangement of the π -stacking, the β packing is divided in cofacial, slipped and brick-layer (Figure 17e). The face-to-face π - π stacking found in γ and β packings is considered as optimal in terms of effective and continuous overlap throughout the material, whereas the presence of edge-to-face interactions favors alternative hopping pathways.

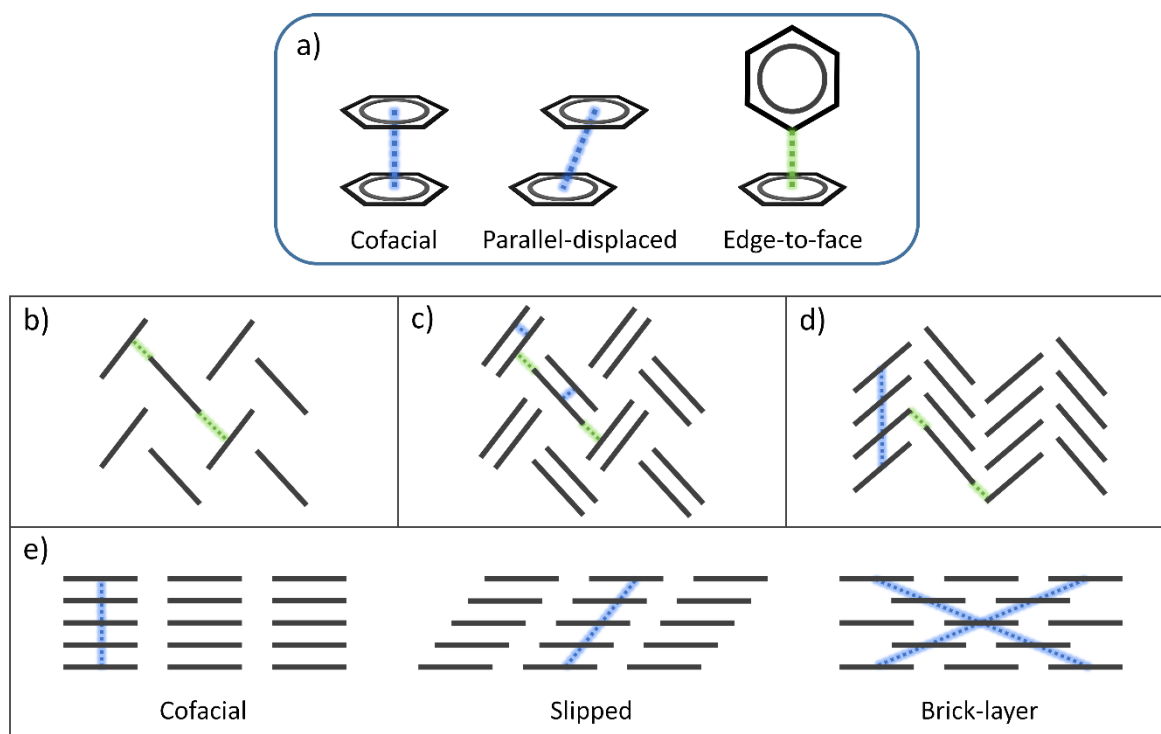


Figure 17. Schematic representation of interactions and packing motifs commonly found in aromatic systems: a) basic interaction geometries represented for a benzene dimer, namely cofacial, parallel-displaced and edge-to-face; b) herringbone packing; c) sandwich herringbone packing; d) γ packing; e) different types of the β (or sheet) packing, namely cofacial, slipped and brick-layer stacking motifs.

The presence of alkyl chains or other groups can endorse another interactions such as aliphatic $C-H \cdots \pi$ or $C-H \cdots C-H$ that are prone to conditioning and reinforcing the packing motif.

4.2. Characterization of a thin film

Since organic semiconductors constitute the active layers of final devices, it is important to also characterize the arrangement within the thin films. Contrarily to XRD measurements of a single crystal or a powder material, which aim the characterization of all Bragg reflections in the 3D space, the analysis of a thin film is centered on the reflection parallel to the substrate. If the thin film possesses an ordered and crystalline arrangement, the XRD will reveal the orientation of the material within it. Knowing the crystal structure of the compound, it is possible to relate the diffraction signal of the film with a lattice plane of the crystal, revealing the preferred orientation (or orientations) of the lattice, as represented in Figure 18.

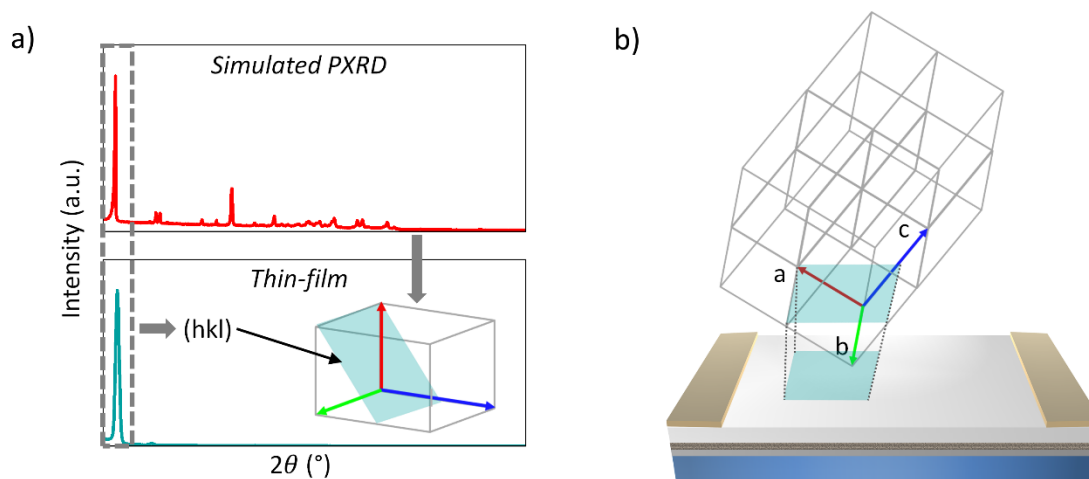


Figure 18. Assignment of the preferred orientation of an organic compound in a thin film: a) PXR simulated from the crystal structure, in which each diffraction is related to a specific lattice plane (above) and the XRD of the thin film displaying a unique preferred orientation (below); b) disposition of the lattice within the thin-film, where the corresponding (hkl) plane is situated parallel to the substrate.

The intensity of the diffractogram is typically related to the degree of order of the material. When comparing the diffractograms of different samples integrating the same compound, a higher intensity is directly associated to a higher degree of order. The comparison of the degree of order between different compounds is not as obvious, since the intensity displayed by the corresponding reflections in the powder samples could highly vary.

In some cases, XRD of thin films using conventional scanning methods only afford weak signals from the film that are eclipsed by those from the substrate. To overcome this problem, the grazing incidence X-ray diffraction (GIXRD) technique can be used instead. This method implies that the measurement is performed at an incident angle lower than the critical angle relative to the surface plane. Hence, the beam does not permeate the thin film as far as the substrate, so the X-ray reflection from the latter is attenuated.

RESULTS AND DISCUSSION

The page features a minimalist design. A thick, dark gray vertical bar runs along the right edge. Two horizontal lines, one thin and one thick, extend from the left margin towards the vertical bar, positioned just below the section header.

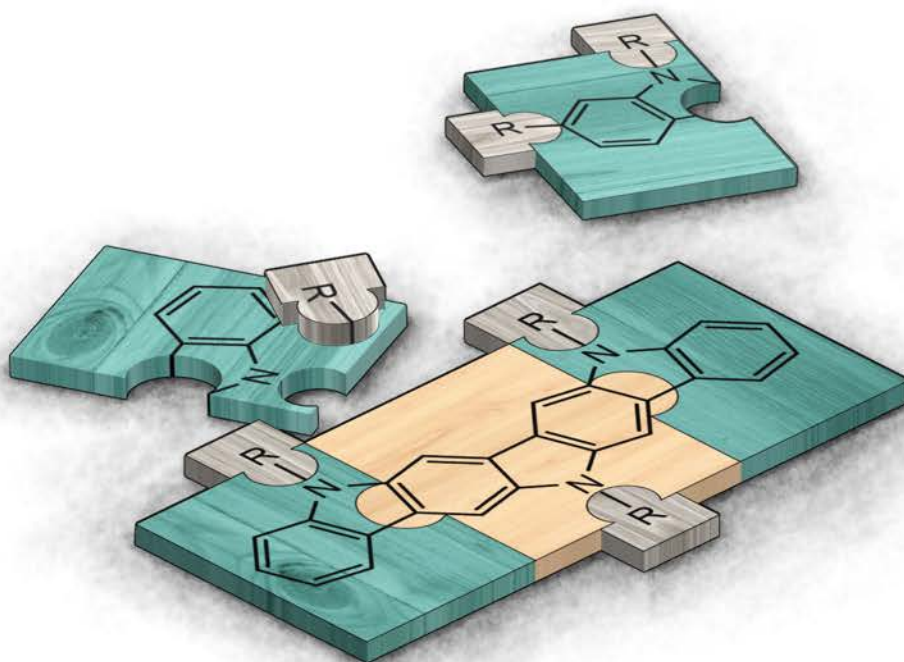
CHAPTER

7

Extending the carbazole heterocycle (I): the diindolocarbazole core

Part of this chapter has been published in:

Acta Cryst. **2022**, *B78*, 253–260.



CHAPTER 1. Extending the carbazole heterocycle (I): the diindolocarbazole core

1.1. Introduction

This first chapter initiates the study of molecular constructions based on the carbazole core with potential semiconductor properties. Indeed, previous studies in our research group have demonstrated the suitability of 9*H*-carbazole as building block.^[122-126] Derived structures featuring more extended systems such as indolo[3,2-*b*]carbazole and diindolo[3,2-*a*:3',2'-*c*]carbazole, best known as triindole, have excelled as p-type semiconductors in organic thin-film transistors.^[124] This does not only apply in terms of charge mobility, but also considering their air and temporal stability. Taking this into account, further investigation of carbazole-based constructions prevailed as an enticing project. The case of the diindolo[3,2-*b*:2',3'-*h*]carbazole core, which is a constitutional isomer of the aforementioned triindole, arose as a plausible and appealing next step in this study. As shown in Figure 1.1, the conversion of triindole into diindolo[3,2-*b*:2',3'-*h*]carbazole **1**, simply referred as diindolocarbazole from now on, implies a structural change from a star-shaped to a ladder-type architecture.

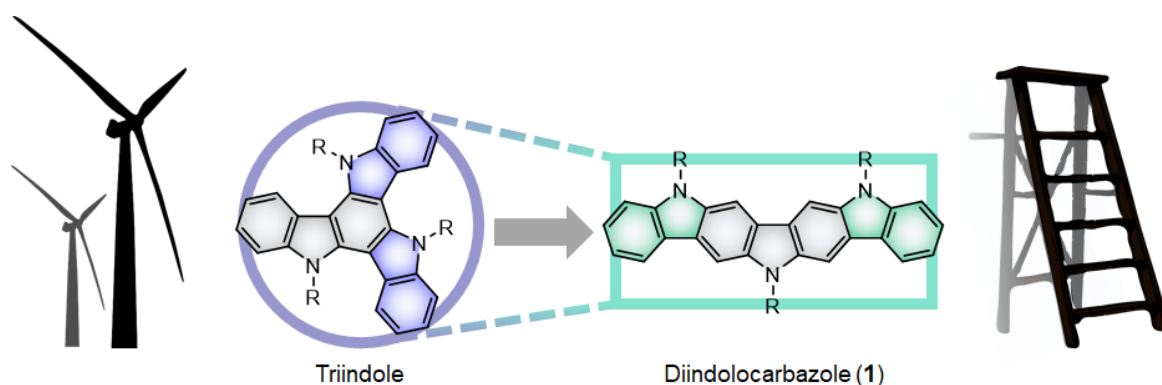


Figure 1.1. Structures of the two examined constitutional isomers of diindolocarbazole: star-shaped diindolo[3,2-*a*:3',2'-*c*]carbazole (triindole) and ladder-type diindolo[3,2-*b*:2',3'-*h*]carbazole (diindolocarbazole **1**). The main carbazole nucleus is highlighted in grey whereas the two indole extensions are highlighted in violet in the former and green in the latter.

Inspired by the outstanding performance of pentacene, the investigation of analogous ladder-type structures has gathered many endeavor within the scientific community.^[127-128] That is, conjugated systems comprised of fused aromatic subunits that are connected linearly through two or more atoms. Contrarily to the wide assortment of

similar ladder-type constructions, however, the case of the diindolocarbazole core still remains surprisingly unexplored. Even though there are a few derivative structures reported in the literature,^[129-133] the information concerning their semiconductor properties is inexistent so far, to the best of our knowledge. Thus, an in-depth study regarding the synthesis, physical characterization and particularly the semiconductor properties of diindolocarbazole-based materials could pave the way towards the settlement of this core in organic electronics.

Regardless of the crucial role of the main aromatic nucleus, other structural factors can be decisive in modulating the semiconductor properties of the material. A prime example is the presence of flexible alkyl chains, which not only enhance the solubility of the material but also exert a great impact on the intermolecular interactions in the solid state.^[24-28] In order to explore the potential of the diindolocarbazole core in this topic, the influence of the alkylation patterning should be also considered in the design.

1.2. Synthesis of the diindolocarbazole core

As aforementioned, there are a few reports on the synthesis of diindolocarbazole-based materials described in the literature. Figure 1.2 collects the most relevant cyclisation reactions for the formation of the carbazole nucleus that have been applied in the synthesis of diindolocarbazole. Leclerc *et al.* pioneered in the synthesis of the diindolocarbazole core in 2004, proposing two distinct strategies towards it. The first approach^[129] culminated with a ring closure through the Cadogan reaction, which is driven by a reductive cyclisation through the nitro group. In this case, two scenarios were contemplated depending on the position of the nitro group (Figure 1.2), which can be situated in the main carbazole nucleus (A) or in the phenyl moiety (B). As stated in the literature, the former procedure was fruitless, whereas the latter required protecting groups in specific positions of carbazole to ensure the formation of the desired regioisomer of diindolocarbazole. Thus, this procedure was remarkably limited and lengthy. In a second work,^[130] they proposed a route incorporating the Ullmann reaction (C), which is a copper-mediated carbon-nitrogen cross-coupling procedure. Even though this synthetic route was equally lengthy, it was successful in the synthesis of *N,N',N''*-trioctyldiindolocarbazole. In fact, it has been employed thereafter in the synthesis of additional derivatives.^[131-132] More recently, Srour *et al.* revised the applicability of the Cadogan reaction *via* method A and described new conditions taking advantage of microwave irradiation for the formation of the main core and different methoxy-containing derivatives.^[132] The resultant synthetic route was considerably more versatile and straightforward than the ones hitherto reported. Thus, it was the one selected to conduct the present study.

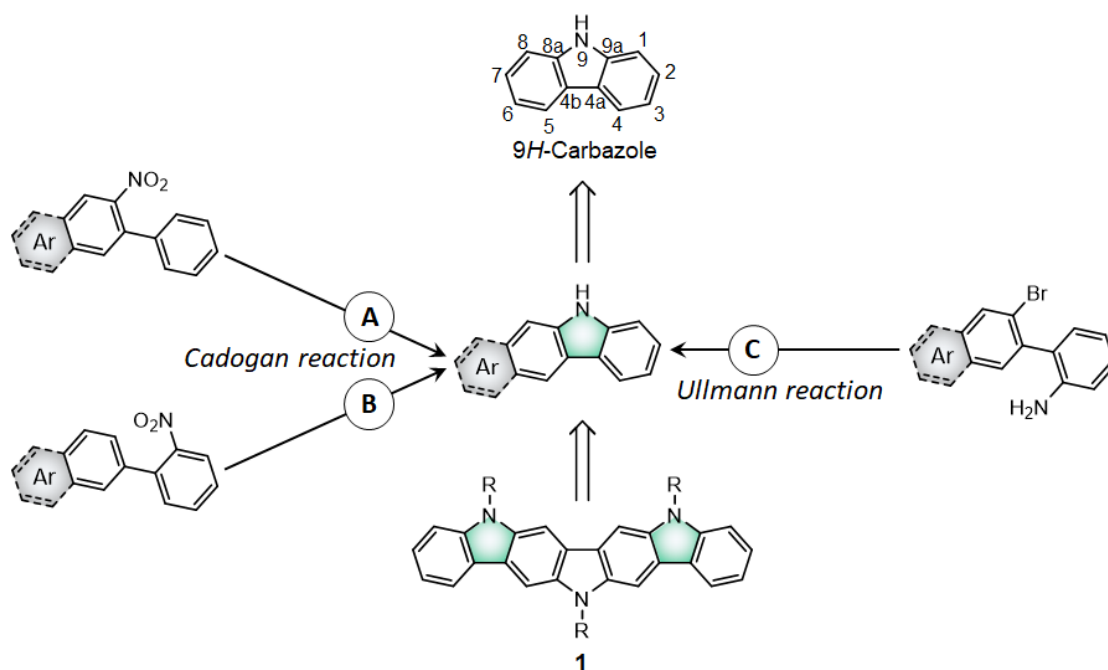


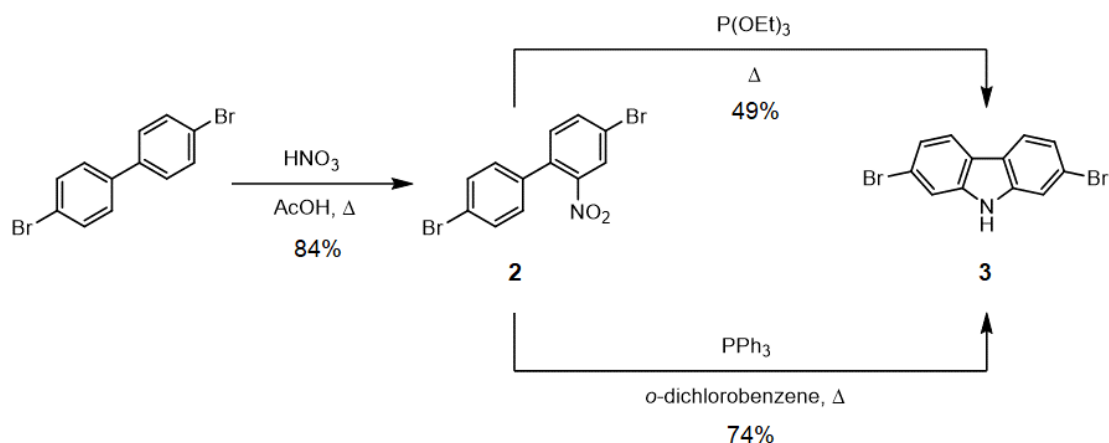
Figure 1.2. Carbazole ring closure towards the construction of the diindolocarbazole core *via* different synthetic approaches: the Cadogan reaction, with the nitro group attached to the central carbazole (A) or to the phenyl moiety (B)^[129] and the Ullmann reaction (C)^[130].

1.2.1. Synthesis through the Cadogan reaction: C-N coupling

This section deals with the synthesis of different diindolocarbazole derivatives utilizing the procedure based on the microwave-assisted Cadogan reaction. The proposed structural variations are focused on evaluating the influence of the alkylation patterning in the solid state arrangement and the performance in final devices.

Synthesis of 2,7-dibromo-9H-carbazole

The synthesis of 2,7-dibromo-9H-carbazole, which stands as an indispensable synthetic building block to construct the diindolocarbazole core, started with the commercially available 4,4'-dibromobiphenyl. Scheme 1.1 depicts the formation of 2,7-dibromo-9H-carbazole, which is likewise based on the Cadogan reaction. The mononitration of 4,4'-dibromobiphenyl employing fuming nitric acid in glacial acetic acid as solvent led to the intermediate **2** in a yield of 84%. The subsequent cyclization was tested using two reported conditions. The first one, involving the use of triethyl phosphite as both reducing agent and solvent,^[134] provided compound **3** in a yield of 49% after 20 hours. The second one, in which triphenylphosphine performed as the reducing agent in *o*-dichlorobenzene as solvent,^[135] certainly implied further advantages. In addition to an easier purification process, the yield increased to a 74% and the reaction time was reduced to only 5 hours.



Scheme 1.1. Preparation of the synthetic building block 2,7-dibromo-9H-carbazole (**3**).

***N*-alkylated diindolocarbazole derivatives**

As a first synthetic goal, five diindolocarbazole derivatives featuring distinct *N*-alkylation patternings were considered, as shown in Figure 1.3.

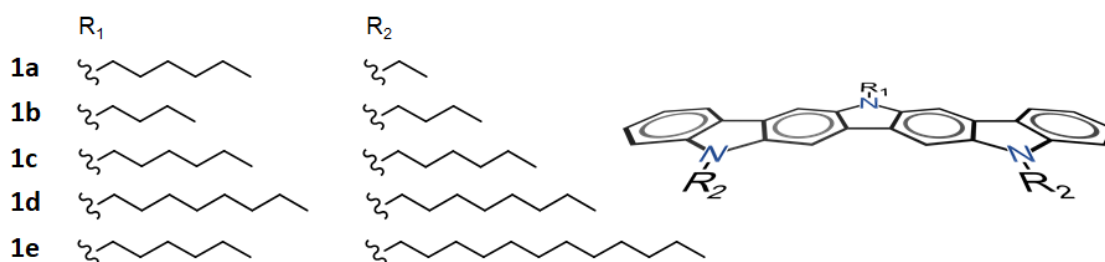
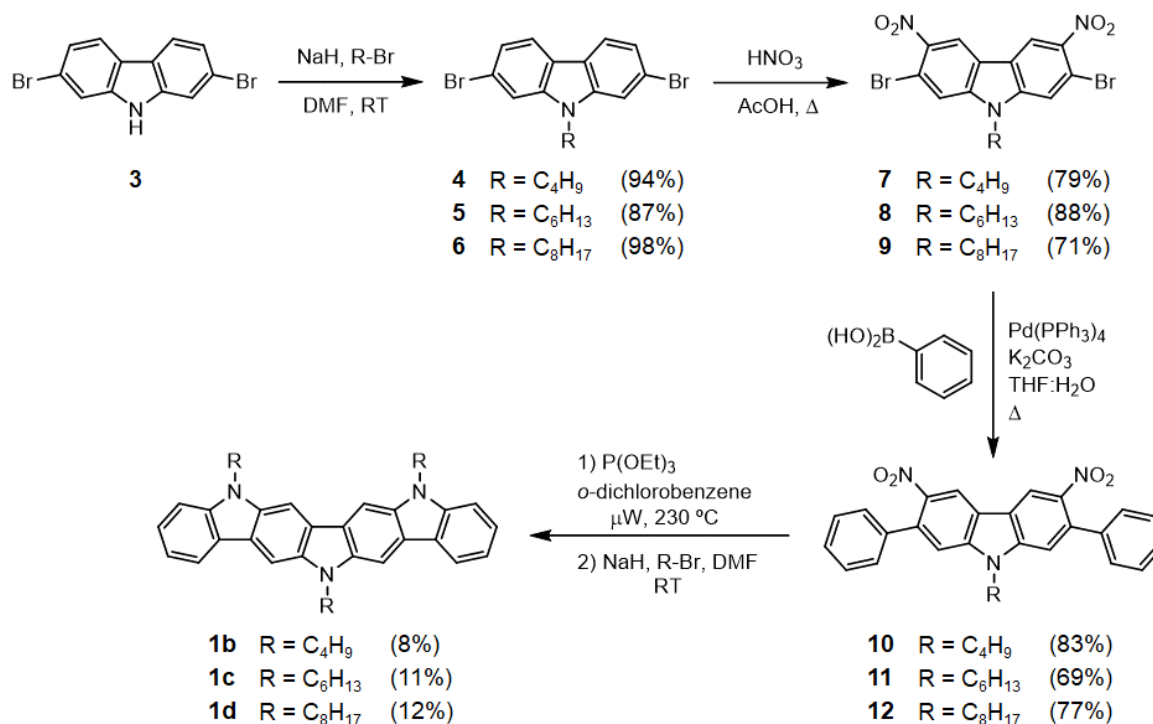


Figure 1.3. Alkylation patterning of the five targeted *N*-alkylated diindolocarbazole derivatives.

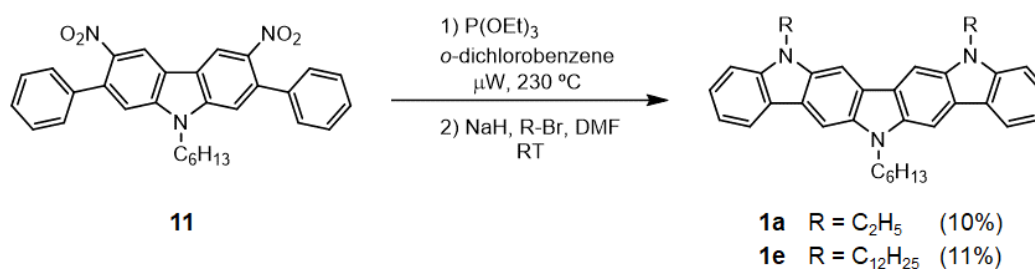
The diindolocarbazole nucleus possesses three nitrogens that can be alkylated, one corresponding to the central carbazole and the other two in the respective indole extensions. Specifically, three of the targeted systems display a homogeneous substitution patterning, namely tributyl- (**1b**), trihexyl- (**1c**) and trioctyl- (**1d**), whereas the other two maintain the hexyl chain on the central carbazole while the peripheral indoles feature either shorter ethyl (**1a**) or longer dodecyl (**1e**) chains. The synthesis of the homogeneously substituted compounds **1b–d** is described in Scheme 1.2. The alkylation of 2,7-dibromo-9H-carbazole was conducted with sodium hydride as base and the corresponding 1-bromoalkane in DMF as solvent. The alkylated compounds **4–6** were obtained in excellent yields around 90%. Subsequently, positions 3 and 6 of the carbazole ring were nitrated using fuming nitric acid in glacial acetic acid under reflux, providing intermediates **7–9** in yields ranging from 71 to 88%. The attachment of the phenyl moieties towards derivatives **10–12** was achieved in similarly high yields (from 69 to 83%) through the Suzuki-Miyaura cross-coupling reaction^[136], utilizing phenylboronic acid, Pd(PPh₃)₄ as catalyst and K₂CO₃ as

base in a mixture of THF and water (6:1 v/v) under reflux. As stated, the cyclisation was carried out *via* the Cadogan reaction, using triethyl phosphite as reducing agent in *o*-dichlorobenzene under microwave irradiation for 2 hours. The final alkylation was performed directly on the resulting precipitate, using analogous conditions to the ones described for the synthesis of **4-6**. Due to the severe insolubility of the non-alkylated intermediates, the alkylation was carried out without any in-between purification. The yields comprising both the cyclisation and the alkylation processes went from 8 to 12%.



Scheme 1.2. Synthesis of the homogeneously *N*-alkylated diindolocarbazole derivatives **1b-d**.

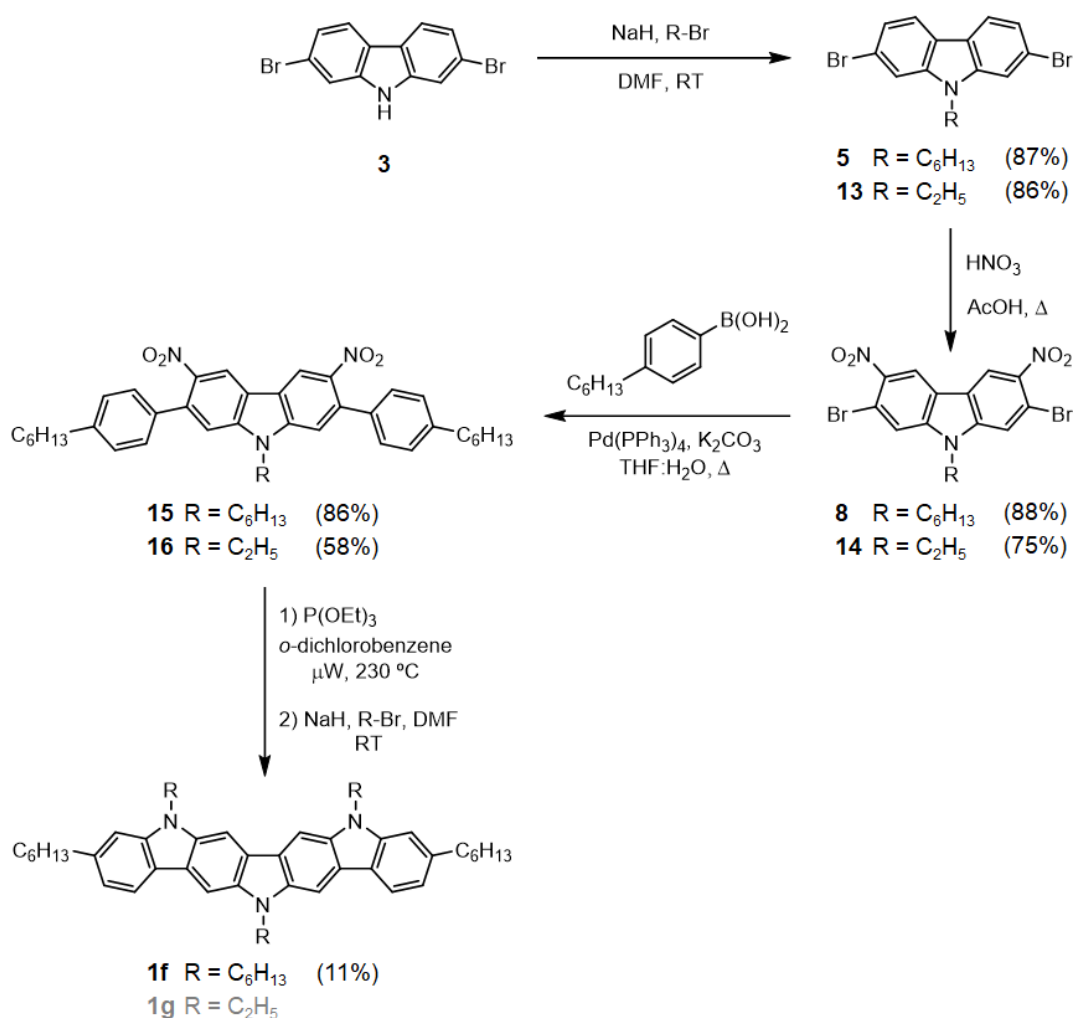
On the other hand, the preparation of the heterogeneously substituted derivatives **1a** and **1e** was achieved from the hexylated intermediate **11**. As described in Scheme 1.3, the cyclisation and posterior alkylation with bromoethane or 1-bromododecane provided derivatives **1a** and **1e**, respectively. The yields are consonant with those of **1b-d**.



Scheme 1.3. Synthesis of the heterogeneously *N*-alkylated diindolocarbazole derivatives **1a** and **1e** from the hexylated intermediate **11**.

Addition of peripheral chains to diindolocarbazole

Another interesting point of study was the tailoring of the alkylation patterning beyond the *N*-alkyl chains. An easy modification was the attachment of peripheral alkyl chains to the aromatic nucleus in a head-tail fashion. In order to evaluate the effects of such addition, the inclusion of two peripheral hexyl chains to the structure of the hexylated derivative **1c** was considered, resulting into the pentahexylated derivative **1f**. Besides, an analog derivative **1g**, possessing shorter *N*-ethyl chains, was envisioned to accentuate the influence of the peripheral chains. The followed route, shown in Scheme 1.4, is analogous to the one employed for the synthesis of the other derivatives.



Scheme 1.4. Synthetic route towards the diindolocarbazole derivatives **1f** and **1g**, featuring peripheral hexyl chains.

The alkylation with bromoethane and the subsequent dinitration, with yields of 86 and 75%, respectively, provided the ethylated intermediate **14**, whereas the synthesis of **8** has been already described. The inclusion of the peripheral hexyl chains was attained by

substituting the phenylboronic acid for 4-hexylphenylboronic acid in the Suzuki reaction, which supplied compounds **15** and **16** in a yield of 86 and 58%, respectively. The final cyclization and hexylation provided derivative **1f** in a comparable yield of 11%. Unfortunately, this synthetic procedure was unsuccessful in the case of the ethylated derivative. In fact, the formation of the tributylated derivative **1b** was already hampered with a lower yield, anticipating the synthetic difficulty regarding the shortest *N*-alkyl chains. As reported in the literature, the formation of higher heteroacenes was also limited employing these conditions, which was attributed to the lack of solubility of the reagents.^[133] Apparently, not even the addition of peripheral hexyl chains was enough to evade this solubility limitation in the case of **1g**. It should be mentioned that the consumption of the starting material was observed in all the cases, implying the formation of numerous by-products in which **1g** was not detected.

1.2.2. Synthesis through the oxidative cyclisation: C-C coupling

The successful synthesis of the diindolocarbazole derivatives **1a–f** reinforced the viability of the procedure based on the microwave-assisted Cadogan reaction. However, the investigation of alternative synthetic strategies that could broaden the range of available structural modifications was equally engaging. Being a relatively unstudied core, the search of more accessible synthetic pathways might result into an innovational advance towards its implementation in the field. Thus, a more synthetically conducted research about this core was considered as a parallel study in this chapter.

The formation of the carbazole heterocycle was surveyed as an initial and simpler approach towards more complex systems like diindolocarbazole. According to the literature, it can be achieved from numerous and diverse methodologies apart from the ones already stated.^[137] However, most of them would be exceedingly difficult to adapt for the synthesis of carbazole-based constructions with large aromatic extensions. Specifically, we prioritized the options that implied versatile and accessible synthetic precursors and had the potential robustness to work with different target compounds. Taking this into account, we considered a promising method as an alternative to the consolidated Cadogan reaction, namely the cyclisation *via* an oxidative palladium-mediated coupling (method D depicted in Figure 1.4). This synthetic method could also open the door to the construction of different carbazole-based structures. The envisioned route implies an even more straightforward synthesis than the one based on the Cadogan ring closure, starting from the commercially available 3,6-dibromo-9*H*-carbazole. Since the Cadogan reaction could not provide derivatives possessing short *N*-alkyl chains like ethyl, it was attempted employing this procedure. The synthesis of the trihexylated **1c** was also tested with this route for comparison.

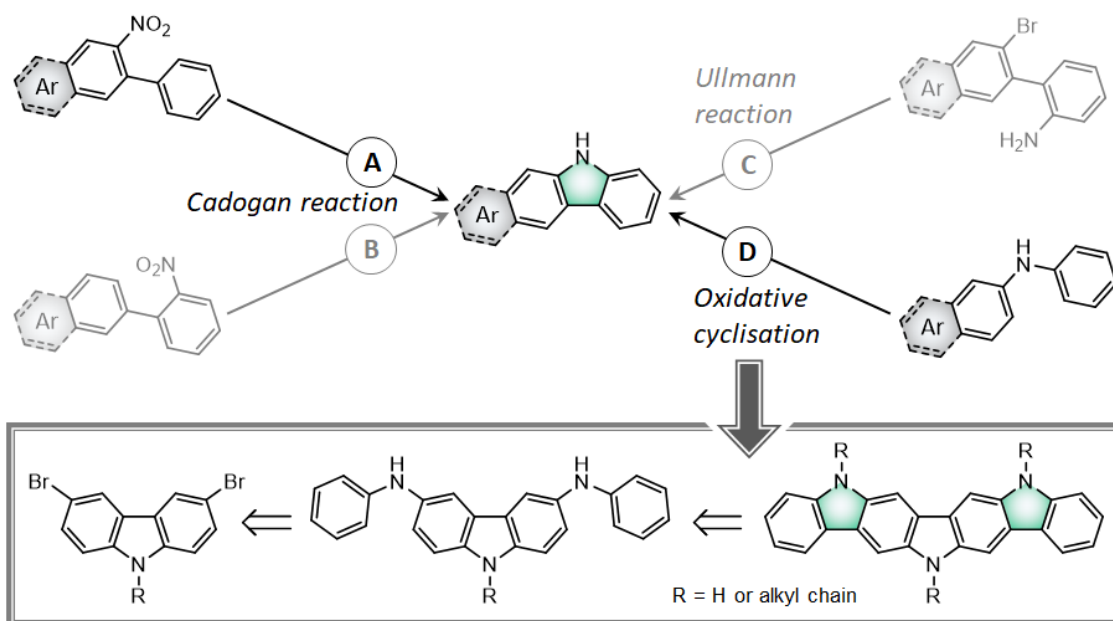
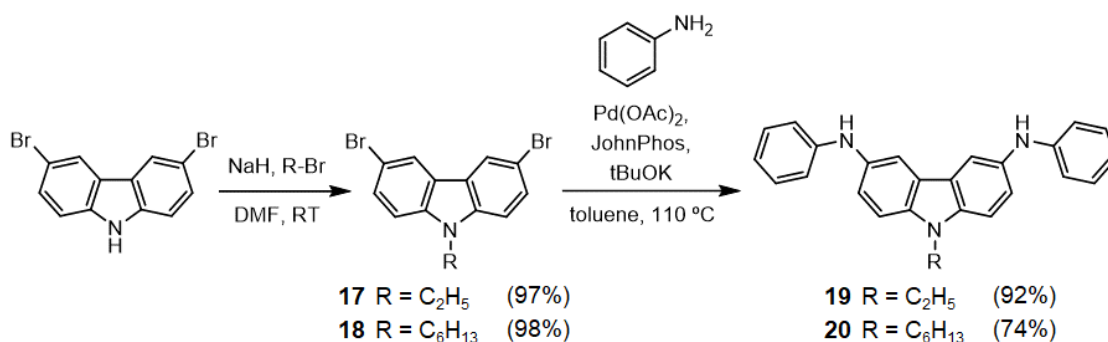


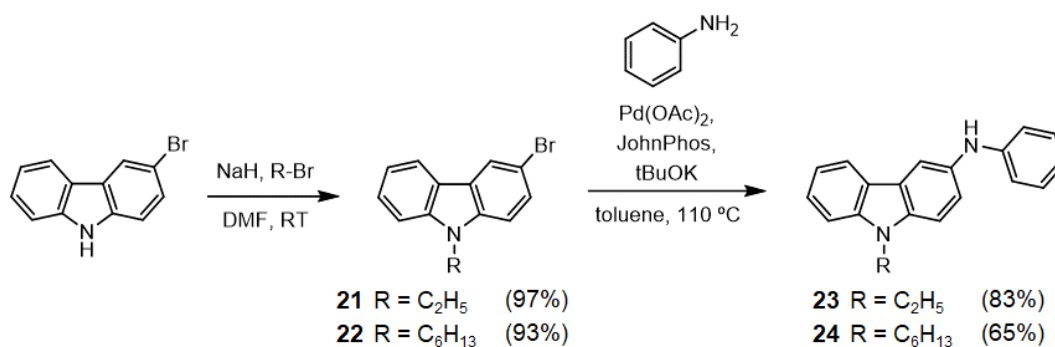
Figure 1.4. Carbazole ring closure towards the construction of the diindolocarbazole core *via* different synthetic approaches, highlighting the method employed to furnish derivatives **1a-f** (A) and the one proposed in this section, based on a carbon-carbon oxidative coupling (D). The corresponding retrosynthesis is also depicted.

As shown in Scheme 1.5, the alkylation of 3,6-dibromo-9*H*-carbazole was performed employing either bromoethane or 1-bromohexane to afford compounds **17** and **18** in excellent yields of 97 and 98%, respectively, under standard conditions. The next step was based on the attachment of aniline through the Buchwald-Hartwig reaction to form compounds **19** and **20**. For this, we pondered among several reported protocols which combined different bases, ligands, solvents and heating conditions.^[138-142] Seemingly, one of the most appropriate protocols was the one reported by Shaya *et al.* featuring Pd(OAc)₂ as catalyst, JohnPhos as ligand and potassium *tert*-butoxide as base in toluene under microwave irradiation.^[138] We tested these conditions in the synthesis of the hexylated compound **20** both under microwave irradiation and conventional heating in an oil bath. Both methods were successful in affording the desired compound in similar yields, i.e. 69% for the former and 74% for the latter. Even though the reaction under microwave irradiation required substantially less time to complete than under conventional heating (1 hour vs. up to 15 hours), the reaction was difficult to scale up and the involved by-products made the purification process rather complex. Thus, all the subsequent reactions were carried out at 110 °C under conventional heating, yielding both the *N*-ethylated (**19**) and the *N*-hexylated (**20**) derivatives (Scheme 1.5).



Scheme 1.5. Synthesis of the disubstituted intermediates **19** and **20**.

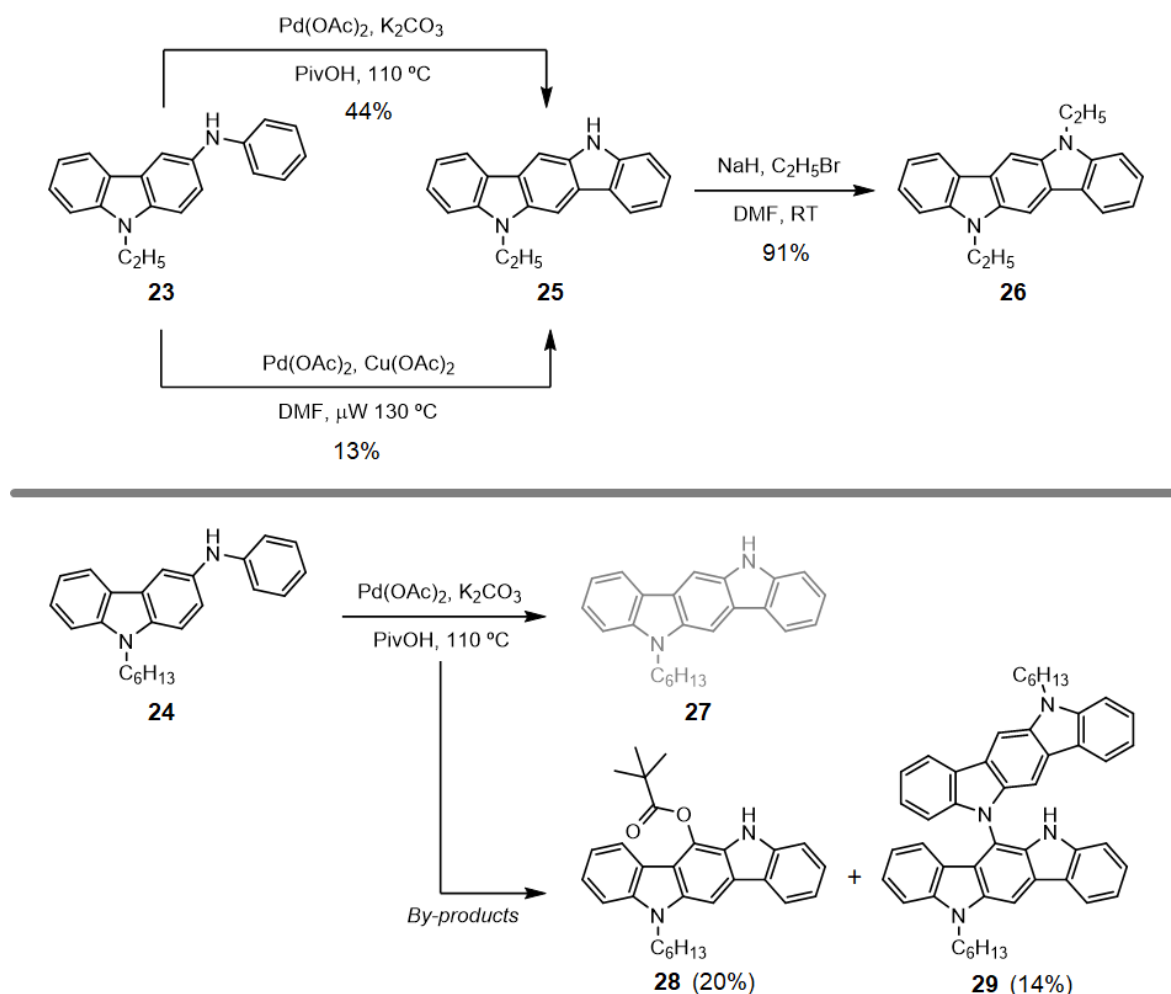
In the case of **19**, these conditions provided an even higher yield of 92%. Regarding the oxidative cyclisation step, we found two alternative Pd(II)-catalyzed procedures for the construction of the carbazole ring, namely acid-mediated^[143–144] and acid-free conditions^[145]. Nevertheless, the synthesis of more extended systems was scarce. The only reported examples implying a twofold reaction were the formation of some derivatives of indolo[3,2-*a*]carbazole through the acid-mediated protocol.^[146] Unfortunately, our first attempts in furnishing the cyclized compounds were fruitless, so we decided to test the coupling conditions on a less complex system to ensure their viability and scope. For this purpose, we synthesized the monoaminated analogs **23** and **24** following the same conditions, as shown in Scheme 1.6. The yields obtained in the Buchwald-Hartwig reaction, with values of 83 and 65% for **23** and **24**, respectively, were equally promising. As observed, the ethylated derivatives provided the highest yields in both cases.



Scheme 1.6. Synthesis of the monosubstituted intermediates **23** and **24**.

The oxidative coupling in the monosubstituted structure **23** was finally successful in affording the desired cyclized product **25** using both conditions, as represented in Scheme 1.7. The acid-mediated coupling, employing catalytic amounts of Pd(OAc)₂ and K₂CO₃ in pivalic acid at 110 °C and air as the terminal oxidant, provided **25** in a satisfactory yield of 44%. Regarding the acid-free conditions, they were carried out under microwave irradiation at 130 °C with Pd(OAc)₂ as catalyst and Cu(OAc)₂ as the terminal oxidant in DMF.

The latter conditions proved less convenient for this coupling, resulting in a lower yield of 13% and a more tedious purification process, so they were discarded. The alkylation of compound **25** under standard conditions yielded the *N*-diethylated indolo[3,2-*b*]carbazole **26** in a 91%. Contrarily, the cyclization of the hexylated counterpart **24** was seemingly more prone in undergoing additional couplings and the targeted product **27** was not obtained. Instead, two main by-products were formed, which were proposed as the structures **28** and **29** shown in Scheme 1.7 based on of their ¹H NMR and MS spectra.



Scheme 1.7. Oxidative coupling of the monoaminated compounds **23** and **24**, affording the targeted compound **25** in the former and by-products **28** and **29** in the latter.

As reported, the use of pivalic acid instead of the hitherto conventional acetic acid drastically reduces the formation of undesired by-products.^[143] However, the inclusion of pivalic acid observed in **28** was also reported as a minor side reaction in the synthesis of mukonine, a carbazole-based alkaloid. On the other hand, an example of the unusual C-N coupling observed in **29** was reported for the reaction of 3-methoxy-9*H*-carbazole using acetic acid as solvent. In the case of **24**, not even the choice of pivalic acid could prevent

the formation of by-products **28** and **29** in a yield of 20 and 14%, respectively. Nevertheless, the occurrence of such unusual C-O and C-N couplings using air as an oxidant could be interesting from a synthetic point of view.^[143] The *N*-ethylated counterparts of **28** and **29** were also detected in the synthesis of **25** as minor by-products.

Taking this information into account, the twofold cyclization of **19** and **20** in pivalic acid was analyzed again. We could determine that in this case the inclusion of pivalic acid occurred before the cyclisation process, impeding the formation of the desired products. Thus, the synthetic studies regarding the oxidative coupling reaction were not continued. The effective synthesis of derivative **25**, however, provides a way to obtain asymmetrically substituted derivatives of the indolo[3,2-*b*]carbazole core. Despite the various well-established synthetic procedures described to obtain this nucleus,^[147] this is the first one that permits an easy and straightforward asymmetric substitution, to the best of our knowledge. Considering the relevant optoelectronic and biological properties of the indolo[3,2-*b*]carbazole scaffold,^[147] this synthetic approach could be a valuable resource for the design of new materials. Not only that, but the aniline-containing intermediates **19–20** and **23–24**, being carbazole-based constructions possessing electro-donating moieties, are interesting candidates to be studied as blue-emitting fluorophores.

1.3. Characterization of the organic materials

1.3.1. Aniline-containing intermediates

As anticipated, the aniline-containing intermediates were surveyed in terms of fluorescent behavior. In fact, another aspect evidenced their potential as blue emitters during the synthetic process. Qualitatively, the emission intensity of these compounds in solution seemed to be relatively affected by the type of solvent. In order to further investigate this, the photophysical characterization was performed in various solvents. Specifically, Table 1.1 collects the fluorescent properties of the *N*-ethylated derivatives **19** and **23**, selected as representatives, in a set of five solvents of different nature. The proposed solvents cover a wide range of polarities and include protic and aprotic examples. As observed, the wavelength of maximum emission ($\lambda_{em,max}$) and the fluorescence quantum yield (Φ_f) of compounds **23** and **19** proved to be slightly conditioned by the solvent in the first four selected ones of Table 1.1. In fact, their emission spectra suffered an expected shift to the red from the least polar solvent, i.e. cyclohexane, to the other ones. The choice of a protic solvent like 1-butanol did not provide a significant effect either. The emission spectra of both compounds in all the solvents tested are represented in Figure 1.5. Regarding the Φ_f ,

it displays slightly higher values in the mono-substituted **23** (ca. 0.17–0.22) than in the di-substituted **19** (ca. 0.12–0.18).

Table 1.1. Optical characteristics of the mono-substituted **23** and the di-substituted **19** compounds recorded in different solvents.

Solvent ^[a]	Compound 23		Compound 19	
	$\lambda_{em,max}$ ^[b] (nm)	Φ_f ^[c]	$\lambda_{em,max}$ ^[b] (nm)	Φ_f ^[c]
CH	398	0.20	418	0.18
DCM	416	0.17	430	0.12
ACN	426	0.21	426	0.15
BuOH	426	0.22	434	0.16
DMSO	434	0.46	442	0.35

[a] Solvents: cyclohexane (CH), dichloromethane (DCM), acetonitrile (ACN), 1-butanol (BuOH) and dimethyl sulfoxide (DMSO). [b] Wavelength of maximum emission ($\lambda_{em,max}$). The emission spectra were recorded after excitation at 300 nm. [c] Fluorescence quantum yields (Φ_f), determined using POPOP as standard.

The most prominent change was found in DMSO, which afforded considerably higher Φ_f values of 0.46 and 0.35 in the case of **23** and **19**, respectively. This implies an almost 3-fold increase with respect to the values registered in the other solvents. The switch from cyclohexane to DMSO in compounds **23** and **19** implied a global red-shift of the $\lambda_{em,max}$ up to 36 and 24 nm, respectively.

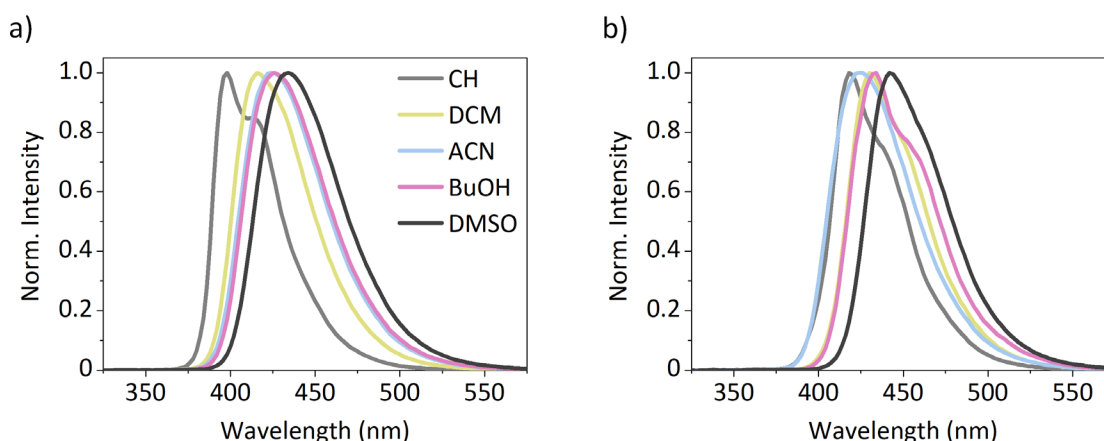


Figure 1.5. Emission spectra of the ethylated derivatives in different solvents: a) the monosubstituted **23** and b) the disubstituted **19**.

It should be noted that the *N*-aniline moiety endows the core with σ bonds where the system can freely rotate. The divergent Φ_f values exhibited in DMSO could be derived from an effective restriction of the intramolecular rotations due to its high viscosity and polarity, enhancing the fluorescence. Indeed, the development of rotor-like materials in which the

fluorescence depends on the medium viscosity represents a topic of study with numerous applications in different fields.^[148–149]

1.3.2. Diindolocarbazole derivatives

Thermal and photophysical properties

The thermal characterization and the photophysical properties in dichloromethane and in the solid state of derivatives **1a–f** and are presented in Table 1.2. The properties of *N*-trihexyltriindole (THT) are also compiled for comparison between the star-shaped and the ladder-type structures of the two constitutional isomers.

Table 1.2. Thermal and photophysical characteristics of the diindolocarbazole derivatives **1a–f** and *N*-trihexyl triindole (THT).

	Thermal properties		Photophysical properties ^[e]				
	T_m ^[a] (°C)	T_d ^[b] (°C)	Solution			Solid state	
			$\lambda_{abs,max}$ (nm)	$\lambda_{em,max}$ (nm)	Φ_f	$\lambda_{abs,max}$ (nm)	$\lambda_{em,max}$ (nm)
THT ^[122]	(-) ^[c]	424 ^[d]	318	395	0.19		
1a	268	329	378	473, 505 _(sh)	0.16	353, 480	494
1b	258	362	378	474, 506 _(sh)	0.15	357, 478	492
1c	170	412	378	474, 506 _(sh)	0.14	358, 477	496
1d	163	416	378	474, 506 _(sh)	0.14	357, 481	468, 500 _(sh)
1e	111	386	378	473, 506 _(sh)	0.16		
1f	170	383	383	468, 501 _(sh)	0.18		

[a] Melting point (T_m) obtained from DSC at a scan rate of 10 °C min⁻¹. [b] Decomposition temperature (T_d) obtained from TGA (5% weight loss) at a heating rate of 10 °C min⁻¹. [c] Not available. [d] Onset decomposition temperature obtained from TGA at a heating rate of 20 °C min⁻¹ from reference 122. [e] Wavelengths of maximum absorption ($\lambda_{abs,max}$) and emission ($\lambda_{em,max}$), with the shoulder peaks indicated as (sh). The emission spectra in dichloromethane were recorded after excitation at 300 nm. The spectra in the solid state were measured after excitation at 350 nm in vacuum-evaporated thin-films of 75 nm deposited over quartz. Fluorescence quantum yields (Φ_f) were determined using POPOP as standard.

As observed, the characteristics of the diindolo[3,2-*b*:2',3'-*h*]carbazole core govern the photophysical properties of derivatives **1a–e** in solution, whereas the impact of the *N*-alkyl chains is not relevant. The attachment of two additional peripheral hexyl chains in derivative **1f**, on the contrary, induces slight shifts in the wavelengths of both the absorption and emission spectra with respect to **1a–e**. For instance, the emission of **1f** peaks at 468 and 501 nm, whereas those of **1a–e** peak at 473 and 506 nm. Therefore, the emission of the diindolocarbazole core is placed into the blue-green region of the visible spectrum, which contrasts with the UV-blue emission of triindole. The fluorescence quantum yields of **1**-based derivatives display similar values to THT, ranging from 0.14 to

0.16 and a slightly higher value of 0.18 in the case of **1f**. On the other hand, the effect of the *N*-alkyl chains becomes substantial in the solid state. The absorption and emission spectra in solution and in the solid state are shown in Figure 1.6. The measurements were performed on vacuum-deposited thin-films of 75 nm over quartz. Whereas the absorption spectra are very similar, the length of the *N*-alkyl chains determines the emission profiles. The longer *N*-alkyl chains, the more similar becomes the emission spectrum in the solid state with respect to that in solution. The broadening of the emission band to the red region due to the formation of aggregates in the solid state is especially notable in the case of **1a**, i.e. the derivative featuring the overall shortest *N*-alkyl chains. Even though the fluorescence quantum yields in the solid state could not be quantified, the intensity was seemingly higher for derivatives featuring longer alkyl chains. A more aliphatic contribution seemingly mitigates the aggregation and subsequent quenching of the fluorescence in the solid state generally seen in organic materials.

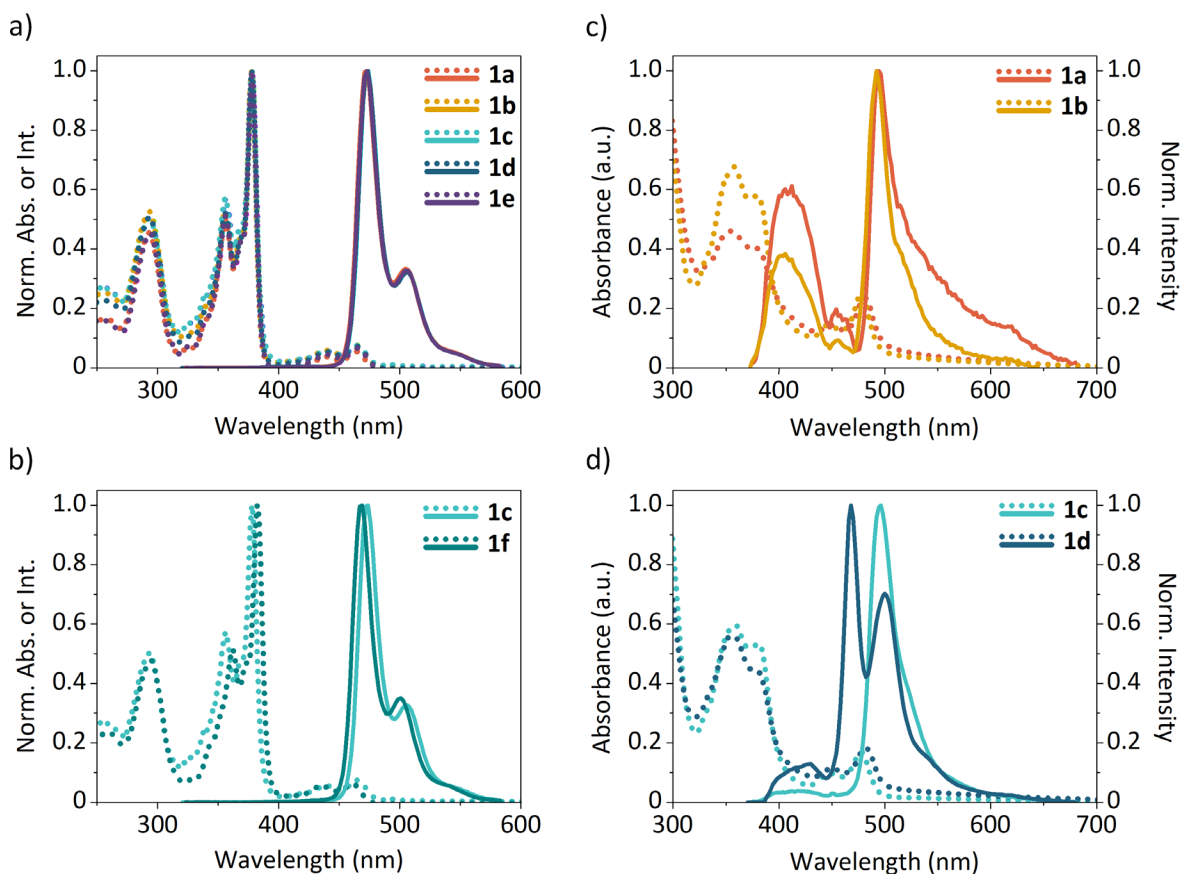


Figure 1.6. Absorption (dotted lines) and emission (solid lines) spectra of the diindolocarbazole derivatives: a) **1a–e** and b) **1c** and **1f** in solution; c) **1a–b** and d) **1c–d** in the solid state.

Regarding the thermal properties, all derivatives presented good thermal stability with decomposition temperatures (T_d) higher than 320 °C, which are convenient for their vacuum-deposition. The TGA scans of all derivatives are represented in Figure A1.1 of the

Appendix. As expected, their melting points (T_m) seem to decrease with the elongation of the *N*-alkyl chains, with values from 268 °C to 111 °C corresponding to derivatives **1a** and **1e**, respectively. Curiously, the inclusion of two additional hexyl chains in **1f** does not imply a decrease of the T_m in regard to **1c**, which corresponds to 170 °C in both cases.

Electrochemical properties

The electrochemical characterization of derivatives **1a–f** is compiled in Table 1.3. The properties of the constitutional isomer THT are also listed for comparison.

Table 1.3. Electrochemical characterization of the diindolocarbazole derivatives **1a–f**.

Compound	$\lambda_{\text{abs,onset}}$ (nm) ^[a]	$E_{\text{gap}}^{\text{opt}}$ (eV) ^[a]	$E_{\text{onset}}^{\text{ox}}$ (V) ^[b]	IP (eV) ^[c]	EA (eV) ^[d]
THT ^[122]	352	3.52	+0.21	5.60	2.07
1a	479	2.59	-0.004	5.39	2.80
1b	478	2.59	-0.002	5.39	2.80
1c	479	2.59	-0.014	5.38	2.79
1d	479	2.59	+0.001	5.39	2.80
1e	478	2.59	-0.010	5.38	2.79
1f	474	2.62	-0.046	5.34	2.72

[a] Optical energy gap ($E_{\text{gap}}^{\text{opt}}$) estimated from the absorption spectrum ($\lambda_{\text{abs,onset}}$). [b] Onset oxidation potential ($E_{\text{onset}}^{\text{ox}}$) vs. Fc^+/Fc determined from CV in 1 mM solutions in dichloromethane. [c] Ionization potential (IP) estimated as $\text{IP} = E_{\text{onset vs. Fc}^+/\text{Fc}}^{\text{ox}} + 5.39$. [d] Electron affinity (EA) estimated as $\text{EA} = \text{IP} - E_{\text{gap}}^{\text{opt}}$.

Again, the electrochemical characterization of derivatives **1a–e** provides analogous results due to the low impact of the alkyl chains in solution. The cyclic voltammograms of derivatives **1c** and **1f** are collected in Figure 1.7 as representatives. As shown, compounds **1a–f** undergo two reversible oxidation processes. Interestingly, all possess rather low onset oxidation potentials, with resulting HOMO energy levels around -5.39 eV that accurately fit the Au electrode work function (-5.1 eV). The linear extension of the π -system of diindolo[3,2-*b*:2',3'-*h*]carbazole results into a drastic reduction of the optical band gaps ($E_{\text{gap}}^{\text{opt}}$) with respect to the carbazole ring, i.e. 4.1 eV.^[124] The achieved values around 2.59 eV for derivatives **1a–e** and 2.62 eV for **1f** are even lower than that of the triindole core and, at the same time, still ameliorate the exceedingly low value of pentacene (1.85 eV)^[150]. As a result, the balanced energy levels of this set of derivatives are well-suited for their application in optoelectronic devices. In particular, the HOMO energy levels are close to that of Au, making them ideal for hole injection and transport, while also being sufficiently low-lying to grant a substantially long-term stability.^[18,133]

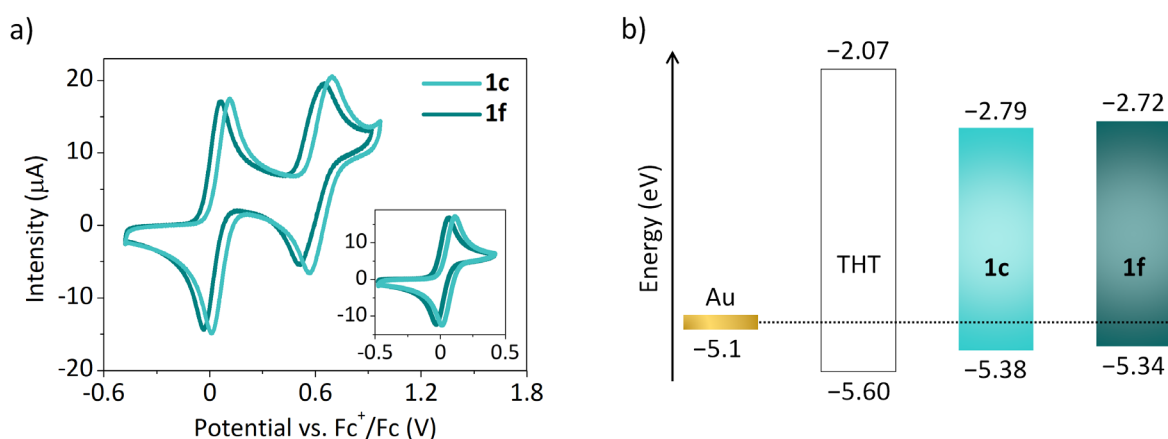


Figure 1.7. Electrochemical characterization: a) cyclic voltammograms of derivatives **1c** and **1f** in dichloromethane, referred to the Fc^+/Fc redox couple (the inset shows only the first oxidation steps); b) schematic representation of the energy levels of *N*-trihexyltriindole (THT), **1c** and **1f** with respect to the gold work function.

1.4. Organic thin-film transistors

The diindolo[3,2-*b*:2',3'-*h*]carbazole derivatives **1a–f** were investigated and characterized as p-type semiconductors in OTFTs. They were tested as vacuum-deposited active layers of 75 nm of thickness in standard bottom gate-top contact devices, using gold as the source and drain electrodes. The effect of two distinct organic dielectric layers recovering the SiO_2 surface was also investigated, namely octadecyltrichlorosilane (OTS) and polystyrene (PS). OTS was chosen as an aliphatic Self-Assembled Monolayer (SAM), whereas PS portrays as an aromatic dielectric polymer. As abovementioned, the evaluation of the stability of the devices also represents a crucial part of this work. Thus, the OTFT characteristics of each set of devices have been measured periodically not only to determine the lifetime of the devices, but also to describe the evolution of the average mobility over time. Table 1.4 collects the data of OTFTs based on compounds **1a–f** in OTS- and PS-treated devices. Specifically, it contains the maximum mobility obtained for a specific device ($\mu_{h,\text{max}}$) and the maximum average mobility ($\mu_{h,\text{avg}}$) registered for a set of analogous devices. Additionally, the average mobility of the set after approximately a year is also collected to evaluate the air and temporal stability. Globally, the obtained hole mobility values cover three orders of magnitude, from 10^{-6} to $10^{-3} \text{ cm}^2 \text{ V}^{-1} \text{ s}^{-1}$, depending on the alkylation patterning and the nature of the interfacial dielectric. In particular, the highest mobility values were extracted with the tributylated **1b** and the trihexylated **1c**, both featuring short-to-medium homogeneous *N*-alkyl chains. In fact, **1b** provided the highest mobility of all OTS-treated devices with a value of $1.1 \times 10^{-3} \text{ cm}^2 \text{ V}^{-1} \text{ s}^{-1}$, whereas it was slightly lower over PS, i.e. $6.7 \times 10^{-4} \text{ cm}^2 \text{ V}^{-1} \text{ s}^{-1}$. The OTFT characteristics of the former are represented in Figure 1.8.

Table 1.4. OTFT hole mobilities of a set of representative devices based on compounds **1a–f** in OTS- and PS-treated substrates, corresponding to the maximum value obtained for a single device and the average mobility of a batch up to 8 devices.

Compd.	SiO ₂ /OTS		SiO ₂ /PS	
	$\mu_{h,max}^{[a]}$ (cm ² V ⁻¹ s ⁻¹)	$\mu_{h,avg}^{[b]}$ (cm ² V ⁻¹ s ⁻¹)	$\mu_{h,max}^{[a]}$ (cm ² V ⁻¹ s ⁻¹)	$\mu_{h,avg}^{[b]}$ (cm ² V ⁻¹ s ⁻¹)
1a	7.8×10^{-5}	6×10^{-5} (6×10^{-5})	1.5×10^{-4}	1×10^{-4} (8×10^{-5})
1b	1.1×10^{-3}	8×10^{-4} (4×10^{-4})	6.7×10^{-4}	5×10^{-4} (3×10^{-4})
1c	1.7×10^{-4}	1×10^{-4} (9×10^{-5})	1.1×10^{-3}	8×10^{-4} (3×10^{-4})
1d	6.3×10^{-5}	6×10^{-5} (2×10^{-5})	2.1×10^{-4}	2×10^{-4} (1×10^{-4})
1e	6.3×10^{-6}	5×10^{-6} (-) ^[c]	4.9×10^{-5}	4×10^{-5} (-) ^[c]
1f	2.1×10^{-4}	2×10^{-4} (1×10^{-5})	7.2×10^{-5}	7×10^{-5} (8×10^{-6}) ^[d]

[a] Maximum hole mobility value for a single device. [b] Maximum average hole mobility value of a set of representative devices collected on the same day. The values in parenthesis correspond to the average mobility registered a year after their fabrication. [c] Not measured. [d] Value after 600 days.

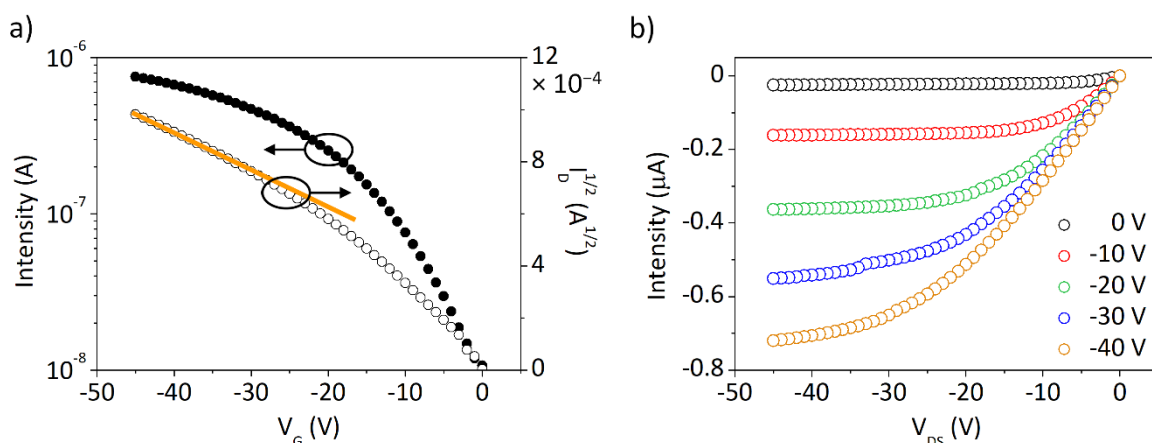


Figure 1.8. OTFT characteristics of a device fabricated with compound **1b** over an OTS-treated substrate, obtained on the day of its fabrication: a) transfer ($V_{DS} = -40$ V) and saturation characteristics; b) output plot at different gate voltages. The colored line in the saturation plot indicates the slope that was used to extract the $\mu_{h,max}$.

Derivative **1c** also outstands with an analogous $\mu_{h,max}$ of 1.1×10^{-3} cm² V⁻¹ s⁻¹, which in this case was registered over PS. The further elongation of the *N*-alkyl chains to the octylated **1d** translates into a descend of the hole mobility, especially over OTS. Indeed, the aliphatic nature of OTS becomes generally unfavorable for this core, since the best results are extracted over PS. Apart from the case of **1b**, this trend is only reversed by accentuating the aliphatic character in the peripheral sides (**1f**).

The heterogeneous alkylation patterning of compounds **1a** and **1e** clearly derives into a decrease of the performance with respect to the homogeneous **1c**, which also features a central *N*-hexyl chain. The shortening of the outer *N*-chains to ethyl in **1a** causes a

substantial downfall of the $\mu_{h,max}$ up to an order of magnitude. The underperformance becomes even more evident with their elongation to dodecyl in **1e**, inducing a 20-fold drop in both dielectrics.

The most noteworthy feature of this core resides in the outstanding temporal and air stability featured by the devices, with a shelf lifetime up to years maintaining a considerably uniform $\mu_{h,avg}$ over time. This prominent asset represents a permanently sought-after characteristic in OTFTs. Indeed, top organic semiconductors like pentacene or TIPS-pentacene fall behind in terms of stability, even when protecting strategies like encapsulation are considered.^[58] Notably, the *N*-alkylation patterning and the organic dielectric modulate the performance of the devices without discrediting their shelf lifetime. Figure 1.9 represents the evolution of the $\mu_{h,avg}$ of the homogeneously substituted derivatives **1b–1d** throughout 900 days. The evolution of derivatives **1a** and **1e** can be found in Figure A1.2 of the Appendix. As observed, OTS-treated devices show their $\mu_{h,max}$ and very consistent $\mu_{h,avg}$ values during the first months after fabrication, with a moderate decline over longer periods of time. On the other hand, the charge mobility values on their PS counterparts tend to reach their maximum several days after their fabrication, stabilizing thereafter in a plateau. Also, the choice of PS implies a superior long-term uniformity of the $\mu_{h,avg}$ and more robustness in front of the *N*-alkylation patterning.

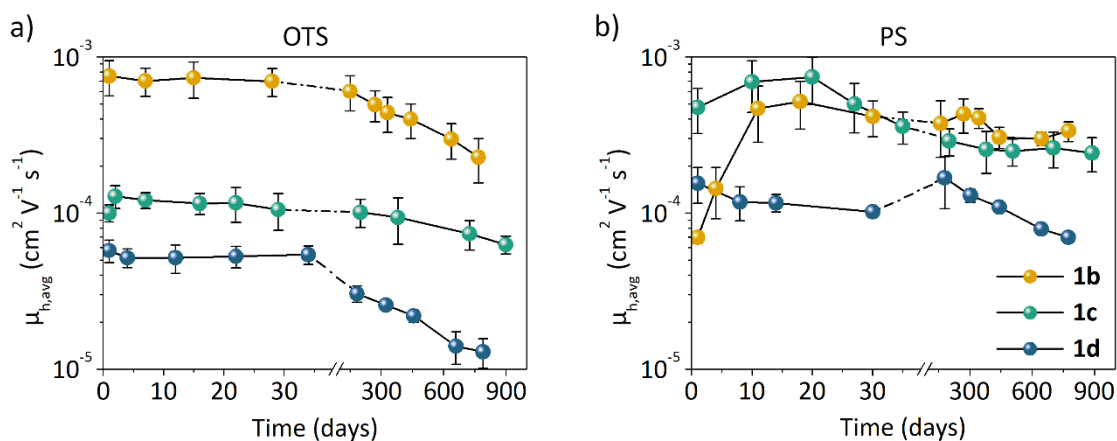


Figure 1.9. Evolution profile of the average hole mobility ($\mu_{h,avg}$) of a set of devices fabricated from compounds **1b**, **1c** and **1d** over: a) OTS and b) PS. The displayed period comprises 900 days starting from the fabrication day.

In fact, the shelf lifetime of this core was demonstrated to be higher than four years with the examples of derivatives **1a** and **1c**, which were the first ones to be tested. A study of such extend has been seldom reported in the literature, proving the potential of these materials. Contrarily, the addition of peripheral chains in **1f** certainly results into a loss of stability. Particularly, the $\mu_{h,avg}$ of **1f** suffers a severe decrease during the first year with both

dielectrics as collected in Table 1.4, whereas the shelf lifetime of the devices does not extend further than two years. A more in-depth discussion of the effect of the peripheral chains in several carbazole-based cores is held in Chapter 3.

All devices tend to exhibit a slight sublinear behavior, i.e. the slope of the extracted μ_h is lower than that of an electrically-equivalent ideal device. In some cases this sublinear behavior accentuates into a hump-like nonlinearity over time. The origin of this particular phenomenon was suggested to be caused from gated Schottky contacts.^[104] Another feature of the studied devices that should be pointed out is the relatively low I_{on}/I_{off} ratios they display. Seemingly, the derivatives that feature longer *N*-alkyl chains (**1d** and **1e**) show the highest I_{on}/I_{off} ratios with values up to 10^3 . This trend was already observed on similar studies regarding different aromatic cores.^[125,151] A more detailed representation of the OTFT characteristics of devices containing derivatives **1a–f** is shown in the Appendix.

The comparison between the diindolocarbazole and triindole cores also comprised a valuable aspect of this study. Overall, the triindole core still outperforms diindolocarbazole to some degree, claiming a $\mu_{h,max}$ of $1 \times 10^{-2} \text{ cm}^2 \text{ V}^{-1} \text{ s}^{-1}$ and an I_{on}/I_{off} ratio of $\sim 10^6$ in the case of the trihexylated derivative over PS-treated devices. Nevertheless, the studied diindolocarbazole derivatives **1a–f** present interestingly high air-stability and early switch-on voltages (as shown in Figure 1.9a). Also, the results in relation to the different alkylation patternings augur certain room of improvement and optimization of the performance of this core.

1.5. Molecular order and disposition in the thin-films

The next stage of this study involves the correlation of the charge transport properties of the diindolocarbazole derivatives with their structural design. As observed, the characterization of the devices has made plain the huge impact of the length of the alkyl chains on the performance of the diindolocarbazole nucleus. In order to shed light on this topic, the analysis of the arrangement of the materials within the films represents an essential information.

1.5.1. Crystallographic study

The elucidation of the single crystal structure of a material grants an insight into its intermolecular arrangement, so it represents a valuable information in organic electronics. Even after considerable attempts regarding all derivatives, however, we could not produce single crystals with the required resolution to define their intermolecular disposition *via* conventional methods. In view of this, we attempted the elucidation of their crystal

structures from Powder X-Ray Diffraction (PXRD). Structure determination from powder diffraction, while by no means routine, has emerged as an alternative option to access crystal structures.^[117] This approach was successful in deciphering the crystal structure of the tributylated derivative **1b**, pioneering as the first reported *N,N,N'*-trialkyldiindolocarbazole construction. **1b** crystallizes in space group *R*-3 of the trigonal system, featuring a high volume unit cell of 12987 Å³ that fits 18 molecules, and dimensions of $a = 52.8790$ Å, $b = 52.8790$ Å, $c = 5.36308$ Å, $\alpha = 90^\circ$, $\beta = 90^\circ$, $\gamma = 120^\circ$ (Figure 1.10).

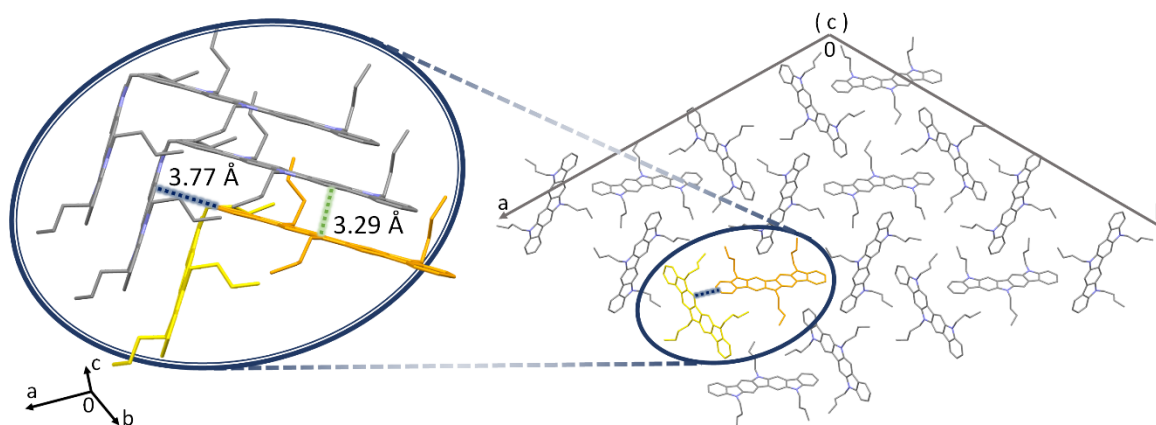


Figure 1.10. Single crystal structures of derivative **1b**, with the cell axes delimiting the unit cells and an amplified region indicating the π - π stacking distance of 3.29 Å through the *c* axis (in green) and the edge-to-face distance of 3.77 Å between stacked columns (in blue).

As observed, **1b** mainly establishes π - π interactions between the aromatic systems of contiguous molecules along the *c* axis, assembling in a slipped parallel fashion. The butyl chains also assist the stacking in this direction with C-H \cdots π interactions. As a result, the shortest π - π stacking distance found corresponds to 3.29 Å, which ensures an adequate overlap and charge transport along the material layers on the basis of the hopping model. Finally, additional C-H \cdots π and aliphatic interactions reinforce the packing of molecules along the plane of the unit cell. Specifically, the edge-to-face C-H \cdots π interactions between molecules belonging to different π -stacked columns feature distances as close as 3.77 Å, which endows the material with a potential alternative mechanism for the hopping of charges.

Apart from **1b**, we could also unravel the crystal structures of derivatives **1a** and **1d** following the same procedure. Their crystal structures are illustrated in Figure 1.11.

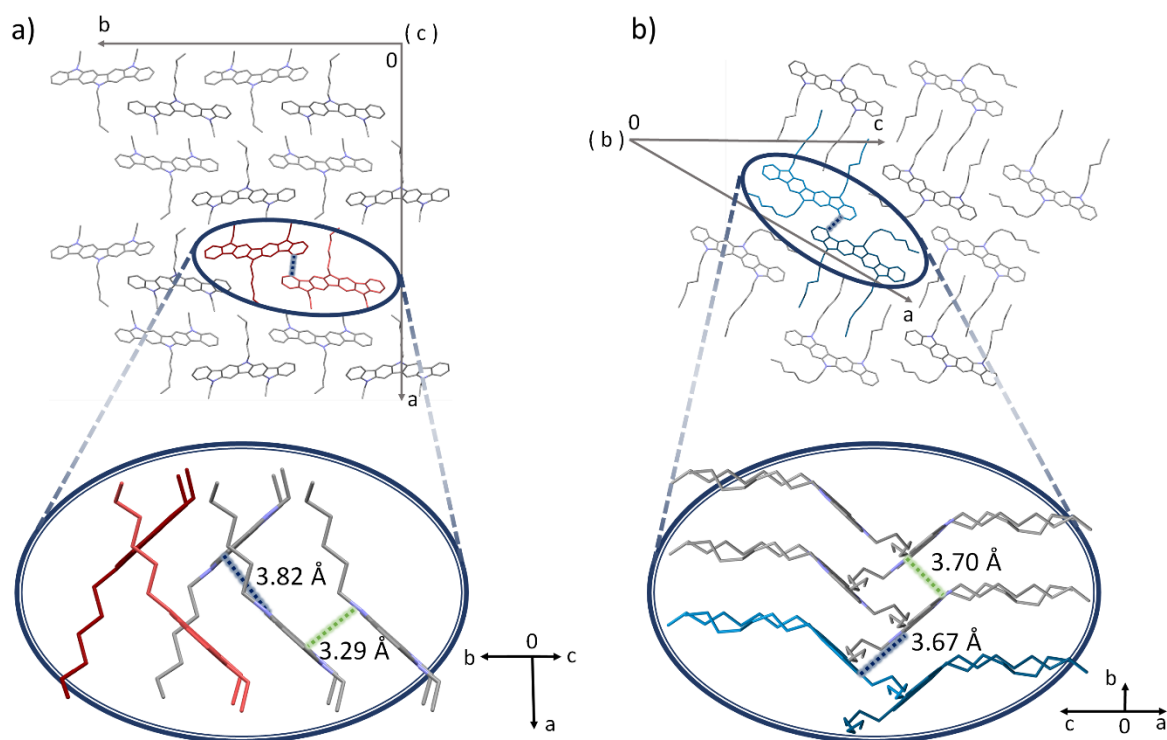


Figure 1.11. Single crystal structures of derivatives: a) **1a** and b) **1d**, with the cell axes delimiting the unit cells and an amplified regions indicating the π - π stacking distances in green (3.29 Å through the c axis in **1a** and 3.70 Å through the b axis in **1d**) and the edge-to-face distances between stacked columns in blue (3.82 Å in **1a** and 3.67 Å in **1d**).

1a crystallizes in space group $Fdd2$ of the orthorhombic system, displaying an also high volume unit cell of 10885 \AA^3 and dimensions of $a = 48.565 \text{ \AA}$, $b = 42.882 \text{ \AA}$, $c = 5.22695 \text{ \AA}$, $\alpha = 90^\circ$, $\beta = 90^\circ$, $\gamma = 90^\circ$ (Figure 1.11a). In general, the disposition of **1a** assimilates to that of **1b**. The arrangement through the shortest c axis also shows a slipped parallel stacking with analogous π - π distances as low as 3.29 Å. In this case, the arrangement along the plane is conditioned by the heterogeneous alkylation of **1a**, with the bulkier hexyl chains intercalated among the π -stacked columns. The edge-to-face distances are slightly higher than in **1b**, i.e. 3.82 Å. **1d** crystallizes in space group $P2_1/c$ of the orthorhombic system, possessing a considerably lower volume unit cell of 4050 \AA^3 ($a = 45.0352 \text{ \AA}$, $b = 4.84267 \text{ \AA}$, $c = 34.8647 \text{ \AA}$, $\alpha = 90^\circ$, $\beta = 32.2^\circ$, $\gamma = 90^\circ$, Figure 1.11b). Despite the similitudes with **1a** and **1b** in regard to the packing through the shortest axis (i.e. the b axis in this case), derivative **1d** possesses greater and less favorable π - π distances of 3.70 Å. Contrarily, the edge-to-face distances are reduced to 3.67 Å. The superior length of the octyl chains emphasizes the presence of aliphatic-predominating regions in the disposition found in the main plane, which could explain the higher I_{on}/I_{off} ratios found in the corresponding devices.^[151]

Overall, the elucidated structures demonstrate the planarity of the diindolocarbazole system, which facilitates the intermolecular overlapping that is sought in organic

electronics. Considering the packing motifs typically seen in polycyclic aromatic hydrocarbons,^[120-121] the arrangement of all three compounds can be associated to a γ type. A γ packing is mainly governed by face-to-face C \cdots C (and C \cdots N in this case) interactions between parallel translated molecules with the support of edge-to-face C-H \cdots π interactions. Contrarily, materials such as pentacene^[152] or indolo[3,2-*b*]carbazole^[124] arrange in a herringbone packing characterized solely by edge-to-face C-H \cdots π interactions. Even though their excellence in organic electronics, the herringbone motif is considered as non-optimal for charge transport because of the generally smaller direct π - π orbital overlap.^[121,153] The elongation of the aromatic system from indolo[3,2-*b*]carbazole to **1** therefore translates into a favorable, more flattened, γ disposition.

1.5.2. GIXRD measurements

The solid-state characterization of the semiconductor layers was achieved by means of Grazing Incidence X-Ray Diffraction (GIXRD). The measurements were performed on vacuum-evaporated films (75 nm of thickness) over OTS- and PS-treated Si/SiO₂ substrates, equivalent to the active layers of the devices. The GIXRD patterns of derivatives **1a-d** and **1f** are shown in Figure 1.12. Compound **1e** has been excluded from this analysis due to its remarkable underperformance in OTFTs.

Compounds **1a-d** exhibit matching profiles in OTS- and PS-treated substrates that only differ in terms of intensity, suggesting that the organic dielectric influences the degree of order within the active layer but not the preferred orientation. All films deposited over OTS exhibit higher intensities, i.e. possess a higher degree of order. This fact is rather unexpected because of the general outperformance of the diindolocarbazole core over PS-treated devices. One plausible explanation could be that the nature of the dielectric alters the charge transport beyond the solid-state organization, implying electronic or structural issues in the interface rather than in the bulk.^[125,154] Once again, these results highlight the special care needed at designing the structure of both the semiconductor material and the device.

The availability of the single crystal structures of **1a**, **1b** and **1d** enabled the indexation of their GIXRD patterns. The diffraction peaks at $2\theta = 7.0$ and 13.9° observed in **1a** films were suggested as the reflection 400 and the complementary 800, respectively, on the basis of the PXRD and the resolved crystal structure. In the case of **1b**, the principal diffraction signal peaking at $2\theta = 7.2^\circ$ was proposed to belong to the reflection 4-20, whereas the peaks of **1d** at $2\theta = 5.1$, 12.8 and 18.2° were assigned to the complementary reflections 202, 505 and 707, respectively.

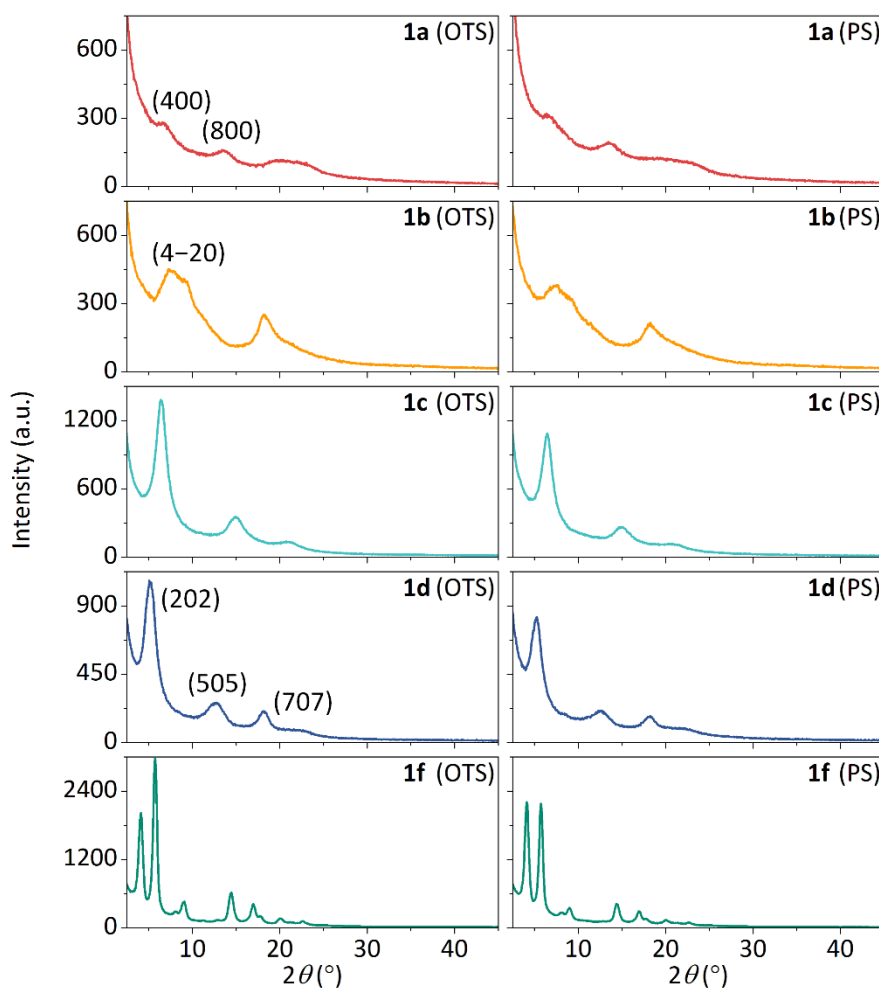


Figure 1.12. Analysis of the solid-state organization: GIXRD patterns corresponding to thin-films (75 nm of thickness) of compounds **1a–d** and **1f** deposited under vacuum over OTS- (left) and PS-treated substrates (right).

This indicates that the planes (400), (4–20) and (202) in **1a**, **1b** and **1d**, respectively, are arranged parallel to the substrate as schematized in Figure 1.13. The π - π stacking directions, which coincide with the *c* axis in structures **1a–b** and the *b* axis in **1d**, are conveniently parallel to the substrate. The proposed dispositions in the thin-films of all three derivatives admit a proper charge transport throughout the semiconductor layers. Nevertheless, the GIXRD of **1a** films stand out due to their exceedingly low degree of order. The underperformance of the heterogeneous **1a** could be associated to the highly disordered or amorphous arrangement within the film. On the other hand, the trioctylated **1d** displays similar $\mu_{h,avg}$ to **1a** despite **1d** features more ordered films. This could be attributed to a poorer π - π overlapping derived from the higher π - π stacking distances (i.e. 3.70 Å) found in the single crystal of **1d**, hampering the transport of charges through the hopping model.

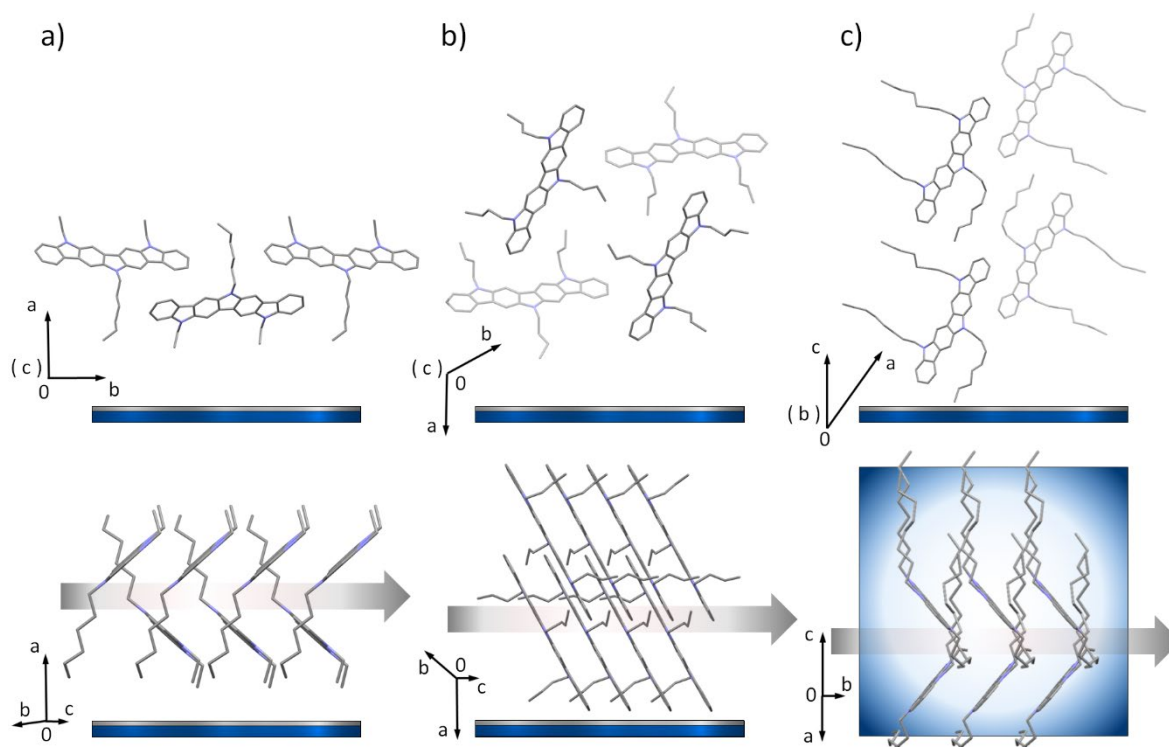


Figure 1.13. Proposed disposition of **1a** (a), **1b** (d) and **1d** (c) within the film from two different perspectives, in accordance to the reflections observed in the GIXRD pattern. The planes (400), (4–20) and (202) are placed parallel to the substrate for **1a**, **1b** and **1d**, respectively. The π - π stacking directions, which are parallel to the substrate, are also indicated. The molecular dispositions depicted for **1a** and **1b** correspond to representative fragments of the unit cells. Hydrogen atoms have been omitted for clarity.

Finally, compound **1f** displays sharper and more intense diffraction peaks with relative intensities that diverge between substrates. In particular, the peak at $2\theta = 5.7^\circ$ has a higher intensity over OTS with respect to the other peaks, something that does not happen over PS. This hints that the outperformance of this derivative over OTS could result from the predominance of a more convenient disposition in it. It is also remarkable that the films of **1f** show several peaks, which could imply the presence of various preferred orientations of the material, justifying the lower performance of **1f** in OTFTs. Unfortunately, the lack of its crystal structure does not permit a more in-depth analysis at this point.

1.6. Conclusions

The microwave-assisted Cadogan reaction permitted the synthesis of five diindolo[3,2-*b*:2',3'-*h*]carbazole derivatives (**1a–e**) featuring alkyl chains with various lengths and patterns. The addition of peripheral hexyl chains was feasible as well, conferring the pentahexylated derivative **1f**. However, the access to derivatives featuring short alkyl chains like ethyl in the central nitrogen is still limited *via* this procedure. Alternatively, the

synthetic investigations of the oxidative cyclisation approach have opened the door to subsequent advances to an even more straightforward route towards this core. Compounds **1a–f** presented adequate photophysical and electrochemical properties for their application as p-type semiconductors, with low IP values that closely match the gold work function. The reported charge mobility values, ranging from 10^{-6} to 10^{-3} $\text{cm}^2 \text{V}^{-1} \text{s}^{-1}$, are highly dependent on the alkylation design and the organic dielectric applied in the SiO_2 /semiconductor interface. Remarkably, a hole mobility as high as 1.1×10^{-3} $\text{cm}^2 \text{V}^{-1} \text{s}^{-1}$ was achieved with the tributylated **1b** over OTS as the organic dielectric and the trihexylated **1c** over PS. The crystal structures, elucidated via PXRD, revealed a convenient γ packing that is accordant with the favorable device performances. In fact, the crystallographic study in conjunction with the GIXRD measures of the thin-films acquainted with the role of the structural design in modulating the device performance. The relationship between the alkylation patterning and the charge mobilities also reveals an appealing outperformance of derivatives possessing short-to-medium and homogeneous *N*-alkyl chains. Overall, the diindolocarbazole core claims a great potential as a hole-transporting semiconductor, supported by its noteworthy air stability and shelf lifetime in OTFT devices, which extends to periods up to several years. This study should therefore usher in the optimization and implementation of this core in organic electronics.

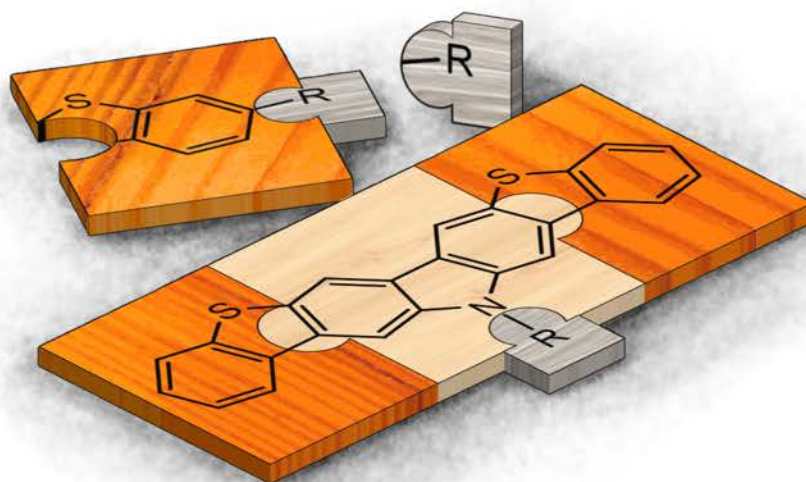
CHAPTER

2

Extending the carbazole heterocycle (II): the bisbenzothienocarbazole core

Part of this chapter has been published in:

Materials, **2021**, *14*, 3487.



CHAPTER 2. Extending the carbazole heterocycle (II): the bisbenzothienocarbazole core

2.1. Introduction

The potential of novel ladder-type constructions has been exemplified in the previous chapter with the study of the diindolocarbazole core. Chapter 2 resumes the investigation of extended structures based on the carbazole heterocycle from a similar approach. Specifically, the fused indole extensions that configure the diindolocarbazole architecture have been replaced with benzothiophene scaffolds. The resulting core, namely 14*H*-bis[1]benzothieno[3,2-*b*:2',3'-*h*]carbazole, substitutes the peripheral nitrogens of diindolocarbazole for sulfurs.

Sulfur-containing heterocycles are well-known building blocks in the search of novel materials within organic electronics. In fact, the suitability of this strategy has been extensively certified with a myriad of examples.^[155–158] Cores such as benzothieno[3,2-*b*][1]benzothiophene (BTBT)^[25,42–44,159–160] or dinaphtho[2,3-*b*:2',3'-*f*]thieno[3,2-*b*]thiophene (DNTT)^[45–46,161–163] are just a few of the sulfurated aromatic systems currently settled amongst the top performing organic semiconductors. Indeed, they do not only excel in terms of charge mobility transport, but also for their remarkable air-stability.^[160,164] In spite of the potential displayed by similar constructions and the endeavor invested in developing a suitable synthetic route^[165–166], there is no reported data of devices integrating the bisbenzothienocarbazole core to date. Thus, an in-depth study of this core emerged as a prime objective to answer the current absence of information.

Taking into account the conclusions extracted from the previous chapter, a special attention has been put in the design of the alkylation patterning. Contrarily to structure **1**, the bisbenzothienocarbazole nucleus does not concede the opportunity to attach alkyl chains to the peripheral heteroatoms. Figure 2.1 depicts two feasible derivatives of the bisbenzothienocarbazole core **30** resulting from model diindolocarbazole structures analyzed in Chapter 1. A possible analog of the hexylated compound **1c** would be derivative **30a**, featuring a lateral configuration with a single *N*-hexyl chain. On the other hand, this core also permits a more head-tail orientated design, emphasizing the elongation through the long axis with peripheral alkyl chains and minimizing the impact of the *N*-alkyl chain. Therefore, the structure of derivative **30b**, possessing two peripheral hexyl chains and the shortest possible *N*-methyl, redesigns the concept of derivative **1f**.

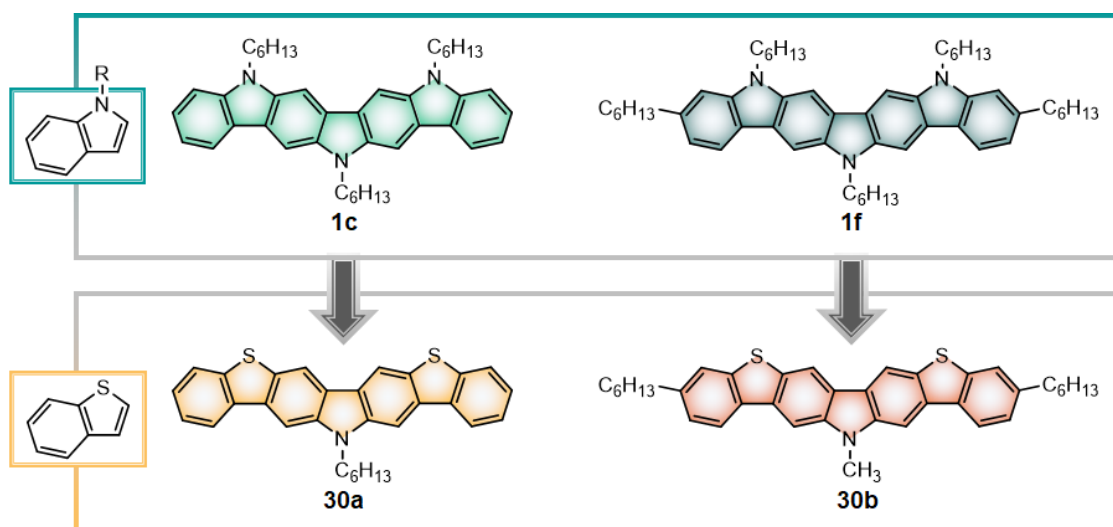
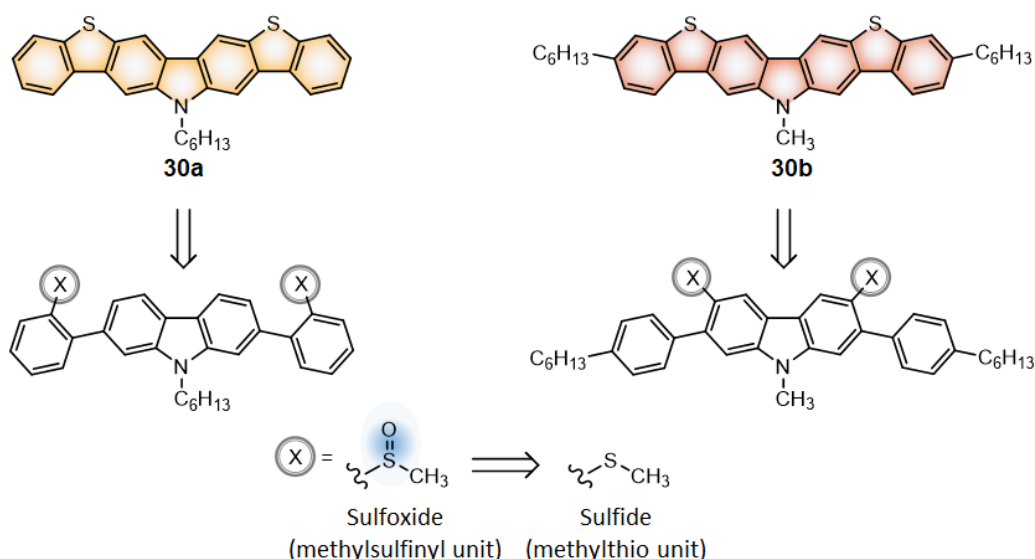


Figure 2.1. Molecular structures of the proposed target derivatives of the bis[1]benzothieno[3,2-*b*:2',3'-*h*]carbazole **30a** and **30b** and their respective diindolocarbazole similes **1c** and **1f**.

2.2. Sulfurated carbazole precursors

The synthesis of derivatives **30a** and **30b** has been carried out according to a reported procedure, which is based on the annulation of the sulfoxide-containing precursors shown in Scheme 2.1.^[165] These precursors are obtained by oxidizing their respective sulfide-containing counterparts. During the early stages of the synthetic process, an intriguing aspect related to these intermediates piqued our attention. As detected, the two pairs of precursors possessed divergent optical properties regarding the emission intensity, depending on the oxidation state of the sulfur. It should be noted that the oxidation of the methylthio unit implies the transformation of an electron-donating into an electron-withdrawing group. The associated electrochemical modulation is therefore prone to affecting the photoluminescence, as evidenced by some published examples.^[167–169] Indeed, the switch from methylsulfinyl to methylthio groups in various fluorophores has been recently reported as a tool for biological imaging probes.^[168–169] Keeping in mind that 9*H*-carbazole also outstands as a building block for its excellent photophysical properties, the analysis of the herein synthesized precursors could derive into attractive findings.

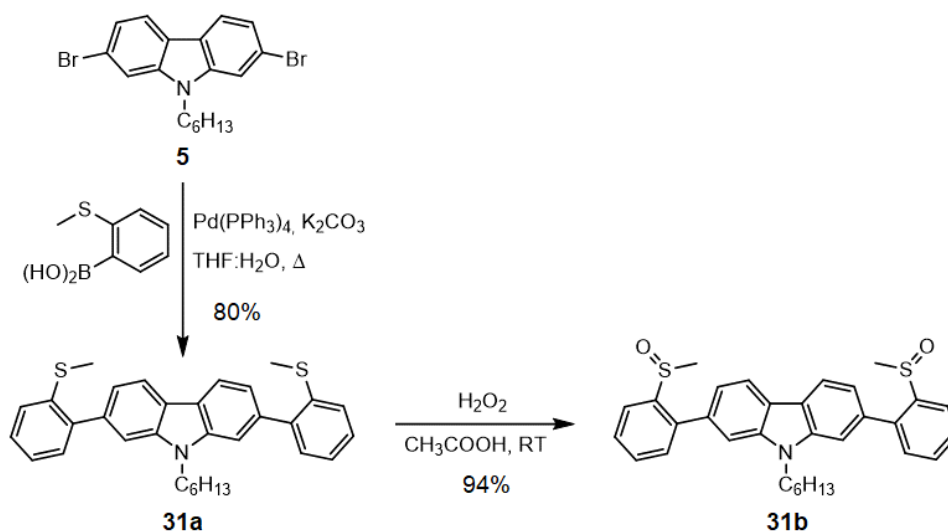
Overall, this section deals with the synthesis of the abovementioned sulfurated carbazole precursors as well as analog structures, in order to analyze the role of the position and the oxidation state of the sulfur moieties in the properties of carbazole-based fluorophores.



Scheme 2.1. Schematic representation of the retrosynthetic approach towards compounds **30a** and **30b**, involving various sulfurated carbazole precursors.

2.2.1. Synthesis

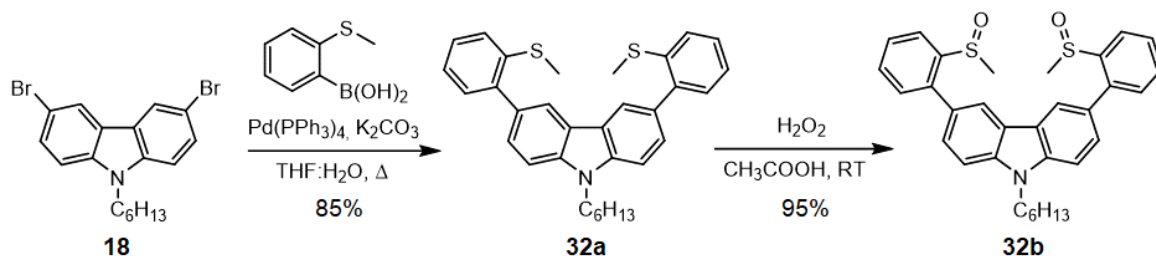
The synthesis of the *meta*-substituted intermediates **31a–b** is represented in Scheme 2.2. It should be clarified that the nomenclature of the sulfurated precursors synthesized in this section includes a letter that denotes the oxidation degree of the sulfur.



Scheme 2.2. Synthesis of the *meta*-substituted intermediates **31a–b**, precursors of the final compound **30a**.

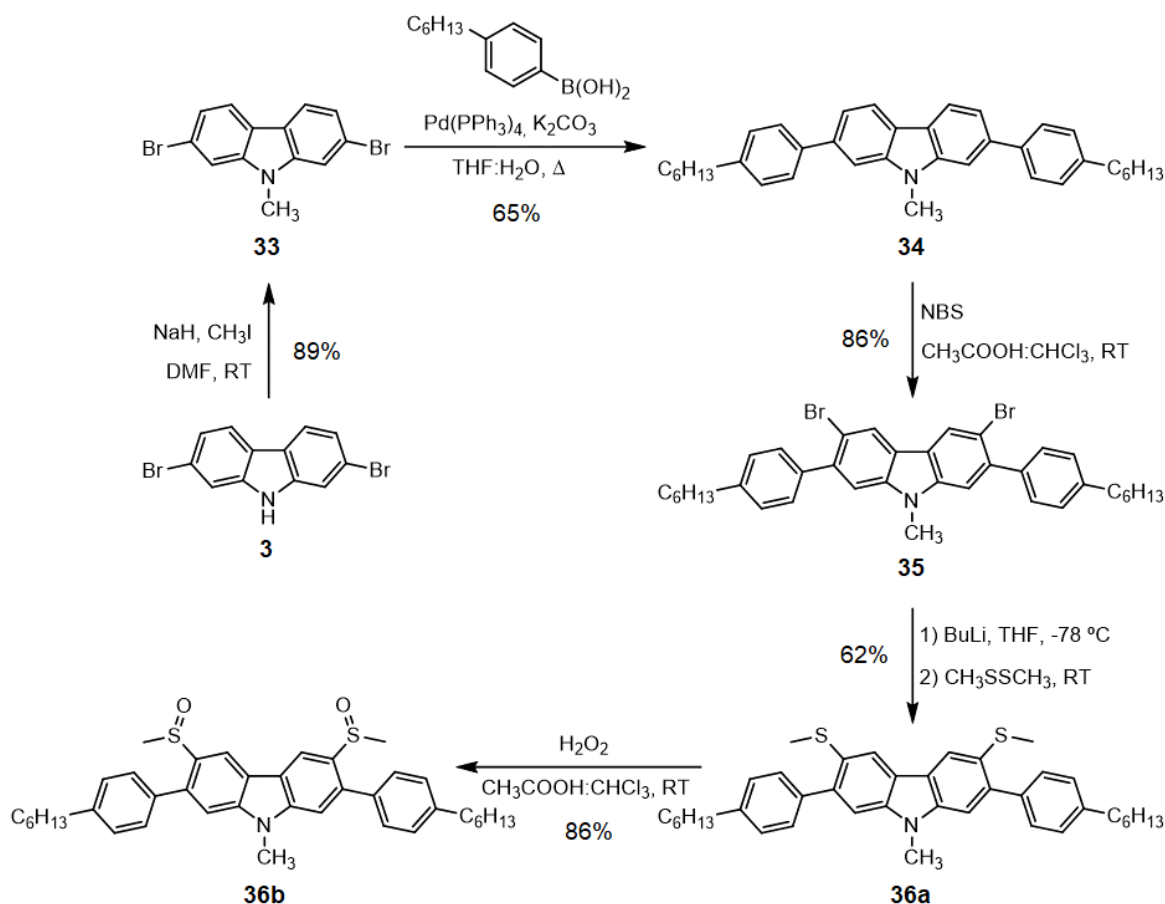
Compound **31a** was obtained from **5** in a yield of 80% through the Suzuki-Miyaura cross-coupling reaction, using 2-methylthiophenylboronic acid, Pd(PPh₃)₄ and K₂CO₃ in a mixture of THF and water under reflux. The subsequent oxidation with H₂O₂ in glacial acetic acid at room temperature led to **31b** in an excellent yield of 94%. Additionally, the synthesis of the

para-substituted analogs **32a–b** was projected with the only purpose of comparing their optical properties with respect to the *meta*-substituted structure **31**. Their synthesis, shown in Scheme 2.3, was performed likewise from **18** as starting material. The formation of the *para*-substituted derivatives **32a–b** was accomplished in similarly high yields of 85 and 95%, respectively.



Scheme 2.3. Synthesis of the *para*-substituted analogs **32a–b**.

The synthesis of precursors **36a–b**, it was achieved from 2,7-dibromo-9*H*-carbazole (**3**) adapting a reported procedure.^[165] The route is depicted in Scheme 2.4.



Scheme 2.4. Synthetic route towards intermediates **36a–b**, precursors of the final compound **30b**.

3 was methylated under standard conditions with iodomethane to afford **33** in a yield of 89%. The Suzuki-Miyaura reaction permitted the attachment of the 4-hexylphenyl scaffold to **33** to provide **34** in a yield of 65%. It was followed by the bromination of positions 3 and 6 of the carbazole ring with *N*-bromosuccinimide (NBS) in a mixture of glacial acetic acid and chloroform at room temperature, providing **35** in a yield of 86%. The substitution of the bromines was performed with *n*-butyllithium in THF at $-78\text{ }^{\circ}\text{C}$ and the subsequent quenching with dimethyl disulfide, which led to compound **36a** in a yield of 62%. Finally, the oxidation to the sulfinylated **36b** with hydrogen peroxide was carried out in a mixture of acetic acid and chloroform in this case, in a yield of 86%.

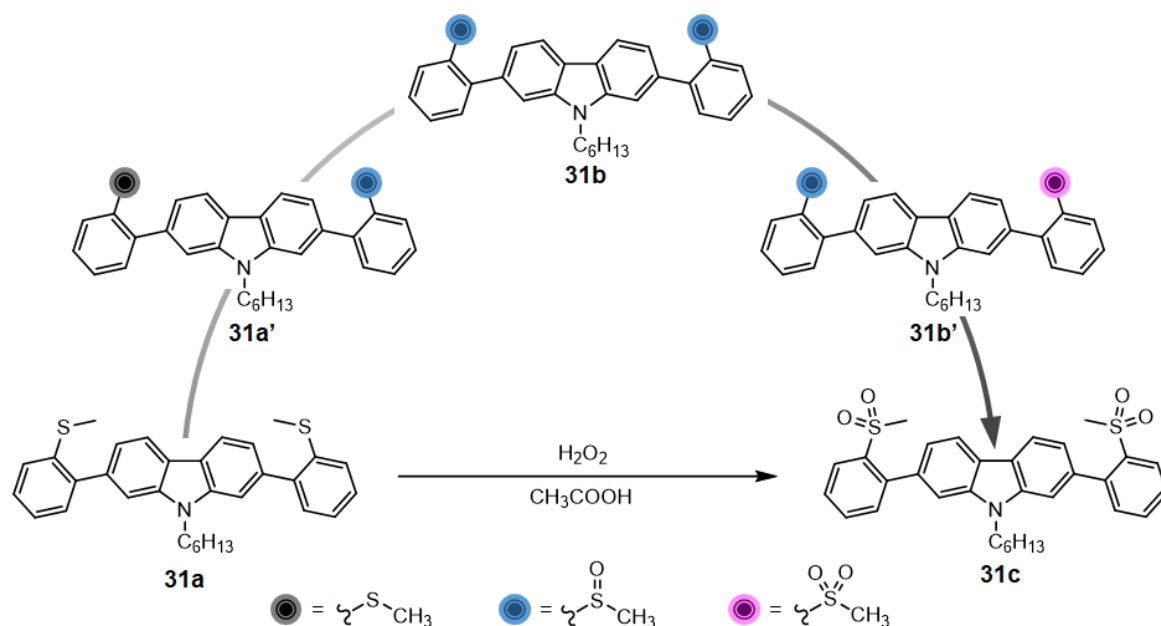
2.2.2. Synthetic study towards the sulfonylated analogs

The premise that the optical properties of structures **31**, **32** and **36** are strongly conditioned by the oxidation degree of the sulfur moieties delineated a completely new objective: the conversion of sulfide to sulfone as the subsequent oxidation state. Thus, the formation of their sulfonyl-containing analogs aroused as an engaging synthetic target to conclude this family of compounds. The presence of sulfone groups in highly performing fluorophores only reinforced the interest in these synthetic targets. Indeed, the integration of sulfones as acceptor bridges or moieties is particularly useful in the search of donor-acceptor molecules for efficient Thermally Activated Delayed Fluorescence (TADF) materials.^[170–174]

In order to accomplish so, the conditions of the oxidation reaction were surveyed in the literature. As observed, standard oxidizing agents such as hydrogen peroxide^[175–177] and *m*-CPBA^[178–180] were the most common choices in this case. Taking into account the success of hydrogen peroxide to convert compounds **31–32a** and **36a** into **31–32b** and **36b**, it was the one employed for the first synthetic approaches towards the *meta*-substituted **31c**. The oxidation to the methylsulfonyl group was directly performed from the methylthio precursor **31a**. Scheme 2.5 depicts the reaction towards **31c** alongside the three in-between intermediates, which includes the methylsulfinyl derivative **31b**.

The initial conditions tested implied analog conditions to the ones employed in the synthesis of **31b**, but using an excess of H_2O_2 instead. Specifically, the original 2.1 equivalents were increased to 15 and 30 with respect to the starting material. Nevertheless, these conditions still provided **31b** regardless of the equivalents of H_2O_2 and the reaction time. Thus, the next step involved the increment of the reaction temperature. In order to evaluate the effect of the temperature and the reaction time in this molecule, several reaction probes were programmed at different temperatures. Each reaction was periodically monitored by UV-Vis/HPLC. The optimal conditions to furnish **31c** were

established at a temperature of 50 °C. The corresponding experimental data is shown in Figure 2.2.



Scheme 2.5. Oxidation reaction from **31a** to **31c**, displaying all the in-between intermediates.

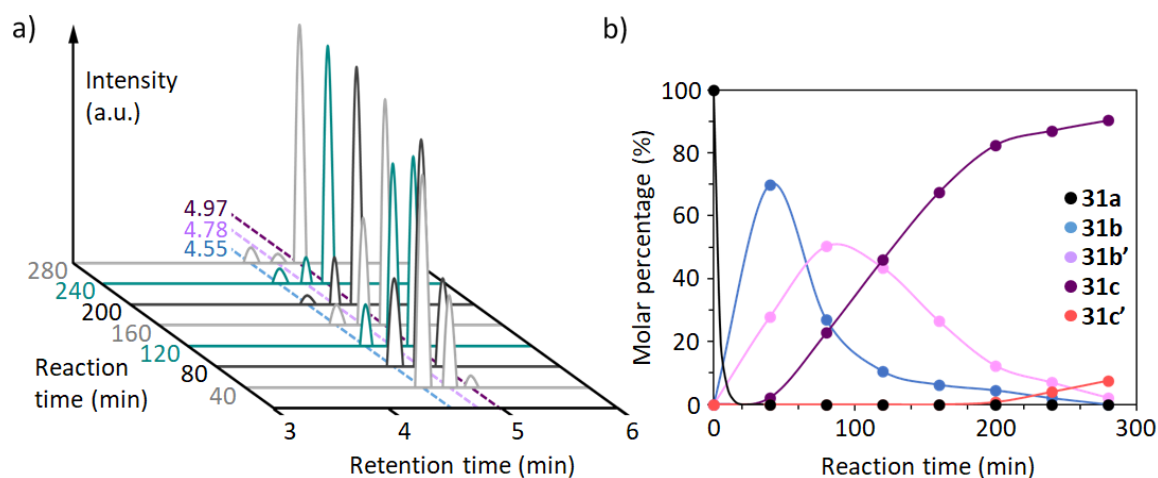


Figure 2.2. Evolution of the different species present in the oxidation process from the *meta*-substituted **31a** to **31c** in front of the reaction time: a) profiles collected by UV-Vis/HPLC, displaying the composition of the crude from seven samples; b) progression of the molar percentage of each specie during the reaction time. The relative intensity areas obtained from UV-Vis/HPLC have been corrected to the actual molar percentage by means of $^1\text{H-NMR}$ spectroscopy. The employed HPLC conditions are detailed in the experimental part.

The conversion from the starting material **31a** to the dimethylsulfinyl derivative **31b** was fast, since neither the starting material **31a** nor the intermediate **31a'** could be detected in the first sample. Thereafter, the reaction species converged progressively to the desired product **31c**, with a conversion higher than 90% after 280 min. It should be mentioned that

the formation of a sixth specie, namely **31c'**, was detected during the final stages of the reaction. This specie eluted simultaneously with **31b** in the employed HPLC conditions ($t_r = 4.6$ min) and possessed a molecular mass of 590.3 g mol^{-1} , implying an increment of 30 g mol^{-1} with respect to **31c**. This suggests the incorporation of two additional oxygen atoms, so it was proposed as a further oxidized by-product. In order to maximize the conversion to **31c** and avoid the raise of by-product **31c'**, the time reaction was set at 4.5 hours. It should be mentioned that the increase of the temperature to $60 \text{ }^\circ\text{C}$ implied a much faster conversion rate, providing the sought **31c** in approximately 60 min. However, these conditions were discarded because the conversion between species was exceedingly sensitive within very short periods of time. Finally, a temperature of $80 \text{ }^\circ\text{C}$ rapidly derived into the formation of **31c'** and the consequent degradation of the product.

Regarding the *para*-substituted **32c**, the chosen conditions provided a similar reaction profile. Overall, the synthesis of the methylsulfonyl derivatives **31c** and **32c** was accomplished in high yields of 80 and 85%, respectively. Even though the sulfonylated counterpart of structure **36** could not be included in this preliminary study, it is likely to be investigated in the future.

2.2.3. Crystal structure

The crystal structure of compound **31a** could be elucidated *via* single-crystal X-ray analysis. Specifically, it crystallized in space group $P12_1/c1$ of the monoclinic system. The molecule does not feature a planar configuration, since the central carbazole and the two *meta*-substituted phenyls adopt high twist angles of 55.99° and 71.77° . The configuration of the molecule and the disposition in the single crystal are represented in Figure 2.3.

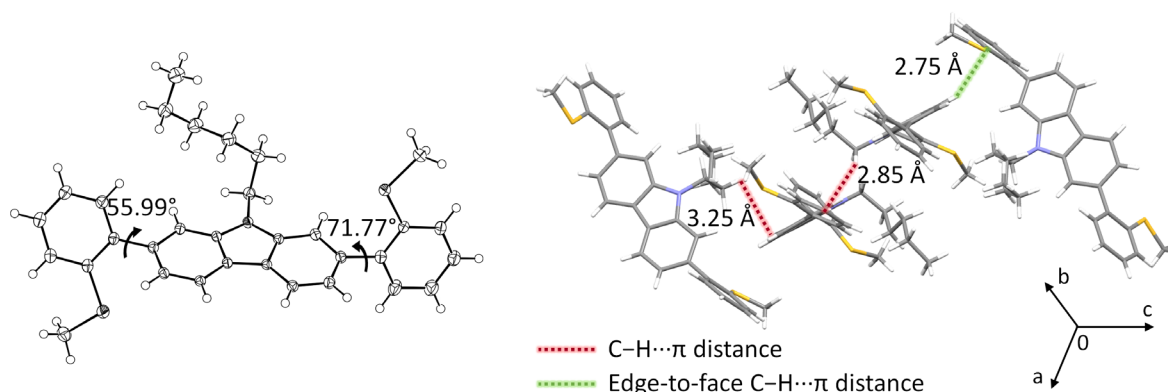


Figure 2.3. X-ray crystal structure **31a**, showing the ORTEP projection (left) and the unit cell (right). The twist angles and representative distances are also indicated.

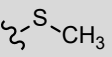
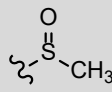
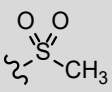
The intermolecular arrangement is mainly governed by aliphatic C-H \cdots π interactions along with edge-to-face aromatic C-H \cdots π interactions. However, the structure lacks the effective

intermolecular π - π interactions that could be interesting in charge transport. The high twist angles between the carbazole nucleus and the phenyl scaffolds, which induce a considerable intermolecular steric hindrance, possibly represent the main obstacle to this.

2.2.4. Optical properties

The photoluminescence data of all the sulfurated carbazole derivatives synthesized so far is compiled in Table 2.1. All derivatives were examined in three different solvents, namely cyclohexane, dichloromethane and acetonitrile, which feature an increasing range of polarities. Apart from the sulfonylated compound **32c**, which will be discussed independently, the optical properties in the tested solvents provided similar results in terms of quantum yields and a slight bathochromic shift from cyclohexane to the two more polar solvents (the corresponding spectra can be found in Figure A2.1 of the Appendix). Taking this into account, the subsequent analysis is centered on the results obtained in dichloromethane as representatives. The absorption and emission spectra in dichloromethane are represented in Figure 2.4.

Table 2.1. Photoluminescence data of the sulfurated carbazole structures featuring sulfide (**31–32,36a**), sulfoxide (**31–32,36b**) and sulfone (**31–32c**) groups in cyclohexane (CH), dichloromethane (DCM) and acetonitrile (ACN).

Structure	Solvent						
		λ_{em} (nm) ^[a]	Φ_f ^[b]	λ_{em} ^[a] (nm)	Φ_f ^[b]	λ_{em} ^[a] (nm)	Φ_f ^[b]
31	CH	384	0.07	377	0.33	381, 396	0.32
	DCM	394	0.03	400	0.34	402	0.32
	ACN	393	0.04	400	0.35	405	0.27
32	CH	360, 379	0.05	363, 382	0.15	355, 374	0.25
	DCM	366, 384	0.05	367, 386	0.12	360, 380, 412	0.38
	ACN	366, 383	0.05	367, 386	0.13	362, 382, 435	0.33
36	CH	406	0.02	384	0.17		
	DCM	424	0.01	387	0.16		
	ACN	431	0.01	390	0.15		

[a] Wavelength of maximum emission ($\lambda_{em,max}$). The emission spectra were recorded after excitation at 300 nm. [b] Fluorescence quantum yields (Φ_f), determined using POPOP as standard.

Both the emission wavelength and the quantum yield of the studied fluorophores proved to be strongly conditioned by the oxidation degree of the sulfur moieties and their bonding positions with respect to the carbazole ring. Derivatives **31–32a**, which contain the 2-methylthiophenyl moiety, display similar emission spectra with respect to their oxidized counterparts **31–32b**. In the case of **31a** and **31b**, the former peaks at 394 nm, while the

latter shows a very slight bathochromic shift, peaking at 400 nm. The shift found in the *para*-substituted compounds **32a** and **32b** is even smaller. Regarding the oxidation to methylsulfonyl groups, the *meta*-substituted **31c** follows the same tendency, displaying a minor bathochromic shift of 2 nm with regard to **31b**. The *para*-substituted **32c**, however, reveals a new emission band peaking at 412 nm that endows it with a distinct emission profile. As a consequence, it displays a greater contribution to the visible spectrum than their less oxidized analogs **32a–b**. Structure **36** also stresses out the key role of the oxidation state of the sulfur in the fluorescence, since in this case is directly attached to carbazole. Contrary to structures **31** and **32**, the oxidation to methylsulfinyl causes a remarkable hypsochromic shift of 37 nm, from 424 to 387 nm for **36a** and **36b**, respectively.

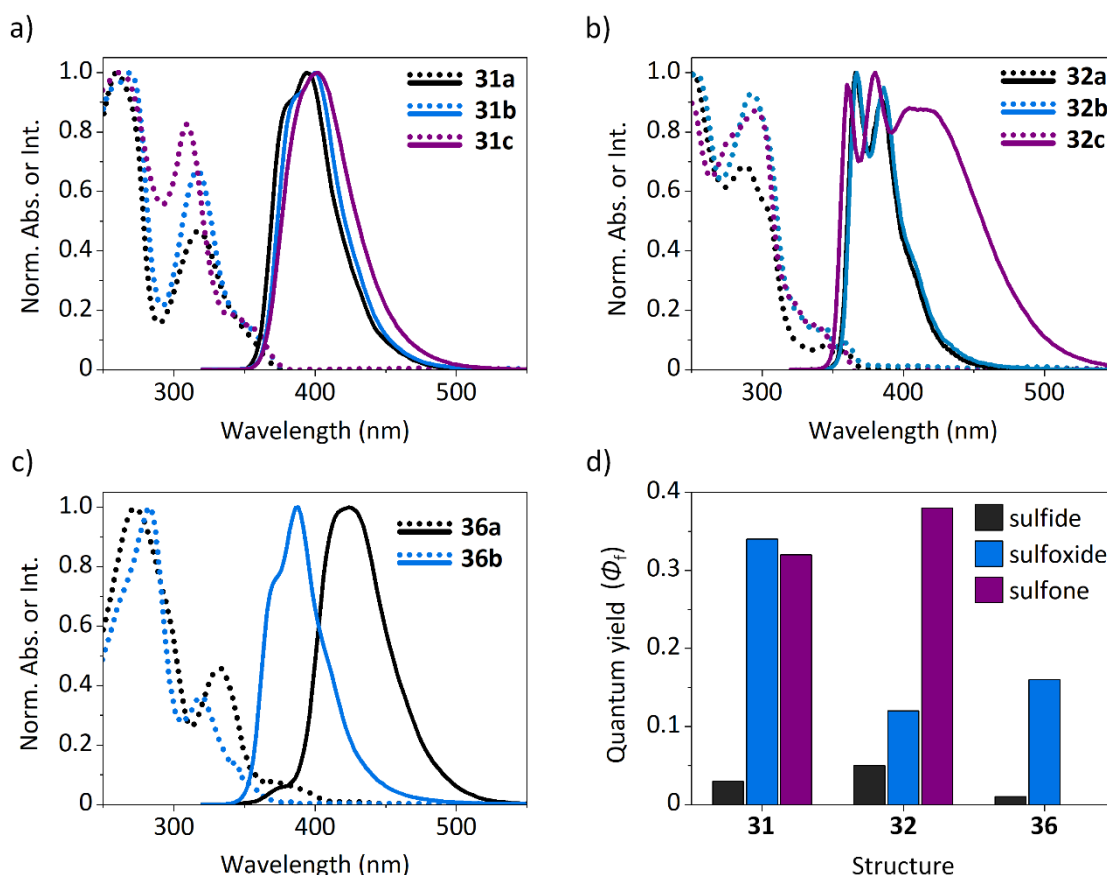


Figure 2.4. Photophysical characterization of the different sulfurated carbazole structures in dichloromethane: absorption (dotted) and emission (solid) spectra of derivatives **31a–c** (a), **32a–c** (b) and **36a–b** (c) at $\lambda_{\text{ex}} = 300$ nm, with their corresponding Φ_f (d).

On the other hand, the fluorescence quantum yields of both sulfide and sulfoxide derivatives provided unexpected results. Several reported methylsulfinyl-containing fluorophores display a much lower quantum yield than their methylthio analogues,^[181] impelling their application in fields such as biological imaging and detection probes.^[168–169] Nevertheless, in our case we found the opposite trend, i.e. the oxidation to sulfoxide leads

to a noteworthy enhancement of the quantum yield with respect to the almost non-emitting sulfide derivatives. Even though there are some examples that follow this tendency,^[167,182] the difference between the quantum yields of both counterparts is seldom as significant as the ones herein reported (Figure 2.5d). Specifically, compounds **31a** and **32a**, featuring the 2-methylthiophenyl unit, display low quantum yields of 0.03 and 0.05, respectively, whereas those of their oxidized analogues **31b** and **32b** increase to 0.34 and 0.12, respectively. The increase observed in the *meta*-substituted carbazole **31** is considerably higher than in the *para*-substituted structure **32**. Besides, the former possess a greater contribution in the blue region of the visible spectrum. In the case of compounds **36a–b**, the difference is even more remarkable, with a 16-fold enhancement between analogues. The fact that the methylthio group is directly bounded to the carbazole heterocycle in structure **36** seemingly makes it more susceptible to the changes in the oxidation state of the sulfur.

The conversion from sulfoxide to sulfone has little effect in the Φ_f of the *meta*-substituted **31** (from 0.34 to 0.32), but implies a 3-fold enhancement in the *para*-substituted **32** (from 0.12 to 0.38). As stated, the sulfonylated **32c** also astounded with the appearance of an additional emission band. This characteristic was suggested to origin through the Twisted Intramolecular Charge Transfer (TICT) mechanism, which manifests in some molecules constructed from donor and acceptor moieties linked by a single bond. This phenomenon implies the coexistence of two different minima in the potential energy surface of the first excited singlet state (S_1): the locally excited (LE) state and the TICT state.^[85,183–184] These two states are correlated with the twist angle of the single bond that connects the D-A system. As schematized in Figure 2.5a, the system first enters the locally excited (LE) state upon photoexcitation, which features a planar configuration. The twist towards a perpendicular geometry promotes the transference of an electron from the donor to the acceptor moiety, which derives into the highly polarized TICT state. Hence, it becomes particularly stable in the presence of polar solvents. As a result, materials featuring TICT exhibit solvatochromism, i.e. solvent-dependent emission. The data collected from different solvents seemingly confirms the occurrence of this phenomenon. Indeed, the combination of the sulfonyl moieties, which are highly electron-withdrawing, with an electro-donating core such as 9*H*-carbazole through a phenyl spacer certainly ushers in a potential TICT process. Figure 2.5b shows the emission spectra of **32c** in the three stated solvents plus DMSO as an even more polar example. As observed, the spectrum registered in the least polar solvent, i.e. cyclohexane, is quite analogous to those of **32a** and **32b**. The subsequent increase of polarity in the rest of solvents accentuates the TICT band in detriment of the normal LE band. In DMSO, which is the most polar solvent tested, the red-shifted TICT band almost dominates the profile of the spectrum. Consequently, the nature

of the solvent also affects the Φ_f of **32c**, with a value that ranges from 0.25 to 0.38 in cyclohexane and dichloromethane, respectively. Thus, the photophysical properties of **32c** can be uniquely altered not only by switching the oxidation state of the sulfur, but also through the polarity of the solvent. This makes the emission characteristics of **32c** abysmally divergent with respect to their less oxidized counterparts **32a–b** in highly polar solvents.

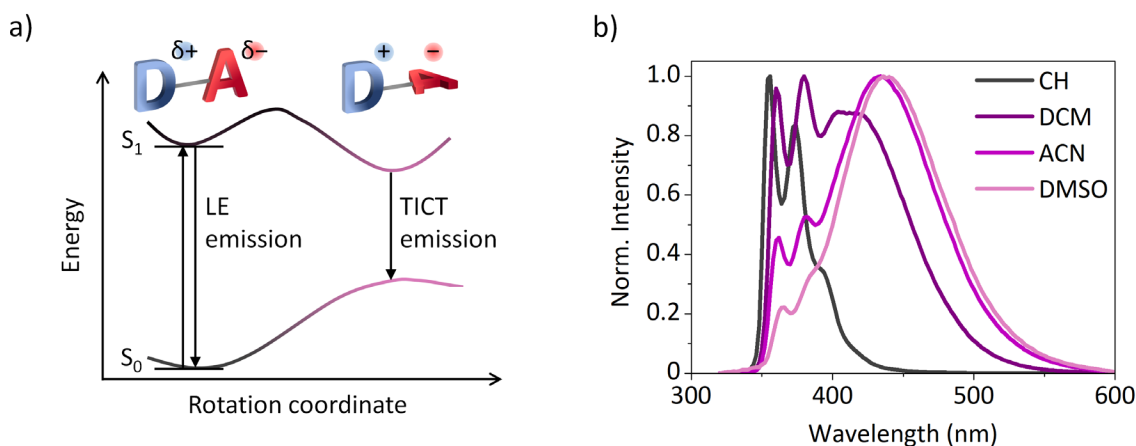
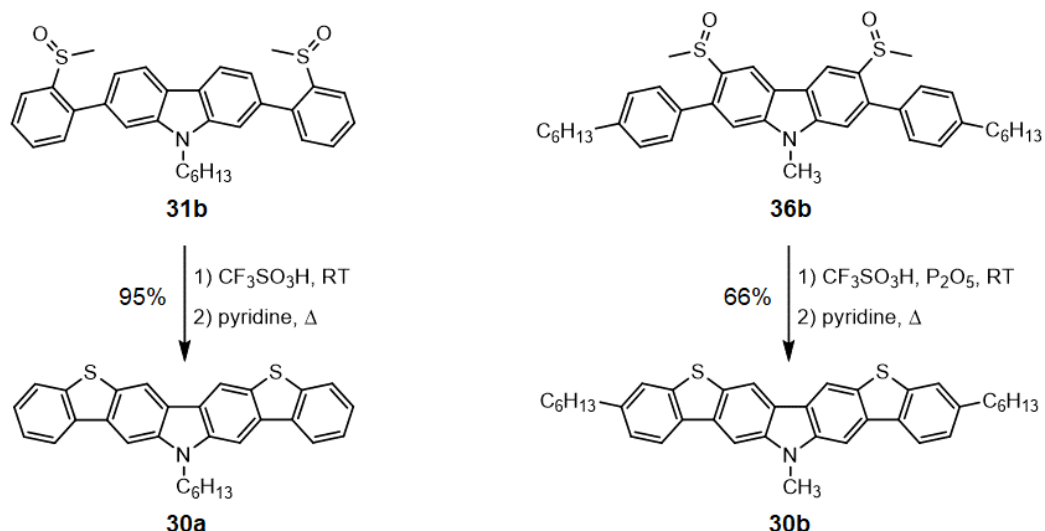


Figure 2.5. a) Schematic representation of the TICT mechanism and b) emission spectra of derivative **32c** in different solvents ($\lambda_{ex} = 300$ nm).

2.3. Bisbenzothienocarbazole derivatives

2.3.1. Synthesis

Scheme 2.6 represents the cyclization of the sulfinylated compounds **31b** and **36b** to obtain the bisbenzothienocarbazole derivatives **30a** and **30b**, respectively. The activation of the methylsulfinyl group,^[185] required for the intramolecular ring closure step, was accomplished using an excess of the strong triflic acid at room temperature for 72 h.^[165] In the cyclisation of **36b**, a small amount of phosphorous pentoxide was also added. This acid-induced condensation led to the cyclized methylsulfonium salt intermediate. Thereafter, the demethylation of the intermediate salts was performed by refluxing them in pyridine for 12 h. The bisbenzothienocarbazole derivatives **30a** and **30b** were obtained in high yields of 95 and 66%, respectively. Despite the considerable length of the synthetic pathways, the corresponding global yields are also remarkable. **30a** was furnished from 2,7-dibromo-9H-carbazole (**3**) in an outstanding global yield of 67% after four steps. Also from **3**, the synthesis of **30b** was achieved in a global yield of 19%, which is equally notable considering that the procedure involves six synthetic steps.



Scheme 2.6. Final cyclization step towards the bisbenzothienocarbazole derivatives **30a** and **30b**.

2.3.2. Characterization of the organic semiconductors

Thermal and photophysical properties

The thermal and optical properties of the bisbenzothienocarbazole derivatives **30a** and **30b** are compiled in Table 2.2.

Table 2.2. Thermal and photoluminescence data in solution and in the solid state of the final compounds **30a** and **30b**.

Compnd.	Thermal properties		Photophysical properties				
	T_m [a] (°C)	T_d [b] (°C)	Solution			Solid state	
			$\lambda_{abs,max}$ [c] (nm)	$\lambda_{em,max}$ [c] (nm)	Φ_f [d]	$\lambda_{abs,max}$ [e] (nm)	$\lambda_{em,max}$ [e] (nm)
30a	197	351	344, 361	438, 466 _(sh)	0.04	284, 370	458
30b	217	408	347, 365	432, 458 _(sh)	0.05	267, 363	474

[a] Melting point (T_m) obtained from DSC at a scan rate of 10 °C min⁻¹. [b] Decomposition temperature (T_d) obtained from TGA (5% weight loss) at a heating rate of 10 °C min⁻¹. [c] Wavelengths of maximum absorption ($\lambda_{abs,max}$) and emission ($\lambda_{em,max}$) in dichloromethane, with the shoulder peaks indicated as (sh). The emission spectra were recorded after excitation at 300 nm. [d] Fluorescence quantum yields (Φ_f), determined using POPOP as standard. [e] The spectra in the solid state were measured in vacuum-evaporated thin films of 75 nm deposited over quartz (λ_{ex} = 350 nm).

The emission of the bisbenzothienocarbazole derivatives, measured in dichloromethane, has an expected bathochromic shift in comparison with their precursors derived from the extension of the aromatic core (e.g. 38 nm from **31b** to **30a**, peaking at 400 and 438 nm, respectively). Accordingly, the fluorescence quantum yields diminish with respect to their methylsulfinyl precursors, with values of 0.04–0.05. The absorption and emission spectra

of both derivatives in dichloromethane and in the solid state are represented in Figure 2.6. Both derivatives exhibit a bathochromic shift in the solid state, which is generally caused by the aggregation of the material. Nevertheless, the photoluminescence of **30a** still preserves a substantial contribution in the blue region of the visible spectrum, peaking at 458 nm. Overall, the $\lambda_{em,max}$ is 20 and 42 nm red-shifted with respect to the value in dichloromethane for **30a** and **30b**, respectively.

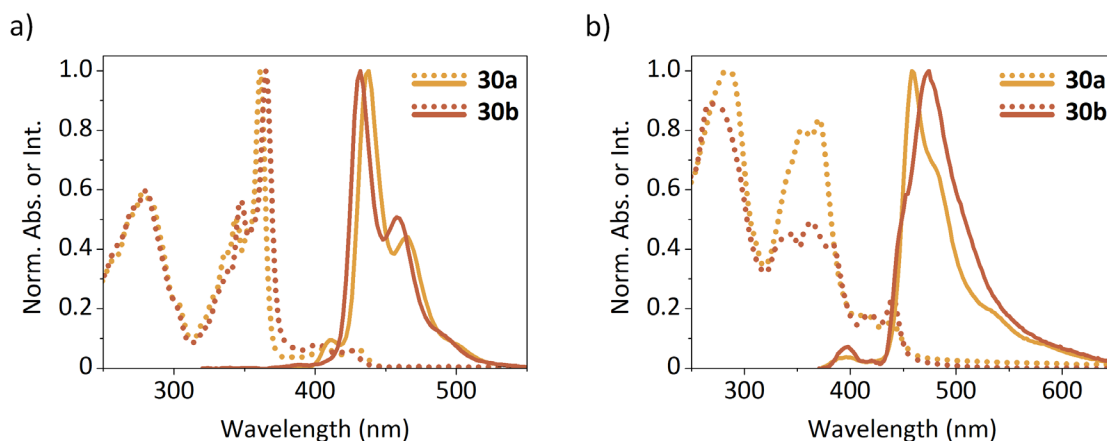


Figure 2.6. Absorption (dotted lines) and emission (solid lines) spectra of derivatives **30a** and **30b** in dichloromethane (a) and in the solid state (b). The emission spectra were registered after excitation at $\lambda_{ex} = 300$ nm in solution and $\lambda_{ex} = 350$ nm in the solid state. The optical properties in the solid state were registered in thin films of 75 nm deposited over quartz plates.

Concerning the thermal properties, both derivatives feature T_d values above 350 °C, which are adequate for the vacuum-deposition process. Remarkably, the peripheral hexyl chains endow derivative **30b** with a higher T_d up to 408 °C on the basis of the 5% weight loss. The TGA measurements are depicted in Figure A2.2. of the Appendix.

Electrochemical properties

The electrochemical characterization of compounds **30a** and **30b**, which is mainly focused on determining whether these compounds possess suitable properties to be applied in OTFTs, is detailed in Table 2.3.

Table 2.3. Electrochemical data of compounds **30a** and **30b**.

Compound	$\lambda_{abs,onset}$ (nm) [a]	E_{gap}^{opt} (eV) [a]	E_{onset}^{ox} (V) [b]	IP (eV) [c]	EA (eV) [d]
30a	442	2.81	0.38	5.77	2.96
30b	437	2.84	0.42	5.81	2.97

[a] Optical energy gap (E_{gap}^{opt}) estimated from the absorption spectrum ($\lambda_{abs,onset}$). [b] Onset oxidation potential (E_{onset}^{ox}) vs. Fc^+/Fc determined from CV in 1 mM solutions in dichloromethane. [c] Ionization potential (IP) estimated as $IP = E_{onset}^{ox} vs. Fc^+/Fc + 5.39$. [d] Electron affinity (EA) estimated as $EA = IP - E_{gap}^{opt}$.

Compounds **30a** and **30b** undergo an oxidation process, which is represented in Figure 2.7a. Both compounds exhibit similar ionization potential (IP) values, calculated from the first oxidation onset potential, and optical gap energy values, estimated from their absorption spectra. The resulting energy levels, represented in Figure 2.7b, have estimated values around -5.80 and -2.97 eV for their HOMO and LUMO energy levels, respectively. Their low-lying HOMO energy levels, which confer more stability against oxidation by atmospheric oxygen,^[18] also benefit the gold work function (i.e. 5.1 eV). Therefore, this family of bisbenzothienocarbazole derivatives are perfectly suitable for their application in hole transporting OTFTs.

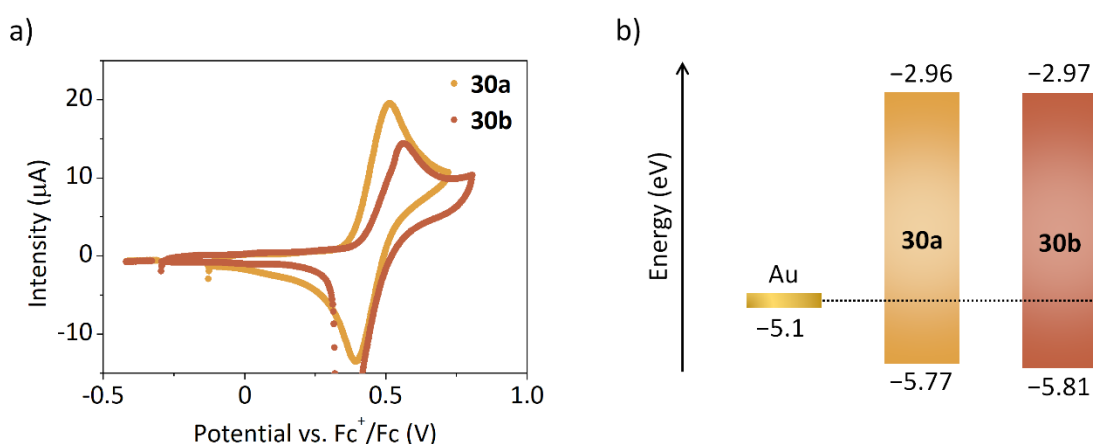


Figure 2.7. Cyclic voltammograms (a), recorded in dichloromethane (1 mM), and estimated energy levels (b) of derivatives **30a** and **30b**.

2.3.3. Organic Thin-Film Transistors

The bisbenzothienocarbazole derivatives **30a** and **30b** have been tested as p-type semiconductors in OTS- and PS-treated devices. The most relevant OTFT characteristics are collected in Table 2.4.

Table 2.4. OTFT characteristics of the devices fabricated from derivatives **30a** and **30b**.

Compound	Dielectric	$\mu_{h,max}$ ($\text{cm}^2 \text{V}^{-1} \text{s}^{-1}$) ^[a]	$\mu_{h,avg}$ ($\text{cm}^2 \text{V}^{-1} \text{s}^{-1}$) ^[b]	I_{on}/I_{off} (A/A) ^[d]
30a	OTS	7.1×10^{-5}	7×10^{-5} (1×10^{-5})	$\sim 10^3$
	PS	4.4×10^{-4}	4×10^{-4} (2×10^{-4})	$\sim 10^4$
30b	OTS	6.5×10^{-4}	6×10^{-4} (-) ^[c]	$\sim 10^3$
	PS	1.1×10^{-3}	1×10^{-3} (-) ^[c]	$\sim 10^4$

[a] Maximum hole mobility value for a single device. [b] Maximum average hole mobility value of a set of representative devices collected on the same day. The values in parenthesis correspond to the average mobility registered ca. 7 months after their fabrication. [c] Not operative. [d] I_{on}/I_{off} ratio.

The best performance was found in PS-treated devices integrating compound **30b**, with mobility values up to $1.1 \times 10^{-3} \text{ cm}^2 \text{ V}^{-1} \text{ s}^{-1}$. In the case of compound **30a**, the highest mobility was also found in PS-treated devices, with a value up to $4.4 \times 10^{-4} \text{ cm}^2 \text{ V}^{-1} \text{ s}^{-1}$, whereas the mobility dropped to $7.1 \times 10^{-5} \text{ cm}^2 \text{ V}^{-1} \text{ s}^{-1}$ in devices containing OTS. As observed, the inclusion of the peripheral hexyl chains in **30b** endows the core with more adaptability regarding the nature of the interfacial organic dielectric. Notably, all devices showed noteworthy I_{on}/I_{off} ratios ranging from 10^3 to 10^4 , being generally superior in devices based on PS as dielectric. This fact correlates with the outperformance of both bisbenzothienocarbazole derivatives over PS. Figure 2.8 displays the transfer and saturation characteristics of representative OTS- and PS-treated devices.

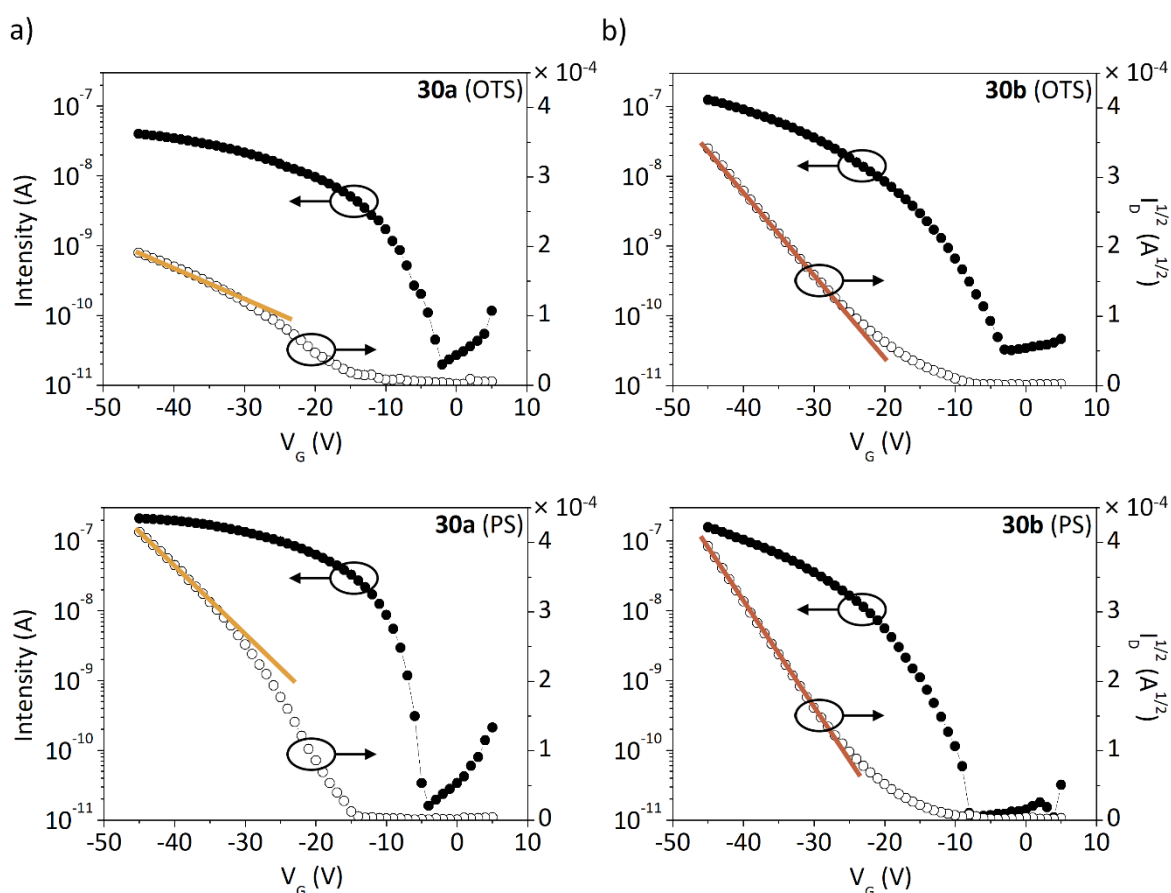


Figure 2.8. Transfer ($V_{DS} = -40 \text{ V}$) and saturation characteristics of OTFT devices integrating derivative **30a** (a) and **30b** (b) over OTS- (above) and PS-treated substrates (below). The mobility was extracted from the slope denoted by the colored line.

Another feature that deserves attention is that all devices fabricated from derivatives **30a** and **30b** tend to exhibit a non-ideal behavior, as observed by the different nonlinearities present in the OTFT saturation characteristics. Devices based on derivative **30a** generally reveal a kink in the saturation characteristics (Figure 2.8a), in which the slope at high V_G is lower and higher at low V_G . The mobility values were extracted from the high V_G region,

according to what is suggested in the literature.^[104–105] Concerning the devices based on **30b**, they show more linear characteristics but still with a significant threshold voltage (Figure 2.8b). These type of nonlinearities diverge from those found for the diindolocarbazole core, which showed a generally sublinear behavior.

All devices, stored under ambient conditions in the dark, were measured periodically to analyze their air-stability. The evolution of the average hole mobility over time is represented in Figure 2.9.

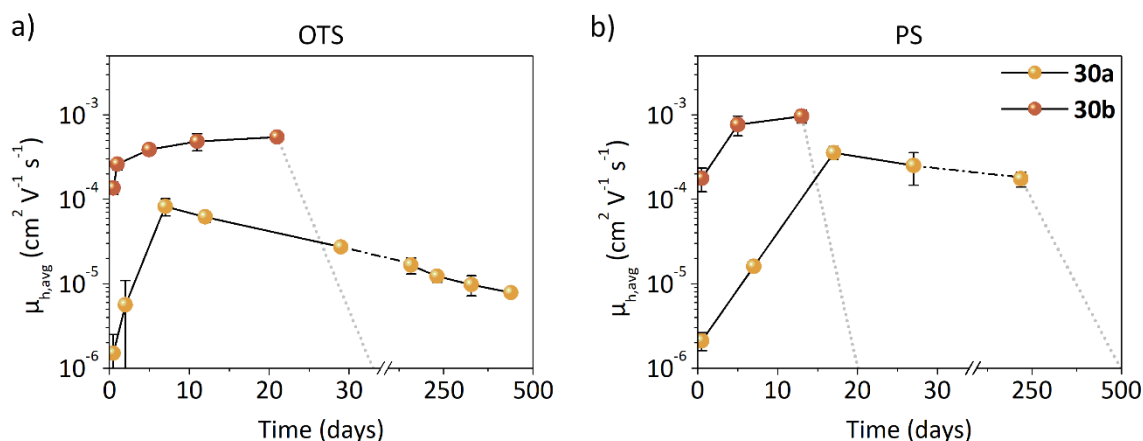


Figure 2.9. Evolution of the $\mu_{h,avg}$ through time of devices fabricated from derivatives **30a** and **30b** over OTS- (a) and PS-treated substrates (b). The dotted lines in grey indicate the period when the devices lost their semiconducting properties and resulted inoperative.

Devices based on compound **30a** featured the longest shelf lifetime and a considerable air-stability. Remarkably, the mobility underwent an abrupt increase from the day of the device manufacturing to some days after, regardless of the chosen organic dielectric. This improvement, which goes up to two orders of magnitude, is generally attributed to the doping of the semiconductor layer as a result of its exposure to air. In fact, this phenomenon was suggested in some examples of sulfurated materials displaying comparable behavior.^[186–187] Thereafter, the $\mu_{h,avg}$ in PS-treated devices barely fluctuates, exhibiting a value up to $2 \times 10^{-4} \text{ cm}^2 \text{ V}^{-1} \text{ s}^{-1}$ after seven months. The OTFT characteristics after seven months are shown in Figure A2.3 of the Appendix. On the other hand, their OTS-treated analogs experimented a persistent decrease of the $\mu_{h,avg}$ up to an order of magnitude in the course of a year. Even though the considerable stability of **30a**-based devices, their lifetime did not extend more than 500 days. In the case of devices integrating derivative **30b**, they display a much shorter shelf lifetime with respect to **30a** despite the similarity of their energy levels. Their $\mu_{h,avg}$ also increased during the first days after the manufacturing over both dielectrics, stabilizing in a plateau. However, the devices collapsed after that, causing the loss of the semiconductor properties. The functioning period of the devices integrating **30b** was determined to be around three weeks over OTS-

treated substrates and a little less over PS-treated ones. Overall, the bisbenzothienocarbazole core claims a great potential as a p-type semiconductor. Even though it could not outpace the unyielding air-stability and shelf lifetime displayed by the diindolocarbazole core **1**, the maximum hole mobility values extracted from both cores are comparable. A more in-depth comparison of the properties and assets of both cores will be held in Chapter 3.

After considering the dependence of the device performance with the alkylation patterning of the bisbenzothienocarbazole core, we decided to further investigate its role in the molecular arrangement and degree of order of the deposited films. With this aim, the single crystal structures and the GIXRD patterns of the films of compounds **30a** and **30b** were analyzed.

2.3.4. Crystal structures

Compound **30b** crystallized in space group P_{-1} of the triclinic system, as illustrated in Figure 2.10.

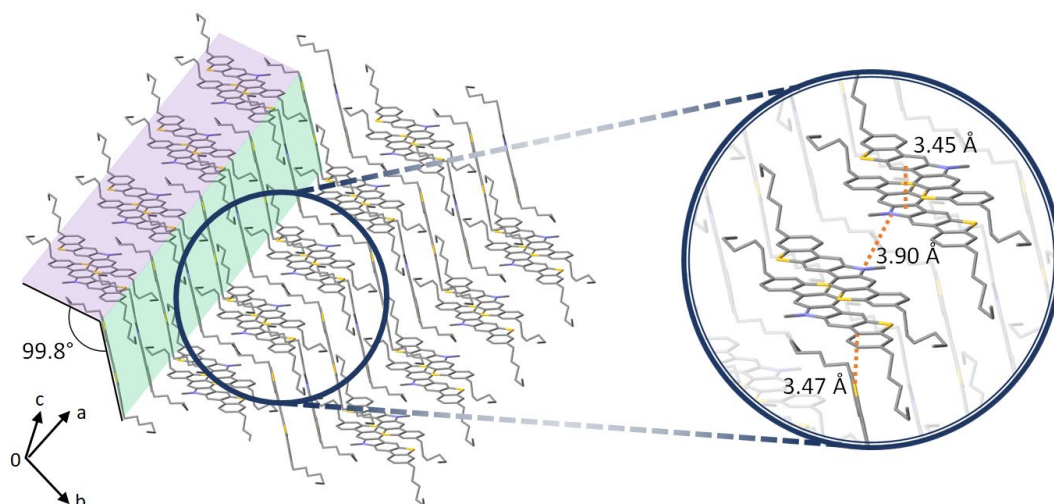


Figure 2.10. Single crystal structure of derivative **30b**, highlighting the corresponding interplanar angle. The amplified region indicates the π - π stacking distance that constitutes the dimer (3.45 Å), the N...N distance between dimers (3.90 Å) and the edge-to-face S... π interaction (3.47 Å). Hydrogen atoms have been omitted for clarity.

Its crystal structure reveals discerned dimers of co-facial molecules disposed in a sandwich herringbone packing. The pair of molecules forming the dimer are separated by 3.45 Å through π - π stacking interactions, affording a significant π -orbital overlap. The intermolecular packing between dimers exhibits a slightly slipped disposition, with the shortest π - π distance corresponding to the separation between nitrogens, i.e. 3.90 Å. This slipped disposition is mostly assisted by tilted edge-to-face C-H... π and S... π interactions,

as well as additional interactions from the peripheral alkyl chains. As a result, the interplanar angle (99.8°) is almost perpendicular, which along the slipped disposition associated with the packing could be a disadvantage for an efficient π - π charge hopping.^[121]

The case of derivative **30a** resulted slightly more intricate. It crystallized in space group $Pna2_1$ of the orthorhombic system in the presence of chloroform, a structure that goes in accordance with the one reported by Gao *et al.*^[165] Additionally, an alternative crystal structure was obtained in different conditions, which crystallized in space group $P2_1/n$ of the orthorhombic system and incorporated an unknown solvent. The two alternative packing motifs found for derivative **30a**, referred as dispositions A and B, respectively, are depicted in Figure 2.11. Despite the efforts invested in producing adequate solvent-free crystals, it was not possible in any of the numerous conditions tested. Thus, these results are not applicable in the correlation of the crystal structure to the arrangement of the material within the device. Nevertheless, they can still provide useful information regarding the molecular structure and the prevalent intermolecular interactions.

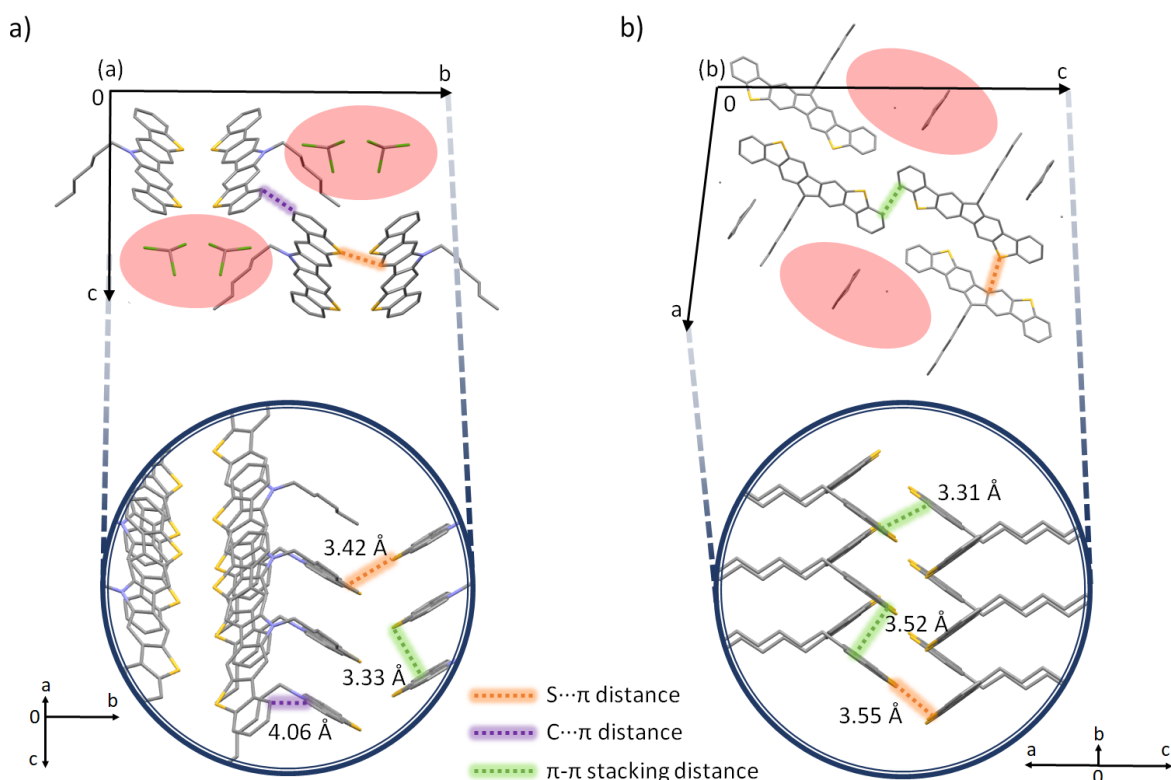


Figure 2.11. Unit cells (above) and amplified regions from a different point of view (below) of the single crystal structures found for derivative **30a**: disposition A, incorporating $CHCl_3$ molecules in the packing (a) and disposition B, in the presence of an unknown solvent (b). The most relevant π - π stacking, $S \cdots \pi$ and $C \cdots \pi$ distances are indicated in green, orange and purple, respectively. The red areas highlight the void regions occupied by solvent molecules in the unit cell. The solvent molecules have been omitted in the amplified regions for clarity. Hydrogen atoms have been also omitted.

30a arranges in a convenient γ -like packing in both dispositions, forming columns of π -stacked molecules separated by 3.33 and 3.52 Å in dispositions A and B, respectively. The columns organize in antiparallel pairs through S $\cdots\pi$ and C-H $\cdots\pi$ edge-to-face interactions, with S $\cdots\pi$ distances of 3.42 and 3.55 Å in structure A and B, respectively. The steric effect exerted by the central *N*-hexyl chains could be the source of this arrangement. Even though the stacking distances are slightly shorter in disposition A, the co-facial molecules forming the columns are only partially overlapped due to their slipped disposition (detailed in the amplified region of Figure 2.11a). It can be also appreciated that the π -stacking direction of the two pairs of columns within the unit cell is not completely parallel. This derives from the aromatic and aliphatic C-H $\cdots\pi$ interactions that govern the arrangement between columns. On the other hand, the overlap in disposition B is superior, with a uniform π -stacking direction. Not only that, but there are also effective π - π stacking interactions between different pairs of columns, with a distance of 3.31 Å (highlighted in Figure 2.11b).

Overall, both dispositions display two distinct regions: one comprising the aromatic cores, which would assist in the transport of charges, and the other aliphatic. Contrarily to **30b**, which features a more compact packing due to the head-tail alkylation patterning, the presence of a central *N*-hexyl chain in **30a** seems unable to grant so. In order to stabilize the packing, compound **30a** strongly depends upon small solvent molecules to fill the voids of the aliphatic region (highlighted in red in Figure 2.11). Specifically, disposition A possesses two voids of 250 Å³ (occupied by chloroform molecules), whereas disposition B features a larger void of 351 Å³, implying that the unknown solvent must be bulkier than chloroform. Considering that the employed vacuum-deposition process is exempt of solvent, the intermolecular organization within the semiconductor layer of the devices could be certainly altered with respect to the available crystallized structures. Thus, the degree of order and morphology of the thin-films will be analyzed.

2.3.5. Molecular order in the thin films

The GIXRD patterns of vacuum-deposited thin-films of derivatives **30a** and **30b** over Si/SiO₂ substrates are shown in Figure 2.12. As predicted, the GIXRD measurements of **30a** vacuum-deposited films reveal generally amorphous layers, with very small diffraction peaks at $2\theta = 4.9$ and 14.5° . Considering the literature, however, the XRD pattern of a drop-casted thin-film of compound **30a** provides sharp and intense diffraction peaks typical of crystalline layers with a high degree of order.^[165] Consequently, the degree of order and the intermolecular disposition of **30a** are greatly conditioned by the deposition conditions. These results support the theory that the presence of small solvent units are necessary to stabilize the intermolecular arrangement and achieve highly ordered films, preventing a superior performance in vacuum-deposited OTFTs. On the other hand, GIXRD

measurements of **30b** films exhibit an exceedingly higher degree of order than those based on **30a** over both dielectrics. Thanks to the availability of the crystal structure of **30b**, we could shed light on its intermolecular disposition within the device. The strong diffraction peak at $2\theta = 3.9^\circ$ was proposed to belong to the reflection 001 in regard to the powder pattern diffractogram and the one simulated from the single crystal structure. This implies that the π - π stacking direction lies parallel to the substrate, facilitating the charge transport. Figure 2.12c schematizes the organization proposed for **30b** over the Si/SiO₂ wafer. The outstanding degree of order and the orientation present in the semiconductor layer could explain the overall better performance of **30b**-based devices.

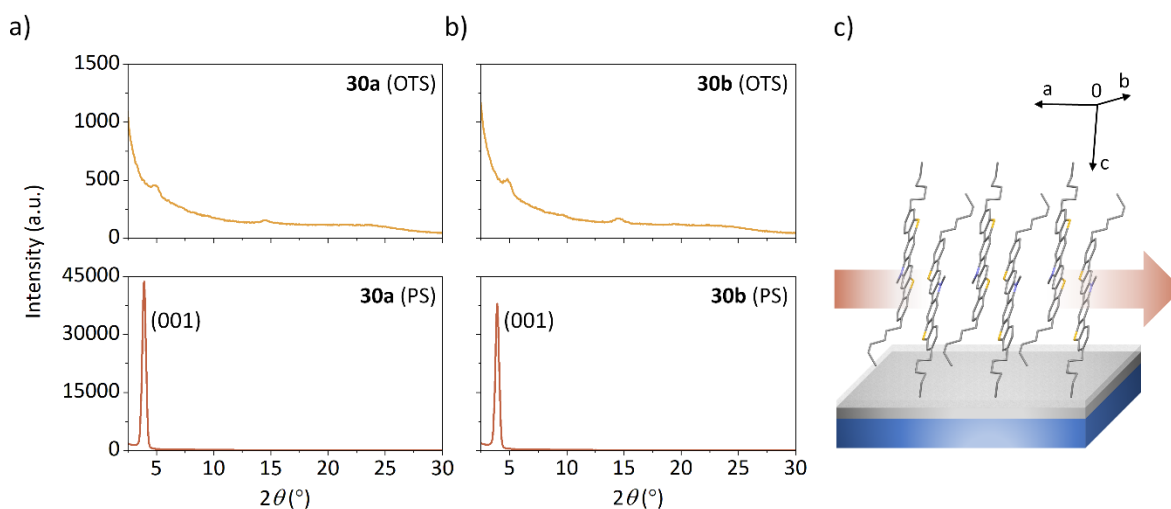


Figure 2.12. GIXRD patterns of vacuum-deposited films of compounds **30a** and **30b** on: (a) OTS- and (b) PS-treated Si/SiO₂ substrates; (c) proposed molecular disposition of **30b** in the film based on the reflections observed in the GIXRD patterns, with the (001) plane placed parallel to the substrate and the arrow indicating the corresponding π - π stacking direction. Hydrogen atoms have been excluded for clarity.

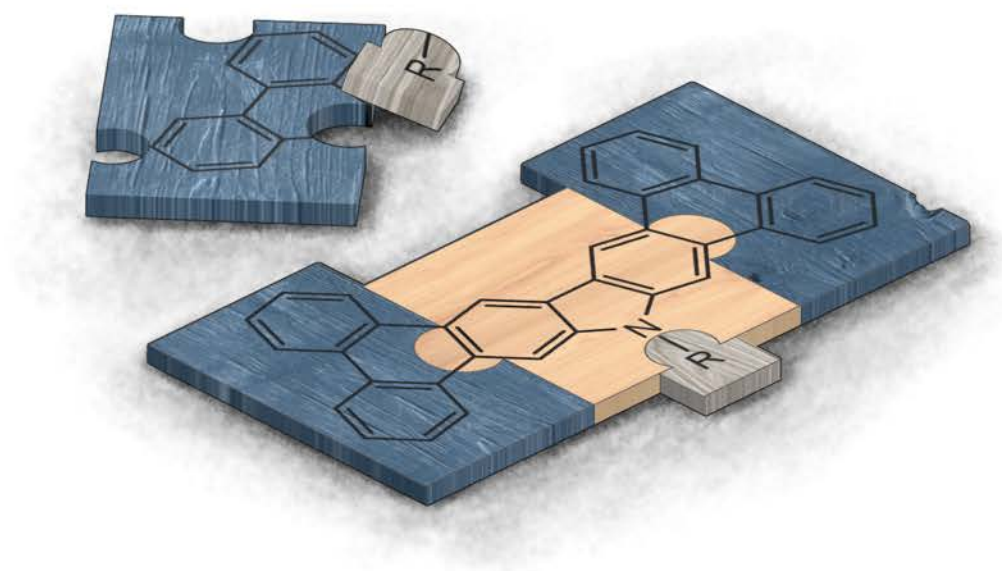
2.4. Conclusions

The two bisbenzothienocarbazole-based derivatives **30a–b**, displaying high thermal stability and appropriate energy levels, have demonstrated great potential as p-type semiconductors. The customized alkylation patternings in combination with the chosen dielectric permitted the modulation and enhancement of the performance of this core in OTFTs. Specifically, the elongated architecture of derivative **30b** afforded a balanced performance both in OTS- and PS-treated devices, with the latter reaching the highest charge mobility value, i.e. $1.1 \times 10^{-3} \text{ cm}^2 \text{ V}^{-1} \text{ s}^{-1}$. As corroborated by means of X-ray diffraction, **30b** provides thin-films with a high degree of order and an intermolecular arrangement suitable for the charge transport. On the other hand, the design of **30a** falls

behind in terms of charge mobility, but alternatively grants a superior shelf lifetime that extends to 500 days.

The analysis of the synthetic precursors also triggered interesting findings related to their optical properties. The successful approach to the sulfonyl-containing counterparts provided an additional perspective. Interestingly, the oxidation state and position of the sulfurated moieties played a key role in tuning the fluorescence of each structure. These results certainly encourage further studies in several applications. Overall, the synthesis of the bisbenzothienocarbazole core furnished a set of compounds with assorted properties and potential within diverse fields.

Extending the carbazole heterocycle (III):
the diphenanthrocarbazole core



CHAPTER 3. Extending the carbazole heterocycle (III): the diphenanthrocarbazole core

3.1. Introduction

Chapter 1 and 2 dealt with the study of ladder-type constructions derived from the fusion of indole and benzothiophene extensions to 9*H*-carbazole, respectively. Considering the promising results that were collected, we decided to exploit this strategy once more. The inclusion of phenanthrene aroused as an interesting alternative, implying an easily accessible choice to expand the 9*H*-carbazole nucleus. In fact, phenanthrene represents a promising scaffold alongside its structural isomer anthracene in the search of fluorophores.^[188–190] Both moieties have been also object of study integrated in different semiconductor molecules and polymers, with great success in performance and stability.^[191–194] The resulting core, namely diphenanthro[9,10-*b*:9',10'-*h*]carbazole, contrasts with the ones previously studied in this work due to the ramified aromatic extensions and the absence of heteroatoms on them. These singular structural features are likely to modify the electronic properties of the core with respect to the hitherto analyzed structures and, consequently, the performance as semiconductor. Figure 3.1 summarizes its structural characteristics in comparison with structures **1** and **30**.

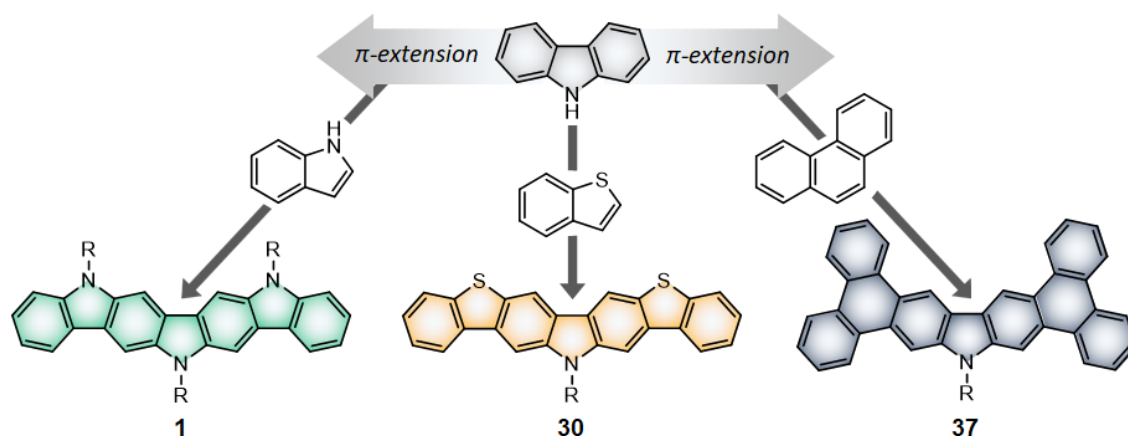
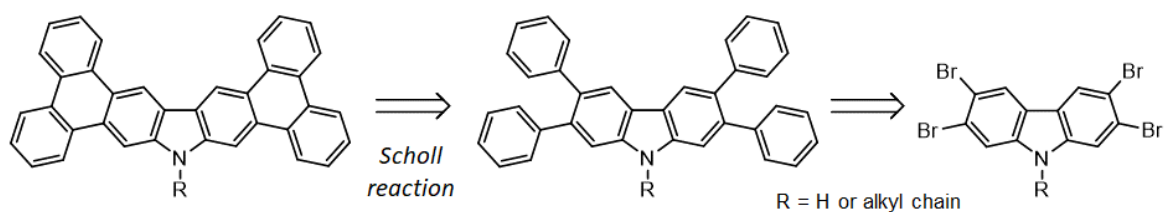


Figure 3.1. Proposed extensions of the 9*H*-carbazole core through the inclusion of different scaffolds: indole (**1**) and benzothiophene (**30**), presented in chapters 1 and 2, respectively; the extension *via* phenanthrene (**37**) conforms the study presented in this chapter.

At the end of this chapter, the properties and performance as semiconductors of the three constructions presented so far will be surveyed and compared to emphasize the advantages and drawbacks of each one.

3.2. Synthesis and design

The synthesis of diphenanthrocarbazole has been envisioned through the Scholl reaction, which can be defined as an acid-catalyzed oxidative condensation of aromatic systems *via* the formation of a carbon-carbon bond.^[195] In fact, the Scholl reaction represents a frequently resorted way to access large polyaromatic constructions through intramolecular couplings.^[195-200] Its application and optimization towards the diphenanthrocarbazole core has been recently surveyed by Kumar *et al.*^[201] but, once again, its semiconductor properties have not been analyzed yet. Thus, this chapter is mostly dedicated to unveil the potential of this core in terms of charge transport in OTFTs. Scheme 3.1 depicts the proposed retrosynthetic approach on the basis of the literature reports, which starts from 2,3,6,7-tetrabromo-9H-carbazole.



Scheme 3.1. Retrosynthetic approach towards the diphenanthrocarbazole core.

The results obtained in the two previous chapters only reinforce the premise that the inclusion of alkyl chains is a key feature to consider in organic electronics. Therefore, the design of the alkylation patterning conferred to this core has been carefully addressed. As stated, the phenanthrene scaffolds endow the diphenanthrocarbazole core with a ramified aromatic system, which permits the addition of differently placed peripheral alkyl chains. The proposed target derivatives are shown in Figure 3.2. Similarly to the strategy employed with the bisbenzothienocarbazole core (**30**, Chapter 2), in this case we opted for a lateral *N*-hexylated derivative (**37a**, analogous to **30a**) and a head-tail fashioned derivative with a short *N*-methyl chain and two peripheral hexyl chains (**37b**, analogous to **30b**). The addition of two supplementary peripheral hexyl chains in **37c** conceived an alternative target derivative that took advantage of the ramified phenanthrene extensions.

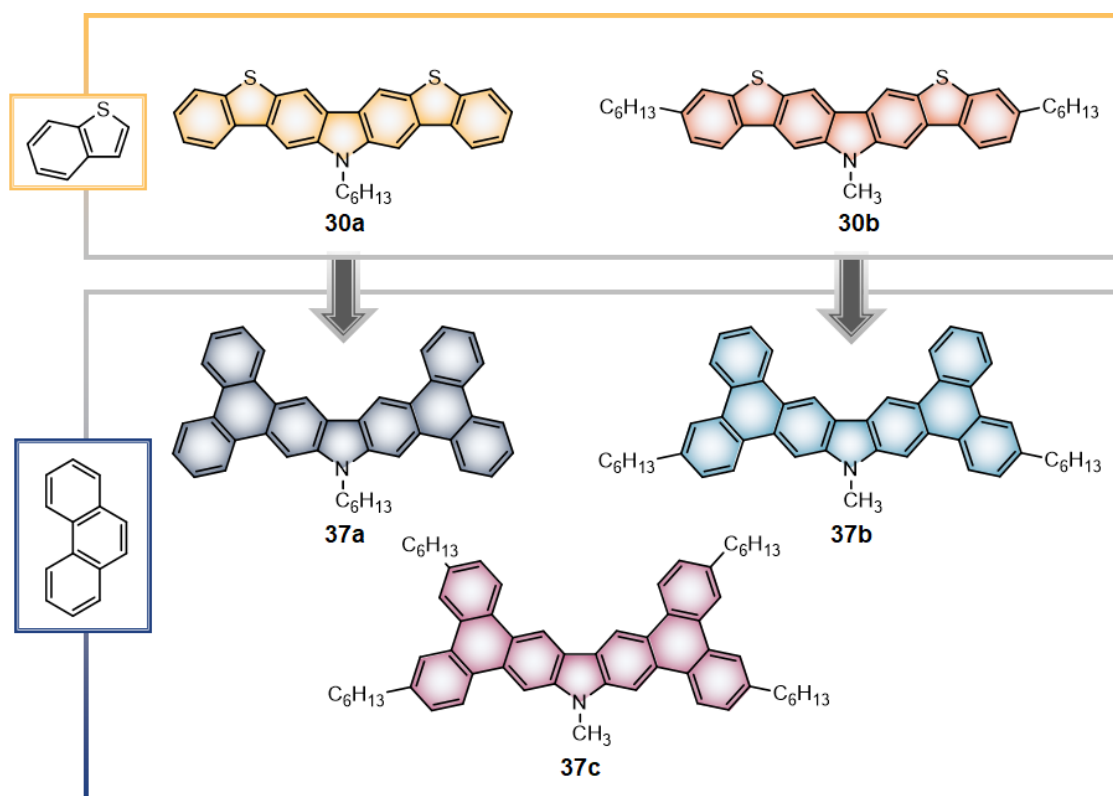
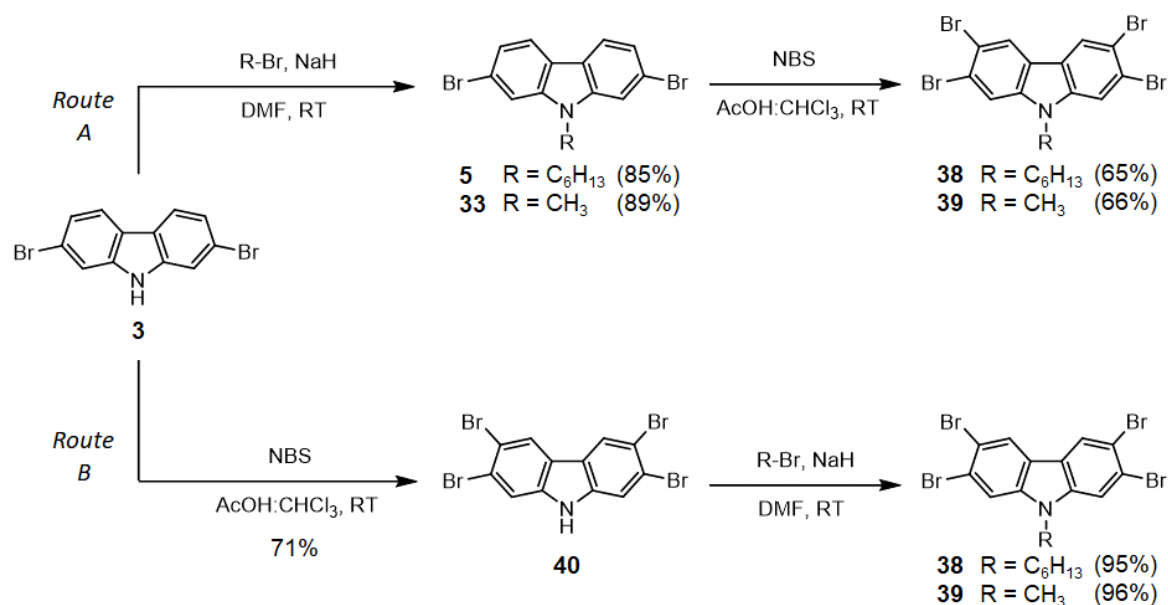


Figure 3.2. Envisioned derivatives of the diphenanthrocarbazole core, inspired by the bisbenzothienocarbazole counterparts **30a–b**: **37a**, featuring an *N*-hexyl chain, **37b** with a shorter *N*-methyl and a pair of peripheral hexyl chains and **37c**, which incorporates an additional pair of peripheral hexyl chains.

3.2.1. Synthesis of the unbounded precursors

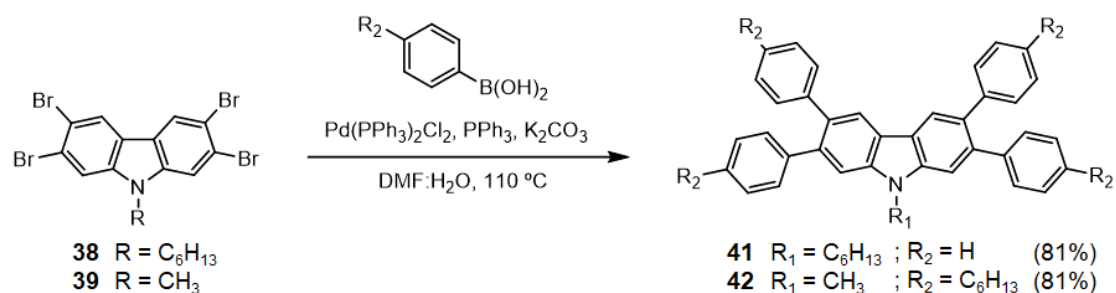
Since *meta* positions (2 and 7) of 9*H*-carbazole are less reactive to electrophilic aromatic substitutions, a direct tetrabromination of 9*H*-carbazole would not lead to the required starting material 2,3,6,7-tetrabromo-9*H*-carbazole. Therefore, its synthesis was achieved from 2,7-dibromo-9*H*-carbazole (**3**). Positions 2 and 7 of **3** are already brominated, so the bromination of the most reactive positions 3 and 6 represents a simpler procedure. The two alternative synthetic routes tested are depicted in Scheme 3.2. Route A initiated with the alkylation of **3**, which was performed under standard conditions using whether 1-bromohexane or methyl iodide to yield **5** and **33**, respectively. Subsequently, the bromination of positions 3 and 6 was achieved with *N*-bromosuccinimide (NBS) in a mixture of acetic acid and chloroform at room temperature. Intermediates **38** and **39** were obtained in a global yield of 55 and 59% from **3**, respectively. It should be mentioned that the equivalents of NBS were carefully adjusted to avoid polybromination at positions 1 and 8 as well. However, the low excess of reagent was translated into a significant presence of the tribrominated by-product, which hampered the yield regardless of the alkyl chain. Also, the separation of the two formed species was complex due to their similar polarities.



Scheme 3.2. Alternative synthetic pathways towards the tetrabrominated intermediates **38** and **39**.

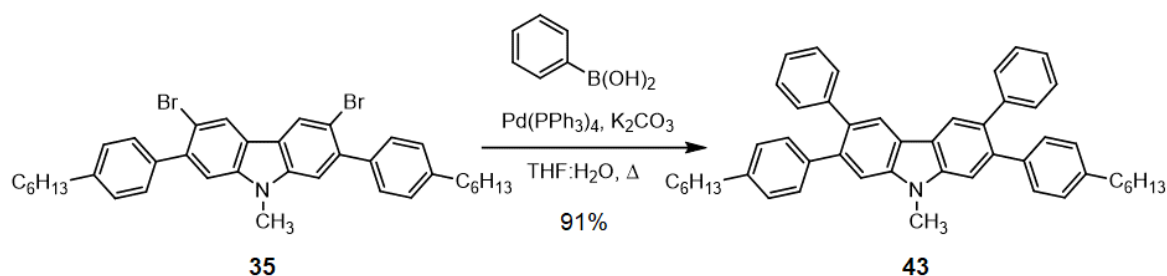
Thus, the two synthetic steps were reversed in an attempt to improve the procedure (route B). The bromination of the non-alkylated **3** led to a slightly higher conversion to the tetrabrominated derivative **40** and implied an easier purification process. The alkylation with 1-bromohexane or methyl iodide provided **38** and **39** in higher global yields of 67 and 68%, respectively. An additional advantage of this route is the convenience to produce derivatives with different alkyl chains, since they are added in the last step.

The next stage consisted in the coupling of the phenyl moieties that would eventually configure the phenanthrene extensions. The attachment of the phenyl groups *via* the Suzuki-Miyaura cross-coupling reaction was achieved using reported conditions. Specifically, the choice of Pd(PPh₃)₂Cl₂ and PPh₃ as catalysts, K₂CO₃ as base, the corresponding boronic acid and a mixture of DMF and water as solvent were successful in the synthesis of tetra- (and even hexa-) phenylated carbazoles.^[201] The choice of DMF as solvent also permits reaching higher reaction temperatures (110 °C in this case) than the hitherto employed THF-based conditions. The synthesis of precursors **41** and **42** from **38** and **39**, respectively, is shown in Scheme 3.3. Compound **41**, precursor of the *N*-hexylated **37a**, was obtained from 2,3,6,7-tetrabromo-9-hexyl-9*H*-carbazole (**38**) and phenylboronic acid in a yield of 81%. **42**, precursor of the tetrahexylated **37c**, was prepared from 2,3,6,7-tetrabromo-9-methyl-9*H*-carbazole (**39**) and 4-hexylphenylboronic acid in an equivalent yield of 81%. The notoriously high yields obtained, considering that it corresponds to a direct fourfold coupling, prove the suitability of these conditions.



Scheme 3.3. Suzuki-Miyaura cross-coupling reaction towards **41** and **42**, precursors of **37a** and **37c**, respectively.

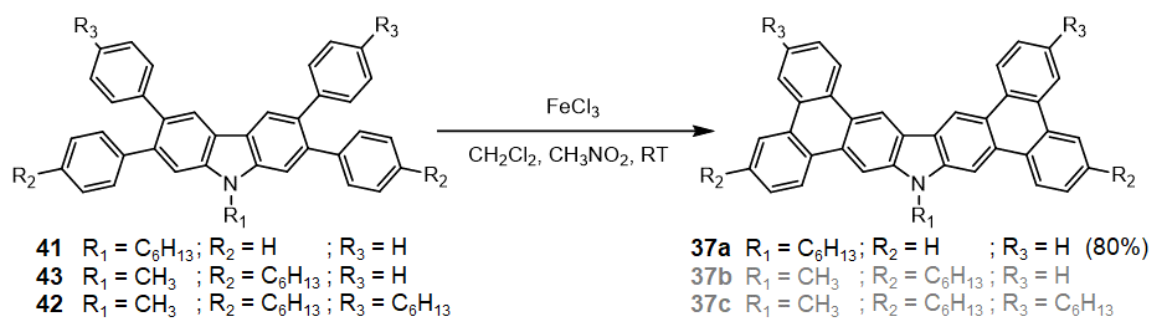
The construction of the diphenanthrocarbazole derivative **37b**, which only features peripheral chains in the two *meta*-substituted phenyls, was achieved from a different approach. Specifically, it was conceived from compound **35**, i.e. an intermediate present in the synthesis of compound **30b** as detailed in the previous chapter. In this case, the twofold coupling was performed under the hitherto employed conditions of the Suzuki-Miyaura reaction (Scheme 3.4). The non-cyclized precursor **43** was obtained in an excellent yield of 91%.



Scheme 3.4. Suzuki-Miyaura cross-coupling reaction towards **43**, precursor of **37b**.

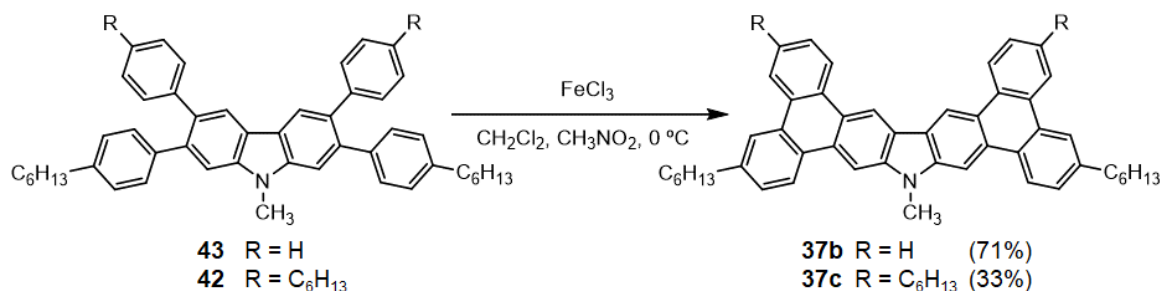
3.2.2. Synthesis of the diphenanthrocarbazole derivatives through the Scholl reaction

Scheme 3.5 summarizes the conditions tested for the synthesis of the three derivatives of diphenanthrocarbazole **37**. The intramolecular cyclization *via* the Scholl reaction was carried out with anhydrous FeCl₃, which acts as both Lewis acid and oxidant,^[196] in a mixture of dichloromethane and nitromethane at room temperature. Compound **37a** was successfully synthesized in a yield of 80%. Nevertheless, the cyclization of precursors possessing peripheral hexyl chains (**42–43**) presumably led to polymerization and other side reactions in these conditions.



Scheme 3.5. Cyclization of intermediates **41–43** towards the final compounds **37a–c** via the Scholl reaction, which was only successful in the case of **37a**.

As reported, the synthesis of a peripherally alkylated oligothiophene nucleus was accomplished via the Scholl reaction under milder conditions.^[202] Specifically, the reaction was carried out at 0 °C within a short period of time. The new conditions were adapted as specified in Scheme 3.6.



Scheme 3.6. Synthesis of derivatives **37b** and **37c** through the Scholl reaction at 0 °C.

The convenient decrease of both the reaction time from the hour-scale to 15 minutes and the temperature from room temperature to 0 °C enabled the formation of the desired products **37b** and **37c** in yields of 71 and 33%, respectively.

3.3. Optoelectronic characterization

In order to evaluate the impact of the extension of the π -system in diphenanthrocarbazole derivatives **37a–c**, their photophysical and electrochemical properties have been compared to those of their uncyclized precursors **41–43**.

3.3.1. Photophysical and thermal properties

The photophysical properties of the non-cyclized precursors **41–43** and the diphenanthrocarbazole derivatives **37a–c** in dichloromethane are collected in Table 3.1 and represented in Figure 3.3a–b.

Table 3.1. Photophysical properties of compounds **41–43** and **37a–c** in dichloromethane.

<i>Uncyclized precursors</i>				<i>Cyclized products</i>			
Compnd.	$\lambda_{\text{abs,max}}$ [a] (nm)	$\lambda_{\text{em,max}}$ [a] (nm)	Φ_f [b]	Compnd.	$\lambda_{\text{abs,max}}$ [a] (nm)	$\lambda_{\text{em,max}}$ [a] (nm)	Φ_f [b]
41	289, 323	402	0.32	37a	334, 369	432, 460	0.19
43	286, 325	402	0.34	37b	336, 373	428, 456	0.19
42	287, 326	404	0.34	37c	338, 375	434, 462	0.17

[a] Wavelength of maximum absorption ($\lambda_{\text{abs,max}}$) and emission ($\lambda_{\text{em,max}}$). The emission spectra were recorded after excitation at 300 nm. [b] Fluorescence quantum yields (Φ_f), determined using POPOP as standard.

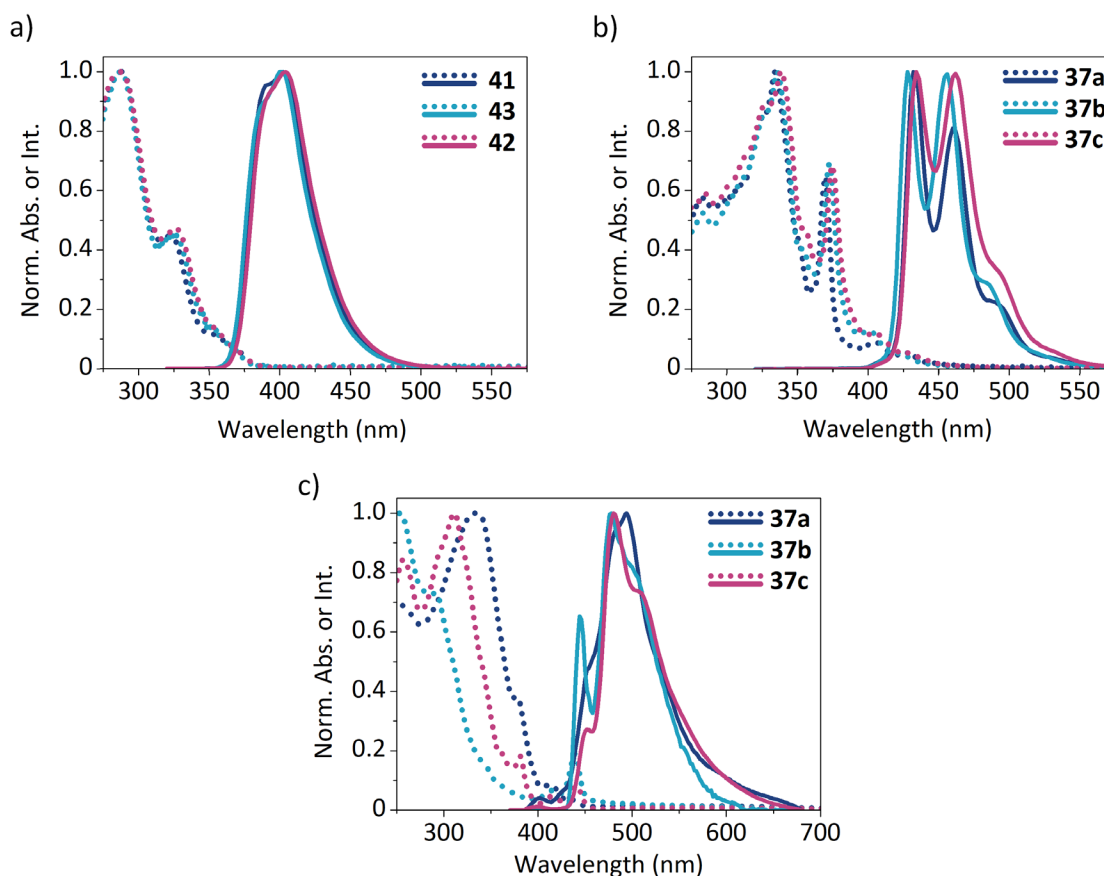


Figure 3.3. Normalized absorption and emission spectra of compounds: a) **41–43** and b) **37a–c** in dichloromethane; c) **37a–c** in the solid state.

All compounds display their maximum absorbance peaks into the UV zone, albeit those of the final compounds **37a–c** are situated at longer wavelengths than those of **41–43**. The same effect applies to their emission, which is centered into the UV-blue zone in **41–43** and displaced into the blue-green region in **37a–c**. The bathochromic shift observed in the final compounds **37a–c** with respect to their uncyclized precursors **41–43** in both the absorption

and emission spectra agrees with the extension of the conjugation of the π -system. The effect of the different alkylation patternings in the absorption and emission spectra is moderate for compounds **37a–c**, with a global wavelength shift that does not exceed 6 nm. In the case of their precursors **41–43**, it is even less significant. Concerning the fluorescence quantum yields, compounds **41–43** display very similar values as high as 0.34, which surpass that of the main 9*H*-carbazole heterocycle, i.e. 0.20.^[122] The addition of the phenyl moieties therefore translates into a direct enhancement of the fluorescence and a more blue-centered emission. The expansion of the π -system in **37a–c** causes an expected slight decrease of the Φ_f (c.a. 0.19), which still equals those of other extended carbazole-based systems such as triindole. In regard to the photophysical results of the cyclized derivatives in the solid state, they are represented in Fig. 3.3c and collected in Table 3.2 alongside their thermal properties. As observed, all derivatives still emit into blue-green region and are slightly conditioned by their alkylation patterning.

Table 3.2. Thermal and photophysical properties in the solid state of the diphenanthrocarbazole derivatives **37a–c**.

Compound	Thermal properties		Photophysical properties	
	T_m (°C) [a]	T_d (°C) [b]	$\lambda_{abs,max}$ (nm) [c]	$\lambda_{em,max}$ (nm) [c]
37a	294	451	254, 331	494
37b	296	445	254, 291	478
37c	217	446	257, 311	480

[a] Melting point (T_m) obtained from DSC at a scan rate of 10 °C min⁻¹. [b] Decomposition temperature (T_d) obtained from TGA (5% weight loss) at a heating rate of 10 °C min⁻¹. [c] Wavelengths of maximum absorption ($\lambda_{abs,max}$) and emission ($\lambda_{em,max}$) in the solid state, measured in vacuum-evaporated thin-films of 75 nm deposited over quartz. The emission spectra were recorded after excitation at 300 nm.

In terms of thermal properties, compounds **37a–c** suit the requisites for an adequate fabrication of the OTFTs. All three derivatives possess similarly high thermal stability, with decomposition temperatures that surpass the 440 °C (the TGA scans are represented in Figure A3.1 of the Appendix). Their melting points are also high, with the tetrahexylated derivative **37c** displaying the lowest value of 217 °C and the other two comparable values around 295 °C.

3.3.2. Electrochemical properties

Compounds **41–43** and **37a–c** underwent an oxidation process, whereas no reduction was observed for any of them. Figure 3.4 illustrates the cyclic voltammograms of all compounds in dichloromethane solutions.

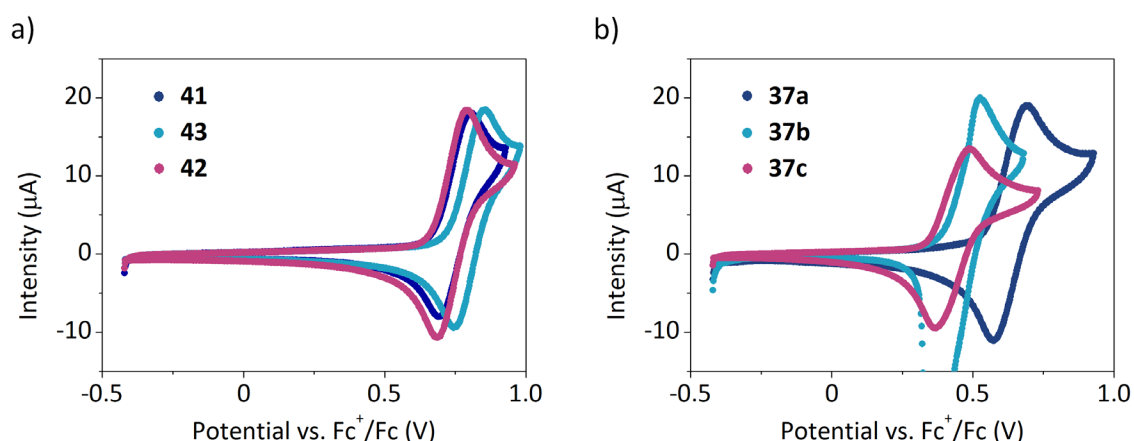


Figure 3.4. Cyclic voltammograms of compounds **41–43** (a) and their cyclized counterparts **37a–c** (b) recorded at a scan rate of 100 mV s⁻¹ in 1 mM dichloromethane solutions.

The electrochemical characterization of the uncyclized precursors **41–43** and the final compounds **37a–c** is summarized in Table 3.3, and their energy levels, represented in Figure 3.5.

Table 3.3. Electrochemical characterization of compounds **41–43** and **37a–c**.

Compound	$\lambda_{\text{abs, onset}}$ (nm) [a]	$E_{\text{gap}}^{\text{opt}}$ (eV) [a]	$E_{\text{onset}}^{\text{ox}}$ (V) [b]	IP (eV) [c]	EA (eV) [d]
41	348	3.56	0.678	6.07	2.51
43	352	3.52	0.729	6.12	2.60
42	354	3.50	0.669	6.06	2.56
37a	427	2.90	0.549	5.94	3.04
37b	422	2.94	0.403	5.79	2.85
37c	429	2.89	0.344	5.73	2.84

[a] Optical energy gap ($E_{\text{gap}}^{\text{opt}}$) estimated from the absorption spectrum ($\lambda_{\text{abs, onset}}$). [b] Onset oxidation potential ($E_{\text{onset}}^{\text{ox}}$) vs. Fc⁺/Fc determined from CV in 1 mM solutions in dichloromethane. [c] Ionization potential (IP) estimated as $\text{IP} = E_{\text{onset vs. Fc}^+/\text{Fc}}^{\text{ox}} + 5.39$. [d] Electron affinity (EA) estimated as $\text{EA} = \text{IP} - E_{\text{gap}}^{\text{opt}}$.

As anticipated from their optical characterization, the extension of the π -conjugated system in structure **37** in comparison to their precursors **41–43** is manifested by the decrease of both the energy band gaps and the ionization potentials. Due to the slightly electron-donating character of the hexyl chains, the two compounds featuring peripheral alkyl chains (**37b–c**) display lower IP values than the bare *N*-hexylated **37a**. This effect is notable only between the cyclized structures. Even though the relatively high IP with respect to the gold work function, compounds **37a–c** are perfectly suitable for their integration in OTFTs. Overall, the diphenanthrocarbazole core possess the potential to perform as p-type semiconductor.

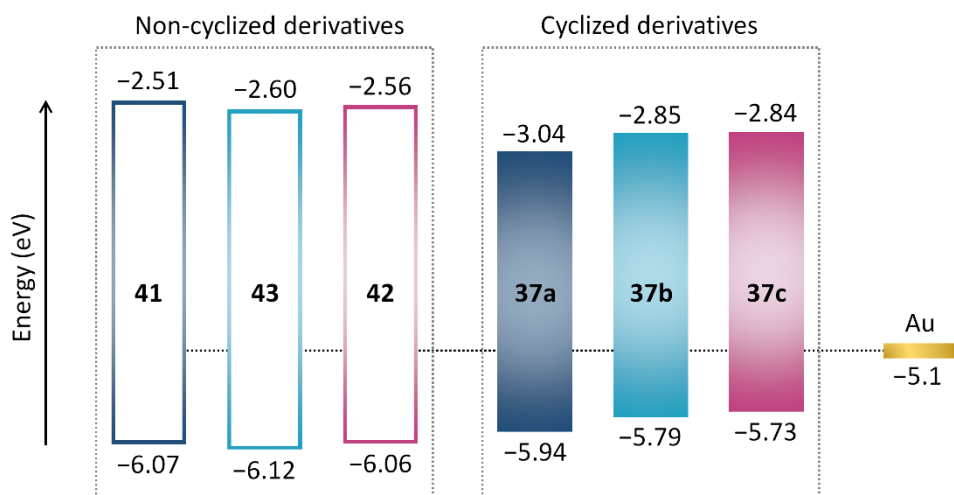


Figure 3.5. Energy levels of compounds **41–43** (left) and their cyclized counterparts **37a–c** (right), with respect to the gold work function.

3.4. Application in final devices and characterization

3.4.1. Organic Thin-Film Transistors

The hole-transporting properties of compounds **37a–c** were analyzed in bottom-gate top-contact OTFTs over *c*-Si/SiO₂ gate/dielectric substrates treated with either octadecyltrichlorosilane (OTS) or polystyrene (PS) and gold as both the source and drain electrodes. Table 3.4 compiles the most relevant characteristics of devices based on compounds **37a–c**.

Table 3.4. OTFT characteristics of the devices fabricated from derivatives **37a–c**.

Compound	Dielectric	$\mu_{h,max}$ (cm ² V ⁻¹ s ⁻¹) ^[a]	$\mu_{h,avg}$ (cm ² V ⁻¹ s ⁻¹) ^[b]	I_{on}/I_{off} (A/A) ^[c]
37a	OTS	4.4×10^{-4}	3×10^{-4} (2×10^{-4})	$\sim 10^3$
	PS	9.7×10^{-5}	8×10^{-5} (6×10^{-5})	$\sim 10^2$
37b	OTS	1.5×10^{-3}	1×10^{-3} (1×10^{-3})	$\sim 10^4$
	PS	1.5×10^{-4}	1×10^{-4} (1×10^{-4})	$\sim 10^2$
37c	OTS	3.0×10^{-3}	3×10^{-3} (4×10^{-4})	$\sim 10^6$
	PS	1.2×10^{-3}	9×10^{-4} (5×10^{-5})	$\sim 10^5$

[a] Maximum hole mobility value for a single device. [b] Maximum average hole mobility value of a set up to 8 representative devices collected on the same day. The values in parenthesis correspond to the average mobility registered ca. one year after their fabrication. [c] Maximum I_{on}/I_{off} ratio.

Once again, the results collected for this core highlight the relevance of the structural design of the material and the device. The choice of OTS as the interfacial organic dielectric implies a clear outperformance with respect to PS, as observed in all three derivatives. This

applies to all the analyzed parameters, i.e. higher mobility values and I_{on}/I_{off} ratios. In this sense, the diphenanthrocarbazole nucleus diverges from the two previously studied cores. Derivative **37c**, with a pronounced head-tail design featuring four peripheral hexyl chains, displayed the best OTFT performance from all the semiconductors studied in this work. Specifically, a hole mobility up to $3.0 \times 10^{-3} \text{ cm}^2 \text{ V}^{-1} \text{ s}^{-1}$ was registered over OTS-treated devices, whereas their PS-treated analogs provided similarly outstanding values up to $1.2 \times 10^{-3} \text{ cm}^2 \text{ V}^{-1} \text{ s}^{-1}$. The OTFT characteristics of representative OTS- and PS-treated devices based on **37c** are represented in Figure 3.6.

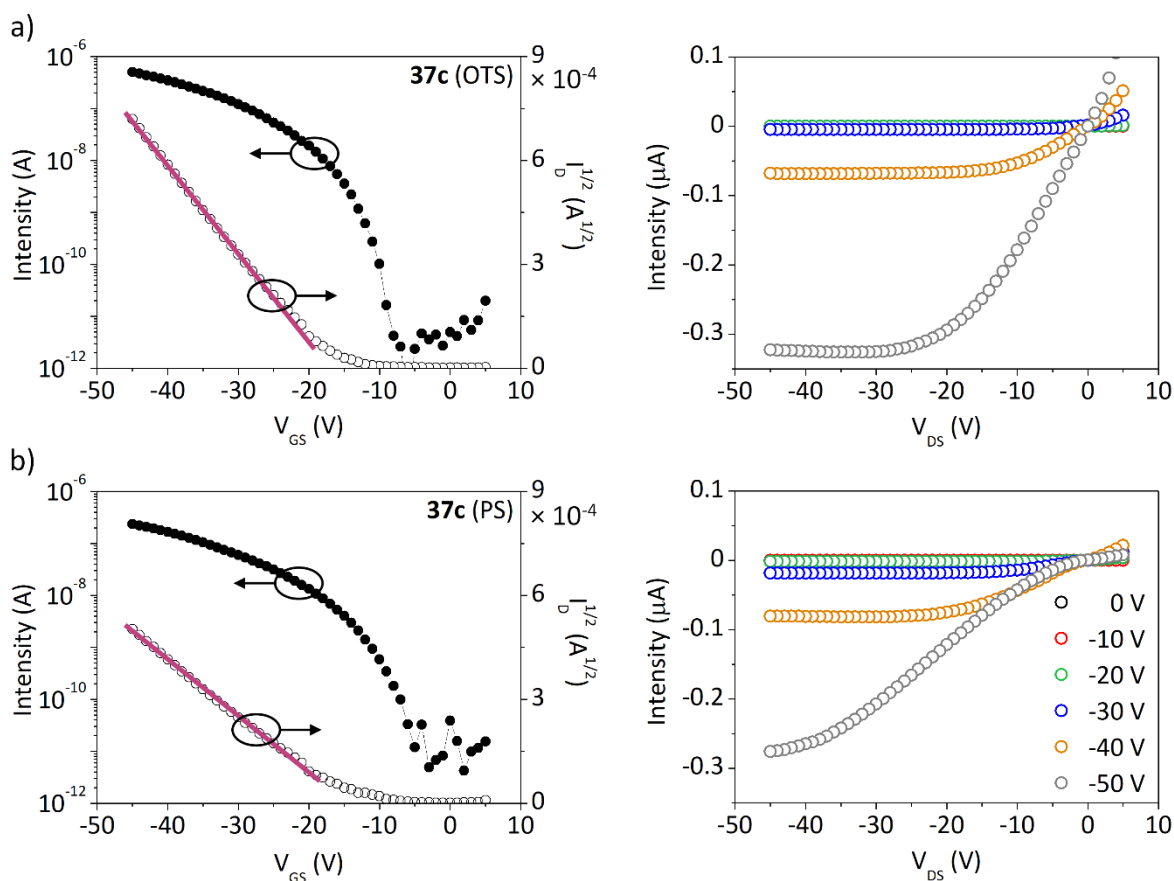


Figure 3.6. OTFT characteristics of **37c** over OTS- (a) and PS-treated (b) substrates: transfer ($V_{DS} = -40 \text{ V}$) and saturation (left) and output (right) characteristics.

As observed, the devices fabricated from **37c** display highly linear characteristics, but with a still significant threshold voltage around -20 V . This feature applies to all three derivatives. The outperformance of **37c** also relies on the excellent I_{on}/I_{off} ratios, estimated to be as high as 10^6 and 10^5 over OTS- and PS-treated devices, respectively. Indeed, the presence of peripheral alkyl chains proves as an effective way to improve the I_{on}/I_{off} ratio. The values obtained for this specific derivative are close to those found for the well-known triindole core.^[125]

All the devices were operative up to a year after their fabrication. The detailed evolution of each set of devices is depicted in Figure 3.7.

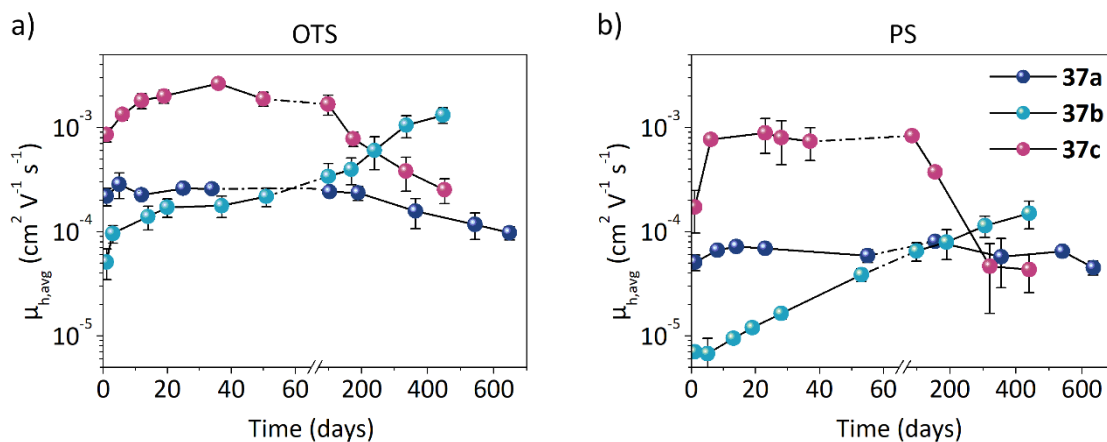


Figure 3.7. Evolution of the charge mobility of devices fabricated from derivatives **37a–c** over OTS- (left) and PS-treated (right) substrates.

Considering the fluctuation of the $\mu_{h,avg}$ values over time, some interesting appreciations can be highlighted. Compound **37a** featured the most uniform performance along its shelf lifetime, which actually extends to an ongoing period of almost two years. The low fluctuation of the mobility as well as its impressive air-stability applies to both OTS- and PS-treated devices. As stated, derivative **37c** displayed outstanding mobility values up to the order of $10^{-3} \text{ cm}^2 \text{ V}^{-1} \text{ s}^{-1}$ over both dielectrics, which were preserved during a considerable period of c.a. 100 days. Subsequently, the $\mu_{h,avg}$ progressively decreased in both OTS- and PS-treated devices, particularly in the latter.

On the other hand, the trend observed in the case of **37b** is certainly anomalous. In fact, the highest mobility obtained for this core was registered more than one year after the fabrication of the devices, regardless of the selected organic dielectric. The evolution from the fabrication day to 15 months after implied an improvement of the charge mobility of more than an order of magnitude (ca. a 20-fold increase). As commented in the previous chapter, p-type organic semiconductors are prone to improve their performances with respect to the fabrication phase due to in-situ oxidation processes. Thus, it is relatively common that devices undergo moderate to abrupt improvements during the first days after fabrication as observed in structure **30**. However, this case highly stands out because of the steadily enhancement of the performance occurred through the course of 15 months. This phenomenon was compared with other reported cases, but studies comprising such extended periods are seldom described. After surveying the literature, a comparable trend was found in DNTT-based devices only when they were exposed to both light and air conditions during their storage.^[203] To explain it, Ding *et al.* suggested that the

gradual twofold increment of the μ_h over 300 days could be due to light-assisted doping by oxygen molecules diffusing into the semiconductor. This case differs from the one herein presented regarding the light exposure during the storage and a more moderate enhancement. Another example was reported by Chiarella *et al.* while describing the stability of an n-type semiconductor based on the perylene diimide nucleus.^[204] In it, the deposited layer suffered morphological transitions due to a spontaneous wetting process, which converted the initially not-compacted film into a continuous one. This process, which was described to happen in a large time-scale up to months, involved a subsequent increase of the charge mobility of several orders of magnitude. However, this second example refers to a distinct deposition technique, namely supersonic molecular beam deposition. Figure 3.8 illustrates the improvement of the OTFT characteristics of **37b** over time on the basis of a representative OTS-treated device.

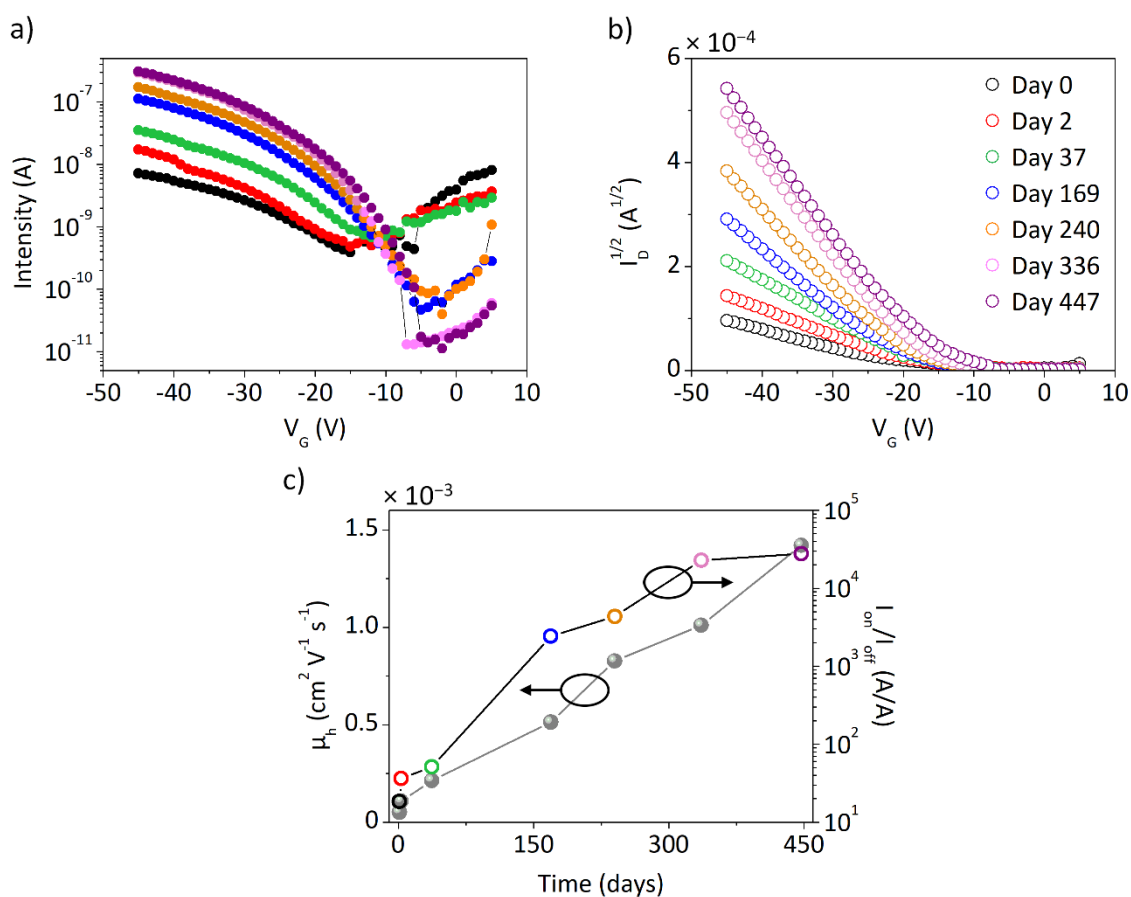


Figure 3.8. Evolution of the OTFT characteristics of a representative OTS-treated device based on **37b** throughout 447 days (ca. 15 months): a) transfer ($V_{DS} = -40$ V) and b) saturation characteristics; c) individual hole mobility values and I_{on}/I_{off} ratios calculated from the corresponding saturation and transfer characteristics, respectively.

As represented, the improvement of the performance occurred over one year extends to all aspects. In fact, the I_{on}/I_{off} ratio increased three orders of magnitude, approximately

from 10^1 to 10^4 . Future measurements will confirm whether this ascending tendency settles **37b** as the best performing semiconductor studied in this work or, to the contrary, finally stabilizes or even starts to decrease. Also, the search of the cause of this anomalous behavior is likely to engage subsequent analyses and studies both from an experimental and theoretical point of view.

3.4.2. Molecular order and morphology

Similarly to the previous chapters, an analysis of the arrangement in the solid state has been carried out. Unfortunately, the information regarding the single crystal structures based on **37** is still limited. The structure of **37a** could be approached by means of single crystal X-ray diffraction, but the presence of an unknown component within the unit cell impeded an in-depth analysis. Investigation towards the elucidation of the single crystal of all three derivatives *via* powder X-ray diffraction is currently ongoing as well.

Single crystal

37a crystallized in space group $P2_1/c$ of the monoclinic system in the presence of an unknown compound. Albeit the inaccuracy of this information with regard to the actual arrangement of the material within the device, it still sheds light on the planarity and main intermolecular interactions. The elucidated structure is depicted in Figure 3.9.

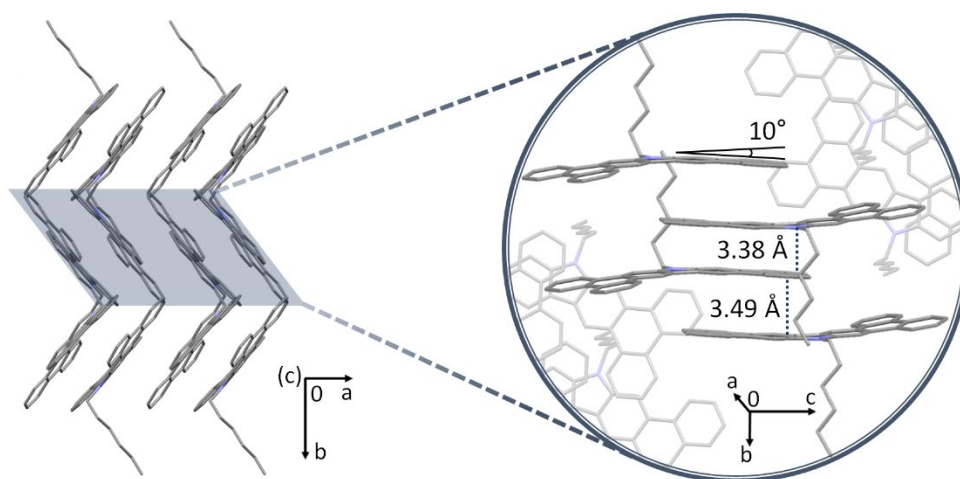


Figure 3.9. Crystal structure of **37a**, with the torsion angle of the aromatic system and the π - π stacking distances highlighted in the amplified region. The unknown compound present in the unit cell and hydrogen atoms have been omitted for clarity.

Contrarily to the other two analyzed nuclei, the aromatic system of the diphenanthrocarbazole core is not entirely planar, or at least the *N*-hexylated variant. Specifically, the phenanthrene extensions deviate approximately 10° with respect to the central ring. Despite the differences, the arrangement of **37a** could be assimilated to a

favorable γ -type packing like that of structure **1**. As highlighted in the amplified region of Figure 3.9, the symmetry within the columns is dimeric with intermolecular π - π distances as short as 3.38 and 3.49 Å. Thus, the π - π stacking found in the packing is advantageous for an effective charge transport throughout the film. The void associated to the unknown impurity corresponds to a moderate volume of 246 Å³. Because of that, this disposition could diverge from the actual arrangement within the device.

It should be mentioned that the single crystal of a different diphenanthrocarbazole derivative is reported in the literature. Specifically, it corresponds to 3,6,14,17-tetrafluoro-10-methyl-10*H*-diphenanthrocarbazole,^[201] an analog structure of **37c** possessing peripheral fluorine moieties instead of hexyl chains. Interestingly, its structure disposes in a very favorable β -type (or sheet) arrangement with promisingly short π - π stacking distances. This precedent gives rise to the premise that the outstanding performance of **37c** could originate due to a similar arrangement, which entices further investigation. The design and study of similar derivatives also represent an engaging project considering the novelty of this core.

Characterization of the thin films

The relationship between the performance of the devices and the role of the molecular order within the thin films has been investigated by means of GIXRD. As shown in Fig. 3.10, the alkylation patterning again exerts certain effects to the degree of order and GIXRD profiles.

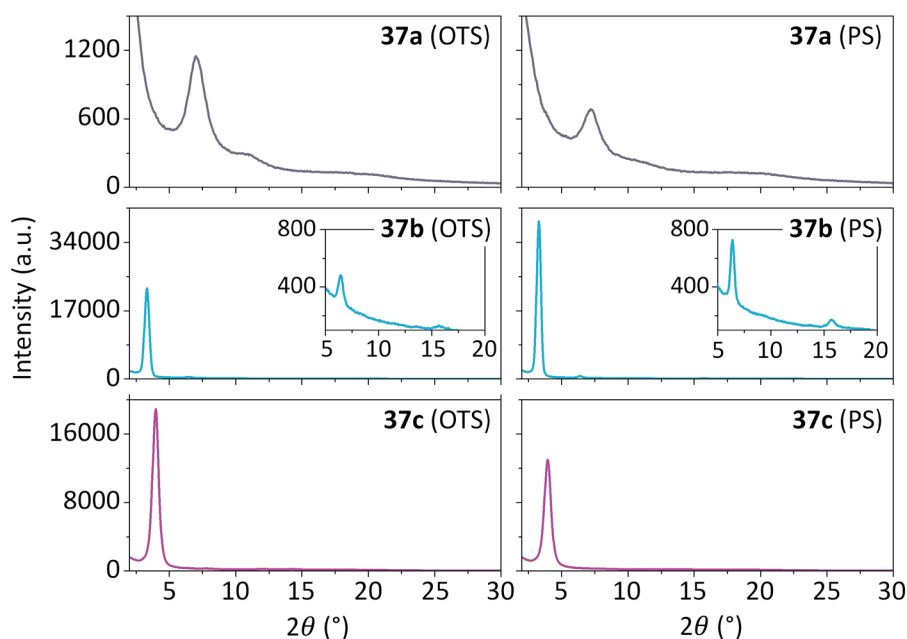


Figure 3.10. GIXRD patterns of derivatives **37a–c** over OTS- (left) and PS-treated (right) substrates. The inset shows an amplification of the secondary peaks observed in the case of **37b**.

All three compounds present GIXRD patterns with discerned diffraction peaks, which correlate with their powder X-ray diffraction. Derivative **37a** displays a main diffraction signal at $2\theta = 7.1^\circ$; derivative **37b** peaks at $2\theta = 3.3^\circ$, with two minor diffractions at 6.4 and 15.7°; in the case of **37c**, the main signal corresponds to a $2\theta = 4.0^\circ$. Since the crystal structure **37a** is not appropriate for comparison due to the embedded impurity and those of **37b–c** are still unavailable, we could not extract further conclusions regarding the intermolecular packing within the device. However, the degree of order of the thin films is equally enlightening.

The choice of the organic dielectric covering the substrate only modulates the degree of order but not the preferred orientation or the intermolecular arrangement. Compounds **37b** and **37c**, featuring peripheral hexyl chains, stand out because of the high degree of order in the thin-films. The secondary diffraction peaks at $2\theta = 6.4$ and 15.7° from the former could be related to complementary planes detected due to the high degree of order of the films. These measurements were performed in analog substrates right after the fabrication of the devices. Thus, the high degree of order found in the **37b**-based films relates to the initial performance of the devices, i.e. the lowest charge mobility values collected. Not only that, but the degree of order detected over the PS-treated substrate is the highest even though the remarkably underperformance of the corresponding devices. In order to evaluate the potential changes in the disposition of the material in the thin films, the GIXRD measurements were repeated after four and twelve months. Overall, the subsequent GIXRD profiles were very similar to the initial ones, with a slight decrease in intensity over OTS and increase over PS (as represented in Figure A3.2 of the Appendix). Hence, these facts prompt the theory that the origin of the improvement observed in the **37b**-based devices is not associated to morphological or structural issues but electronic ones instead. Similarly to the example of DNTT introduced in the previous section, the gradual enhancement might be induced *via* doping by oxygen.

3.5. Overview: influence of the studied extensions on 9H-carbazole

In this section, the photophysical, electrochemical and semiconductor properties of the three heretofore studied cores will be briefly surveyed. The bare *N*-hexylated derivatives as well as the derivatives featuring peripheral hexyl chains will be also compared.

Optically, a few remarks can be pointed out. The absorption spectra of all structures show low-energy bands that are associated to the $S_0 \rightarrow S_1$ transition,^[133,165,201] as shown in Figure 3.11. These transitions occur in the 400–430 nm region in structures **30** and **37**, whereas they require less energy in the case of **1** (found at 440–460 nm), conditioning the

energy of the optical band gap. The stronger absorption band (378 nm in **1**, 361 nm in **30** and 369 nm in **37**), which is assigned to the $S_0 \rightarrow S_2$ transition,^[133] also follows the same tendency. This also translates into the fluorescence, in which the emission of structure **1** features a higher contribution to the green region than the other cores. Thus, the indole extensions confer a considerably higher bathochromic shift to the carbazole nucleus than the benzothiophene and phenanthrene ones. Structure **37** features the highest fluorescence quantum yield, with values up to 0.19, which contrasts with the 0.05 of **30**.

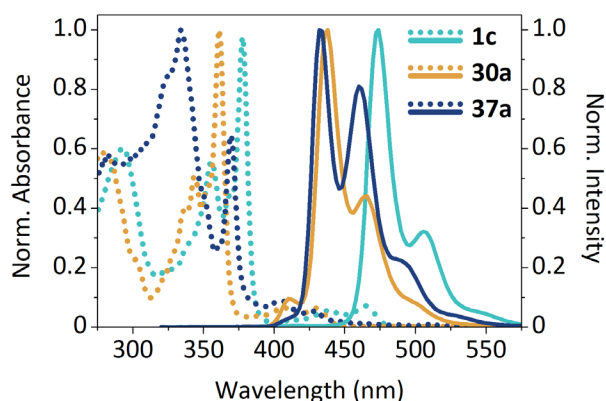


Figure 3.11. Absorption (dotted) and emission (solid) spectra of the *N*-hexylated derivatives **1c**, **30a** and **37a** in dichloromethane solutions.

Another comparison that should be highlighted implies the energy levels of the three structures, which are represented in Figure 3.12.

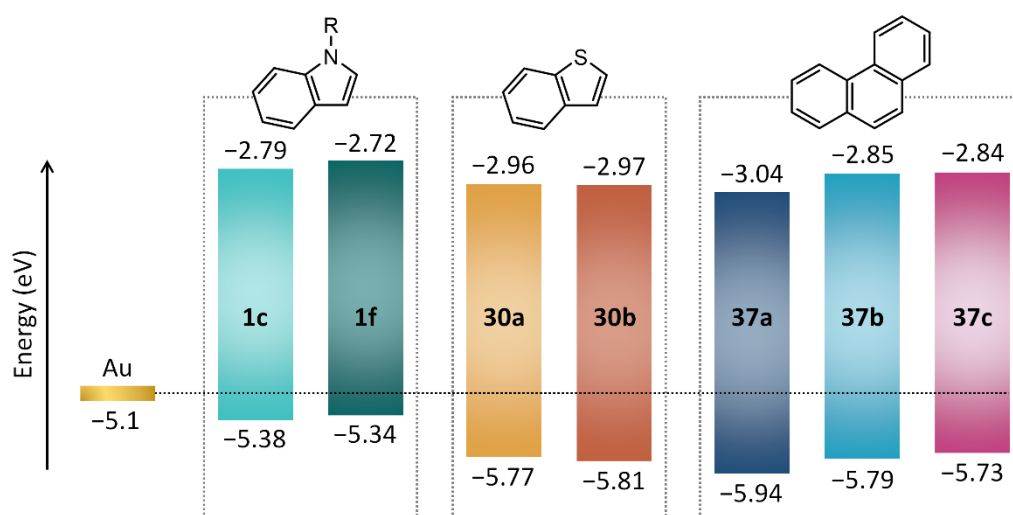


Figure 3.12. Energy levels with respect to the gold work function of derivatives **1c,f**, **30a–b** and **37a–c**.

As observed, the diindolocarbazole core **1** features the lowest ionization potentials. This suggests that the HOMO energy levels are less stabilized, but at the same time confer a

more suitable fit to the gold work function. Electrochemically, cores **30** and **37** display quite analogous characteristics typically found in p-type semiconductors. The impact of adding peripheral hexyl chains is more significant in the case of **37**, with a slight, gradual destabilization of the energy levels from **37a** to **37c**.

Finally, the analysis of the performance of all three carbazole-based cores in OTFTs is the most enlightening, considering the objectives of this Thesis. Since the charge transport properties of the devices have been extensively examined in each chapter, this section will be centered on a global comparison of the extensions applied to the carbazole heterocycle. Figure 3.13 illustrates the evolution of the $\mu_{h,avg}$ over time of devices integrating the three cores. For a rapid analysis, the graphics compare the *N*-hexylated derivatives (**1c**, **30a** and **37a**) with compounds possessing peripheral hexyl chains (**1f**, **30b** and **37b-c**) over both organic dielectrics.

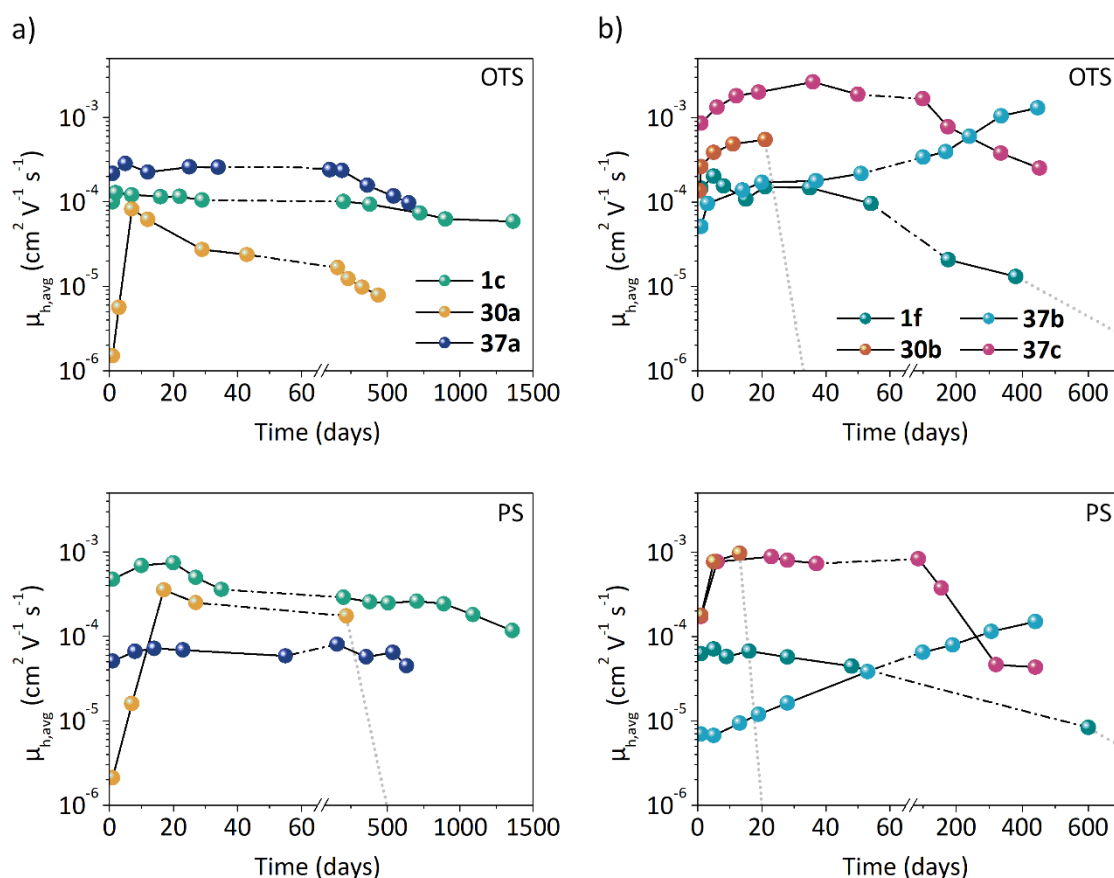


Figure 3.13. Evolution of the charge mobility of devices fabricated from the *N*-hexylated derivatives **1c**, **30a** and **37a** (a) and their analogs displaying peripheral hexyl chains **1f**, **30b** and **37b-c** (b) over OTS- (above) and PS-treated (below) substrates. The dotted lines in grey indicate the estimated period of time in which the active layer of some devices lost their semiconductor properties.

Overall, the addition of peripheral hexyl chains endows all cores with higher charge mobility values. As explained in the corresponding sections, derivatives featuring

peripheral hexyl chains exhibit remarkably higher intensities in their GIXRD profiles, which can be attributed to a higher degree of order within the films. The upgrade in the $\mu_{h,avg}$ is especially notorious in OTS-based devices. The only exceptions to that are the pentahexylated derivative **1f**, featuring a surrounding alkylation patterning, when deposited over PS and the early measurements of **37b**. Omitting the anomalous behavior of **37b**, however, derivatives featuring peripheral hexyl chains cannot keep up their parent constructions in terms of stability, i.e. prolonged shelf lifetime and low variability of the $\mu_{h,avg}$.

The sulfurated structure **30** clearly falls behind from a stability point of view, with a shelf lifetime below 500 days in the case of **30a** and 3 weeks in **30b**. Contrarily, the diindolocarbazole (**1**) and diphenanthrocarbazole (**37**) cores outstand with extended shelf lifetimes and relatively low fluctuation of the $\mu_{h,avg}$ over time. The promising packing in a γ -like motif displayed by all the elucidated crystal structures of **1** (**1a**, **1b** and **1d**) and **37** (**37a**) also augur further optimization of the devices. Additionally, the synthetic routes towards **1** and **37** are quite versatile, especially the straightforward synthesis of the latter. The facile attachment of diverse peripheral alkyl chains to it, which greatly modulate its performance, is indeed convenient. With all these factors in mind, the diphenanthrocarbazole core presents the highest potential with regard to subsequent studies.

3.6. Conclusions

The benefits of the Scholl reaction in the search of new organic semiconductors have been evidenced in the successful formation of diphenanthrocarbazole derivatives. The cyclization towards diphenanthrocarbazole furnishes the required π -conjugation extent, which is translated into adequate optoelectronic characteristics. Therefore, the study of this promising core concludes the trilogy of ladder-type carbazole-based systems envisioned in this work. Even when compared with the two heretofore studied cores, the diphenanthrocarbazole core stands out for the excellent semiconductor properties, air-stability and robustness. Not only that, but the facile access to differently substituted derivatives, such as the addition of peripheral hexyl chains surveyed in this chapter, anticipate a great potential in the field. This core, which is clearly favored by the functionalization of the SiO₂ surface with OTS, has displayed the highest charge mobility registered so far. Specifically, the strongly head-tail orientated design of **37c**, featuring four peripheral hexyl chains, grants the core with a $\mu_{h,max}$ up to $3.0 \times 10^{-3} \text{ cm}^2 \text{ V}^{-1} \text{ s}^{-1}$ in OTS- and $1.2 \times 10^{-3} \text{ cm}^2 \text{ V}^{-1} \text{ s}^{-1}$ in PS-treated devices. On the other hand, the doubly alkylated analog **37b** displays an anomalous and periodic enhancement regardless of the organic dielectric, implying an approximate 20-fold increase of the $\mu_{h,avg}$ and three orders of magnitude in the

$I_{\text{on}}/I_{\text{off}}$ ratio through the course of 15 months. Consequently, the results over OTS culminate to an also notorious $\mu_{\text{h,max}}$ up to $1.5 \times 10^{-3} \text{ cm}^2 \text{ V}^{-1} \text{ s}^{-1}$. All derivatives claim an ongoing shelf lifetime up to years. The first results regarding the intermolecular arrangement suggest an appealing γ packing and an outstanding degree of order within the films, confirming the suitability of this construction and motivating further research.

CHAPTER

4

Beyond 9*H*-carbazole: the potential
of the dibenzothiophene nucleus



CHAPTER 4. Beyond 9H-carbazole: the potential of the dibenzothiophene nucleus

4.1. Introduction

The enticing performance of the diphenanthrocarbazole core, outpacing the rest of the studied carbazole-extended systems in terms of charge mobility, promoted our interest on structures with ramified π -systems rather than entirely linear. In this context, the potential of the Scholl reaction in the design of new semiconductors was reinforced. Indeed, this reaction provides an easy and versatile synthetic approach towards not only variants of specific cores but also a vast range of completely new and unique constructions. Taking this into account, the perspective over alternative building blocks beyond 9H-carbazole appeared as a coherent next step to continue the search of novel materials. Specifically, the application of the Scholl reaction in extending the dibenzo[*b,d*]thiophene heterocycle, i.e. the sulfurated equivalent of 9H-carbazole, seemed particularly appealing. As discussed in Chapter 2, the inclusion of sulfur as heteroatom is currently a well-known resource in the search of improved semiconductors.

Hence, tetrabromothiophene (TBT) assumes the role of synthetic starting material in this chapter. Figure 4.1 illustrates the synthetic strategy envisioned for the extension of dibenzothiophene from tetrabromothiophene, which is analogous to the procedure employed in the synthesis of **37** in the previous chapter. The resulting system is known as diphenanthro[9,10-*b*:9',10'-*d*]thiophene.

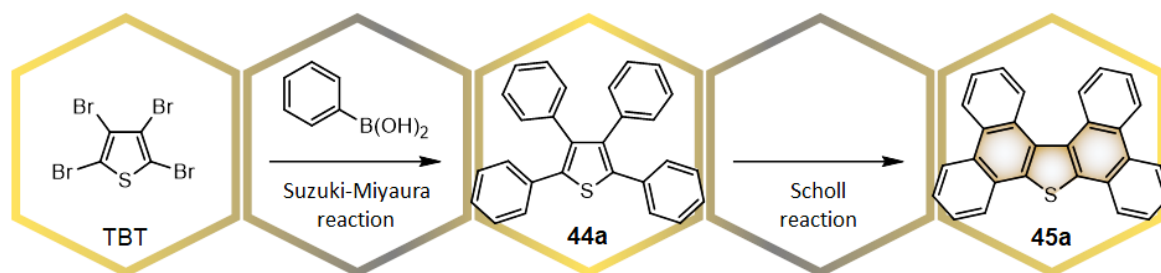


Figure 4.1. Synthetic strategy towards ramified π -extended system diphenanthro[9,10-*b*:9',10'-*d*]thiophene derived from the dibenzo[*b,d*]thiophene core (highlighted in orange), which starts from the commercially available tetrabromothiophene (TBT).

In fact, the easy availability of tetrabromothiophene as starting material and the immense library of commercially-available aromatic boronic acids provide an open field of investigation. So far, several reported polycyclic structures derived from dibenzothiophene

have been synthesized using this approach, proving its adequacy.^[205–207] Contrarily to the hitherto studied compounds, the final structure **45** does not feature a planar π -system due to the steric hindrance between the upper phenyl scaffolds. Nevertheless, the integration of derived structures as hole transporting semiconductors in devices such as single crystal FETs^[205] and perovskite solar cells^[206] demonstrates the potential of this architecture regardless of its non-planarity.

One of the main objectives of this chapter is therefore the evaluation of the synthetic scope of the Scholl reaction in the design of new structures along with their optoelectronic characterization. The incorporation of scaffolds of different nature to the parent structure **45a**, such as aliphatic, aromatic, electron-donating or electron-withdrawing groups, are interesting both for modulating the optoelectronic properties of the core and from a synthetic point of view. Also, the integration of larger aromatic scaffolds would provide an even larger extension of the π -system, giving access to completely new constructions. It should be noted that the interest of this synthetic approach resides not only in the final cyclized compounds but also in the unbounded intermediates, especially regarding their photophysical properties.

4.2. Precedents of AIE studies on propeller-shaped materials

Many studies acknowledge several analogue structures of **44**, often called propeller-shaped molecules, as well-known models of the unique aggregation-induced emission (AIE) phenomenon.^[208–209] Equivalent structures incorporating nitrogen, silicon, phosphorus or even 1,2,3,4-tetraphenyl-1,3-cyclopentadiene, which does not include heteroatoms, are some of the representative examples featuring AIE that collects Figure 4.2. Apart from tetraphenylfuran (TPF), which displays the opposite phenomenon of aggregation-caused quenching (ACQ), the AIE effect observed for tetraphenylthiophene is by far the weakest from the ones compiled in Figure 4.2.^[209] The anomalous behavior of **44a** with respect to its counterparts has been object of several recent studies. As revealed by the single crystal of **44a**, the main reason of this behavior seemingly resides into the weak intermolecular interactions present in the packing.^[209–211] Typically, the lack of emission in solution of this type of constructions is attributed to the free rotation of phenyls, which promotes a non-radiative decay rather than emissive. Alternatively, calculations over 1,1-dimethyl-2,3,4,5-tetraphenylsilole (TPS)^[212] and 1,2,3,4-tetraphenyl-1,3-cyclopentadiene (TPC)^[213] suggest that the main deactivating mechanism of the emission in propeller-shaped molecules could be through a ring puckering pathway occurred in the central heterocycle. In either way, both mechanisms are suppressed with the formation of aggregates due to the additional restrictions established.

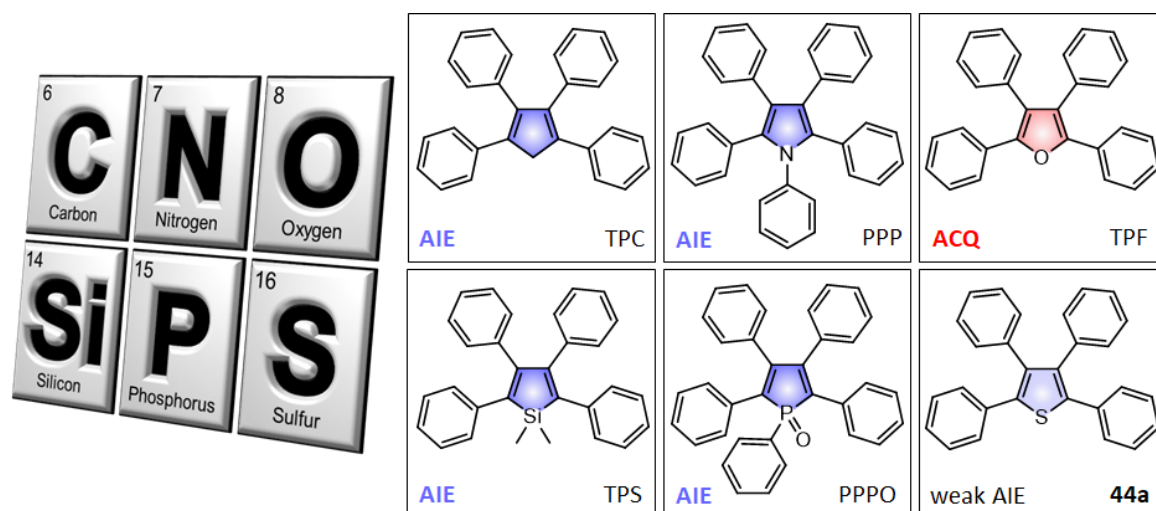


Figure 4.2. Analogue structures of the herein studied tetraphenylthiophene (**44a**) that display AIE: 1,2,3,4-tetraphenyl-1,3-cyclopentadiene (TPC)^[214], 1,2,3,4,5-pentaphenylpyrrole (PPP)^[215], 1,1-dimethyl-2,3,4,5-tetraphenylsilole (TPS)^[216] and 1,2,3,4,5-pentaphenylphosphole oxide (PPPO)^[217]. Contrarily, tetraphenylfuran (TPF) displays the opposite effect ACQ. Adapted from ref. 209.

Since the AIEgens shown in Figure 4.2 also lack effective π - π interactions, this translates into an enhancement of the fluorescence in the solid state. Unfortunately, this does not apply in the case of **44a**. Stojanović *et al.* shed light on the role of the triplet states on the relaxation mechanisms and proposed a non-radiative pathway exclusive for **44a**, involving the stretching between carbon and sulfur.^[211] In this case, the loose packing found for **44a** still permits such mechanism in the solid state, justifying the anomalously weak AIE it exhibits. Most of these studies coincide on the need to impose additional constraints to **44** to achieve effective AIE. Indeed, Gu *et al.* demonstrated the enhancement of emission of **44a** under high pressure, as a result of the inhibition of the non-radiative vibrational process.^[212] Also, Guo *et al.* described several mesogens based on the **44** nucleus for luminescent liquid crystals displaying AIE, proving the effectiveness of the rational addition of scaffolds.^[218]

Hence, the synthesis of different derivatives of **44** brings the opportunity to further extend this study and get insight into the topic. The aimed inclusion of different groups to tetraphenylthiophene or the substitution of phenyls with larger and more hindering scaffolds could be a proper feature to restrict the structure in the solid state, unlocking the AIE phenomenon.

4.3. Homogeneously substituted compounds

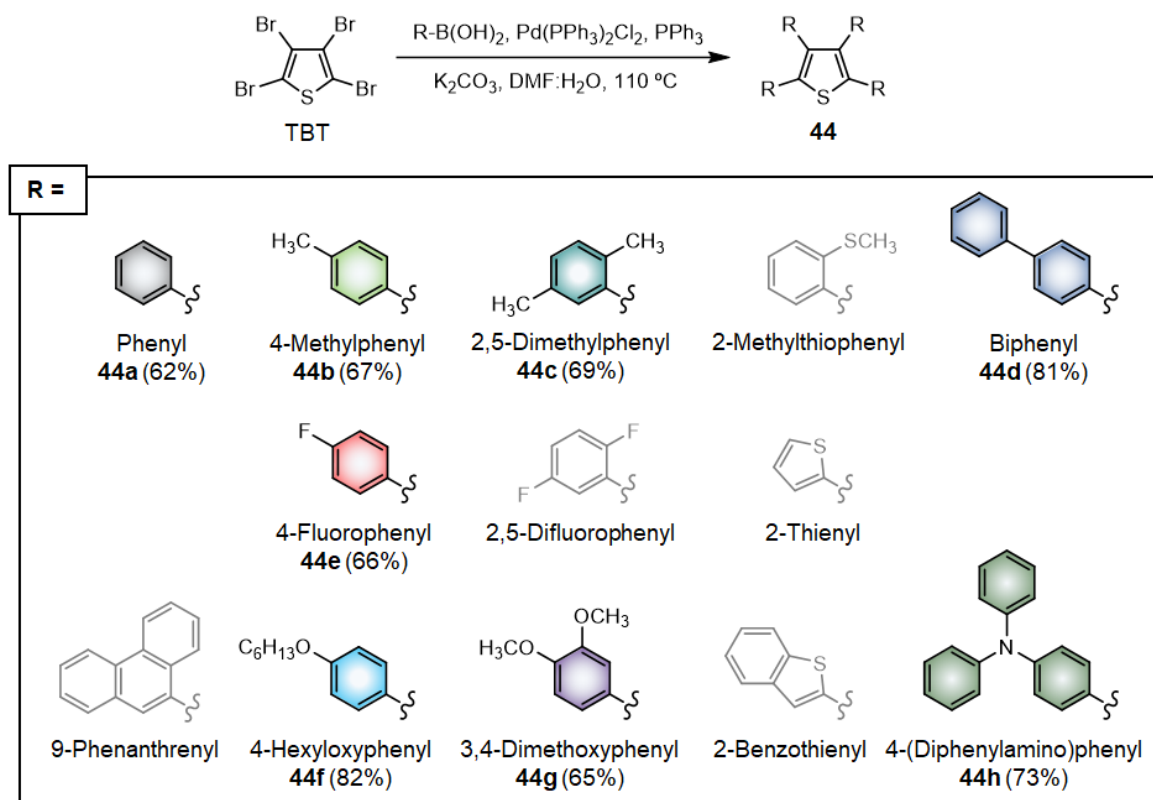
As stated, this Chapter deals with the search of new materials with potential interest in diverse topics within organic optoelectronics using an alternative strategy. In the first

stages of this study, the design and choice of scaffolds will not be entirely rational but conducted in an untargeted way. Starting from a wide and assorted collection of arylboronic acids, this strategy permits a rapid evaluation of the scope and limitations of the envisioned synthesis and the structural features that yield the sought properties. From this information, the design can be modulated accordingly in future studies. In an initial approach, the study will focus on homogeneously substituted compounds, that is, products derived from a simultaneous tetra-substitution of the corresponding scaffold.

4.3.1. Synthesis

Step I: Suzuki-Miyaura cross-coupling reaction

The first step concerning the fourfold Suzuki-Miyaura cross-coupling reaction was attempted using the same conditions that afforded the analogous compounds **37a–c** in Chapter 3, namely the use of the corresponding boronic acid, catalytic Pd(PPh₃)₂Cl₂ and PPh₃, K₂CO₃ as base and a mixture of DMF and water as solvent at 110 °C. Scheme 4.1 illustrates the employed conditions as well as the assortment of arylboronic acids tested along with the resultant products.



Scheme 4.1. Synthesis of several derivatives of the intermediate structure **44** through a fourfold Suzuki-Miyaura cross-coupling reaction using TBT (1 mmol), the arylboronic acids specified below (4.5 mmol), Pd(PPh₃)₂Cl₂ (0.05 mmol), PPh₃ (0.1 mmol) and K₂CO₃ (20 mmol) in DMF:H₂O (22.5 mL, 6:1 v/v). The colored intermediates **44a–g** represent the ones successfully prepared employing these conditions.

As stated, the synthesized structures based on the non-substituted **44a** were obtained from a diverse selection of boronic acids, which comprises several phenyl scaffolds substituted with a variety of groups in different positions, sulfurated heterocycles and the bulky 9-phenanthrenyl system. Additionally, the incorporation of the 4-(diphenylamino)phenyl moiety was projected since it represents a well-known building block in the search of AIEgens.^[88,219–221] The reported conditions were successful in the coupling of eight out of the thirteen proposed boronic acids, with promising yields from 62 to 82%. These results are quite notable considering that the synthesis implies a simultaneous tetra-substitution.

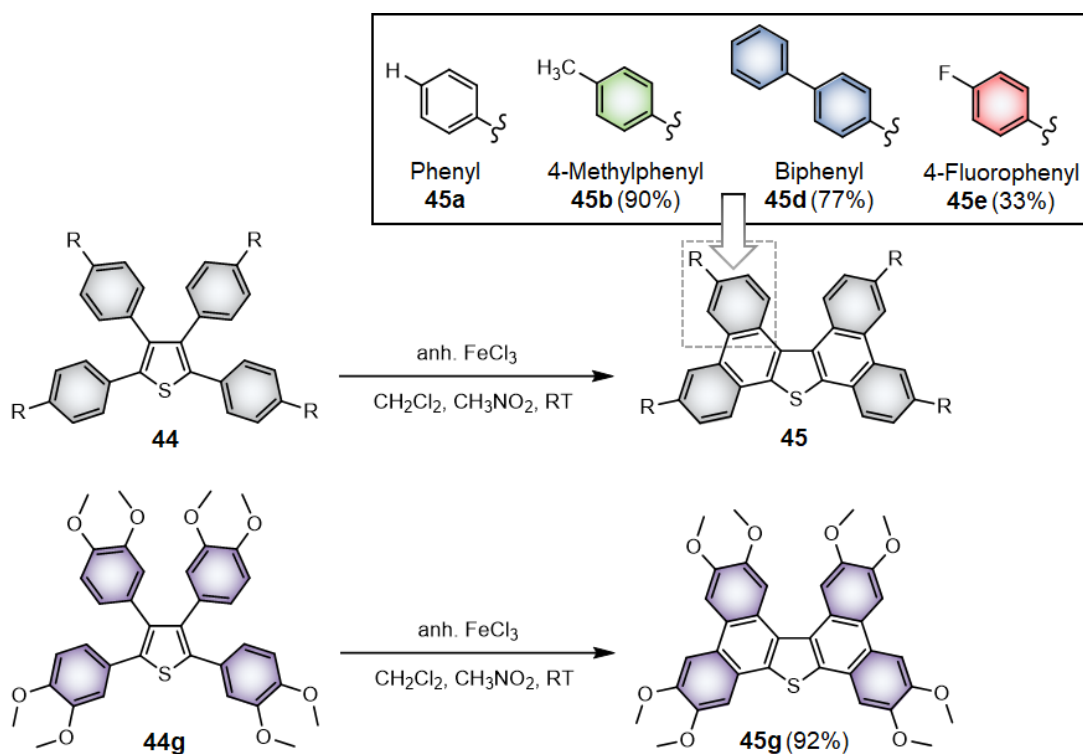
Regarding the unsuccessful couplings, several aspects should be mentioned. The reaction with 9-phenanthrenylboronic acid afforded some compounds that could not be identified nor characterized as the sought tetra-substituted product due to their severe insolubility and difficulty to ionize via mass-spectrometry. On the other hand, none of the reactions comprising sulfurated boronic acids afforded the desired products. Specifically, reactions with 2-methylthiophenyl and 2-thienylboronic acids only led to di-substituted products in positions 2 and 5, which in the case of 2-thiophene also implied the loss of one or both of the remaining bromines. In the case of 2-benzothiophenylboronic acid, however, the reactants were consumed through undesired polymerization or degradation side reactions. This was similarly observed for 2,5-difluorophenylboronic acid, despite their different structural and electrochemical compositions.

The precedents of fourfold couplings of sulfurated heterocycles to tetrabromothiophene employing the Suzuki-Miyaura reaction are scarce, hinting the limitations of the procedure on this substrate.^[222] Alternatively, the few successful examples did not imply the coupling of the corresponding boronic acid, but substitutes such as the respective pinacol ester^[223] or the trihydroxyboronate salt^[224] were used instead. Seemingly, the Stille^[225] and Kumada^[226–227] cross-coupling reactions are also plausible choices in this case. Considering that the extension of dibenzothiophene with four sulfurated heterocycles already appears in a few reported examples, further research in this direction was discarded.

With respect to the dehalogenation side reaction, some examples revealed that it is prone to happen in cross-coupling reactions depending on factors such as the substrate and the solvent.^[228–229] After surveying the literature, this undesired process was found to hamper the Suzuki-Miyaura reaction in analogue heterocycles containing N-H, such as pyrrole^[230] and pyrazole^[231]. In the case of thiophene, the dehalogenation of 4,5-dibromothiophene-2-carboxaldehyde was also reported.^[232] Remarkably, all these examples suffered from dehalogenation only on *meta* (β) positions with respect to the heteroatom.

Step II: Scholl reaction

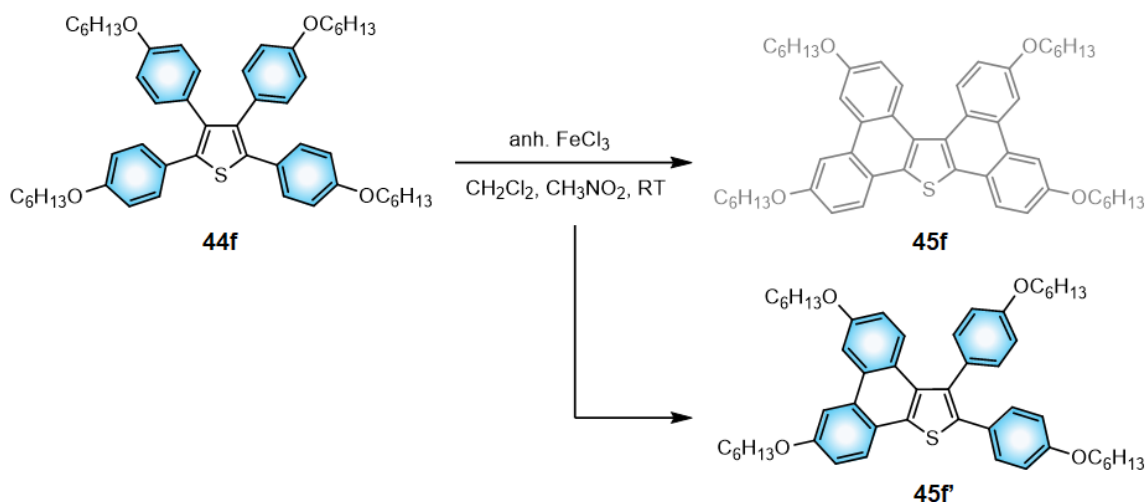
The Scholl reaction was carried out with an excess of anhydrous FeCl₃ in a mixture of dichloromethane and nitromethane at room temperature. Scheme 4.2 shows the cyclization conditions towards some derivatives of **45**.



Scheme 4.2. Synthesis of the cyclized compounds derived from structure **45** through the Scholl reaction. The cyclisation towards **45g** is shown apart to specify the resulting regioisomer.

The synthesis of the parent compound **45a** was hampered with the formation of a complex mixture of by-products, which prevented its proper purification and characterization. As stated in the literature, the Scholl reaction occasionally fails in the cyclisation of small and non-substituted compounds, leading instead to different by-products.^[233] *Ortho*- and *para*-positions are prone to undergoing undesired couplings, making the unprotected position 4 of **45a** particularly vulnerable to oligomerization. The new synthetic strategy reported recently by Maddala *et al.* could be addressed to circumvent this inconvenience in subsequent designs.^[234] Contrarily, compounds **45b** and **45d**, which possess a methyl and phenyl substituent in position 4, respectively, were obtained in very good yields. The synthesis of **45g** also proved the efficacy of suitably placed directing groups, resulting in an even higher yield of 92% with excellent regioselectivity. Concerning the incorporation of fluorine as an electron-withdrawing group in **45e**, the synthesis proceeded substantially slower and provided a lower yield of 33%, but it was still successful. Unexpectedly, the cyclization of **44f**, which is a priori similar to the ones stated in Scheme 4.2, only led to the

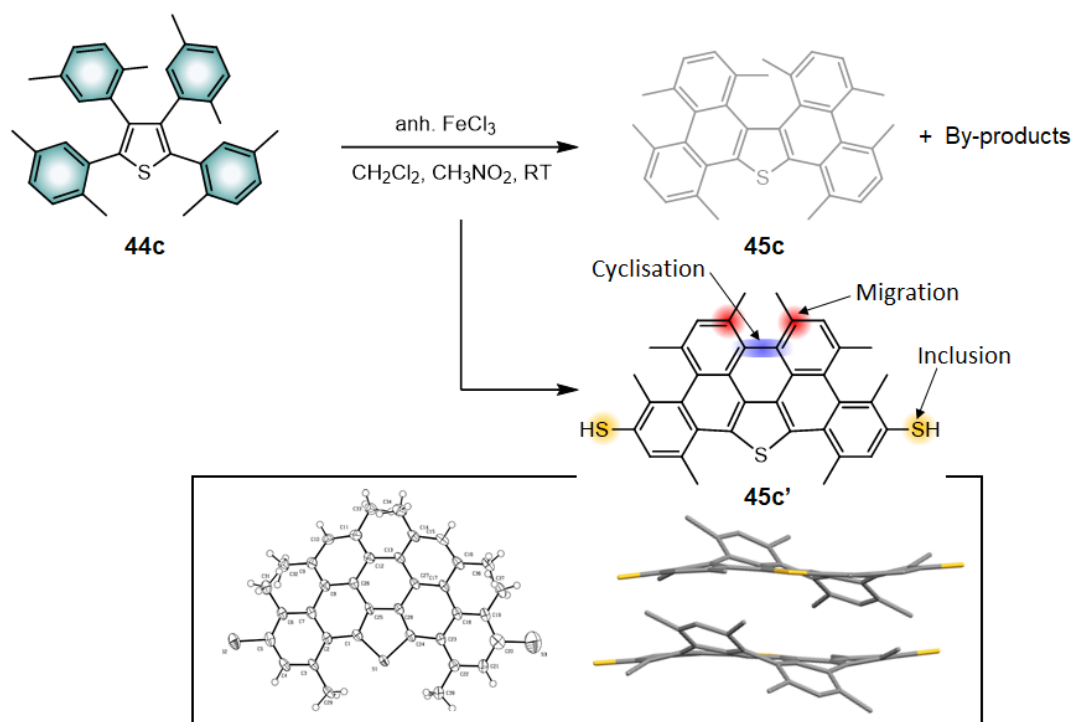
monocyclized intermediate instead of the envisioned product **45f**. As observed, the first cyclization already progressed at a slow rate, whereas the second one could not be detected even after 24 hours (Scheme 4.3).



Scheme 4.3. Cyclization reaction of **44f** under the studied Scholl conditions, in which only the monocyclized intermediate **45f'** was formed.

The cyclization of **44c** was a particularly interesting case. The strategy of incorporating methyl groups at positions 2 and 5 was intended as an additional obstacle to test the robustness of the Scholl reaction. In fact, the envisioned product would feature an even more twisted structure derived from the steric hindrance between the methyl groups. Even though the consumption of **44c** was complete, the crude was composed by traces of multiple by-products and the expected **45c** could not be detected. Despite the efforts, the purification process did not permit a proper separation and characterization of individual by-products. Nevertheless, one of them successfully crystallized during the purification step, which enabled its structural characterization *via* single crystal resolution. The synthetic procedure as well as the elucidated crystal structure are shown in Scheme 4.4. As observed, the elucidated crystal structure demonstrates the migration of two methyl groups into adjacent and less hindered positions. It also suggests an additional cyclization between the phenyls bounded to positions 3 and 4 of thiophene, which could be driven by the migration of the methyl groups. The unexpected introduction of sulfur moieties suggested by the crystal structure highlights the reactivity of unprotected *para* positions. The availability of sulfur in the reaction could only be explained by the occasional cleavage of the thiophene ring in alternative side reactions. Albeit the very low yield, the occurrence of this by-product proves the viability of numerous side reactions under the Scholl conditions that hampered the formation of **45c**. According to the literature, these unusual rearrangements have been demonstrated in different substrates,^[235] especially in highly

hindered or twisted cores.^[236–238] Unfortunately, none of the side reactions was predominant enough to furnish a major by-product in a reasonable yield to enable a further analysis.



Scheme 4.4. Cyclization reaction of **44c** under the Scholl conditions and the proposed structure of one of the by-products on the basis of the crystal structure elucidation.

4.3.2. Crystal structures

The structures of **44b** and **44e** could be elucidated by means of single crystal X-ray diffraction and were compared with that of **44a** reported from the literature.^[209] Their structures are represented in Figure 4.3. **44a** was described to crystallize in space group I2 of the monoclinic system. **44b** also crystallized in the monoclinic system but in space group $P2_1/n$. Their crystal structures dispose differently but present several similarities. **44a** arranges in a displaced parallel way, with certainly high distances of 4.75 Å between aromatic systems and 6.05 Å between sulfur atoms. As described in the introduction, these large distances impede aggregation but still permit the free rotation of the phenyl moieties and other processes, so the AIE phenomenon is not unlocked. The disposition of **44b** changes to a displaced antiparallel packing, with distances between sulfurs of 4.73 and 6.54 Å. The presence of methyl groups apparently tightens the packing but it still conserves relatively high distances between aromatics, which could be beneficial for the sought effect.

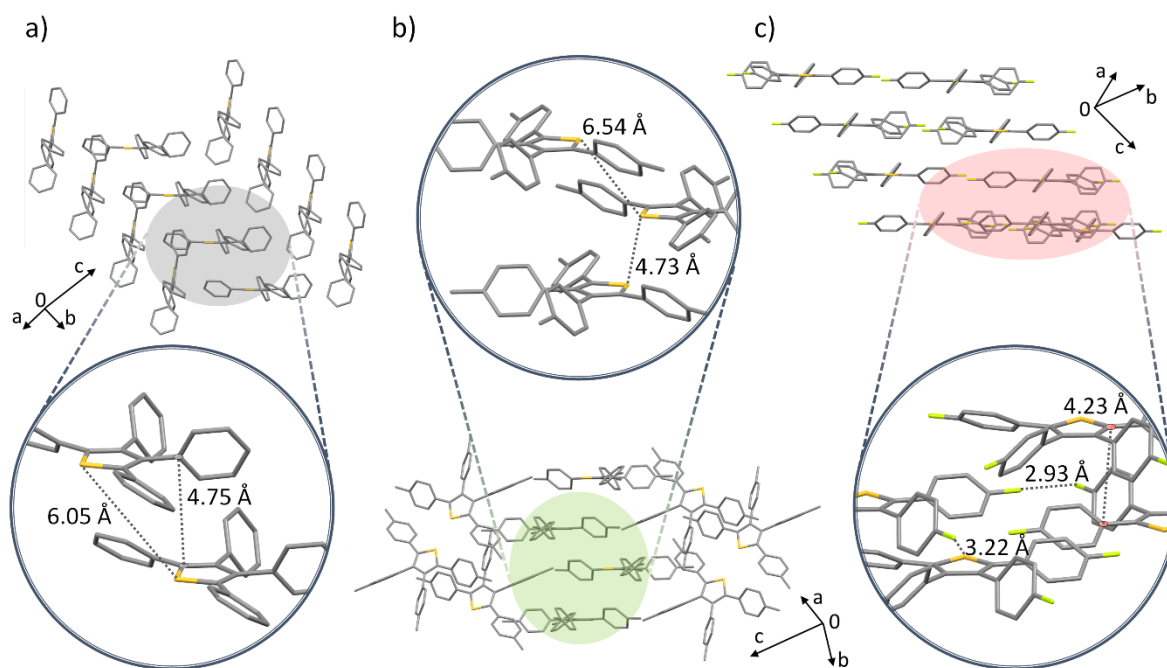


Figure 4.3. Single crystal structures of derivatives: a) **44a**^[209] CCDC number: 1494294; b) **44b** and c) **44e**.

On the other hand, **44e** crystallized in space group P_{-1} of the triclinic system. Contrarily to **44a** and **44b**, the packing of **44e** is also conditioned by the interactions between fluorine moieties. The distance between lateral fluorine atoms is 2.93 Å, which contributes to a more compact distribution. As a result, the material adopts a cofacial packing that can be associated to a β or displaced lamellar motif. In this case, the sulfur heteroatoms are not aligned and display even higher distances of 6.14 and 7.37 Å. Despite the still relatively long intermolecular π - π distances of ca. 4.23 Å, this type of arrangement seems a priori more prone to aggregation. It should be noticed that the phenyl moieties are not planar with respect to the thiophene nucleus in any of the three derivatives.

4.3.3. Photophysical properties

The optical properties of derivatives **44a–h** and their cyclized counterparts **45** in dichloromethane solutions are collected in Table 4.1. All derivatives emit into the UV-blue region of the spectrum. The addition of electron-donating groups to **44a** causes a slight bathochromic shift on both the $\lambda_{\text{abs,onset}}$ of the absorbance spectrum and the maximum $\lambda_{\text{em,max}}$. The magnitude of the shift in the emission spectrum depends on the substituent, which gradually increases from 6 to 28 nm for the *p*-methylated **44b** and the biphenylated **44d**, respectively. Notably, the emission of **44d** also displays two secondary peaks in the UV region at 352 and 368 nm. The addition of the 4-(diphenylamino)phenyl moieties in **44h** results into an even larger bathochromic shift of 57 nm that places its emission into the blue-green region. On the other side, the addition of fluorine in **44e** derives into a small

hypsochromic shift of 4 nm with respect to **44a**. It is also significant the hypsochromic shift of 19 nm displayed by **44c**. The absorption and emission spectra of all derivatives are represented in Figure 4.4.

Table 4.1. Optical properties of the non-cyclized derivatives **44a–h** and their cyclized counterparts in dichloromethane.

	Unbounded compounds			Cyclized compounds			
	$\lambda_{\text{abs,onset}}$ ^[a] (nm)	$\lambda_{\text{em,max}}$ ^[b] (nm)	Φ_f ^[c]	$\lambda_{\text{abs,onset}}$ ^[a] (nm)	$\lambda_{\text{em,max}}$ ^[b] (nm)	Φ_f ^[c]	
44a	358	400	0.02	45a ^[d]	380	394	0.05
44b	363	406	0.02	45b	383	384, 400	0.04
44c	318	381	<0.01				
44d	392	352, 368, 428	0.09	45d	408	409, 429	0.21
44e	354	396	0.02	45e	379	403	0.04
44f	373	416	0.02				
44g	382	424	0.02	45g	395	393, 412	0.04
44h	430	457	0.14				

[a] Absorption onset wavelength ($\lambda_{\text{abs,onset}}$). [b] Wavelength of maximum emission ($\lambda_{\text{em,max}}$), recorded after excitation at 300 nm. [c] Fluorescence quantum yields (Φ_f), determined using POPOP as standard. [d] Results from reference 234.

The study of the Φ_f of the open intermediates **44** was equally interesting as a prelude to the AIE analysis. As observed, most of them displayed values similar to that of the parent **44a** ($\Phi_f = 0.02$ in solution). Comparatively, the analogue **41** studied in the previous chapter, which possesses 9*H*-carbazole as the central heterocycle instead of thiophene, displays a much higher quantum yield value of 0.33 in solution. On the other hand, **44d** and **44h** outstand with higher values of 0.09 and 0.14, respectively, whereas **44c** is almost non-emitting. Hence, the inclusion of methyl groups in positions 2 and 5, intended as a further restriction to the free rotation of the phenyl moieties, resulted into the loss of fluorescence. In fact, the photophysical properties of **44c** are more similar to those of the bare thiophene nucleus^[239] than those of the rest of derivatives. Seemingly, the restriction caused by the 2,5-dimethyl substituents in the phenyl moieties derives into a loss of conjugation with the thiophene nucleus, explaining the anomalous hypsochromic shift.

Unexpectedly, the cyclisation process also induced a hypsochromic shift of the emission spectrum with respect to the open intermediates. Typically, the expansion of the π -system is translated into an augment of the emission wavelength due to the higher conjugation. In this case, however, the non-planarity of the molecule prevents an extended π -conjugation thorough the system. Again, the fluorinated derivative **45e** displays the opposite trend,

which in this case implies an increase of the maximum emission wavelength from 396 to 403 nm. Concerning the Φ_f of the cyclized compounds, the phenylated **45d** stands out again with a divergent value of 0.21, outpacing by far the ca. 0.04 displayed by the rest of analogues.

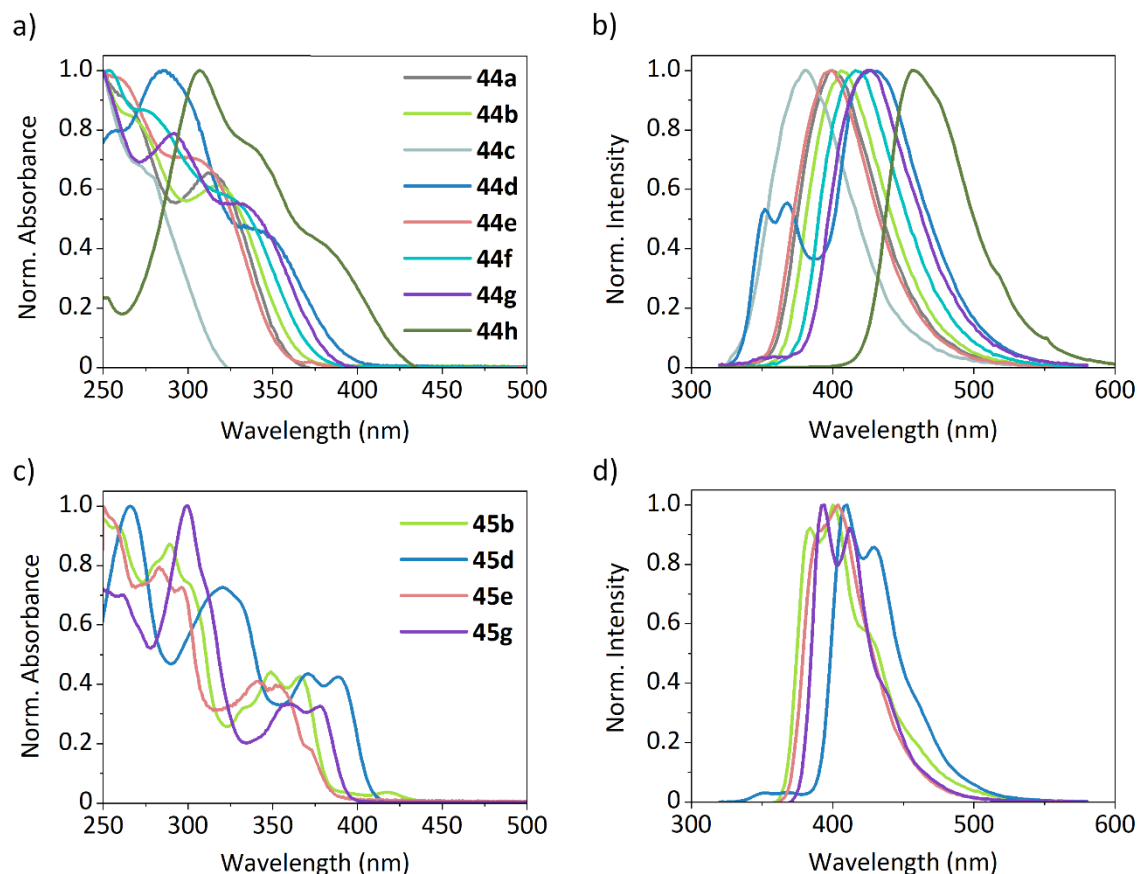


Figure 4.4. Photophysical characterization of the open intermediates **44** and their cyclized counterparts **45**: normalized absorbance (a) and emission (b) of **44**-based derivatives; normalized absorbance (c) and emission (d) of **45**-based derivatives. The emission spectra were recorded in dichloromethane after excitation at 300 nm.

As a first approach to analyze the fluorescent behavior in the aggregate state, a selection of the open derivatives were measured in THF solutions with an increasing percentage of water. Specifically, the emission spectra of derivatives **44b**, **44d**, **44e** and **44h** were recorded in 10^{-5} M solutions of THF and THF:H₂O mixtures of 75:25, 50:50, 25:75 and 5:95 v/v. The addition of higher proportions of water promotes the formation of aggregates due to the loss of solubility of the organic compounds. Nevertheless, none of the analyzed derivatives exhibited conclusive signs of AIE. Compounds **44b** and **44e** displayed similar profiles to that reported for **44a**.^[209] The first impressions suggest that the differences found in their packing motifs are not enough or suitable to unlock the AIE. On the other hand, the higher Φ_f values in solution of derivatives **44d** and **44h** hinted alternative

emissive pathways and, seemingly, these were not increased in the aggregate state. The emission spectra of all compounds and the evolution of the emission intensity in different aqueous percentages can be found in the Appendix (Figure A4.3).

4.3.4. Electrochemical properties

The electrochemical properties of the cyclized derivatives are compiled in Table 4.2 and their cyclic voltammograms and energy levels, represented in Figure 4.5.

Table 4.2. Electrochemical characterization of the cyclized compounds **45**.

Compound	$E_{\text{gap}}^{\text{opt}}$ (eV) [a]	$E_{\text{onset}}^{\text{ox}}$ (V) [b]	IP (eV) [c]	EA (eV) [d]
45b	3.24	0.58	5.97	2.73
45d	3.04	0.57	5.96	2.92
45e	3.27	0.88	6.27	3.00
45g	3.14	0.40	5.79	2.65

[a] Optical energy gap ($E_{\text{gap}}^{\text{opt}}$) estimated from the absorption spectrum ($\lambda_{\text{abs, onset}}$).

[b] Onset oxidation potential ($E_{\text{onset}}^{\text{ox}}$) vs. Fc^+/Fc determined from CV in 1 mM

solutions in dichloromethane. [c] Ionization potential (IP) estimated as

$\text{IP} = E_{\text{onset vs. Fc}^+/\text{Fc}}^{\text{ox}} + 5.39$. [d] Electron affinity (EA) estimated as $\text{EA} = \text{IP} - E_{\text{gap}}^{\text{opt}}$.

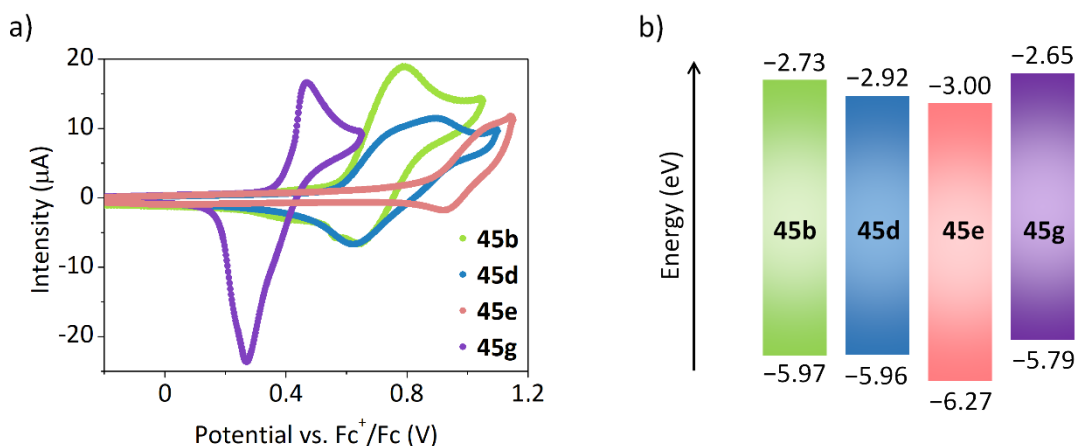


Figure 4.5. Electrochemical characterization of the synthesized derivatives of cyclized structure **45**: a) cyclic voltammograms recorded at a scan rate of 100 mV s^{-1} in 1 mM dichloromethane solutions; b) estimated energy levels.

All derivatives underwent an oxidation process, so the ionization potentials were estimated accordingly. The analyzed **45**-based compounds display rather high ionization potentials close to 6 eV, which could be disadvantageous due to the misalignment with regard to the gold work function (ca. 5.1 eV). As expected, the addition of electro-donating moieties in **45b**, **45d** and **45g** provides lower IP, i.e. a destabilization of the HOMO energy level. The progression of their values goes from 5.97 to a more convenient 5.79 eV in the case of

octamethoxylated **45g**. Contrarily, the addition of fluorine as an electro-withdrawing group in **45e** results in the opposite effect, with an exceedingly high IP value of 6.27 eV.

Globally, structure **45** possesses interesting characteristics that can be modulated with the easy incorporation of diverse substituents. As a result, the evaluation of their potential in optoelectronic applications can be surveyed in subsequent studies.

4.4. Heterogeneously substituted compounds

Given the success of the synthetic approach towards the extended dibenzothiophene derivatives based on **45**, the access to more complex and diverse structures seemed especially interesting. However, the attachment of bulky π -extended scaffolds could easily derive into major solubility problems as observed on the tetra-substitution of 9-phenanthrenyl groups. With this in mind, the combination of bulky aromatic moieties with alkylated ones appeared as a plausible solution. That is, a heterogeneous substitution of tetrabromothiophene concerning positions α and β , which implies two consecutive two-fold substitutions rather than a homogeneous tetrasubstitution. This strategy could also enable the synthesis of derivatives possessing sulfurated heterocycles in positions 3 and 4, mitigating the steric hindrance of phenyls to furnish a more planar structure as demonstrated by some crystal structures.^[224] As discussed, the Suzuki-Miyaura conditions applied for the tetrasubstitution of thiophenyl and benzothiophenyl moieties failed in achieving so, but proved adequate for the formation of disubstituted derivatives.

4.4.1. Design and synthesis

The projected heterogeneous approach aims at structures combining diverse extended scaffolds with 4-hexylphenyl to preserve some solubility. Specifically, 9-phenanthrenyl and 4-dibenzothiienyl were considered as substituents in α positions, whereas 2-benzothiienyl was projected in β positions to attenuate the steric hindrance (Figure 4.6).

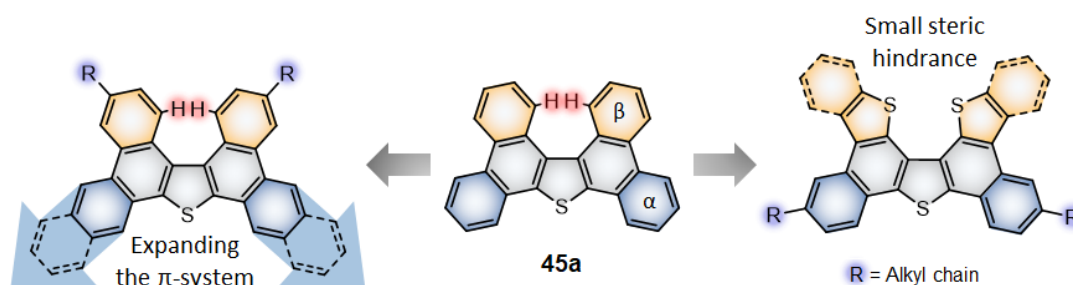


Figure 4.6. Examples of generic structures derived from **45a** displaying a heterogeneous substitution in α (blue) and β (yellow) positions with respect to the central thiophene.

Step I: Suzuki-Miyaura cross-coupling reaction

Even though the initial study was more focused on the scope and robustness of the Scholl reaction in differently substituted intermediates, this first step emerged again as the bottleneck towards the final cyclized compounds. Since the inclusion of sulfurated scaffolds led to a partial debromination process using DMF as solvent, the search of milder analogue conditions was a requisite. The standard conditions employed in Chapters 1 and 2, involving a mixture of THF and water (6:1 v/v) and Pd(PPh₃)₄ as catalyst were an appropriate option in the case of a disubstitution. After surveying the literature, a third procedure implying toluene and water (10:3 v/v) as solvent and Pd(PPh₃)₂Cl₂ as catalyst was also promising to overcome the debromination problems.^[240] Table 4.3 compiles the synthetic scheme to furnish intermediates **46** and **48** and the respective yields under the specific conditions.

Table 4.3. Specific conditions and yields obtained on the consecutive couplings necessary to obtain the di-substituted **46** and tetra-substituted **48** heterogeneous intermediates.

1) R₁-B(OH)₂, Pd catalyst
K₂CO₃, solvent:H₂O, Δ

2) R₂-B(OH)₂, Pd catalyst, K₂CO₃, Δ

R ₁	Solvent	Yield 46 (%)	Yield 47 (%)	R ₂	Yield 48 (%)	Yield 49 (%)	2 steps 48 (%) [c]	One-pot 48 (%) [d]
a 	THF	26	23		55	43 ^[b]	31	70
	Toluene	12	6					
	DMF	56	(-) ^[a]					
b 	THF	46	(-) ^[a]		76	(-) ^[a]	35	53
	DMF	Debromination						
c 	THF	45	(-) ^[a]		52	(-) ^[a]	23	34
	Toluene	19	71					
	DMF	Debromination						

[a] Not detected. [b] Corresponding to the by-product **49a'**. [c] Global synthetic yield from TBT, considering the two separate Suzuki-Miyaura reactions. [d] Synthetic yield from TBT employing the one-pot procedure.

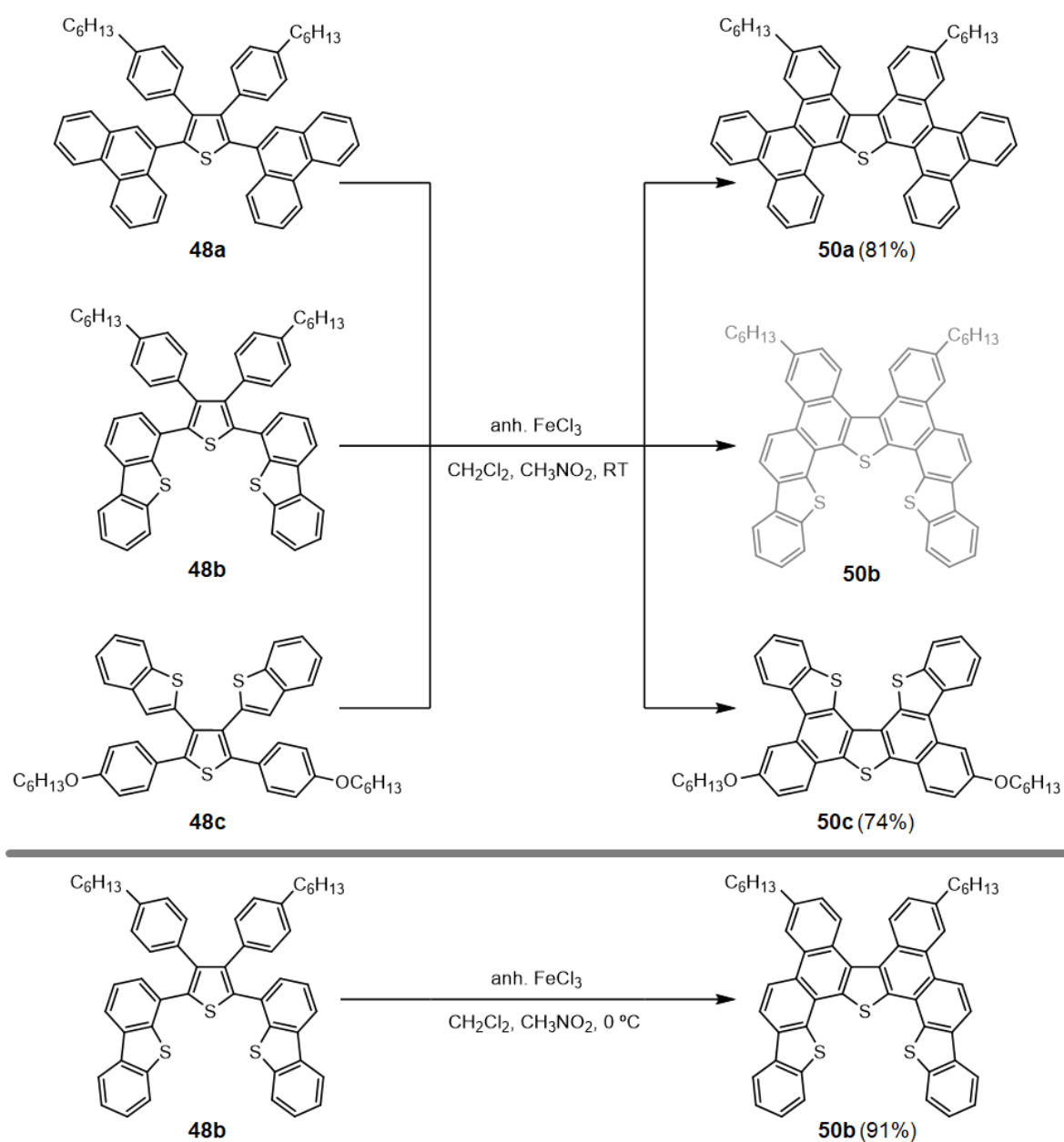
As shown, the choice between solvents resulted critical depending on the boronic acid. As a result, each coupling required a customized synthetic procedure. The presence of the mono-substituted counterparts **47** and **49**, which in some cases hampered the formation of the desired intermediates **46** and **48** in good yields, is also detailed. The use of toluene was clearly disadvantageous in cases **46a** and **46c**, so it was not tested in the synthesis of **46b**. The former provided very low yields of both **46a** and **47a** (12 and 6%, respectively) along with the formation of a major by-product with unknown structure, whereas the latter provided the undesired **47c** in a much higher yield than the targeted **46c** (71 and 19%, respectively). Concerning the use of THF, it was the preferred option in the synthesis of derivatives **46b** and **46c**, providing moderate yields of 46 and 45%, respectively, with no appreciative formation of the monosubstituted by-product. In both cases, the use of DMF derived into dehalogenation of β positions.

Contrarily, the coupling of 9-phenanthrenyl in THF furnished the mono- and di-substituted products in similar yields (23 and 26%, respectively), whereas in DMF the intermediate **46a** was obtained in a yield of 56%. Hence, the reaction with 9-phenanthrenylboronic acid required the harsher conditions provided by the DMF procedure to result into an acceptable yield, whereas the dehalogenation side reaction was not detected. These results point again that the presence of heteroatoms in the arylboronic acid makes tetrabromothiophene more prone to dehalogenation. The subsequent couplings were carried out employing the conditions that provided the best results for the first ones, namely the use of DMF to obtain **48a** and THF for **48b** and **48c**. **48a** was obtained in a yield of 55%, whereas **48b** and **48c** were obtained in yields of 76 and 52%, respectively. The problem with the mono-substitution was only detected in the case of **48a**, which derived into a 43% of the mono-substituted and mono-debrominated by-product **49a'** instead of **49a**. Overall, the global yields considering both couplings had values around 30%.

The synthesis of the tetra-substituted intermediates was also tested one-pot, which performs both couplings subsequently in the same system without any in-between work-up. Notably, this procedure not only favored a more straightforward synthetic way towards precursors **48a–c**, but also provided them in remarkably higher yields. For instance, the one-pot procedure yielded **48a** in a 70%, which outstandingly surpasses the overall yield of 31% obtained with the two separate couplings. The success of the one-pot procedure makes the heterogeneous extension of dibenzothiophene even more accessible. As observed, the twofold coupling of sulfurated scaffolds was possible both in positions α and β , as demonstrated in the formation of **46b** and **48c**, respectively. Hence, the search of alternative cross-coupling conditions was not necessary.

Step II: Scholl reaction

The cyclization employing the Scholl reaction was achieved for all three compounds, affording the expected structures (illustrated in Scheme 4.5).



Scheme 4.5. Synthesis of the cyclized products **50a–c** using the Scholl reaction. The cyclization of **50b** required a temperature of 0 °C to be successful.

It should be noted that the cyclization of compound **50b** under standard conditions derived into polymerization and other side reactions, similarly to the results described in the previous chapter for **37b** and **37c**. Again, the reduction of both the time and the temperature of the reaction (0 °C for 20 minutes) was appropriate, resulting in an excellent

yield of 91%. Compounds **50a** and **50c** were also obtained in high yields of 81 and 74%, respectively.

The herein analyzed synthetic approach opens the door towards new and diverse molecular constructions based on extended dibenzothiophene cores. The heterogeneous substitution, which permits more versatility and tunability, can be easily carried out with diverse scaffolds in two synthetic steps due to the success of the one-pot procedure.

4.4.2. Optoelectronic characterization

Photophysical properties

The optical properties of the heterogeneously substituted compounds **48a–c** and their cyclized counterparts **50a–c** are collected in Table 4.4.

Table 4.4. Optical properties of the non-cyclized derivatives **48a–c** and their cyclized counterparts **50a–c**.

	Unbounded compounds			Cyclized compounds			
	$\lambda_{\text{abs,max}}$ [a] (nm)	$\lambda_{\text{em,max}}$ [a] (nm)	Φ_f [b]	$\lambda_{\text{abs,max}}$ [a] (nm)	$\lambda_{\text{em,max}}$ [a] (nm)	Φ_f [b]	
48a	256, 304	418	0.02	50a	255, 432	454, 475 _(sh)	0.10
48b	241, 333	412	0.01	50b	318, 398	402, 424 _(sh)	0.05
48c	291	420	<0.01	50c	255, 326	396, 414 _(sh)	0.03

[a] Wavelengths of maximum absorption ($\lambda_{\text{abs,max}}$) and emission ($\lambda_{\text{em,max}}$), with the shoulder peaks indicated as (sh). The emission spectra were recorded after excitation at 300 nm. [b] Fluorescence quantum yields (Φ_f), determined using POPOP as standard.

The non-cyclized derivatives display similar $\lambda_{\text{em,max}}$ values around 415 nm, which place their emission in the UV-blue region. All three compounds exhibit low fluorescence quantum yields, even lower than those of their homogeneously substituted counterparts in the instances of **48b–c**. As observed in the homogeneous structure, the cyclisation to derivatives **50b–c** implies a hypsochromic shift of the $\lambda_{\text{em,max}}$ despite the augment of the absorption wavelengths. This also occurs regardless of the presumably planar structure of **50c**, which would imply an effective extension of the conjugation. Oppositely, **50a** experiences a considerable bathochromic shift with respect to its non-cyclized counterpart of 36 nm. The cyclization of all structures also derives into an increment of the Φ_f , with a maximum value of 0.10 in the case of **50a**. The absorption and emission spectra of all materials are shown in Figure 4.7.

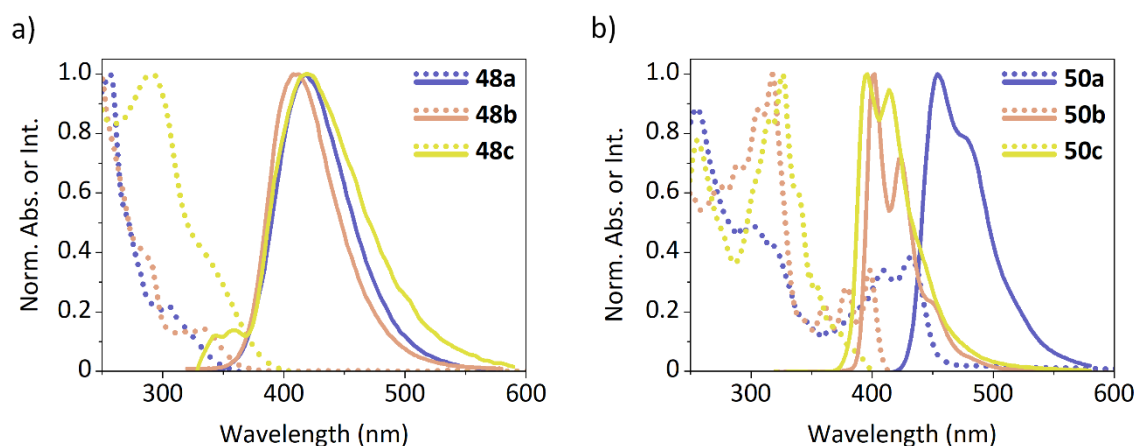


Figure 4.7. Normalized absorbance (dotted) and emission (solid) spectra of the open intermediates **48a–c** (left) and their cyclized counterparts **50a–c** (right).

Derivative **48a** was also surveyed in terms of AIE in an equivalent procedure to that applied to the homogeneously substituted compounds. In this material, the increment of the water percentage up to a 50% caused an increase of the emission intensity followed by a slight bathochromic shift. Beyond this percentage the intensity decreased and, surprisingly, so did the emission wavelength. Although these early findings are not pertinent to qualify this material as an AIEgen, justify further investigation in this direction. The emission spectra and evolution of the maximum intensity and wavelength with respect to the percentage of water are represented in Figure 4.8.

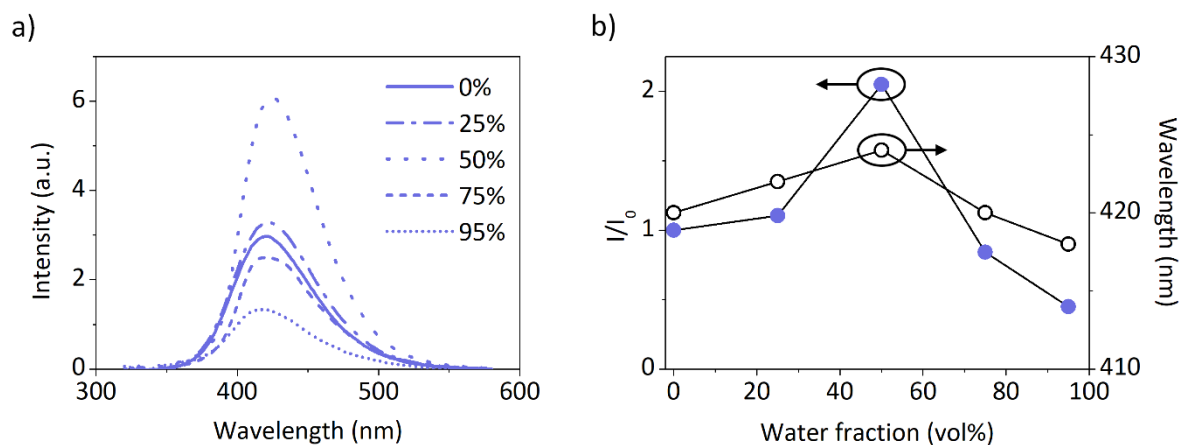


Figure 4.8. Emission properties of derivative **48a** (10^{-5} M) dissolved in THF solutions featuring different water percentages: a) emission spectra; b) plot of the emission maximum intensity (or relative emission intensity (I/I_0)) and wavelength *versus* the composition of the aqueous mixture.

Thermal and electrochemical properties

The thermal and electrochemical characterization of the final compounds **50a–c** is collected in Table 4.5.

Table 4.5. Thermal and electrochemical data of the cyclized compounds **50a–c**.

Compound	T_m [a] (°C)	T_d [b] (°C)	$\lambda_{\text{abs,onset}}$ [c] (nm)	$E_{\text{gap}}^{\text{opt}}$ [c] (eV)	$E_{\text{onset}}^{\text{ox}}$ [d] (V)	IP [e] (eV)	EA [f] (eV)
50a	-	425	452	2.74	0.50	5.89	3.15
50b	271	468	410	3.03	0.50	5.89	2.86
50c	246	415	374	3.32	0.54	5.93	2.61

[a] Melting point (T_m) obtained from DSC at a scan rate of 10 °C min⁻¹. [b] Decomposition temperature (T_d) obtained from the 5% weight loss in TGA at a heating rate of 10 °C min⁻¹. [c] Optical energy gap ($E_{\text{gap}}^{\text{opt}}$) estimated from the absorption spectrum ($\lambda_{\text{abs,onset}}$). [d] Onset oxidation potential ($E_{\text{onset}}^{\text{ox}}$) vs. Fc⁺/Fc determined from CV in 1 mM solutions in dichloromethane. [e] Ionization potential (IP) estimated as IP = $E_{\text{onset vs. Fc}^+/\text{Fc}}^{\text{ox}}$ + 5.39. [f] Electron affinity (EA) estimated as EA = IP - $E_{\text{gap}}^{\text{opt}}$.

All three derivatives possess high thermal stability, with T_d values that surpass the 415 °C on the basis of the 5% weight loss (the TGA scans are represented in Figure A4.1 of the Appendix). Thus, they are suitable to be vacuum deposited. Their melting points (T_m) are also found at high temperatures, namely 271 and 246 °C for **50b** and **50c**, respectively. In the case of **50a**, if any, it was not detected below 300 °C. All compounds undergo an oxidation process, which seems reversible only in the case of **50a**. The cyclic voltammograms and energy levels of compounds **50a–c** are depicted in Figure 4.9. The intensity displayed by derivatives **50b–c** is lower due to solubility issues. The resulting IP values are very similar, but slightly lower than that of the parent structure **44a** (6.01 eV). This makes them more suitable with regard to the gold work function. Contrarily, their optical band gaps are highly divergent. Unexpectedly, the derivative that should feature the most planar π -system on the basis of its structural design and the reported precedents, namely **50c**, presents the highest optical band gap (3.32 eV).

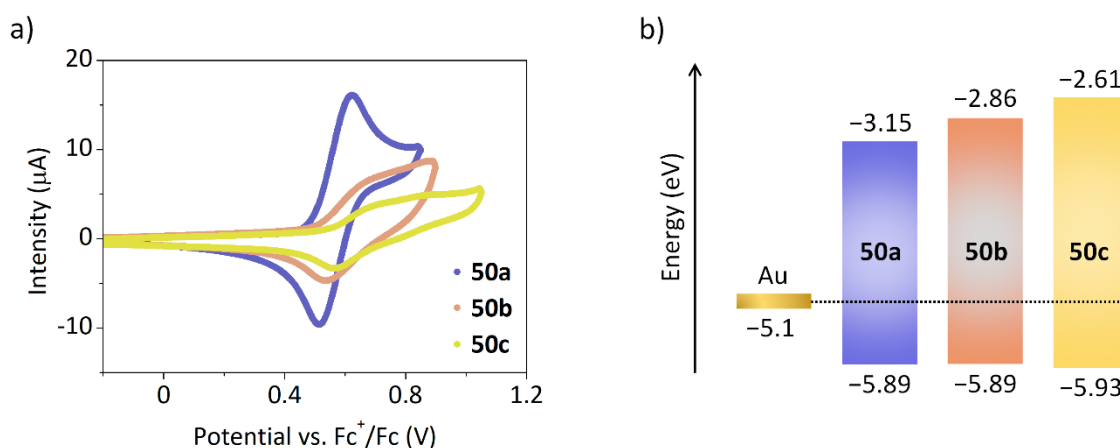


Figure 4.9. Electrochemical characterization of the cyclized derivatives **50a–c**: a) cyclic voltammograms recorded at a scan rate of 100 mV s⁻¹ in 1 mM dichloromethane solutions; b) estimated energy levels with respect to the gold work function.

Globally, all three compounds feature appropriate characteristics for their integration as p-type semiconductors in OTFT devices.

4.4.3. Organic Thin-Film Transistors

Compounds **50a–c** were tested as p-type semiconductors in standard bottom gate-top contact OTFTs. As a proof of concept, they were integrated in PS-treated devices. The OTFT characteristics are collected in Table 4.6.

Table 4.6. OTFT characteristics of devices fabricated from derivatives **50a–c** over PS-treated substrates.

Compound	Dielectric	$\mu_{h,max}$ ($\text{cm}^2 \text{V}^{-1} \text{s}^{-1}$) ^[a]	$\mu_{h,avg}$ ($\text{cm}^2 \text{V}^{-1} \text{s}^{-1}$) ^[b]	I_{on}/I_{off} (A/A) ^[c]
50a	PS	6.9×10^{-5}	6.3×10^{-5} (5.8×10^{-5})	10^3
50b	PS	5.1×10^{-6}	4.6×10^{-6} (-) ^[d]	10^2
50c	PS	8.0×10^{-5}	5.9×10^{-5} (-) ^[d]	10^3

[a] Maximum hole mobility value for a single device. [b] Maximum average hole mobility value of a set of representative devices collected on the same day. The values in parenthesis correspond to the average mobility registered ca. one year after their fabrication. [c] Maximum I_{on}/I_{off} ratio. [d] Not operative.

The first results suggest a great potential of this type of constructions regardless of the degree of planarity of the aromatic system. Specifically, the non-planar compound **50a** displayed a maximum $\mu_{h,avg}$ of $6.3 \times 10^{-5} \text{ cm}^2 \text{V}^{-1} \text{s}^{-1}$, slightly outpacing the $5.9 \times 10^{-5} \text{ cm}^2 \text{V}^{-1} \text{s}^{-1}$ of **50c**. The OTFT characteristics of the former are represented in Figure 4.10. Even considering that the extracted charge mobility values fall short with respect to those of the carbazole-based cores, they are still engaging due to their unique and diverse structural features. On the other hand, compound **50b** clearly underperformed with an average hole mobility of $4.6 \times 10^{-6} \text{ cm}^2 \text{V}^{-1} \text{s}^{-1}$, i.e. one order of magnitude below the other two compounds. In terms of stability, **50a** outstands with a shelf lifetime up to a year, which grants it a potential comparable to the hitherto studied cores based on 9H-carbazole. Its charge mobility reveals again a gradual increase over time, which culminates several months after the fabrication. Thereafter, it stabilizes in a plateau. Even though the variation is less substantial than the one observed in compound **37b** (Chapter 3), it still represents an overall 6-fold improvement. Contrarily, compounds **50b** and **50c** displayed poorer air-stability, with a functional period that do not extend further than a few weeks. Therefore, the structures possessing sulfurated scaffolds apart from the central thiophene suffer from early degradation, similarly to the case of structure **30**. The evolution of the charge mobility of all three cores is represented in the Appendix (Figure A4.2).

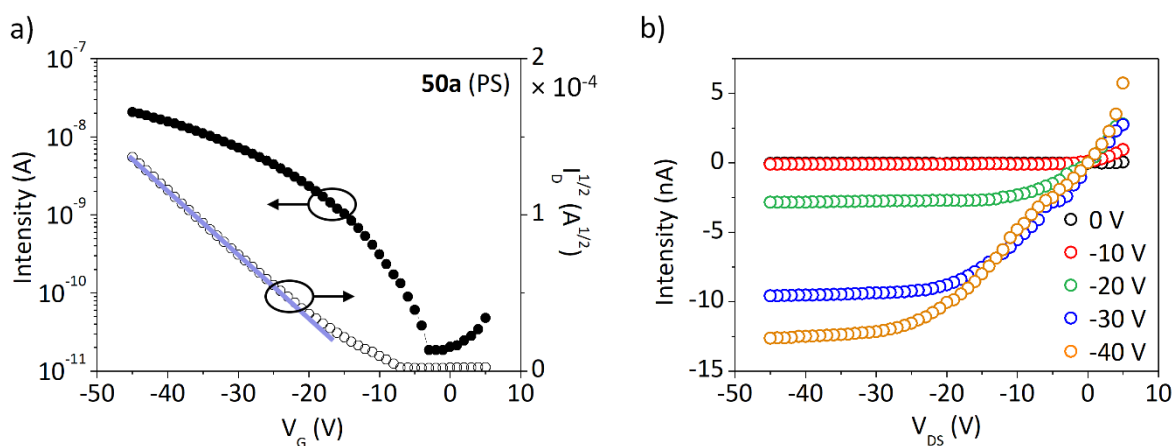


Figure 4.10. OTFT characteristics of a device fabricated from **50a** over a PS-treated substrate: a) transfer ($V_{DS} = -40$ V), saturation and b) output characteristics. The shown data corresponds to the maximum charge mobility obtained, which was registered 230 days after the fabrication.

4.5. Conclusions

The synthesis of differently substituted and derived structures of diphenanthro[9,10-*b*:9',10'-*d*]thiophene, an extended system based on the dibenzothiophene heterocycle, has been accomplished through sequential Suzuki-Miyaura and Scholl reactions. Synthetically, the fourfold Suzuki-Miyaura coupling was successful in a wide array of arylboronic acids in yields exceeding 60%, except for, basically, the sulfurated ones. Once again, the Scholl reaction has settled as an excellent way to construct novel materials with potential in optoelectronics, especially when the *para*-positions are protected or in the presence of suitably placed directing groups. The first approach towards homogeneously substituted derivatives has permitted the coupling of scaffolds of diverse nature, fine-tuning the photophysical and electrochemical properties of both the open and the cyclized nuclei (**44** and **45**, respectively).

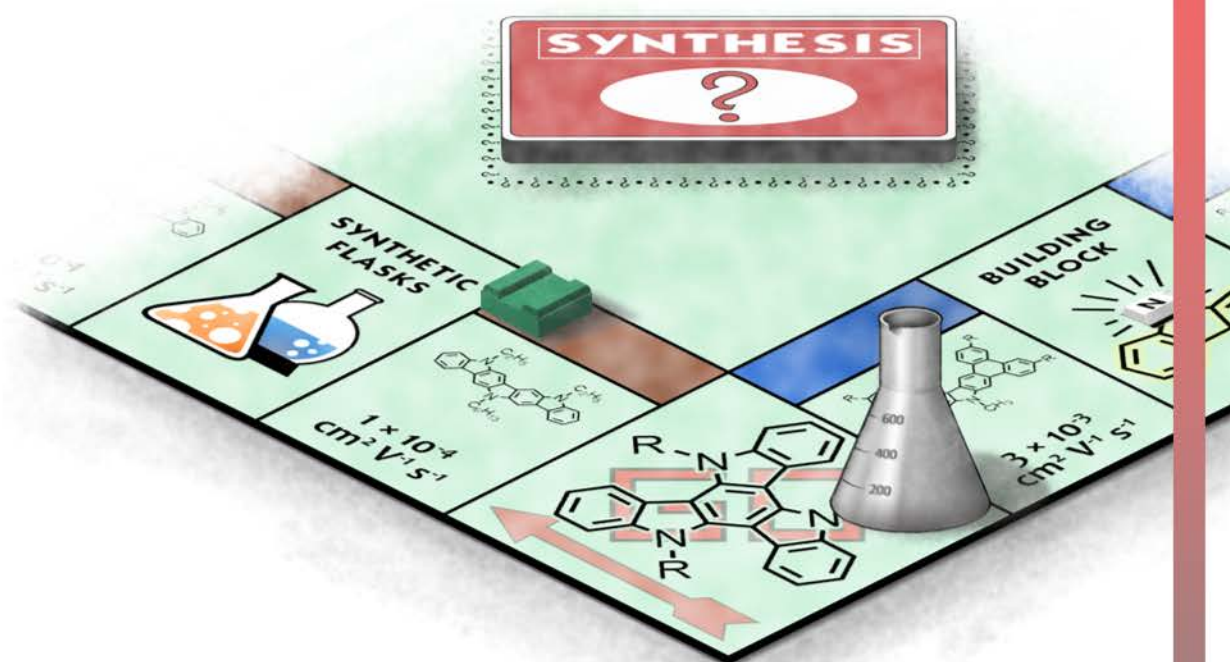
On this basis, we could also envision alternative and novel designs based on a heterogeneous substitution. The research of alternative conditions in the Suzuki-Miyaura coupling was key to avoid the incompatibility of certain substrates. As a result, we could not only adapt and meliorate the protocol for each specific case, but also pave the way to new architectures. Besides, the access to heterogeneously substituted thiophenes has been facilitated by means of the one-pot procedure, implying a straightforward synthesis to the cyclized structures **50a–c** in just two steps with excellent yields. The integration of the **50**-based derivatives in OTFT devices shed light on the role of the chosen scaffolds, ushering in subsequent tailored modifications. Remarkably, derivative **50a** afforded the best performance for this set of products, with a $\mu_{h,avg}$ of $6.3 \times 10^{-5} \text{ cm}^2 \text{ V}^{-1} \text{ s}^{-1}$ deposited over PS and a shelf lifetime that extends beyond one year. Additionally, its non-cyclized

counterpart **48a** hinted potential AIE characteristics. The results extracted from this study therefore encourage new perspectives and further investigation in different directions.

CHAPTER

5

Back to the start:
remodeling the triindole core



CHAPTER 5. Back to the start: remodeling the triindole core

5.1. Introduction

The research of new organic semiconductors presented throughout the previous chapters has provided numerous structures with interesting applications, especially as active layers in OTFTs. Even considering the particular advantages of each material, the triindole core still reigns as the material possessing the highest charge mobility value developed in our research group. Indeed, the hole mobility of the trimethylated triindole (TMT) reached values up to $9 \times 10^{-3} \text{ cm}^2 \text{ V}^{-1} \text{ s}^{-1}$ over OTS-treated devices, whereas its trihexylated analogue (THT) displayed slightly higher values up to $1 \times 10^{-2} \text{ cm}^2 \text{ V}^{-1} \text{ s}^{-1}$ over PS as the organic dielectric.^[125] These promising results, in conjunction with the knowledge derived from the previous chapters, can be translated into interesting modifications in order to further enhance the triindole core.

Figure 5.1 compiles feasible structural derivatives based on the triindole nucleus. The first projected modification consists on the extension of triindole with σ -bonded aromatic heterocycles. In fact, the attachment of different aromatic moieties in various positions of triindole has been already demonstrated in our group as a valid strategy to modulate the properties of the main triindole core.^[123,126] The effect over the physical properties, intermolecular arrangement and OTFT performance has been analyzed applying moieties such as benzene, naphthalene, thiophene and benzothiophene. Considering the self-evident potential of 9*H*-carbazole, its choice as the added scaffold appeared as an interesting design. On the other hand, the conversion of triindole to trioxatruxene and trithiatruxene, namely its oxygen and sulfur-containing counterparts, implies the same synthetic strategy applied to diindolocarbazole in Chapter 2. As stated thorough the thesis, sulfurated heterocycles are especially appealing in organic electronics. Given that triindole already exhibits impressive properties, the integration of sulfur could represent a key innovation. Regarding the oxygenated analogue, it not only involves unique properties but also emerged as a more accessible derivative to study in the development of a suitable synthetic procedure for trithiatruxene. In fact, computational studies also predict the engaging properties of these cores.^[241-242] Finally, the importance of the alkylation patterning has been amply demonstrated with several examples. Thus, this aspect appears again as a convenient structural modification to consider.

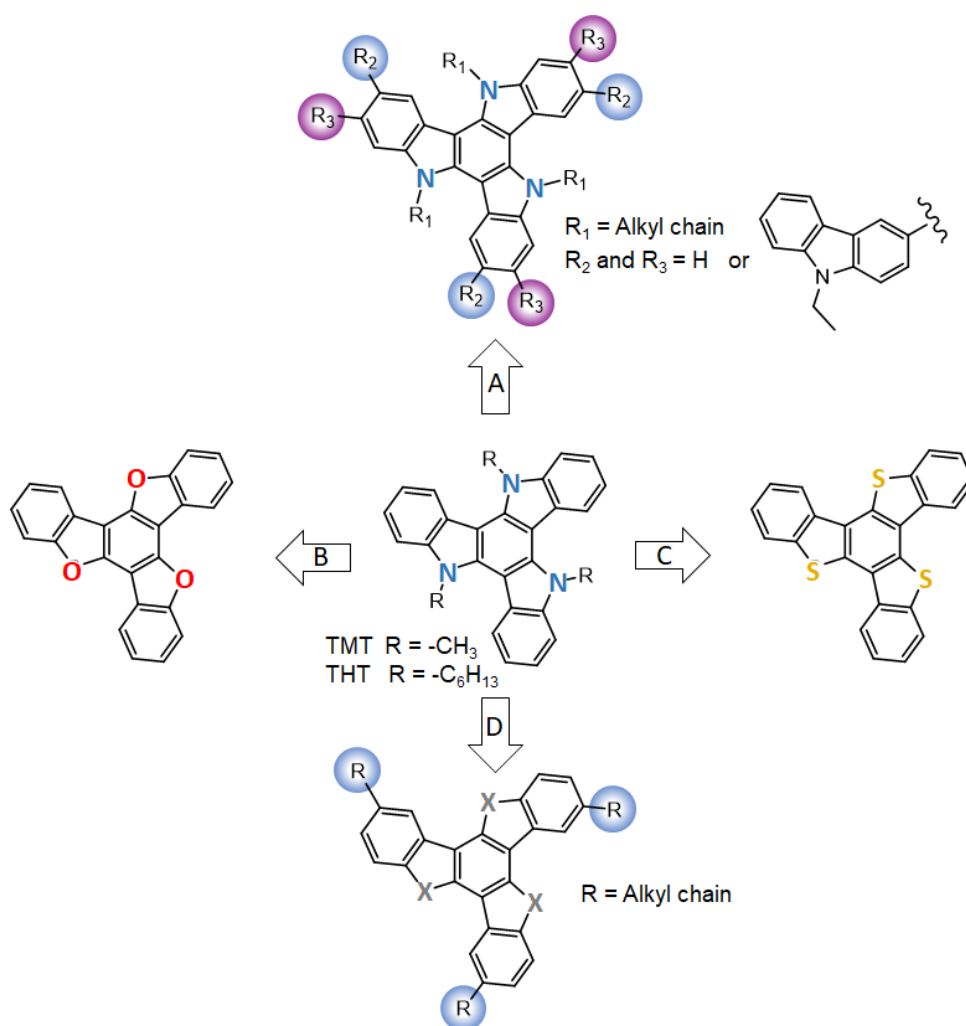


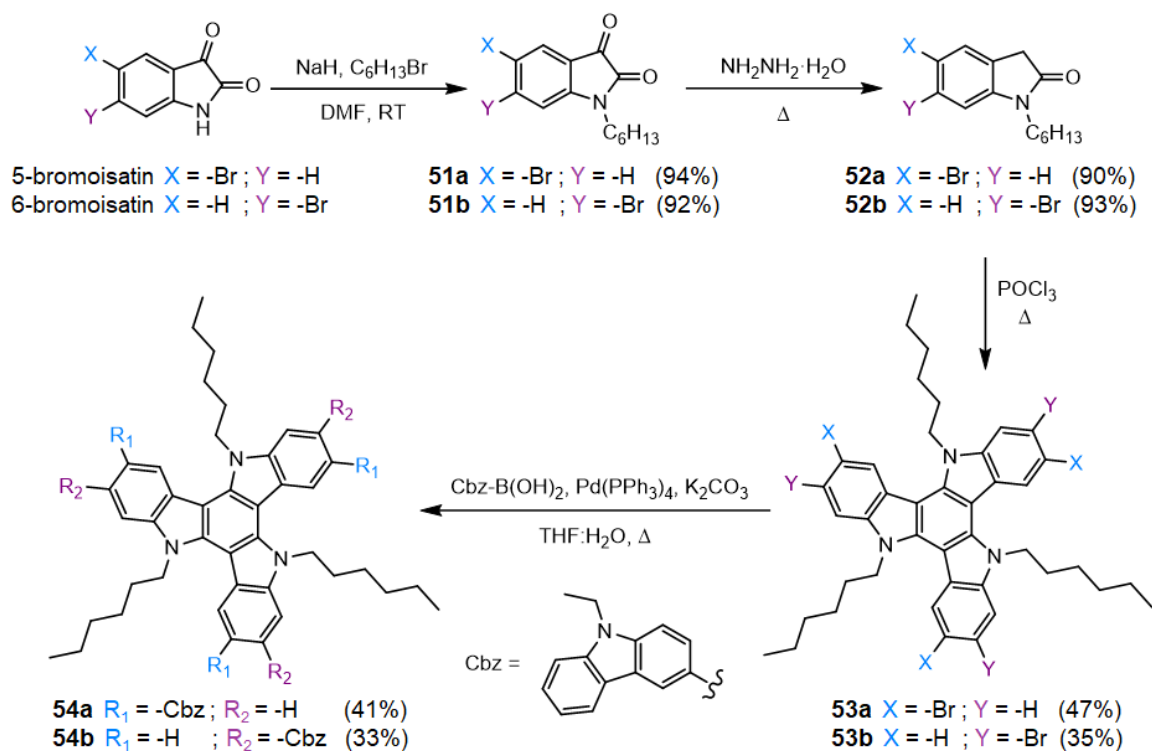
Figure 5.1. Envisioned modifications of the triindole core: attachment of additional aromatic moieties at positions 3, 8 and 13 (blue) or 2, 7 and 12 (purple) (A), substitution of nitrogen by oxygen (B) or sulfur (C) and inclusion of alkyl chains to positions 3, 8 and 13 of the aforementioned cores (D).

Therefore, this chapter aims the synthesis of different triindole-based cores and derivatives with great potential in organic optoelectronics, as well as their optoelectronic characterization, in order to smooth the path towards their application in final devices.

5.2. Design and synthesis

5.2.1. Triindole derivatives

The synthetic procedure utilized for the formation of the triindole derivatives **54a–b**, incorporating the 9-ethyl-9*H*-carbazol-3-yl moiety, is described in Scheme 5.1.

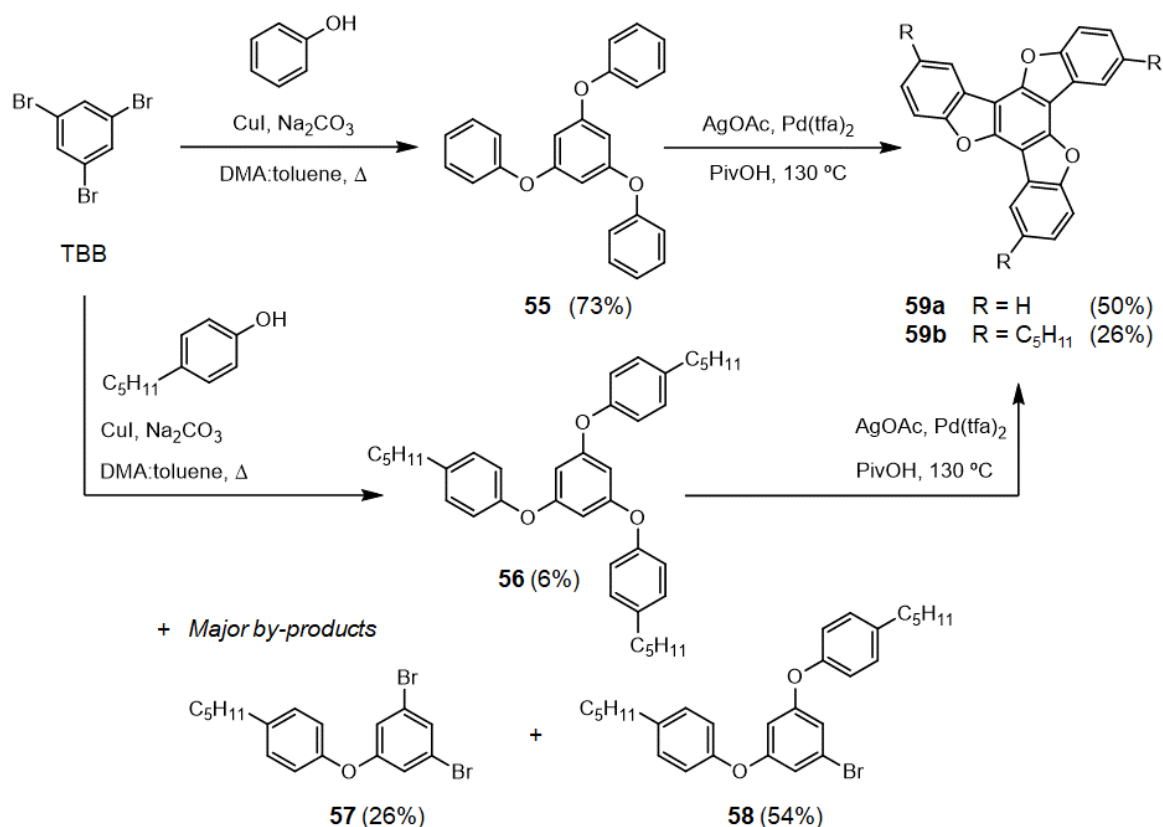


Scheme 5.1. Synthetic route towards derivatives **54a** and **54b** from 5-bromoisatin and 6-bromoisatin, respectively.

This procedure, optimized in our research group,^[123,126] started with the *N*-hexylation of the respective brominated isatin under standard conditions to obtain compounds **51a** and **51b** almost quantitatively. The following step involved the reduction of isatin to oxindole with hydrazine, forming **52a** and **52b** in excellent yields of 90 and 93%, respectively. The cyclocondensation with POCl₃ furnished the tribrominated triindoles **53a** and **53b** in good yields of 47 and 35%. Finally, the introduction of the carbazole moieties was achieved through the Suzuki-Miyaura reaction under standard conditions, providing the final compounds **54a** and **54b** in yields of 41 and 33%.

5.2.2. Trioxatruxene core

Contrarily to the case of triindole, oxygen does not permit the attachment of alkyl chains in the trioxatruxene core. Hence, the synthesis of an additional derivative possessing peripheral alkyl chains apart from the main core was planned. It should be mentioned that the synthesis of the main trioxatruxene core **59** has been already reported by means of two different approaches.^[243–244] The reported studies specially highlight the interesting long-life phosphorescence of this core. However, the information regarding its optoelectronic properties, especially concerning the application in devices, is still scarce. The synthetic route employed to obtain the main core **59a** and the alkylated derivative **59b** is depicted in Scheme 5.2.



Scheme 5.2. Synthetic route towards the trioxatruxene core **59a** and its tri-pentylated derivative **59b** from 1,3,5-tribromobenzene (TBB).

The coupling between phenol and 1,3,5-tribromobenzene to furnish the triether intermediates **55** and **56** was achieved through the Ullmann condensation, using CuI as catalyst, Na₂CO₃ as base and a mixture of DMA and toluene as solvent.^[245] The addition of toluene is required to eliminate the formed water by means of azeotropic distillation in a Dean-Stark apparatus. The threefold coupling was not complete in the case of 4-pentylphenol, so the intermediate **56** was obtained in a yield of 6% regardless of the reaction time (up to a week) and equivalents added, which is notably lower than the 73% obtained for **55**. The preferred product seemed to be the di-substituted **58** in this case, which was isolated in a yield of 54%.

The subsequent triple cyclization reaction was conducted with Pd(tfa)₂ as catalyst and silver acetate as oxidant in pivalic acid, following a reported method.^[243] The obtained yield for **59a** (50%) was comparable to the one described in the literature. Concerning **59b**, it was furnished in a more moderate yield of 26%. As expected, the non-alkylated **59a** suffers from high insolubility, which hampers its applicability in certain topics.

5.2.3. Trithiatruxene core

The introduction of sulfurs in the triindole structure to form the trithiatruxene core represents a highly promising project. Surprisingly, though, the synthesis of trithiatruxene still remains seldom reported. After surveying the literature, only one case had been described during the first stages of this study, which corresponded to an early synthetic research by Bergman *et al.* in 1986.^[246] This reported synthesis was carried out following a strategy similar to the cyclocondensation of oxindole to triindole seen in section 5.2.1. In this case, it involved the cyclocondensation of benzo[*b*]thiophen-3(2*H*)-one under acidic conditions, in which the use of dichloroacetic acid afforded the best results. However, this procedure seemingly implied a tedious purification process due to the appearance of diverse by-products, the availability of the starting material was limited and was quite inflexible in incorporating additional moieties to the final core. Thus, alternative methodologies to form the dibenzothiophene heterocycle were examined as models to apply in the construction of trithiatruxene.^[247-248] The most relevant and promising ones are collected in Figure 5.2.

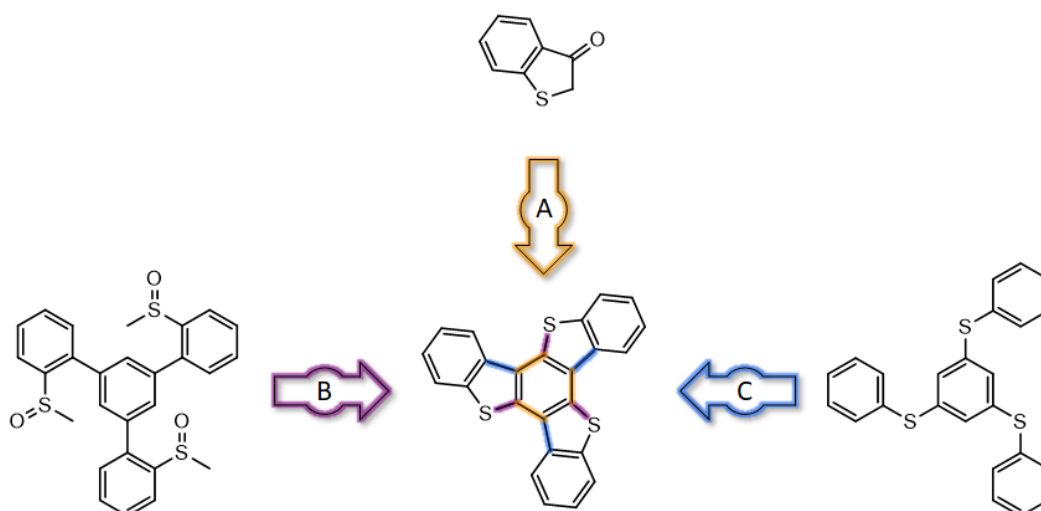


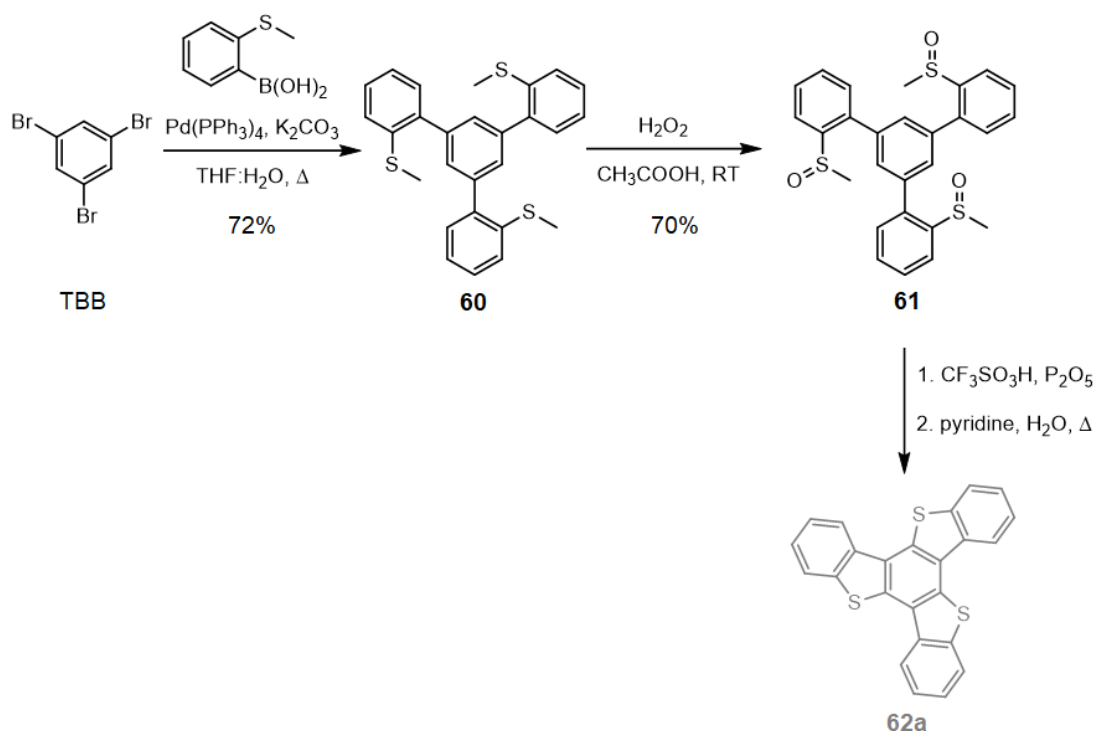
Figure 5.2. Alternative synthetic strategies towards the formation of the trithiatruxene core: the cyclocondensation described by Bergman *et al.*^[246] under acidic conditions (route A, highlighted in orange), cyclisation *via* C-S coupling (route B, highlighted in purple) and cyclisation *via* C-C coupling (route C, highlighted in blue). The bonds formed in each approach towards trithiatruxene are highlighted accordingly.

Two alternative synthetic routes were examined apart from the cyclocondensation reported in the literature (route A). Route B was tested in this case due to the great success in the C-S coupling with triflic acid concerning the synthesis of compounds **30a-b** in Chapter 2. On the other hand, route C implies the cyclization through the formation of the C-C bonds. The application in this case was contemplated as an analogous procedure of the one described in the synthesis of trioxatruxenes **59a-b**. A few examples hinted the viability of

such conditions regarding sulfurated compounds in place of their oxygenated counterparts.^[247,249] Even though the most part of the reported results implied the formation of dibenzothiophene derivatives, the synthesis of benzo[1,2-*b*;4,5-*b'*]bis[*b*]benzothiophene also proved the efficacy in the formation of two cycles simultaneously.^[247]

Route B: Cyclisation through the carbon-sulfur coupling

This approach is based on the coupling between carbon and sulfur *via* the condensation of the methylsulfinyl groups. As stated in Chapter 2, the application in twofold couplings was advantageous to furnish several sulfurated structures. Regarding a threefold coupling, an example of another sulfurated star-shaped molecule was reported by Zou *et al.*,^[250] reinforcing its potential in this case. As observed in Scheme 5.3, this synthetic approach is quite straightforward from the commercially available 1,3,5-tribromobenzene (TBB).



Scheme 5.3. Synthetic approach towards **62a** based on the cyclisation through the carbon-sulfur bonds, starting from TBB.

The precursor **60** was obtained from TBB through the Suzuki-Miyaura cross-coupling reaction in a yield of 72%. The oxidation of the methylthio groups to **61** was achieved with hydrogen peroxide in acetic acid at room temperature in a yield of 70%. The final condensation was carried out with triflic acid and P₂O₅ and the subsequent demethylation, with a mixture of pyridine and water. Unfortunately, it was not successful. After several attempts, only the mono-cyclized compound could be detected by mass-spectrometry.

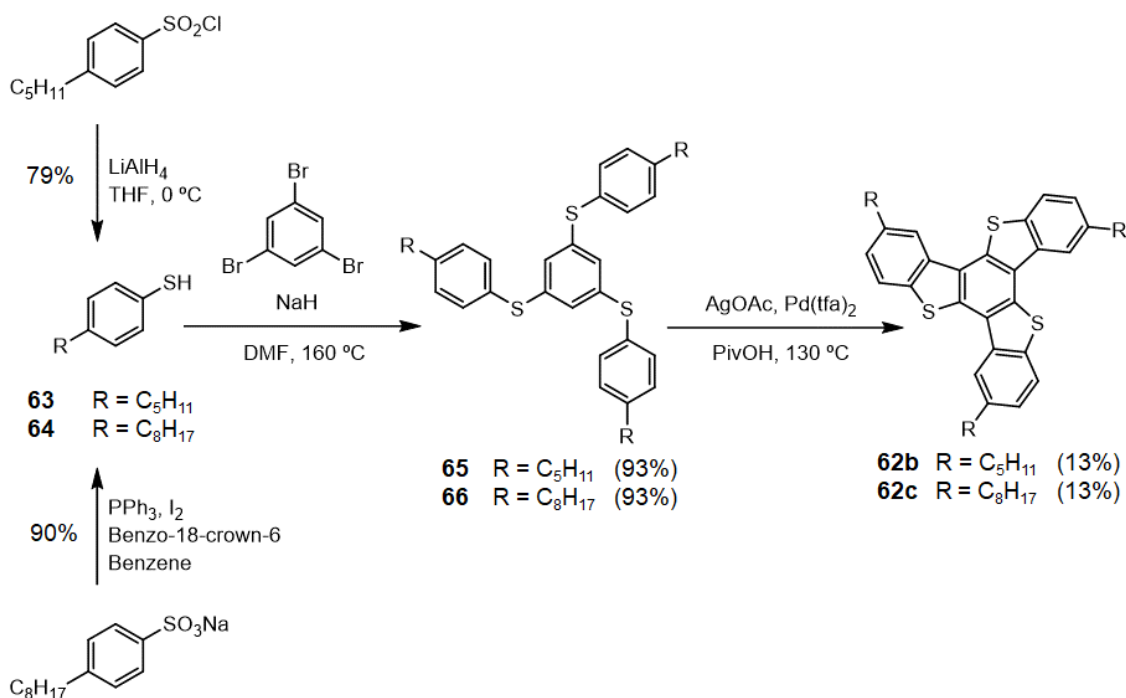
One plausible explanation could be related to the ionized intermediate involved in the condensation process, which proceeds previously to the demethylation reaction. It requires the accumulation of three positive charges in close positions, which probably impedes the formation of the completely cyclized intermediate. The subsequent condensation of the mono-cyclized compound was equally fruitless. Hence, further studies in this direction were discarded.

Route C: Cyclisation through the carbon-carbon coupling

As aforementioned, this synthetic approach was conceived as an analogous procedure to the one tested for the synthesis of trioxatruxene. Equivalent cyclisation conditions, i.e. the use of Pd(tfa)₂ as catalyst, AgOAc as oxidant in pivalic acid as solvent, had been appropriate to form diverse dibenzothiophene-based molecules.^[247,249] Thus, all the references pointed to the suitability of this approach to synthesize the targeted nucleus. In a parallel way to the development of this study, however, similar conditions were described by Nakamura *et al.*^[251] as an appropriate method for the synthesis of derivatives of **62** featuring *tert*-butyl chains. Thereafter, the published procedure was the one employed in this study. In view of the reported structures, the design of the new addressed derivatives of **62** was focused on the incorporation of linear alkyl chains of different length. Apart from improving the solubility, which was anticipated to be as low as that of **59a**, the alkylation patterning greatly modulates the core performance.

The envisioned derivatives **62b** and **62c**, featuring pentyl and octyl chains, respectively, are depicted in Scheme 5.4 along with the followed synthetic routes. As shown, the targeted compounds require the corresponding alkylated thiophenols as starting materials. However, the commercial availability of such thiophenols is limited only to derivatives featuring the shortest of the alkyl chains, whereas their oxidized counterparts, such as the sulfonyl chloride or the sulfonate salt, are more commonly found. For that reason, two alternative reduction procedures were tested depending on the starting material. In the case of **63**, the reduction was conducted from 4-pentylbenzenesulfonyl chloride using LiAlH₄ in THF as solvent.^[252-253] Regarding **64**, the starting material was the sodium 4-octylbenzenesulfonate, so the reduction was carried out with PPh₃ as reducing agent, iodine and benzo-18-crown-6 in benzene.^[254-255] The subsequent addition of water is required in order to cleave the sulfur bonds of the dimeric species. The excellent yields of 79 and 90% for **63** and **64**, respectively, demonstrate the viability of both procedures depending on the available starting material. It should be mentioned that the incorporation of alternative alkyl chains is feasible through the sulfonation of the corresponding alkylbenzene and its subsequent reduction employing the aforementioned conditions. The next step corresponded to the nucleophilic substitution of the thiophenols to 1,3,5-

tribromobenzene to form the respective trithioethers (**65–66**).^[251] Contrarily to phenol, the attachment of thiophenols **63** and **64** was achieved without the presence of metals as catalysts due to the stronger nucleophilic character of sulfur. Specifically, it was carried out using NaH as base and DMF as solvent, resulting in analogous yields of 93%. The final cyclization was achieved with rather low yields of 13% for both **62b** and **62c**.



Scheme 5.4. Synthetic route towards the trithiatruxene derivatives **62b** and **62c** from 4-pentylbenzenesulfonyl chloride and sodium 4-octylbenzenesulfonate, respectively.

5.3. Physical characterization

5.3.1. Thermal and photophysical properties

The thermal and photophysical characterization of the synthesized derivatives based on the triindole core is compiled in Table 5.1. The properties of the parent *N*-trihexylated triindole are also described for comparison.

The tendency observed in terms of the T_d indicates that the materials possess a considerable air-stability, with values surpassing the 370 °C considering the onset. Cores **59** and **62** feature similar T_d values that increment with the attachment of longer alkyl chains. On the other hand, the T_m of the trialkylated derivatives of **59** are lower than those of **62**, on the basis of the values found for the tripentylated **59b** and **62b** (98 and 144 °C, respectively). In fact, the T_m of derivatives **59b** and **62c** are alarmingly low, which could originate malformations in the semiconductor layers during an occasional vacuum-

deposition process. On the other hand, the triindole derivatives **54a–b** and the bare trioxatruxene **59a** do not display T_m below 300 °C.

Table 5.1. Thermal and optical properties of the triindole-derived structures **54a–b**, **59a–b** and **62b–c**. The information regarding the parent *N*-trihexylated triindole (THT) is also listed.

Compound	T_m (°C) [a]	T_d (°C) [d]	$\lambda_{abs,max}$ (nm) [f]	$\lambda_{em,max}$ (nm) [f]	Φ_f [f]
THT ^[125]	(-) ^[b]	424 ^[e]	318	395	0.19
54a	(-) ^[c]	420	336	396 _(sh) , 411	0.17
54b	(-) ^[c]	430	346	422	0.27
59a	-	371	268	346, 360 _(sh)	0.17
59b	98	418	271	350, 364 _(sh)	0.19
62b	144	436	293	372, 390, 410	0.01
62c	68	458	293	372, 390, 410	0.01

[a] Melting point (T_m) obtained from DSC at a scan rate of 10 °C min⁻¹. [b] Not reported. [c] Only processes involving low ΔH were detected. [d] Onset decomposition temperature (T_d) obtained from TGA at a heating rate of 10 °C min⁻¹. [e] Onset decomposition temperature obtained from TGA at a heating rate of 20 °C min⁻¹ from reference 125. [f] Wavelengths of maximum absorption ($\lambda_{abs,max}$) and emission ($\lambda_{em,max}$) in dichloromethane. The emission spectra were recorded after excitation at 300 nm. Fluorescence quantum yields (Φ_f) were determined using POPOP as standard.

The absorption and emission spectra of all compounds are represented in Figure 5.3. The addition of carbazole moieties in THT derives into a red-shift in both the absorption and emission. The bathochromic shift is larger in the meta-substituted **54b** than in the para-substituted **54a**, which could indicate a higher π -conjugation between the triindole nucleus and the carbazole scaffolds in the former.

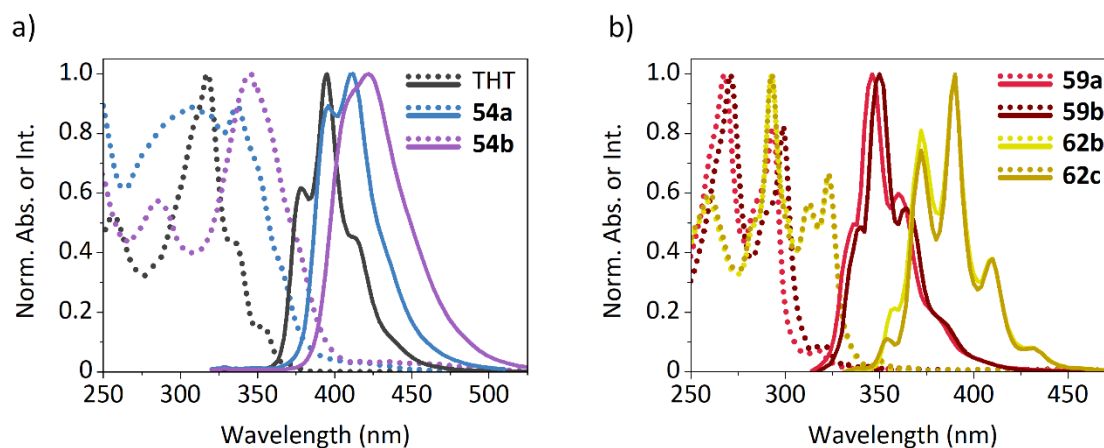


Figure 5.3. Absorption and emission spectra in dichloromethane of the triindole-based materials ($\lambda_{ex} = 300$ nm): a) substituted triindoles **54a–b** with respect to the parent THT; b) trioxatruxenes **59a–b** and trithiatruxenes **62b–c**.

The Φ_f is also higher in **54b**, whereas the value corresponding to **54a** assimilates to that of the parent THT. The inclusion of oxygen and sulfur, however, causes a hypsochromic shift with respect to THT, especially in the oxygenated structure **59**. Whereas compounds **59a–b** maintain similar Φ_f values to the triindole core, the substitution with sulfur causes derivatives **62b–c** to be almost non-emitting. Likewise, a comparable drop in the Φ_f has been reported from the diindolocarbazole core **1** to the sulfurated analog **30**.

5.3.2. Electrochemical properties

The electrochemical characterization of the materials synthesized in this chapter is summarized in Table 5.2 (the corresponding CV are compiled in Figure A5.1 of the Appendix). This data can shed light on the potential of these structures as semiconductors and assist in future applications.

Table 5.2. Electrochemical properties of the triindole-derived structures **54a–b**, **59a–b** and **62b–c**. The information regarding the parent *N*-trihexylated triindole (THT) is also listed.

Compound	$\lambda_{\text{abs,onset}}$ (nm) [a]	$E_{\text{gap}}^{\text{opt}}$ (eV) [a]	$E_{\text{onset}}^{\text{ox}}$ (V) [b]	IP (eV) [c]	EA (eV) [d]
THT ^[125]	352	3.52	0.21	5.60	2.07
54a	382	3.25	0.14	5.53	2.28
54b	396	3.13	0.06	5.45	2.32
59a	300	4.14	1.01	6.40	2.26
59b	310	4.00	0.94	6.33	2.33
62b	333	3.73	0.74	6.13	2.40
62c	332	3.74	0.73	6.12	2.38

[a] Optical energy gap ($E_{\text{gap}}^{\text{opt}}$) estimated from the absorption spectrum ($\lambda_{\text{abs,onset}}$). [b] Onset oxidation potential ($E_{\text{onset}}^{\text{ox}}$) vs. Fc^+/Fc determined from CV in 1 mM solutions in dichloromethane. [c] Ionization potential (IP) estimated as $\text{IP} = E_{\text{onset vs. Fc}^+/\text{Fc}}^{\text{ox}} + 5.39$. [d] Electron affinity (EA) estimated as $\text{EA} = \text{IP} - E_{\text{gap}}^{\text{opt}}$.

According to the effects observed in the optical properties, the attachment of carbazole scaffolds into the THT structure prompts a reduction of the $E_{\text{gap}}^{\text{opt}}$ especially in **54b**, granting values similar to the studied ladder-type cores. The resulting energy levels, depicted in Figure 5.4, also provide a better fit to the gold work function than the parent THT. On the other hand, the blue shift described for structures **59** and **62** with respect to THT translates in this case into very high $E_{\text{gap}}^{\text{opt}}$ values. It is indeed prominent with the inclusion of oxygen, which provides exceedingly high values above 4.00 eV that are analogous to that of the carbazole heterocycle (4.14 eV)^[124]. In combination with their also high $E_{\text{onset}}^{\text{ox}}$, structures **59** and **62** feature low-lying HOMO energy levels that, in the case of the oxygen-containing **59a–b**, are especially misaligned with the gold work function (Figure 5.4). These

characteristics may difficult their implementation as p-type semiconductors. The substitution with sulfur (**62b–c**) slightly corrects it, but the IP values still exceed the 6 eV.

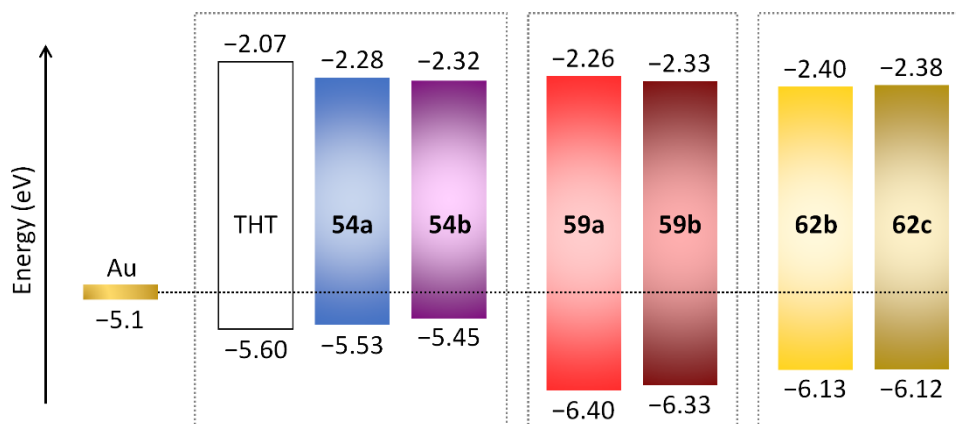


Figure 5.4. Energy levels of the triindole-based materials with respect to the gold work function and the parent structure THT.

5.4. Conclusions

The synthetic modifications projected for the triindole core, namely the inclusion of carbazole moieties and the substitution of nitrogen for oxygen or sulfur, have been successfully carried out. The extension *via* the attachment of carbazole scaffolds in compounds **54a** and **54b** afforded interesting modulations of the main core, such as the red-shift of both the absorption and emission spectra and the reduction of the optical energy gap and the ionization potential. As a consequence, their HOMO energy levels better fit the gold work function. All these variations are more acute in **54b**, which is substituted in the *meta*-positions with respect to the nitrogens, and also features a higher Φ_f of 0.27. The oxygen-containing trioxatruxene nucleus **59a** could also be prepared, as well as its pentylated derivative **59b** as a more soluble variant. However, the exceedingly high optical energy gaps and low-lying HOMO energy levels could hamper the viability or applicability of this core as semiconductor. On the other hand, the first attempt towards the trithiatruxene core, involving the route through the carbon-sulfur coupling, was fruitless. However, it was achieved making use of the carbon-carbon coupling route. The reduction of the commercially-available sulfonyl chloride and sulfonate salt precursors to sulfur led to the synthesis of derivatives with peripheral pentyl and octyl chains (**62b** and **62c**, respectively). Albeit displaying more promising electrochemical characteristics than the trioxatruxene, the ionization potential of trithiatruxene is still quite low-lying. Overall, this chapter settles the bases for the subsequent integration of triindole-based nuclei in organic devices.

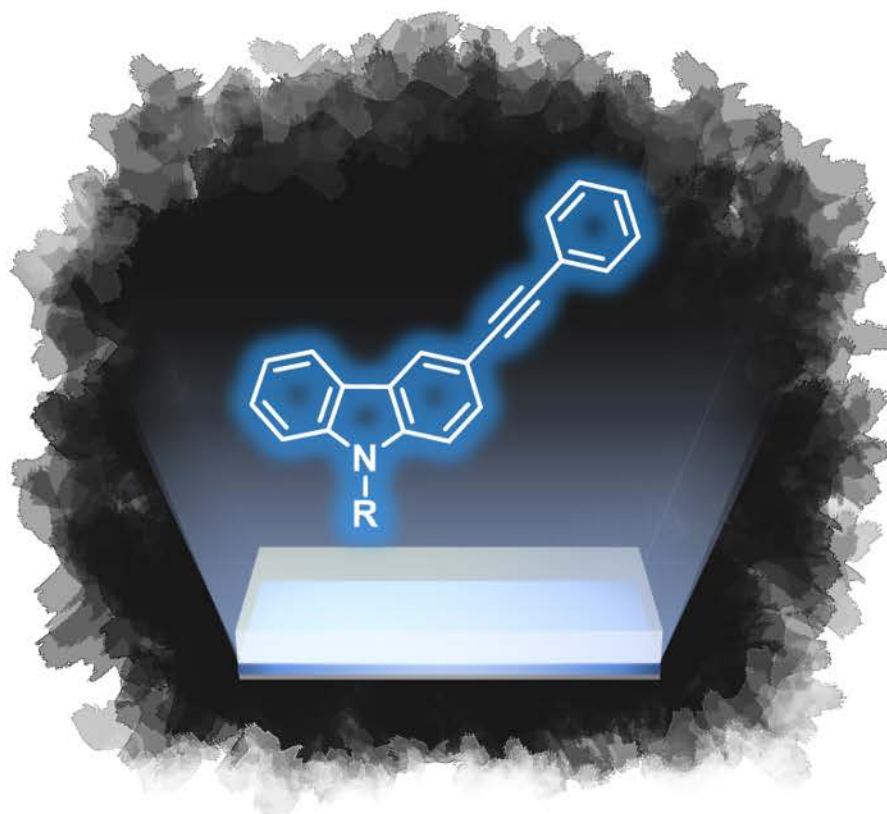
CHAPTER

6

Shedding light on the performance of the 3-(phenylethynyl)-9*H*-carbazole unit in OLED devices

Part of this chapter has been published in:

Opt. Mater. **2021**, *111*, 110696.



CHAPTER 6. Shedding light on the performance of the 3-(phenylethynyl)-9H-carbazole unit in OLED devices

6.1. Introduction

Throughout the previous chapters, most of the efforts have been focused on studying and implementing materials with regard to their charge transport properties. Even though the extensive reports and analyses of their optical properties, the functional study of potential applications arising from them have been rather overshadowed. The current importance and spread of the OLED technology makes self-evident the relevance of this field within organic electronics. Nevertheless, the still limited availability of efficient and stable fluorophores and the high production cost of the manufacturing techniques enact as the bottleneck for a conclusive settlement in the industry.^[68–69] In particular, the key towards full operational OLEDs resides in the improvement of blue emitters, necessary in both full-color displays and WOLEDs.^[76–77] On the other hand, the introduction of the solution processing strategy represents an alternative for the low-cost production of flat displays and lighting.^[69,256–258] Taking into account the importance of this still advancing technology, further investigation is required to pave the way towards an economical and versatile source of lighting.

Therefore, this final chapter pretends to exploit the well-known optical attributes of the 9H-carbazole heterocycle in this direction. Additionally, the carbazole core acts as a relatively weak π -donor moiety, which is of interest to the research on deep-blue dyes.^[82,259–261] According to the *Commission Internationale de l'Eclairage*, the deep-blue emission is defined with a y -axis value not higher than 0.1. The structures of the envisioned carbazole derivatives consist in the attachment of additional aromatic moieties to the carbazole core through a triple bond spacer. This spacer provides rigidity and planarity, favoring conjugation and a reasonable π -electron delocalization.^[262–264] The 3-(phenylethynyl)-9H-carbazole unit, depicted in Figure 6.1, is indeed an appealing building block towards deep-blue fluorophores. The potential of this scaffold has been demonstrated in our research group with a variety of derived structures.^[265–266]

This study presents the development and characterization of new blue-emitting compounds and their integration in solution-processed OLED devices. Specifically, these compounds have been investigated as blue emitters in non-doped OLEDs and in combination with commercially available iridium (III) complexes in WOLEDs (Figure 6.1).

The optimization and fine-tuning of the composition of the device also represents an important part of this chapter. The resulting emissive layer, which consists of a bulk heterojunction, is designed to display tunable white light.

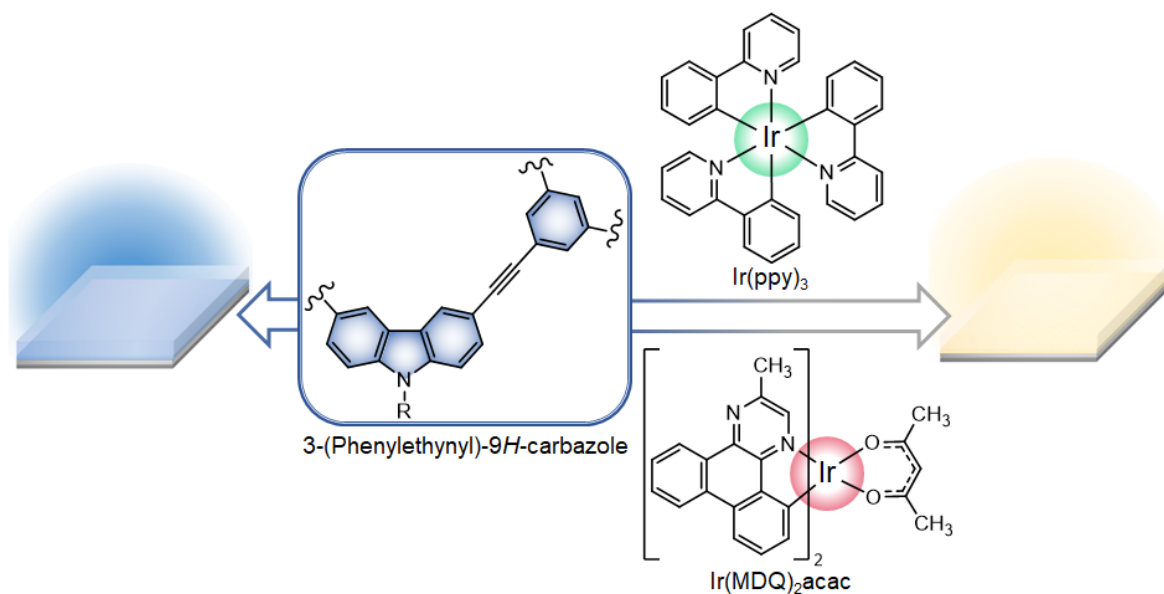


Figure 6.1. Molecular structures of the 3-(phenylethynyl)-9H-carbazole unit and the commercially available iridium complexes tris(2-phenylpyridine)iridium (III) (Ir(ppy)₃) and bis(2-methyldibenzo[*f,h*]quinoxaline)(acetylacetonate) iridium (III) (Ir(MDQ)₂acac), displaying green and red emission, respectively.

6.2. Design and synthesis

As stated, the structural design of new fluorophores in this chapter was envisioned from the 3-(phenylethynyl)-9H-carbazole unit as building block. With this in mind, two new molecular constructions have been considered, namely 6,6'-bis(phenylethynyl)-9H,9'H-3,3'-bicarbazole (**67**) and 1,3,5-tris((9H-carbazol-3-yl)ethynyl)benzene (**68**). As shown in Figure 6.2, two 3-(phenylethynyl)-9H-carbazole units are bonded through positions 3 and 3' of the carbazole heterocycles in the former, whereas three carbazole moieties are attached to a central benzene ring in the latter. Again, the incorporation of *N*-alkyl chains of different lengths has been analyzed. Apart from being a crucial factor in conferring an adequate intermolecular disposition, in this case they can provide the solubility that requires the solution processing. It should be also mentioned that materials capable of forming continuous and morphologically stable films are particularly sought for the successful operation of the devices.^[267] Thus, amorphous molecular materials possessing glass transition temperatures (T_g) above room temperature appear as the most appropriate candidates. In this way, the inclusion of longer alkyl chains like *n*-hexyl or the ramified 2-ethylhexyl can promote the desired morphology.

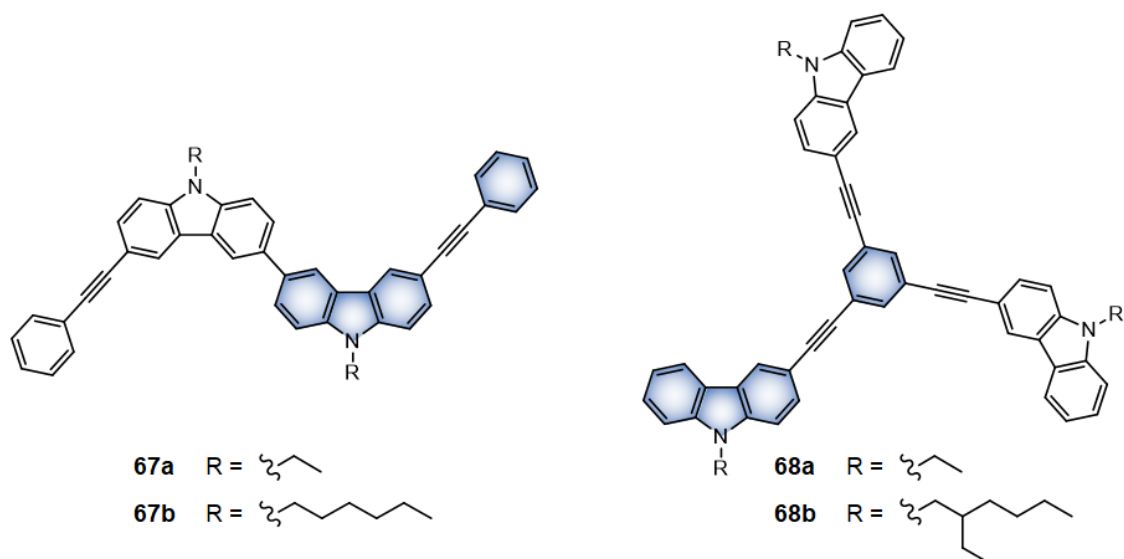
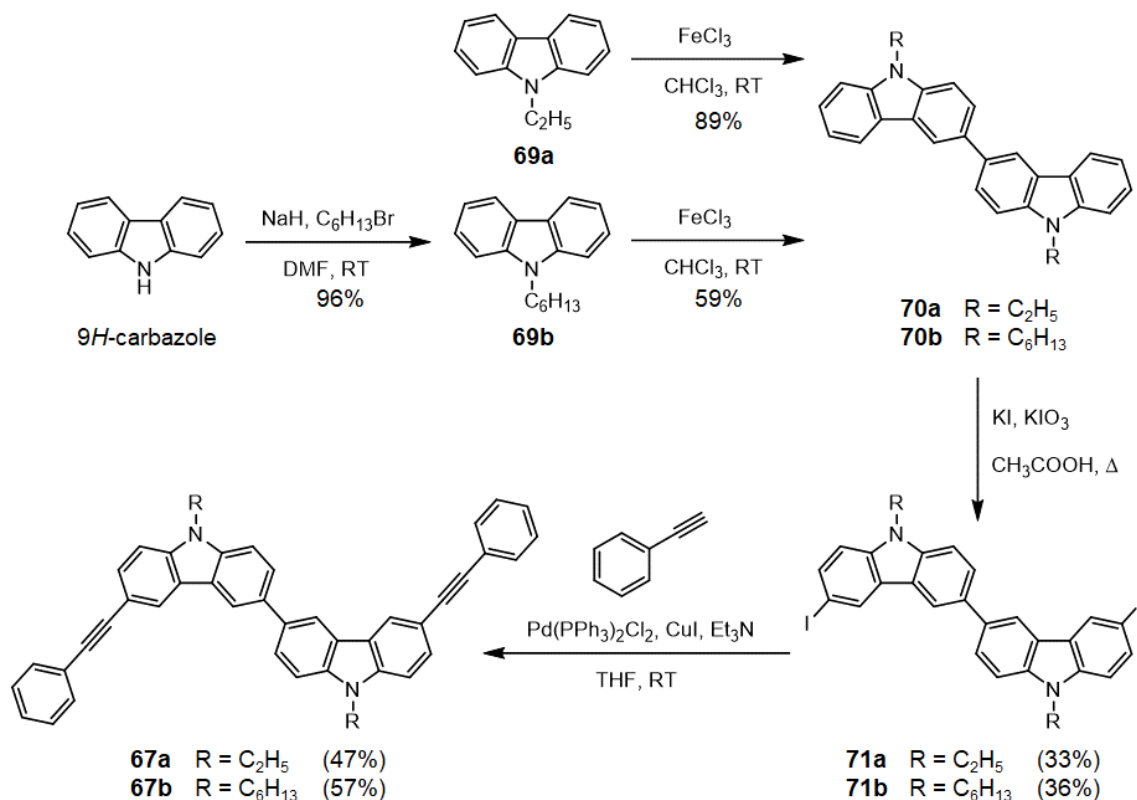


Figure 6.2. Structural design of the 6,6'-bis(phenylethynyl)-9H,9'H-3,3'-bicarbazole derivatives **67a–b** and the 1,3,5-tris((9H-carbazol-3-yl)ethynyl)benzene derivatives **68a–b**. A 3-(phenylethynyl)-9H-carbazole fragment is highlighted in blue in each construction.

6.2.1. 6,6'-bis(phenylethynyl)-9H,9'H-3,3'-bicarbazole derivatives

The synthetic route followed to furnish the 6,6'-bis(phenylethynyl)-9H,9'H-3,3'-bicarbazole derivatives **67a–b** is depicted in Scheme 6.1.

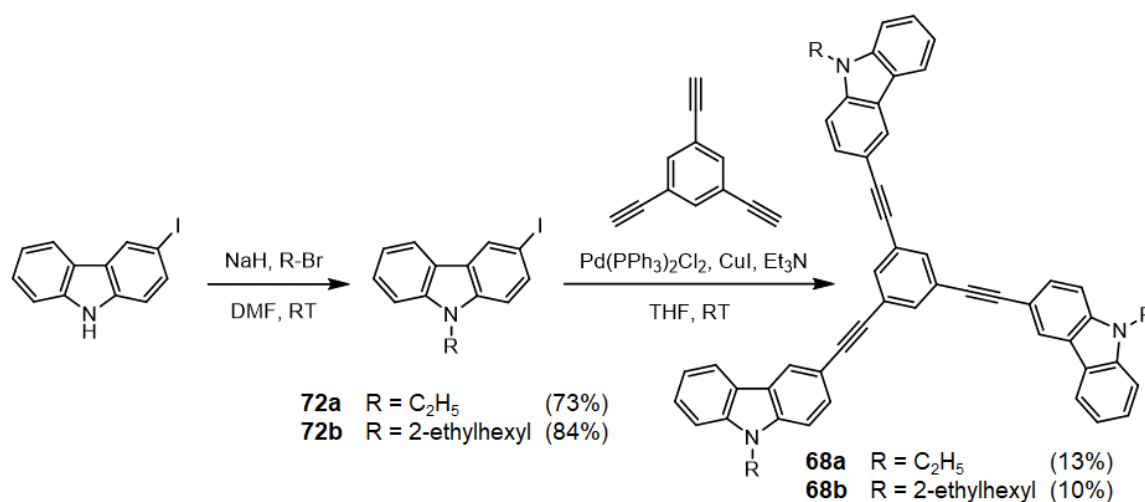


Scheme 6.1. Synthetic route towards structures **67a** and **67b**.

The alkylation of 9*H*-carbazole under standard conditions provided the hexylated compound **69b** in an excellent yield of 96%, whereas the ethylated counterpart **69a** is commercially available. The bicarbazole backbone was prepared by oxidative dimerization of the corresponding alkylated 9*H*-carbazoles using FeCl₃ in anhydrous chloroform for 30 min at room temperature.^[268] Notably, the reaction towards the ethylated **70a** provided a much higher yield of 89% in comparison with the hexylated **70b**, i.e. 58%. The iodination in positions 6 and 6' using KI and KIO₃ in acetic acid^[269] afforded intermediates **71a–b** in similar yields of 33 and 36%, respectively. Finally, the Sonogashira coupling reaction^[270] between **71a–b** and phenylacetylene, using Pd(PPh₃)₂Cl₂ as catalyst, copper (I) iodide as co-catalyst and triethylamine as base in anhydrous THF at room temperature yielded the final compounds **67a–b** in a 47 and 57%, respectively.

6.2.2. 1,3,5-tris((9*H*-carbazol-3-yl)ethynyl)benzene derivatives

Compounds **68a–b** were synthesized as described in Scheme 6.2. The commercially available 3-iodo-9*H*-carbazole was alkylated under standard conditions to afford compounds **72a–b** in yields of 73 and 84%, respectively. Compounds **68a–b** were also obtained through analogous conditions of the Sonogashira coupling reaction, but in this case employing 1,3,5-triethynylbenzene and **72a–b** as reactants. Albeit the rather low yields obtained, i.e. up to 13%, the synthesis of compounds **68a–b** was accomplished in a simple, two-step strategy. It should be mentioned that an alternative synthetic approach for **68a–b** had been previously investigated, implying the attachment of the triple bond to the corresponding alkylated 3-iodo-9*H*-carbazole and the subsequent attachment of three 3-ethynyl-9*H*-carbazole units to 1,3,5-tribromobenzene through Sonogashira coupling reactions. This second approach, however, proved to be inappropriate.^[123]



Scheme 6.2. Synthetic route towards derivatives **68a** and **68b** from 3-iodo-9*H*-carbazole.

6.3. Characterization of the fluorophores

6.3.1. Thermal and photophysical properties

The thermal and photophysical properties of compounds **67a–b** and **68a–b** are summarized in Table 6.1. All compounds possess an extraordinary thermal stability, with onset decomposition temperatures higher than 430 °C. The highest values correspond to the ethylated derivatives **67a** and **68a**. Also, compounds **67b** and **68a–b** display adequate glass transitions above room temperature, which is mandatory for the morphological stability of the film. In the case of derivatives **67b** and **68b**, featuring longer alkyl chains, this transition occurs at lower temperatures of 59 and 52 °C, respectively.

Table 6.1. Thermal and photophysical characterization of derivatives **67a–b** and **68a–b**.

Comp.	Thermal properties [a]			Photophysical properties					
	T_d (°C)	T_g (°C)	T_m (°C)	Solution			Solid state		
				$\lambda_{abs,max}$ [b] (nm)	$\lambda_{em,max}$ [b] (nm)	Φ_f [c]	$\lambda_{em,max}$ [d] (nm)	Φ_f [e]	CIE [f]
67a	474	-	-	313, 337	416	0.11	428	0.07	(0.20, 0.20)
67b	440	59	132	313, 337	416	0.11	428	0.21	(0.17, 0.10)
68a	515	132	250	304, 332	369, 380	0.82	410	0.08	(0.17, 0.11)
68b	433	52	126	304, 332	369, 380	0.80	400	0.07	(0.17, 0.12)

[a] The decomposition temperatures (T_d), corresponding to the 5% weight loss, were obtained from TGA performed at a heating rate of 20 °C min⁻¹. The glass transition temperatures (T_g) and melting points (T_m) were obtained from DSC performed at a scan rate of 10 °C min⁻¹. [b] Wavelengths of maximum absorption ($\lambda_{abs,max}$) and emission ($\lambda_{em,max}$) in THF solutions (10⁻⁵ M). The emission spectra were recorded at $\lambda_{ex} = \lambda_{abs,max}$. [c] Fluorescence quantum yields (Φ_f), determined using POPOP as standard ($\lambda_{ex} = 300$ nm). [d] The spectra in the solid state were measured films deposited over quartz ($\lambda_{ex} = 320$ and 330 nm in **67a–b** and **68a–b**, respectively). [e] Fluorescence quantum yields (Φ_f) in the solid state, determined using an integrating sphere. [f] CIE coordinates calculated from the emission spectra.

The fluorescence measurements in THF show a maximum at 416 nm for compounds **67a–b** and a double peak at 369 and 380 nm for compounds **68a–b**. The structural disposition of the aromatic system influences considerably, since the bicarbazole derivatives **67a–b** emit at higher wavelengths than the triethynylbenzene-centered **68a–b**. The corresponding spectra are represented in Figure 6.3. Concerning the alkylation patterning, it does not influence the optical properties of neither of the two cores in solution but it is decisive in determining the emission in the solid state. The narrow difference between **68a** and **68b** in the solid state (**68a**, with shorter ethyl chains, is 10 nm red-shifted with respect to **68b**) contrasts with the change of the emitted color between **67a** and **67b**. Specifically, the hexylated **67b**, with a sharp band peaking at 428 nm, is the only one strictly showing deep-

blue coordinates. Although **67a** peaks at the same wavelength, it displays a much broader band that results into blue-green emission.

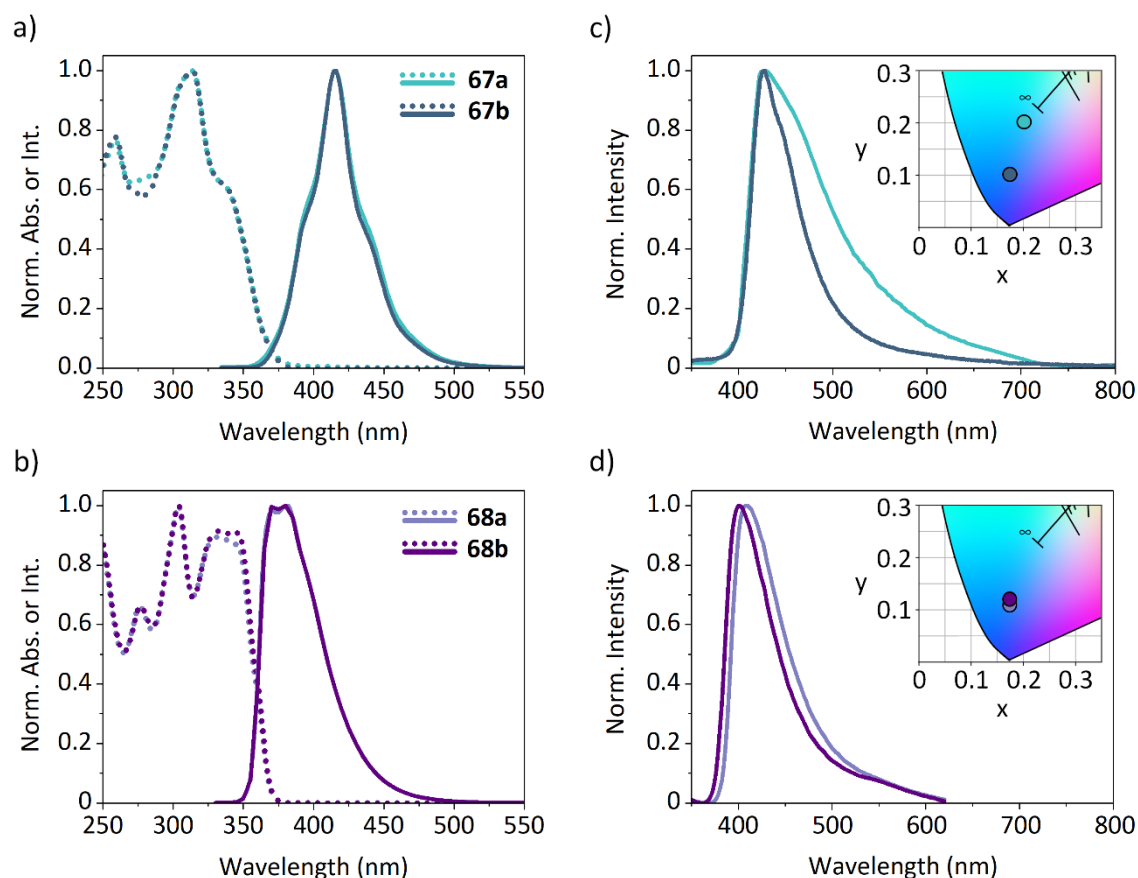


Figure 6.3. Absorption (dotted lines) and emission (solid lines) spectra of compounds: a) **67a–b** in THF ($\lambda_{\text{ex}} = \lambda_{\text{abs,max}}$); b) **68a–b** in THF ($\lambda_{\text{ex}} = \lambda_{\text{abs,max}}$); c) **67a–b** in the solid state ($\lambda_{\text{ex}} = 320$ nm); b) **68a–b** in the solid state ($\lambda_{\text{ex}} = 330$ nm). The inset graphs depict their CIE coordinates in the solid state.

The divergent behavior of **67a** and **67b** in the solid state extends likewise to their respective fluorescence quantum yields. Both derivatives display an equivalent Φ_f of 0.11 in solution, which in the solid state drops to 0.07 in **67a** and increases to a notable value of 0.21 in **67b**. Therefore, the optical properties of the bicarbazole-based system **67** in the solid state are highly dependent on the alkyl chain nature. Regarding compounds **68a–b**, they provide outstanding Φ_f values in solution up to 0.82 and 0.80, respectively. However, the values in the solid state diminish in both derivatives, resulting in values of 0.08 and 0.07 for **68a** and **68b**, respectively. An in-depth analysis of this phenomenon from a structural point of view is held in the following section.

6.3.2. Single crystals

In order to further investigate the divergent optical properties found for derivatives **67a–b** in the solid state, their single crystal structures were investigated by means of single crystal X-ray diffraction (Figure 6.4).

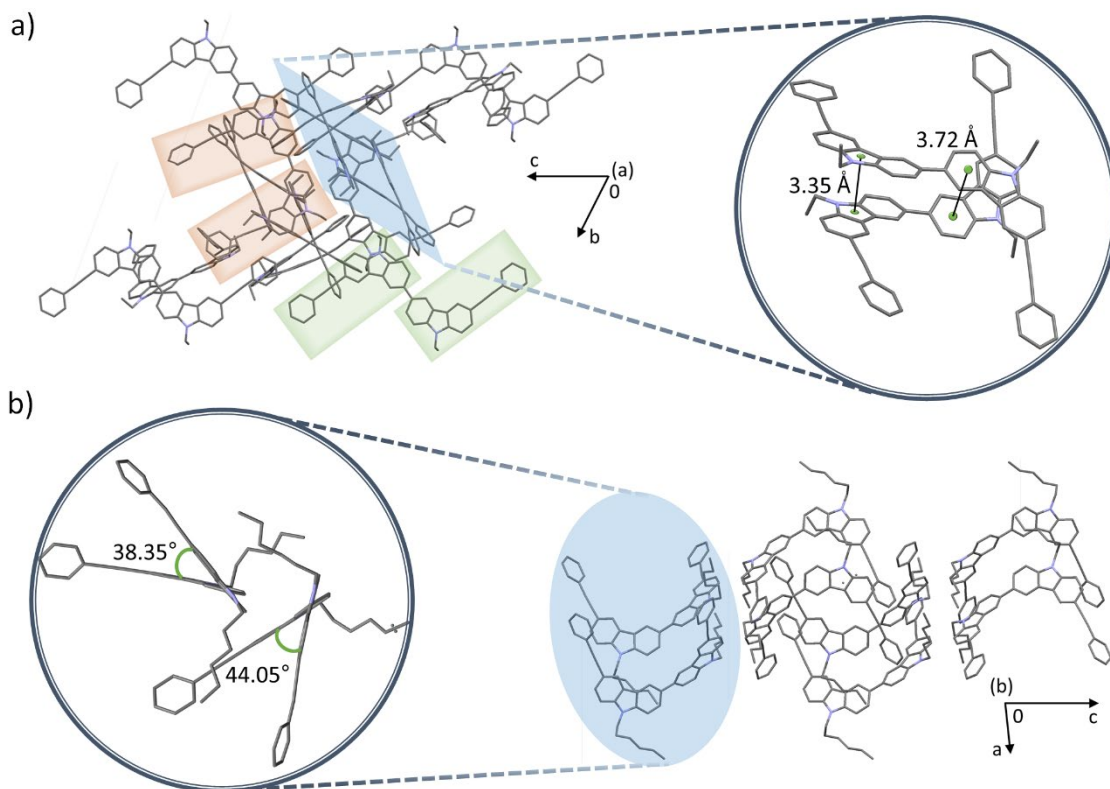


Figure 6.4. Single crystal structures of compounds a) **67a** and b) **67b**. The blue regions of the crystal structures have been magnified to detail a representative set of π - π distances for **67a** and the dihedral angles for **67b** from a different point of view. The structure of **67a** also highlights an example of a bicarbazole system arranged in the *trans* form (green) and in the *cis* form (orange). Hydrogen atoms have been omitted for clarity.

The ethylated derivative **67a** crystallized in space group P_{-1} of the triclinic system. The disposition of **67a** suggests aggregation of the π -system between adjacent molecules, with π - π stacking distances as short as 3.35 Å. In fact, the distribution of the aromatic moieties is defined by the overall high planarity of the molecules, with torsion angles between the carbazole rings that go from 2 to 36°. The triple bond spacers also grant a minimum deviation of the planarity within the 3-(phenylethynyl)-9*H*-carbazole units. Therefore, the broadening of the emission band found in the solid state is likely originated by aggregation. The slight decrease of the quantum yield (from 0.11 in solution to 0.07 in the solid state) also agrees with the presence of π - π stacking interactions, as described by the aggregation-caused quenching phenomenon. Peculiarly, the unit cell contains molecules displaying the bicarbazole system in two different arrangements, namely *cis* and *trans* dispositions.

Regarding compound **67b**, it crystallized in space group $P2_1/c$ of the monoclinic system. As anticipated from the sharp peak with a minimum red-shift in the solid-state emission, the disposition of **67b** within the unit cell does not show any appreciative π - π stacking interaction. Indeed, the shortest intermolecular π - π stacking distances found possess exceedingly high values of 4.83 Å. On the contrary, edge-to-face and aliphatic C-H \cdots π interactions are predominant and determine the intermolecular packing motif. Regarding the intramolecular disposition, neither the phenyl nor the carbazole rings are coplanar with each other, with a deviation of planarity that disfavor aggregation. As stated, compound **67b** provides enhanced emission in the solid state, featuring quantum yield values of 0.11 and 0.21 in solution and in the solid state, respectively. These results also agree with the reported crystallographic data, pointing out once again that the choice of the alkyl chain length requires special care in certain cores.

Even though the crystal structures of the triethynylbenzene derivatives **68a–b** could not be elucidated, some considerations can be made. Contrarily to structure **67**, which possesses a sigma bond between the two carbazole rings with a certain dihedral angle, structure **68** only features triple bond spacers to connect the different aromatic rings. The considerable decay of their quantum yield could be correlated to a higher planarity conferred by the rigidity of the triple bond spacers, making this structure more prone to aggregation-caused quenching. Overall, these results highlight the special interest in the structural design of **67b**, displaying enhanced deep-blue emission in the solid state.

6.3.3. Electrochemical properties

The electrochemical properties of compounds **67a–b** and **68a–b** are detailed in Table 6.2. The definition of the energy levels of the synthesized materials is indispensable in this case, since the architecture of the device needs to be designed accordingly.

Table 6.2. Electrochemical data of compounds **67a–b** and **68a–b**.

Compound	$\lambda_{\text{abs, onset}}$ (nm) [a]	$E_{\text{gap}}^{\text{opt}}$ (eV) [a]	$E_{\text{onset}}^{\text{ox}}$ (V) [b]	IP (eV) [c]	EA (eV) [d]
67a	370	3.35	0.41	5.80	2.45
67b	370	3.35	0.41	5.80	2.45
68a	371	3.34	0.57	5.96	2.62
68b	371	3.34	0.61	6.00	2.66

[a] Optical energy gap ($E_{\text{gap}}^{\text{opt}}$) estimated from the absorption spectrum ($\lambda_{\text{abs, onset}}$). [b] Onset oxidation potential ($E_{\text{onset}}^{\text{ox}}$) vs. Fc^+/Fc determined from CV in 1 mM solutions in dichloromethane. [c] Ionization potential (IP) estimated as $\text{IP} = E_{\text{onset vs. Fc}^+/\text{Fc}}^{\text{ox}} + 5.39$. [d] Electron affinity (EA) estimated as $\text{EA} = \text{IP} - E_{\text{gap}}^{\text{opt}}$.

All compounds undergo an oxidation process, which is reversible for compounds **67a–b** and irreversible for compounds **68a–b** (Figure 6.5). A second irreversible oxidation process was also observed in derivatives **67a–b**. As opposed to the first oxidation step, the second one displays a different profile depending on the length of the alkyl chains. No reduction processes were detected for any of them. Taking into account their energy levels, all of them display the characteristics typically found in p-type semiconductors. It should be noticed that the IP values obtained for the bicarbazole derivatives are lower than those of the triethynylbenzene derivatives, whereas their optical band gaps are almost equivalent (ca. 3.35 eV). On the basis of the estimated energy level values, the most convenient electrodes and interlayers will be selected.

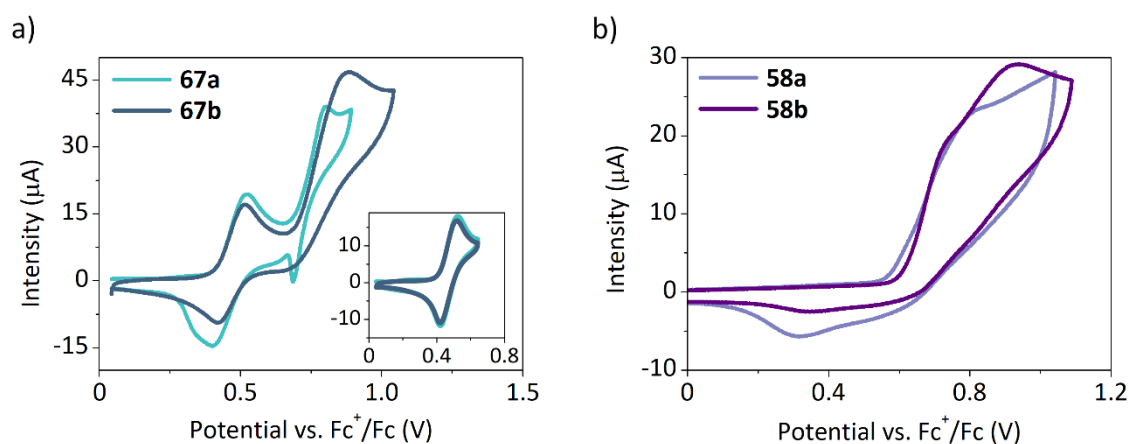


Figure 6.5. Cyclic voltammograms in dichloromethane referred to the Fc⁺/Fc redox couple of derivatives: a) **67a–b**, with their first oxidation steps represented in the inset; b) **68a–b**.

6.4. Organic Light-Emitting Diodes

In view of the resulting photophysical and electrochemical characterization, compounds **67a–b** and **68a–b** are good candidates to be explored within the OLED technology. Apart from their strong emission within the blue region of the visible spectrum, all compounds display p-type semiconducting properties. This fact was corroborated by means of the Time of Flight (TOF) technique, which stands as an alternative method for determining the charge mobility of a material. Both structures exhibited similar hole-transporting properties, with mobility values around $10^{-3} \text{ cm}^2 \text{ V}^{-1} \text{ s}^{-1}$ at high electric fields up to $9 \times 10^5 \text{ V cm}^{-1}$.^[122–123] As a proof of concept, they have been tested as emissive layer components alone in non-doped OLEDs and in combination with iridium (III) complexes in the search of white-emitting OLEDs.

The chosen device architecture, which features a simple multilayer design compatible with the solution processing, is depicted in Figure 6.6 alongside the energy levels of all the

components. Specifically, it consists of ITO/PEDOT:PSS (25 nm)/a mixture of **compound**:Ir(ppy)₃:Ir(MDQ)₂acac/TPBi (20 nm)/Ca (14 nm)/Al (100 nm). The composition and thickness of the emissive layer depend on the type of device. The fabrication of the devices was performed by the subsequent deposition of the components over pretreated commercial glass substrates coated with an ITO film. A requisite for the solution deposition of multilayered devices is the choice of orthogonal solvents, that is, solvents that dissolve the component to deposit but do not solubilize or damage the underlaid films. In our case, the hole-transporting layer (PEDOT:PSS) and the emissive layer were solution-processed and the electron-transporting layer (TPBi) and the cathode bilayer (calcium and aluminum) were vacuum-deposited. The appropriate pick of PEDOT:PSS, which is deposited in water, permits the use of a wide selection of non-polar organic solvents to solubilize and process the synthesized derivatives and the iridium (III) complexes.

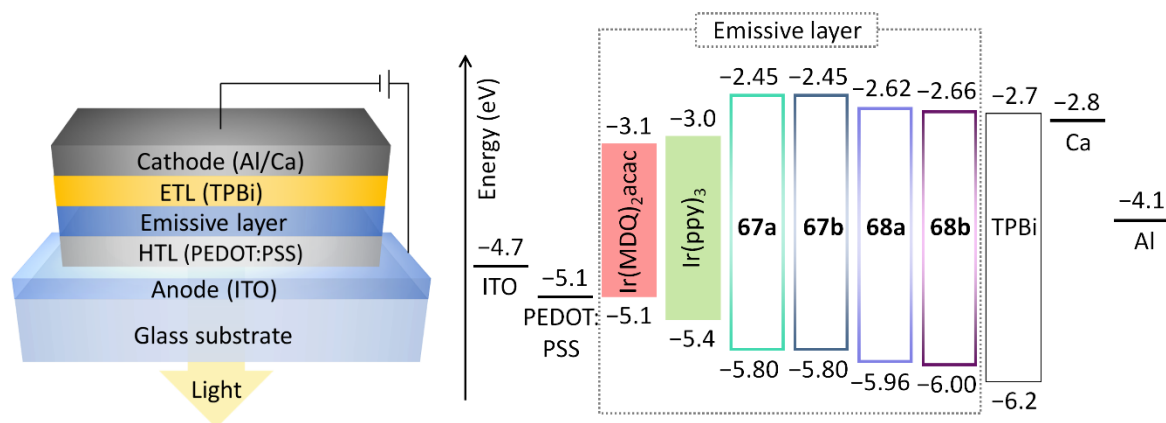


Figure 6.6. Schematic representation of the OLED architecture along with the energy levels of all the components: ITO (Indium Tin Oxide) as anode, PEDOT:PSS (poly(3,4-ethylenedioxythiophene) polystyrene sulfonate) as HTL (Hole-Transporting Layer), the emissive layer (which contains only one of the synthesized fluorophores in the non-doped devices and incorporates the iridium complexes Ir(ppy)₃^[258] and Ir(MDQ)₂acac^[271] in WOLEDs), TPBi (2,2',2''-(1,3,5-Benzinetriyl)-tris(1-phenyl-1-*H*-benzimidazole)) as ETL (Electron-Transporting Layer) and a bilayer of calcium and aluminum as the cathode.

6.4.1. Non-doped devices

As a first approach, we fabricated non-doped OLEDs to evaluate the effectiveness of the synthesized compounds as blue emitters. It was also important to test and define the best conditions to prepare the devices. The deposition of the emissive layer *via* solution-processing was examined with commonly used solvents. All compounds were deposited using tetrahydrofuran (THF) and chlorobenzene (CB), as collected in Table 6.3. The use of cyclohexanone (CHO) was discarded because of the poor performance of the corresponding device (**67b** in device 4). Essentially, devices fabricated from THF solutions underperformed in front of the ones fabricated using CB, in terms of both luminance and

current efficiency. The resulting turn-on voltage and thickness of the films were also considerably higher for those prepared from THF. Hence, CB was selected for the fabrication of all the subsequent devices.

Table 6.3. Characteristics of OLED devices fabricated from compounds **67a–b** and **68a–b**.

	Device	Solvent ^[a]	<i>d</i> (nm) ^[c]	<i>V</i> _{on} (V) ^[d]	<i>L</i> _{max} (cd m ⁻²) ^[e]	CE (cd A ⁻¹) ^[f]
67a	1	THF	51 ± 2	5.2	38	0.05
	2	CB	33 ± 2	3.8	108	0.26
	3	- ^[b]	35 ± 1	4.3	217	0.22
67b	4	CHO	33 ± 2	5.7	9	0.04
	5	THF	49 ± 8	7.8	15	0.02
	6	CB	37 ± 4	5.0	43	0.05
	7	- ^[b]	34 ± 2	3.5	121	0.34
68a	8	THF	77 ± 6	6.4	19	0.04
	9	CB	43 ± 4	4.9	38	0.09
68b	10	THF	79 ± 2	8.2	44	0.12
	11	CB	44 ± 4	4.5	96	0.47

[a] Solvent used to prepare the spin-coated emissive layer, namely tetrahydrofuran (THF), chlorobenzene (CB) and cyclohexanone (CHO). [b] The emissive layer was vacuum-evaporated. [c] Average thickness of the emitting layer, determined with a profilometer. [d] Turn-on voltage, defined as the voltage necessary to provide a luminance of 1 cd m⁻². [e] Maximum luminance. [f] Maximum current efficiency.

All bicarbazole-based (**67a–b**) and triethynylbenzene-based (**68a–b**) compounds displayed luminance values from 10¹ to 10² cd m⁻². Remarkably, the best luminance and current efficiency values were achieved with derivatives **67a** and **68b**, which correspond to the ethylated derivative for the former structure and the 2-ethylhexylated derivative for the latter, respectively. Figure 6.7 represents the OLED characteristics of the devices fabricated using chlorobenzene as solvent. Regarding the electroluminescence of the devices, none of the compounds **67a–b** and **68a–b** achieved strict deep-blue coordinates. Similarly to their photoluminescence in the solid state, all devices showed blue emission with the exception of those fabricated from derivative **67a**, which displayed blue-green emission.

Additionally, analogue devices featuring vacuum-evaporated derivatives **67a–b** as active layers were prepared for comparison (devices 3 and 7). Unfortunately, compounds **68a–b** resulted inappropriate for this technique even though their extraordinarily high thermal stability. As expected, the vacuum-deposited devices outdid all their solution-processed counterparts. The ethylated **67a** exhibited a maximum luminance of 217 cd m⁻², whereas the hexylated **67b** displayed a high current efficiency of 0.34 cd A⁻¹. It should be mentioned that the substitution of PEDOT:PSS for MoO₃ as an alternative HTL was considered in

vacuum-deposited devices, since its application is incompatible with the solution-processing. However, both derivatives underperformed in this case despite the closer work function value of MoO₃ (5.6 eV) to the HOMO energy level of structure **67**. Overall, the relatively small difference between both deposition techniques does not discredit the advantages of the solution-processing.

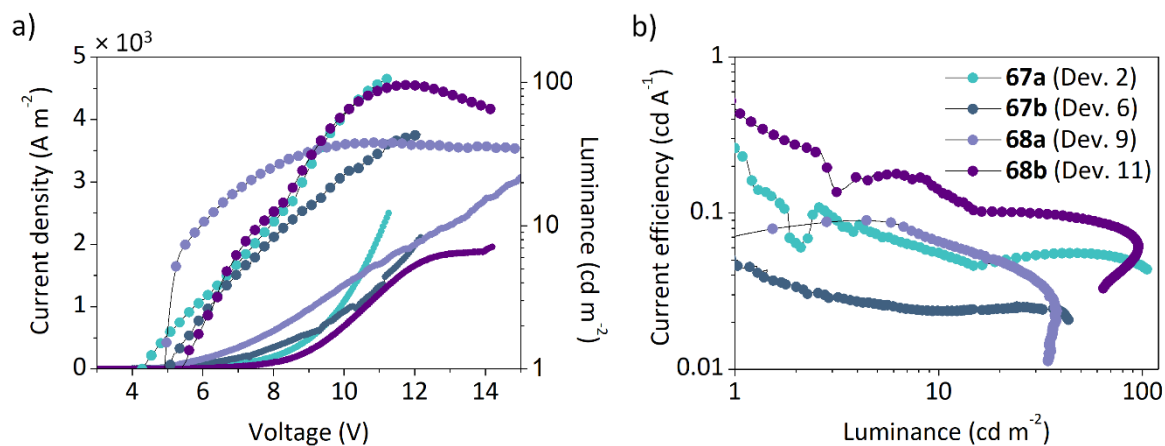


Figure 6.7. Characterization of devices featuring derivatives **67a–b** and **68a–b** deposited using chlorobenzene as solvent: a) current density and luminance; b) current efficiency.

6.4.2. Iridium-containing devices

Going one step further, we evaluated the synthesized compounds in the preparation of WOLEDs. It should be pointed out that, even if pure white is denoted with the CIE coordinates (0.33, 0.33), the definition of white light in terms of illumination extends to a wide range of color coordinates that can be described by the Planckian locus. The color temperature represents a well-known way to classify the assortment of white light shades, so the analysis of this parameter is also discussed.

Each blue-emitting material was combined with the commercially available Ir(ppy)₃ and Ir(MDQ)₂acac complexes in different ratios using chlorobenzene as solvent. The first attempts, however, proved that the ethylated derivative **68a** was not suitable for this study due to the low quality of the solution-deposited layers incorporating iridium complexes. Despite the great potential in non-doped devices, its analog **68b** also underperformed in this assembly. The decrease of both the luminance and the current efficiency was especially evident with the low ratios of iridium needed to emit pure white light. A similar trend was observed in the case of derivative **67a**, which in addition deviated slightly from the sought white light due to its blue-green emission in the solid state. Thus, **67a** and **68b** were not optimal for this study and were not considered for further experiments (the optoelectronic characterization of devices incorporating derivatives **67a** and **68b** with different ratios of iridium is summarized in Table A6.1 and Figure A6.1 of the Appendix).

On the contrary, devices composed of derivative **67b** revealed it as the best candidate to perform as both host and blue emitter in WOLEDs. The phosphorescence spectra of compounds **67b** and **68b** (Figure A6.2 of the Appendix) indicate that compound **67b** possesses a higher triplet energy than **68b**, with values of 2.66 and 2.56 eV, respectively. This is associated to a more effective host-to-guest energy transfer,^[272–273] which correlates to the better results obtained with **67b** than with **68b** in doped devices. Table 6.4 highlights the optoelectronic properties of a set of some fabricated devices featuring a selection of representative ratios.

Table 6.4. Characteristics of iridium-containing OLED devices fabricated from compound **67b**.

Dev.	67b	Ir(ppy) ₃ ^[a]	Ir(MDQ) ₂ acac ^[a]	V _{on} ^[b] (V)	L _{max} ^[c] (cd m ⁻²)	CE ^[d] (cd A ⁻¹)	CIE ^[e]	CCT ^[f] (K)
12	100	1.00	-	3.7	186	1.73	(0.28, 0.57)	-
13	100	-	1.00	4.8	142	0.39	(0.52, 0.40)	1974
14	100	0.12	0.12	4.2	58	0.03	(0.35, 0.33)	4852
15	100	0.25	0.25	3.8	66	0.22	(0.42, 0.40)	3276
16	100	0.50	0.25	3.2	199	0.44	(0.40, 0.43)	3782
17	100	0.25	0.50	3.9	98	0.21	(0.47, 0.40)	2457
18	100	0.50	0.50	3.4	204	0.66	(0.45, 0.44)	3012
19	100	1.00	1.00	3.7	288	1.57	(0.47, 0.45)	2821

[a] Proportion (w/w) of the iridium complexes in front of **67b** (ratio of **67b**:Ir(ppy)₃:Ir(MDQ)₂acac. [b] Turn-on voltage, defined as the voltage necessary to provide a luminance of 1 cd m⁻². [c] Maximum luminance. [d] Maximum current efficiency, calculated at an operating voltage higher than the V_{on}. [e] CIE coordinates calculated from the corresponding electroluminescence spectrum at 10 V in devices 12–13 and at 8 V in devices 14–19. [f] Correlated color temperature (CCT) calculated from the corresponding CIE coordinates using the McCamy's approximation (ref. 112).

The first tests (devices 12–13) were performed in combination with a single iridium emitter as references. Notably, the combination with the green-emitting Ir(ppy)₃ (device 12), which features a triplet energy level closer to that of the blue emitter, outperforms that with the red one Ir(MDQ)₂acac (device 13). This applies to both the luminance and the current efficiency. In fact, the former outdoes with a maximum current efficiency value of 1.73 cd A⁻¹ in front of 0.39 cd A⁻¹ of the latter, pointing out the relevance of balanced triplet energy levels. It has to be mentioned that the results on this part refer to devices with different chromaticity, so the comparison of their parameters should be taken with prudence. Nevertheless, this tendency is also observed by comparing devices 16 and 17, which display similar CIE coordinates. The former, with a higher amount of green-emitting Ir(ppy)₃, doubles both the maximum luminance and current efficiency of the latter, in which the red-emitting Ir(MDQ)₂acac predominates. The overlap between the absorption and emission spectra of the synthesized compounds and the ones reported for both iridium

complexes^[274–275] also assists the feasibility of host-to-guest energy transfer. Accordingly, devices incorporating both iridium complexes in higher ratios tend to display higher luminance and current efficiency values. Figure 6.8 represents the OLED characteristics of devices featuring a single iridium complex (12–13) and those with an equal amount of them (14–15, 17–19). Notably, all devices possess turn-on voltages below 5 V, which conveniently decrease in the presence of Ir(ppy)₃. This fact also agrees with a favorable adjustment of the triplet energy levels.

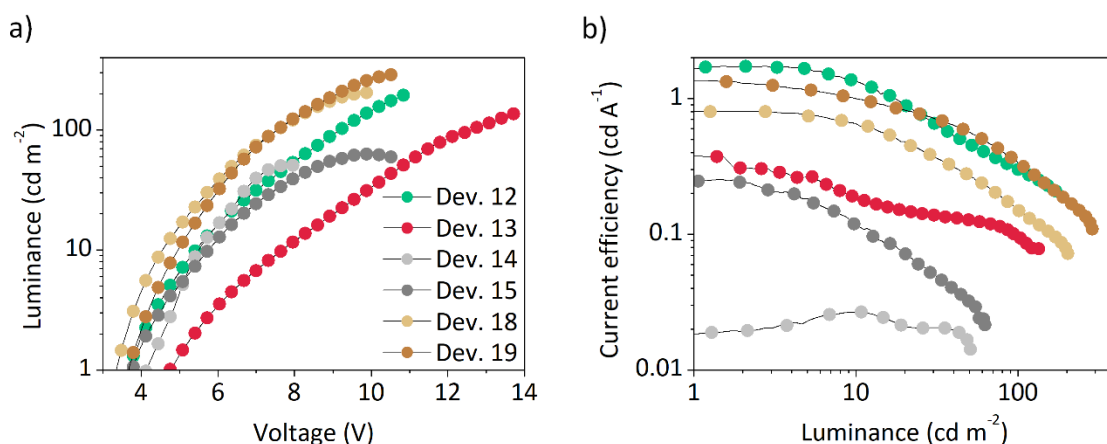


Figure 6.8. Characteristics of some of the devices featuring **67b** in combination with Ir(ppy)₃ and Ir(MDQ)₂acac: a) luminance and b) current efficiency.

The chromaticity of the devices provided encouraging results as well. Figure 6.9 depicts the electroluminescent properties of the abovementioned devices. It should be noted that the combination of both complexes is necessary to produce light with pure white coordinates (0.33, 0.33). Specifically, it was achieved in a ratio of 100:0.12:0.12 of **67b**:Ir(MDQ)₂acac:Ir(ppy)₃ (device 14) applying a voltage of 6 V, with a correlated color temperature of 5617 K. This derives from the perfectly balanced emission of all three components, as observed in Figure 6.10a. Nevertheless, the equivalent emission of Ir(MDQ)₂acac and Ir(ppy)₃ is lost at higher proportions of iridium than the aforementioned (devices 15, 18 and 19). The red emission corresponding to Ir(MDQ)₂acac then surpasses the green one from Ir(ppy)₃. This phenomenon was observed even in devices incorporating higher proportions of the latter. Device 16, regardless of the outweigh of Ir(ppy)₃, provides an electroluminescent spectrum clearly dominated by the red emission of Ir(MDQ)₂acac (Figure 6.10b). The chromaticity data seems to further support the thesis of an energy transfer from host to guest towards Ir(MDQ)₂acac. As a result, the emission acquires color coordinates that favorably approximate the Planckian locus (represented in Figure 6.9c). In fact, the color temperature tends to lower values at higher percentages of iridium, i.e. warmer white in terms of illumination. Therefore, the produced white light can be fine-tuned with small variations of the emissive layer composition.

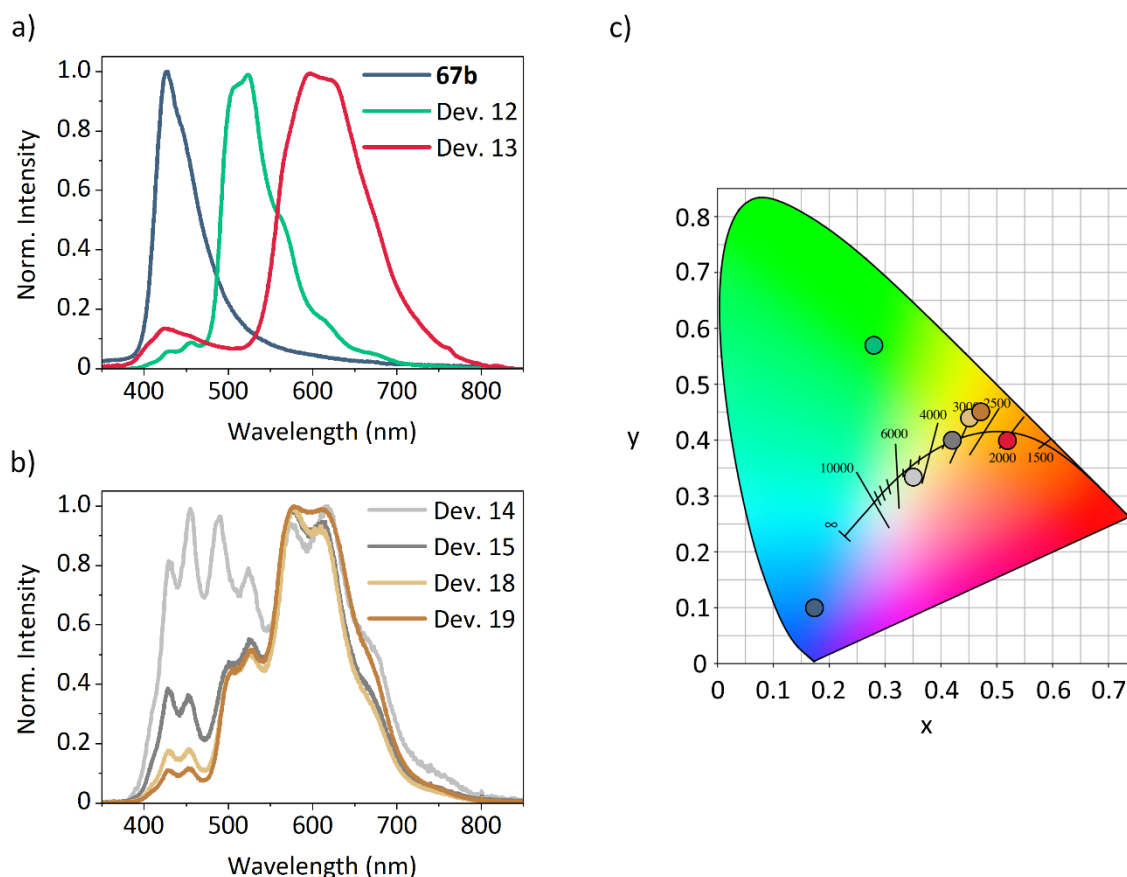


Figure 6.9. Optical characterization of devices featuring **67b** in combination of Ir(ppy)₃ and Ir(MDQ)₂acac: a) devices containing a single iridium complex (12 and 13) alongside the photoluminescence in the solid state of **67b**; b) devices containing different 1:1 iridium ratios (14–15 and 18–19); c) correlated color coordinates represented in the CIE 1931 color space chromaticity diagram with the Planckian locus (the transversal lines indicate the color temperatures in K).

It is also significant the influence of the applied voltage as modulator of the emitted white color. Figure 6.10 shows the electroluminescent spectra of devices 14, 16 and 18 and their resulting CIE coordinates at different voltages to exemplify this effect (the CIE and CCT values of devices 12–19 at different voltages are compiled in Table A6.2 of the Appendix). Considering the studied devices, the contribution to the blue emission of the host **67b** and the green Ir(ppy)₃ are generally maximized at lower voltages, whereas more transference to the red Ir(MDQ)₂acac is observed at higher voltages. This points to an additional voltage-dependent energy transfer towards the red-emitting Ir(MDQ)₂acac, so the color temperature can be controlled working with the voltage as a modulating factor.

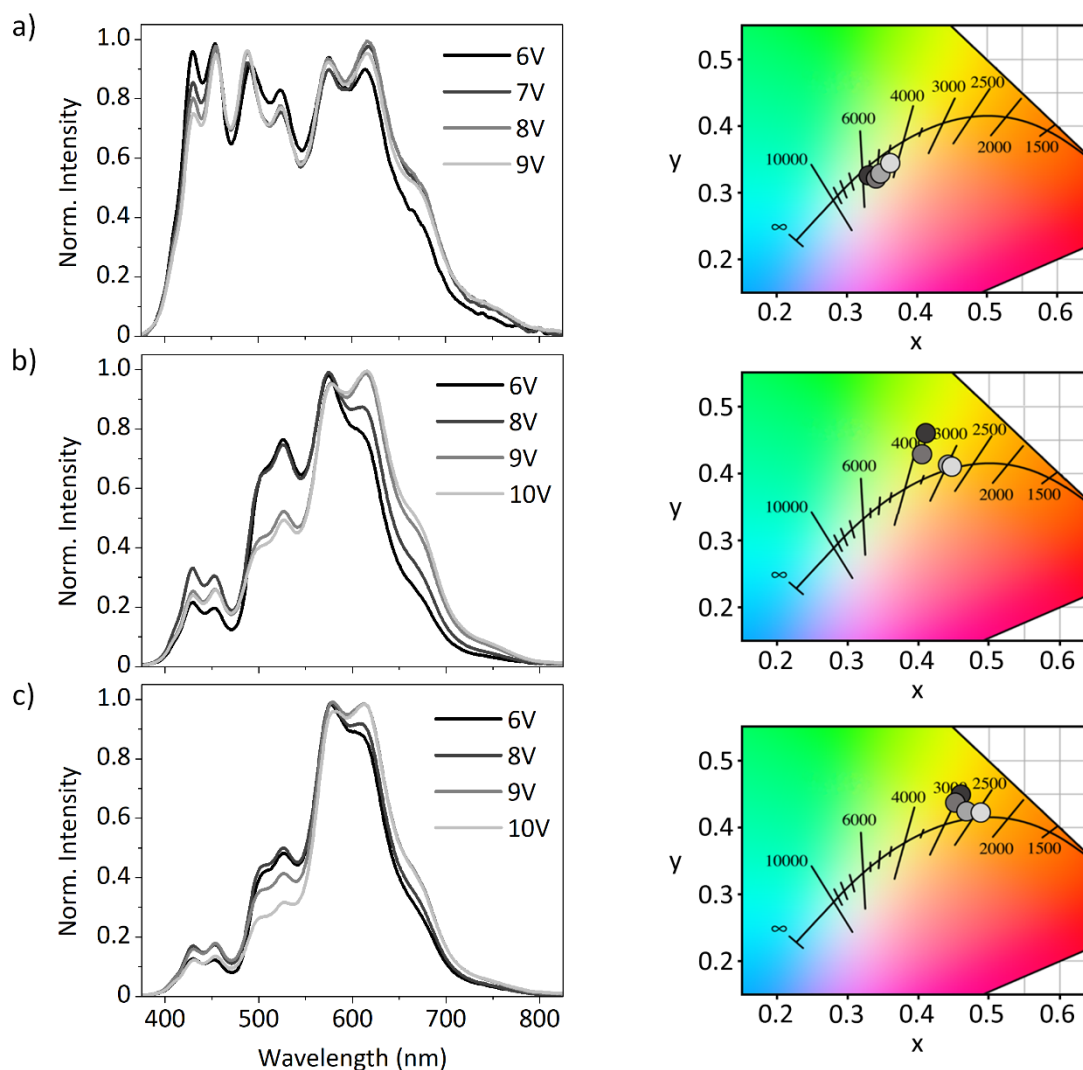


Figure 6.10. Electroluminescence spectra and the corresponding CIE coordinates at different applied voltages (the lower represented in black and the higher in pale grey) of: a) Device 12 (100:0.12:0.12), b) device 16 (100:0.50:0.25) and c) device 18 (100:0.50:0.50).

6.5. Conclusions

Two new carbazole-based structures featuring two different *N*-alkyl chain lengths have been developed for their application as blue fluorophores. All the synthesized compounds display interesting optoelectronic properties that are influenced by their structural features. Indeed, the length of the *N*-alkyl chains is crucial in the bicarbazole-based derivatives **67a–b**, determining the intermolecular arrangement and, therefore, their optical properties in the solid state. In particular, the *N*-hexylated derivative **67b** is the only one that displays enhanced emission in the solid state and in the deep-blue region. Contrarily, the triethynylbenzene derivatives **68a–b** display very high Φ_f in solution (ca. 0.80) within the UV-blue region, whereas the values in the solid state diminish to 0.07.

The integration of all compounds in non-doped blue OLEDs *via* solution-processing highlighted chlorobenzene as the most appropriate solvent for the deposition. The best results were collected with derivative **67a**, with a maximum luminance up to 108 cd m^{-2} that is comparative to that of the vacuum-deposited counterpart. On the other hand, **67b** also stands out as the most appropriate derivative to perform as host for iridium complexes in solution-processed WOLEDs. The emission of the resulting devices, which depends on the ratio of the iridium complexes and the applied voltage, covers a vast range of correlated color temperatures. In fact, the combination of **67b** with a 0.12% of each iridium complex provided pure white coordinates at 6 V. An increase to 1% of each complex implied the best performance, with a luminance up to 288 cd m^{-2} and a CE of 1.57 cd A^{-1} and a warm white emission of 2821 K at 8V.

These first results, far from being competitive with the current state-of-the-art OLED technology, still demonstrate the flexibility and potential of **67b** in the manufacture of WOLEDs. Also, it proves the feasibility to emit white light in a vast range of temperatures by fine-tuning the ternary composition of the emissive layer and the applied voltage.

CONCLUSIONS



CONCLUSIONS

The main results and conclusions extracted from the carbazole-based materials surveyed in this work, from their synthesis to their application in final devices, are compiled herein.

The π -extension of the carbazole nucleus towards different ladder-type cores has been confirmed as an effective approach to furnish air-stable p-type semiconductors for OTFTs. Indeed, the diindolocarbazole (**1**), the bisbenzothienocarbazole (**30**) and the diphenanthrocarbazole (**37**) systems have exhibited outstanding hole mobility values up to $10^{-3} \text{ cm}^2 \text{ V}^{-1} \text{ s}^{-1}$ with shelf lifetimes that in some instances could even surpass the milestone of 1000 days. Specifically, the synthesis of several diindolocarbazole derivatives through the microwave-assisted Cadogan reaction has revealed that a homogeneous *N*-alkylation pattern with short-to-medium chains provides the best performance in this core. Concerning the bisbenzothienocarbazole and the diphenanthrocarbazole cores, the addition of peripheral alkyl chains to confer a head-tail fashion derives into overall enhanced charge mobility values. However, it is accomplished in most cases with a consequent destabilization of the charge mobility over time or a detriment of the shelf lifetime of the devices. The choice between OTS and PS as the interfacial organic dielectrics prompt an alternative way to improve the device performance, being PS more favorable for cores **1** and **30** and OTS for **37**. Comparatively, the diindolocarbazole and diphenanthrocarbazole structures emerge as the most promising building blocks, especially the latter. The γ -type packing detected on their crystal structures, their preeminent air and temporal stability and their easier functionalization and more accessible synthetic processes augur a huge impact into the electronic field.

Alternatively, the π -extension of the dibenzothiophene nucleus accomplished *via* the Scholl reaction has provided a new perspective towards diverse structures. Synthetically, the coupling and subsequent cyclization succeeded in a wide array of arylboronic acids with excellent yields. The first approach to homogeneously substituted derivatives, featuring scaffolds of diverse nature, has permitted the fine-tuning of the physical properties of both the open and the cyclized structures (2,3,4,5-tetraphenylthiophene **44** and diphenanthro[9,10-*b*:9',10'-*d*]thiophene **45**, respectively). In a second stage, we could also envision alternative and novel designs based on a heterogeneous substitution of thiophene (**50a–c**), which was facilitated by means of a one-pot procedure. Their integration in OTFT devices shed light on the role of the chosen scaffolds, ushering in subsequent tailored modifications. Derivative **50a**, which incorporates two phenanthrene extensions, afforded

the best performance with a $\mu_{h,avg}$ of $6.3 \times 10^{-5} \text{ cm}^2 \text{ V}^{-1} \text{ s}^{-1}$ deposited over PS and a shelf lifetime that extends beyond one year.

The synthetic modifications projected for the triindole core have been also successful. The inclusion of carbazole moieties to different positions of triindole afforded a modulation of its physical properties, such as the reduction of both the optical energy gap and the ionization potential to move closer to the gold work function. Besides, the synthesis of the analog nuclei trioxatruxene and trithiatruxene and the attachment of peripheral alkyl chains has been successfully accomplished. Even though their high ionization potentials anticipate a challenging integration in OTFTs, these systems will be exploited in ongoing studies.

Finally, the potential of 9*H*-carbazole in the optoelectronic field has been reaffirmed with the synthesis of two blue-emitting structures based on the 3-phenylethynylcarbazole unit: 6,6'-bis(phenylethynyl)-9*H*,9'*H*-3,3'-bicarbazole (**67**) and 1,3,5-tris((9*H*-carbazol-3-yl)ethynyl)benzene (**68**). The integration in non-doped blue OLEDs *via* solution-processing highlighted chlorobenzene as the most appropriate solvent for the deposition step. The best results were collected with the *N*-ethylated **67a**, with a maximum luminance up to 108 cd m^{-2} that is comparative to that of the vacuum-deposited counterpart. On the other hand, the *N*-hexylated **67b** not only stands out for displaying enhanced emission in the solid state within the deep-blue region, but also to effectively perform as host for iridium complexes in WOLEDs. The resultant emission, which depends on the ternary composition and the applied voltage, covers a vast range of correlated color temperatures.

Overall, the wide array of materials analyzed so far prove the potential of the 9*H*-carbazole nucleus as building block to furnish air-stable organic semiconductors for different applications. The results collected and presented throughout this Thesis, far from concluding the research over these materials, are likely to open the door to subsequent investigations.

REFERENCES

The page features a minimalist design. A thick, dark gray vertical bar runs along the right edge. Two horizontal lines, one slightly above the other, extend from the left margin towards the right, ending at the vertical bar. The word "REFERENCES" is centered between these two lines.

REFERENCES

- [1] Prasad, S.; Schumacher, H.; Gopinath, A. *High speed electronics and optoelectronics: devices and circuits*; Cambridge University Press: Cambridge, 2009; pp. 3–8.
- [2] Cheng, K. Y. *III-V compound semiconductors and devices: an introduction to fundamentals*; Springer Nature Switzerland AG: Switzerland, 2020; pp. 1–19.
- [3] Eley, D. Phthalocyanines as semiconductors. *Nature* **1948**, *162*, 819.
- [4] Akamatu, H.; Inokuchi, H.; Matsunaga, Y. Electrical conductivity of the perylene–bromine complex. *Nature* **1954**, *173*, 168–169.
- [5] Shirakawa, H.; Louis, E. J.; MacDiarmid, A. G.; Chiang, C. K.; Heeger, A. J. Synthesis of electrically conducting organic polymers: halogen derivatives of polyacetylene, (CH)_x. *J. Chem. Soc., Chem. Commun.* **1977**, 578–580.
- [6] Shirakawa, H. The discovery of polyacetylene film: the dawning of an era of conducting polymers (Nobel Lecture). *Angew. Chem., Int. Ed.* **2001**, *40*, 2575–2580.
- [7] The Nobel Prize in Chemistry 2000. NobelPrize.org. Nobel Prize Outreach AB 2022. <<https://www.nobelprize.org/prizes/chemistry/2000/summary/>>
- [8] Wang, C.; Dong, H.; Jiang, L.; Huanli, D. Organic semiconductor crystals. *Chem. Soc. Rev.* **2017**, *47*, 422–500.
- [9] Wu, F.; Liu, Y.; Zhang, J.; Duan, S.; Ji, D.; Yang, H. Recent advances in high-mobility and high-stretchability organic field-effect transistors: from materials, devices to applications. *Small Methods* **2021**, *5*, 2100676.
- [10] Varghese, M. A.; Anjali, A.; Harshini, D.; Nagarajan, S. Organic light-emitting transistors: from understanding to molecular design and architecture. *ACS Appl. Electron. Mater.* **2021**, *3*, 550–573.
- [11] Scaccabarozzi, A. D.; Basu, A.; Aníés, F.; Liu, J.; Zapata-Arteaga, O.; Warren, R.; Firdaus, Y.; Nugraha, M. I.; Lin, Y.; Campoy-Quiles, M.; Koch, N.; Müller, C.; Tsetseris, L.; Heeney, M.; Anthopoulos, T. D. Doping approaches for organic semiconductors. *Chem. Rev.* **2021**, *122*, 4420–4492.
- [12] Jiang, H.; Zhu, S.; Cui, Z.; Li, Z.; Liang, Y.; Zhu, J.; Hu, P.; Zhang, H.-L.; Hu, W. High-performance five-ring-fused organic semiconductors for field-effect transistors. *Chem. Soc. Rev.* **2022**, *51*, 3071–3122.
- [13] Guo, X.; Xu, Y.; Ogier, S.; Ng, T. N.; Caironi, M.; Perinot, A.; Li, L.; Zhao, J.; Tang, W.; Sporea, R. A.; Nejm, A.; Carrabina, J.; Cain, P.; Yan, F. current status and opportunities of organic thin-film transistor technologies. *IEEE Trans. Electron Devices* **2017**, *64*, 1906–1921.
- [14] Zou, S.-J.; Shen, Y.; Xie, F.-M.; Chen, J.-D.; Li, Y.-Q.; Tang, J.-X. Recent advances in organic light-emitting diodes: toward smart lighting and displays. *Mater. Chem. Front.* **2020**, *4*, 788–820.
- [15] Hong, G.; Gan, X.; Leonhardt, C.; Zhang, Z.; Seibert, J.; Busch, J. M.; Bräse, S. A brief history of OLEDs—emitter development and industry milestones. *Adv. Mater.* **2021**, *33*, 2005630.
- [16] Liu, Y.; Li, B.; Ma, C.-Q.; Huang, F.; Feng, G.; Chen, H.; Hou, J.; Yan, L.; Wei, Q.; Luo, Q.; Bao, Q.; Ma, W.; Liu, W.; Li, W.; Wan, X.; Hu, X.; Han, Y.; Li, Y.; Zhou, Y.; Zou, Y.; Chen, Y.; Li, Y.;

- Chen, Y.; Tang, Z.; Hu, Z.; Zhang, Z.-G.; Bo, Z. Recent progress in organic solar cells (Part I material science). *Sci. China Chem.* **2022**, *65*, 224–268.
- [17] Luo, D.; Jang, W.; Babu, D. D.; Kim, M. S.; Wang, D. H.; Kyaw, A. K. K. Recent progress in organic solar cells based on non-fullerene acceptors: materials to devices. *J. Mater. Chem. A* **2022**, *10*, 3255–3295.
- [18] Bronstein, H.; Nielsen, C. B.; Schroeder, B. C.; McCulloch, I. The role of chemical design in the performance of organic semiconductors. *Nat. Rev. Chem.* **2020**, *4*, 66–77.
- [19] Ueberricke, L.; Mastalerz, M. Triptycene end-capping as strategy in materials chemistry to control crystal packing and increase solubility. *Chem. Rec.* **2021**, *21*, 558–573.
- [20] Klues, M.; Witte, G. Crystalline packing in pentacene-like organic semiconductors. *CrystEngComm* **2018**, *20*, 63–74.
- [21] Wang, C.; Dong, H.; Hu, W.; Liu, Y.; Zhu, D. Semiconducting π -conjugated systems in field-effect transistors: a material odyssey of organic electronics. *Chem. Rev.* **2012**, *112*, 2208–2267.
- [22] Olivier, Y.; Lemaire, V.; Brédas, J. L.; Cornil, J. Charge hopping in organic semiconductors: influence of molecular parameters on macroscopic mobilities in model one-dimensional stacks. *J. Phys. Chem. A* **2006**, *110*, 6356–6364.
- [23] Shirota, Y.; Kageyama, H. Charge carrier transporting molecular materials and their applications in devices. *Chem. Rev.* **2007**, *107*, 953–1010.
- [24] Lei, T.; Wang, J.-Y.; Pei, J. Roles of flexible chains in organic semiconducting materials. *Chem. Mater.* **2014**, *26*, 594–603.
- [25] He, K.; Li, W.; Tian, H.; Zhang, J.; Yan, D.; Geng, Y.; Wang, F. Asymmetric conjugated molecules based on [1]benzothieno[3,2-*b*][1]benzothiophene for high-mobility organic thin-film transistors: influence of alkyl chain length. *ACS Appl. Mater. Interfaces* **2017**, *9*, 35427–35436.
- [26] Shao, J.; Zhang, X.; Tian, H.; Geng, Y.; Wang, F. Donor–acceptor–donor conjugated oligomers based on isoindigo and anthra[1,2-*b*]thieno[2,3-*d*]thiophene for organic thin-film transistors: the effect of the alkyl side chain length on semiconducting properties. *J. Mater. Chem. C* **2015**, *3*, 7567–7574.
- [27] Mišićák, R.; Novota, M.; Weis, M.; Cigáň, M.; Šiffalovič, P.; Nádaždy, P.; Kožíšek, J.; Kožíšková, J.; Pavúk, M.; Putala, M. Effect of alkyl side chains on properties and organic transistor performance of 2,6-bis(2,2'-bithiophen-5-yl)naphthalene. *Synth. Met.* **2017**, *233*, 1–14.
- [28] Khatun, M. N.; Dey, A.; Meher, N.; Iyer, P. K. Long alkyl chain induced OFET characteristic with low threshold voltage in an n-type perylene monoimide semiconductor. *ACS Appl. Electron. Mater.* **2021**, *3*, 3575–3587.
- [29] The Nobel Prize in Physics 1956. NobelPrize.org. Nobel Prize Outreach AB 2022. <<https://www.nobelprize.org/prizes/physics/1956/summary/>>
- [30] The Nobel Prize in Physics 2000. NobelPrize.org. Nobel Prize Outreach AB 2022. <<https://www.nobelprize.org/prizes/physics/2000/summary/>>
- [31] Tsumura, A.; Kozuka, H.; Ando, T. Macromolecular electronic device: Field-effect transistor with a polythiophene thin film. *Appl. Phys. Lett.* **1986**, *49*, 1210–1212.

- [32] Koezuka, H.; Tsumura, A.; Ando, T. Field-effect transistor with polythiophene thin film. *Synth. Met.* **1987**, *18*, 699–704.
- [33] Paterson, A. F.; Singh, S.; Fallon, K. J.; Hodsden, T.; Han, Y.; Schroeder, B. C.; Bronstein, H.; Heeney, M.; McCulloch, I.; Anthopoulos, T. D. Recent progress in high-mobility organic transistors: a reality check. *Adv. Mater.* **2018**, *30*, 1801079.
- [34] Liu, X.; Guo, Y.; Ma, Y.; Chen, H.; Mao, Z.; Wang, H.; Yu, G.; Liu, Y. Flexible, low-voltage and high-performance polymer thin-film transistors and their application in photo/thermal detectors. *Adv. Mater.* **2014**, *26*, 3631–3636.
- [35] Reese, C.; Roberts, M.; Ling, M.; Bao, Z. Organic thin film transistors. *Mater. Today* **2004**, *7*, 20–27.
- [36] Bittle, E. G.; Basham, J. I.; Jackson, T. N.; Jurchescu, O. D.; Gundlach, D. J. Mobility overestimation due to gated contacts in organic field-effect transistors. *Nat. Commun.* **2016**, *7*, 10908.
- [37] Peng, H.; He, X.; Jiang, H. Greater than $10 \text{ cm}^2 \text{ V}^{-1} \text{ s}^{-1}$: A breakthrough of organic semiconductors for field-effect transistors. *InfoMat* **2021**, *3*, 613–630.
- [38] Chang, H.; Li, W.; Tian, H.; Geng, Y.; Wang, H.; Yan, D.; Wang, T. High performance of rubrene thin film transistor by weak epitaxy growth method. *Org. Electron.* **2015**, *20*, 43–48.
- [39] Klauk, H.; Halik, M.; Zschieschang, U.; Schmid, G.; Radlik, W.; Weber, W. High-mobility polymer gate dielectric pentacene thin film transistors. *J. Appl. Phys.* **2002**, *92*, 5259–5263.
- [40] Roberts, M. E.; Mannsfeld, S. C. B.; Queraltó, N.; Reese, C.; Locklin, J.; Knoll, W.; Bao, Z. Water-stable organic transistors and their application in chemical and biological sensors. *PNAS* **2008**, *105*, 12134–12139.
- [41] Park, S. K.; Jackson, T. N.; Anthony, J. E.; Mourey, D. A. High mobility solution processed 6,13-bis(triisopropyl-silylethynyl) pentacene organic thin film transistors. *Appl. Phys. Lett.* **2007**, *91*, 063514.
- [42] Yuan, Y.; Giri, G.; Ayzner, A. L.; Zoombelt, A. P.; Mannsfeld, S. C. B.; Chen, J.; Nordlund, D.; Toney, M. F.; Huang, J.; Bao, Z. Ultra-high mobility transparent organic thin film transistors grown by an off-centre spin-coating method. *Nat. Commun.* **2014**, *5*, 3005.
- [43] Iino, H.; Usui, T.; Hanna, J. Liquid crystals for organic thin-film transistors. *Nat Commun* **2015**, *6*, 6828.
- [44] Amin, A. Y.; Khassanov, A.; Reuter, K.; Meyer-Friedrichsen, T.; Halik, M. Low-voltage organic field effect transistors with a 2-tridecyl[1]benzothieno[3,2-*b*][1]benzothiophene semiconductor layer. *J. Am. Chem. Soc.* **2012**, *134*, 16548–16550.
- [45] Yamamoto, T.; Takimiya, K. Facile synthesis of highly π -extended heteroarenes, dinaphtho[2,3-*b*:2',3'-*f*]chalcogenopheno[3,2-*b*]chalcogenophenes, and their application to field-effect transistors. *J. Am. Chem. Soc.* **2007**, *129*, 2224–2225.
- [46] Nakayama, K.; Hirose, Y.; Soeda, J.; Yoshizumi, M.; Uemura, T.; Uno, M.; Li, W.; Kang, M. J.; Yamagishi, M.; Okada, Y.; Miyazaki, E.; Nakazawa, Y.; Nakao, A.; Takimiya, K.; Takeya, J. Patternable solution-crystallized organic transistors with high charge carrier mobility. *Adv. Mater.* **2011**, *23*, 1626–1629.

- [47] Okamoto, T.; Kumagai, S.; Fukuzaki, E.; Ishii, H.; Watanabe, G.; Niitsu, N.; Annaka, T.; Yamagishi, M.; Tani, Y.; Sugiura, H.; Watanabe, T.; Watanabe, S.; Takeya, J. Robust, high-performance n-type organic semiconductors. *Sci. Adv.* **2020**, *6*, eaaz0632.
- [48] Xu, X.; Yao, Y.; Shan, B.; Gu, X.; Liu, D.; Liu, J.; Xu, J.; Zhao, N.; Hu, W.; Miao, Q. Electron mobility exceeding $10 \text{ cm}^2 \text{ V}^{-1} \text{ s}^{-1}$ and band-like charge transport in solution-processed n-channel organic thin-film transistors. *Adv. Mater.* **2016**, *28*, 5276–5283.
- [49] Chu, M.; Fan, J.-X.; Yang, S.; Liu, D.; Ng, C.-F.; Dong, H.; Ren, A.-M.; Miao, Q. Halogenated tetraazapentacenes with electron mobility as high as $27.8 \text{ cm}^2 \text{ V}^{-1} \text{ s}^{-1}$ in solution-processed n-channel organic thin-film transistors. *Adv. Mater.* **2018**, *30*, 1803467.
- [50] Huang, X.; Sheng, P.; Tu, Z.; Zhang, F.; Wang, J.; Geng, H.; Zou, Y.; Di, C.-A.; Yi, Y.; Sun, Y.; Xu, W.; Zhu, D. A two-dimensional π -*d* conjugated coordination polymer with extremely high electrical conductivity and ambipolar transport behaviour. *Nat Commun.* **2015**, *6*, 7408.
- [51] Sheraw, C. D.; Jackson, T. N.; Eaton, D. L.; Anthony, J. E. Functionalized pentacene active layer organic thin-film transistors. *Adv. Mater.* **2003**, *15*, 2009–2011.
- [52] Jurchescu, O. D.; Popinciuc, M.; van Wees, B. J.; Palstra, T. T. M. Interface-controlled, high-mobility organic transistors. *Adv Mater.* **2007**, *19*, 688–692.
- [53] Feng, L.; Tang, W.; Zhao, J.; Yang, R.; Hu, W.; Li, Q.; Wang, R.; Guo, X. Unencapsulated air-stable organic field effect transistor by all solution processes for low power vapor sensing. *Sci. Rep.* **2016**, *6*, 20671.
- [54] Mitsui, C.; Okamoto, T.; Yamagishi, M.; Tsurumi, J.; Yoshimoto, K.; Nakahara, K.; Soeda, J.; Hirose, Y.; Sato, H.; Yamano, A.; Uemura, T.; Takeya, J. High-performance solution-processable N-shaped organic semiconducting materials with stabilized crystal phase. *Adv. Mater.* **2014**, *26*, 4546–4551.
- [55] Abbaszadeh, D.; Kunz, A.; Kotadiya, N. B.; Mondal, A.; Andrienko, D.; Michels, J. J.; Wetzelaer, G. A.; Blom, P. W. Electron trapping in conjugated polymers. *Chem. Mater.* **2019**, *31*, 6380–6386.
- [56] Usta, H.; Risko, C.; Wang, Z.; Huang, H.; Deliomeroglu, M.; Zhukhovitskiy, A.; Facchetti, A.; Marks, T. Design, synthesis, and characterization of ladder-type molecules and polymers. Air-stable, solution-processable n-channel and ambipolar semiconductors for thin-film transistors via experiment and theory. *J. Am. Chem. Soc.* **2009**, *131*, 5586–608.
- [57] Sirringhaus, H. Reliability of organic field-effect transistors. *Adv. Mater.* **2009**, *21*, 3859–3873.
- [58] Chen, X.; Wang, Z.; Qi, J.; Hu, Y.; Huang, Y.; Sun, S.; Sun, Y.; Gong, W.; Luo, L.; Zhang, L.; Du, H.; Hu, X.; Han, C.; Li, J.; Ji, D.; Li, L.; Hu, W. Balancing the film strain of organic semiconductors for ultrastable organic transistors with a five-year lifetime. *Nat. Commun.* **2022**, *13*, 1480.
- [59] Bernanose, A.; Comte, M.; Vouaux, P. Sur un nouveau mode d'émission lumineuse chez certains composés organiques. *J. Chim. Phys.* **1953**, *50*, 64–68.
- [60] Pope, M.; Kallmann, H. P.; Magnante, P. Electroluminescence in Organic Crystals. *J. Chem. Phys.* **1963**, *38*, 2042–2043.
- [61] Parker, C.; Hatchard, C. Triplet-singlet emission in fluid solutions. Phosphorescence of eosin. *Trans. Faraday Soc.* **1961**, *57*, 1894–1904.

- [62] Tang, C. W.; VanSlyke, S. A. Organic electroluminescent diodes. *Appl. Phys. Lett.* **1987**, *51*, 913–915.
- [63] Chen, H. W.; Lee, J. H.; Lin, B. Y.; Chen, S.; Wuet, S.-T. Liquid crystal display and organic light-emitting diode display: present status and future perspectives. *Light Sci. Appl.* **2018**, *7*, 17168.
- [64] Image extracted from <<https://www.trustedreviews.com/reviews/sony-xr-65a95k>> (author: Kob Monney; image under Creative Commons license: CC BY-NC-ND 4.0; download date: 2022/08/12)
- [65] Image extracted from <<https://www.flickr.com/photos/eu2016nl/27798923486/>> (author: EU2016 NL; image under the Creative Commons license CC BY 2.0; download date: 2022/08/12)
- [66] Image extracted from <<https://www.flickr.com/photos/nanpalmero/39516115240/>> (author: Nan Palmero; image under the Creative Commons license CC BY 2.0; download date: 2022/08/12)
- [67] Image extracted from <<https://www.trustedreviews.com/reviews/nintendo-switch-oled>> (author: Ryan Jones; image under the Creative Commons license CC BY-NC-ND 4.0; download date: 2022/08/12)
- [68] Salehi, A.; Fu, X.; Shin, D.-H.; So, F. Recent advances in OLED optical design. *Adv. Funct. Mater.* **2019**, *29*, 1808803.
- [69] Jou, J.-H.; Sahoo, S.; Dubey, D. K.; Yadav, R. A. K.; Swayamprabha, S. S.; Chavhan, S. D. Molecule-based monochromatic and polychromatic OLEDs with wet-process feasibility. *J. Mater. Chem. C* **2018**, *6*, 11492–11518.
- [70] Birks, J. B. *Photophysics of aromatic molecules*; Wiley: London, 1970.
- [71] Hong, Y.; Lam, J. W. Y.; Tang, B. Z. Aggregation-induced emission. *Chem. Soc. Rev.* **2011**, *40*, 5361–5388.
- [72] Bauri, J.; Choudhary, R. B.; Mandal, G. Recent advances in efficient emissive materials-based OLED applications: a review. *J. Mater. Sci.* **2021**, *56*, 18837–18866.
- [73] Ha, J. M.; Hur, S. H.; Pathak, A.; Jeong, J.-E.; Woo, H. Y. Recent advances in organic luminescent materials with narrowband emission. *NPG Asia Mater.* **2021**, *13*, 53.
- [74] Thejo Kalyani, N.; Dhoble, S. J. Novel materials for fabrication and encapsulation of OLEDs. *Renew. Sustain. Energy Rev.* **2015**, *44*, 319–347.
- [75] Yang, X.; Xu, X.; Zhou, G. Recent Advances of the emitters for high performance deep-blue organic light-emitting diodes. *J. Mater. Chem. C* **2015**, *3*, 913–944.
- [76] Liu, B.; Li, X.-L.; Tao, H.; Zou, J.; Xu, M.; Wang, L.; Peng, J.; Cao, Y. Manipulation of exciton distribution for high-performance fluorescent/phosphorescent hybrid white organic light-emitting diodes. *J. Mater. Chem. C* **2017**, *5*, 7668–7683.
- [77] Dong, H.; Jiang, H.; Wang, J.; Guan, Y.; Hua, J.; Gao, X.; Bo, B.; Wang, J. High-efficiency and color-stable warm white organic light-emitting diodes utilizing energy transfer from interface exciplex. *Org. Electron.* **2018**, *62*, 524–529.
- [78] Zheng, C.-J.; Zhao, W.-M.; Wang, Z.-Q.; Huang, D.; Ye, J.; Ou, X.-M.; Zhang, X.-H.; Lee, C.-S.; Lee, S.-T. Highly efficient non-doped deep-blue organic light-emitting diodes based on anthracene derivatives. *J. Mater. Chem.* **2010**, *20*, 1560–1566.

- [79] Fleetham, T.; Li, G.; Wen, L.; Li, J. Efficient “pure” blue OLEDs employing tetradentate Pt complexes with a narrow spectral bandwidth. *Adv. Mater.* **2014**, *26*, 7116–7121.
- [80] Chan, C. Y.; Cui, L. S.; Kim, J. U.; Nakanotani, H.; Adachi, C. Rational molecular design for deep-blue thermally activated delayed fluorescence emitters. *Adv. Funct. Mater.* **2018**, *28*, 1706023.
- [81] Grybauskaite-Kaminskiene, G.; Volyniuk, D.; Mimaite, V.; Bezikonnyi, O.; Bucinskas, A.; Bagdziunas, G.; Grazulevicius, J. V. Aggregation-enhanced emission and thermally activated delayed fluorescence of derivatives of 9-phenyl-9H-carbazole: effects of methoxy and *tert*-butyl substituents. *Chem. Eur. J.* **2018**, *24*, 9581–9591.
- [82] Joseph, V.; Thomas, K. R. J.; Sahoo, S.; Singh, M.; Jou, J.-H. Simple carbazole based deep-blue emitters: the effect of spacer, linkage and end-capping cyano group on the photophysical and electroluminescent properties. *Dyes Pigm.* **2018**, *151*, 310–320.
- [83] Ong, B. S.; Wu, Y. W.; Li, Y. Organic semiconductors based on polythiophene and indolo[3,2-*b*]carbazole. In *Organic electronics: materials, manufacturing and applications*; Klauk, H., Ed.; WILEY-VCH: Weinheim, Germany, 2006; pp 75–107.
- [84] Wex, B.; Kaafarani, B. R. Perspective on carbazole-based organic compounds as emitters and hosts in TADF applications. *J. Mater. Chem. C* **2017**, *5*, 8622–8653.
- [85] Valeur, B. *Molecular fluorescence: principles and applications*; Wiley-VCH: Weinheim, Germany, 2001.
- [86] Crosby, G. A.; Demas, J. N. Measurement of photoluminescence quantum yields. Review. *J. Phys. Chem.* **1971**, *75*, 991–1024.
- [87] Mei, J.; Hong, Y.; Lam, J. W. Y.; Qin, A.; Tang, Y.; Tang, B. Z. Aggregation-induced emission: the whole is more brilliant than the parts. *Adv. Mater.* **2014**, *26*, 5429–5479.
- [88] Mei, J.; Leung, N. L. C.; Kwok, R. T. K.; Lam, J. W. Y.; Tang, B. Z. Aggregation-induced emission: together we shine, united we soar! *Chem. Rev.* **2015**, *115*, 11718–11940.
- [89] Uoyama, H.; Goushi, K.; Shizu, K.; Nomura, H.; Adachi, C. Highly efficient organic light-emitting diodes from delayed fluorescence. *Nature* **2012**, *492*, 234–238.
- [90] Yang, Z.; Mao, Z.; Xie, Z.; Zhang, Y.; Liu, S.; Zhao, J.; Xu, J.; Chi, Z.; Aldred, M. P. Recent advances in organic thermally activated delayed fluorescence materials. *Chem. Soc. Rev.* **2017**, *46*, 915–1016.
- [91] Shi, Y.-Z.; Wu, H.; Wang, K.; Yu, J.; Ou, X.-M.; Zhang, X.-H. Recent progress in thermally activated delayed fluorescence emitters for nondoped organic light emitting diodes. *Chem. Sci.* **2022**, *13*, 3625–3651.
- [92] Cardona, C. M.; Li, W.; Kaifer, A. E.; Stockdale, D.; Bazan, G. C. Electrochemical considerations for determining absolute frontier orbital energy levels of conjugated polymers for solar cell applications. *Adv. Mater.* **2011**, *23*, 2367–2371.
- [93] Bard, A. J.; Faulkner, L. R. *Electrochemical methods: fundamentals and applications*; WILEY-VCH: New York, 2001.
- [94] Bujak, P.; Kulszewicz-Bajer, I.; Zagorska, M.; Maurel, V.; Wielgus, I.; Pron, A. Polymers for electronics and spintronics. *Chem. Soc. Rev.* **2013**, *42*, 8895–8999.
- [95] Elgrishi, N.; Rountree, K. J.; McCarthy, B. D.; Rountree, E. S.; Eisenhart, T. T.; Dempsey, J. L. A practical beginner’s guide to cyclic voltammetry. *J. Chem. Educ.* **2018**, *95*, 197–206.

- [96] Savéant, J.-M. *Elements of molecular and biomolecular electrochemistry*; John Wiley & Sons: Hoboken, NJ, USA, 2006, pp 5–10.
- [97] Leng, Y. *Materials characterization: introduction to microscopic and spectroscopic methods*; Wiley-VCH: Weinheim, Germany, 2013.
- [98] Kokil, A.; Yang, K.; Kumar, J. Techniques for characterization of charge carrier mobility in organic semiconductors. *J. Polym. Sci., Part B: Polym. Phys.* **2012**, *50*, 1130–1144.
- [99] Singh, M.; Kaur, N.; Comini, E. The role of self-assembled monolayers in electronic devices. *J. Mater. Chem. C* **2020**, *8*, 3938–3955.
- [100] Feriancová, L.; Kmentová, I.; Micjan, M.; Pavúk, M.; Weis, M.; Putala, M. Synthesis and effect of the structure of bithienyl-terminated surfactants for dielectric layer modification in organic transistor. *Materials* **2021**, *14*, 6345.
- [101] Lee, H. S.; Kim, D. H.; Cho, J. H.; Hwang, M.; Jang, Y.; Cho, K. Effect of the phase states of self-assembled monolayers on pentacene growth and thin-film transistor characteristics. *J. Am. Chem. Soc.* **2008**, *130*, 10556–10564.
- [102] Hasan, M. M.; Islam, M. M.; Li, X.; He, M.; Manley, R.; Chang, J.; Zhelev, N.; Mehrotra, K.; Jang, J. Interface engineering with polystyrene for high-performance, low-voltage driven organic thin film transistor. *IEEE Trans. Electron Devices* **2020**, *67*, 1751–1756.
- [103] Torsi, L.; Magliulo, M.; Manoli, K.; Palazzo, G. Organic field-effect transistor sensors: a tutorial review. *Chem. Soc. Rev.* **2013**, *42*, 8612–8628.
- [104] Choi, H. H.; Cho, K.; Frisbie, C. D.; Sirringhaus, H.; Podzorov, V. Critical assessment of charge mobility extraction in FETs. *Nat. Mater.* **2018**, *17*, 2–7.
- [105] McCulloch, I.; Salleo, A.; Chabinyk, M. Avoid the kinks when measuring mobility. *Science* **2016**, *352*, 1521–1522.
- [106] Minaev, B.; Baryshnikov, G.; Agren, H. Principles of phosphorescent organic light emitting devices. *Phys. Chem. Chem. Phys.* **2014**, *16*, 1719–1758.
- [107] Adachi, C.; Sandanayaka, A. S. D. The leap from organic light-emitting diodes to organic semiconductor laser diodes. *CCS Chem.* **2020**, *2*, 1203–1216.
- [108] Nehate, S. D.; Prakash, A.; Mani, P. D.; Sundaram, K. B. Work function extraction of indium tin oxide films from MOSFET devices. *ECS J. Solid State Sci. Technol.* **2018**, *7*, 87–90.
- [109] Zhu, X.-H.; Peng, J.; Cao, Y.; Roncali, J. Solution-processable single-material molecular emitters for organic light-emitting devices. *Chem. Soc. Rev.* **2011**, *40*, 3509–3524.
- [110] Baldo, M. A.; Forrest, S. R.; Thompson, M. E. In *Organic electroluminescence*; Kafafi, Z. H., Ed.; Taylor & Francis Group: Boca Raton, FL, USA, 2005; pp 267–305.
- [111] Zhang, T.; He, S.-J.; Wang, D.-K.; Jiang, N.; Lu, Z.-H. A multi-zoned white organic light-emitting diode with high CRI and low color temperature. *Sci. Rep.* **2016**, *6*, 20517.
- [112] McCamy, C. S. Correlated color temperature as an explicit function of chromaticity coordinates. *Color Res. Appl.* **1992**, *17*, 142–144.
- [113] Massa, W. *Crystal structure determination*, 2nd ed.; Springer: Germany, 2004, pp 1–26.
- [114] Leng, Y. *Materials characterization: introduction to microscopic and spectroscopic methods*; Wiley-VCH: Weinheim, Germany, 2013, pp 45–77.
- [115] Wen, Y.; Liu, Y.; Guo, Y.; Yu, G.; Hu, W. Experimental techniques for the fabrication and characterization of organic thin films for field-effect transistors. *Chem. Rev.* **2011**, *111*, 3358–3406.

- [116] Rychkov, D. A.; Arkhipov, S. G.; Boldyreva, E. V. Simple and efficient modifications of well known techniques for reliable growth of high-quality crystals of small bioorganic molecules. *J. Appl. Cryst.* **2014**, *47*, 1435–1442.
- [117] Meden, A.; Radosavljevic Evans, I. Structure determination from powder diffraction data: past, present and future challenges. *Cryst. Res. Technol.* **2015**, *50*, 747–758.
- [118] Černý, R. Crystal structures from powder diffraction: principles, difficulties and progress. *Crystals* **2017**, *7*, 142.
- [119] Bergese, P.; Bontempi, E.; Colombo, I.; Depero, L. E. Micro X-ray diffraction on capillary powder samples: a novel and effective technique for overcoming preferred orientation. *J. Appl. Cryst.* **2001**, *34*, 663–665.
- [120] Desiraju, G. R.; Gavezzotti, A. Crystal structures of polynuclear aromatic hydrocarbons. Classification, rationalization and prediction from molecular structure. *Acta Cryst.* **1989**, *B45*, 473–482.
- [121] Campbell, J. E.; Yang, J.; Day, G. M. Predicted energy–structure–function maps for the evaluation of small molecule organic semiconductors. *J. Mater. Chem. C* **2017**, *5*, 7574–7584.
- [122] Reig Canyelles, M. *Carbazole-based materials for organic thin-film transistors and organic light-emitting diodes*. PhD Thesis, University of Barcelona, Barcelona, 2017.
- [123] Cuadrado Santolaria, A. *Semiconductores orgánicos derivados del carbazol y su aplicación en dispositivos electrónicos*. PhD Thesis, University of Barcelona, Barcelona, 2019.
- [124] Reig, M.; Puigdollers, J.; Velasco, D. Molecular order of air-stable p-type organic thin-film transistors by tuning the extension of the π -conjugated core: The cases of indolo[3,2-*b*]carbazole and triindole semiconductors. *J. Mater. Chem. C* **2015**, *3*, 506–513.
- [125] Reig, M.; Bagdziunas, G.; Ramanavicius, A.; Puigdollers, J.; Velasco, D. Interface engineering and solid-state organization for triindole-based p-type organic thin-film transistors. *Phys. Chem. Chem. Phys.* **2018**, *20*, 17889–17898.
- [126] Cuadrado, A.; Cuesta, J.; Puigdollers, J.; Velasco, D. Air stable organic semiconductors based on diindolo[3,2-*a*:3',2'-*c*]carbazole. *Org. Electron.* **2018**, *62*, 35–42.
- [127] Cai, Z.; Awais, M. A.; Zhang, N.; Yu, L. Exploration of syntheses and functions of higher ladder-type π -conjugated heteroarenes. *Chem* **2018**, *4*, 2538–2570.
- [128] Chen, J.; Yang, K.; Zhou, X.; Guo, X. Ladder-type heteroarene-based organic semiconductors. *Chem. Asian J.* **2018**, *13*, 2587–2600.
- [129] Bouchard, J.; Wakim, S.; Leclerc, M. Synthesis of diindolocarbazoles by Cadogan reaction: route to ladder oligo(*p*-aniline)s. *J. Org. Chem.* **2004**, *69*, 5705–5711.
- [130] Wakim, S.; Bouchard, J.; Blouin, N.; Michaud, A.; Leclerc, M. Synthesis of diindolocarbazoles by Ullmann reaction: a rapid route to ladder oligo(*p*-aniline)s. *Org. Lett.* **2004**, *6*, 3413–3416.
- [131] Blouin, N.; Michaud, A.; Wakim, S.; Boudreault, P.-L. T.; Leclerc, M.; Vercelli, B.; Zecchin, S.; Zotti, G. Optical, electrochemical, magnetic, and conductive properties of new polyindolocarbazoles and polydiindolocarbazoles. *Macromol. Chem. Phys.* **2006**, *207*, 166–174.
- [132] Kawano, S.; Kato, M.; Soumiya, S.; Nakaya, M.; Onoe, J.; Tanaka, K. Columnar liquid crystals from a giant macrocycle mesogen. *Angew. Chem., Int. Ed.* **2018**, *57*, 167–171.

- [133] Srour, H.; Doan, T.-H.; Da Silva, E.; Whitby, R. J.; Witulski, B. Synthesis and molecular properties of methoxysubstituted diindolo[3,2-*b*:2',3'-*h*]carbazoles for organic electronics obtained by a consecutive twofold Suzuki and twofold Cadogan reaction. *J. Mater. Chem. C* **2016**, *4*, 6270–6279.
- [134] Müllen, K.; Dierschke, F.; Grimsdale, A. C. Efficient synthesis of 2,7-dibromocarbazoles as components for electroactive materials. *Synthesis* **2003**, *2003*, 2470–2472.
- [135] Freeman, A. W.; Urvoy, M.; Criswell, M. E. Triphenylphosphine-mediated reductive cyclization of 2-nitrobiphenyls: a practical and convenient synthesis of carbazoles. *J. Org. Chem.* **2005**, *70*, 5014–5019.
- [136] Miyaura, N.; Suzuki, A. Palladium-catalyzed cross-coupling reactions of organoboron compounds. *Chem. Rev.* **1995**, *95*, 2457–2483.
- [137] Schmidt, A. W.; Reddy, K. R.; Knölker, H.-J. Occurrence, biogenesis, and synthesis of biologically active carbazole alkaloids. *Chem. Rev.* **2012**, *112*, 3193–3328.
- [138] Shaya, J.; Deschamps, M.-A.; Michel, B. Y.; Burger, A. Air-stable Pd catalytic systems for sequential one-pot synthesis of challenging unsymmetrical aminoaromatics. *J. Org. Chem.* **2016**, *81*, 7566–7573.
- [139] Sasabe, H.; Hayasaka, Y.; Komatsu, R.; Nakao, K.; Kido, J. Highly luminescent π -conjugated terpyridine derivatives exhibiting thermally activated delayed fluorescence. *Chem. Eur. J.* **2017**, *23*, 114–119.
- [140] Nguyen, W. H.; Bailie, C. D.; Burschka, J.; Moehl, T.; Grätzel, M.; McGehee, M. D.; Sellinger, A. Molecular engineering of organic dyes for improved recombination lifetime in solid-state dye-sensitized solar cells. *Chem. Mater.* **2013**, *25*, 1519–1525.
- [141] Bagdžiūnas, G.; Grybauskaitė, G.; Kostiv, N.; Ivaniuk, K.; Volyniuk, D.; Lazauskas, A. Green and red phosphorescent organic light-emitting diodes with ambipolar hosts based on phenothiazine and carbazole moieties: photoelectrical properties, morphology and efficiency. *RSC Adv.* **2016**, *6*, 61544–61554.
- [142] Coeffard, V.; Müller-Bunz, H.; Guiry, P. J. The synthesis of new oxazoline-containing bifunctional catalysts and their application in the addition of diethylzinc to aldehydes. *Org. Biomol. Chem.* **2009**, *7*, 1723–1734.
- [143] Liégault, B.; Lee, D.; Huestis, M. P.; Stuart, D. R.; Fagnou, K. Intramolecular Pd(II)-catalyzed oxidative biaryl synthesis under air: reaction development and scope. *J. Org. Chem.* **2008**, *73*, 5022–5028.
- [144] Watanabe, T.; Oishi, S.; Fujii, N.; Ohno, H. Palladium-catalyzed direct synthesis of carbazoles via one-pot *N*-arylation and oxidative biaryl coupling: synthesis and mechanistic study. *J. Org. Chem.* **2009**, *74*, 4720–4726.
- [145] Sridharan, V.; Martín, M. A.; Menéndez, J. C. Acid-free synthesis of carbazoles and carbazolequinones by intramolecular Pd-catalyzed, microwave-assisted oxidative biaryl coupling reactions – efficient syntheses of murrayafoline A, 2-methoxy-3-methylcarbazole, and glycozolidine. *Eur. J. Org. Chem.* **2009**, *2009*, 4614–4621.
- [146] Yang, C.; Lin, K.; Huang, L.; Pan, W.-D.; Liu, S. Facile synthesis of indolo[3,2-*a*]carbazoles via Pd-catalyzed twofold oxidative cyclization. *Beilstein J. Org. Chem.* **2016**, *12*, 2490–2494.
- [147] Janosik, T.; Rannug, A.; Rannug, U.; Wahlström, N.; Slätt, J.; Bergman, J. Chemistry and properties of indolocarbazoles. *Chem. Rev.* **2018**, *118*, 9058–9128.

- [148] Lee, S.-C.; Heo, J.; Woo, H. C.; Lee, J.-A.; Seo, Y. H.; Lee, C.-L.; Kim, S.; Kwon, O.-P. Fluorescent molecular rotors for viscosity sensors. *Chem. Eur. J.* **2018**, *24*, 13706–13718.
- [149] Xia, T.; Wang, L.; Qu, Y.; Rui, Y.; Cao, J.; Hu, Y.; Yang, J.; Wu, J.; Xu, J. A thermoresponsive fluorescent rotor based on a hinged naphthalimide for a viscometer and a viscosity-related thermometer. *J. Mater. Chem. C* **2016**, *4*, 5696–5701.
- [150] Jiang, W.; Li, Y.; Wang, Z. Heteroarenes as high performance organic semiconductors. *Chem. Soc. Rev.* **2013**, *42*, 6113–6127.
- [151] Reig, M.; Puigdollers, J.; Velasco, D. Solid-state organization of n-type carbazole-based semiconductors for organic thin-film transistors. *Phys. Chem. Chem. Phys.* **2017**, *20*, 1142–1149.
- [152] Campbell, R. B.; Robertson, J. M.; Trotter, J. The crystal structure of hexacene, and a revision of the crystallographic data for tetracene and pentacene. *Acta Cryst.* **1962**, *15*, 289–290.
- [153] Yao, Z.-F.; Wang, J.-Y.; Pei, J. Control of π - π stacking via crystal engineering in organic conjugated small molecule crystals. *Cryst. Growth Des.* **2018**, *18*, 7–15.
- [154] Sirringhaus, H. 25th anniversary article: organic field-effect transistors: the path beyond amorphous silicon. *Adv. Mater.* **2014**, *26*, 1319–1335.
- [155] Takimiya, K.; Shinamura, S.; Osaka, I.; Miyazaki, E. Thienoacene-based organic semiconductors. *Adv. Mater.* **2011**, *23*, 4347–4370.
- [156] Okamoto, T. Next-generation organic semiconductors driven by bent-shaped π -electron cores. *Polym. J.* **2019**, *51*, 825–833.
- [157] Sugiyama, M.; Jancke, J.; Uemura, T.; Kondo, M.; Inoue, Y.; Namba, N.; Araki, T.; Fukushima, T.; Sekitani, T. Mobility enhancement of DNTT and BTBT derivative organic thin-film transistors by triptycene molecule modification. *Org. Electron.* **2021**, *96*, 106219.
- [158] Takimiya, K.; Osaka, I.; Mori, T.; Nakano, M. Organic semiconductors based on [1]benzothieno[3,2-*b*][1]benzothiophene substructure. *Acc. Chem. Res.* **2014**, *47*, 1493–1502.
- [159] Minemawari, H.; Yamada, T.; Matsui, H.; Tsutsumi, J.; Haas, S.; Chiba, R.; Kumai, R.; Hasegawa, T. Inkjet printing of single-crystal films. *Nature* **2011**, *475*, 364–367.
- [160] Babuji, A.; Temiño, I.; Perez-Rodríguez, A.; Solomeshch, O.; Tessler, N.; Vila, M.; Li, J.; Mas-Torrent, M.; Ocal, C.; Barrena, E. Double beneficial role of fluorinated fullerene dopants on organic thin-film transistors: structural stability and improved performance. *ACS Appl. Mater. Interfaces* **2020**, *12*, 28416–28425.
- [161] Kang, M. J.; Doi, I.; Mori, H.; Miyazaki, E.; Takimiya, K.; Ikeda, M.; Kuwabara, H. Alkylated dinaphtho[2,3-*b*:2',3'-*f*]thieno[3,2-*b*]thiophenes (C_n -DNTTs): organic semiconductors for high-performance thin-film transistors. *Adv. Mater.* **2011**, *23*, 1222–1225.
- [162] Borchert, J. W.; Peng, B.; Letzkus, F.; Burghartz, J. N.; Chan, P. K. L.; Zojer, K.; Ludwigs, S.; Klauk, H. Small contact resistance and high-frequency operation of flexible low-voltage inverted coplanar organic transistors. *Nat. Commun.* **2019**, *10*, 1119.
- [163] Peng, B.; Cao, K.; Lau, A. H. Y.; Chen, M.; Lu, Y.; Chan, P. K. L. Crystallized monolayer semiconductor for ohmic contact resistance, high intrinsic gain, and high current density. *Adv. Mater.* **2020**, *32*, 2002281.
- [164] Zschieschang, U.; Ante, F.; Yamamoto, T.; Takimiya, K.; Kuwabara, H.; Ikeda, M.; Sekitani, T.; Someya, T.; Kern, K.; Klauk, H. Flexible low-voltage organic transistors and circuits based

- on a high-mobility organic semiconductor with good air stability. *Adv. Mater.* **2010**, *22*, 982–985.
- [165] Gao, P.; Feng, X.; Yang, X.; Enkelmann, V.; Baumgarten, M.; Müllen, K. Conjugated ladder-type heteroacenes bearing pyrrole and thiophene ring units: facile synthesis and characterization. *J. Org. Chem.* **2008**, *73*, 9207–9213.
- [166] Gao, P.; Cho, D.; Yang, X.; Enkelmann, V.; Baumgarten, M.; Müllen, K. Heteroheptacenes with fused thiophene and pyrrole rings. *Chem. A Eur. J.* **2010**, *16*, 5119–5128.
- [167] Ding, F.; Xia, D.; Sun, W.; Chen, W.; Yang, Y.; Lin, K.; Zhang, F.; Guo, X. Sulfur-containing bent N-heteroacenes. *Chem. A Eur. J.* **2019**, *25*, 15106–15111.
- [168] Sun, T.; Xia, L.; Huang, J.; Gu, Y.; Wang, P. A highly sensitive fluorescent probe for fast recognition of DTT and its application in one- and two-photon imaging. *Talanta* **2018**, *187*, 295–301.
- [169] Zhang, L.; Peng, S.; Sun, J.; Yao, J.; Kang, J.; Hu, Y.; Fang, J. A specific fluorescent probe reveals compromised activity of methionine sulfoxide reductases in Parkinson's disease. *Chem. Sci.* **2017**, *8*, 2966–2972.
- [170] Zhang, Q.; Li, B.; Huang, S.; Nomura, H.; Tanaka, H.; Adachi, C. Efficient blue organic light-emitting diodes employing thermally activated delayed fluorescence. *Nat. Photonics* **2014**, *8*, 326–332.
- [171] Jankus, V.; Data, P.; Graves, D.; McGuinness, C.; Santos, J.; Bryce, M. R.; Dias, F. B.; Monkman, A. P. Highly efficient TADF OLEDs: how the emitter–host interaction controls both the excited state species and electrical properties of the devices to achieve near 100% triplet harvesting and high efficiency. *Adv. Funct. Mater.* **2014**, *24*, 6178–6186.
- [172] Wang, J.; Yang, Y.; Jiang, C.; He, M.; Yao, C.; Zhang, J. Ultrapure deep-blue aggregation-induced emission and thermally activated delayed fluorescence emitters for efficient OLEDs with CIE_y < 0.1 and low efficiency roll-offs. *J. Mater. Chem. C* **2022**, *10*, 3163–3171.
- [173] Wong, M. Y.; Zysman-Colman, E. Purely organic thermally activated delayed fluorescence materials for organic light-emitting diodes. *Adv. Mater.* **2017**, *29*, 1605444.
- [174] Jürgensen, N.; Kretzschmar, A.; Höfle, S.; Freudenberg, J.; Bunz, U. H. F.; Hernandez-Sosa, G. Sulfone-based deep blue thermally activated delayed fluorescence emitters: solution-processed organic light-emitting diodes with high efficiency and brightness. *Chem. Mater.* **2017**, *29*, 9154–9161.
- [175] Zhang, X.; Chen, J.-X.; Wang, K.; Shi, Y.-Z.; Fan, X.-C.; Zhang, S.-L.; Wu, L.; Li, Y.-Q.; Ou, X.-M.; Zhang, X.-H. Charge-transfer transition regulation of thermally activated delayed fluorescence emitters by changing the valence of sulfur atoms. *J. Mater. Chem. C* **2020**, *8*, 17457.
- [176] Yang, S.-Y.; Tian, Q.-S.; Yu, Y.-J.; Zou, S.-N.; Li, H.-C.; Khan, A.; Wu, Q.-H.; Jiang, Z.-Q.; Liao, L.-S. Sky-blue thermally activated delayed fluorescence with intramolecular spatial charge transfer based on a dibenzothiophene sulfone emitter. *J. Org. Chem.* **2020**, *85*, 10628–10637.
- [177] Cao, L.; Zhang, L.; Wei, Q.; Zhang, J.; Chen, D.; Wang, S.; Su, S.; Wang, T.; Ge, Z. Bipolar fluorophores based on intramolecular charge-transfer moieties of sulfone for nondoped deep blue solution-processed organic light-emitting diodes. *Dyes Pigm.* **2020**, *176*, 108242.

- [178] Wu, J.; Yin, J.; Chen, S.; Xiao, H.; Yan, B.; Yang, Q. Synthesis, aggregation-induced emission properties and mechanofluorochromic behavior of sulfur connected bis(tetraphenylethene) luminogens. *Dyes Pigm.* **2021**, *186*, 108978.
- [179] Kerr, W. J.; Knox, G. J.; Reid, M.; Tuttle, T.; Bergare, J.; Bragg, R. A. Computationally-guided development of a chelated NHC-P iridium(III) complex for the directed hydrogen isotope exchange of aryl sulfones. *ACS Catal.* **2020**, *10*, 11120–11126.
- [180] Wang, F.; Rao, W.; Wang, S.-Y. Nickel-catalyzed reductive thiolation of unactivated alkyl bromides and arenesulfonyl cyanides. *J. Org. Chem.* **2021**, *86*, 8970–8979.
- [181] Lee, W.; Jenks, W. S. Photophysics and photostereomutation of aryl methyl sulfoxides. *J. Org. Chem.* **2001**, *66*, 474–480.
- [182] Yoshida, T.; Moriyama, Y.; Nakano, S. Fluorescence properties of 2-substituted 6-, 7- or 8-methoxyquinoline-4-carboxylic acid derivatives. *Chem. Pharm. Bull.* **1992**, *40*, 1322–1324.
- [183] Wang, C.; Chi, W.; Qiao, Q.; Tan, D.; Xu, Z.; Liu, X. Twisted intramolecular charge transfer (TICT) and twists beyond TICT: from mechanisms to rational designs of bright and sensitive fluorophores. *Chem. Soc. Rev.* **2021**, *50*, 12656–12678.
- [184] Sasaki, S.; Drummen, G. P. C.; Konishi, G. Recent advances in twisted intramolecular charge transfer (TICT) fluorescence and related phenomena in materials chemistry. *J. Mater. Chem. C* **2016**, *4*, 2731–2743.
- [185] Mancuso, A. J.; Swern, D. Activated dimethyl sulfoxide: useful reagents for synthesis. *Synthesis* **1981**, *1981*, 165–185.
- [186] Mai, J.; Tang, N.; He, W.; Zou, Z.; Luo, C.; Zhang, A.; Fan, Z.; Wu, S.; Zeng, M.; Gao, J.; Zhou, G.; Lu, X.; Liu, J.-M. Effects of ambient gases on the electrical performance of solution-processed c8-btbt thin-film transistors. *Nanoscale Res. Lett.* **2019**, *14*, 169.
- [187] Xie, P.; Liu, T.; He, P.; Dai, G.; Jiang, J.; Sun, J.; Yang, J. The effect of air exposure on device performance of flexible C8-BTBT organic thin-film transistors with hygroscopic insulators. *Sci. China Mater.* **2020**, *63*, 2551–2559.
- [188] Raouafi, S.; Aloui, F.; Raouafi, A.; Hassine, B. B. Synthesis and characterization of phenanthrene derivatives for optoelectronic applications. *C. R. Chim.* **2017**, *20*, 697–703.
- [189] Wang, Y.; Fang, D.; Fu, T.; Ali, M. U.; Shi, Y.; He, Y.; Hu, Z.; Yan, C.; Mei, Z.; Meng, H. Anthracene derivative based multifunctional liquid crystal materials for optoelectronic devices. *Mater. Chem. Front.* **2020**, *4*, 3546–3555.
- [190] Baviera, G. S.; Donate, P. M. Recent advances in the syntheses of anthracene derivatives. *Beilstein J. Org. Chem.* **2021**, *17*, 2028–2050.
- [191] Wang, C.; Dong, H.; Hu, W.; Liu, Y.; Zhu, D. Semiconducting π -conjugated systems in field-effect transistors: a material odyssey of organic electronics. *Chem. Rev.* **2012**, *112*, 2208–2267.
- [192] Kim, H.; Schulte, N.; Zhou, G.; Müllen, K.; Laquai, F. A high gain and high charge carrier mobility indenofluorene-phenanthrene copolymer for light amplification and organic lasing. *Adv. Mater.* **2011**, *23*, 894–897.
- [193] Chen, M.; Yan, L.; Zhao, Y.; Murtaza, I.; Meng, H.; Huang, W. Anthracene-based semiconductors for organic field-effect transistors. *J. Mater. Chem. C* **2018**, *6*, 7416–7444.

- [194] Tian, H.; Shi, J.; Dong, S.; Yan, D.; Wang, L.; Geng, Y.; Wang, F. Novel highly stable semiconductors based on phenanthrene for organic field-effect transistors. *Chem. Commun.* **2006**, 3498–3500.
- [195] Jassas, R. S.; Mughal, E. U.; Sadiq, A.; Alsantali, R. I.; Al-Rooqi, M. M.; Naeem, N.; Moussa, Z.; Ahmed, S. A. Scholl reaction as a powerful tool for the synthesis of nanographenes: a systematic review. *RSC Adv.* **2021**, *11*, 32158–32202.
- [196] Grzybowski, M.; Skonieczny, K.; Butenschön, H.; Gryko, D. T. Comparison of oxidative aromatic coupling and the Scholl reaction. *Angew. Chem., Int. Ed.* **2013**, *52*, 9900–9930.
- [197] Quernheim, M.; Golling, F. E.; Zhang, W.; Wagner, M.; Räder, H.-J.; Nishiuchi, T.; Müllen, K. The precise synthesis of phenylene-extended cyclic hexa-*peri*-hexabenzocoronenes from polyarylated [*n*]cycloparaphenylenes by the Scholl reaction. *Angew. Chem. Int. Ed.* **2015**, *54*, 10341–10346.
- [198] García-Frutos, E. M.; Omenat, A.; Barbera, J.; Serrano, J. L.; Gómez-Lor, B. Highly ordered π -extended discotic liquid-crystalline triindoles. *J. Mater. Chem.* **2011**, *21*, 6831–6836.
- [199] Ponugoti, N.; Parthasarathy, V. Rearrangements in Scholl reaction. *Chem. Eur. J.* **2022**, *28*, e202103530.
- [200] Maeda, C.; Nagahata, K.; Shirakawa, T.; Ema, T. Azahelicene-fused BODIPY analogues showing circularly polarized luminescence. *Angew. Chem. Int. Ed.* **2020**, *59*, 7813–7817.
- [201] Kumar, S.; Tao, Y.-T. Synthesis of polyarylated carbazoles: discovery toward soluble phenanthro- and tetraceno-fused carbazole derivatives. *J. Org. Chem.* **2015**, *80*, 5066–5076.
- [202] Wang, J.; Xu, H.; Li, B.; Cao, X.-P.; Zhang, H.-L. Synthesis and characterization of new planar butterfly-shaped fused oligothiophenes. *Tetrahedron* **2012**, *68*, 1192–1197.
- [203] Ding, Z.; Abbas, G.; Assender, H. E.; Morrison, J. J.; Yeates, S. G.; Patchett, E. R.; Taylor, D. M. Effect of oxygen, moisture and illumination on the stability and reliability of dinaphtho[2,3-*b*:2',3'-*f*]thieno[3,2-*b*]thiophene (DNTT) OTFTs during operation and storage. *ACS Appl. Mater. Interfaces* **2014**, *6*, 15224–15231.
- [204] Chiarella, F.; Chianese, F.; Barra, M.; Parlato, L.; Toccoli, T.; Cassinese, A. Spontaneous wetting dynamics in perylene diimide n-type thin films deposited at room temperature by supersonic molecular beam. *J. Phys. Chem. C* **2016**, *120*, 26076–26082.
- [205] Venkateswarlu, S.; Prakoso, S. P.; Kumar, S.; Kuo, M.-Y.; Tao, Y.-T. Benzophenanthrothiophenes: syntheses, crystal structures, and properties. *J. Org. Chem.* **2019**, *84*, 10990–10998.
- [206] Venkateswarlu, S.; Lin, Y.-D.; Lee, K.-M.; Liao, K.-L.; Tao, Y.-T. Thiophene-fused butterfly-shaped polycyclic arenes with a diphenanthro[9,10-*b*:9',10'-*d*]thiophene core for highly efficient and stable perovskite solar cells. *ACS Appl. Mater. Interfaces* **2020**, *12*, 50495–50504.
- [207] Zhao, K.-C.; Du, J.-Q.; Wang, H.-F.; Zhao, K.-Q.; Hu, P.; Wang, B.-Q.; Monobe, H.; Heinrich, B.; Donnio, B. Board-like fused-thiophene liquid crystals and their benzene analogs: facile synthesis, self-assembly, p-type semiconductivity, and photoluminescence. *Chem. Asian J.* **2019**, *14*, 462–470.
- [208] Luo, J.; Xie, Z.; Lam, J. W. Y.; Cheng, L.; Chen, H.; Qiu, C.; Kwok, H. S.; Zhan, X.; Liu, Y.; Zhuc, D.; Tang, B. Z. Aggregation-induced emission of 1-methyl-1,2,3,4,5-pentaphenylsilole. *Chem. Commun.* **2001**, 1740–1741.

- [209] Nie, H.; Hu, K.; Cai, Y.; Peng, Q.; Zhao, Z.; Hu, R.; Chen, J.; Su, S.-J.; Qin, A.; Tang, B. Z. Tetraphenylfuran: aggregation-induced emission or aggregation-caused quenching? *Mater. Chem. Front.* **2017**, *1*, 1125–1129.
- [210] Stojanović, L.; Crespo-Otero, R. Aggregation-induced emission in the tetraphenylthiophene crystal: the role of triplet states. *J. Phys. Chem. C* **2020**, *124*, 17752–17761.
- [211] Gu, Y.; Li, N.; Shao, G.; Wang, K.; Zou, B. Mechanism of different piezoresponsive luminescence of 2,3,4,5-tetraphenylthiophene and 2,3,4,5-tetraphenylfuran: a strategy for designing pressure-induced emission enhancement materials. *J. Phys. Chem. Lett.* **2020**, *11*, 678–682.
- [212] Peng, X.-L.; Ruiz-Barragan, S.; Li, Z.-S.; Li, Q.-S.; Blancafort, L. Restricted access to a conical intersection to explain aggregation induced emission in dimethyl tetraphenylsilole. *J. Mater. Chem. C* **2016**, *4*, 2802–2810.
- [213] Stojanović, L.; Crespo-Otero, R. Understanding aggregation induced emission in a propeller-shaped blue emitter. *ChemPhotoChem* **2019**, *3*, 907–915.
- [214] Zeng, Q.; Li, Z.; Dong, Y.; Di, C.; Qin, A.; Hong, Y.; Ji, L.; Zhu, Z.; Jim, C. K. W.; Yu, G.; Li, Q.; Li, Z.; Liu, Y.; Qin A. J.; Tang, B. Z. Fluorescence enhancements of benzene-cored luminophors by restricted intramolecular rotations: AIE and AIEE effects. *Chem. Commun.* **2007**, 70–72.
- [215] Feng, X.; Tong, B.; Shen, J.; Shi, J. B.; Han, T.; Chen, L.; Zhi, J.; Lu, P.; Ma, Y.; Dong, Y. Aggregation-induced emission enhancement of aryl-substituted pyrrole derivatives. *J. Phys. Chem. B* **2010**, *114*, 16731–16736.
- [216] Yu, G.; Yin, S.; Liu, Y.; Chen, J.; Xu, X.; Sun, X.; Ma, D.; Zhan, X.; Peng, Q.; Shuai, Z.; Tang, B. Z.; Zhu, D.; Fang, W.; Luo, Y. Structures, electronic states, photoluminescence, and carrier transport properties of 1,1-disubstituted 2,3,4,5-tetraphenylsiloles. *J. Am. Chem. Soc.* **2005**, *127*, 6335–6346.
- [217] Bu, F.; Wang, E.; Peng, Q.; Hu, R.; Qin, A.; Zhao, Z.; Tang, B. Z. Structural and theoretical insights into the AIE attributes of phosphindole oxide: the balance between rigidity and flexibility. *Chem. Eur. J.* **2015**, *21*, 4440–4449.
- [218] Guo, L.-X.; Xing, Y.-B.; Wang, M.; Sun, Y.; Zhang, X.-Q.; Lin, B.-P.; Yang, H. Luminescent liquid crystals bearing an aggregation-induced emission active tetraphenylthiophene fluorophore. *J. Mater. Chem. C* **2019**, *7*, 4828–4837.
- [219] Niu, G.; Zheng, X.; Zhao, Z.; Zhang, H.; Wang, J.; He, X.; Chen, Y.; Shi, X.; Ma, C.; Kwok, R. T. K.; Lam, J. W. Y.; Sung, H. H. Y.; Williams, I. D.; Wong, K. S.; Wang, P.; Tang, B. Z. Functionalized acrylonitriles with aggregation-induced emission: structure tuning by simple reaction-condition variation, efficient red emission, and two-photon bioimaging. *J. Am. Chem. Soc.* **2019**, *141*, 15111–15120.
- [220] Zhang, Y.-P.; Teng, Q.; Yang, Y.-S.; Cao, J.-Q.; Xue, J.-J. Aggregation-induced emission properties of triphenylamine chalcone compounds. *J. Fluoresc.* **2021**, *31*, 807–815.
- [221] Liu, L.; Ma, J.; Pan, J.; Li, D.; Wang, H.; Yang, H. The preparation of novel triphenylamine-based AIE-effect fluorescent probe for selectively detecting mercury(II) ion in aqueous solution. *New J. Chem.* **2021**, *45*, 5049–5059.
- [222] Đăng, T. T.; Đăng, T. T.; Rasool, N.; Villinger, A.; Reinke, H.; Fischer, C.; Langer, P. Regioselective palladium(0)-catalyzed cross-coupling reactions and metal-halide exchange reactions of tetrabromothiophene: optimization, scope and limitations. *Adv. Synth. Catal.* **2009**, *351*, 1595–1609.

- [223] Liu, X.; Wang, Y.; Gao, J.; Jiang, L.; Qi, X.; Hao, W.; Zou, S.; Zhang, H.; Li, H.; Hu, W. Easily solution-processed, high-performance microribbon transistors based on a 2D condensed benzothiophene derivative. *Chem. Commun.* **2014**, *50*, 442–444.
- [224] Wang, J.; Xu, H.; Li, B.; Cao, X.-P.; Zhang, H.-L. Synthesis and characterization of new planar butterfly-shaped fused oligothiophenes. *Tetrahedron*, **2012**, *68*, 1192–1197.
- [225] Urieta-Mora, J.; Zimmermann, I.; Aragón, J.; Molina-Ontoria, A.; Ortí, E.; Martín, N.; Nazeeruddin, M. K. Dibenzoquinethiophene- and dibenzosexithiophene-based hole-transporting materials for perovskite solar cells. *Chem. Mater.* **2019**, *31*, 6435–6442.
- [226] Xing, Y.; Xu, X.; Wang, F.; Lu, P. Optical properties of a series of tetraarylthiophenes. *Opt. Mater.* **2006**, *29*, 407–409.
- [227] Muraoka, H.; Tanifuji, T.; Ogawa, S. Systematic synthesis and characterization of a series of tetra(5-aryl-2-thienyl)thiophenes. *Chem. Lett.* **2011**, *40*, 964–966.
- [228] Sherwood, J.; Clark, J. H.; Fairlamb, I. J. S.; Slattery, J. M. Solvent effects in palladium catalyzed cross-coupling reactions. *Green Chem.* **2019**, *21*, 2164–2213.
- [229] Ahmadi, Z.; McIndoe, J. S. A mechanistic investigation of hydrodehalogenation using ESI-MS. *Chem. Commun.* **2013**, *49*, 11488–11490.
- [230] Handy, S. T.; Bregman, H.; Lewis, J.; Zhang, X.; Zhang, Y. An unusual dehalogenation in the Suzuki coupling of 4-bromopyrrole-2-carboxylates. *Tetrahedron Lett.* **2003**, *44*, 427–430.
- [231] Jedinák, L.; Zátopková, R.; Zemánková, H.; Šustková, A.; Cankař, P. The Suzuki-Miyaura cross-coupling reaction of halogenated aminopyrazoles: method development, scope, and mechanism of dehalogenation side reaction. *J. Org. Chem.* **2017**, *82*, 157–169.
- [232] Handy, S. T.; Mayi, D. Regioselective double Suzuki couplings of 4,5-dibromothiophene-2-carboxaldehyde. *Tetrahedron Lett.* **2007**, *48*, 8108–8110.
- [233] King, B. T.; Kroulík, J.; Robertson, C. R.; Rempala, P.; Hilton, C. L.; Korinek, J. D.; Gortari, L. M. Controlling the Scholl reaction. *J. Org. Chem.* **2007**, *72*, 2279–2288.
- [234] Maddala, S.; Panua, A.; Venkatakrishnan, P. Steering Scholl oxidative heterocoupling by tuning topology and electronics for building thiananographenes and their functional N-/C-congeners. *Chem. Eur. J.* **2021**, *27*, 16013–16020.
- [235] Liu, J.; Narita, A.; Osella, S.; Zhang, W.; Schollmeyer, D.; Beljonne, D.; Feng, X.; Müllen, K. Unexpected Scholl reaction of 6,7,13,14-tetraarylbenzo[k]tetraphene: selective formation of five-membered rings in polycyclic aromatic hydrocarbons. *J. Am. Chem. Soc.* **2016**, *138*, 2602–2608.
- [236] Nobusue, S.; Fujita, K.; Tobe, Y. Skeletal rearrangement of twisted polycyclic aromatic hydrocarbons under scholl reaction conditions. *Org. Lett.* **2017**, *19*, 3227–3230.
- [237] Ormsby, J. L.; Black, T. D.; Hilton, C. L.; Bharat; King, B. T. Rearrangements in the Scholl oxidation: implications for molecular architectures. *Tetrahedron* **2008**, *64*, 11370–11378.
- [238] Pradhan, A. *Distorted arenes by Scholl cyclizations, towards twisted carbon nanoribbons*. PhD Thesis, Université Sciences et Technologies, Bordeaux I, 2013.
- [239] Piotrowski, P.; Zarębska, K.; Skompska, M.; Kaim, A. Electrodeposition and properties of donor-acceptor double-cable polythiophene with high content of pendant fulleropyrrolidine moieties. *Electrochim. Acta* **2014**, *148*, 145–152.
- [240] Saini, K. M.; Saunthwal, R. K.; Verma, A. K. Pd-Catalyzed one-pot sequential cross-coupling reactions of tetrabromothiophene. *Org. Biomol. Chem.* **2017**, *15*, 10289–10298.

- [241] Tripathi, A.; Prabhakar, C. Optoelectronic and charge-transport properties of truxene, isotruxene, and its heteroatomic (N, O, Si, and S) analogs: A DFT study. *J. Phys. Org. Chem.* **2019**, *32*, e3944.
- [242] Yin, J.; Chaitanya, K.; Ju, X.-H. Theoretical design of benzo[1,2-b:3,4-b':5,6-b'']tristhianaphthene and its derivatives as high performance organic semiconductors. *J. Theor. Comput. Chem.* **2015**, *14*, 1550058.
- [243] Kaida, H.; Satoh, T.; Nishii, Y.; Hirano, K.; Miura, M. Synthesis of benzobis- and benzotrisbenzofurans by palladium-catalyzed multiple intramolecular C–H/C–H coupling. *Chem. Lett.* **2016**, *45*, 1069–1071.
- [244] Ogaki, T.; Ohta, E.; Oda, Y.; Sato, H.; Matsui, Y.; Kumeda, M.; Ikeda, H. Intramolecular triple cyclization strategy for sila- and oxa-analogues of truxene with long-lived phosphorescence. *Asian J. Org. Chem.* **2017**, *6*, 290–296.
- [245] Jeon, I.; Tan, L.; Baek, J. Self-Controlled Synthesis of Hyperbranched Poly(etherketone)s from A₂ + B₃ Approach in Poly(phosphoric acid). *J. Polym. Sci., Part A: Polym. Chem.* **2009**, *47*, 3326–3336.
- [246] Bergman, J.; Egestad, B. Cyclocondensation of 3(2H)-benzo[b]thiophenone and oxidation products obtained during these reactions. *Tetrahedron*, **1986**, *42*, 763–773.
- [247] Che, R.; Wu, Z.; Li, Z.; Xiang, H.; Zhou, X. Synthesis of dibenzothiophenes by pd-catalyzed dual C–h activation from diaryl sulfides. *Chem. Eur. J.* **2014**, *20*, 7258–7261.
- [248] Gao, P.; Beckmann, D.; Tsao, H. N.; Feng, X.; Enkelmann, V.; Pisulaz, W.; Müllen, K. Benzo[1,2-*b*:4,5-*b'*]bis[*b*]benzothiophene as solution processible organic semiconductor for field-effect transistors. *Chem. Commun.* **2008**, 1548–1550.
- [249] Kaida, H.; Satoh, T.; Hirano, K.; Miura, M. Synthesis of thieno[3,2-*b*]benzofurans by palladium-catalyzed intramolecular C–H/C–H coupling. *Chem. Lett.* **2015**, *44*, 1125–1127.
- [250] Zou, S.; Wang, Y.; Gao, J.; Liu, X.; Hao, W.; Zhang, H.; Zhang, H.; Xie, H.; Yang, C.; Li, H.; Hu, W. Synthesis, characterization, and field-effect transistor performance of a two-dimensional starphene containing sulfur. *J. Mater. Chem. C* **2014**, *2*, 10011.
- [251] Nakamura, S.; Okamoto, M.; Tohnai, N.; Nakayama, K.; Nishii, Y.; Miura, M. Synthesis and properties of tri-*tert*-butylated trioxa and trithia analogues of truxene. *Bull. Chem. Soc. Jpn.* **2020**, *93*, 99–108.
- [252] Hasegawa, J.; Hamada, M.; Miyamoto, T.; Nishide, K.; Kajimoto, T.; Uenishi, J.; Node, M. The application of phenylmethanethiol and benzenethiol derivatives as odorless organosulfur reagents in the synthesis of thiosugars and thioglycosides. *Carbohydr. Res.*, **2005**, *340*, 2360–2368.
- [253] Madumo, G. K.; Moshapo, P. T.; Kiefe, H. H. Effects of lipophilicity, protecting group and stereochemistry on the antimalarial activity of carbohydrate-derived thiochromans. *Med. Chem. Res.* **2018**, *27*, 817–833.
- [254] Fujimori, K.; Togo, H.; Oae, S. Iodine catalyzed reduction of arenesulfonic acid to the arenethiol with triphenylphosphine. *Tetrahedron Lett.* **1980**, *21*, 4921–4924.
- [255] Oae, S.; Togo, H. Reduction of sulfonic acids and related organosulfur compounds with triphenylphosphine–iodine system. *Bull. Chem. Soc. Jpn.* **1983**, *56*, 3802–3812.
- [256] Liu, D.; Tian, W.; Feng, Y.; Zhang, X.; Ban, X.; Jiang, W.; Sun, Y. Achieving 20% external quantum efficiency for fully solution-processed organic light-emitting diodes based on

- thermally activated delayed fluorescence dendrimers with flexible chains. *ACS Appl. Mater. Interfaces* **2019**, *11*, 16737–16748.
- [257] Zheng, X.; Liu, Y.; Zhu, Y.; Ma, F.; Feng, C.; Yu, Y.; Hu, H.; Li, F. Efficient inkjet-printed blue OLED with boosted charge transport using host doping for application in pixelated display. *Opt. Mater.* **2020**, *101*, 109755.
- [258] Aizawa, N.; Pu, Y.-J.; Watanabe, M.; Chiba, T.; Ideta, K.; Toyota, N.; Igarashi, M.; Suzuri, Y.; Sasabe, H.; Kido, J. Solution-processed multilayer small-molecule light-emitting devices with high-efficiency white-light emission. *Nat. Commun.* **2014**, *5*, 5756.
- [259] Lin, S.-L.; Chan, L.-H.; Lee, R.-H.; Yen, M.-Y.; Kuo, W.-J.; Chen, C.-T.; Jeng, R.-J. Highly efficient carbazole- π -dimesitylborane bipolar fluorophores for nondoped blue organic light-emitting diodes. *Adv. Mater.* **2008**, *20*, 3947–3952.
- [260] Yu, M.; Wang, S.; Shao, S.; Ding, J.; Wang, L.; Jing, X.; Wang, F. Starburst 4,4',4''-tris(carbazol-9-yl)-triphenylamine-based deep-blue fluorescent emitters with tunable oligophenyl length for solution-processed undoped organic light emitting diodes. *J. Mater. Chem. C* **2015**, *3*, 861–869.
- [261] Jou, J.-H.; Li, J.-L.; Sahoo, S.; Dubey, D. K.; Yadav, R. A. K.; Joseph, V.; Thomas, K. R. J.; Wang, C.-W.; Jayakumar, J.; Cheng, C.-H. Enabling a 6.5% external quantum efficiency deep-blue organic light-emitting diode with a solution-processable carbazole-based emitter. *J. Phys. Chem. C* **2018**, *122*, 24295–24303.
- [262] Kato, S.; Noguchi, H.; Kobayashi, A.; Yoshihara, T.; Tobita, S.; Nakamura, Y. Bicarbazoles: systematic structure-property investigations on a series of conjugated carbazole dimers. *J. Org. Chem.* **2012**, *77*, 9120–9133.
- [263] Zhao, B.; Jia, X.; Liu, J.; Ma, X.; Zhang, H.; Wang, X.; Wang, T. Synthesis and characterization of novel 1,4-bis(carbazolyl)benzene derivatives with blue-violet two-photon-excited fluorescence. *Ind. Eng. Chem. Res.* **2016**, *55*, 1801–1807.
- [264] Slodek, A.; Filapek, M.; Schab-Balcerzak, E.; Grucela, M.; Kotowicz, S.; Janeczek, H.; Smolarek, K.; Mackowski, S.; Malecki, J. G.; Jedrzejowska, A.; Szafraniec-Gorol, G.; Chrobok, A.; Marcol, B.; Krompiec, S.; Matussek, M. Highly luminescence anthracene derivatives as promising materials for OLED applications. *Eur. J. Org. Chem.* **2016**, *23*, 4020–4031.
- [265] Reig, M.; Gozálvez, C.; Bujaldon, R.; Bagdziunas, G.; Ivaniuk, K.; Kostiv, N.; Volyniuk, D.; Grazulevicius, J. V.; Velasco, D. Easy accessible blue luminescent carbazole-based materials for organic light-emitting diodes. *Dyes Pigm.* **2017**, *137*, 24–35.
- [266] Reig, M.; Bubniene, G.; Cambarau, W.; Jankauskas, V.; Getautis, V.; Palomares, E.; Martínez-Ferrero, E.; Velasco, D. New solution-processable carbazole derivatives as deep blue emitters for organic light-emitting diodes. *RSC Adv.* **2016**, *6*, 9247–9253.
- [267] Stroehriegl, P.; Grazulevicius, J. V. Charge-transporting molecular glasses. *Adv. Mater.* **2002**, *14*, 1439–1452.
- [268] Wang, H.; Chen, G.; Xu, X.; Chen, H.; Ji, S. The synthesis and optical properties of benzothiazole-based derivatives with various π -electron donors as novel bipolar fluorescent compounds. *Dyes Pigm.* **2010**, *86*, 238–248.
- [269] Tucker, S. H. Iodination in the carbazole series. *J. Chem. Soc.* **1926**, *129*, 546–553.
- [270] Chinchilla, R.; Nájera, C. The Sonogashira reaction: a booming methodology in synthetic organic chemistry. *Chem. Rev.* **2007**, *107*, 874–922.

- [271] Xie, Y.-M.; Cui, L.-S.; Liu, Y.; Zu, F.-S.; Li, Q.; Jiang, Z.-Q.; Liao, L.-S. Efficient blue/white phosphorescent organic light-emitting diodes based on a silicon-based host material via a direct carbon–nitrogen bond. *J. Mater. Chem. C* **2015**, *3*, 5347–5353.
- [272] Zhu, L.; Wu, Z.; Chen, J.; Ma, D. Reduced efficiency roll-off in all-phosphorescent white organic light-emitting diodes with an external quantum efficiency of over 20%. *J. Mater. Chem. C* **2015**, *3*, 3304–3310.
- [273] Li, Y.; Zhou, L.; Cui, R.; Jiang, Y.; Zhao, X.; Liu, W.; Zhu, Q.; Cui, Y.; Zhang, H. High performance red organic electroluminescent devices based on a trivalent iridium complex with stepwise energy levels. *RSC Adv.* **2016**, *6*, 71282–71286.
- [274] King, S. M.; Al-Attar, H. A.; Evans, R. J.; Congreve, A.; Beeby, A.; Monkman, A. P. The use of substituted iridium complexes in doped polymer electrophosphorescent devices: the influence of triplet transfer and other factors on enhancing device performance. *Adv. Funct. Mater.* **2006**, *16*, 1043–1050.
- [275] Chang, Y.-L.; Song, Y.; Wang, Z.; Helander, M. G.; Qiu, J.; Chai, L.; Liu, Z.; Scholes, G. D.; Lu, Z. Highly efficient warm white organic light-emitting diodes by triplet exciton conversion. *Adv. Funct. Mater.* **2013**, *23*, 705–712.
- [276] Ghalgaoui, A.; Shimizu, R.; Hosseinpour, S.; Álvarez-Asencio, R.; McKee, C.; Johnson, C.M.; Rutland, M.W. Monolayer study by VSFS: in situ response to compression and shear in a contact. *Langmuir* **2014**, *30*, 3075–3085.
- [277] Song, D.; Wang, H.; Zhu, F.; Yang, J.; Tian, H.; Geng, Y.; Yan, D. Phthalocyanato tin(IV) dichloride: an air-stable, high-performance, n-type organic semiconductor with a high field-effect electron mobility. *Adv. Mater.* **2008**, *20*, 2142–2144.
- [278] Boulouf, A.; Louër, D. Powder pattern indexing with the dichotomy method. *J. Appl. Cryst.* **2004**, *37*, 724–731.
- [279] Coelho, A. A. *TOPAS* and *TOPAS-Academic*: an optimization program integrating computer algebra and crystallographic objects written in C++. *J. Appl. Cryst.* **2018**, *51*, 210–218.
- [280] Coelho, A. A.; Evans, J.; Evans, I.; Kern, A.; Parsons, S. The TOPAS symbolic computation system. *Powder Diffr.* **2011**, *26*, S22–S25.
- [281] Young, D. C. *Computational Chemistry*; Wiley-Interscience: 2001; Appendix A.1.6, p. 330.

EXPERIMENTAL PART



EXPERIMENTAL PART

1. Materials, solvents and reagents

All chemicals were of commercial grade and used as received. All solvents were dried and degassed by standard methods. Tetrahydrofuran was distilled from sodium/benzophenone whereas dichloromethane and acetonitrile were distilled from CaH₂. Anhydrous commercially available DMF was stored over activated 4 Å molecular sieves under nitrogen atmosphere. Anhydrous CHCl₃ was purchased from Sigma-Aldrich and stored under nitrogen atmosphere. Reactions were monitored by thin layer chromatography (TLC) using aluminium sheets coated with silica gel or neutral alumina (Merck, 60 F254). Visualization of TLC plates was achieved using ultraviolet light (254 nm and also 365 nm in the case of fluorophores). Flash chromatography was carried out over commercial silica gel (VWR, 40-63 µm) or neutral alumina (Sigma-Aldrich; activated, neutral, Brockmann Activity I). As specified, the use of neutralized silica gel was necessary in some cases. It was prepared by mixing commercial silica gel (200 mg) with triethylamine (5 mL) in dichloromethane (500 mL), followed by the removal of the solvents under reduced pressure.

2. Instrumentation and methods

2.1. Characterization of organic compounds

- **NMR spectroscopy.** ¹H NMR and ¹³C NMR spectra were collected on a Varian Mercury 400 MHz, a Bruker 400 MHz Avance III or a Bruker Avance Neo 500 MHz instrument. NMR spectra were processed using the MestRec Nova software (version 14.2.0) and referenced with the solvent signal.
- **Mass spectrometry.** MALDI-TOF was performed on an Applied Biosystems MDS SCIEX 4800 equipment in the Reflector mode. High resolution mass spectrometry (HRMS) was performed on a LC/MSD-TOF Agilent Technologies instrument by the electrospray (ESI-MS) technique.
- **UV-Vis spectroscopy.** UV-Vis spectra were registered using a Varian Cary UV-Vis-NIR 500E.
- **Fluorescence spectroscopy.** Emission spectra were recorded with a PTI fluorimeter equipped with a 220B lamp power supply, an 815 photomultiplier detection system and

a Felix 32 software. The estimation of the fluorescence quantum yields (Φ_f) in solution was achieved using optically-matched solutions of a standard following a literature protocol, as described by eqn. (3) in the General part.^[86] The employed standard was 1,4-bis(5-phenyl-2-oxazolyl)benzene (POPOP) dissolved in cyclohexane, which exhibits a fluorescence quantum yield of 0.93 after excitation at 300 nm. The measurements of the quantum yields in the solid state were determined by means of an integrating sphere. The AIE analyses were performed with THF:H₂O mixtures of different proportion prepared in-situ into the quartz cuvette under continuous stirring. The solutions were prepared by adding with a micropipette 60 μ L of a solution containing the compound in THF (0.5 mM) and the corresponding volume of THF and H₂O up to 3 mL to dilute the compound to 10 μ M.

- **Cyclic voltammetry (CV).** Cyclic voltammograms were collected in cylindrical three-electrode cell using a microcomputer-controlled potentiostat/galvanostat Autolab with PGSTAT30 equipment and GPES software. The reference electrode was an Ag/Ag⁺ electrode (1 mM AgNO₃ in acetonitrile), whereas the counter and working electrodes consisted of a platinum wire and a glassy-carbon electrode, respectively. All voltammetric curves were recorded under quiescent conditions, at a scan rate of 100 mV s⁻¹ and under argon atmosphere. All solutions were prepared in distilled dichloromethane (1 mM). Tetrabutylammonium hexafluorophosphate (TBAP) was used as the supporting electrolyte (0.1 M). All potentials were referred to the Fc⁺/Fc redox couple employing the $E^0(\text{Fc}^+/\text{Fc})$, which was experimentally determined before recording the cyclic voltammograms of the samples. The ionization potential values (IP) were estimated from the onset of the first oxidation peak as $\text{IP} = E_{\text{onset}}^{\text{OX}} + 5.39$, where 5.39 eV corresponds to the formal potential of the Fc⁺/Fc couple in the Fermi scale.^[92] The electron affinity values (EA) were calculated as $\text{EA} = \text{IP} - E_{\text{gap}}$. The optical gap energy values (E_{gap}) were estimated from λ_{onset} of the absorption spectra.
- **Thermogravimetric analyses (TGA).** TGA were performed using a TA Instruments Q50 instrument at a heating rate of 10 °C min⁻¹ under nitrogen atmosphere.
- **Differential scanning calorimetry (DSC).** DSC analyses were performed on a TA Instruments Q2000 calorimeter at a scan rate of 10 °C min⁻¹ under nitrogen atmosphere.
- **High-performance liquid chromatography (HPLC).** HPLC analyses were performed in a Waters Alliance 2795 instrument equipped with a PDA detector (Waters 2996) and a MS detector (Waters ZQ 2000). The separation was carried out with an X-Terra MS C₁₈ column (Waters, 3.5 μ m, 4.6×50 mm). The applied eluent was composed of a mixture of water and acetonitrile (90:10 v/v) containing a 0.1% of formic acid.

2.2. Fabrication and characterization of OTFTs

Both the fabrication and characterization of OTFT devices were performed in the facilities of the *Universitat Politècnica de Catalunya (Departament d'Enginyeria Electrònica)*, under the supervision of Prof. Joaquim Puigdollers.

- **Materials.** The fabrication of the OTFT devices was based on the bottom-gate top-contact geometry. The substrates were composed of thermally oxidized crystalline silicon wafers (p-type). Each substrate possessed a specific and known SiO₂ thickness that was used in the extraction of the mobility. The SiO₂ thickness of the substrates employed throughout this work went from 100 to 135 nm.
- **Pretreatment of the substrates.** Part of the SiO₂ coating of the gate side of the substrates was removed by applying a drop of an ammonium fluoride solution onto the surface. Then, the excess of solution was removed and the wafers were cleaned by subsequent ultrasonic treatments in acetone, isopropyl alcohol and Milli-Q water (10 min each). Finally, the substrates were dried with a nitrogen blow and heated at 100 °C for 5 min.
- **Modification of the dielectric surface.** The SiO₂ surface was treated with either octadecyltrichlorosilane (OTS) as a self-assembled monolayer (SAM) or a layer of polystyrene (PS) to modulate the device performance:
 - For the formation of the OTS SAM onto the SiO₂ surface, the substrates were immersed in a solution of OTS in toluene (2 mM) at room temperature for 24 hours.^[276-277] After, the substrates were cleaned by subsequent ultrasonic treatments in toluene (5 min), acetone (10 min) and isopropyl alcohol (10 min), and dried with a nitrogen blow and heated at 100 °C for 5 minutes.
 - The deposition of PS was carried out through the spin coating technique. For this purpose, 0.1 mL of a solution of PS in toluene (4 mg mL⁻¹) was cast onto the substrate in order to entirely cover the surface. The substrate was spun at 1500 rpm for 5 s and 2500 rpm for 30 s with a P6700 spin coater and subsequently heated at 120 °C for 1 hour.

As characterized in previous investigations of our research group,^[122] the contact angles for bare SiO₂, PS- and OTS-treated SiO₂ surfaces possess values of 14°, 74° and 92°, respectively (Figure 1).

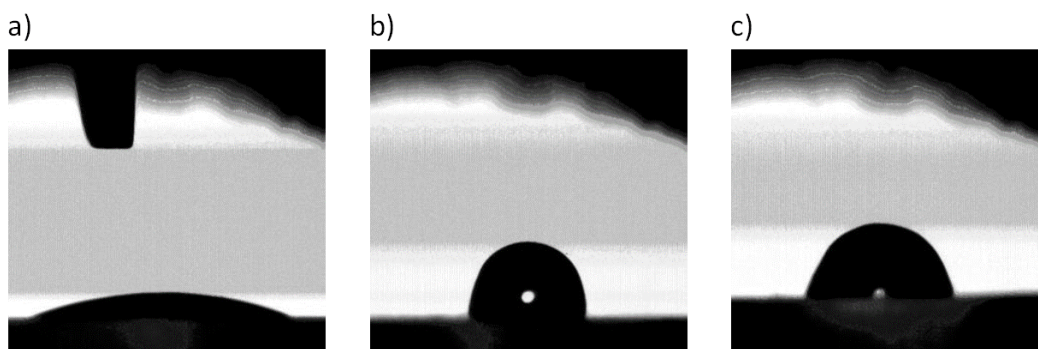


Figure 1. Measurement of the contact angle with a water drop on: a) a bare SiO₂ substrate; b) an OTS-treated substrate; c) a PS-treated substrate. From ref. 122.

- **Vacuum deposition process.** The organic compounds were deposited by thermal evaporation under vacuum in a chamber with a pressure below 10^{-6} mbar. The sublimation temperature for each compound was controlled manually to maintain the deposition at a stable rate of $0.2\text{--}0.3 \text{ \AA s}^{-1}$ until a thickness of 75 nm was obtained. The wafers were subsequently transferred to another vacuum system to deposit the golden contacts. The drain and source electrodes as well as the organic layers were defined by a metallic mask, providing a channel length and width of 80 μm and 2 mm, respectively.
- **Measurements.** The resultant OTFTs were characterized under ambient conditions in the dark. The electrical characteristics were recorded employing a Keithley 2636A source meter. The devices were stored under ambient conditions in the dark.

2.3. Fabrication and characterization of OLEDs

Both the fabrication and characterization of OLED devices were carried out in the facilities of the Technological Center of Catalonia Eurecat (Printed Electronics & Embedded Devices Unit), under the supervision of Dr. Eugenia Martínez and Dr. Nikola Peřinka.

- **OLED fabrication.** The glass substrates coated with ITO (10 Ω/sq , Psiotec Ltd.) were cleaned by subsequent ultrasonic treatments in acetone, isopropanol and ethanol (15 minutes each) and finally dried with a nitrogen blow. After, the substrates were treated with plasma/O₂ (10 sccm, 120 W, 60 s). The PEDOT:PSS (Clevios P VP AI4083, H. C. Starck GmbH) layer was deposited over the plasma treated ITO *via* spin-coating (4000 rpm/60s) and then annealed at 120 °C for 3h, resulting in homogeneous layers of 30 nm. The active layer was also deposited through spin-coating using solutions containing the corresponding blue emitter (**57–58**) in a concentration of 10 mg mL⁻¹ (the specific solvents are detailed in Table 6.3 of Chapter 6). In the case of iridium containing solutions, they were prepared in chlorobenzene in a concentration of 10 mg mL⁻¹ of blue emitter with different iridium ratio, in a proportion (w/w) of

compound: Ir(MDQ)₂(acac):Ir(ppy)₃ expressed as 100:x:y (x and y are detailed in Table 6.4. of Chapter 6). The active layers were spin-coated under ambient conditions (1000 rpm/60 s) and dried under vacuum for 1 h. All the subsequent steps were carried out under nitrogen ambience inside a Glovebox. The TPBi (20 nm), Ca (14 nm) and Al (100 nm, Kurt & Lesker) were deposited by thermal evaporation under high vacuum (1×10^{-7} mbar), using shadow masks defining 9 devices per substrate with an active device area of 5 mm². The devices were encapsulated with epoxy resin (Ossila E132), then covered by cover glass 20×20 mm (Deltalab, D102020), and subsequently cured in an UV oven Dymax 2000-PC for 60 s.

- **Profilometry.** The thicknesses of the layers were determined with a Dektak XT, Veeco profilometer.
- **OLED characterization.** The optoelectronic characterization of the devices was performed under ambient conditions with a Keithley 2604B SourceMeter and a photodiode (Thorlabs, SM1PD2A) governed by an in house software. The electroluminescence spectra were recorded with a spectrophotometer Ocean Optics USB2000+ and using SpectraSuite software.

2.4. X-ray diffraction measurements

The X-ray diffraction measurements and analyses were performed by the researchers integrating the X-Ray Diffraction Unit of the CCiTUB. Specifically, the X-ray diffraction and elucidation of the crystal structures of monocrystalline materials were performed by Dr. Mercè Font; the powder X-ray diffraction and the subsequent elucidation of the crystal structures was accomplished by Dr. Cristina Puigjaner, Dr. Xavier Alcobé and Anna Vilche; the GIXRD of thin films was carried out by Dr. Josep Maria Bassas.

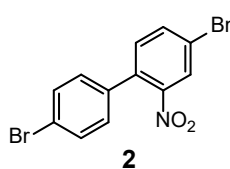
- **X-Ray diffraction of monocrystalline materials.** The single-crystal elucidation was achieved on a D8 Venture System equipped with a multilayer monochromator and a Mo microfocus ($\lambda = 0.71073 \text{ \AA}$) or Cu ($\lambda = 1.54178 \text{ \AA}$). The frames were integrated using the Bruker SAINT Software package (version SAINT V8.38A) with a narrow-frame algorithm. The structure resolution and refinement were performed using the Bruker SHELXTL Software package (version APEX v2018 7-2).
- **Powder X-Ray diffraction.** PXRD patterns were obtained on a PANalytical X'Pert PRO MPD diffractometer of 240 mm of radius in a transmission configuration with a spinner glass capillary sample holder, using Cu K α radiation ($\lambda = 1.5418 \text{ \AA}$) with a focalizing elliptic mirror and a PIXcel detector working at a maximum detector active length of 3.347 A° . The sample was placed in a Hilgenberg glass capillary (0.5 mm of diameter).

Incident and diffracted beam 0.01 radians soller slits and incident beam slits defining a beam height of 0.4 mm. 22 consecutive 2θ scans were measured and added from 2 to 70° in 2θ , with a step size of 0.013° and a measuring time of 700 s per step. The indexing process was achieved by means of the dichotomy algorithm implemented in the program DICVOL04^[278]. The pattern matching was carried out through the Pawley (1981) refinement by means of the TOPAS Software (Version 6)^[279–280]. The starting model for the crystal structure determination was previously optimized with the program SPARTAN^[281]. The crystal structure was solved using the Global Optimization Simulated Annealing approach integrated in TOPAS. The crystal structure was subsequently refined by the Rietveld (1969) method, also by means of TOPAS Software.

- **Grazing Incidence X-Ray Diffraction (GIXRD) of thin films.** The analyzed thin-films (75 nm thickness) were vacuum-deposited over either OTS- or PS-treated Si/SiO₂ substrates. Out-of-plane GIXRD measurements of thin films were collected in a PANalytical X'Pert PRO MRD diffractometer. It possesses a PIXcel detector, a parabolic Göbel mirror at the incident beam and a parallel plate collimator at the diffracted beam, with Cu K α radiation ($\lambda = 1.5418 \text{ \AA}$) and a work power of 45 kV \times 40 mA. An optimized angle of incidence around 0.17° was used for the measurements.

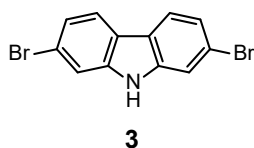
3. Synthetic procedures and characterization data

3.1. 4,4'-Dibromo-2-nitro-1,1'-biphenyl (**2**)



4,4'-dibromobiphenyl (21.5 g, 69.0 mmol) was dissolved in glacial acetic acid (320 mL) at 100°C . After, fuming nitric acid (108 mL) was slowly added with a dropping funnel. Thereafter, the reaction mixture was stirred for 60 min at 100°C and then, cooled to room temperature. The product was precipitated by adding water to the mixture, filtered, washed thoroughly with a solution of NaHCO₃ and dried. Compound **2** was obtained as a pale yellow solid in a yield of 84% (20.6 g, 57.7 mmol). ¹H NMR (400 MHz, CDCl₃) δ (ppm): 8.03 (d, $J = 2.0$ Hz, 1H), 7.76 (dd, $J = 8.3, 2.0$ Hz, 1H), 7.56 (d, $J = 8.4$ Hz, 2H), 7.29 (d, $J = 8.3$ Hz, 1H), 7.16 (d, $J = 8.4$ Hz, 2H).

3.2. 2,7-Dibromo-9H-carbazole (**3**)



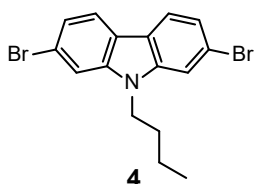
Method 1: **2** (2.18 g, 6.10 mmol) was dissolved in P(OEt)₃ (10 mL, 58 mmol) and the mixture was stirred for 20 h under reflux. After cooling down to room temperature, the excess of P(OEt)₃ was slowly removed with an air stream. The crude was purified by flash column

chromatography using a mixture of hexane and ethyl acetate (20:1 v/v) as eluent. Compound **3** was obtained as a white solid in a yield of 49% (0.964 g, 2.97 mmol).

Method 2: **2** (4.77 g, 13.4 mmol) and PPh₃ (8.89 g, 33.9 mmol) were dissolved in *o*-dichlorobenzene (27 mL) under nitrogen and the mixture was stirred for 6 h under reflux. Then, the system was cooled down to room temperature and the solvent was slowly removed with an air stream. The crude was purified by flash column chromatography using a mixture of hexane and ethyl acetate (20:1 v/v) as eluent. Compound **3** was obtained as a white solid in a yield of 74% (3.21 g, 9.89 mmol).

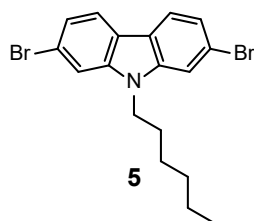
¹H NMR (400 MHz, CDCl₃) δ (ppm): 8.06 (s, 1H), 7.88 (d, *J* = 8.3 Hz, 2H), 7.59 (d, *J* = 1.7 Hz, 2H), 7.36 (dd, *J* = 8.3, 1.7 Hz, 2H).

3.3. 2,7-Dibromo-9-butyl-9H-carbazole (**4**)



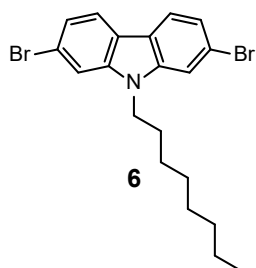
3 (1.50 g, 4.62 mmol) was dissolved in anhydrous DMF (5 mL) under nitrogen. NaH (0.277 g, 60% in mineral oil, 6.92 mmol) was added and the solution was stirred for 30 min at room temperature. Then, 1-bromobutane (1.0 mL, 9.2 mmol) was added and the reaction was stirred overnight. After, it was diluted with water and the product was extracted with dichloromethane. The organic layers were dried over anhydrous MgSO₄, filtered and the solvent was removed under reduced pressure. The crude was purified by flash column chromatography using hexane as eluent. Compound **4** was obtained as a white solid in a yield of 94% (1.65 g, 4.32 mmol). ¹H NMR (400 MHz, CDCl₃) δ (ppm): 7.89 (d, *J* = 8.2 Hz, 2H), 7.53 (d, *J* = 1.7 Hz, 2H), 7.34 (dd, *J* = 8.2, 1.7 Hz, 2H), 4.21 (t, *J* = 7.3 Hz, 2H), 1.83 (m, 2H), 1.40 (m, 2H), 0.97 (t, *J* = 7.3 Hz, 3H).

3.4. 2,7-Dibromo-9-hexyl-9H-carbazole (**5**)



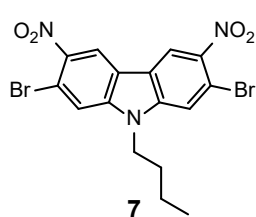
Analogously to the procedure described in section 3.3, this synthesis was carried out with **3** (3.05 g, 9.39 mmol), NaH (0.563 g, 60% in mineral oil, 14.1 mmol) and 1-bromohexane (2.6 mL, 19 mmol) in anhydrous DMF (10 mL). Compound **5** was obtained as a white solid in a yield of 87% (3.32 g, 8.12 mmol). ¹H NMR (400 MHz, CDCl₃) δ (ppm): 7.89 (d, *J* = 8.3 Hz, 2H), 7.53 (d, *J* = 1.5 Hz, 2H), 7.34 (dd, *J* = 8.3, 1.5 Hz, 2H), 4.20 (t, *J* = 7.4 Hz, 2H), 1.84 (m, 2H), 1.43–1.26 (m, 6H), 0.88 (t, *J* = 7.0 Hz, 3H).

3.5. 2,7-Dibromo-9-octyl-9H-carbazole (6)



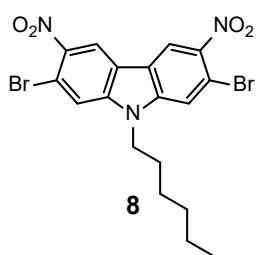
Analogously to the procedure described in section 3.3, this synthesis was carried out with **3** (1.50 g, 4.62 mmol), NaH (0.277 g, 60% in mineral oil, 6.92 mmol) and 1-bromooctane (1.6 mL, 9.2 mmol) in anhydrous DMF (5 mL). Compound **6** was obtained as a white solid in a yield of 98% (1.98 g, 4.52 mmol). $^1\text{H NMR}$ (400 MHz, CDCl_3) δ (ppm): 7.89 (d, $J = 8.3$ Hz, 2H), 7.53 (d, $J = 1.7$ Hz, 2H), 7.34 (dd, $J = 8.3$, 1.7 Hz, 2H), 4.19 (t, $J = 7.4$ Hz, 2H), 1.84 (m, 2H), 1.42–1.18 (m, 10H), 0.87 (t, $J = 6.9$ Hz, 3H).

3.6. 2,7-Dibromo-9-butyl-3,6-dinitro-9H-carbazole (7)



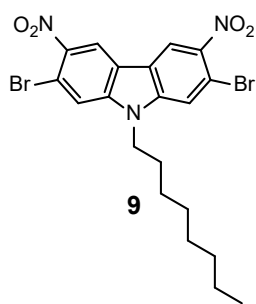
4 (1.65 g, 4.32 mmol) was dissolved in glacial acetic acid (16 mL) at 80 °C. Thereafter, the temperature was raised to 100 °C and fuming nitric acid (2 mL) was slowly added with a dropping funnel. The reaction was stirred for 90 min at 100 °C and then, cooled to room temperature. The product was precipitated by adding water to the mixture, filtered and dried. Further purification was carried out by subsequent recrystallizations from a mixture of dichloromethane and ethanol. Compound **7** was obtained as a pale yellow solid in a yield of 79% (1.61 g, 3.41 mmol). $^1\text{H NMR}$ (400 MHz, CDCl_3) δ (ppm): 8.74 (s, 2H), 7.77 (s, 2H), 4.32 (t, $J = 7.3$ Hz, 2H), 1.90 (m, 2H), 1.42 (m, 2H), 1.01 (t, $J = 7.3$ Hz, 3H).

3.7. 2,7-Dibromo-9-hexyl-3,6-dinitro-9H-carbazole (8)



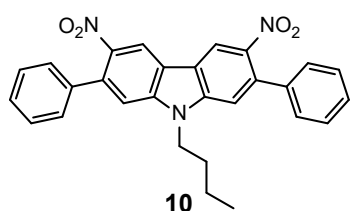
Analogously to the procedure described in section 3.6, this synthesis was carried out with **5** (6.08 g, 14.9 mmol) and fuming nitric acid (5.9 mL) in glacial acetic acid (43 mL). Further purification was carried out by dissolving the product in the minimum amount of dichloromethane and precipitating it by the slow addition of hexane. Compound **8** was obtained as a pale yellow solid in a yield of 88% (6.54 g, 13.1 mmol). $^1\text{H NMR}$ (400 MHz, CDCl_3) δ (ppm): 8.74 (s, 2H), 7.76 (s, 2H), 4.31 (t, $J = 7.3$ Hz, 2H), 1.89 (m, 2H), 1.44–1.26 (m, 6H), 0.89 (t, $J = 7.0$ Hz, 3H).

3.8. 2,7-Dibromo-3,6-dinitro-9-octyl-9H-carbazole (9)



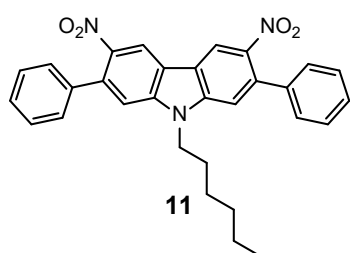
Analogously to the procedure described in section 3.6, this synthesis was carried out with **6** (1.98 g, 4.52 mmol) and fuming nitric acid (2 mL) in glacial acetic acid (17 mL). Further purification was carried out by subsequent recrystallizations from a mixture of dichloromethane and ethanol. Compound **9** was obtained as a pale yellow solid in a yield of 71% (1.69 g, 3.21 mmol). $^1\text{H NMR}$ (400 MHz, CDCl_3) δ (ppm): 8.74 (s, 2H), 7.76 (s, 2H), 4.31 (t, $J = 7.3$ Hz, 2H), 1.90 (m, 2H), 1.42–1.21 (m, 10H), 0.87 (t, $J = 6.9$ Hz, 3H).

3.9. 9-Butyl-3,6-dinitro-2,7-diphenyl-9H-carbazole (10)



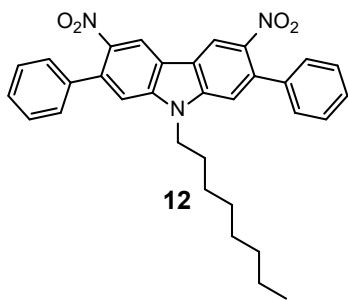
7 (620 mg, 1.32 mmol), phenylboronic acid (417 mg, 3.42 mmol), $\text{Pd}(\text{PPh}_3)_4$ (76 mg, 0.066 mmol) and K_2CO_3 (1090 mg, 7.90 mmol) were dissolved in a previously purged mixture of THF and H_2O (28 mL, 6:1 v/v). The system was further purged with nitrogen and the solution was stirred under reflux overnight. Then, the product was extracted with dichloromethane. The combined organic extract was dried over anhydrous MgSO_4 , filtered and the solvent was removed under reduced pressure. The crude was purified by flash column chromatography using a mixture of hexane and ethyl acetate (10:1 v/v) as eluent. Compound **10** was obtained as a yellow solid in a yield of 83% (506 mg, 1.09 mmol). $^1\text{H NMR}$ (400 MHz, CDCl_3) δ (ppm): 8.81 (s, 2H), 7.53–7.41 (m, 10H), 7.40 (s, 2H), 4.37 (t, $J = 7.3$ Hz, 2H), 1.88 (m, 2H), 1.40 (m, 2H), 0.96 (t, $J = 7.4$ Hz, 3H).

3.10. 9-Hexyl-3,6-dinitro-2,7-diphenyl-9H-carbazole (11)



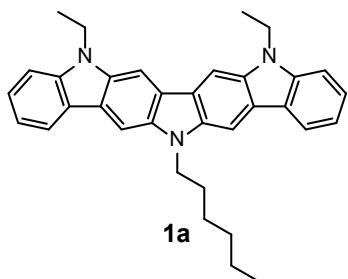
Analogously to the procedure described in section 3.9, this synthesis was carried out with **8** (600 mg, 1.20 mmol), phenylboronic acid (381 mg, 3.13 mmol), $\text{Pd}(\text{PPh}_3)_4$ (60 mg, 0.060 mmol) and K_2CO_3 (995 mg, 7.21 mmol) in THF: H_2O (25.2 mL, 6:1 v/v). The crude was purified using a mixture of hexane and ethyl acetate (20:1 v/v) as eluent. Compound **11** was obtained as a yellow solid in a yield of 69% (407 mg, 0.825 mmol). $^1\text{H NMR}$ (400 MHz, CDCl_3) δ (ppm): 8.81 (s, 2H), 7.52–7.41 (m, 10H), 7.39 (s, 2H), 4.35 (t, $J = 7.4$ Hz, 2H), 1.94–1.85 (m, 2H), 1.42–1.20 (m, 6H), 0.85 (t, $J = 7.1$ Hz, 3H).

3.11. 3,6-Dinitro-9-octyl-2,7-diphenyl-9H-carbazole (**12**)



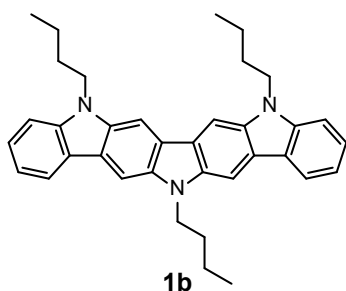
Analogously to the procedure described in section 3.9, this synthesis was carried out with **9** (701 mg, 1.33 mmol), phenylboronic acid (429 mg, 3.45 mmol), Pd(PPh₃)₄ (77 mg, 0.066 mmol) and K₂CO₃ (1102 mg, 7.97 mmol) in THF:H₂O (28 mL, 6:1 v/v). The crude was purified using a mixture of hexane and ethyl acetate (20:1 v/v) as eluent. Compound **12** was obtained as a yellow solid in a yield of 77% (530 mg, 1.02 mmol). ¹H NMR (400 MHz, CDCl₃) δ (ppm): 8.81 (s, 2H), 7.52–7.41 (m, 10H), 7.39 (s, 2H), 4.35 (t, *J* = 7.3 Hz, 2H), 1.89 (m, 2H), 1.40–1.15 (m, 10H), 0.84 (t, *J* = 6.9 Hz, 3H).

3.12. 5,8-Diethyl-14-hexyl-8,14-dihydro-5H-diindolo[3,2-*b*:2',3'-*h*]carbazole (**1a**)



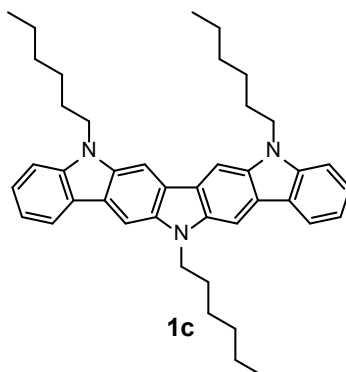
11 (200 mg, 0.405 mmol) was dissolved in *o*-dichlorobenzene (6 mL) in a microwave vial and purged with nitrogen. Then, P(OEt)₃ (0.83 mL, 4.8 mmol) was added and the sealed tube was heated under microwave irradiation at 230 °C for 2 h. After cooling to room temperature, hexane was added to the mixture to precipitate the cyclized intermediate, which was filtered and dried. Without further purification, the solid and NaH (25 mg, 60% in mineral oil, 0.63 mmol) were dissolved in anhydrous DMF (4 mL) under nitrogen. The solution was stirred for 30 min at room temperature and then, bromoethane (0.14 mL, 1.3 mmol) was added and stirred overnight. After, the solution was diluted with water and the product was extracted with dichloromethane. The combined organic extract was dried over anhydrous MgSO₄, filtered and the solvent was removed under reduced pressure. The crude was purified by flash column chromatography using a mixture of hexane and ethyl acetate (250:1 v/v) as eluent. Compound **1a** was obtained as a bright yellow solid in a yield of 10% (20 mg, 0.041 mmol). ¹H NMR (500 MHz, C₆D₆) δ (ppm): 8.31 (d, *J* = 7.7 Hz, 2H), 8.21 (s, 2H), 8.17 (s, 2H), 7.51 (ddd, *J* = 8.3, 7.1, 1.2 Hz, 2H), 7.33 (ddd, *J* = 7.4, 7.4, 0.9 Hz, 2H), 7.22 (d, *J* = 8.1 Hz, 2H), 4.24 (t, *J* = 7.3 Hz, 2H), 4.05 (q, *J* = 7.2 Hz, 4H), 1.87–1.79 (m, 2H), 1.33–1.25 (m, 2H), 1.17–1.11 (m, 4H), 1.14 (t, *J* = 7.2 Hz, 6H), 0.79 (t, *J* = 7.1 Hz, 3H). ¹³C NMR (125 MHz, C₆D₆) δ (ppm): 141.8, 138.2, 135.8, 126.0, 124.0, 123.8, 123.8, 120.8, 118.6, 108.6, 99.2, 99.1, 43.7, 37.7, 31.9, 28.9, 27.4, 22.9, 14.2, 13.6. HRMS (ESI-MS) (*m/z*): calculated for C₃₄H₃₅N₃ M⁺, 485.2825; found 485.2822.

3.13. 5,8,14-Tributyl-8,14-dihydro-5H-diindolo[3,2-*b*:2',3'-*h*]carbazole (**1b**)



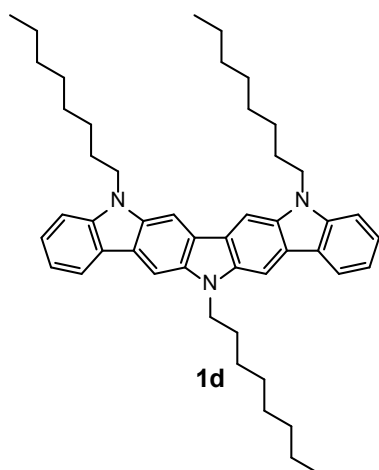
Analogously to the procedure described in section 3.12, this synthesis was carried out with **10** (192 mg, 0.412 mmol) and $\text{P}(\text{OEt})_3$ (0.83 mL, 4.8 mmol) in *o*-dichlorobenzene (6 mL). Then, NaH (26 mg, 60% in mineral oil, 0.65 mmol) and 1-bromobutane (0.13 mL, 1.21 mmol) in anhydrous DMF (5 mL). The crude was purified using a mixture of hexane and dichloromethane (20:1 v/v) as eluent. Compound **1b** was obtained as a bright yellow solid in a yield of 8% (17 mg, 0.033 mmol). ^1H NMR (400 MHz, C_6D_6) δ (ppm): 8.32 (d, $J = 7.8$ Hz, 2H), 8.31 (s, 2H), 8.17 (s, 2H), 7.53 (ddd, $J = 8.2, 7.1, 1.2$ Hz, 2H), 7.34 (m, 2H), 7.30 (d, $J = 8.1$ Hz, 2H), 4.21 (t, $J = 7.1$ Hz, 2H), 4.07 (t, $J = 7.1$ Hz, 4H), 1.78 (m, 2H), 1.66 (m, 4H), 1.34–1.10 (m, 6H), 0.76 (t, $J = 7.4$ Hz, 3H), 0.70 (t, $J = 7.3$ Hz, 6H). ^{13}C NMR (100 MHz, C_6D_6) δ (ppm): 142.4, 138.2, 136.3, 126.0, 123.8, 123.8, 123.7, 120.8, 118.5, 108.9, 99.3, 99.2, 43.5, 43.2, 31.3, 31.1, 21.0, 20.9, 14.1, 14.0. HRMS (ESI-MS) (m/z): calculated for $\text{C}_{36}\text{H}_{39}\text{N}_3$ M^+ , 513.3138; found 513.3139.

3.14. 5,8,14-Trihexyl-8,14-dihydro-5H-diindolo[3,2-*b*:2',3'-*h*]carbazole (**1c**)



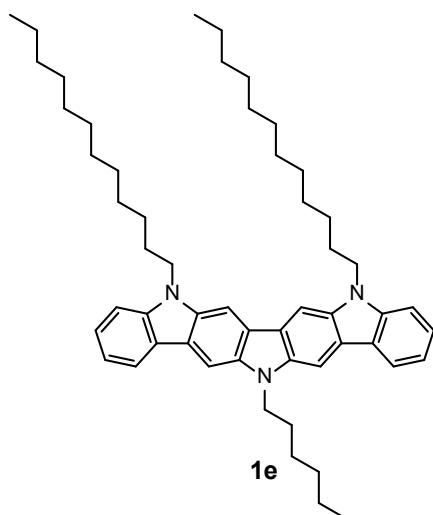
Analogously to the procedure described in section 3.12, this synthesis was carried out with **11** (200 mg, 0.405 mmol) and $\text{P}(\text{OEt})_3$ (0.83 mL, 4.8 mmol) in *o*-dichlorobenzene (6 mL). Then, NaH (25 mg, 60% in mineral oil, 0.63 mmol) and 1-bromohexane (0.18 mL, 1.3 mmol) in anhydrous DMF (3 mL). The crude was purified using a mixture of hexane and ethyl acetate (250:1 v/v) as eluent. Compound **1c** was obtained as a bright yellow solid in a yield of 11% (27 mg, 0.046 mmol). ^1H NMR (500 MHz, C_6D_6) δ (ppm): 8.33 (s, 2H), 8.32 (d, $J = 7.8$ Hz, 2H), 8.19 (s, 2H), 7.52 (ddd, $J = 8.2, 7.1, 1.2$ Hz, 2H), 7.35–7.31 (m, 2H), 7.32 (d, $J = 8.2$, 2H), 4.23 (t, $J = 7.3$ Hz, 2H), 4.09 (t, $J = 7.3$ Hz, 4H), 1.83 (m, 2H), 1.71 (m, 4H), 1.30 (m, 2H), 1.19 (m, 4H), 1.16–1.03 (m, 12H), 0.80 (t, $J = 7.1$ Hz, 6H), 0.80 (t, $J = 7.1$ Hz, 3H). ^{13}C NMR (125 MHz, C_6D_6) δ (ppm): 142.4, 138.2, 136.3, 126.0, 123.8, 123.8, 123.7, 120.8, 118.5, 108.9, 99.3, 99.1, 43.7, 43.4, 31.9, 31.9, 29.1, 28.9, 27.4, 27.3, 22.9, 22.9, 14.2, 14.2. HRMS (ESI-MS) (m/z): calculated for $\text{C}_{42}\text{H}_{51}\text{N}_3$ M^+ , 597.4078; found 597.4082.

3.15. 5,8,14-Trioctyl-8,14-dihydro-5H-diindolo[3,2-*b*:2',3'-*h*]carbazole (**1d**)



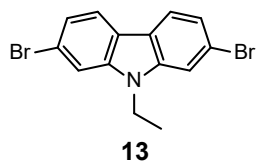
Analogously to the procedure described in section 3.12, this synthesis was carried out with **12** (214 mg, 0.410 mmol) and P(OEt)₃ (0.83 mL, 4.8 mmol) in *o*-dichlorobenzene (6 mL). Then, NaH (26 mg, 60% in mineral oil, 0.66 mmol) and 1-bromooctane (0.23 mL, 1.3 mmol) in anhydrous DMF (5 mL). The crude was purified using hexane as eluent. Compound **1d** was obtained as a bright yellow solid in a yield of 12% (33 mg, 0.048 mmol). ¹H NMR (400 MHz, C₆D₆) δ (ppm): 8.35 (s, 2H), 8.32 (d, *J* = 8.1 Hz, 2H), 8.20 (s, 2H), 7.53 (ddd, *J* = 8.3, 7.2, 1.2 Hz, 2H), 7.35–7.31 (m, 4H), 4.26 (t, *J* = 7.1 Hz, 2H), 4.12 (t, *J* = 7.2 Hz, 4H), 1.86 (m, 2H), 1.75 (m, 4H), 1.38–1.07 (m, 30H), 0.87 (t, *J* = 7.1 Hz, 6H), 0.84 (t, *J* = 7.0 Hz, 3H). ¹³C NMR (125 MHz, C₆D₆) δ (ppm): 142.4, 138.2, 136.3, 126.0, 123.8, 123.8, 123.8, 120.8, 118.5, 108.9, 99.3, 99.2, 43.7, 43.4, 32.2, 32.2, 29.8, 29.8, 29.6, 29.5, 29.1, 28.9, 27.7, 27.7, 23.0, 23.0, 14.3, 14.3. HRMS (ESI-MS) (*m/z*): calculated for C₄₈H₆₃N₃ M⁺, 681.5017; found 681.5007.

3.16. 5,8-Didodecyl-14-hexyl-8,14-dihydro-5H-diindolo[3,2-*b*:2',3'-*h*]carbazole (**1e**)



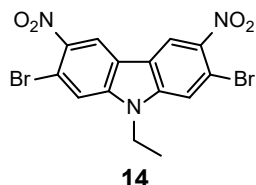
Analogously to the procedure described in section 3.12, this synthesis was carried out with **11** (200 mg, 0.405 mmol) and P(OEt)₃ (0.83 mL, 4.8 mmol) in *o*-dichlorobenzene (6 mL). Then, NaH 25 mg, 60% in mineral oil, 0.63 mmol) and 1-bromododecane (0.30 mL, 1.3 mmol) in anhydrous DMF (6 mL). The crude was purified using hexane as eluent. Compound **1e** was obtained as a bright yellow solid in a yield of 11% (34 mg, 0.044 mmol). ¹H NMR (500 MHz, C₆D₆) δ (ppm): 8.35 (s, 2H), 8.32 (d, *J* = 7.6 Hz, 2H), 8.18 (s, 2H), 7.55–7.51 (m, 2H), 7.35–7.31 (m, 2H), 7.34 (d, *J* = 7.7 Hz, 2H), 4.26 (t, *J* = 7.2 Hz, 4H), 4.14 (t, *J* = 7.3 Hz, H), 1.87–1.80 (m, 2H), 1.80–1.73 (m, 4H), 1.37–1.10 (m, 42H), 0.91 (t, *J* = 6.9 Hz, 6H), 0.80 (t, *J* = 7.0 Hz, 3H). ¹³C NMR (125 MHz, C₆D₆) δ (ppm): 142.4, 138.2, 136.3, 126.0, 123.8, 123.8, 123.7, 120.8, 118.6, 108.9, 99.3, 99.2, 43.7, 43.4, 32.4, 31.9, 30.2, 30.1, 30.0, 30.0, 29.9, 29.8, 27.7, 27.4, 26.9, 23.1, 22.9, 14.4, 14.3. HRMS (ESI-MS) (*m/z*): calculated for C₅₄H₇₅N₃ M⁺, 765.5956; found 765.5962.

3.17. 2,7-Dibromo-9-ethyl-9H-carbazole (13)



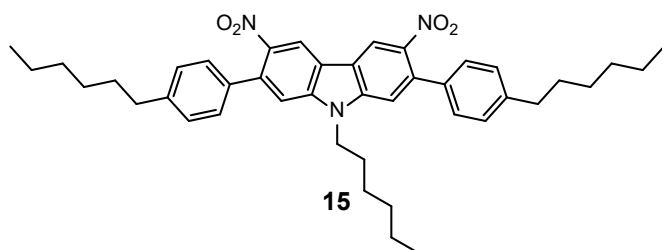
3 (1.50 g, 4.61 mmol) was dissolved in anhydrous DMF (5 mL) under nitrogen. NaH (0.282 g, 60% in mineral oil, 7.05 mmol) was added and the solution was stirred for 30 min at room temperature. Then, bromoethane (0.69 mL, 9.2 mmol) was added and the reaction was stirred overnight. After, it was diluted with water to favor the precipitation of the product, which was filtered off, washed thoroughly with water and dried. The solid was purified by flash column chromatography using hexane as eluent. Compound **13** was obtained as a white solid in a yield of 86% (1.40 g, 3.95 mmol). ¹H NMR (400 MHz, CDCl₃) δ (ppm): 7.90 (d, *J* = 8.2 Hz, 2H), 7.55 (d, *J* = 1.6 Hz, 2H), 7.34 (dd, *J* = 8.2, 1.6 Hz, 2H), 4.29 (q, *J* = 7.2 Hz, 2H), 1.43 (t, *J* = 7.2 Hz, 3H).

3.18. 2,7-Dibromo-9-ethyl-3,6-dinitro-9H-carbazole (14)



13 (1.385 g, 3.923 mmol) was dissolved in glacial acetic acid (10 mL) at 80 °C. Thereafter, the temperature was raised to 100 °C and fuming nitric acid (1.34 mL) was slowly added with a dropping funnel. The reaction was stirred for 90 min at 100 °C and then, cooled to room temperature. The product was precipitated by adding water to the mixture and then it was filtered and dried. Further purification was carried out by dissolving the product in the minimum amount of dichloromethane and precipitating it by the slow addition of hexane. Compound **14** was obtained as a pale yellow solid in a yield of 75% (1.295 g, 2.923 mmol). ¹H NMR (400 MHz, CDCl₃) δ (ppm): 8.75 (s, 2H), 7.79 (s, 2H), 4.40 (q, *J* = 7.3 Hz, 2H), 1.52 (t, *J* = 7.3 Hz, 3H).

3.19. 9-Hexyl-2,7-bis(4-hexylphenyl)-3,6-dinitro-9H-carbazole (15)

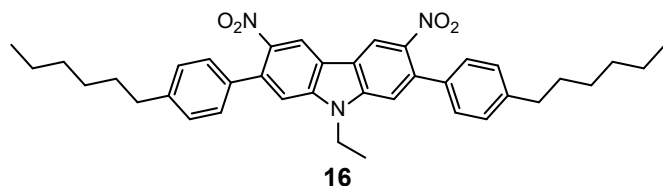


8 (500 mg, 1.00 mmol), 4-hexylphenylboronic acid (537 mg, 2.60 mmol), Pd(PPh₃)₄ (58 mg, 0.050 mmol) and K₂CO₃ (830 mg, 6.01 mmol) were dissolved in a previously purged mixture of THF and H₂O (17.5 mL, 6:1 v/v). The system was further purged with nitrogen and the solution was stirred under reflux overnight. Then, the product was extracted with dichloromethane. The combined organic extract was dried over anhydrous MgSO₄, filtered and the solvent was removed under reduced pressure. The crude was purified by flash column chromatography using a mixture of hexane and ethyl acetate (10:1 v/v) as eluent. Compound **15** was obtained as a yellow solid in a yield of 86% (568 mg, 0.859 mmol). ¹H NMR (400 MHz, CDCl₃) δ (ppm): 8.76 (s,

2H), 7.38 (s, 2H), 7.34 (d, $J = 8.1$ Hz, 4H), 7.29 (d, $J = 8.1$ Hz, 4H), 4.34 (t, $J = 7.3$ Hz, 2H), 2.69 (t, $J = 7.8$ Hz, 4H), 1.93–1.83 (m, 2H), 1.73–1.63 (m, 4H), 1.45–1.25 (m, 18H), 0.92 (t, $J = 7.0$ Hz, 6H), 0.85 (t, $J = 6.9$ Hz, 3H).

3.20. 9-Ethyl-2,7-bis(4-hexylphenyl)-3,6-dinitro-9H-carbazole (16)

Analogously to the procedure described in section 3.19, this synthesis was carried out with **14** (500 mg, 1.13 mmol), 4-hexylphenylboronic acid (605 mg, 2.93 mmol), Pd(PPh₃)₄ (65 mg, 0.056 mmol) and K₂CO₃ (934 mg, 6.77 mmol) in a mixture of THF and H₂O (23.7 mL, 6:1 v/v).

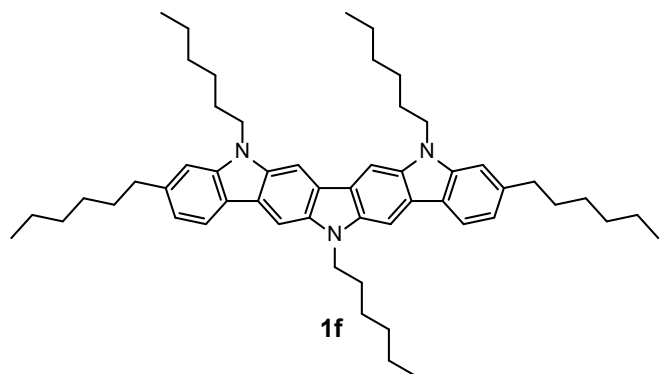


The crude was purified using a mixture of hexane and ethyl acetate (20:1 v/v) as eluent. Compound **16** was obtained as a yellow solid in a

yield of 58% (397 mg, 0.655 mmol). ¹H NMR (400 MHz, CDCl₃) δ (ppm): 8.77 (s, 2H), 7.39 (s, 2H), 7.34 (d, $J = 8.1$ Hz, 4H), 7.29 (d, $J = 8.1$ Hz, 4H), 4.42 (q, $J = 7.2$ Hz, 2H), 2.69 (t, $J = 7.8$ Hz, 4H), 1.73–1.63 (m, 4H), 1.48 (t, $J = 7.2$ Hz, 3H), 1.43–1.27 (m, 12H), 0.92 (t, $J = 7.0$ Hz, 6H).

3.21. 3,5,8,10,14-Pentahexyl-8,14-dihydro-5H-diindolo[3,2-b:2',3'-h]carbazole (1f)

15 (271 mg, 0.410 mmol) was dissolved in *o*-dichlorobenzene (6 mL) in a microwave vial and purged with nitrogen. Then, P(OEt)₃ (0.83 mL, 4.8 mmol) was added and the sealed tube was heated under microwave irradiation at 230 °C for 2 h. After cooling to room

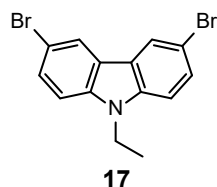


temperature, hexane was added to the mixture to precipitate the cyclized intermediate, which was filtered and dried. Without further purification, the solid and NaH (15 mg, 60% in mineral oil, 0.38 mmol) were dissolved in anhydrous DMF (5 mL) under nitrogen. The solution was

stirred for 30 min at room temperature and then, 1-bromohexane (0.20 mL, 1.4 mmol) was added and stirred for 3 h. After, the solution was diluted with water and the product was extracted with dichloromethane. The combined organic extract was dried over anhydrous MgSO₄, filtered and the solvent was removed under reduced pressure. The crude was purified by flash column chromatography using a mixture of hexane and ethyl acetate (500:1 v/v) as eluent. Compound **1f** was obtained as a bright yellow solid in a yield of 11% (34 mg, 0.044 mmol). ¹H NMR (500 MHz, C₆D₆) δ (ppm): 8.42 (s, 2H), 8.36 (d, $J = 7.9$ Hz, 2H), 8.27 (s, 2H), 7.39 (d, $J = 1.3$ Hz, 2H), 7.30 (dd, $J = 7.9, 1.3$ Hz, 2H), 4.33 (t, $J = 7.3$ Hz, 2H),

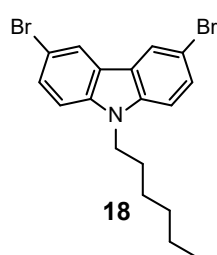
4.23 (t, $J = 7.2$ Hz, 4H), 2.99 (t, $J = 7.7$ Hz, 4H), 1.97–1.80 (m, 10H), 1.58–1.13 (m, 30H), 1.03–0.97 (m, 6H), 0.93–0.80 (m, 9H). ^{13}C NMR (125 MHz, C_6D_6) δ (ppm): 142.9, 141.2, 138.2, 136.5, 123.8, 123.5, 122.0, 120.7, 119.5, 108.5, 99.2, 98.9, 43.7, 43.4, 37.5, 32.8, 32.3, 31.9, 29.6, 29.1, 28.9, 27.4, 27.4, 23.1, 22.9, 14.4, 14.3. HRMS (ESI-MS) (m/z): calculated for $\text{C}_{54}\text{H}_{75}\text{N}_3 \text{M}^+$, 765.5956; found 765.5954.

3.22. 3,6-Dibromo-9-ethyl-9H-carbazole (17)



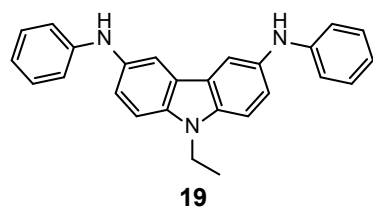
3,6-Dibromo-9H-carbazole (0.508 g, 1.56 mmol) was dissolved in anhydrous DMF (2 mL) under nitrogen. NaH (0.092 g, 60% in mineral oil, 2.3 mmol) was added and the solution was stirred for 30 min at room temperature. Then, bromoethane (0.23 mL, 3.1 mmol) was added and the reaction was stirred overnight. After, it was diluted with water and the resultant precipitate was filtered and dried. The solid was purified by flash column chromatography using hexane as eluent. Compound **17** was obtained as a white solid in a yield of 97% (0.534 g, 1.51 mmol). ^1H NMR (400 MHz, CDCl_3) δ (ppm): 8.14 (d, $J = 1.9$ Hz, 2H), 7.51 (dd, $J = 8.5$, 1.9 Hz, 2H), 7.19 (d, $J = 8.5$ Hz, 2H), 4.20 (q, $J = 7.2$ Hz, 2H), 1.35 (t, $J = 7.2$ Hz, 3H).

3.23. 3,6-Dibromo-9-hexyl-9H-carbazole (18)



Analogously to the procedure described in section 3.22, this synthesis was carried out with 3,6-dibromo-9H-carbazole (0.500 g, 1.54 mmol), NaH (0.092 g, 60% in mineral oil, 2.3 mmol) and 1-bromohexane (0.432 mL, 3.08 mmol) in anhydrous DMF (2 mL). Compound **18** was obtained as a white solid in a yield of 98% (0.615 g, 1.50 mmol). ^1H NMR (400 MHz, CDCl_3) δ (ppm): 8.14 (d, $J = 2.0$ Hz, 2H), 7.55 (dd, $J = 8.7$, 2.0 Hz, 2H), 7.26 (d, $J = 8.7$ Hz, 2H), 4.23 (t, $J = 7.2$ Hz, 2H), 1.87–1.76 (m, 2H), 1.39–1.20 (m, 6H), 0.86 (t, $J = 7.1$ Hz, 3H).

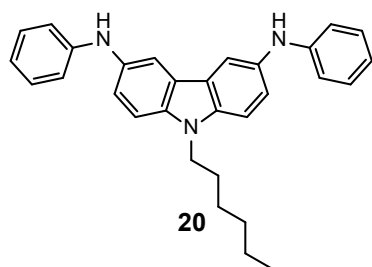
3.24. 9-Ethyl-3,6-bis[*N*-phenylamino]-9H-carbazole (19)



17 (520 mg, 1.47 mmol), tBuOK (364 mg, 3.24 mmol), $\text{Pd}(\text{AcO})_2$ (33 mg, 0.15 mmol) and JohnPhos (132 mg, 0.441 mmol) were dissolved in toluene (6 mL) under nitrogen in a previously dried reaction tube. The system was heated at 100 °C for 5 min. Then, aniline (325 μL , 3.54 mmol) was added and the mixture was stirred at 110 °C overnight. After, the mixture was diluted with water and the product was extracted with AcOEt. The combined organic extract was dried over Na_2SO_4 , filtered and the solvent was removed under reduced pressure. The crude was purified by flash column chromatography in neutralized silica using a mixture of

hexane and AcOEt (20:1 v/v) as eluent. Compound **19** was obtained as a white solid in a yield of 92% (0.513 g, 1.36 mmol). ^1H NMR (400 MHz, DMSO- d_6) δ (ppm): 7.91 (s, 2H), 7.79 (d, $J = 2.1$ Hz, 2H), 7.50 (d, $J = 8.7$ Hz, 2H), 7.24 (dd, $J = 8.7, 2.2$ Hz, 2H), 7.15 (m, 4H), 6.96 (m, 4H), 6.68 (t, $J = 7.2$ Hz, 2H), 4.38 (q, $J = 7.0$ Hz, 2H), 1.32 (t, $J = 7.0$ Hz, 3H).

3.25. 9-Hexyl-3,6-bis[*N*-phenylamino]-9*H*-carbazole (**20**)



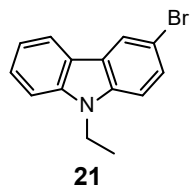
Method 1: **18** (150 mg, 0.367 mmol), tBuOK (91 mg, 0.81 mmol), Pd(AcO) $_2$ (7 mg, 0.03 mmol) and JohnPhos (26 mg, 0.088 mmol) were dissolved in toluene (2 mL) under nitrogen in a previously dried reaction tube. Then, aniline (80 μL , 0.88 mmol) was added and the mixture was stirred at 130 $^\circ\text{C}$ under microwave irradiation for 1 h. After, the

mixture was diluted with water and the product was extracted with AcOEt. The combined organic extract was dried over Na $_2$ SO $_4$, filtered and the solvent was removed under reduced pressure. The crude was purified by flash column chromatography in neutral alumina using a mixture of hexane and AcOEt (20:1 v/v) as eluent. Compound **20** was obtained as a white solid in a yield of 69% (0.109 g, 0.251 mmol).

Method 2: Analogously to the procedure described in section 3.24, this synthesis was carried out with **18** (400 mg, 0.978 mmol), tBuOK (241 mg, 2.15 mmol), Pd(AcO) $_2$ (22 mg, 0.098 mmol) and JohnPhos (88 mg, 0.29 mmol) in toluene (6 mL). The crude was purified in neutralized silica using a mixture of hexane and AcOEt (15:1 v/v) as eluent. Compound **20** was obtained as a white solid in a yield of 74% (0.313 g, 0.721 mmol).

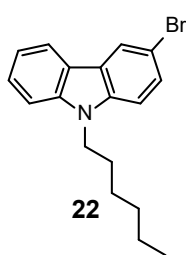
^1H NMR (400 MHz, DMSO- d_6) δ (ppm): 7.91 (s, 2H), 7.79 (d, $J = 2.1$ Hz, 2H), 7.48 (d, $J = 8.7$ Hz, 2H), 7.23 (dd, $J = 8.7, 2.1$ Hz, 2H), 7.15 (m, 4H), 6.96 (m, 4H), 6.68 (t, $J = 7.2$ Hz, 2H), 4.32 (t, $J = 7.0$ Hz, 2H), 1.75 (m, 2H), 1.33–1.19 (m, 6H), 0.83 (t, $J = 7.0$ Hz, 3H).

3.26. 3-Bromo-9-hexyl-9*H*-carbazole (**21**)



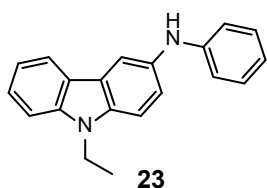
Analogously to the procedure described for the formation of **17**, this synthesis was carried out with 3-bromo-9*H*-carbazole (1.00 g, 4.06 mmol), NaH (0.243 g, 60% in mineral oil, 6.09 mmol) and bromoethane (0.60 mL, 8.1 mmol) in anhydrous DMF (5 mL). Compound **21** was obtained as a white solid in a yield of 97% (1.08 g, 3.95 mmol). ^1H NMR (400 MHz, CDCl $_3$) δ (ppm): 8.19 (d, $J = 2.2$ Hz, 1H), 8.02 (d, $J = 7.8$ Hz, 1H), 7.52 (dd, $J = 8.6, 2.2$ Hz, 1H), 7.47 (ddd, $J = 8.2, 7.2, 1.0$ Hz, 1H), 7.38 (dd, $J = 8.2, 1.0$ Hz, 1H), 7.25–7.19 (m, 2H), 4.31 (q, $J = 7.2$ Hz, 2H), 1.39 (t, $J = 7.2$ Hz, 3H).

3.27. 3-Bromo-9-ethyl-9H-carbazole (**22**)



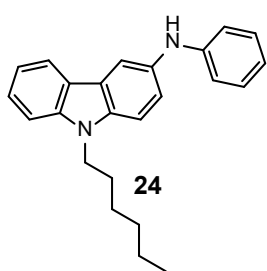
Analogously to the procedure described in section 3.26, this synthesis was carried out with 3-bromo-9H-carbazole (1.00 g, 4.06 mmol), NaH (0.243 g, 60% in mineral oil, 6.10 mmol) and 1-bromohexane (1.2 mL, 8.1 mmol) in anhydrous DMF (5 mL). Compound **22** was obtained as a white solid in a yield of 93% (1.26 g, 3.82 mmol). ^1H NMR (400 MHz, CDCl_3) δ (ppm): 8.20 (d, $J = 2.0$ Hz, 1H), 8.04 (d, $J = 7.8$ Hz, 1H), 7.53 (dd, $J = 8.5, 2.0$ Hz, 1H), 7.51–7.45 (m, 1H), 7.40 (d, $J = 8.2$ Hz, 1H), 7.28 (d, $J = 8.5$ Hz, 1H), 7.26–7.21 (m, 1H), 4.27 (t, $J = 7.3$ Hz, 2H), 1.90–1.80 (m, 2H), 1.42–1.21 (m, 6H), 0.86 (t, $J = 7.0$ Hz, 3H).

3.28. 9-Ethyl-3-[N-phenylamino]-9H-carbazole (**23**)



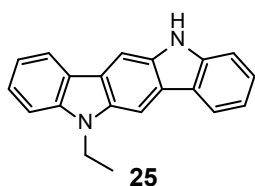
Analogously to the procedure described in section 3.24, this synthesis was carried out with **21** (500 mg, 1.82 mmol), tBuOK (225 mg, 2.01 mmol), $\text{Pd}(\text{AcO})_2$ (20 mg, 0.091 mmol) and JohnPhos (82 mg, 0.27 mmol) in toluene (9 mL) and aniline (200 μL , 2.19 mmol). The crude was purified in neutralized silica using a mixture of hexane and AcOEt (100:1 v/v) as eluent. Compound **23** was obtained as a white solid in a yield of 83% (432 mg, 1.51 mmol). ^1H NMR (400 MHz, $\text{DMSO}-d_6$) δ (ppm): 8.08 (d, $J = 7.8$ Hz, 1H), 7.94 (s, 1H), 7.88 (d, $J = 2.1$ Hz, 1H), 7.55 (dd, $J = 8.4, 6.8$ Hz, 2H), 7.42 (ddd, $J = 8.3, 7.0, 1.2$ Hz, 1H), 7.26 (dd, $J = 8.7, 2.1$ Hz, 1H), 7.22–7.09 (m, 3H), 6.97 (d, $J = 7.6$ Hz, 2H), 6.70 (t, $J = 7.2$ Hz, 1H), 4.41 (q, $J = 7.1$ Hz, 2H), 1.31 (t, $J = 7.1$ Hz, 3H).

3.29. 9-Hexyl-3-[N-phenylamino]-9H-carbazole (**24**)



Analogously to the procedure described in section 3.24, this synthesis was carried out with **22** (324 mg, 0.981 mmol), tBuOK (121 mg, 1.08 mmol), $\text{Pd}(\text{AcO})_2$ (17 mg, 0.075 mmol) and JohnPhos (44 mg, 0.15 mmol) in toluene (9 mL) and aniline (107 μL , 1.18 mmol). The crude was purified by flash column chromatography in neutralized silica using hexane as eluent. Compound **24** was obtained as a white solid in a yield of 65% (220 mg, 0.642 mmol). ^1H NMR (400 MHz, $\text{DMSO}-d_6$) δ (ppm): 8.08 (d, $J = 7.8$ Hz, 1H), 7.94 (s, 1H), 7.87 (d, $J = 2.1$ Hz, 1H), 7.54 (dd, $J = 8.4, 6.8$ Hz, 2H), 7.42 (ddd, $J = 8.3, 7.0, 1.2$ Hz, 1H), 7.25 (dd, $J = 8.7, 2.1$ Hz, 1H), 7.22–7.09 (m, 3H), 6.97 (d, $J = 7.6$ Hz, 2H), 6.70 (t, $J = 7.2$ Hz, 1H), 4.35 (t, $J = 7.0$ Hz, 2H), 1.75 (m, 2H), 1.33–1.19 (m, 6H), 0.83 (t, $J = 7.0$ Hz, 3H).

3.30. 5-Ethyl-5,11-dihydro-indolo[3,2-*b*]carbazole (25)

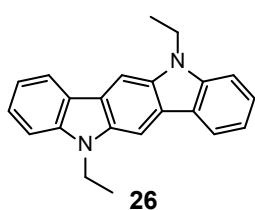


Method 1: **23** (150 mg, 0.524 mmol), K_2CO_3 (7.2 mg, 0.052 mmol) and $Pd(AcO)_2$ (5.9 mg, 0.026 mmol) were dissolved in pivalic acid (0.95 g) in a reaction tube and the mixture was stirred at 110 °C for 17 h under air. After, the mixture was cooled to room temperature, diluted with dichloromethane and washed with a solution of $NaHCO_3$. The organic extract was dried over anhydrous $MgSO_4$, filtered and the solvent was removed under reduced pressure. The crude was purified by flash column chromatography in neutralized silica using a mixture of hexane and AcOEt (20:1 v/v) as eluent. Compound **25** was obtained as a pale brown solid in a yield of 44% (66 mg, 0.23 mmol).

Method 2: **23** (100 mg, 0.349 mmol), $Cu(AcO)_2$ (127 mg, 0.70 mmol) and $Pd(AcO)_2$ (31 mg, 0.14 mmol) were dissolved in anhydrous DMF (250 μ L) in a reaction tube under nitrogen and the mixture was stirred for 1 h at 130 °C under microwave irradiation. After, the mixture was cooled to room temperature, diluted with dichloromethane and washed with a solution of $NaHCO_3$. The organic extract was dried over anhydrous $MgSO_4$, filtered and the solvent was removed under reduced pressure. The crude was purified by flash column chromatography in neutralized silica using a mixture of hexane and AcOEt (20:1 v/v) as eluent. Compound **25** was obtained as a pale brown solid in a yield of 13% (13 mg, 0.046 mmol).

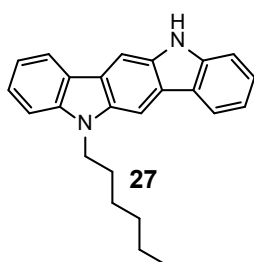
1H NMR (400 MHz, $DMSO-d_6$) δ (ppm): 11.06 (s, 1H), 8.28 (s, 1H), 8.24 (d, $J = 7.7$ Hz, 2H), 8.16 (s, 1H), 7.56 (d, $J = 8.3$ Hz, 1H), 7.49–7.42 (m, 2H), 7.38 (dd, $J = 7.5, 7.5$ Hz, 1H), 7.20–7.11 (m, 2H), 4.53 (q, $J = 7.0$ Hz, 2H), 1.39 (t, $J = 7.0$ Hz, 3H).

3.31. 5,11-Diethyl-5,11-dihydro-indolo[3,2-*b*]carbazole (26)



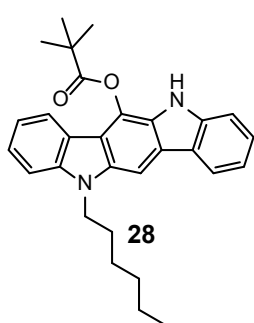
25 (50 mg, 0.18 mmol) was dissolved in anhydrous DMF (2 mL) under nitrogen. NaH (11 mg, 60% in mineral oil, 0.26 mmol) was added and the solution was stirred for 30 min at room temperature. Then, bromoethane (30 μ L, 0.35 mmol) was added and the reaction was stirred overnight. After, it was diluted with water and the product was extracted with dichloromethane. The combined organic extract was dried with $MgSO_4$, filtered and the solvent was removed under reduced pressure. The crude was purified by flash column chromatography using hexane and dichloromethane (5:1 v/v) as eluent. Compound **26** was obtained as a pale brown solid in a yield of 91% (50 mg, 0.16 mmol). 1H NMR (400 MHz, $DMSO-d_6$) δ (ppm): 8.34 (s, 2H), 8.28 (d, $J = 7.7$ Hz, 2H), 7.58 (d, $J = 8.2$ Hz, 2H), 7.46 (dd, $J = 8.1, 7.4$ Hz, 2H), 7.19 (dd, $J = 7.4, 7.4$ Hz, 2H), 4.54 (q, $J = 7.1$ Hz, 4H), 1.38 (t, $J = 7.1$ Hz, 6H).

3.32. 5-Hexyl-5,11-dihydro-indolo[3,2-*b*]carbazole (27)



Analogously to the procedure described in method 1 of section 3.30, this synthesis was carried out with **24** (198 mg, 0.578 mmol), K_2CO_3 (8.0 mg, 0.058 mmol) and $Pd(AcO)_2$ (7.5 mg, 0.033 mmol) in pivalic acid (1.05 g). The crude was purified by flash column chromatography in neutral alumina using a mixture of hexane and dichloromethane (5:1 v/v) as eluent. Nevertheless, compound **27** could not be detected.

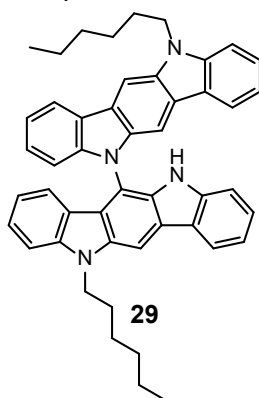
3.33. 11-Hexyl-5,11-dihydro-indolo[3,2-*b*]carbazol-6-yl pivalate (28)



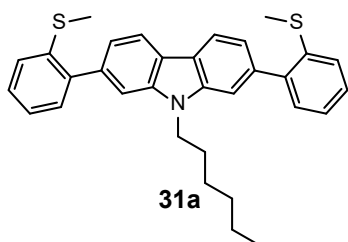
Compound **28** was obtained in a yield of 20% (51 mg, 0.12 mmol) as a by-product of the cyclization conditions described in section 3.32. 1H NMR (400 MHz, $DMSO-d_6$) δ (ppm): 10.63 (s, 1H), 8.28 (d, $J = 7.6$ Hz, 1H), 8.24 (s, 1H), 8.00 (d, $J = 7.8$ Hz, 1H), 7.60 (d, $J = 8.3$ Hz, 1H), 7.56 (d, $J = 8.1$ Hz, 1H), 7.50–7.41 (m, 2H), 7.20 (dd, $J = 7.4, 7.3$ Hz, 1H), 7.19 (dd, $J = 7.5, 7.4$ Hz, 1H), 4.49 (t, $J = 7.0$ Hz, 2H), 1.85 (m, 2H), 1.62 (s, 9H), 1.49–1.19 (m, 6H), 0.82 (t, $J = 7.2$ Hz, 3H). HRMS (ESI-MS) (m/z): calculated for $C_{29}H_{33}N_2O_2$ ($M+H$) $^+$, 441.2537; found 441.2551.

3.34. 11,11'-Dihexyl-5,11-dihydro-11*H*-5,6'-biindolo[3,2-*b*]carbazole (29)

Compound **29** was obtained in a yield of 14% (28 mg, 0.041 mmol) as a by-product of the cyclization conditions described in section 3.32. 1H NMR (400 MHz, $DMSO-d_6$) δ (ppm): δ 10.84 (s, 1H), 8.64 (s, 1H), 8.61 (s, 1H), 8.55 (d, $J = 7.5$ Hz, 1H), 8.41 (d, $J = 7.9$ Hz, 1H), 7.91 (d, $J = 7.8$ Hz, 1H), 7.54 (d, $J = 7.9$ Hz, 2H), 7.54 (s, 1H), 7.39–7.19 (m, 7H), 6.93 (dd, $J = 7.5, 7.5$ Hz, 1H), 6.79 (d, $J = 7.8$ Hz, 1H), 6.52 (dd, $J = 7.5, 7.5$ Hz, 1H), 6.10 (d, $J = 7.9$ Hz, 1H), 4.68–4.51 (m, 4H), 1.95 (m, 4H), 1.55–1.21 (m, 12H), 0.88 (t, $J = 8.4$ Hz, 3H), 0.87 (t, $J = 8.4$ Hz, 3H). MS (ESI-MS) (m/z): calculated for $C_{48}H_{46}N_4$ M^+ , 678.4; found 678.5.



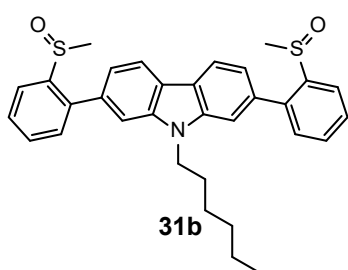
3.35. 9-Hexyl-2,7-bis(2-methylthiophenyl)-9*H*-carbazole (31a)



5 (1.15 g, 2.80 mmol), 2-methylthiophenylboronic acid (1.22 g, 7.28 mmol), $Pd(PPh_3)_4$ (0.16 g, 0.14 mmol) and K_2CO_3 (2.33 g, 16.8 mmol) were placed in a round-bottom flask. Then, the system was purged with nitrogen. A previously purged mixture of THF and water (6:1 v/v, 58 mL) was added to the flask and stirred under reflux overnight. The reaction mixture was extracted with

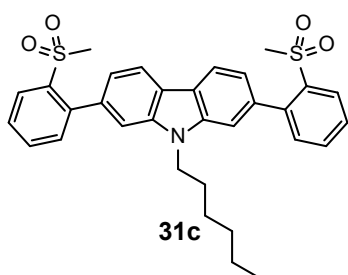
CH₂Cl₂. Then, the combined organic extract was dried over anhydrous MgSO₄, filtered and the solvent was removed under reduced pressure. The crude was purified by flash column chromatography using a mixture of hexane and dichloromethane (20:1 v/v) as eluent. Compound **31a** was obtained as a white solid in a yield of 80% (1.11 g, 2.25 mmol). ¹H NMR (400 MHz, CDCl₃) δ (ppm): 8.14 (d, *J* = 8.0 Hz, 2H), 7.47 (d, *J* = 8.0 Hz, 2H), 7.40–7.31 (m, 6H), 7.29–7.23 (m, 4H), 4.30 (t, *J* = 7.3 Hz, 2H), 2.37 (s, 6H), 1.94–1.83 (m, 2H), 1.45–1.20 (m, 6H), 0.84 (t, *J* = 7.1 Hz, 3H). ¹³C NMR (100 MHz, CDCl₃) δ (ppm): 141.9, 140.8, 138.2, 137.7, 130.5, 127.9, 125.3, 124.8, 122.2, 120.5, 120.2, 109.9, 43.4, 31.8, 29.3, 27.2, 22.7, 16.1, 14.2. HRMS (ESI-MS) (*m/z*): calculated for C₃₂H₃₄NS₂ (M+H)⁺, 496.2127; found 496.2131.

3.36. 9-Hexyl-2,7-bis(2-methylsulfinylphenyl)-9H-carbazole (31b)



31a (602 mg, 1.21 mmol) was dissolved in glacial acetic acid (40 mL) and cooled at 0 °C. Hydrogen peroxide (35%, 218 μL, 2.55 mmol) was added carefully and the mixture was stirred overnight at room temperature. After, the solvents were removed under reduced pressure. The crude was purified by flash column chromatography using a mixture of hexane and ethyl acetate (1:1 v/v) as eluent. Compound **31b**, corresponding to a diastereomeric mixture, was obtained as a pale yellow solid in a yield of 94% (600 mg, 1.14 mmol). ¹H NMR (400 MHz, CDCl₃) δ (ppm): 8.19 (d, *J* = 7.9, 2H), 8.17 (s + s', d, *J* = 7.9, 2H), 7.67 (s + s', dd, *J* = 7.6, 7.4 Hz, 2H), 7.60 (s + s', dd, *J* = 7.4, 7.4 Hz, 2H), 7.25 (s + s', d, *J* = 7.4 Hz, 2H), 7.46 (s, 2H), 7.25 (dd, *J* = 7.9, 1.4 Hz, 2H), 4.32 (t, *J* = 7.2 Hz, 2H), 2.34 (s, 6H), 1.87 (m, 2H), 1.45–1.20 (m, 6H), 0.83 (t, *J* = 7.1 Hz, 3H). ¹³C NMR (100 MHz, CDCl₃) δ (ppm): 144.2, 141.1, 140.3, 136.0, 130.8, 130.8, 128.8, 123.6, 122.4, 121.2, 120.5, 109.7, 43.6, 41.6, 31.7, 29.3, 27.3, 22.7, 14.1. HRMS (ESI-MS) (*m/z*): calculated for C₃₂H₃₄NO₂S₂ (M+H)⁺, 528.2025; found 528.2023.

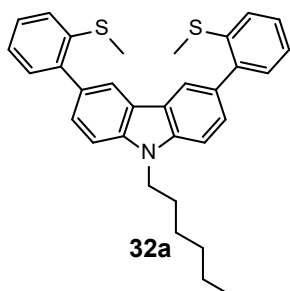
3.37. 9-Hexyl-2,7-bis(2-methylsulfonylphenyl)-9H-carbazole (31c)



31a (105 mg, 0.212 mmol) was dissolved in glacial acetic acid (3.5 mL) at 50 °C. Hydrogen peroxide (35%, 516 μL, 6.00 mmol) was added carefully and the mixture was stirred at 50 °C for 4.5 h. After, the mixture was poured into a solution of NaHCO₃ and was extracted with dichloromethane. The combined organic extract was dried over anhydrous MgSO₄ and the solvent was removed under reduced pressure. The crude was purified by flash column chromatography using a mixture of hexane and ethyl acetate (2:1 v/v) as eluent. Compound

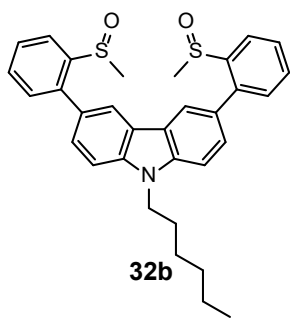
31c was obtained as a white solid in a yield of 80% (95 mg, 0.17 mmol). ^1H NMR (400 MHz, CDCl_3) δ (ppm): 8.30 (dd, $J = 8.0, 1.4$ Hz, 2H), 8.18 (d, $J = 8.0$ Hz, 2H), 7.72–7.67 (m, 4H), 7.63–7.57 (m, 2H), 7.53 (dd, $J = 7.5, 1.4$ Hz, 2H), 7.30 (dd, $J = 8.0, 1.5$ Hz, 2H), 4.33 (t, $J = 7.3$ Hz, 2H), 2.57 (s, 6H), 1.94–1.85 (m, 2H), 1.39–1.19 (m, 6H), 0.81 (t, $J = 7.0$ Hz, 3H). HRMS (ESI-MS) (m/z): calculated for $\text{C}_{32}\text{H}_{34}\text{NO}_4\text{S}_2$ ($\text{M}+\text{NH}_4$) $^+$, 577.2189; found 577.2178.

3.38. 9-Hexyl-3,6-bis(2-methylthiophenyl)-9H-carbazole (32a)



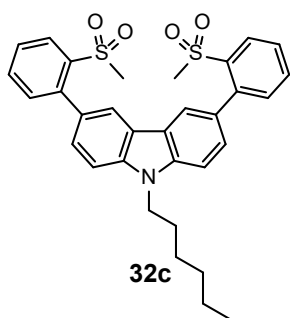
Analogously to the procedure described in section 3.35, this synthesis was carried out with **18** (1.15 g, 2.81 mmol), 2-methylthiophenylboronic acid (1.23 g, 7.31 mmol), $\text{Pd}(\text{PPh}_3)_4$ (0.16 g, 0.14 mmol) and K_2CO_3 (2.33 g, 16.9 mmol) in a mixture of THF and water (6:1 v/v, 58 mL). Compound **32a** was obtained as a white solid in a yield of 85% (1.19 g, 2.40 mmol). ^1H NMR (400 MHz, CDCl_3) δ (ppm): 8.12 (d, $J = 1.7$ Hz, 2H), 7.54 (dd, $J = 8.1, 1.7$ Hz, 2H), 7.46 (d, $J = 8.4$ Hz, 2H), 7.38–7.28 (m, 4H), 7.33 (d, $J = 8.1$ Hz, 2H), 7.25–7.20 (m, 2H), 4.34 (t, $J = 7.4$ Hz, 2H), 1.99–1.89 (m, 2H), 1.53–1.28 (m, 6H), 0.90 (t, $J = 7.0$ Hz, 3H). ^{13}C NMR (100 MHz, CDCl_3) δ (ppm): 141.8, 140.4, 137.7, 131.4, 130.7, 127.6, 127.4, 125.1, 124.8, 123.0, 121.4, 108.4, 43.6, 31.8, 29.2, 27.2, 22.7, 16.1, 14.2. HRMS (ESI-MS) (m/z): calculated for $\text{C}_{32}\text{H}_{34}\text{NS}_2$ ($\text{M}+\text{H}$) $^+$, 496.2127; found 496.2122.

3.39. 9-Hexyl-3,6-bis(2-methylsulfinylphenyl)-9H-carbazole (32b)



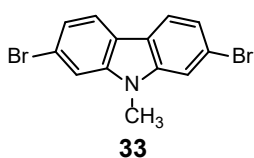
Analogously to the procedure described in section 3.36, this synthesis was carried out with **32a** (0.250 g, 0.504 mmol) and hydrogen peroxide (35%, 93 μL , 1.1 mmol) in glacial acetic acid (17 mL). Compound **32b**, corresponding to a diastereomeric mixture, was obtained as a pale yellow solid in a yield of 95% (0.254 g, 0.481 mmol). ^1H NMR (400 MHz, CDCl_3) δ (ppm): 8.17–8.13 (m, 2H), 8.11–8.07 (m, 2H), 7.65–7.55 (m, 4H), 7.55–7.48 (m, 4H), 7.45 and 7.42 (dd + dd', $J = 7.4, 1.3$ Hz, 2H), 4.38 (t, $J = 7.4$ Hz, 2H), 2.37 and 2.35 (s + s', 6H), 2.00–1.91 (m, 2H), 1.53–1.29 (m, 6H), 0.90 (t, $J = 7.1$ Hz, 3H). ^{13}C NMR (100 MHz, CDCl_3) δ (ppm): 144.3, 140.7, 140.2, 131.1, 131.0, 130.9, 130.8, 129.2, 128.5, 127.5, 123.6, 123.0, 121.3, 121.3, 109.3, 43.7, 41.7, 41.7, 31.7, 29.2, 27.2, 22.72, 14.1. HRMS (ESI-MS) (m/z): calculated for $\text{C}_{32}\text{H}_{34}\text{NO}_2\text{S}_2$ ($\text{M}+\text{H}$) $^+$, 528.2025; found 528.2024.

3.40. 9-Hexyl-3,6-Bis(2-methylsulfonylphenyl)-9H-carbazole (32c)



Analogously to the procedure described in section 3.37, this synthesis was carried out with **32a** (62 mg, 0.13 mmol) and hydrogen peroxide (35%, 321 μ L, 3.75 mmol) in glacial acetic acid (2.5 mL). Compound **32c** was obtained as a white solid in a yield of 86% (60 mg, 0.11 mmol). $^1\text{H NMR}$ (400 MHz, CDCl_3) δ (ppm): 8.27 (dd, $J = 8.2, 1.5$ Hz, 2H), 8.18 (dd, $J = 1.5, 0.6$ Hz, 2H), 7.69–7.63 (m, 4H), 7.59–7.54 (m, 2H), 7.51 (dd, $J = 8.2, 0.6$ Hz, 2H), 7.48 (dd, $J = 7.5, 1.4$ Hz, 2H), 4.38 (t, $J = 7.4$ Hz, 2H), 2.60 (s, 6H), 2.00–1.91 (m, 2H), 1.54–1.28 (m, 6H), 0.91 (t, $J = 7.0$ Hz, 3H). HRMS (ESI-MS) (m/z): calculated for $\text{C}_{32}\text{H}_{34}\text{NO}_4\text{S}_2$ ($\text{M}+\text{NH}_4$) $^+$, 577.2189; found 577.2185.

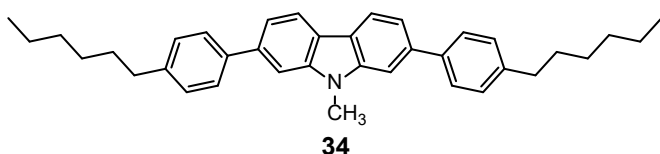
3.41. 2,7-Dibromo-9-methyl-9H-carbazole (33)



3 (0.749 g, 2.31 mmol) was dissolved in anhydrous DMF (5 mL) under nitrogen. NaH (0.138 g, 60% in mineral oil, 3.46 mmol) was added and the solution was stirred for 30 min at room temperature. Then, iodomethane (0.29 mL, 4.6 mmol) was added and the reaction was stirred overnight. After, it was diluted with water and the resultant precipitate was filtered and dried. The crude was purified by flash column chromatography using hexane as eluent. Compound **33** was obtained as a white solid in a yield of 89% (0.693 g, 2.04 mmol). $^1\text{H NMR}$ (400 MHz, CDCl_3) δ (ppm): 7.89 (d, $J = 8.3$ Hz, 2H), 7.55 (d, $J = 1.7$ Hz, 2H), 7.35 (dd, $J = 8.3, 1.7$ Hz, 2H), 3.79 (s, 3H).

3.42. 2,7-Bis(4-hexylphenyl)-9-methyl-9H-carbazole (34)

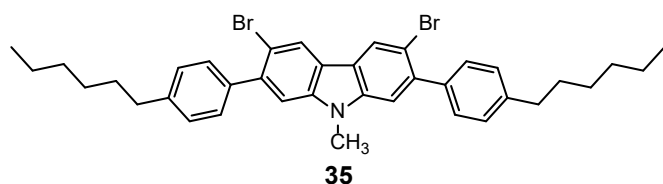
33 (1.00 g, 2.95 mmol), 4-hexylphenylboronic acid (1.58 g, 7.67 mmol), $\text{Pd}(\text{PPh}_3)_4$ (0.17 g, 0.15 mmol) and K_2CO_3 (2.44 g, 17.7 mmol) were dissolved in a mixture of THF and water



(6:1 v/v, 62 mL) under nitrogen and stirred under reflux overnight. The reaction mixture was extracted with CH_2Cl_2 . The combined organic extract was dried over anhydrous MgSO_4 , filtered and the solvent was removed under reduced pressure. The crude was purified by flash column chromatography using a mixture of hexane and ethyl acetate (100:1 v/v) as eluent. Compound **34** was obtained as a white solid in a yield of 65% (0.970 g, 1.93 mmol). $^1\text{H NMR}$ (400 MHz, CDCl_3) δ (ppm): 8.12 (d, $J = 8.1$ Hz, 2H), 7.66 (d, $J = 7.9$ Hz, 4H), 7.58 (d, $J = 1.5$ Hz, 2H), 7.48 (dd, $J = 8.1, 1.5$ Hz, 2H), 7.30 (d, $J = 7.9$ Hz, 4H), 3.93 (s, 3H), 2.68 (t, $J = 7.9$ Hz, 4H), 1.68 (m, 4H), 1.43–1.29 (m, 12H), 0.91 (t, $J = 7.0$ Hz, 6H).

3.43. 3,6-Dibromo-2,7-bis(4-hexylphenyl)-9-methyl-9H-carbazole (35)

34 (0.968 g, 1.93 mmol) was dissolved in a mixture of glacial acetic acid and chloroform (1:1 v/v, 70 mL) at 0 °C. *N*-bromosuccinimide (0.704 g, 3.96 mmol) was added in portions and

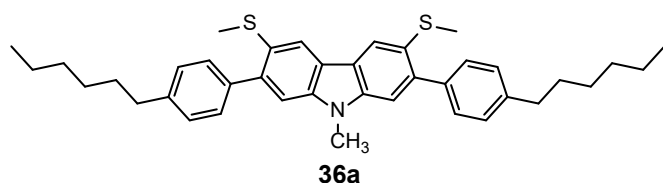


the mixture was stirred overnight at room temperature in the dark. After, the reaction was quenched with water and the product was extracted

with CH₂Cl₂. The combined organic extract was dried over anhydrous MgSO₄, filtered and the solvent was removed under reduced pressure. The crude was purified by flash column chromatography using hexane as eluent. Compound **35** was obtained as a white solid in a yield of 86% (1.09 g, 1.65 mmol). ¹H NMR (400 MHz, CDCl₃) δ (ppm): 8.32 (s, 2H), 7.43 (d, *J* = 8.1 Hz, 4H), 7.34 (s, 2H), 7.29 (d, *J* = 8.1 Hz, 4H), 3.78 (s, 3H), 2.69 (t, *J* = 7.8 Hz, 4H), 1.69 (m, 4H), 1.45–1.29 (m, 12H), 0.91 (t, *J* = 7.0 Hz, 6H).

3.44. 2,7-Bis(4-hexylphenyl)-9-methyl-3,6-bis(methylthio)-9H-carbazole (36a)

35 (510 mg, 0.776 mmol) was dissolved in anhydrous THF (30 mL) under nitrogen and cooled to -78 °C. *n*-Butyllithium (2.5 M in hexane, 0.78 mL, 1.9 mmol) was carefully added

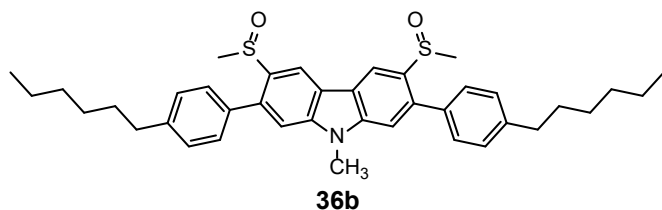


and stirred for 1 h. Then, dimethyl disulfide (0.17 mL, 1.9 mmol) was added dropwise, and the mixture was stirred at room temperature

overnight. The mixture was slowly poured into water under continuous agitation and after, the product was extracted with CH₂Cl₂. The combined organic extract was dried over anhydrous MgSO₄, filtered and the solvent was removed under reduced pressure. The crude was purified by flash column chromatography using a mixture of hexane and dichloromethane (10:1 v/v) as eluent. Compound **36a** was obtained as a white solid in a yield of 62% (287 mg, 0.484 mmol). ¹H NMR (400 MHz, CDCl₃) δ (ppm): 8.08 (s, 2H), 7.45 (d, *J* = 7.9 Hz, 4H), 7.28 (d, *J* = 7.9 Hz, 4H), 7.28 (s, 2H), 3.79 (s, 3H), 2.69 (t, *J* = 7.8 Hz, 4H), 2.41 (s, 6H), 1.69 (m, 4H), 1.45–1.29 (m, 12H), 0.91 (t, *J* = 6.9 Hz, 6H). ¹³C NMR (100 MHz, CDCl₃) δ (ppm): 142.3, 140.9, 140.2, 139.0, 129.7, 128.2, 126.9, 122.0, 120.2, 110.7, 36.0, 31.9, 31.6, 29.4, 29.3, 22.8, 18.4, 14.3.

3.45. 2,7-Bis(4-hexylphenyl)-9-methyl-3,6-bis(methylsulfinyl)-9H-carbazole (36b)

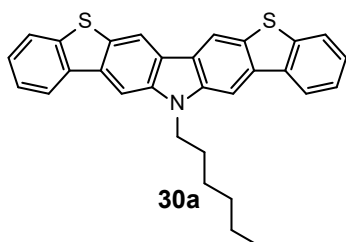
36a (200 mg, 0.337 mmol) was dissolved in a mixture of glacial acetic acid and chloroform (1:1 v/v, 24 mL). Hydrogen peroxide (35%, 61 μ L, 0.72 mmol) was subsequently added and



the mixture was stirred overnight at room temperature. The solvents were removed under reduced pressure and the crude was purified by flash column chromatography

using a mixture of hexane and ethyl acetate (1:1 v/v) as eluent. Compound **36b**, corresponding to a diastereomeric mixture, was obtained as a pale yellow solid in a yield of 86% (182 mg, 0.291 mmol). ^1H NMR (400 MHz, CDCl_3) δ (ppm): 8.96 and 8.95 (s and s', 2H), 7.41 and 7.40 (d and d', $J = 8.0$ Hz, 4H), 7.36 (s and s', 2H), 7.31 (d, $J = 8.0$ Hz, 4H), 3.91 (s, 3H), 2.70 (t, $J = 7.8$ Hz, 4H), 2.48 and 2.44 (s and s', 6H), 1.69 (m, 4H), 1.45–1.30 (m, 12H), 0.91 (t, $J = 7.0$ Hz, 6H). ^{13}C NMR (100 MHz, CDCl_3) δ (ppm): 143.4, 143.4, 143.0, 142.9, 138.4, 138.2, 136.0, 135.5, 135.5, 129.6, 129.5, 129.0, 128.9, 128.9, 122.5, 122.4, 117.3, 117.2, 110.7, 110.7, 42.7, 42.5, 35.8, 31.8, 31.5, 29.8, 29.1, 22.7, 14.2.

3.46. 14-Hexyl-14H-bis[1]benzothieno[3,2-b:2',3'-h]carbazole (30a)

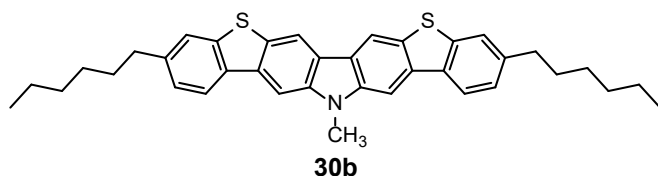


31b (200 mg, 0.379 mmol) and phosphorus pentoxide (27 mg, 0.19 mmol) were dissolved in trifluoromethanesulfonic acid (5.7 mL) in a round-bottom flask equipped with a drying tube, and the mixture was stirred at room temperature for 72 h. The crude was poured into a mixture of ice-water (50 mL) and the

resulting yellow precipitate was filtered. The precipitate was then dissolved in pyridine (30 mL) and refluxed overnight. The product was precipitated by adding water to the mixture, filtered and purified by flash column chromatography using a mixture of hexane and dichloromethane (10:1 v/v) as eluent. Compound **30a** was obtained as a bright yellow solid in a yield of 95% (166 mg, 0.358 mmol). ^1H NMR (400 MHz, CDCl_3) δ (ppm): 8.49 (s, 2H), 8.24–8.20 (m, 2H), 8.04 (s, 2H), 7.84–7.79 (m, 2H), 7.46–7.39 (m, 4H), 4.45 (t, $J = 7.3$ Hz, 2H), 2.01–1.92 (m, 2H), 1.44–1.19 (m, 6H), 0.82 (t, $J = 7.2$ Hz, 3H). ^{13}C NMR (100 MHz, CDCl_3) δ (ppm): 140.6, 140.5, 135.8, 134.7, 130.5, 126.8, 124.2, 123.4, 123.1, 121.5, 114.2, 100.5, 43.6, 31.8, 28.7, 27.2, 22.7, 14.2.

3.47. 3,10-Dihexyl-14-methyl-14H-bis[1]benzothieno[3,2-*b*:2',3'-*h*]carbazole (**30b**)

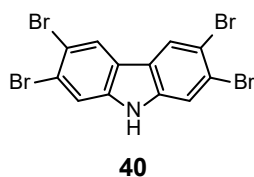
36b (182 mg, 0.291 mmol) and phosphorus pentoxide (21 mg, 0.15 mmol) were dissolved in trifluoromethanesulfonic acid (4.4 mL) and stirred at room temperature for 72 h. The



crude was poured into a mixture of ice-water (50 mL) and the resulting yellow precipitate was filtered. The precipitate was then dissolved in

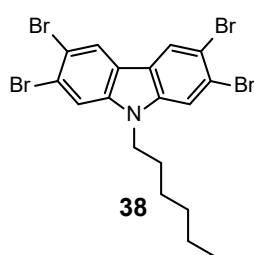
pyridine (25 mL) and refluxed overnight. The product was precipitated by adding water to the mixture, filtered and purified by flash column chromatography using a mixture of hexane and dichloromethane (10:1 v/v) as eluent. Compound **30b** was obtained as a dark yellow solid in a yield of 66% (107 mg, 0.190 mmol). ¹H NMR (400 MHz, CDCl₃) δ (ppm): 8.50 (s, 2H), 8.16 (d, *J* = 8.1 Hz, 2H), 8.04 (s, 2H), 7.68 (s, 2H), 7.31 (dd, *J* = 8.1, *J* = 1.5 Hz, 2H), 4.03 (s, 3H), 2.78 (t, *J* = 7.8 Hz, 4H), 1.73 (m, 4H), 1.45–1.27 (m, 12H), 0.90 (t, *J* = 7.1 Hz, 6H). ¹³C NMR (125 MHz, CDCl₃) δ (ppm): 142.1, 141.2, 140.6, 134.8, 133.7, 130.5, 125.2, 122.9, 122.5, 121.2, 114.0, 100.0, 36.7, 31.9, 31.8, 29.2, 22.8, 14.3.

3.48. 2,3,6,7-Tetrabromo-9H-carbazole (**40**)



3 (0.750 g, 2.31 mmol) was dissolved in a mixture of glacial acetic acid and chloroform (1:1 v/v, 70 mL) at 0 °C. *N*-bromosuccinimide (0.842 g, 4.73 mmol) was added in portions and the mixture was stirred overnight at room temperature in the dark. Then, the reaction was quenched with water and the product was extracted with CH₂Cl₂. The organic layers were washed with a saturated solution of NaHCO₃, dried over anhydrous MgSO₄, filtered and the solvent was removed under reduced pressure. The crude was purified by flash column chromatography using a mixture of hexane and ethyl acetate (10:1 v/v) as eluent. Compound **40** was obtained as a white solid in a yield of 71% (0.795 g, 1.65 mmol). ¹H NMR (400 MHz, CDCl₃) δ (ppm): 8.25 (s, 2H), 8.10 (s, 1H), 7.74 (s, 2H).

3.49. 2,3,6,7-Tetrabromo-9-hexyl-9H-carbazole (**38**)

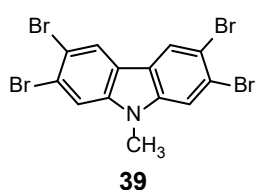


Method 1 (from 5): Analogously to the procedure described in section 3.48, this synthesis was carried out with **5** (0.792 g, 1.94 mmol) and *N*-bromosuccinimide (0.706 g, 3.97 mmol) in a mixture of glacial acetic acid and chloroform (1:1 v/v, 50 mL). The crude was purified by flash column chromatography using hexane as eluent. Compound **38** was obtained as a white solid in a yield of 65% (0.713 g, 1.26 mmol).

Method 2 (from 40): **40** (0.200 g, 0.414 mmol) was dissolved in anhydrous DMF (3 mL) under nitrogen. NaH (0.024 g, 60% in mineral oil, 0.62 mmol) was added and the solution was stirred for 30 min at room temperature. Then, 1-bromohexane (0.12 mL, 0.82 mmol) was added and the reaction was stirred overnight. After, it was diluted with water and the product was extracted with CH₂Cl₂. The organic layers were dried over anhydrous MgSO₄, filtered and the solvent was removed under reduced pressure. The crude was purified by flash column chromatography using hexane as eluent. Compound **38** was obtained as a white solid in a yield of 91% (0.210 g, 0.370 mmol).

¹H NMR (400 MHz, CDCl₃) δ (ppm): 8.24 (s, 2H), 7.66 (s, 2H), 4.16 (t, *J* = 7.3 Hz, 2H), 1.87–1.77 (m, 2H), 1.38–1.24 (m, 6H), 0.88 (t, *J* = 7.0 Hz, 3H).

3.50. 2,3,6,7-Tetrabromo-9-methyl-9H-carbazole (**39**)



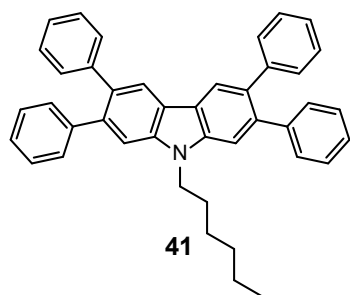
Analogously to the procedures described in section 3.49, this synthesis was carried out as follows:

Method 1 (from 33): **33** (0.670 g, 1.98 mmol) and *N*-bromosuccinimide (0.726 g, 4.08 mmol) in a mixture of glacial acetic and chloroform (1:1 v/v, 70 mL). The crude was purified by flash column chromatography using a mixture of hexane and ethyl acetate (100:1 v/v) as eluent. Compound **39** was obtained as a white solid in a yield of 66% (0.650 g, 1.31 mmol).

Method 2 (from 40): **40** (0.456 g, 0.944 mmol) and NaH (0.057 g, 60% in mineral oil, 1.4 mmol) in anhydrous DMF (3 mL). Then, iodomethane (0.117 mL, 1.888 mmol). The crude was purified by flash column chromatography using hexane as eluent. Compound **39** was obtained as a white solid in a yield of 96% (0.449 g, 0.904 mmol).

¹H NMR (400 MHz, CDCl₃) δ (ppm): 8.24 (s, 2H), 7.68 (s, 2H), 3.77 (s, 3H).

3.51. 9-Hexyl-2,3,6,7-tetraphenyl-9H-carbazole (**41**)

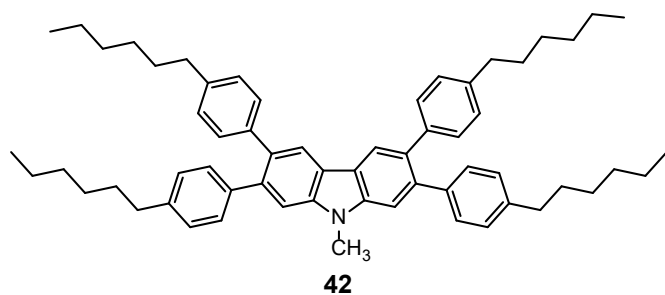


38 (0.593 g, 1.05 mmol), phenylboronic acid (0.583 g, 4.78 mmol), Pd(PPh₃)₂Cl₂ (0.037 g, 0.053 mmol), PPh₃ (0.027 g, 0.10 mmol) and K₂CO₃ (2.93 g, 21.2 mmol) were dissolved in a mixture of DMF and H₂O (27.9 mL, 9:1 v/v) under nitrogen and stirred at 110 °C overnight. After cooling to room temperature, the mixture was poured into water and the resultant precipitate was filtered off and dried. The solid was purified by flash column chromatography using a mixture of hexane and dichloromethane (from 100:1 to 25:1 v/v) as eluent. Compound **41** was obtained as a white

solid in a yield of 81% (0.477 g, 0.858 mmol). ^1H NMR (400 MHz, CDCl_3) δ (ppm): 8.15 (s, 2H), 7.44 (s, 2H), 7.32–7.15 (m, 12H), 4.36 (t, $J = 7.3$ Hz, 2H), 1.98–1.88 (m, 2H), 1.50–1.23 (m, 6H), 0.87 (t, $J = 6.9$ Hz, 3H).

3.52. 2,3,6,7-Tetrakis(4-hexylphenyl)-9-methyl-9H-carbazole (42)

Analogously to the procedure described in section 3.51, this synthesis was carried out with **39** (0.450 g, 0.906 mmol), 4-hexylphenylboronic acid (0.840 g, 4.08 mmol), $\text{Pd}(\text{PPh}_3)_2\text{Cl}_2$ (0.034 g, 0.048 mmol), PPh_3 (0.024 g, 0.091 mmol) and K_2CO_3 (2.51 g, 18.1 mmol) in a

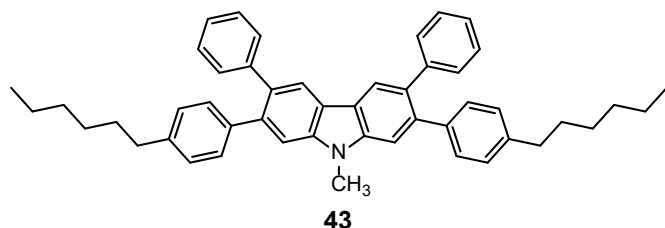


mixture of DMF and H_2O (25 mL, 9:1 v/v). Then, the product was extracted with CH_2Cl_2 . The organic layers were dried over anhydrous MgSO_4 , filtered and the solvent was removed under reduced pressure. The crude was purified by flash column

chromatography using a mixture of hexane and dichloromethane (20: v/v) as eluent. Compound **42** was obtained as a white solid in a yield of 81% (0.606 g, 0.737 mmol). ^1H NMR (400 MHz, CDCl_3) δ (ppm): 8.11 (s, 2H), 7.42 (s, 2H), 7.17 (d, $J = 8.1$ Hz, 4H), 7.13 (d, $J = 8.1$ Hz, 4H), 7.06 (d, $J = 8.1$ Hz, 4H), 7.03 (d, $J = 8.1$ Hz, 4H), 3.90 (s, 3H), 2.59 (t, $J = 6.9$ Hz, 4H), 2.57 (t, $J = 6.9$ Hz, 4H), 1.66–1.55 (m, 8H), 1.36–1.25 (m, 24H), 0.92–0.86 (m, 12H).

3.53. 3,6-Bis(4-hexylphenyl)-2,7-diphenyl-9-methyl-9H-carbazole (43)

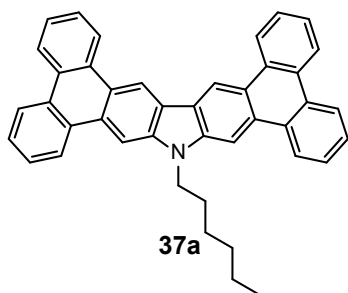
35 (0.501 g, 0.760 mmol), phenylboronic acid (0.252 g, 2.07 mmol), $\text{Pd}(\text{PPh}_3)_4$ (0.045 g, 0.039 mmol) and K_2CO_3 (0.630 g, 4.56 mmol) were dissolved in a mixture of THF and H_2O (16.3 mL, 6:1 v/v) under nitrogen. The solution was stirred under reflux overnight. Then,



the product was extracted with CH_2Cl_2 . The organic layers were dried over anhydrous MgSO_4 , filtered and the solvent was removed under reduced pressure. The crude was

purified by flash column chromatography using a mixture of hexane and dichloromethane (20:1 v/v) as eluent. Compound **43** was obtained as a white solid in a yield of 91% (0.452 g, 0.691 mmol). ^1H NMR (400 MHz, CDCl_3) δ (ppm): 8.13 (s, 2H), 7.44 (s, 2H), 7.25–7.19 (m, 10H), 7.18 (d, $J = 8.0$ Hz, 4H), 7.07 (d, $J = 8.0$ Hz, 4H), 3.91 (s, 3H), 2.59 (t, $J = 7.7$ Hz, 4H), 1.65–1.57 (m, 4H), 1.35–1.27 (m, 12H), 0.89 (t, $J = 6.7$ Hz, 6H).

3.54. 10-hexyl-10H-diphenanthro[9,10-*b*:9',10'-*h*]carbazole (**37a**)

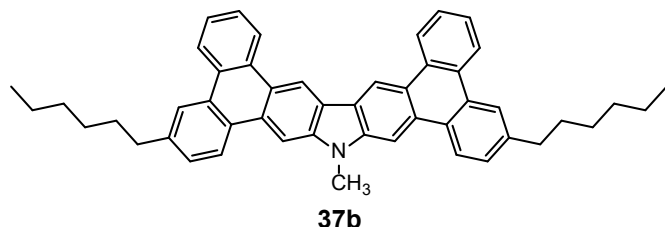


41 (0.278 g, 0.500 mmol) was dissolved in anhydrous dichloromethane (15 mL) under nitrogen atmosphere. Then, a previously purged solution of anhydrous FeCl₃ (1.62 g, 10.0 mmol) in nitromethane (5 mL) was added and the mixture was stirred for 3 h at room temperature. After, the reaction was diluted with methanol and the resultant precipitate was filtered off and thoroughly washed with the same solvent.

The precipitate was dried and purified by flash column chromatography using a mixture of hexane and dichloromethane (20:1 v/v) as eluent. Compound **37a** was obtained as a yellow solid in a yield of 80% (0.221 g, 0.401 mmol). ¹H NMR (400 MHz, CDCl₃) δ (ppm): 9.60 (s, 2H), 8.96 (d, *J* = 8.2 Hz, 2H), 8.82 (d, *J* = 8.1 Hz, 2H), 8.71 (dd, *J* = 8.4, 8.4 Hz, 4H), 8.59 (s, 2H), 7.81–7.61 (m, 8H), 4.65 (t, *J* = 7.2 Hz, 2H), 2.25–2.04 (m, 2H), 1.65–1.25 (m, 6H), 0.91 (t, *J* = 7.2 Hz, 3H). ¹³C NMR (125 MHz, CDCl₃) δ (ppm): 142.5, 131.1, 130.5, 130.2, 129.6, 128.8, 127.5, 127.3, 127.2, 126.3, 124.0, 123.7, 123.6, 123.5, 123.2, 123.2, 115.4, 101.3, 43.4, 31.8, 29.9, 28.9, 27.3, 22.8, 14.2. HRMS (ESI-MS) (*m/z*): calculated for C₄₂H₃₃N M⁺, 551.2608; found 551.2611.

3.55. 6,14-Dihexyl-10-methyl-10H-diphenanthro[9,10-*b*:9',10'-*h*]carbazole (**37b**)

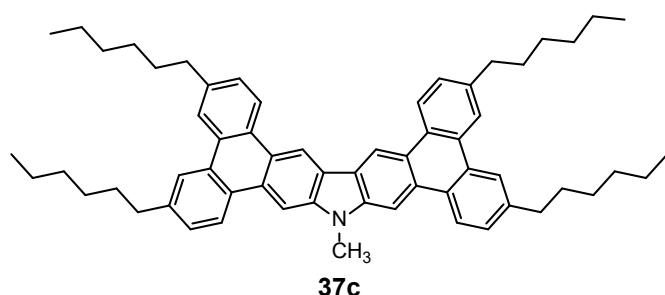
43 (0.220 g, 0.336 mmol) was dissolved in anhydrous dichloromethane (10.2 mL) under nitrogen atmosphere. Then, a previously purged solution of anhydrous FeCl₃ (1.09 g,



6.72 mmol) in nitromethane (3.4 mL) was added and the mixture was stirred for 15 min at 0 °C. After, the reaction was diluted with methanol and the resultant precipitate was

filtered off and thoroughly washed with the same solvent. The precipitate was dried and purified by flash column chromatography in neutral alumina using a mixture of hexane and ethyl acetate (20:1 v/v) as eluent. Compound **37b** was obtained as a bright yellow solid in a yield of 71% (0.154 g, 0.237 mmol). ¹H NMR (400 MHz, CDCl₃) δ (ppm): 9.29 (s, 2H), 8.80 (d, *J* = 8.1 Hz, 2H), 8.63 (d, *J* = 7.8 Hz, 2H), 8.59 (d, *J* = 8.5 Hz, 2H), 8.42 (s, 2H), 8.26 (s, 2H), 7.70–7.64 (m, 2H), 7.63–7.58 (m, 2H), 7.49 (dd, *J* = 8.3, 1.7 Hz, 2H), 3.87 (s, 3H), 2.87 (t, *J* = 7.7 Hz, 4H), 1.86–1.75 (m, 4H), 1.52–1.32 (m, 12H), 0.93 (t, *J* = 7.1 Hz, 6H). ¹³C NMR (100 MHz, CDCl₃) δ (ppm): 142.7, 141.9, 131.2, 130.0, 129.6, 128.8, 128.4, 127.9, 127.3, 126.0, 123.5, 123.5, 123.4, 123.2, 123.0, 122.8, 115.0, 100.6, 36.5, 32.0, 31.8, 29.3, 29.3, 22.8, 14.3.

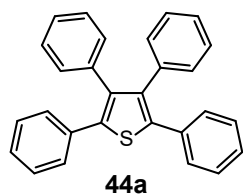
3.56. 3,6,14,17-Tetrahexyl-10-methyl-10H-diphenanthro[9,10-*b*:9',10'-*h*]-carbazole (**37c**)



Analogously to the procedure described in section 3.55, this synthesis was carried out with **42** (0.411 g, 0.500 mmol) and anhydrous FeCl₃ (1.62 g, 10.0 mmol) in anhydrous dichloromethane (15 mL) and nitromethane (5 mL). The

precipitate was dried and purified by flash column chromatography in neutral alumina using a mixture of hexane and ethyl acetate (50:1 v/v) as eluent. Further purification was carried out by precipitating the product in the eluent mixture and removing the solvent. Compound **37c** was obtained as a bright yellow solid in a yield of 33% (0.135 g, 0.165 mmol). ¹H NMR (400 MHz, CDCl₃) δ (ppm): 9.50 (s, 2H), 8.84 (d, *J* = 8.4 Hz, 2H), 8.72 (d, *J* = 8.5 Hz, 2H), 8.50 (s, 2H), 8.48 (s, 2H), 8.46 (s, 2H), 7.57 (dd, *J* = 8.5, 1.0 Hz, 2H), 7.53 (dd, *J* = 8.4, 1.0 Hz, 2H), 4.14 (s, 3H), 2.91 (t, *J* = 7.8 Hz, 8H), 1.87–1.77 (m, 8H), 1.52–1.33 (m, 24H), 0.93 (t, *J* = 7.0 Hz, 6H), 0.92 (t, *J* = 7.0 Hz, 6H). ¹³C NMR (100 MHz, CDCl₃) δ (ppm): 142.4, 141.6, 140.5, 130.0, 129.2, 129.1, 128.7, 128.5, 128.0, 127.6, 123.5, 123.4, 123.2, 123.0, 122.8, 122.8, 114.64, 100.45, 36.5, 32.1, 32.0, 31.9, 29.4, 29.4, 31.9, 29.4, 29.4, 22.9, 22.9, 14.3, 14.3.

3.57. 2,3,4,5-Tetraphenylthiophene (**44a**)

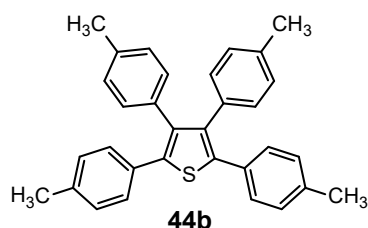


General procedure: Tetrabromothiophene (0.402 g, 1.01 mmol), phenylboronic acid (0.554 g, 4.54 mmol), Pd(PPh₃)₂Cl₂ (0.035 g, 0.050 mmol), PPh₃ (0.028 g, 0.11 mmol) and K₂CO₃ (2.76 g, 20.0 mmol) were dissolved in a mixture of DMF and H₂O (22.5 mL, 8:1 v/v) under nitrogen and stirred at 110 °C overnight. After cooling to room

temperature, the reaction mixture was diluted with water and the resulting precipitate was filtered off and dried. The solid was purified by flash column chromatography using hexane as eluent.

Compound **44a** was obtained as a white solid in a yield of 62% (0.241 g, 0.620 mmol). ¹H NMR (400 MHz, CDCl₃) δ (ppm): 7.25–7.18 (m, 10H), 7.15–7.08 (m, 6H), 6.99–6.94 (m, 4H).

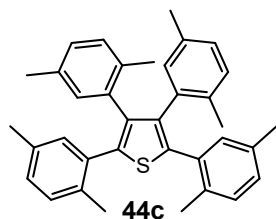
3.58. 2,3,4,5-Tetra-*p*-tolylthiophene (44b)



As described in section 3.57, this synthesis was carried out with tetrabromothiophene (0.400 g, 1.00 mmol), *p*-tolylboronic acid (0.633 g, 4.66 mmol), Pd(PPh₃)₂Cl₂ (0.037 g, 0.053 mmol), PPh₃ (0.027 g, 0.10 mmol) and K₂CO₃ (2.80 g, 20.3 mmol) in a mixture of DMF and H₂O (22.5 mL, 8:1 v/v).

The precipitate was purified using hexane as eluent. Compound **44b** was obtained as a white solid in a yield of 67% (0.296 g, 0.666 mmol). ¹H NMR (400 MHz, CDCl₃) δ (ppm): 7.11 (d, *J* = 8.1 Hz, 4H), 7.02 (d, *J* = 8.1 Hz, 4H), 6.92 (d, *J* = 8.0 Hz, 4H), 6.84 (d, *J* = 8.0 Hz, 4H), 2.30 (s, 6H), 2.26 (s, 6H).

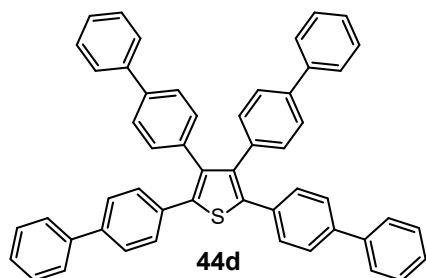
3.59. 2,3,4,5-Tetrakis(2,5-dimethylphenyl)thiophene (44c)



As described in section 3.57, this synthesis was carried out with tetrabromothiophene (0.400 g, 1.00 mmol), 2,5-dimethylphenylboronic acid (0.670 g, 4.47 mmol), Pd(PPh₃)₂Cl₂ (0.036 g, 0.051 mmol), PPh₃ (0.028 g, 0.11 mmol) and K₂CO₃ (2.76 g, 20.0 mmol) in a mixture of DMF and H₂O (22.5 mL, 8:1 v/v).

After diluting with water, the product was extracted with dichloromethane. The combined organic extract was dried over anhydrous MgSO₄, filtered and the solvent was removed under reduced pressure. The crude was purified using hexane as eluent. Compound **44c** was obtained as a white solid in a yield of 69% (0.343 g, 0.685 mmol). ¹H NMR (400 MHz, CDCl₃) δ (ppm): 7.10–7.04 (m, 2H), 7.00–6.91 (m, 4H), 6.82–6.66 (m, 6H), 2.22 (s, 3H), 2.21 (s, 3H), 2.16 (s, 3H), 2.14 (s, 3H), 2.08 (s, 3H), 2.05 (s, 3H), 1.93 (s, 3H), 1.79 (s, 3H).

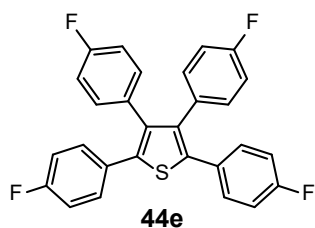
3.60. 2,3,4,5-Tetrakis([1,1'-biphenyl]-4-yl)thiophene (44d)



As described in section 3.57, this synthesis was carried out with tetrabromothiophene (0.400 g, 1.00 mmol), 4-biphenylboronic acid (0.930 g, 4.70 mmol), Pd(PPh₃)₂Cl₂ (0.036 g, 0.051 mmol), PPh₃ (0.026 g, 0.099 mmol) and K₂CO₃ (2.75 g, 20.0 mmol) in a mixture of DMF and H₂O (22.5 mL, 8:1 v/v). The precipitate was purified using a mixture of hexane and dichloromethane (3:1 v/v) as eluent.

Compound **44d** was obtained as a pale yellow solid in a yield of 81% (0.563 g, 0.813 mmol). ¹H NMR (400 MHz, CDCl₃) δ (ppm): 7.62–7.56 (m, 8H), 7.50 (d, *J* = 8.4 Hz, 4H), 7.46–7.41 (m, 8H), 7.41–7.35 (m, 8H), 7.35–7.27 (m, 4H), 7.12 (d, *J* = 8.4 Hz, 4H).

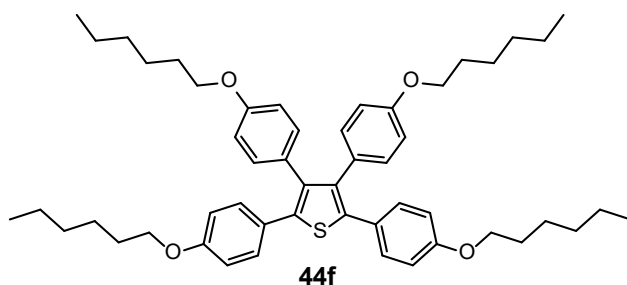
3.61. 2,3,4,5-Tetrakis(4-fluorophenyl)thiophene (44e)



As described in section 3.57, this synthesis was carried out with tetrabromothiophene (0.402 g, 1.01 mmol), 4-fluorophenylboronic acid (0.711 g, 5.08 mmol), Pd(PPh₃)₂Cl₂ (0.036 g, 0.051 mmol), PPh₃ (0.026 g, 0.099 mmol) and K₂CO₃ (2.73 g, 19.8 mmol) in a mixture of DMF and H₂O (22.5 mL, 8:1 v/v). After diluting with water, the product was extracted with dichloromethane. The combined organic extract was dried over anhydrous MgSO₄, filtered and the solvent was removed under reduced pressure. The crude was purified using hexane as eluent. Compound **44e** was obtained as a white solid in a yield of 66% (0.306 g, 0.664 mmol). ¹H NMR (400 MHz, CDCl₃) δ (ppm): 7.17 (dd, *J* = 8.8, 5.3 Hz, 4H), 6.94 (dd, *J* = 8.8, 8.5 Hz, 4H), 6.91–6.81 (m, 8H).

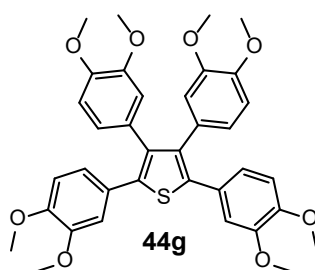
3.62. 2,3,4,5-Tetrakis(4-hexyloxyphenyl)thiophene (44f)

As described in section 3.57, this synthesis was carried out with tetrabromothiophene (0.401 g, 1.00 mmol), 4-hexyloxyphenylboronic acid (1.00 g, 4.50 mmol), Pd(PPh₃)₂Cl₂ (0.035 g, 0.050 mmol), PPh₃ (0.026 g, 0.099 mmol) and K₂CO₃ (2.76 g, 20.0 mmol) in a mixture of DMF and H₂O (22.5 mL, 8:1 v/v). After diluting with water, the product was



extracted with dichloromethane. The combined organic extract was dried over anhydrous MgSO₄, filtered and the solvent was removed under reduced pressure. The crude was purified in neutralized silica using a mixture of hexane and dichloromethane (10:1 v/v) as eluent. Compound **44f** was obtained as a white solid in a yield of 82% (0.649 g, 0.822 mmol). ¹H NMR (400 MHz, CDCl₃) δ (ppm): 7.13 (d, *J* = 8.6 Hz, 4H), 6.84 (d, *J* = 8.5 Hz, 4H), 6.74 (d, *J* = 8.6 Hz, 4H), 6.65 (d, *J* = 8.5 Hz, 4H), 3.91 (t, *J* = 6.6 Hz, 4H), 3.87 (t, *J* = 6.6 Hz, 4H), 1.79–1.70 (m, 8H), 1.48–1.38 (m, 8H), 1.37–1.27 (m, 16H), 0.91 (t, *J* = 6.8 Hz, 12H).

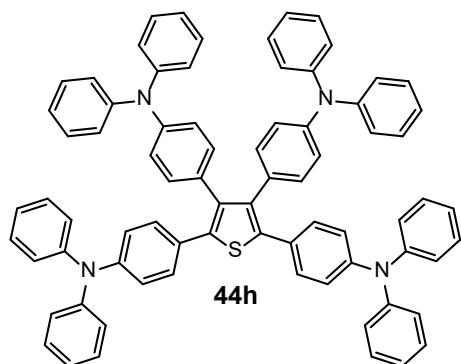
3.63. 2,3,4,5-Tetrakis(3,4-dimethoxyphenyl)thiophene (44g)



As described in section 3.57, this synthesis was carried out with tetrabromothiophene (0.605 g, 1.51 mmol), 3,4-dimethoxyphenylboronic acid (1.23 g, 6.76 mmol), Pd(PPh₃)₂Cl₂ (0.056 g, 0.080 mmol), PPh₃ (0.040 g, 0.15 mmol) and K₂CO₃ (4.16 g, 30.15 mmol) in a mixture of DMF and H₂O (22.5 mL, 8:1 v/v). The precipitate was purified using dichloromethane as

eluent. Compound **44g** was obtained as a pale brown solid in a yield of 65% (0.613 g, 0.975 mmol). ¹H NMR (400 MHz, CDCl₃) δ (ppm): 6.92 (dd, *J* = 8.4, 2.0 Hz, 2H), 6.77 (d, *J* = 8.4 Hz, 2H), 6.73 (d, *J* = 2.0 Hz, 2H), 6.68 (d, *J* = 8.2 Hz, 2H), 6.58 (dd, *J* = 8.2, 1.9 Hz, 2H), 6.52 (d, *J* = 1.9 Hz, 2H), 3.87 (s, 6H), 3.82 (s, 6H), 3.59 (s, 6H), 3.52 (s, 6H).

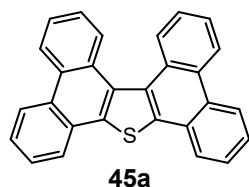
3.64. 2,3,4,5-Tetrakis(4-(diphenylamino)phenyl)thiophene (**44h**)



As described in section 3.57, this synthesis was carried out with tetrabromothiophene (0.397 g, 0.993 mmol), 4-(diphenylamino)phenyl boronic acid (1.28 g, 4.44 mmol), Pd(PPh₃)₂Cl₂ (0.042 g, 0.060 mmol), PPh₃ (0.027 g, 0.10 mmol) and K₂CO₃ (2.76 g, 20.0 mmol) in a mixture of DMF and H₂O (22.5 mL, 8:1 v/v). The precipitate was purified in

neutralized silica using a mixture of hexane and dichloromethane (10:1 v/v) as eluent. Compound **44h** was obtained as a bright yellow solid in a yield of 73% (0.772 g, 0.730 mmol). ¹H NMR (400 MHz, CDCl₃) δ (ppm): 7.22–7.15 (m, 6H), 7.15–7.07 (m, 12H), 7.06–7.01 (m, 8H), 6.99–6.88 (m, 18H), 6.88–6.80 (m, 12H). MS (MALDI-TOF) (*m/z*): calculated for C₇₆H₅₆N₄S M⁺, 1056.4; found 1056.5.

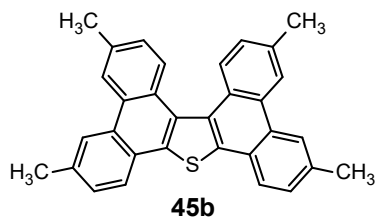
3.65. Diphenanthro[9,10-*b*:9',10'-*d*]thiophene (**45a**)



General procedure: **44a** (0.194 g, 0.500 mmol) was dissolved in anhydrous dichloromethane (15 mL) under nitrogen atmosphere. Then, a previously purged solution of anhydrous FeCl₃ (1.46 g, 9.00 mmol) in nitromethane (5 mL) was added and the mixture was stirred for 1.5 h at room temperature. After, the reaction was diluted with methanol and the resultant precipitate was filtered off and thoroughly washed with the same solvent. The precipitate was dried and purified by flash column chromatography using a mixture of hexane and ethyl acetate (10:1 v/v) as eluent.

Compound **45a**, however, could not be completely isolated from the different by-products. MS (MALDI-TOF) (*m/z*): calculated for C₂₈H₁₆S M⁺, 384.1; found 384.1.

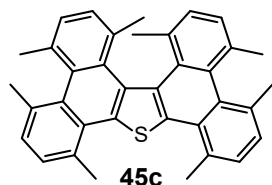
3.66. 3,6,12,15-Tetramethyldiphenanthro[9,10-*b*:9',10'-*d*]thiophene (**45b**)



As described in section 3.65, this synthesis was carried out with **44b** (0.223 g, 0.502 mmol) and anhydrous FeCl₃ (1.46 g, 9.00 mmol) in anhydrous dichloromethane (15 mL) and nitromethane (5 mL) for 5 h. The precipitate was thoroughly washed with methanol and dried. Compound

45b was obtained as a pale yellow solid in a yield of 90% (0.199 g, 0.452 mmol). ^1H NMR (400 MHz, CDCl_3) δ (ppm): 8.65 (d, $J = 8.4$ Hz, 2H), 8.51 (s, 4H), 8.12 (d, $J = 8.2$ Hz, 2H), 7.50 (dd, $J = 8.4, 1.2$ Hz, 2H), 7.36 (dd, $J = 8.2, 1.5$ Hz, 2H), 2.66 (s, 6H), 2.65 (s, 6H).

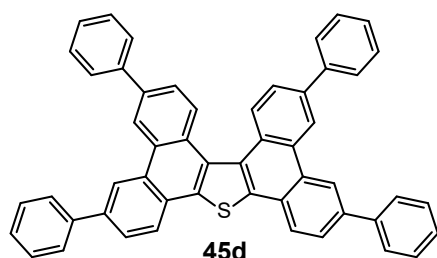
3.67. 1,4,5,8,10,13,14,17-Octamethyldiphenanthro[9,10-*b*:9',10'-*d*]thiophene (45c)



As described in section 3.65, this synthesis was carried out with **44c** (0.250 g, 0.500 mmol) and anhydrous FeCl_3 (1.46 g, 9.00 mmol) in anhydrous dichloromethane (15 mL) and nitromethane (5 mL) for 1.5 h. The precipitate was dried and purified using hexane as eluent.

Nevertheless, compound **45c** was not detected among the several by-products.

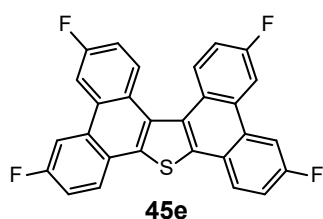
3.68. 3,6,12,15-Tetraphenyldiphenanthro[9,10-*b*:9',10'-*d*]thiophene (45d)



As described in section 3.65, this synthesis was carried out with **44d** (0.348 g, 0.502 mmol) and anhydrous FeCl_3 (1.46 g, 9.00 mmol) in anhydrous dichloromethane (15 mL) and nitromethane (5 mL) for 3.5 h. The precipitate was thoroughly washed with methanol and dried. Compound **45d** was obtained as a

pale yellow solid in a yield of 77% (0.267 g, 0.388 mmol). ^1H NMR (400 MHz, CDCl_3) δ (ppm): 8.90 (d, $J = 1.7$ Hz, 2H), 8.88 (d, $J = 1.7$ Hz, 2H), 8.78 (d, $J = 8.5$ Hz, 2H), 8.22 (d, $J = 8.2$ Hz, 2H), 7.88 (dd, $J = 8.2, 1.7$ Hz, 2H), 7.85–7.77 (m, 8H), 7.76 (dd, $J = 8.5, 1.7$ Hz, 2H), 7.58–7.52 (m, 8H), 7.49–7.42 (m, 4H).

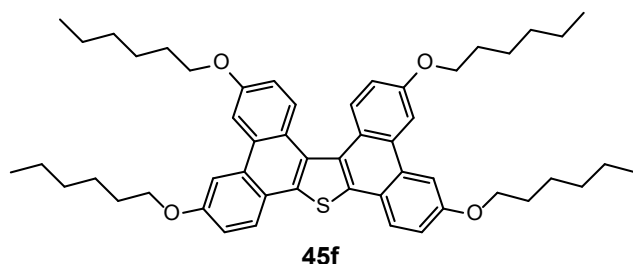
3.69. 3,6,12,15-Tetrafluorodiphenanthro[9,10-*b*:9',10'-*d*]thiophene (45e)



As described in section 3.65, this synthesis was carried out with **44e** (0.230 g, 0.500 mmol) and anhydrous FeCl_3 (1.46 g, 9.00 mmol) in anhydrous dichloromethane (15 mL) and nitromethane (5 mL) for 72 h. The precipitate was thoroughly washed with methanol and dried. Compound **45e** was obtained

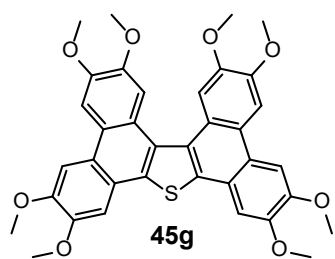
as a white solid in a yield of 33% (0.076 g, 0.17 mmol). ^1H NMR (400 MHz, CDCl_3) δ (ppm): 8.68 (dd, $J = 9.1, 5.8$ Hz, 2H), 8.27–8.19 (m, 5H), 7.52–7.46 (d, $J = 2.4$ Hz, 2H), 7.39–7.31 (m, 2H).

3.70. 3,6,12,15-Tetrahexyloxydiphenanthro[9,10-*b*:9',10'-*d*]thiophene (45f)



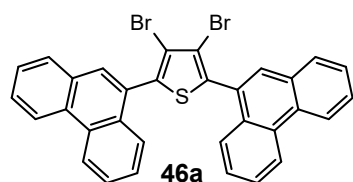
As described in section 3.65, this synthesis was carried out with **44f** (0.200 g, 0.253 mmol) and anhydrous FeCl₃ (0.739 g, 4.55 mmol) in anhydrous dichloromethane (7.6 mL) and nitromethane (2.5 mL) for 24 h. The precipitate was thoroughly washed with methanol and dried. Nevertheless, compound **45f** was not formed and only the monocyclized compound **45f'** was detected.

3.71. 2,3,6,7,11,12,15,16-Octamethoxydiphenanthro[9,10-*b*:9',10'-*d*]thiophene (45g)



As described in section 3.65, this synthesis was carried out with **44g** (0.459 g, 0.730 mmol) and anhydrous FeCl₃ (2.13 g, 13.1 mmol) in anhydrous dichloromethane (22 mL) and nitromethane (7.5 mL) for 7 h. The precipitate was thoroughly washed with methanol and dried. Compound **45g** was obtained as a white solid in a yield of 92% (0.491 g, 0.671 mmol). ¹H NMR (400 MHz, CDCl₃) δ (ppm): 8.12 (s, 2H), 7.91 (s, 2H), 7.90 (s, 2H), 7.54 (s, 2H), 4.18 (s, 12H), 4.16 (s, 6H), 3.85 (s, 6H).

3.72. 3,4-Dibromo-2,5-di(phenanthren-9-yl)thiophene (46a)



Method 1 (THF): Tetrabromothiophene (0.600 g, 1.50 mmol), phenanthren-9-ylboronic acid (0.700 g, 3.15 mmol), Pd(PPh₃)₄ (0.087 g, 0.075 mmol) and K₂CO₃ (2.08 g, 15.1 mmol) were dissolved in a mixture of THF and H₂O (52.5 mL, 6:1 v/v) under nitrogen and stirred under reflux overnight. After cooling to room temperature, the reaction mixture was diluted with water and the product was extracted with dichloromethane. The organic layers were dried over anhydrous MgSO₄, filtered and the solvent was removed under reduced pressure. The crude was purified by flash column chromatography using a mixture of hexane and dichloromethane (20:1 v/v) as eluent. Compound **46a** was obtained as a pale yellow solid in a yield of 26% (0.235 g, 0.395 mmol).

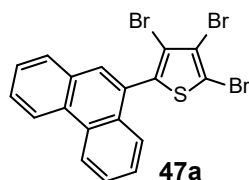
Method 2 (toluene): Tetrabromothiophene (0.398 g, 0.996 mmol), phenanthren-9-ylboronic acid (0.466 g, 2.10 mmol), Pd(PPh₃)₂Cl₂ (0.037 g, 0.053 mmol), PPh₃ (0.027 g, 0.10 mmol) and K₂CO₃ (1.39 g, 10.0 mmol) were dissolved in a mixture of toluene and H₂O (65 mL, 10:3 v/v) under nitrogen and stirred at 110 °C for 24 h. After cooling to room

temperature, the reaction mixture was diluted with water and the product was extracted with dichloromethane. The organic layers were dried over anhydrous MgSO_4 , filtered and the solvent was removed under reduced pressure. The crude was purified by flash column chromatography using hexane as eluent. Compound **46a** was obtained as a pale yellow solid in a yield of 12% (0.074 g, 0.12 mmol).

Method 3 (DMF): Tetrabromothiophene (0.404 g, 1.01 mmol), phenanthren-9-ylboronic acid (0.466 g, 2.10 mmol), $\text{Pd}(\text{PPh}_3)_2\text{Cl}_2$ (0.036 g, 0.051 mmol), PPh_3 (0.027 g, 0.10 mmol) and K_2CO_3 (1.38 g, 10.0 mmol) were dissolved in a mixture of DMF and H_2O (22.5 mL, 9:1 v/v) under nitrogen and stirred at 110 °C overnight. After cooling to room temperature, the reaction mixture was diluted with water and the product was extracted with dichloromethane. The organic layers were dried over anhydrous MgSO_4 , filtered and the solvent was removed under reduced pressure. The crude was purified by flash column chromatography using hexane as eluent. Compound **46a** was obtained as a pale yellow solid in a yield of 56% (0.335 g, 0.564 mmol).

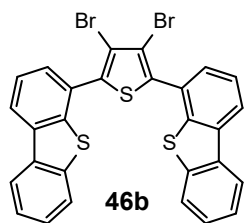
^1H NMR (400 MHz, CDCl_3) δ (ppm): 8.81 (d, $J = 8.1$ Hz, 2H), 8.77 (d, $J = 8.2$ Hz, 2H), 7.98 (dd, $J = 8.0, 1.3$ Hz, 2H), 7.97 (dd, $J = 8.0, 1.1$ Hz, 2H), 7.96 (s, 2H), 7.78–7.65 (m, 8H).

3.73. 2,3,4-Tribromo-5-(phenanthren-9-yl)thiophene (47a)



Compound **47a** was obtained as a pale yellow by-product in the synthesis of **46a** (section 3.72) in a yield of 23% (0.169 g, 0.340 mmol) in method 1 and 6% (0.030 g, 0.060 mmol) in method 2. ^1H NMR (400 MHz, CDCl_3) δ (ppm): 8.83 (d, $J = 8.0$ Hz, 1H), 8.81 (d, $J = 8.1$ Hz, 1H), 7.93 (dd, $J = 7.9, 1.4$ Hz, 1H), 7.86 (s, 1H), 7.77–7.71 (m, 1H), 7.69–7.62 (m, 2H), 7.51 (dd, $J = 8.2, 1.3$ Hz, 1H), 7.41–7.35 (m, 1H).

3.74. 2,5-Bis(dibenzo[b,d]thiophen-4-yl)-3,4-dibromothiophene (46b)

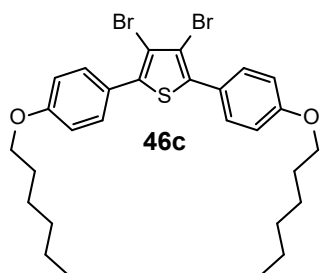


Method 1 (THF): As described in section 3.72 (method 1), this synthesis was carried out with tetrabromothiophene (0.603 g, 1.51 mmol), 4-dibenzothienylboronic acid (0.820 g, 3.60 mmol), $\text{Pd}(\text{PPh}_3)_4$ (0.087 g, 0.075 mmol) and K_2CO_3 (2.07 g, 15.0 mmol) in a mixture of THF and H_2O (52.5 mL, 6:1 v/v). The crude was dissolved in a small volume of dichloromethane and was precipitated by the slow addition of hexane. The resultant solid was collected by filtration. Compound **46b** was obtained as a yellow solid in a yield of 46% (0.419 g, 0.691 mmol).

Method 3 (DMF): As described in section 3.72 (method 3), this synthesis was carried out with tetrabromothiophene (0.400 g, 1.00 mmol), 4-dibenzothiénylboronic acid (0.479 g, 2.10 mmol), Pd(PPh₃)₂Cl₂ (0.035 g, 0.050 mmol), PPh₃ (0.026 g, 0.10 mmol) and K₂CO₃ (1.38 g, 10.0 mmol) in a mixture of DMF and H₂O (22.5 mL, 9:1 v/v). Compound **46b** could not be obtained with this method.

¹H NMR (500 MHz, CDCl₃) δ (ppm): 8.26 (dd, *J* = 7.8, 1.2 Hz, 2H), 8.24–8.19 (m, 2H), 7.90–7.85 (m, 2H), 7.67 (dd, *J* = 7.4, 1.2 Hz, 2H), 7.61 (dd, *J* = 7.8, 7.4 Hz, 2H), 7.54–7.47 (m, 4H).

3.75. 3,4-Dibromo-2,5-bis(4-(hexyloxy)phenyl)thiophene (46c)



Method 1 (THF): As described in section 3.72 (method 1), this synthesis was carried out with tetrabromothiophene (0.402 g, 1.01 mmol), 4-hexyloxyphenylboronic acid (0.468 g, 2.11 mmol), Pd(PPh₃)₄ (0.060 g, 0.052 mmol) and K₂CO₃ (1.38 g, 10.0 mmol) in a mixture of THF and H₂O (35 mL, 6:1 v/v). The crude was purified by flash column chromatography using a mixture of

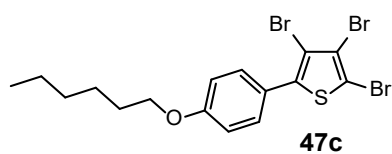
hexane and dichloromethane (20:1 v/v) as eluent. Compound **46c** was obtained as a pale brown solid in a yield of 45% (0.269 g, 0.453 mmol).

Method 2 (toluene): As described in section 3.72 (method 2), this synthesis was carried out with tetrabromothiophene (0.399 g, 0.998 mmol), 4-hexyloxyphenylboronic acid (0.466 g, 2.10 mmol), Pd(PPh₃)₂Cl₂ (0.037 g, 0.053 mmol), PPh₃ (0.026 g, 0.099 mmol) and K₂CO₃ (1.50 g, 10.9 mmol) in a mixture of toluene and H₂O (65 mL, 10:3 v/v). The crude was purified by flash column chromatography using hexane as eluent. Compound **46c** was obtained as a pale brown solid in a yield of 19% (0.114 g, 0.191 mmol).

Method 3 (DMF): As described in section 3.72 (method 3), this synthesis was carried out with tetrabromothiophene (0.400 g, 1.00 mmol), 4-hexyloxyphenylboronic acid (0.467 g, 2.10 mmol), Pd(PPh₃)₂Cl₂ (0.035 g, 0.050 mmol), PPh₃ (0.028 g, 0.11 mmol) and K₂CO₃ (1.40 g, 10.2 mmol) in a mixture of DMF and H₂O (22.5 mL, 9:1 v/v). Compound **46c** could not be obtained with this method.

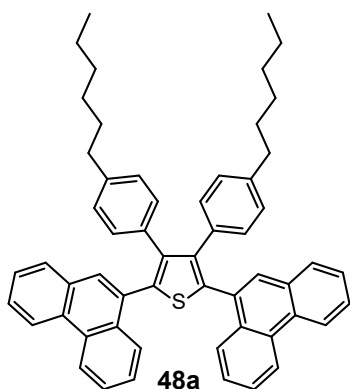
¹H NMR (400 MHz, CDCl₃) δ (ppm): 7.56 (d, *J* = 8.8 Hz, 4H), 6.96 (d, *J* = 8.8 Hz, 4H), 4.00 (t, *J* = 6.5 Hz, 4H), 1.84–1.77 (m, 4H), 1.54–1.30 (m, 12H), 0.92 (t, *J* = 7.0 Hz, 6H).

3.76. 2,3,4-Tribromo-5-(4-(hexyloxy)phenyl)thiophene (47c)



Compound **47c** was obtained as a white by-product in the synthesis of **46c** employing method 2 (section 3.75) in a yield of 71% (0.352 g, 0.708 mmol). $^1\text{H NMR}$ (400 MHz, CDCl_3) δ (ppm): 7.47 (d, $J = 8.8$ Hz, 2H), 6.95 (d, $J = 8.8$ Hz, 2H), 3.99 (t, $J = 6.5$ Hz, 2H), 1.83–1.76 (m, 2H), 1.52–1.30 (m, 6H), 0.91 (t, $J = 7.0$ Hz, 3H).

3.77. 3,4-Bis(4-hexylphenyl)-2,5-di(phenanthren-9-yl)thiophene (48a)

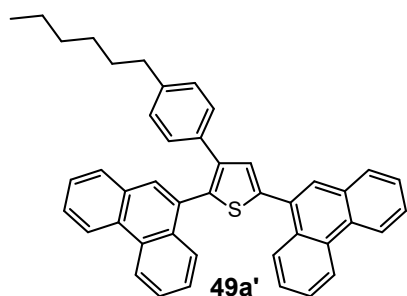


From 46a: **46a** (0.313 g, 0.527 mmol), 4-hexylphenylboronic acid (0.230 g, 1.11 mmol), $\text{Pd}(\text{PPh}_3)_2\text{Cl}_2$ (0.020 g, 0.028 mmol), PPh_3 (0.014 g, 0.053 mmol) and K_2CO_3 (0.722 g, 5.23 mmol) were dissolved in a mixture of DMF and H_2O (11.3 mL, 8:1 v/v) under nitrogen and stirred at 110 °C overnight. After cooling to room temperature, the reaction mixture was diluted with water and the product was extracted with dichloromethane. The organic layers were dried over anhydrous MgSO_4 , filtered off and the solvent was removed under reduced pressure. The crude was purified by flash column chromatography using hexane as eluent. Compound **48a** was obtained as a colorless oil in a yield of 55% (0.218 g, 0.288 mmol).

From TBT (one-pot procedure): Tetrabromothiophene (0.604 g, 1.51 mmol), phenanthren-9-ylboronic acid (0.713 g, 3.21 mmol), $\text{Pd}(\text{PPh}_3)_2\text{Cl}_2$ (0.055 g, 0.078 mmol), PPh_3 (0.039 g, 0.15 mmol) and K_2CO_3 (2.16 g, 15.7 mmol) were dissolved in a mixture of DMF: H_2O (33.8 mL, 8:1 v/v) under nitrogen and stirred at 85 °C overnight. After cooling to room temperature, 4-hexylphenylboronic acid (0.742 g, 3.60 mmol), $\text{Pd}(\text{PPh}_3)_2\text{Cl}_2$ (0.053 g, 0.076 mmol), PPh_3 (0.039 g, 0.15 mmol) and K_2CO_3 (2.07 g, 15.0 mmol) were also added to the reaction mixture and the system was purged again with nitrogen. The reaction was further stirred at 85 °C reflux overnight. Then, the reaction mixture was diluted with water and the resultant precipitate was filtered. The precipitate was purified by flash column chromatography using hexane as eluent. Compound **48a** was obtained as a pale yellow solid in a yield of 70% (0.795 g, 1.05 mmol).

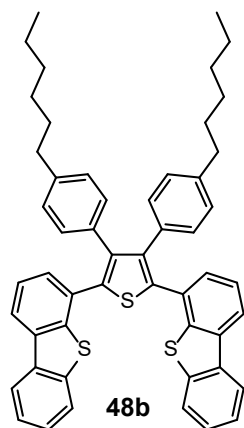
$^1\text{H NMR}$ (400 MHz, CDCl_3) δ (ppm): 8.68 (d, $J = 8.3$ Hz, 4H), 8.06 (d, $J = 8.3$ Hz, 2H), 7.90 (s, 2H), 7.85 (dd, $J = 7.9, 1.1$ Hz, 2H), 7.69–7.63 (m, 2H), 7.62–7.56 (m, 4H), 7.51–7.45 (m, 2H), 6.87 (d, $J = 8.0$ Hz, 4H), 6.68 (d, $J = 8.0$ Hz, 4H), 2.33 (t, $J = 7.6$ Hz, 4H), 1.42–1.33 (m, 4H), 1.24–1.03 (m, 12H), 0.82 (t, $J = 6.9$ Hz, 6H).

3.78. 3-(4-Hexylphenyl)-2,5-di(phenanthren-9-yl)thiophene (49a')



Compound **49a'** was obtained as a by-product in the synthesis of **48a** from **46a** (section 3.77) in a yield of 43% (0.135 g, 0.226 mmol). $^1\text{H NMR}$ (400 MHz, CDCl_3) δ (ppm): 8.81 (d, $J = 8.1$ Hz, 1H), 8.74 (d, $J = 8.2$ Hz, 3H), 8.58 (dd, $J = 7.8, 1.7$ Hz, 1H), 8.02 (d, $J = 8.2$ Hz, 1H), 8.02 (s, 1H), 7.97 (s, 1H), 7.95 (d, $J = 7.9$ Hz, 1H), 7.90 (d, $J = 7.9$ Hz, 1H), 7.77–7.60 (m, 8H), 7.52–7.47 (m, 1H), 7.25 (d, $J = 8.2$ Hz, 2H), 6.90 (d, $J = 8.2$ Hz, 2H), 2.44 (t, $J = 7.6$ Hz, 2H), 1.47 (m, 2H), 1.28–1.16 (m, 6H), 0.83 (t, $J = 6.7$ Hz, 3H). MS (MALDI-TOF) (m/z): calculated for $\text{C}_{44}\text{H}_{34}\text{S}$ ($M-2\text{H}$) $^+$, 594.2; found 594.3.

3.79. 2,5-Bis(dibenzo[b,d]thiophen-4-yl)-3,4-bis(4-hexylphenyl)thiophene (48b)

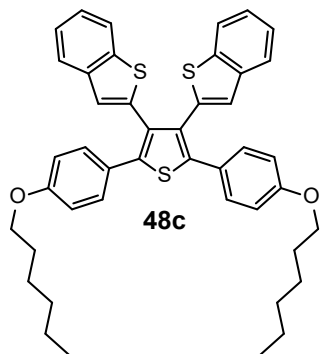


From 46b: **46b** (0.398 g, 0.656 mmol), 4-hexylphenylboronic acid (0.351 g, 1.71 mmol), $\text{Pd}(\text{PPh}_3)_4$ (0.039 g, 0.034 mmol) and K_2CO_3 (0.945 g, 6.85 mmol) were dissolved in a mixture of THF and H_2O (23.3 mL, 6:1 v/v) under nitrogen and stirred under reflux overnight. After cooling to room temperature, the reaction mixture was diluted with water and the product was extracted with dichloromethane. The organic layers were dried over anhydrous MgSO_4 , filtered and the solvent was removed under reduced pressure. The crude was purified by flash column chromatography using a mixture of hexane and dichloromethane (20:1 v/v) as eluent. Compound **48b** was obtained as a yellow solid in a yield of 76% (0.381 g, 0.495 mmol).

From TBT (one-pot procedure): Tetrabromothiophene (0.602 g, 1.51 mmol), 4-dibenzo[b,d]thienylboronic acid (0.850 g, 3.72 mmol), $\text{Pd}(\text{PPh}_3)_4$ (0.090 g, 0.078 mmol) and K_2CO_3 (2.11 g, 15.3 mmol) were dissolved in a mixture of THF and H_2O (52.5 mL, 6:1 v/v) under nitrogen and stirred under reflux overnight. After cooling to room temperature, 4-hexylphenylboronic acid (0.745 g, 3.62 mmol), $\text{Pd}(\text{PPh}_3)_4$ (0.087 g, 0.075 mmol) and K_2CO_3 (2.10 g, 15.2 mmol) were also added to the reaction mixture and the system was purged again with nitrogen. The reaction was further stirred under reflux overnight. Then, the reaction mixture was diluted with water and the product was extracted with dichloromethane. The organic layers were dried over anhydrous MgSO_4 , filtered and the solvent was removed under reduced pressure. The crude was purified by flash column chromatography using a mixture of hexane and dichloromethane (25:1 v/v) as eluent. Compound **48b** was obtained as a white solid in a yield of 53% (0.608 g, 0.790 mmol).

^1H NMR (400 MHz, CDCl_3) δ (ppm): 8.18–8.12 (m, 2H), 8.07 (dd, $J = 7.7, 1.3$ Hz, 2H), 7.84–7.78 (m, 2H), 7.50–7.39 (m, 4H), 7.33 (dd, $J = 7.7, 7.6$ Hz, 2H), 7.27 (dd, $J = 7.6, 1.2$ Hz, 2H), 6.85 (d, $J = 8.0$ Hz, 4H), 6.80 (d, $J = 8.0$ Hz, 4H), 2.44 (t, $J = 7.6$ Hz, 4H), 1.48 (m, 4H), 1.34–1.12 (m, 12H), 0.85 (t, $J = 6.8$ Hz, 6H).

3.80. 3,4-Bis(benzo[b]thiophen-2-yl)-2,5-bis(4-hexyloxyphenyl)thiophene (**48c**)

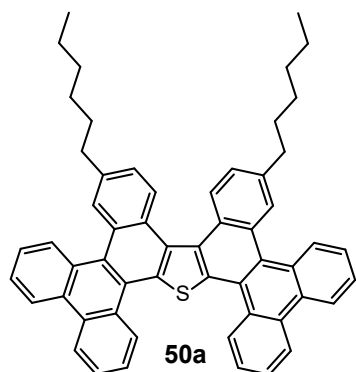


*From **46c***: **46c** (0.360 g, 0.606 mmol), 2-benzothierylboronic acid (0.280 g, 1.58 mmol), $\text{Pd}(\text{PPh}_3)_4$ (0.038 g, 0.033 mmol) and K_2CO_3 (0.851 g, 6.17 mmol) were dissolved in a mixture of THF and H_2O (23.3 mL, 6:1 v/v) under nitrogen and stirred under reflux overnight. After cooling to room temperature, the reaction mixture was diluted with water and the product was extracted with dichloromethane. The organic layers were dried over anhydrous MgSO_4 , filtered and the solvent was removed under reduced pressure. The crude was purified by flash column chromatography using a mixture of hexane and dichloromethane (10:1 v/v) as eluent. Compound **48c** was obtained as a white solid in a yield of 52% (0.221 g, 0.315 mmol).

From TBT (one-pot procedure): Tetrabromothiophene (0.600 g, 1.50 mmol), 4-hexyloxyphenylboronic acid (0.802 g, 3.61 mmol), $\text{Pd}(\text{PPh}_3)_4$ (0.092 g, 0.080 mmol) and K_2CO_3 (2.10 g, 15.2 mmol) were dissolved in a mixture of THF and H_2O (52.5 mL, 6:1 v/v) under nitrogen and stirred under reflux overnight. After cooling to room temperature, 2-benzothierylboronic acid (0.641 g, 3.60 mmol), $\text{Pd}(\text{PPh}_3)_4$ (0.087 g, 0.075 mmol) and K_2CO_3 (2.07 g, 15.0 mmol) were also added to the reaction mixture and the system was purged again with nitrogen. The reaction was further stirred under reflux overnight. Then, the reaction mixture was diluted with water and the product was extracted with dichloromethane. The organic layers were dried over anhydrous MgSO_4 , filtered and the solvent was removed under reduced pressure. The crude was purified by flash column chromatography using a mixture of hexane and dichloromethane (20:1 v/v) as eluent. Compound **48c** was obtained as a white solid in a yield of 34% (0.353 g, 0.503 mmol).

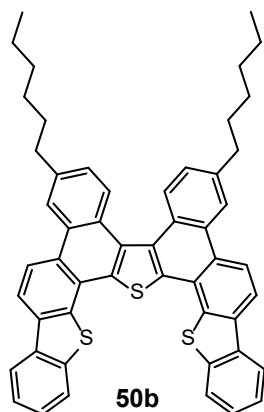
^1H NMR (400 MHz, CDCl_3) δ (ppm): 7.64 (m, 2H), 7.58 (m, 2H), 7.28 (d, $J = 8.5$ Hz, 4H), 7.26–7.18 (m, 4H), 7.01 (s, 2H), 6.77 (d, $J = 8.5$ Hz, 4H), 3.90 (t, $J = 6.5$ Hz, 4H), 1.74 (m, 4H), 1.47–1.26 (m, 12H), 0.90 (t, $J = 6.8$ Hz, 6H).

3.81. 10,15-Dihexylbenzo[11,12]chryseno[5,6-*b*]benzo[11,12]chryseno[6,5-*d*]thiophene (50a)



48a (218 mg, 0.288 mmol) was dissolved in anhydrous dichloromethane (8.6 mL) under nitrogen atmosphere. Then, a purged solution of anhydrous FeCl₃ (841 mg, 5.18 mmol) in nitromethane (2.9 mL) was added and stirred for 3.5 h. The reaction was then diluted with methanol. The resultant precipitate was filtered and thoroughly washed with methanol. The product was purified by flash column chromatography using hexane as eluent. Compound **50a** was obtained as a bright yellow solid in a yield of 81% (175 mg, 0.232 mmol). ¹H NMR (400 MHz, CDCl₃) δ (ppm): 9.42 (d, *J* = 8.2 Hz, 2H), 8.97–8.90 (m, 2H), 8.87–8.76 (m, 6H), 8.63 (s, 2H), 7.89 (dd, *J* = 7.6, 7.5 Hz, 2H), 7.82 (dd, *J* = 7.6, 7.5 Hz, 2H), 7.78–7.71 (m, 4H), 7.41 (d, *J* = 8.5 Hz, 2H), 2.86 (t, *J* = 7.8 Hz, 4H), 1.82–1.71 (m, 4H), 1.49–1.39 (m, 4H), 1.38–1.27 (m, 8H), 0.90 (t, *J* = 6.8 Hz, 6H).

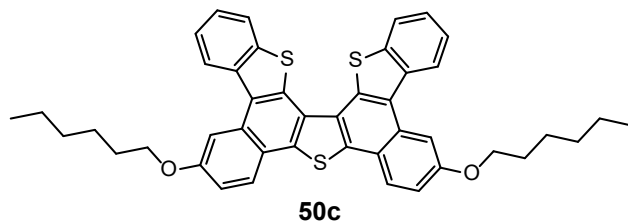
3.82. Compound 50b



48b (351 mg, 0.456 mmol) was dissolved in anhydrous dichloromethane (13.7 mL) under nitrogen atmosphere at 0 °C. Then, a purged solution of anhydrous FeCl₃ (1.33 g, 8.21 mmol) in nitromethane (4.2 mL) was added and stirred for 20 min at 0 °C. The reaction was then diluted with methanol. The resultant precipitate was filtered and thoroughly washed with methanol. The product was further purified by subsequent crystallizations from hexane/dichloromethane mixtures. Compound **50b** was obtained as a pale yellow solid in a yield of 93% (323 mg, 0.422 mmol). ¹H NMR (400 MHz, CDCl₃) δ (ppm): 8.94 (d, *J* = 8.7 Hz, 2H), 8.80 (d, *J* = 8.5 Hz, 2H), 8.65 (s, 2H), 8.56–8.48 (d, *J* = 8.5 Hz, 2H), 8.43–8.36 (m, 2H), 8.26–8.19 (m, 2H), 7.65–7.59 (m, 4H), 7.43 (d, *J* = 8.4 Hz, 2H), 2.95 (t, *J* = 8.0 Hz, 4H), 1.91–1.81 (m, 4H), 1.54–1.32 (m, 12H), 0.94 (t, *J* = 6.8 Hz, 6H).

3.83. Compound 50c

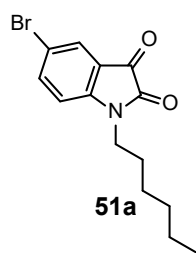
48c (221 mg, 0.315 mmol) was dissolved in anhydrous dichloromethane (9.5 mL) under



nitrogen atmosphere. Then, a purged solution of anhydrous FeCl₃ (1.06 g, 6.52 mmol) in nitromethane (3.2 mL) was added and stirred for 1 h. The reaction was then diluted with

methanol. The resultant precipitate was filtered and thoroughly washed with methanol. The product was further purified by subsequent crystallizations from hexane/dichloromethane mixtures. Compound **50c** was obtained as a pale yellow solid in a yield of 74% (163 mg, 0.234 mmol). ¹H NMR (400 MHz, CDCl₃) δ (ppm): 8.84 (d, *J* = 8.2 Hz, 2H), 8.47 (s, 2H), 8.31 (d, *J* = 8.4 Hz, 2H), 8.16 (d, *J* = 7.3 Hz, 2H), 7.67–7.62 (m, 2H), 7.59–7.53 (m, 2H), 7.35 (d, *J* = 8.4 Hz, 2H), 4.29 (t, *J* = 6.5 Hz, 4H), 2.02–1.93 (m, 4H), 1.67–1.57 (m, 4H), 1.48–1.38 (m, 8H), 0.97 (t, *J* = 6.8 Hz, 6H).

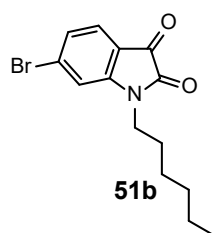
3.84. 5-bromo-1-hexylisatin (51a)



5-Bromoisatin (7.47 g, 33.2 mmol), K₂CO₃ (13.7 g, 99.5 mmol) and 1-bromohexane (7 mL, 50 mmol) were dissolved in anhydrous DMF (35 mL) under nitrogen. Then, the mixture was stirred overnight at room temperature. After, the product was precipitated by the addition of water and filtered off. Compound **51a** was obtained as a red solid in a yield of 94% (9.64 g, 31.2 mmol). ¹H NMR (400 MHz, CDCl₃) δ (ppm): 7.70–7.68

(m, 2H), 6.80 (d, *J* = 9 Hz, 1H), 3.70 (t, *J* = 7 Hz, 2H), 1.71–1.63 (m, 2H), 1.36–1.28 (m, 6H), 0.88 (t, *J* = 7 Hz, 3H).

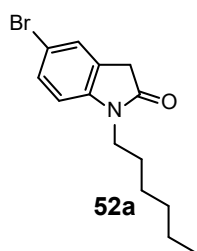
3.85. 6-bromo-1-hexylisatin (51b)



Analogously to the procedure described in section 3.84, this synthesis was carried out with 6-bromoisatin (3.00 g, 13.3 mmol), K₂CO₃ (5.49 g, 39.8 mmol) and 1-bromohexane (2.2 mL, 16 mmol) in anhydrous DMF (20 mL). Compound **51b** was obtained as a red solid in a yield of 90% (3.72 g, 12.0 mmol). ¹H NMR (400 MHz, CDCl₃) δ (ppm): 7.46 (d, *J* = 8 Hz,

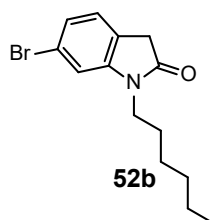
1H), 7.27 (dd, *J* = 8, 2 Hz, 1H), 7.06 (d, *J* = 2 Hz, 1H), 3.69 (t, *J* = 7 Hz, 2H), 1.72–1.64 (m, 2H), 1.42–1.25 (m, 6H), 0.89 (t, *J* = 7 Hz, 3H).

3.86. 5-bromo-1-hexyloxindole (**52a**)



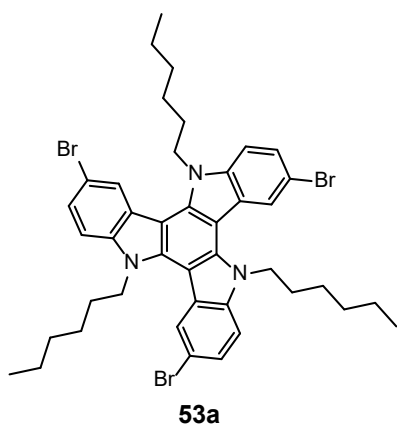
51a (3.49 g, 11.3 mmol) was dissolved in a NH_2NH_2 hydrate solution (30 mL, 80%) and was stirred overnight under reflux. After cooling to room temperature, the solution was diluted with aqueous HCl (4 M). The product was extracted with dichloromethane. The combined organic extract was dried over anhydrous MgSO_4 , filtered and the solvent was removed under reduced pressure. The crude was purified by flash column chromatography using a mixture of hexane and dichloromethane (1:1 v/v) as eluent. Compound **52a** was obtained as a white solid in a yield of 90% (2.98 g, 10.1 mmol). ^1H NMR (400 MHz, CDCl_3) δ (ppm): 7.40–7.39 (m, 2H), 6.70 (d, $J = 8$ Hz, 1H), 3.67 (t, $J = 7$ Hz, 2H), 3.51 (s, 2H), 1.60–1.67 (m, 2H), 1.25–1.37 (m, 6H), 0.88 (t, $J = 7$ Hz, 3H).

3.87. 6-bromo-1-hexyloxindole (**52b**)



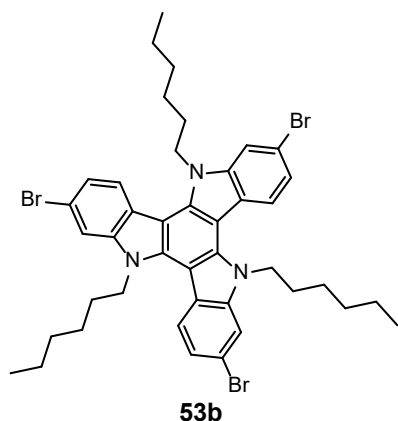
Analogously to the procedure described in section 3.86, this synthesis was carried out with **51b** (3.49 g, 11.3 mmol) in a NH_2NH_2 hydrate solution (30 mL, 80%). Compound **52b** was obtained as a white solid in a yield of 93% (3.10 g, 10.5 mmol). ^1H NMR (400 MHz, CDCl_3) δ (ppm): 7.15 (dd, $J = 8, 2$ Hz, 1H), 7.09 (d, $J = 8$ Hz, 1H), 6.95 (d, $J = 2$ Hz, 1H), 3.66 (t, $J = 8$ Hz, 2H), 3.45 (s, 2H), 1.68–1.61 (m, 2H), 1.40–1.28 (m, 6H), 0.89 (t, $J = 7$ Hz, 3H).

3.88. 3,8,13-Tribromo-5,10,15-trihexyl-10,15-dihydro-5H-diindolo[3,2- α :3',2'-c]carbazole (**53a**)



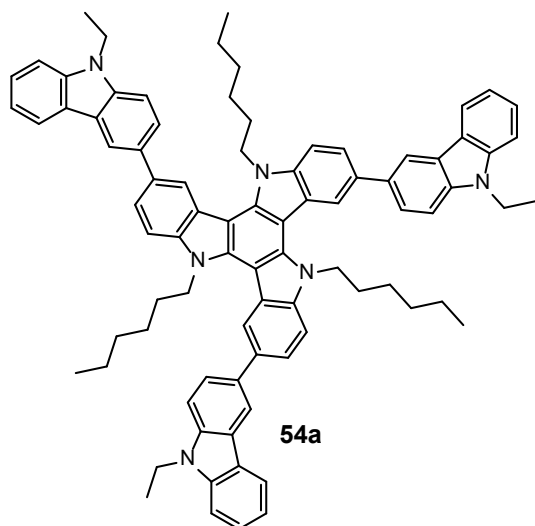
52a (2.07 g, 7.00 mmol) was dissolved in POCl_3 (5.8 mL) and stirred under reflux for 7 h. After, the crude was slowly and carefully poured into a beaker containing water under stirring and the formation of a green precipitate was observed. The solution was neutralized with sodium hydroxide and the precipitate was filtered off and thoroughly washed with water. The precipitate was dissolved in ethyl acetate and precipitated by the addition of hexane and the resultant solid was filtered off. Compound **53a** was obtained as a pale grey solid in a yield of 47% (0.912 g, 1.09 mmol). ^1H NMR (400 MHz, CDCl_3) δ (ppm): 8.27 (d, $J = 2$ Hz, 3H), 7.53 (dd, $J = 9, 2$ Hz, 3H), 7.45 (d, $J = 9$ Hz, 3H), 4.68 (t, $J = 8$ Hz, 6H), 2.03–1.95 (m, 6H), 1.42–1.23 (m, 18H), 0.84 (t, $J = 7$ Hz, 9H).

3.89. 2,7,12-Tribromo-5,10,15-trihexyl-10,15-dihydro-5H-diindolo[3,2-*a*:3',2'-*c*]carbazole (53b)



Analogously to the procedure described in section 3.88, this synthesis was carried out with **52b** (3.0 g, 10 mmol) in POCl₃ (10 mL). Compound **53b** was obtained as a pale grey solid in a yield of 35% (1.0 g, 1.2 mmol). ¹H NMR (400 MHz, CDCl₃) δ (ppm): 8.06 (d, *J* = 9 Hz, 3H), 7.73 (d, *J* = 2 Hz, 3H), 7.43 (dd, *J* = 9 Hz, *J* = 2 Hz, 3H), 4.78 (t, *J* = 8 Hz, 6H), 1.94–1.87 (m, 6H), 1.30–1.16 (m, 18H), 0.80 (t, *J* = 7 Hz, 9H).

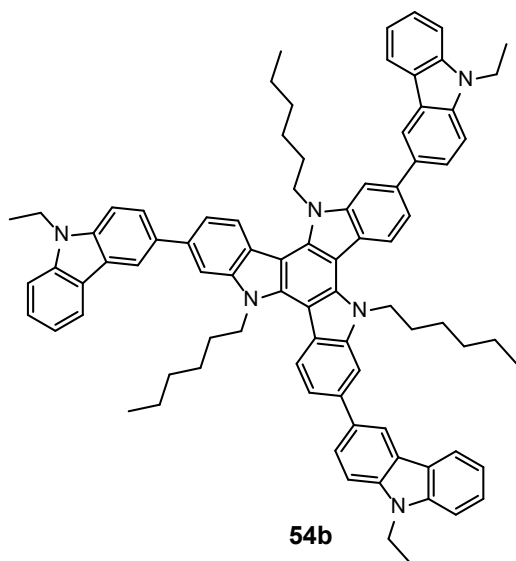
3.90. 3,8,13-Tris(9-ethyl-9H-carbazol-3-yl)-5,10,15-trihexyl-10,15-dihydro-5H-diindolo[3,2-*a*:3',2'-*c*]carbazole (54a)



53a (110 mg, 0.132 mmol), 9-ethyl-9H-carbazol-3-ylboronic acid (189 mg, 0.791 mmol), Pd(PPh₃)₄ (7.6 mg, 0.0066 mmol) and K₂CO₃ (327 mg, 2.37 mmol) were dissolved in a mixture of THF and water (7 mL, 6:1 v/v) and stirred at 150 °C under microwave irradiation for 2 h. After cooling to room temperature, the product was extracted with dichloromethane. The combined organic extract was dried over anhydrous MgSO₄, filtered and the solvent was removed under

reduced pressure. The crude was purified by flash column chromatography in neutral alumina using a mixture of hexane and dichloromethane (1:1 v/v) as eluent. Further purification was performed by dissolving the product in the minimum amount of dichloromethane and precipitating it by slowly adding hexane and filtering it off. Compound **54a** was obtained as a pale yellow solid in a yield of 41% (63 mg, 0.053 mmol). ¹H NMR (400 MHz, CDCl₃) δ (ppm): 8.62 (s, 3H), 8.46 (d, *J* = 1.7 Hz, 3H), 8.21 (d, *J* = 7.6 Hz, 3H), 7.89 (dd, *J* = 8.4, 1.8 Hz, 3H), 7.80 (d, *J* = 8.4 Hz, 3H), 7.74 (d, *J* = 8.4 Hz, 3H), 7.56 (d, *J* = 8.4 Hz, 3H), 7.54–7.49 (m, 3H), 7.47 (d, *J* = 7.9 Hz, 3H), 7.30–7.24 (m, 3H), 5.04 (t, *J* = 7.7 Hz, 6H), 4.46 (q, *J* = 7.2 Hz, 6H), 2.16 (m, 6H), 1.52 (t, *J* = 7.2 Hz, 9H), 1.35–1.13 (m, 18H), 0.61 (t, *J* = 7.3 Hz, 9H).

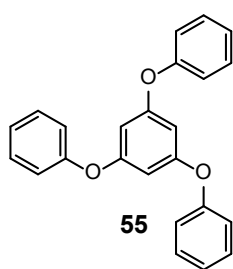
3.91. 2,7,12-Tris(9-ethyl-9*H*-carbazol-3-yl)-5,10,15-trihexyl-10,15-dihydro-5*H*-diindolo[3,2-*a*:3',2'-*c*]carbazole (54b)



53b (302 mg, 0.362 mmol), 9-ethyl-9*H*-carbazol-3-ylboronic acid (518 mg, 2.17 mmol), Pd(PPh₃)₄ (22 mg, 0.019 mmol) and K₂CO₃ (894 mg, 6.48 mmol) were dissolved in a mixture of THF and water (22.7 mL, 6:1 v/v) and stirred under reflux overnight. After cooling to room temperature, the product was extracted with dichloromethane. The combined organic extract was dried over anhydrous MgSO₄, filtered and the solvent was removed under reduced pressure. The crude was purified by flash column chromatography in neutralized silica using a

mixture of hexane and ethyl acetate (10:1 v/v) as eluent. Further purification was performed by dissolving the product in the minimum amount of dichloromethane and precipitating it by slowly adding hexane and filtering it off. Compound **54b** was obtained as a pale yellow solid in a yield of 33% (138 mg, 0.117 mmol). ¹H NMR (400 MHz, CDCl₃) δ (ppm): 8.53 (d, *J* = 1.5 Hz, 3H), 8.42 (d, *J* = 8.4 Hz, 3H), 8.25 (d, *J* = 7.7 Hz, 3H), 7.96 (dd, *J* = 8.3, 1.7 Hz, 3H), 7.95 (d, *J* = 1.0 Hz, 3H), 7.74 (dd, *J* = 8.4, 1.7 Hz, 3H), 7.58 (d, *J* = 8.4 Hz, 3H), 7.55–7.50 (m, 3H), 7.47 (d, *J* = 8.0 Hz, 3H), 7.33–7.27 (m, 3H), 5.09 (t, *J* = 7.8 Hz, 6H), 4.47 (q, *J* = 7.2 Hz, 6H), 2.13 (m, 6H), 1.51 (t, *J* = 7.2 Hz, 9H), 1.48–1.23 (m, 18H), 0.84 (t, *J* = 7.0 Hz, 9H).

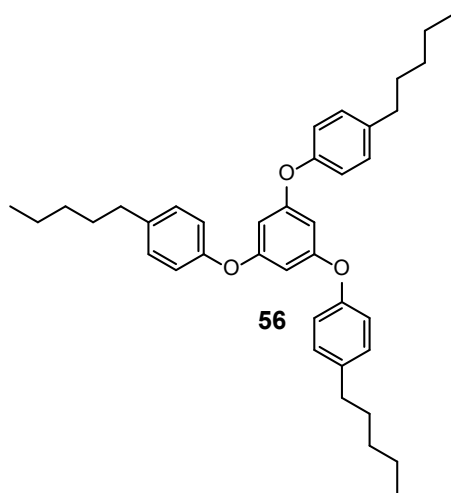
3.92. 1,3,5-Triphenoxybenzene (55)



1,3,5-Tribromobenzene (4.04 g, 12.8 mmol), phenol (4.01 g, 42.6 mmol), CuI (0.461 g, 2.42 mmol) and Na₂CO₃ (5.13 g, 48.4 mmol) were put in a round-bottom flask equipped with a Dean-Stark apparatus under nitrogen. Then, DMA (30 mL) and toluene (5 mL) were carefully added and the mixture was stirred at 160 °C for 96 h. After, the mixture was poured into water and the product was extracted with

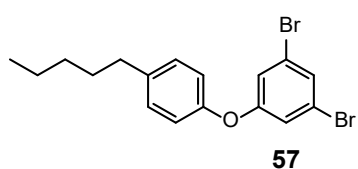
dichloromethane. The combined organic extract was dried over anhydrous MgSO₄, filtered through alumina and the solvent was removed under reduced pressure. The crude was purified by flash column chromatography using hexane as eluent. Compound **55** was obtained as a white solid in a yield of 73% (3.31 g, 9.33 mmol). ¹H NMR (400 MHz, CDCl₃) δ (ppm): 7.33 (m, 6H), 7.11 (t, *J* = 7.4 Hz, 3H), 7.03 (d, *J* = 8.0 Hz, 6H), 6.37 (s, 3H).

3.93. 1,3,5-Tris(4-pentylphenoxy)benzene (56)



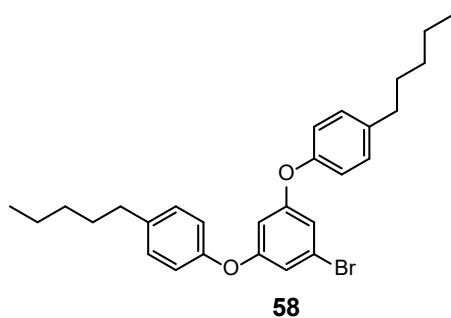
Analogously to the procedure described in section 3.92, this synthesis was carried out with 1,3,5-tribromobenzene (2.32 g, 7.37 mmol), 4-pentylphenol (3.95 g, 24.0 mmol), CuI (0.270 g, 1.42 mmol) and Na₂CO₃ (2.93 g, 27.6 mmol) in DMA (24 mL) and toluene (4 mL) for 75 h. Compound **56** was obtained as a colorless oil in a yield of 6% (0.242 g, 0.428 mmol). ¹H NMR (400 MHz, CDCl₃) δ (ppm): 7.11 (d, *J* = 8.4 Hz, 6H), 6.92 (d, *J* = 8.4 Hz, 6H), 6.30 (s, 3H), 2.55 (t, *J* = 7.7 Hz, 6H), 1.63–1.53 (m, 6H), 1.38–1.25 (m, 12H), 0.89 (t, *J* = 6.8 Hz, 9H).

3.94. 1,3-Dibromo-5-(4-pentylphenoxy)benzene (57)



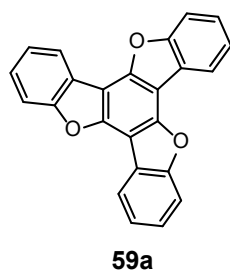
Compound **57** was obtained as a by-product in the synthesis of **56** (section 3.93) in a yield of 26% (0.765 g, 1.92 mmol). ¹H NMR (400 MHz, CDCl₃) δ (ppm): 7.34 (t, *J* = 1.6 Hz, 1H), 7.18 (d, *J* = 8.5 Hz, 2H), 7.04 (d, *J* = 1.6 Hz, 2H), 6.94 (d, *J* = 8.5 Hz, 2H), 2.60 (t, *J* = 7.8 Hz, 2H), 1.67–1.57 (m, 2H), 1.38–1.29 (m, 4H), 0.91 (t, *J* = 6.9 Hz, 3H).

3.95. 1-Bromo-3,5-bis(4-pentylphenoxy)benzene (58)



Compound **58** was obtained as a by-product in the synthesis of **56** (section 3.93) in a yield of 54% (1.91 g, 3.97 mmol). ¹H NMR (400 MHz, CDCl₃) δ (ppm): 7.15 (d, *J* = 8.5 Hz, 4H), 6.94 (d, *J* = 8.5 Hz, 4H), 6.76 (d, *J* = 2.2 Hz, 2H), 6.56 (t, *J* = 2.2 Hz, 1H), 2.59 (t, *J* = 7.7 Hz, 4H), 1.61 (m, 4H), 1.40–1.25 (m, 8H), 0.90 (t, *J* = 6.9 Hz, 6H).

3.96. Tris[1]benzofurano[2,3-a:2',3'-c:2'',3''-e]benzene (59a)

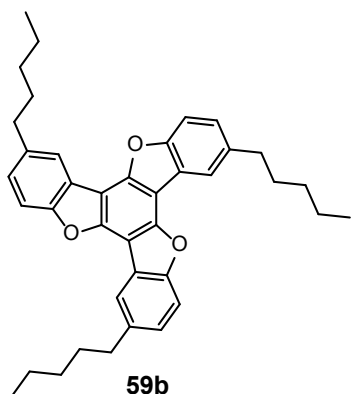


55 (142 mg, 0.401 mmol), AgOAc (400 mg, 2.40 mmol) and Pd(tfa)₂ (6.6 mg, 0.020 mmol) were dissolved in pivalic acid (5.43 g) in a Schlenk tube and stirred in an oil bath at 130 °C for 16 h. Then, the crude was filtered through alumina and diluted with dichloromethane. The solution was washed with a solution of NaHCO₃ to remove the pivalic acid. The organic extract was dried over anhydrous MgSO₄, filtered and the solvent was removed under reduced pressure. The crude was purified by flash column

chromatography using dichloromethane as eluent. The product was further purified by subsequent crystallizations from a mixture of dichloromethane and hexane. Compound **59a** was obtained as colorless crystals in a yield of 50% (70.0 mg, 0.201 mmol). ^1H NMR (400 MHz, CDCl_3) δ (ppm): 8.40 (m, 3H), 7.79 (m, 3H), 7.54 (m, 6H).

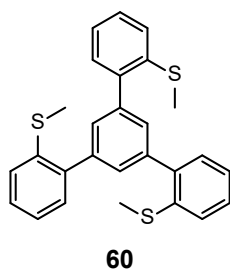
3.97. 3,8,13-Tripentyltris[1]benzofurano[2,3-a:2',3'-c:2'',3''-e]benzene (59b)

Analogously to the procedure described in section 3.96, this synthesis was carried out with **56** (112 mg, 0.198 mmol), AgOAc (203 mg, 1.22 mmol) and $\text{Pd}(\text{tfa})_2$ (3.6 mg, 0.011 mmol) in pivalic acid (2.71 g). The crude was purified by flash column chromatography using hexane as eluent. Compound **59b** was obtained as a white solid in a yield of 26% (28.9 mg, 0.0517 mmol). ^1H NMR (400 MHz, CDCl_3) δ (ppm): 8.17 (d, $J = 1.8$ Hz, 3H), 7.68 (d, $J = 8.4$ Hz, 3H), 7.34 (dd, $J = 8.4, 1.8$ Hz, 3H), 2.87 (t, $J = 7.7$ Hz, 6H), 1.85–1.75 (m, 6H), 1.48–1.36 (m, 12H), 0.94 (t, $J = 7.1$ Hz, 9H).



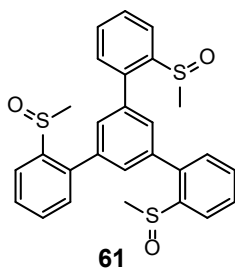
3.98. 1,3,5-Tris(2-methylthiophenyl)benzene (60)

1,3,5-Tribromobenzene (0.700 g, 2.22 mmol), 2-(methylthio)phenylboronic acid (1.46 g, 8.67 mmol), $\text{Pd}(\text{PPh}_3)_4$ (128 mg, 0.111 mmol) and K_2CO_3 (2.78 g, 20.0 mmol) were dissolved under nitrogen in a mixture of THF and water (70 mL, 6:1 v/v) and stirred overnight under reflux. After cooling, the product was extracted with dichloromethane. The combined organic extracts were dried over MgSO_4 , filtered and the solvent was removed under reduced pressure. The crude was purified by flash column chromatography using a mixture of hexane and dichloromethane (10:1 v/v) as eluent. Compound **60** was obtained as a white solid in a yield of 72% (0.715 g, 1.61 mmol). ^1H NMR (400 MHz, CDCl_3) δ (ppm): 7.52 (s, 3H), 7.37–7.34 (m, 3H), 7.33–7.29 (m, 6H), 7.24–7.16 (m, 3H), 2.39 (s, 9H).



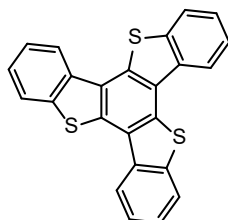
3.99. 1,3,5-Tris(2-methylsulfinylphenyl)benzene (61)

60 (0.400 g, 0.900 mmol) was dissolved in glacial acetic acid (30 mL) and then, hydrogen peroxide (247 μL , 35%, 2.88 mmol) was added carefully. The reaction was stirred at room temperature for 7 h. After, the product was extracted with dichloromethane. The combined organic extract was dried over anhydrous MgSO_4 , filtered and the solvent was removed under reduced pressure. Compound **61**, corresponding to a diastereomeric mixture, was obtained as a white solid in a yield of 70%



(0.308 g, 0.626 mmol). $^1\text{H NMR}$ (400 MHz, CDCl_3) δ (ppm): 8.19–8.15 (m, 3H), 7.72–7.62 (m, 3H), 7.64–7.57 (m, 3H), 7.51–7.36 (m, 6H), [2.61, 2.54 and 2.48 (s, s' and s'', 9H)]. MS (ESI-MS) (m/z): calculated for $\text{C}_{27}\text{H}_{24}\text{O}_3\text{S}_3$ ($\text{M}+\text{H}$) $^+$, 493.1; found 493.2. Calculated for $\text{C}_{27}\text{H}_{24}\text{O}_3\text{S}_3$ ($\text{M}+\text{Na}$) $^+$, 515.1; found 515.2.

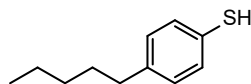
3.100. Tris[1]benzothieno[2,3- α :2',3'- c :2'',3''- e]benzene (62a)



62a

61 (0.308 g, 0.900 mmol) was dissolved in trifluoromethanesulfonic acid (5 mL) in a round-bottom flask equipped with a drying tube, and the mixture was stirred at room temperature for 22 h. Then, the solution was carefully and slowly poured into a mixture of pyridine and water (90 mL, 1:8 v/v) and it was refluxed for 22 h. After cooling, the product was extracted with dichloromethane, dried over anhydrous MgSO_4 , filtered and the solvent was removed under reduced pressure. Nevertheless, compound **62a** could not be detected.

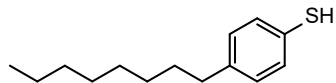
3.101. 4-Pentylbenzenethiol (63)



63

4-pentylbenzene-1-sulfonyl chloride (1.00 g, 3.77 mmol) was dissolved in anhydrous THF (20 mL) under nitrogen at 0 °C. Then, a solution of LiAlH_4 in anhydrous THF (11 mL, 1 M, 11 mmol) was added to the reaction dropwise and the mixture was stirred at room temperature for 24 h. The reaction was quenched with a mixture of concentrated HCl and H_2O (220 mL, 1:10 v/v) and the product was extracted with ethyl acetate. The organic layers were dried over MgSO_4 , filtered and the solvent was removed under reduced pressure. The crude was purified by flash column chromatography using hexane as eluent. Compound **63** was obtained as a colorless oil in a yield of 79% (0.537 g, 2.98 mmol). $^1\text{H NMR}$ (400 MHz, CDCl_3) δ (ppm): 7.21 (d, $J = 8.2$ Hz, 2H), 7.06 (d, $J = 8.2$ Hz, 2H), 3.39 (s, 1H), 2.55 (t, $J = 6.8$ Hz, 2H), 1.63–1.52 (m, 2H), 1.39–1.24 (m, 4H), 0.90 (t, $J = 6.4$ Hz, 3H).

3.102. 4-Octylbenzenethiol (64)

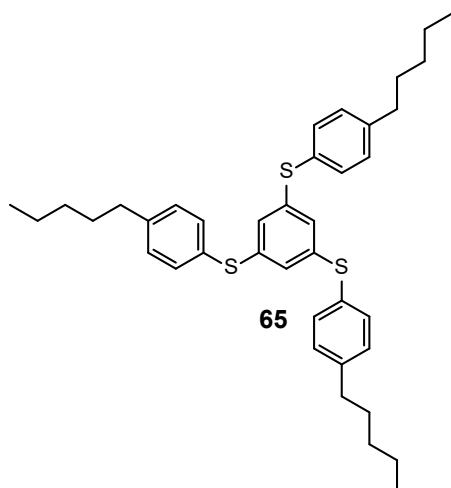


64

Sodium 4-octylbenzenesulfonate (1.50 g, 5.14 mmol) was dissolved in benzene (5 mL) and the solution was refluxed and dehydrated for 30 min under nitrogen using a Dean-Stark apparatus. Afterwards, PPh_3 (6.74 g, 25.7 mmol) and benzo-18-crown-6 (0.803 g, 2.57 mmol) were added to the reaction and the system was purged again with nitrogen. Next, a solution of iodine (1.30 g, 5.14 mmol) in benzene (5 mL) was added dropwise with a dropping funnel and the mixture was refluxed for 24 h. Then, a mixture of water and dioxane (4 mL, 1:1 v/v) was added and the system was further stirred overnight under

reflux to cleave the disulfide bonds. After cooling to room temperature, the mixture was diluted with ethyl acetate and washed with water. The organic layers were dried over anhydrous MgSO_4 , filtered and the solvent was removed under reduced pressure. The crude was purified by flash column chromatography using hexane as eluent. Compound **64** was obtained as a colorless oil in a yield of 90% (1.05 g, 4.77 mmol). ^1H NMR (400 MHz, CDCl_3) δ (ppm): 7.20 (d, $J = 8.2$ Hz, 2H), 7.05 (d, $J = 8.2$ Hz, 2H), 3.38 (s, 1H), 2.54 (t, $J = 7.6$ Hz, 2H), 1.61–1.51 (m, 2H), 1.33–1.20 (m, 10H), 0.88 (t, $J = 6.8$ Hz, 3H).

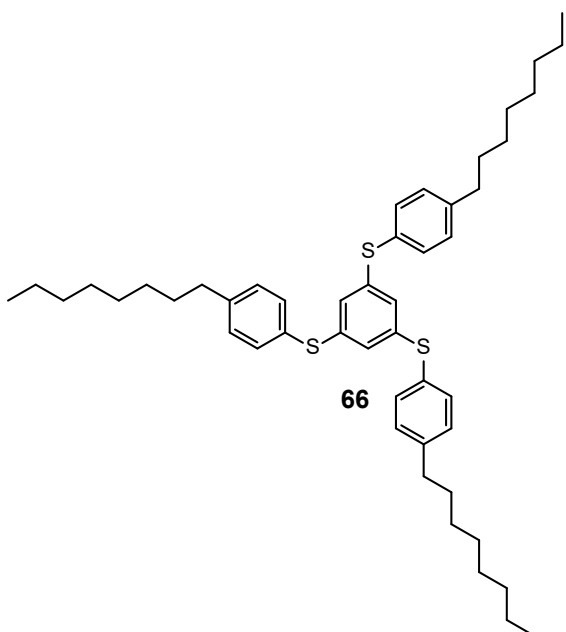
3.103. 1,3,5-Tris((4-pentylphenyl)thio)benzene (**65**)



63 (0.968 g, 5.37 mmol) was dissolved in anhydrous DMF (5 mL) under nitrogen. Then, NaH (0.260 g, 60% dispersion in mineral oil, 6.50 mmol) was added the solution was stirred for 30 min at room temperature. Next, 1,3,5-tribromobenzene (0.508 g, 1.63 mmol) was added and the reaction was refluxed for 24 h. After cooling to room temperature, the mixture was diluted with water and extracted with ethyl acetate. The organic layers were dried over anhydrous MgSO_4 , filtered and the solvent was removed under reduced

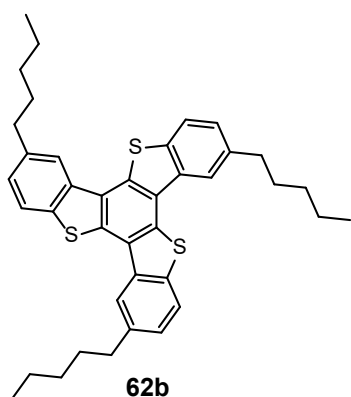
pressure. The crude was purified by flash column chromatography using hexane as eluent. Compound **65** was obtained as a yellow oil in a yield of 93% (0.936 g, 1.53 mmol). ^1H NMR (400 MHz, CDCl_3) δ (ppm): 7.25 (d, $J = 8.1$ Hz, 6H), 7.10 (d, $J = 8.1$ Hz, 6H), 6.83 (s, 3H), 2.58 (t, $J = 7.7$ Hz, 6H), 1.66–1.56 (m, 6H), 1.42–1.23 (m, 12H), 0.90 (t, $J = 6.7$ Hz, 9H).

3.104. 1,3,5-Tris((4-octylphenyl)thio)benzene (**66**)



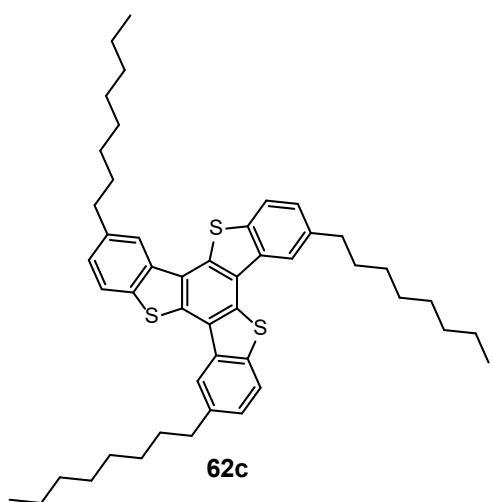
Analogously to the procedure described in section 3.103, this synthesis was carried out with **64** (0.954 g, 3.26 mmol) and NaH (0.158 g, 60% dispersion in mineral oil, 3.95 mmol) in anhydrous DMF (5 mL). Then, 1,3,5-tribromobenzene (0.308 g, 0.989 mmol). Compound **66** was obtained as a colorless oil in a yield of 93% (0.680 g, 0.921 mmol). ^1H NMR (400 MHz, CDCl_3) δ (ppm): 7.24 (d, $J = 8.1$ Hz, 6H), 7.09 (d, $J = 8.1$ Hz, 6H), 6.82 (s, 3H), 2.59 (t, $J = 7.8 =$ Hz, 6H), 1.64–1.56 (m, 6H), 1.38–1.22 (m, 30H), 0.88 (t, $J = 6.9$ Hz, 9H).

3.105. 3,8,13-Tripentyltris[1]benzothieno[2,3-*a*:2',3'-*c*:2'',3''-*e*]benzene (62b)



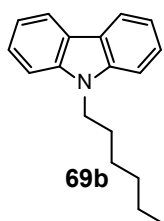
65 (245 mg, 0.400 mmol), Pd(tfa)₂ (40 mg, 0.12 mmol), AgOAc (801 mg, 4.80 mmol) and K₂CO₃ (166 mg, 1.20 mmol) were placed in a microwave vial. Then, pivalic acid (5.4 g) was added and the reaction was stirred at 130 °C for 48 h under air. After, the mixture was poured into water and the product was extracted with dichloromethane and ethyl acetate. The combined organic extract was dried over anhydrous MgSO₄, filtered through a celite pad and the solvent was removed under reduced pressure. The crude was purified by flash column chromatography using hexane as eluent. Compound **62a** was obtained as a white solid in a yield of 13% (32 mg, 0.053 mmol). ¹H NMR (400 MHz, CDCl₃) δ (ppm): 8.48 (d, *J* = 1.3 Hz, 3H), 8.02 (d, *J* = 8.1 Hz, 3H), 7.46 (dd, *J* = 8.5, 1.3 Hz, 3H), 2.96 (t, *J* = 7.0 Hz, 6H), 1.90–1.80 (m, 6H), 1.52–1.40 (m, 12H), 0.96 (t, *J* = 7.0 Hz, 9H).

3.106. 3,8,13-Trioctyltris[1]benzothieno[2,3-*a*:2',3'-*c*:2'',3''-*e*]benzene (62c)



Analogously to the procedure described in section 3.105, this synthesis was carried out with **66** (294 mg, 0.398 mmol), Pd(tfa)₂ (40 mg, 0.12 mmol), AgOAc (801 mg, 4.80 mmol) and K₂CO₃ (166 mg, 1.20 mmol) in pivalic acid (5.4 g). Compound **62b** was obtained as a white solid in a yield of 13% (38 mg, 0.051 mmol). ¹H NMR (400 MHz, CDCl₃) δ (ppm): 8.47 (d, *J* = 1.3 Hz, 3H), 8.01 (d, *J* = 8.1 Hz, 3H), 7.45 (dd, *J* = 8.1, 1.3 Hz, 3H), 2.96 (t, *J* = 7.8 Hz, 6H), 1.89–1.80 (m, 6H), 1.51–1.26 (m, 30H), 0.88 (t, *J* = 7.0 Hz, 9H).

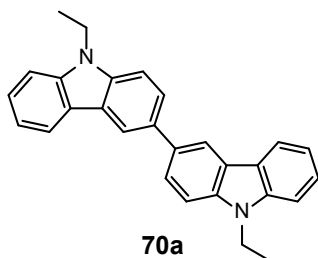
3.107. 9-Hexyl-9*H*-carbazole (69b)



9*H*-carbazole (10.1 g, 60.4 mmol) was dissolved in anhydrous DMF (40 mL) under nitrogen. NaH (2.7 g, 60% in mineral oil, 67 mmol) was added and the solution was stirred for 30 min at room temperature. Then, 1-bromohexane (9.6 mL, 68 mmol) was added and the reaction was stirred overnight. After, it was diluted with water and the product was extracted with dichloromethane. The combined organic layers were dried over anhydrous MgSO₄, filtered and the solvent was removed under reduced pressure. The crude was purified by flash column chromatography using hexane as eluent. Compound **69b** was obtained as a white

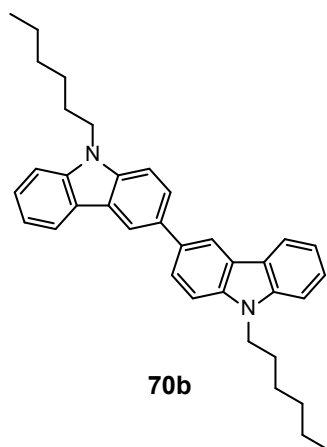
solid in a yield of 96% (14.6 g, 58.1 mmol). ^1H NMR (400 MHz, CDCl_3) δ (ppm): 8.11 (d, $J = 7.8$ Hz, 2H), 7.47 (ddd, $J = 8.1, 6.9, 1.2$ Hz, 2H), 7.41 (d, $J = 8.2$ Hz, 2H), 7.23 (ddd, $J = 7.8, 6.9, 1.2$ Hz, 2H), 4.30 (t, $J = 7.4$ Hz, 2H), 1.92–1.83 (m, 2H), 1.45–1.23 (m, 6H), 0.87 (t, $J = 7.1$ Hz, 3H).

3.108. 9,9'-Diethyl-9*H*,9'*H*-3,3'-bicarbazole (70a)



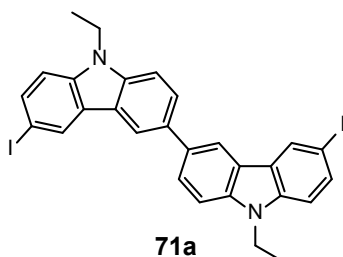
9-Ethyl-9*H*-carbazole (**69a**) (5.1 g, 26 mmol) was dissolved in anhydrous CHCl_3 (40 mL) under inert atmosphere. Next, anhydrous FeCl_3 (16.1 g, 102 mmol) was added, and the reaction mixture was stirred at room temperature for 30 minutes. After, the mixture was diluted with methanol (ca. 100 mL) and the solvent was removed under reduced pressure. The crude was purified by flash column chromatography using a mixture of hexane and dichloromethane (10:1 v/v) as eluent. Compound **70a** was obtained as a white solid in a yield of 89% (4.4 g, 11 mmol). ^1H NMR (400 MHz, CDCl_3) δ (ppm): 8.42 (d, $J = 1.8$ Hz, 2H), 8.20 (d, $J = 7.8$ Hz, 2H), 7.84 (dd, $J = 8.4, 1.8$ Hz, 2H), 7.51 (d, $J = 8.4$ Hz, 2H), 7.48 (ddd, $J = 8.1, 7.5, 1.2$ Hz, 2H), 7.44 (d, $J = 7.5$ Hz, 2H), 7.26 (ddd, $J = 8.1, 7.8, 1.2$ Hz, 2H), 4.43 (q, $J = 7.9$ Hz, 4H), 1.49 (t, $J = 7.9$ Hz, 6H).

3.109. 9,9'-Dihexyl-9*H*,9'*H*-3,3'-bicarbazole (70b)



Analogously to the procedure described in section 3.108, this synthesis was carried out with **69b** (5.1 g, 20 mmol) and anhydrous FeCl_3 (13 g, 80 mmol) in anhydrous CHCl_3 (38 mL). Compound **70b** was obtained as a white solid in a yield of 58% (2.9 g, 5.8 mmol). ^1H NMR (400 MHz, CDCl_3) δ (ppm): 8.42 (d, $J = 1.7$ Hz, 2H), 8.20 (d, $J = 7.8$ Hz, 2H), 7.84 (dd, $J = 8.5, 1.7$ Hz, 2H), 7.52–7.43 (m, 6H), 7.26 (ddd, $J = 7.8, 7.0$ Hz, 1.0 Hz, 2H), 4.35 (t, $J = 7.2$ Hz, 4H), 1.97–1.88 (m, 4H), 1.49–1.27 (m, 12H), 0.89 (t, $J = 7.2$ Hz, 6H).

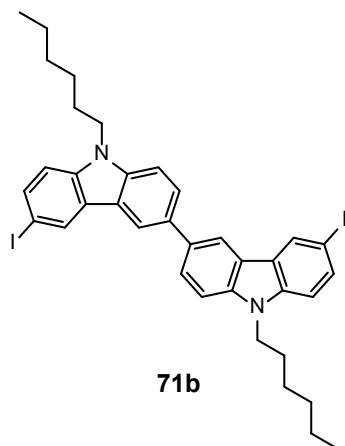
3.110. 9,9'-Diethyl-6,6'-diiodo-9*H*,9'*H*-3,3'-bicarbazole (71a)



70a (1.6 g, 4.1 mmol) was dissolved in glacial acetic acid (60 mL) under reflux. Then, KI (0.91 g, 5.5 mmol) was added, and the mixture was stirred under reflux for 10 minutes. Afterwards, KIO_3 (1.3 g, 6.1 mmol) was added and the mixture was stirred under reflux for 40 minutes. The crude was cooled down to room temperature and the resultant precipitate was

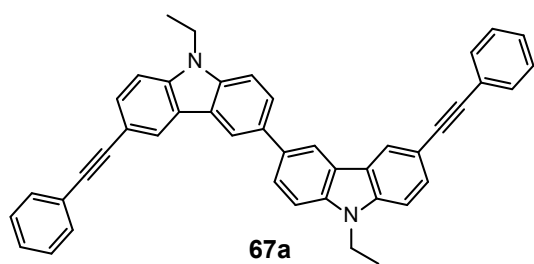
filtered off. The precipitate was washed with NaHCO₃ (sat.) and dried. The solid was purified by flash column chromatography using a mixture of hexane and ethyl acetate (20:1 v/v) as eluent. Compound **71a** was obtained as a brown solid in a yield of 33% (0.87 g, 1.4 mmol). ¹H NMR (400 MHz, CDCl₃) δ (ppm): 8.50 (d, *J* = 1.6 Hz, 2H), 8.34 (d, *J* = 1.6 Hz, 2H), 7.84 (dd, *J* = 8.6, 1.6 Hz, 2H), 7.73 (dd, *J* = 8.5, 1.6 Hz, 2H), 7.50 (d, *J* = 8.6 Hz, 2H), 7.23 (d, *J* = 8.5 Hz, 2H), 4.39 (q, *J* = 7.4 Hz, 4H), 1.25 (t, *J* = 7.4 Hz, 6H).

3.111. 9,9'-Dihexyl-6,6'-diiodo-9*H*,9'*H*-3,3'-bicarbazole (**71b**)



Analogously to the procedure described in section 3.110, **70b** (1.5 g, 3.1 mmol) in glacial acetic acid (50 mL). Then, KI (0.69 g, 4.1 mmol) and KIO₃ (0.98 g, 4.6 mmol) were added by steps. After stirring at reflux for 15 minutes, the solution was neutralized with NaHCO₃ (sat.) and the product was extracted with dichloromethane. The combined organic layers were dried over anhydrous MgSO₄, filtered and the solvent was removed under reduced pressure. The crude was purified by flash column chromatography using a mixture of hexane and CH₂Cl₂ (20:1 v/v) as eluent. Compound **71b** was obtained as a brown solid in a yield of 36% (0.83 g, 1.1 mmol). ¹H NMR (400 MHz, CDCl₃) δ (ppm): 8.49 (d, *J* = 1.6 Hz, 2H), 8.33 (d, *J* = 1.6 Hz, 2H), 7.82 (dd, *J* = 8.8, 1.6 Hz, 2H), 7.72 (dd, *J* = 8.8, 1.6 Hz, 2H), 7.48 (d, *J* = 8.8 Hz, 2H), 7.21 (d, *J* = 8.8 Hz, 2H), 4.31 (t, *J* = 7.3 Hz, 4H), 1.90–1.87 (m, 4H), 1.40–1.25 (m, 12H), 0.88 (t, *J* = 7.0 Hz, 6H).

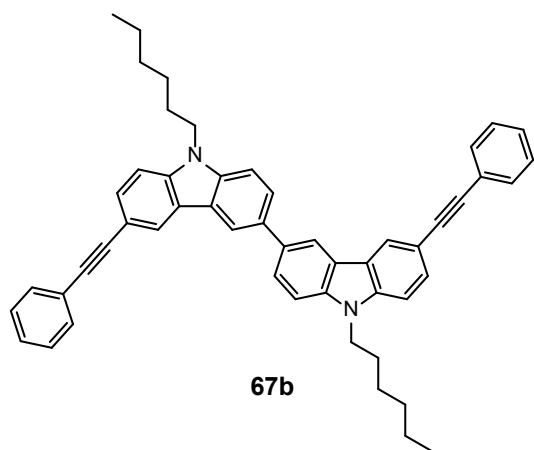
3.112. 9,9'-Diethyl-6,6'-bis(phenylethynyl)-9*H*,9'*H*-3,3'-bicarbazole (**67a**)



71a (0.46 g, 0.72 mmol), CuI (12 mg, 0.063 mmol) and Pd(PPh₃)₂Cl₂ (21 mg, 0.018 mmol) were placed in a round-bottomed flask. Then, the system was evacuated in vacuo and filled up with nitrogen thrice. Next, triethylamine (0.24 mL, 1.7 mmol), phenylacetylene (0.19 mL, 1.7 mmol) and anhydrous THF (20 mL) were added. The reaction mixture was stirred at room temperature for 24 hours. After, the solvent was removed under reduced pressure and the crude was purified by flash column chromatography using a mixture of hexane and ethyl acetate (20:1 v/v) as eluent. Compound **67a** was obtained as a white solid in a yield of 47% (0.20 g, 0.33 mmol). ¹H NMR (400 MHz, CDCl₃) δ (ppm): 8.42 (d, *J* = 1.4 Hz, 2H), 8.41 (d, *J* = 1.1 Hz, 2H), 7.86 (dd, *J* = 8.5, 1.7 Hz, 2H), 7.67 (dd, *J* = 8.3, 1.4 Hz, 2H), 7.61 (dd, *J* = 8.3, 1.6 Hz, 4H), 7.52 (d, *J* = 8.3 Hz, 2H), 7.41 (d, *J* = 8.4 Hz, 2H),

7.36–7.32 (m, 6H), 4.43 (q, $J = 7.3$ Hz, 4H), 1.51 (t, $J = 7.3$ Hz, 6H). ^{13}C NMR (100 MHz, CDCl_3) δ (ppm): 140.2, 139.6, 133.8, 131.6, 129.5, 128.5, 127.9, 126.1, 124.4, 124.1, 123.3, 123.1, 119.3, 113.5, 109.3, 108.8, 91.3, 87.7, 38.1, 14.7. HRMS (ESI-MS) (m/z): calculated for $\text{C}_{44}\text{H}_{33}\text{N}_2$ ($\text{M}+\text{H}$) $^+$, 589.2638; found 589.2637.

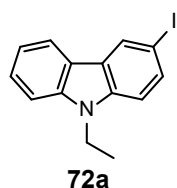
3.113. 9,9'-Dihexyl-6,6'-bis(phenylethynyl)-9H,9'H-3,3'-bicarbazole (67b)



Analogously to the procedure described in section 3.112, this synthesis was carried out with **71b** (0.308 g, 0.410 mmol), CuI (8 mg, 0.04 mmol), $\text{Pd}(\text{PPh}_3)_2\text{Cl}_2$ (14 mg, 0.020 mmol), triethylamine (0.17 mL, 1.2 mmol) and phenylacetylene (0.13, 1.2 mmol) in anhydrous THF (18 mL). The crude was purified using a mixture of hexane and dichloromethane (5:1 v/v) as eluent. Compound **67b** was obtained as a white solid in a yield of 57% (0.165 g, 0.235

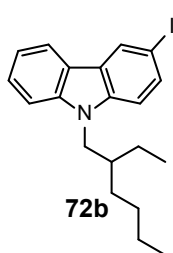
mmol). ^1H NMR (400 MHz, CDCl_3) δ (ppm): 8.42 (d, $J = 1.6$ Hz, 2H), 8.41 (d, $J = 1.4$ Hz, 2H), 7.85 (dd, $J = 8.5, 1.6$ Hz, 2H), 7.67 (dd, $J = 8.4, 1.4$ Hz, 2H), 7.60 (dd, $J = 8.3, 1.6$ Hz, 4H), 7.51 (d, $J = 8.5$ Hz, 2H), 7.39 (d, $J = 8.4$ Hz, 2H), 7.37–7.33 (m, 6H), 4.32 (t, $J = 7.2$ Hz, 4H), 1.95–1.87 (m, 4H), 1.44–1.37 (m, 4H), 1.36–1.28 (m, 8H), 0.87 (t, $J = 7.0$ Hz, 6H). ^{13}C NMR (100 MHz, CDCl_3) δ (ppm): 140.6, 139.9, 133.6, 131.5, 129.3, 128.3, 127.7, 125.9, 124.2, 124.0, 123.1, 123.1, 119.0, 113.2, 109.3, 108.8, 90.9, 87.6, 43.3, 31.6, 29.0, 27.0, 22.6, 14.0. HRMS (ESI-MS) (m/z): calculated for $\text{C}_{52}\text{H}_{49}\text{N}_2$ ($\text{M}+\text{H}$) $^+$, 701.3890; found 701.3897.

3.114. 9-Ethyl-3-iodo-9H-carbazole (72a)



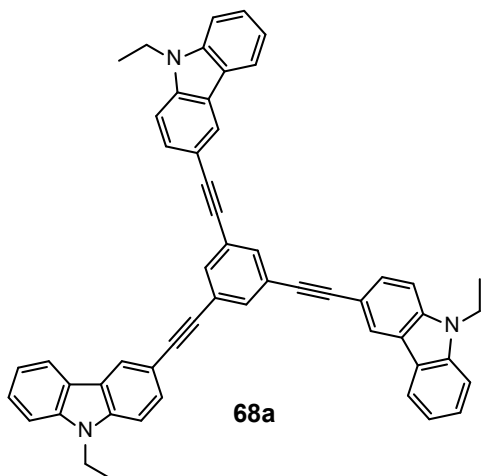
3-Iodo-9H-carbazole (1.50 g, 5.12 mmol) was dissolved in anhydrous DMF (6 mL) under nitrogen. NaH (0.307 g, 60% in mineral oil, 7.68 mmol) was added and the solution was stirred for 30 min at room temperature. Then, bromoethane (0.85 mL, 7.8 mmol) was added and the reaction was stirred overnight. After, it was diluted with water and the product was extracted with dichloromethane. The combined organic extract was dried over anhydrous MgSO_4 , filtered and the solvent was removed under reduced pressure. The crude was purified by flash column chromatography using hexane as eluent. Compound **71a** was obtained as a white solid in a yield of 73% (1.65 g, 4.32 mmol). ^1H NMR (400 MHz, CDCl_3) δ (ppm): 8.30 (s, 1H), 8.19 (d, $J = 8$ Hz, 1H), 7.62–7.54 (m, 3H), 7.52–7.47 (m, 1H), 7.27–7.22 (m, 1H), 4.49 (q, $J = 7$ Hz, 2H), 3.53 (s, 1H), 1.40 (t, $J = 7$ Hz, 3H).

3.115. 9-(2-Ethylhexyl)-3-iodo-9H-carbazole (72b)



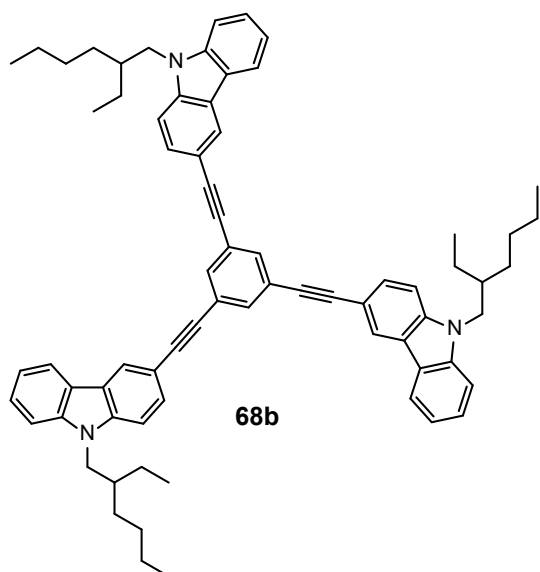
Analogously to the procedure described in section 3.114, this synthesis was carried out with 3-iodo-9H-carbazole (1.00 g, 3.41 mmol) and NaH (0.200 g, 60% in mineral oil, 5.00 mmol) in anhydrous DMF (5 mL). Then, 1-bromo-2-ethylhexane (0.91 mL, 5.1 mmol). The crude was purified by flash column chromatography using hexane as eluent. Compound **71b** was obtained as a white solid in a yield of 84% (1.16 g, 2.86 mmol). ¹H NMR (400 MHz, acetone-*d*₆) δ (ppm): 8.50 (d, *J* = 2 Hz, 1H), 8.18 (d, *J* = 8 Hz, 1H), 7.72 (dd, *J* = 9 Hz, *J* = 2 Hz, 1H), 7.56 (d, *J* = 9 Hz, 1H), 7.51–7.47 (m, 1H), 7.43 (d, *J* = 9 Hz, 1H), 7.25–7.21 (m, 1H), 4.30 (d, *J* = 8 Hz, 2H), 2.14–2.07 (m, 1H), 1.46–1.17 (m, 8H), 0.91 (t, *J* = 8 Hz, 3H), 0.81 (t, *J* = 7 Hz, 3H).

3.116. 1,3,5-Tris((9-ethyl-9H-carbazol-3-yl)ethynyl)benzene (68a)



72a (920 mg, 2.85 mmol), triethynylbenzene (300 mg, 2.00 mmol), Pd(PPh₃)₂Cl₂ (210 mg, 0.299 mmol) and CuI (91 mg, 0.48 mmol) and were dissolved in anhydrous THF (40 mL) under inert atmosphere. Afterwards, triethylamine (1.0 mL, 7.2 mmol) was added and the reaction mixture was stirred at room temperature overnight. Then, the solvent was removed under reduced pressure and the crude was purified by flash column chromatography using a mixture of hexane and CH₂Cl₂ (3:1 v/v) as eluent. Compound **72a** was obtained as a white solid in a yield of 13% (87 mg, 0.12 mmol). ¹H NMR (400 MHz, CDCl₃) δ (ppm): 8.34 (d, *J* = 1.3 Hz, 3H), 8.13 (d, *J* = 7.8 Hz, 3H), 7.73 (s, 3H), 7.67 (dd, *J* = 8.4, 1.3 Hz, 3H), 7.51 (ddd, *J* = 8.1, 7.3 Hz, 1.1 Hz, 3H), 7.44 (d, *J* = 8.1 Hz, 3H), 7.41 (d, *J* = 8.4 Hz, 3H), 7.26 (dd, *J* = 7.8, 7.3 Hz, 3H), 4.40 (q, *J* = 7.7 Hz, 6H), 1.47 (d, *J* = 7.7 Hz, 9H). ¹³C NMR (100 MHz, CDCl₃) δ (ppm): 140.5, 139.9, 133.5, 129.5, 126.3, 124.7, 124.4, 123.2, 122.7, 120.8, 119.6, 113.1, 108.7, 108.7, 92.0, 86.6, 37.9, 14.0. HRMS (ESI-MS) (*m/z*): calculated for C₅₄H₄₀N₃ (M+H)⁺, 730.3217; found 730.3213.

3.117. 1,3,5-Tris((9-(2-ethylhexyl)-9H-carbazol-3-yl)ethynyl)benzene (**68b**)



Analogously to the procedure described in section 3.116, this synthesis was carried out with **72b** (1.26 g, 3.11 mmol), triethynylbenzene (326 mg, 2.17 mmol), Pd(PPh₃)₂Cl₂ (222 mg, 0.317 mmol), CuI (103 mg, 0.517 mmol) and triethylamine (1.4 mL, 10 mmol) in anhydrous THF (40 mL). The crude was purified by flash column chromatography using a mixture of hexane and CH₂Cl₂ (5:1 v/v). Compound **72b** was obtained as a white solid in a yield of 10% (100 mg, 0.102 mmol). ¹H NMR (400 MHz, CDCl₃) δ

(ppm): 8.33 (d, *J* = 1.2 Hz, 3H), 8.12 (d, *J* = 7.4 Hz, 3H), 7.73 (s, 3H), 7.65 (dd, *J* = 8.4, 1.2 Hz, 3H), 7.49 (dd, *J* = 8.4, 8.1 Hz, 3H), 7.41 (d, *J* = 8.4 Hz, 3H), 7.37 (d, *J* = 8.4 Hz, 3H), 7.26 (dd, *J* = 8.1, 7.4 Hz, 3H) 4.19 (d, *J* = 7.1 Hz, 6H), 2.20–2.05 (m, 3H), 1.43–1.21 (m, 24H), 0.93 (t, *J* = 7.2 Hz, 9H), 0.87 (t, *J* = 7.2 Hz, 9H). ¹³C NMR (100 MHz, CDCl₃) δ (ppm): 141.5, 140.9, 133.5, 129.5, 126.2, 124.7, 124.3, 123.0, 122.6, 120.7, 119.5, 113.0, 109.4, 109.2, 92.0, 86.6, 47.7, 39.6, 31.2, 29.0, 24.6, 23.2, 14.2, 11.1. HRMS (ESI-MS) (*m/z*): calculated for C₇₂H₇₆N₃ (M+H)⁺, 982.6034; found 982.6043.

APPENDIX



LIST OF PUBLICATIONS

Scientific publications

5. "Insight into the diindolocarbazole core as an air-stable semiconductor for OTFTs"
ACS Appl. Electron. Mater., to be submitted in October 2022.
R. Bujaldón, A. Vilche, X. Alcobé, J. Puigdollers, C. Puigjaner, D. Velasco.
4. "Powder X-ray diffraction as a powerful tool to exploit in organic electronics: shedding light on the first *N,N',N''*-trialkyldiindolocarbazole"
Acta Cryst. **2022**, *B78*, 253–260.
A. Vilche, **R. Bujaldón**, X. Alcobé, D. Velasco, C. Puigjaner.
3. "Towards the bisbenzothienocarbazole core: a route of sulfurated carbazole derivatives with assorted optoelectronic properties and applications"
Materials, **2021**, *14*, 3487.
R. Bujaldón, J. Puigdollers, D. Velasco.
2. "Exploring the 3-(phenylethynyl)-9*H*-carbazole unit in the search of deep-blue emitting fluorophores"
Opt. Mater. **2021**, *111*, 110696.
R. Bujaldón, N. Peřinka, M. Reig, A. Cuadrado, C. Fabregat, M. Font-Bardía, E. Martínez-Ferrero, D. Velasco.
1. "Easy accessible blue luminescent carbazole-based materials for Organic Light-Emitting Diodes"
Dyes Pigm. **2017**, *137*, 24–35.
M. Reig, C. Gozálviz, **R. Bujaldón**, G. Bagdziunas, K. Ivaniuk, N. Kostiv, D. Volyniuk, J. V. Grazulevicius, D. Velasco.

Poster presentations in congresses

7. "Tuning the Optoelectronic Properties of Sulfurated Carbazole Derivatives: the Case of the Bisbenzothienocarbazole Core"
R. Bujaldón, J. Puigdollers, D. Velasco
7th International Fall School on Organic Electronics (IFSOE 2021), Moscow, Russia (online, September 2021).

6. “Carbazole-based deep-blue dyes for the application in solution-processable white OLEDs”
R. Bujaldón, M. Reig, N. Peřinka, A. Cuadrado, E. Martínez-Ferrero, D. Velasco
10th International Conference on Materials for Advanced Technologies (ICMAT 2019), Singapore, Singapore (June 2019).
5. “Novel diindolocarbazole semiconductors for organic thin-film transistors”
D. Velasco, **R. Bujaldón**, J. Puigdollers
10th International Conference on Materials for Advanced Technologies (ICMAT 2019), Singapore, Singapore (June 2019).
4. “Structural optimization of the diindolocarbazole core as semiconductor for organic thin-film transistors”
R. Bujaldón, J. Puigdollers, D. Velasco
IN²UB 2019 Meeting, Barcelona, Catalonia, Spain (June 2019).
3. “The effect of the substitution patterns of the triindole core on the thin film crystallinity for high performance organic thin-film transistors”
M. Reig, A. Cuadrado, **R. Bujaldón**, J. Puigdollers, D. Velasco
24th International Conference on Science and Technology of Synthetic Metals (ICSM 2018), Busan, South Korea (July 2018).
2. “Amplification of the optical mechanotransducing abilities of carbazole-containing liquid crystal elastomers”
D. Heras, **R. Bujaldón**, M. Reig, J. Garcia-Amorós, D. Velasco
24th Gordon Research Conference on Liquid Crystals, Biddeford, Maine, USA (June 2017).
1. “Influence of the crystallinity of the organic thin film layer in OTFTs”
A. Cuadrado, **R. Bujaldón**, M. Reig, J. Puigdollers, D. Velasco
13th International Conference on Organic Electronics (ICOE 2017), Saint Petersburg, Russia (June 2017).

Oral presentations in congresses

1. “Extending the carbazole core towards enhanced organic semiconductors”
R. Bujaldón
Advanced Materials Workshop, St. St. Constantine and Helena, Varna, Bulgaria (July 2019).

SUMMARY

The increasing demand on next-generation displays encourages an exhaustive research on the development of new and enhanced semiconductors. Apart from the conventional inorganic materials, organic-based semiconductors can also fulfil this role while affording unique features. Indeed, organic materials claim coveted properties such as electronic tunability and the feasibility to fabricate flexible displays with large areas at a lower cost, thus finding enormous applicability in different optoelectronic devices. The capability to transport charges in organic compounds is strongly related to the molecular design, which determines key factors such as the electronic profile and the disposition in the solid state. In this context, the aim of this Thesis is focalized on the synthesis and application of new organic semiconductors designed from a common building block: the carbazole heterocycle. The envisioned applications go from Organic Thin-Film Transistors (OTFTs) to Organic Light-Emitting Diodes (OLEDs).

As an initial approach towards p-type semiconductors, the π -system of the carbazole nucleus has been extended to furnish three ladder-type constructions, namely diindolocarbazole, bisbenzothienocarbazole and diphenanthrocarbazole. The main molecular backbones have been tailored with the inclusion of different alkylation patternings. The integration of the resulting compounds in OTFT devices led to hole mobility values ranging from 10^{-6} up to 10^{-3} $\text{cm}^2 \text{V}^{-1} \text{s}^{-1}$, accentuating the importance of both the molecular and the device architecture. The most promising materials arise from the homogeneous *N*-alkylation of diindolocarbazole with short-to-medium chains and the incorporation of peripheral alkyl chains to the diphenanthrocarbazole core. The availability of these cores is facilitated by accessible synthetic procedures, which conclude with a microwave-assisted Cadogan reaction in the former and the Scholl reaction in the latter. As corroborated by means of X-ray diffraction, both cores arrange in a favorable gamma packing in the solid state that justify these enticing results. Remarkably, all the studied compounds feature an extraordinary air-stability, with some of the devices featuring a shelf lifetime that surpass the milestone of 1000 days.

As a second strategy, the carbazole core has been substituted by its sulfurated analog dibenzothiophene as the main building block. By means of sequential Suzuki-Miyaura and Scholl reactions, diverse diphenanthro[9,10-*b*:9',10'-*d*]thiophene derivatives have been synthesized from the commercially available tetrabromothiophene. The envisioned synthetic route could provide not only homogeneous structures, but also heterogeneous

ones in a two-step procedure. The latter systems also behaved as p-type semiconductors, with hole mobility values up to $6 \times 10^{-5} \text{ cm}^2 \text{ V}^{-1} \text{ s}^{-1}$ in OTFTs.

The redesign of the triindole core, which is a well-known carbazole-based semiconductor, constituted another part of this Thesis. Specifically, it included the synthesis and physical characterization of triindole analogs, featuring: carbazole moieties attached to different positions, oxygen or sulfur substituting the nitrogen as heteroatom and the inclusion of peripheral alkyl chains. The collected results prompt further study in this direction.

Finally, the promising optical properties of the 3-(phenylethynyl)-9*H*-carbazole unit have been exploited in the OLED technology. The two analyzed constructions, i.e. 6,6'-bis(phenylethynyl)-9*H*,9'*H*-3,3'-bicarbazole and 1,3,5-tris((9*H*-carbazol-3-yl)ethynyl)-benzene, exhibited blue emission in the solid state and in solution-processed OLEDs. The hexylated derivative of the first system, apart from emitting in the sought deep-blue region, also stood out as the most appropriate to perform as host for iridium complexes in white OLEDs. The emission of the fabricated devices covered a wide range of white hues, depending on the composition and the applied voltage

SUPPLEMENTARY INFORMATION

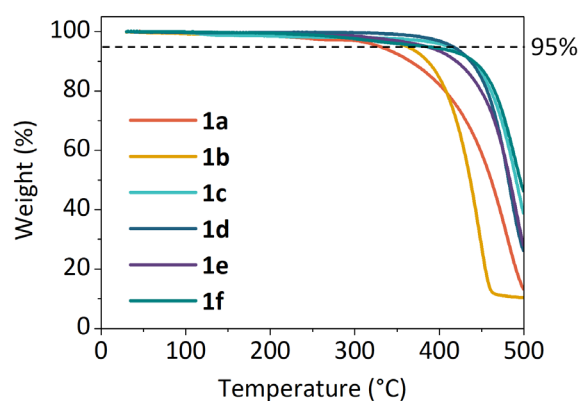


Figure A1.1. TGA scans of compounds **1a–f**, recorded at a heating rate of 10 °C min^{-1} . The decomposition temperature (T_d) was estimated as the 5% weight loss.

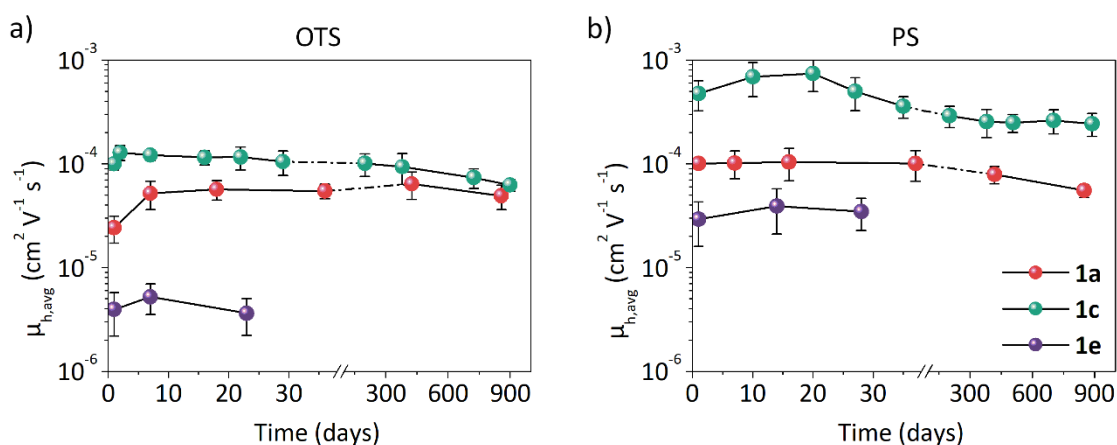


Figure A1.2. Evolution profile of the average hole mobility ($\mu_{h,avg}$) of a set of devices fabricated from the heterogeneously alkylated derivatives **1a** and **1e** along with **1c** as comparison, over: a) OTS- and b) PS-treated substrates. The displayed period comprises 900 days starting from the fabrication day.

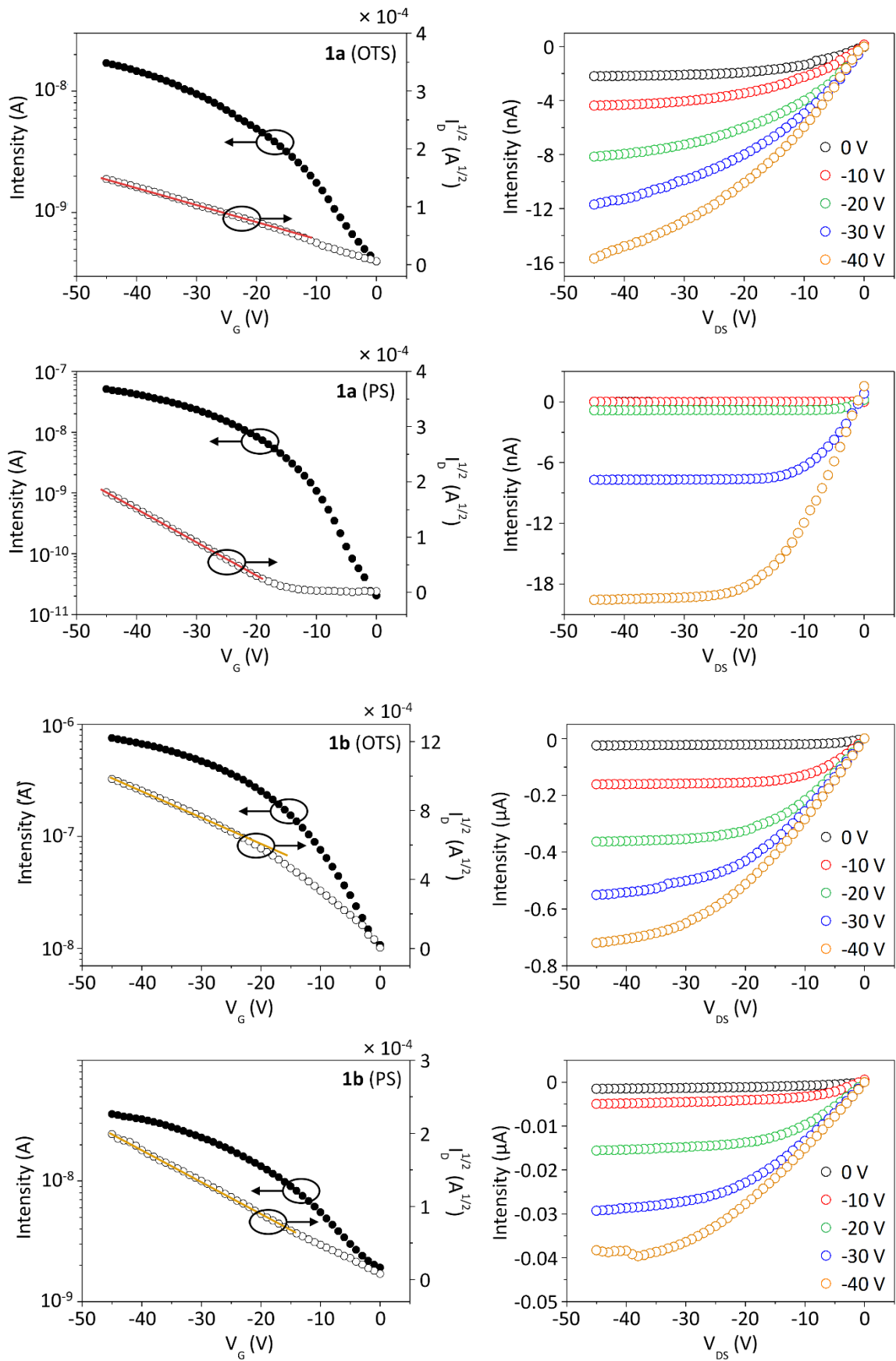


Figure A1.3. OTFT characteristics of derivatives **1a–b** over OTS- and PS-treated substrates: transfer ($V_{DS} = -40$ V) and saturation (left) and output (right), collected on the day of fabrication.

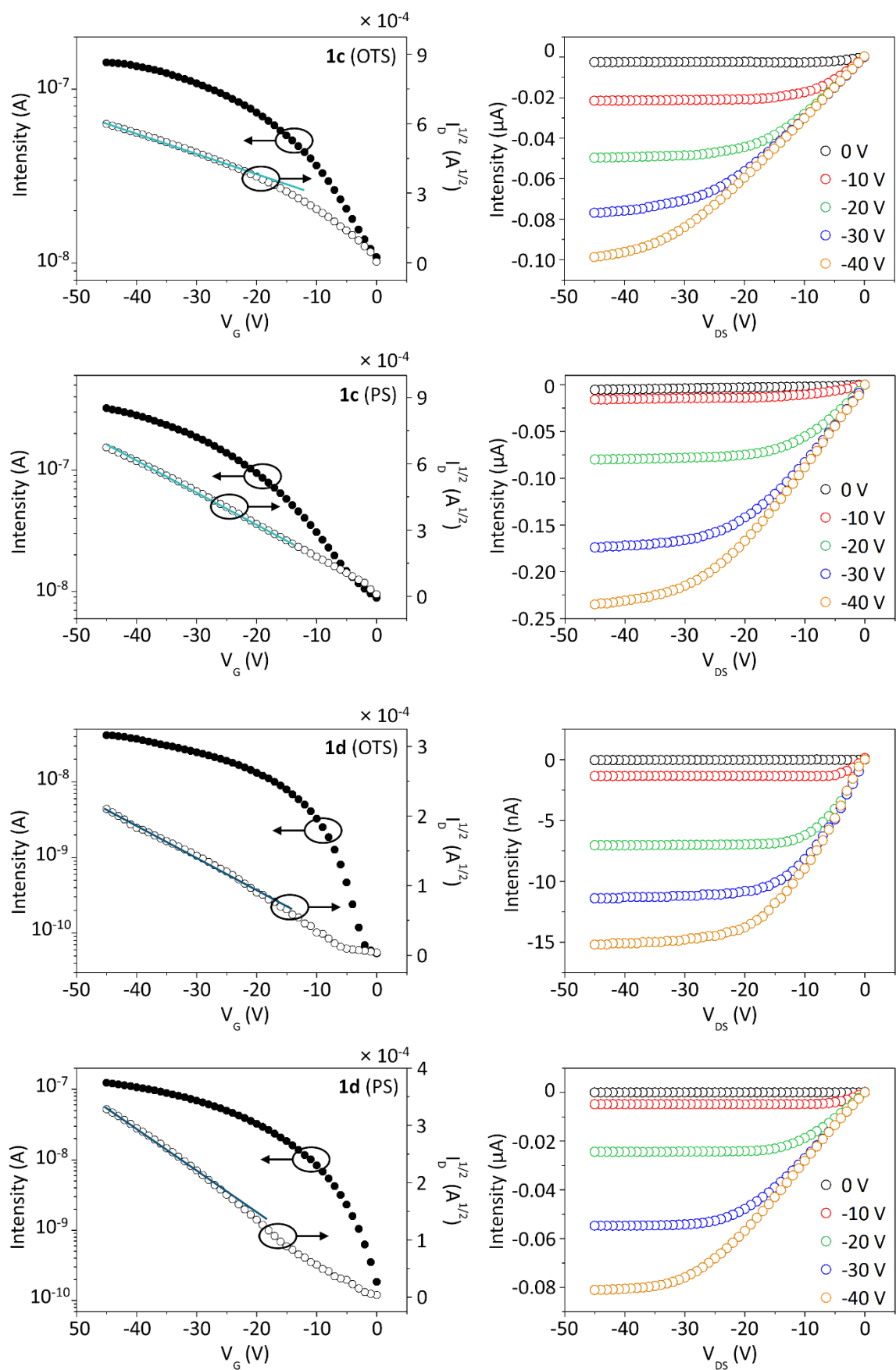


Figure A1.4. OTFT characteristics of derivatives **1c–d** over OTS- (a) and PS-treated (b) substrates: transfer ($V_{DS} = -40$ V) and saturation (left) and output (right), collected on the day of fabrication.

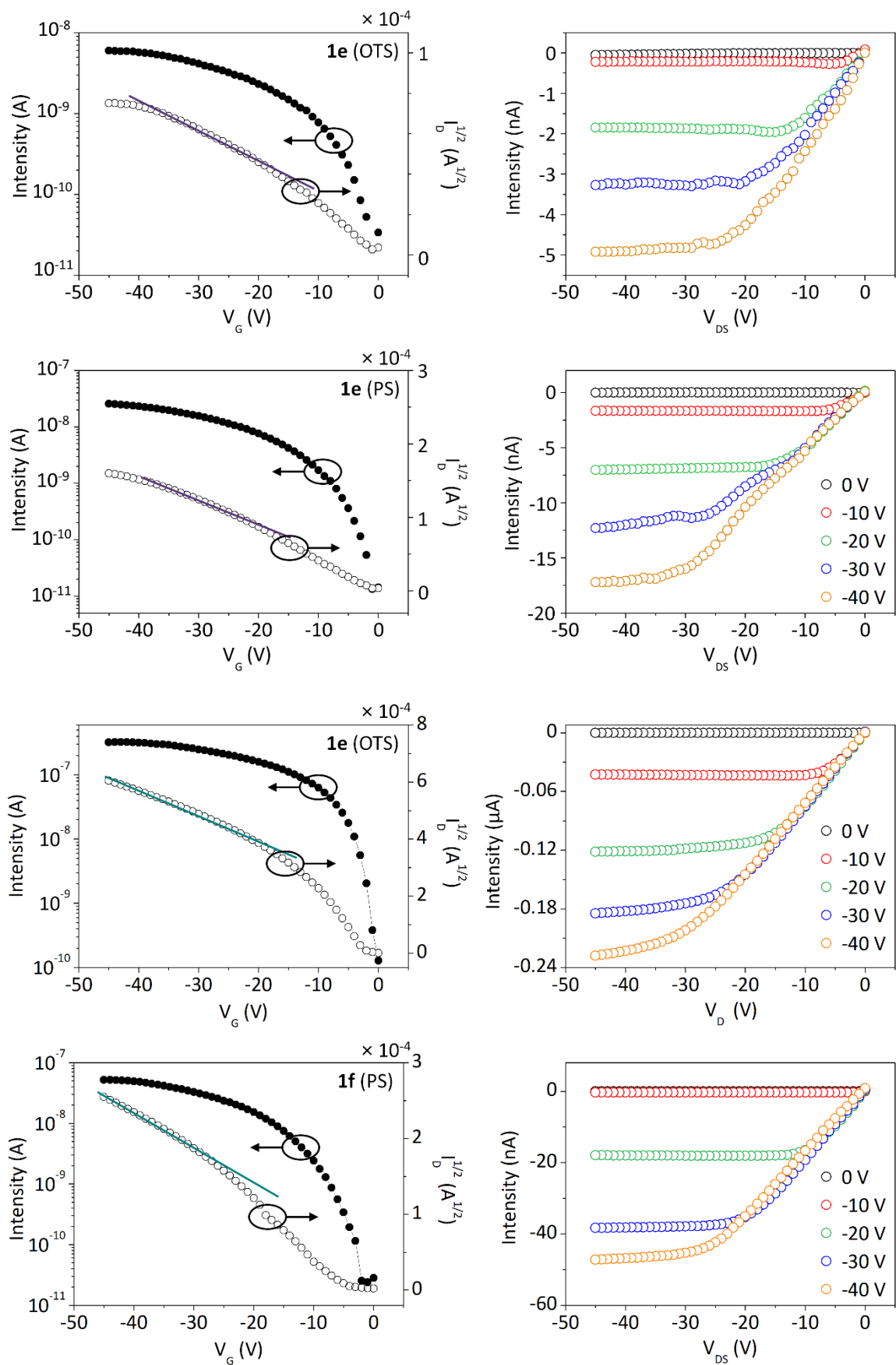


Figure A1.5. OTFT characteristics of derivatives **1e-f** over OTS- (a) and PS-treated (b) substrates: transfer ($V_{DS} = -40$ V) and saturation (left) and output (right), collected on the day of fabrication.

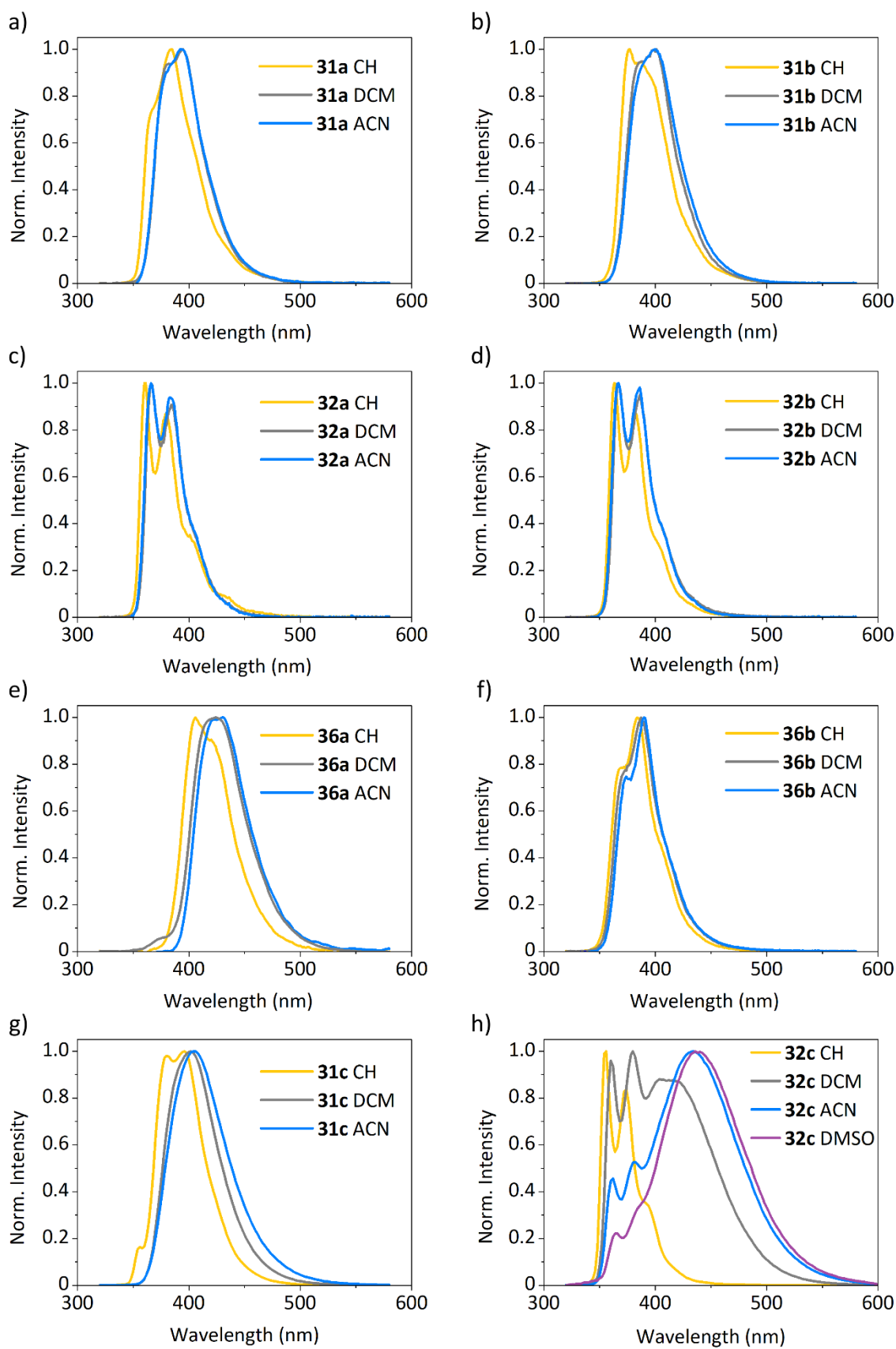


Figure A2.1. Emission spectra in cyclohexane (CH), dichloromethane (DCM), acetonitrile (ACN) and dimethylsulfoxide (DMSO) of compounds **31a** (a), **31b** (b), **32a** (c), **32b** (d), **36a** (e), **36b** (f), **31c** (g), **32c** (h).

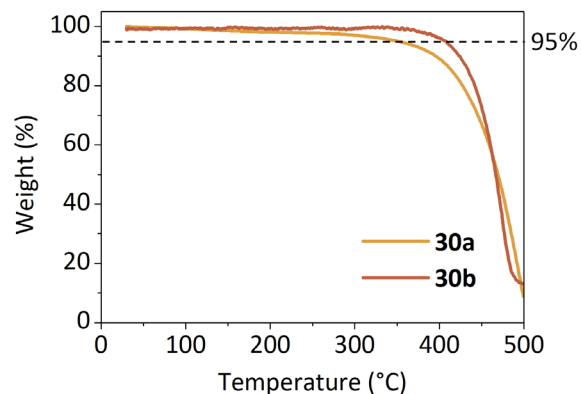


Figure A2.2. TGA scans of compounds **30a–b**, recorded at a heating rate of $10\text{ }^{\circ}\text{C min}^{-1}$. The decomposition temperature (T_d) was estimated as the 5% weight loss.

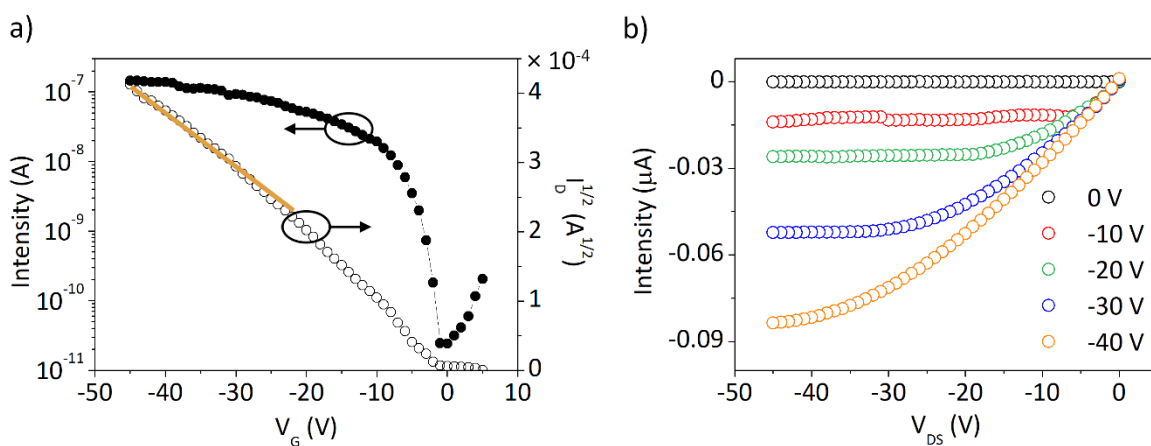


Figure A2.3. OTFT characteristics of a PS-treated device integrating compound **30a** seven months after the fabrication: (a) transfer ($V_{DS} = -40\text{ V}$) and saturation; (b) output.

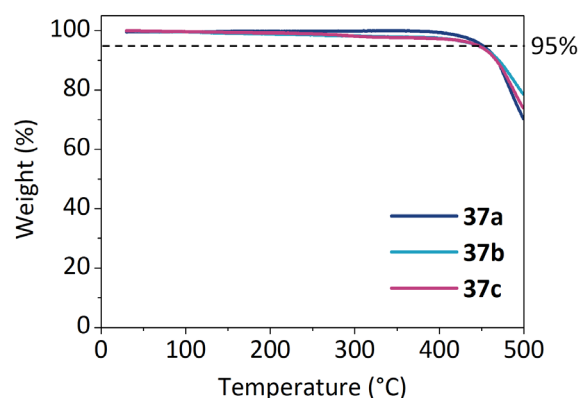


Figure A3.1. TGA scans of compounds **37a–c**, recorded at a heating rate of $10\text{ }^{\circ}\text{C min}^{-1}$. The decomposition temperature (T_d) was estimated as the 5% weight loss.

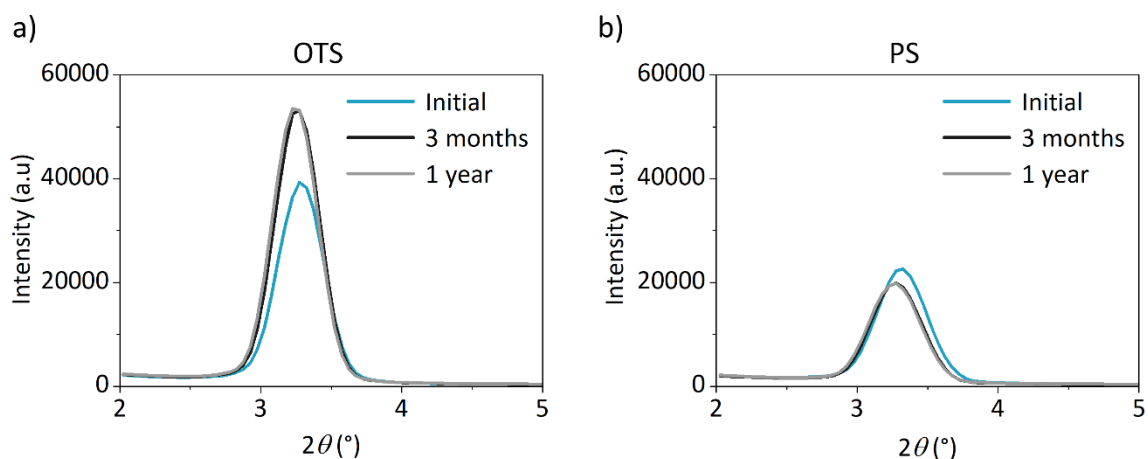


Figure A3.2. GIXRD profiles of **37b** deposited over OTS- (a) and PS-treated (b) substrates collected right after the deposition, after 3 months and after 1 year.

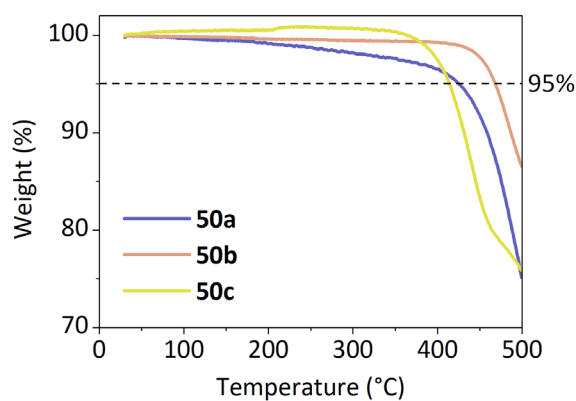


Figure A4.1. TGA scans of compounds **50a-c**, recorded at a heating rate of 10 °C min^{-1} . The decomposition temperature (T_d) was estimated as the 5% weight loss.

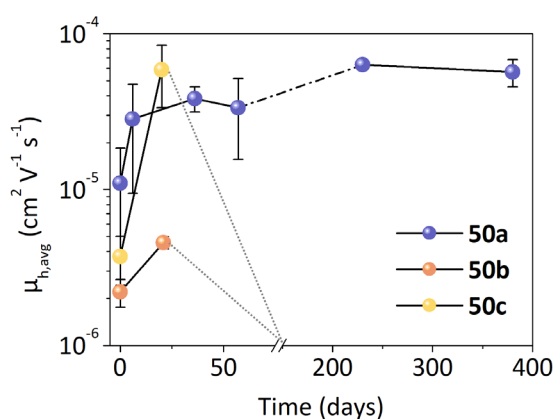


Figure A4.2. Evolution profile of the average hole mobility ($\mu_{h,avg}$) of a set of devices fabricated from derivatives **50a-c** over PS-treated substrates. The displayed period comprises 400 days starting from the fabrication day.

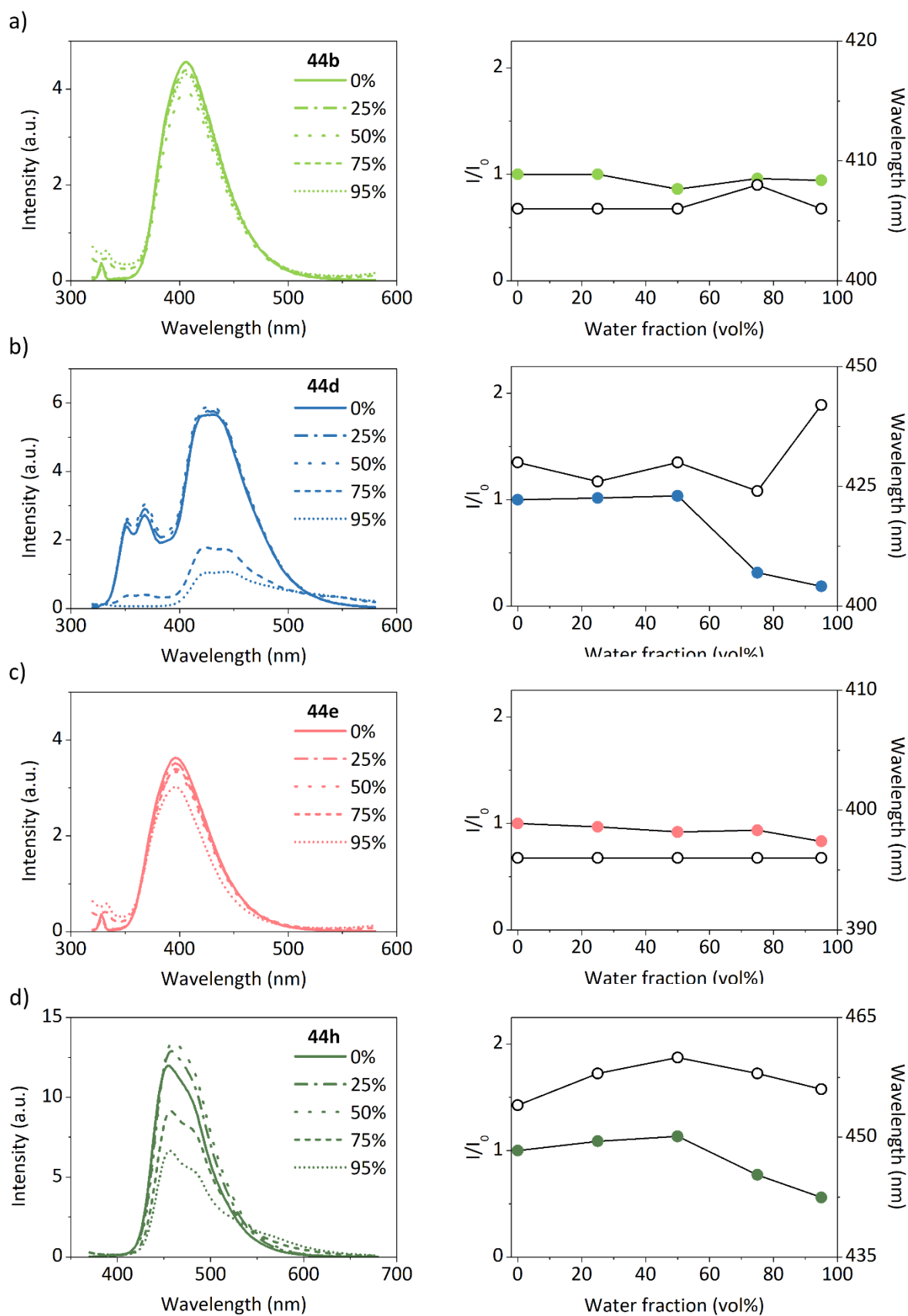


Figure A4.3. Emission spectra (left) and plot of the relative emission intensity (I/I_0) and wavelength *versus* the composition of the aqueous mixture (right) of derivatives **44b** (a), **44d** (b), **44e** (c) and **44h** (d) (10^{-5} M) in THF solutions featuring different water percentages.

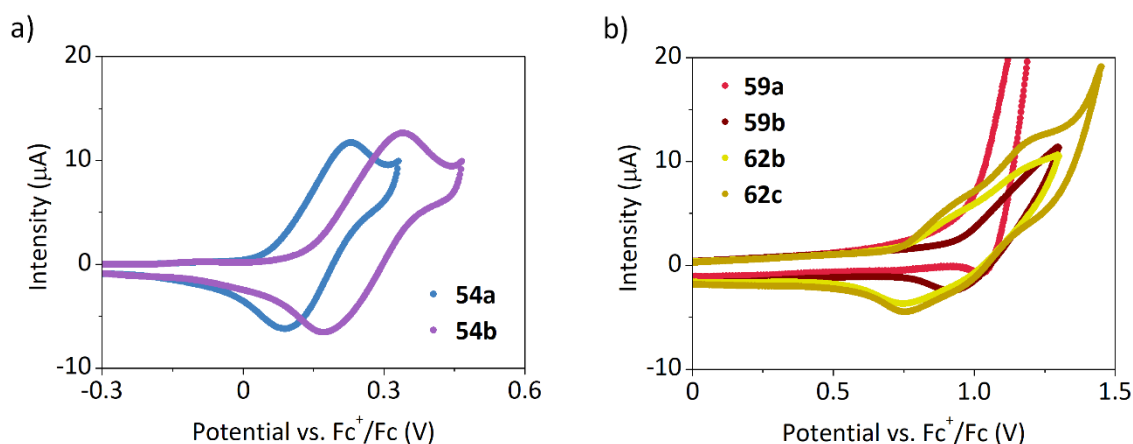


Figure A5.1. Cyclic voltammeteries in dichloromethane referred to the Fc^+/Fc redox couple of derivatives: a) **54a–b**; b) **59a–b** and **62b–c**.

Table A6.1. Characteristics of iridium-containing OLED devices fabricated from **67a** and **68b**.

Dev.	Compound	Composition [a]	V_{on} [b] (V)	L_{max} [c] (cd m^{-2})	CE [d] (cd A^{-1})	CIE [e]	CCT [f] (K)
20	67a	100 : 0.12 : 0.12	7.1	23	0.03	(0.32, 0.38)	5813
21		100 : 0.75 : 0.75	4.0	261	0.18	(0.50, 0.42)	2300
22	68b	100 : 0.12 : 0.12	5.8	31	0.02	(0.36, 0.39)	4655
23		100 : 0.75 : 0.75	5.9	174	0.23	(0.51, 0.46)	2446

[a] Proportion (w/w) of the iridium complexes in front of **67a** or **68b** (ratio of **compound**: $\text{Ir}(\text{ppy})_3$: $\text{Ir}(\text{MDQ})_2\text{acac}$). [b] Turn-on voltage, defined as the voltage necessary to provide a luminance of 1 cd m^{-2} . [c] Maximum luminance. [d] Maximum current efficiency, calculated at an operating voltage higher than the V_{on} . [e] CIE coordinates calculated from the corresponding electroluminescence spectrum at 8 V. [f] Correlated color temperature (CCT) calculated from the corresponding CIE coordinates using the McCamy's approximation.

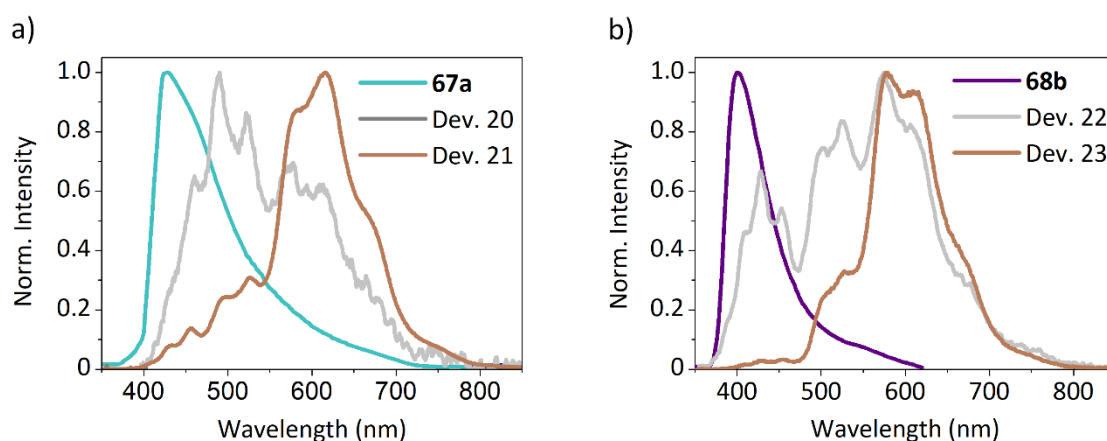


Figure A6.1. Optical properties of compounds **67a** and **68b** and the corresponding iridium-containing WOLEDs: photoluminescence in the solid state and electroluminescence spectra of a) compound **67a** and devices 20 and 21, respectively; b) compound **68b** and devices 22 and 23, respectively.

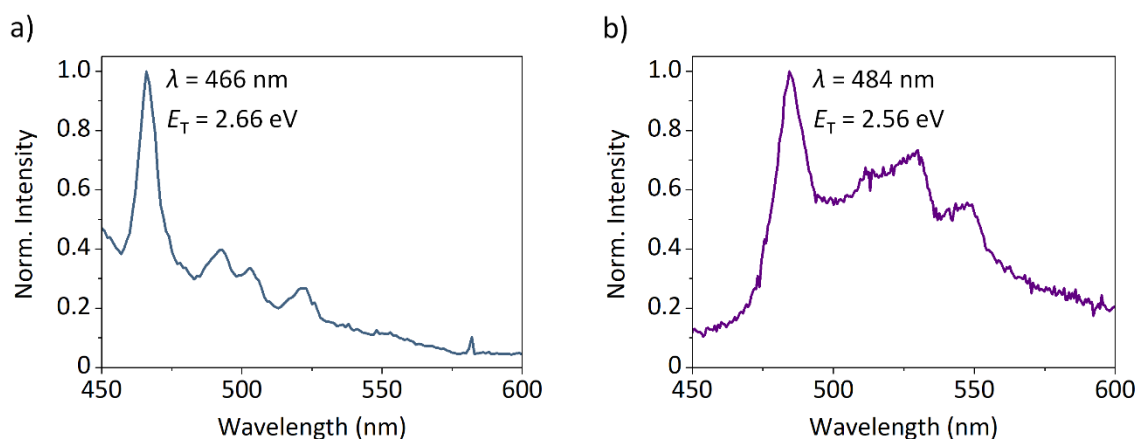


Figure A6.2. Phosphorescence spectra of compounds **67b** (a) and **68b** (b) recorded in THF at 10 μ M at 77K, and their triplet energies (E_T) estimated from the $\lambda_{\text{max,em}}$.

Table A6.2. Characteristics of iridium-containing OLED devices fabricated from compound **67b**.

Dev.	Composition ^[a]	6 V		8 V		10 V	
		CIE	CCT ^[b] (K)	CIE	CCT ^[b] (K)	CIE	CCT ^[b] (K)
12	100:1.00:0	-	-	(0.28, 0.59)	-	(0.28, 0.57)	-
13	100:0:1.00	-	-	(0.52, 0.40)	1974	(0.52, 0.40)	1974
14	100:0.12:0.12	(0.33, 0.33)	5617	(0.35, 0.33)	4852	-	-
15	100:0.25:0.25	(0.42, 0.42)	3335	(0.42, 0.40)	3276	(0.50, 0.41)	2199
16	100:0.50:0.25	(0.41, 0.46)	3860	(0.40, 0.43)	3782	(0.45, 0.41)	2889
17	100:0.25:0.50	(0.48, 0.42)	2557	(0.47, 0.40)	2457	(0.49, 0.40)	2226
18	100:0.50:0.50	(0.46, 0.45)	2988	(0.45, 0.44)	3012	(0.49, 0.42)	2436
19	100:1.00:1.00	(0.50, 0.45)	2556	(0.47, 0.45)	2821	(0.53, 0.42)	1994

[a] Proportion (w/w) of the iridium complexes in front of **67b** (ratio of **67b**:Ir(ppy)₃:Ir(MDQ)₂acac.
[b] Correlated color temperature (CCT) calculated from the corresponding CIE coordinates using the McCamy's approximation.